Noise Source Location and Flow Field Measurements on Supersonic Jets and Implications Regarding Broadband Shock Noise

Gary G. Podboy, Mark P. Wernet, Michelle M. Clem, and Amy F. Fagan
Glenn Research Center, Cleveland, Ohio

NASA STI Program . . . in Profile

Since its founding, NASA has been dedicated to the advancement of aeronautics and space science. The NASA Scientific and Technical Information (STI) Program plays a key part in helping NASA maintain this important role.

The NASA STI Program operates under the auspices of the Agency Chief Information Officer. It collects, organizes, provides for archiving, and disseminates NASA's STI. The NASA STI Program provides access to the NASA Technical Report Server—Registered (NTRS Reg) and NASA Technical Report Server—Public (NTRS) thus providing one of the largest collections of aeronautical and space science STI in the world. Results are published in both non-NASA channels and by NASA in the NASA STI Report Series, which includes the following report types:

- TECHNICAL PUBLICATION. Reports of completed research or a major significant phase of research that present the results of NASA programs and include extensive data or theoretical analysis. Includes compilations of significant scientific and technical data and information deemed to be of continuing reference value. NASA counter-part of peer-reviewed formal professional papers, but has less stringent limitations on manuscript length and extent of graphic presentations.

- TECHNICAL MEMORANDUM. Scientific and technical findings that are preliminary or of specialized interest, e.g., "quick-release" reports, working papers, and bibliographies that contain minimal annotation. Does not contain extensive analysis.

- CONTRACTOR REPORT. Scientific and technical findings by NASA-sponsored contractors and grantees.

- CONFERENCE PUBLICATION. Collected papers from scientific and technical conferences, symposia, seminars, or other meetings sponsored or co-sponsored by NASA.

- SPECIAL PUBLICATION. Scientific, technical, or historical information from NASA programs, projects, and missions, often concerned with subjects having substantial public interest.

- TECHNICAL TRANSLATION. English-language translations of foreign scientific and technical material pertinent to NASA's mission.

For more information about the NASA STI program, see the following:

- Access the NASA STI program home page at http://www.sti.nasa.gov

- E-mail your question to help@sti.nasa.gov

- Fax your question to the NASA STI Information Desk at 757-864-6500

- Telephone the NASA STI Information Desk at 757-864-9658

- Write to:
  NASA STI Program
  Mail Stop 148
  NASA Langley Research Center
  Hampton, VA 23681-2199

Noise Source Location and Flow Field Measurements on Supersonic Jets and Implications Regarding Broadband Shock Noise

Gary G. Podboy, Mark P. Wernet, Michelle M. Clem, and Amy F. Fagan
Glenn Research Center, Cleveland, Ohio

Acknowledgments

Level of Review: This material has been technically reviewed by technical management.

Available from

Noise Source Location and Flow Field Measurements on Supersonic Jets and Implications Regarding Broadband Shock Noise

Gary G. Podboy, Mark P. Wernet, Michelle M. Clem, and Amy F. Fagan
National Aeronautics and Space Administration
Glenn Research Center
Cleveland, Ohio 44135

Abstract

An experiment was conducted in an effort to obtain data that would provide a better understanding of the origins of broadband shock noise (BBSN). Phased array noise source location and two types of flow field data (background oriented schlieren and particle image velocimetry) were acquired on unheated, single-stream jets. Results are presented for one subsonic and four supersonic operating conditions. These data show that BBSN is created primarily in the downstream portion of the shock train with peak BBSN production occurring near where the average size of the turbulent structures is equal to the shockcell spacing. These data tend to validate theories that BBSN is created by turbulent structures that are as large or larger than the shock spacing.

Introduction

Supersonic jets operated at off-design (imperfectly expanded) conditions generate broadband shock noise (BBSN) when the turbulent eddies in the shear layer interact with the quasi-stationary shockcells in the jet plume. BBSN is often the dominant noise component in supersonic jets for broadside and upstream observation angles and appears as one or more humps in the acoustic spectra. Harper-Bourne and Fisher (Ref. 1) explained that BBSN is created by the constructive interference of noise generated at adjacent shockcells when large-scale turbulent structures in the shear layer pass through the shocks.

For decades, researches have investigated ways of either weakening the shocks or altering the nature of the turbulent structures in the shear layer in an attempt to reduce BBSN. However, it is still a significant noise problem for supersonic, military aircraft. For the U.S. Navy, the two most important noise issues are hearing loss developed by flight crew working on aircraft carriers and community noise issues around Naval Air Bases and training sites. Recently, GE and NAVAIR collaborated (Ref. 2) in an effort to develop noise reduction technologies for legacy aircraft with a near-term goal of reducing noise levels by 3 dB. A static engine test of an F404 engine demonstrated that chevrons could be used to reduce noise levels over a wide operating range from low power all the way up to full afterburner conditions while providing minimal impact on performance. The chevrons are thought to have induced the formation of stream-wise counter-rotating vortices that increase the mixing of the jet plume with the ambient air which, in turn, causes the peak jet velocity to decay more rapidly with distance downstream of the nozzle exit and a reduction in jet noise. The chevrons also alter both the shockcell structure and the intensity and scale of the turbulence causing a reduction in BBSN.

BBSN is also a problem for commercial, subsonic aircraft. It contributes to interior cabin noise at cruise conditions especially for passengers sitting in that part of the cabin aft of the engines. As explained by Mengle et al., (Ref. 3) commercial aircraft create BBSN "when flight Mach numbers exceed 0.6 and when thrust requirements are high, such as when the aircraft climbs to a new cruise altitude or during the initial phase of a cruise segment." At these conditions, the nozzles operate under-expanded and a series of shockcells are created in the jet plume. The resulting BBSN contributes significantly to the interior noise problem. Like on supersonic aircraft, the chevrons found on many of today's commercial aircraft are intended to alter the interaction between the turbulence and the shockcells so that BBSN is reduced.

The purpose of this paper is to present noise source localization and flow field data obtained on supersonic jets during tests conducted at the NASA Glenn Research Center. Most of these data were obtained in 2011 and 2012 as part of a series of experiments referred to as the Jet-Surface Interaction Tests (JSIT). The noise source localization data were obtained with a microphone phased array and the flow field data were obtained with both background oriented schlieren (BOS) and particle image velocimetry systems. Examining the source location and flow field data together provides some valuable insight into how BBSN is created in supersonic jets.

Nomenclature

b	acoustic source strength estimated from beamforming
c	the speed of sound
c_{amb}	ambient speed of sound
c_j	speed of sound in jet
C, CSM	cross spectral matrix
D	nozzle exit diameter
g	steering vector
M_a	acoustic Mach number, (V_j/c_{amb})
M_j	ideally-expanded Mach number, (V_j/c_j)
NPR	nozzle total pressure ratio, $(P_{j\ total}/P_{amb})$
OB	octave band

P_j	nozzle plenum pressure
ω	angular frequency
SPL	sound pressure level
T_j	jet temperature
TSR	nozzle static temperature ratio, ($T_{j\ static}/T_{amb}$)
u,w	fluctuating velocity components measured in the streamwise plane
V	velocity
V_j	ideally-expanded jet exit velocity
w	normalized steering vector
x	axial distance downstream of nozzle exit
$\vec{x}$	grid point location
$\vec{y}$	microphone location

Test Facility and Hardware

These experiments were conducted using the Small Hot Jet Acoustic Rig (SHJAR) located at the NASA John H. Glenn Research Center (GRC) in Cleveland, Ohio, USA. The SHJAR is a single-stream nozzle test rig used for fundamental jet noise research. It can accommodate air mass flow rates of up to 6 lb/sec (2.7 kg/s), nozzle exhaust temperatures ranging from ambient to 1300 °F (980 K), and nozzles as large as 3 in. (7.62 cm) in diameter. The test rig is located within the Aeroacoustic Propulsion Laboratory (AAPL), a 19.8 m radius anechoic geodesic dome. Both the floor and the dome's interior surface are covered with sound absorbing acoustic wedges. The facility acoustic instrumentation includes a far-field microphone array made up of 24 microphones arranged in a circular arc at 5° intervals from 50 to 165° from the jet upstream axis and located 150 in. (3.81 m, 75 nozzle diameters) from the nozzle exit. Brown et al. (Ref. 4) provide more information regarding SHJAR and the acoustic characteristics of the AAPL facility.

Data were acquired using two SMC series nozzles that have been tested extensively in the past at NASA Glenn (Refs. 5 and 6) SMC000 is a convergent nozzle that serves as a baseline for most SHJAR tests. SMC016 is a convergent-divergent (C-D) nozzle that was designed using the method of characteristics to provide an ideally expanded flow at $M_j = 1.5$. Both nozzles have a 2 in. (5.08 cm) exit diameter.

Test Conditions

Results will be presented for the five operating conditions listed in Table 1. The different conditions will be identified by the setpoint number listed in this table. Two conditions were set using the convergent SMC000 nozzle, one subsonic and one supersonic. The other three were set with the convergent-divergent SMC016 nozzle. These three were all supersonic; one under-expanded, one ideally-expanded, and one over-expanded. All five setpoints correspond to unheated jets.

Background Oriented Schlieren Data Acquisition and Processing

The shockcells generated in the supersonic jets were visualized using background oriented schlieren (BOS). BOS is based on background distortion or an apparent movement of the background when imaged through a density field onto a detector plane. An incoherent light source uniformly illuminates a background consisting of a high-contrast random dot pattern which is imaged by a camera and lens system. While the background can be illuminated from either side of the flow, the background and camera are placed so that the light traveling from the background must pass through the flow to reach the camera. If there is no flow then there is no refractive index gradient and the light will travel from the background undisturbed and the background will appear normal. When flow is added, however, density variations will be present and, acting as the refractive index gradient, cause the light to refract as it travels from the background to the imaging camera. The background image will look distorted as the dots appear shifted by some number of pixels on the camera's detector plate. The pixel shift is calculated by correlation methods between the image pairs (with and without flow) in small sub-regions across the image using algorithms originally developed for computing the particle displacement in particle image velocimetry (PIV) image pairs (Ref. 7). Unlike PIV, however, the flow is not seeded for BOS and the computed pixel shift indicates only the relative strength of the density gradients in the flow, providing no velocity information. Unique to BOS, the density gradient can be distinguished in the two orthogonal directions of the background plane. Additional information on the theory behind BOS and the general BOS setup used is available in Clem et al. (Ref. 8).

A schematic of the BOS setup, looking into the plane of the nozzle, is shown in Figure 1. A 10 W, 530 nm LED is used as the incident light source for the system. The LED is mounted 0.6 m behind the background in order to uniformly back-illuminate the 0.9 by 0.7 m target, consisting of a high contrast random dot pattern. The dot pattern is composed of 0.7 mm diameter white dots on a black background and has approximately a 32 percent fill ratio. The size of the dots in the pattern was chosen such that one dot would span 2 to 3 pixels after being imaged through the optical system. The pattern was printed onto clear film and mounted onto Plexiglas, which enabled the incident light traveling through the flow to be focused by a Nikon 105 mm lens onto the 36 by 24 mm detector of a Princeton Instruments EC11000 scientific-grade CCD camera. The resulting 12-bit images were captured at an exposure time of 275 ms with a resolution of 4008×2672 pixels, consisting of 9 μm^2 pixels. The large detector size facilitated achievement of the desired 0.45 by 0.35 m field of view within the facility constraints. The background was placed at a distance of 2.8 m from the focusing lens of the camera. The experiment was designed so that the nozzle was located a distance of 1.4 m (halfway) between the background and the camera lens. This setup maximizes sensitivity of the BOS system by placing the refractive index

gradient (jet flow in this case) at the midpoint between the background and camera (Ref. 9).

The BOS setup was mounted on an axial traversing system and was translated downstream with an approximate range of $0 \leq x/D \leq 20$. BOS reference and data images were acquired for each appropriate combination of axial and radial positions for each set point. Note that all of the reference data for each combination of axial and radial positions were acquired during no flow conditions prior to starting the flow each day, while the image data were acquired upon reaching the desired test conditions. The time lag between reference data and flow data increased as a run went on, increasing the likelihood that the physical aspects of the background may have changed. The pixel shifts, in both the axial and radial directions, between the corresponding BOS reference and data images were calculated with an averaged data value for every 8×8 pixel sub-region, resulting in a spatial resolution of 0.97 mm per sub-region. Once processed, the results from 10 separate instantaneous images were averaged to produce the final image. The measurement uncertainty (EBOS) for a given image displacement (in pixels) is computed using the displacement vector peak positioning error (σ) so that EBOS = σ/*(image displacement)*. Given an optimized background pattern close to the one used here, σ = 0.1 pixel and the full-scale uncertainty is 1.7 percent for a maximum pixel displacement of approximately 6 (as observed in the BOS images below).

Particle Image Velocimetry Data Acquisition and Processing

Particle image velocimetry (PIV) was used to map the velocity field in the jet plume. PIV data were acquired in two modes: two-component streamwise, and three-component cross-stream. Brown and Wernet (Ref. 10) presented both streamwise and cross-stream results in a previous paper. Only two-component streamwise data will be presented in this paper. Seeding of the jet flow was achieved using 0.4 μm alumina particles, suspended in low-pH alcohol, and sprayed into the flow upstream of the settling chamber of the SHJAR. Seeding of the ambient was provided by a pair of MDG™ oil foggers, located in the framework of the SHJAR and directed around the jet plume by a pair of 1 m-diameter room fans. The measurement plane was illuminated using a dual head 400 mJ/pulse Nd:YAG laser system. The laser beams were formed into 1 by 350 mm light sheets using cylindrical and spherical lenses.

A dual side-by-side camera configuration was used to maximize the field of view while maintaining high spatial resolution PIV vector maps. High resolution (4008×2672 pixel) PIV cameras were used with the 4008 pixel axis oriented vertically. The cameras were equipped with 180 mm focal length lenses and positioned so that their fields of view overlapped by 25 mm. Both cameras were connected to a single computer system via a CameraLink™ PCI card and the 400 frame pair data sequences were acquired and streamed to disk

at a rate of 2 frame pairs/camera/second. The two camera views were registered using a grid pattern target with a fiducial mark in the overlapping region of the cameras' fields of view. The physical registration of the two cameras was used in the setup of the vector processing grids in the left and right camera images so that no interpolation was required in the merging of the left/right vector maps. The final merged camera vector map covered an area of 308×405 mm. The flow field of interest could generally be acquired using four axial measurement stations.

Since the AAPL is open to the environment during testing, the SHJAR could not be operated in complete darkness. To accommodate this situation, optical backdrops for the cameras were provided and were offset a suitable distance to minimize any influence on the ambient seeded flow distribution. The frame straddle cameras used in the PIV systems incorporate fast acting shutters in front of the CCD arrays to minimize the duration of the frame-straddled second exposures to nominally 12 ms, down from the camera fixed 240 ms second frame integration period. The complete PIV system, including all cameras and backdrops, data acquisition computers, laser hardware and optics were rigidly mounted on a large axial traverse located downstream of the nozzle exit plane. The travel range of the traverse was approximately 2.5 m, with a positioning accuracy of 1.0 mm.

Velocity vector maps for each camera were computed from the image pairs using the in-house PIVPROC software. The software utilizes conventional multi-pass DPIV cross-correlation processing algorithms and incorporates error detection based on image correlation signal to noise ratio. First pass interrogation region sizes of 64×64 pixels on 32 pixel centers and final pass interrogation region sizes of 32×32 pixels on 16 pixel centers were used to process image pairs from the cameras. The data were processed using LogLut intensity filters and Subregion Distortion processing.

The standard PIV system used to acquire the streamwise velocity data only gives the axial and radial components. The total turbulent velocities presented in this paper were computed as:

$$\text{Total Turbulent Velocity} = \sqrt{u^2 + w^2}$$

On some of the figures this quantity is also referred to as the "RMS velocity."

Phased Array Data Acquisition and Processing

Figure 2 shows a front view of the OptiNav Array48 phased array system used during this test. This system consists of 48 Earthworks M30 microphones flush-mounted to a 1 by 1 m aluminum plate. The microphones are arranged in a series of log spirals in an effort to reduce sidelobes (errors in the phased array data). One of the five log spirals is indicated by the darker microphones in Figure 2. The microphones have 1/4 in. (0.635 cm) diameter diaphragms and a flat frequency response over a

frequency range of 5 Hz to 30 kHz. They can be used to measure sound fields with amplitudes as high as 142 dB before they begin to saturate (136 dB when flush mounted in the array plate).

A photograph of the back of the microphone array is shown in Figure 3. This photo shows the microphones mounted to the back of the array plate and a camera located at the center of the plate. There is a hole in the center of the plate through which the camera can take a photo of the "field of view" of the phased array system. The phased array data reduction software superimposes the acoustic source localization data on top of the image taken with the phased array camera.

The phased array data were reduced using classical beamforming in the frequency domain. The first step in the data reduction process was to compute the cross spectral matrix, C, from the array data using the periodogram method with Hanning windowing functions and 50 percent block overlap. The diagonal elements of the cross spectral matrix are then deleted (set to zero, yielding $\overline{C}$), and the beamforming result, b, at a given grid point, k, is computed using the classical beamforming expression

$$ b_k = \mathbf{w}'_\mathbf{k} \overline{\mathbf{C}} \mathbf{w}_\mathbf{k} $$

where $\mathbf{w}_\mathbf{k}$ is a normalized version of the steering vector $\boldsymbol{g}_k$, and b represents the apparent strength of the acoustic source located at grid point k as estimated from the beamforming. The individual elements of $\boldsymbol{g}_k$ represent the Green's function for a monopole located at grid point k as observed by microphone i. In free space with no flow

$$ g_{ki} = \frac{e^{j\frac{\omega}{c}|\vec{y}_i - \vec{x}_k|}}{|\vec{y}_i - \vec{x}_k|} $$

where $\vec{x}_k$ and $\vec{y}_i$ denote the locations of grid point k and microphone i, respectively. A beamforming result is computed for each point in a beamforming grid. The results corresponding to an entire grid are then displayed as color contour maps (known as beamform maps). Each contour map corresponds to a selected frequency band, and shows the location of the dominant noise source or sources in the band as a two-dimensional color contour map overlaid on top of a photograph taken with the phased array camera. The color contours correspond to the location and strength of the noise sources found within an image plane (the beamform grid) parallel to the array plate at some specified distance away from the array. The dynamic range of the color contours (max value minus min value) is the same for each beamform map (i.e., processed frequency band), but the peak value can vary from map to map. The color contour maps presented later in this paper all have a 7 dB dynamic range.

All of the phased array data were acquired with the array mounted on a stationary support stand located between the nozzle and the far field array. Figure 4 shows the array located on this stand during a jet-surface interaction test. The array was at this same location when the bare jet (no surface) phased array data presented in this report were acquired. The center of the array was at the same height as the jet centerline, 10 ft (3.05 m) above the floor, and the array plate was parallel to, and 2.82 m (about 55 nozzle diameters) away from, the jet centerline. Since the nozzles have different lengths, the axial location of the phased array relative to the two nozzle exit locations was slightly different. With the SMC000 nozzle, the array was located such that a line normal to the center of the array intersected the jet centerline at the nozzle exit, while with the SMC016 nozzle the array normal intersected the jet centerline 5 in. (12.7 cm) upstream of the nozzle exit. The polar angle between a ray directed downstream through the jet axis and a line spanning from the array center to the center of the nozzle exit was 90° when the SMC000 nozzle was tested, and 92° with the SMC016 nozzle. The array aperture was roughly 20°.

Results

Flow Field: PIV and BOS

Figure 5 shows BOS results obtained on the convergent-divergent SMC016 nozzle for three supersonic operating conditions: setpoint 11606 (over-expanded), setpoint 11610 (ideally-expanded), and setpoint 11617 (under-expanded). Two images are shown for each setpoint: the top image is a 2D gray-scale map of the density gradients in the nozzle flow; the bottom image shows a line plot that depicts the variation in the 2D gray-scale map along a line passing through the jet centerline. In each plot, results are presented such that the nozzle exit is at the left boundary and the flow moves from left to right. The light gray, dashed, vertical grid lines plotted in each of the three centerline variation plots are located 0.5D apart. The wavelike oscillation depicted in the centerline plots for the two off-design conditions (blue and black lines) are due to the shocks in the flow, and the wavelength of the oscillation is a measure of the shock spacing. The gray-scale 2D map for the ideally-expanded condition (setpoint 11610) shows what appear to be oblique shocks and expansion waves in the flow, but the centerline plot (red) does not show the same sort of oscillation depicted in the centerline plots provided for the off-design conditions. This indicates that the shocks at the ideally-expanded condition are very weak, as expected. The plot at the very bottom of Figure 5 shows how shock spacing (in units of nozzle diameter, D) varies with downstream distance (nondimensionalized as x/D) for the two off-design operating conditions. These data indicate that shock spacing increases and the shock train elongates as NPR is increased between setpoints 11606 (over-expanded) and 11617 (under-expanded). Shocks extend about 7D and 15D downstream at the over-expanded and under-expanded conditions, respectively. At each of these two off-design conditions, the shocks get closer together as distance downstream of the nozzle increases.

Figure 6 shows PIV results for one subsonic (setpoint 7, SMC000 nozzle) and three supersonic operating conditions: setpoint 11606, 11610, and 11617, all with the SMC016 nozzle. The four color contour maps show mean velocities (flow speed) measured with the PIV system configured to measure the flow in a plane passing through the jet centerline. A separate colorbar is provided for each contour map (located above each map). In each of the six plots provided in the figure, the nozzle exit would be located at the left boundary, and nondimensional axial distance (x/D) downstream of the exit is plotted along the abscissa. The line plots provided just below the contour maps show the variation in mean velocity along the jet centerline for each of the four operating conditions. Like the BOS data discussed above, these clearly show the wavelike oscillation caused by the shocks at the two off-design supersonic operating conditions; unlike the BOS data, a discernable wavelike oscillation (albeit much weaker) is also shown for the ideally-expanded supersonic condition, setpoint 11610. The line plots provided in the bottom plot show how the shock spacing varies with downstream distance for the three supersonic cases as measured with PIV, and for the two off-design cases with BOS. The shock spacing results presented for the two different measurement systems are shown to be in good agreement.

BBSN is generated by the interaction between the turbulent structures and the shocks in the flow. Consequently, it is worthwhile to examine the unsteadiness in the jet flows. Figure 7 shows total turbulent velocities, $(\sqrt{u^2 + w^2})$, measured with the PIV system for the same four operating conditions. In this figure all four contour maps are plotted using the same colorbar (shown at the top of the figure). The line plots provided in the plot just below the four contour maps show the variation in the total turbulent velocity measured along the jet centerline at the four operating conditions; while the line plots provided in the bottom plot show this same variation along the upper lipline of the nozzle. The bottom set of line plots indicate that the location along the upper lipline corresponding to the peak turbulent velocity moves downstream as NPR is increased through the three supersonic setpoints - peaking at about 6.5, 9.5 and 14D downstream of the nozzle exit at the over-, ideally-, and under-expanded conditions, respectively. Although the location changes considerably, the magnitude of the peak remains relatively constant. It is nearly the same at the over- and ideally-expanded conditions (about 90 m/s) and increases only slightly (to about 105 m/s) as NPR is increased further to the under-expanded condition. Consequently, it is likely that any differences in the BBSN produced at the different operating conditions (discussed further below) are not simply due a change in the turbulence level.

Figure 8 shows turbulence length scale computed from the instantaneous PIV velocity vector maps for each of the four operating conditions. Each line plot shows the variation in turbulence length scale with distance downstream of the nozzle. Each plotted value is the average of the length scale measured in the upper and lower liplines at the corresponding axial location. This length scale corresponds to that computed from the axial velocity component in the axial (downstream)

direction, L_{ux} (often referred to as L_{11}) using the method discussed by Bridges and Wernet (Ref. 11). The data presented above illustrated that the flow fields corresponding to these four operating conditions were quite different. Figure 8 indicates, however, that the turbulent structures grow in the shear layer at about the same rate regardless of operating condition.

Flow Field and Source Location Combined

Figures 9 to 91 show both flow field and source location results for a subsonic jet. These data were obtained using the convergent SMC000 nozzle at setpoint 7 ($M_a = 0.90$, TSR = 0.835). These figures show the PIV measured flow field results discussed above for this operating condition along with source location data measured with the Optinav Array48 phased array system. Eighty-three figures are presented for this operating condition; each figure shows phased array results corresponding to a different 1/12th octave frequency band, with the lowest processed frequency presented first. The contour plot at the bottom left is the beamform map corresponding to the processed frequency band. The narrow plot just above the beamform map shows a red slider that designates the location of the peak in the beamform map. This plot, and each plot above it, is 20D wide. The top plot in the right column shows PSD spectra (1 Hz bin width) computed from the output of the microphone closest to the center of the microphone array. This is a conventional, single-microphone spectrum (i.e., not a product of the phased array beamforming). All of the single microphone spectra presented in this report have been scaled to a distance equal to 100D from the jet centerline by subtracting $20\log_{10}(100/55)$ dB from the spectra measured at 55D. The data were not corrected for atmospheric attenuation. The bottom plot in the right column of each figure shows the distance between the peak in the beamform maps and the nozzle exit (in units of nozzle diameters, D) as a function of frequency. This type of plot will be referred to herein as a peak location plot. The x-location of the red asterisks superimposed on the two plots in the right column designate the Strouhal number (St) corresponding to the plotted beamform map. The noise source location data indicates that the loudest noise comes from locations between 7 and 10D downstream of the nozzle exit. The flow field data indicate that this corresponds to a region just downstream of the potential core where the total turbulent velocities are highest.

The results shown in Figures 9 to 91 are typical of subsonic jets (Ref. 12). They show (1) broad, rounded acoustic spectra, and (2) the peak noise source located relatively far downstream at low frequency and moving gradually closer to the nozzle exit as frequency is increased. Data from subsonic jets all tend to have these same characteristics because there is only one source of noise in these jets, the turbulent mixing that occurs between the jet and the ambient air.

Figures 92 to 137 show results for the highest Mach number, under-expanded test case. These figures show PIV and BOS flow field as well as phased array noise source location results. Unlike the haystack-shaped spectra of the subsonic jet, the

acoustic spectra presented here (upper right plot) show an elevated hump associated with BBSN (at 0.35 < St < 0.87, or 3 kHz < f < 7.5 kHz). Moving up in frequency through these figures shows that the peak noise source location initially moves toward the nozzle exit, much like in a subsonic jet. It moves upstream to x = 8D at St = 0.35 (the low frequency end of the BBSN hump), then starts moving downstream. It continues to move downstream to x = 16D at about St = 0.87 (the high frequency end of the BBSN hump). The flow field data indicate that x = 16D is about the axial location where the shocks are no longer visible. Near St = 1.0, beyond the high frequency end of the hump, the peak noise source location jumps back upstream, before this pattern (downstream movement followed by a jump back upstream) repeats once again. This upstream-downstream-upstream-downstream movement of the peak noise source location shows up in the peak location plots as the repeated shark-fin-like pattern. These phased array data are indicating that the dominant BBSN hump is created between 8 and 16D downstream of the nozzle exit in the latter half of the shock train, and that the highest frequency BBSN in the hump is created by very weak shocks near the end of the shock train.

The spectrum provided for this under-expanded case shows one dominant hump rising above the higher frequency broadband shock noise, to the right of the hump. The BBSN theory put forth by Tam (Ref. 13) suggests that the elevated region of high frequency noise is actually made up of a series of humps centered about different frequencies. These humps are illustrated in Figure 138 (taken from Miller (Ref. 14)). Sometimes multiple humps are visible in the acoustic spectra obtained from shock-containing jets. Normally, however, the lowest frequency hump is much easier to identify than the others. These humps are thought to be created by turbulent eddies which are large enough to span one or more shockcells. The interaction of these large eddies with the shocks generates highly correlated noise radiating from multiple shocks simultaneously. According to Harper-Bourne and Fisher (Ref. 1), at the peak frequency in each hump "radiation from all sources interferes constructively," while on either side of the peak "this constructive interference is less complete and hence lower levels of noise are anticipated." The lowest frequency hump is created by the interference of sound waves coming from adjacent shocks (1 shock spacing apart), the second hump is created by the interference of waves coming from every-other shock (2 shock spacings apart), etc. The BBSN theories put forth by both Tam (Ref. 13) and Morris (Ref. 15) suggest that in order for the turbulent structures to generate significant BBSN they must be at least as large as the shock spacing. Based on this, one might expect BBSN to be generated only in that region of the flow downstream of the intersection point of the shock spacing and length scale curves shown in the plot just above the beamform maps, i.e., at locations downstream of x = 12D. The phased array data, however, are indicating that BBSN is also generated at locations as far upstream as x = 8D. This might be explained by the fact that the turbulent length scales plotted here represent the *average* size of the turbulent

structures at a given axial location. Some eddies would grow faster than these average eddies. These faster growing eddies would be able to generate BBSN upstream of the intersection point. This intersection point represents the axial location where the average size of the turbulent structures in the shear layer matches the shock spacing. This is where the noise associated with the peak of the BBSN hump appears to come from. It is a "hot spot" for the generation of BBSN.

These data also suggest an explanation as to why the frequency of the BBSN increases as the turbulent structures move downstream. The structures grow in size as they move downstream, while the shocks get closer together. Assuming a constant convection speed, the structures would pass through the shocks at a higher rate (and generate higher frequency noise) as they move downstream.

As mentioned above, the peak noise source location moves downstream as frequency increases through the dominant BBSN hump. Then, the peak noise source location jumps back upstream, followed by another downstream movement. The peak source location plot provided in Figures 92 to 137 shows a total of three such downstream movements: (1) at 0.38 < St < 0.93, or 3.3 kHz < f < 7.9 kHz, (2) at 1.00 < St < 1.45, or 8.7 kHz < f < 12.6 kHz and (3) at 1.81 < St < 2.07, or 15 kHz < f < 18 kHz. As explained previously (Ref. 12), each downstream movement is thought to be associated with a different BBSN hump. In the spectra, however, only the lowest-frequency hump is identifiable. The other two tend to blend together into a smooth region free of humps. This suggests that the downstream movement of the peak noise source location is a more sensitive indicator of the generation of BBSN than the spectra itself. The first hump is generated at locations between 8 and 16D downstream of the nozzle exit; a second hump between 12 and 15D downstream; and a third hump between 13.5 and 14.5D downstream. This indicates that some of the same shocks that contribute to the production of the first hump also produce the higher frequency humps. These data also suggest that the constructive interference of sound waves that produces the BBSN at a given frequency and observer location comes primarily from a small number of shocks, not from all the shocks at the same time.

Combined flow field and source location data for the lowest Mach number supersonic case tested with the convergent-divergent SM016 nozzle, the over-expanded jet condition, are shown in Figures 139 to 192. Compared to the high Mach number case just discussed (Figs. 92 to 137), the BOS and PIV centerline variation plots presented here show the shocks closer together and not extending as far downstream. Consequently, at this lower Mach number the shock spacing curve (shown in red) is lower on the plot and its intersection with the turbulence length scale curve occurs much further upstream (at 5D vs. 12.5D). In this set of figures, the peak noise source location moves toward the nozzle as frequency increases until around St = 0.65, where it reaches x = 4D, then starts moving downstream. It continues to move downstream until it gets to about x = 7D at St = 1.5. The flow field data indicate that this is near the axial location where the shocks disappear. As before,

the data are indicating that BBSN is produced by the weaker shocks near the tail end of the shock train. In the previous dataset (under-expanded, setpoint 11617) the loudest shock noise occurred at the peak of the BBSN hump; in contrast, in this dataset the loudest shock noise is the screech tone occurring at $St = 0.811$. In both cases, however, the loudest shock noise is generated near the axial location corresponding to the intersection of the shock spacing and turbulence length scale curves. In both cases this intersection point is a "hot spot" for shock noise. The three shark-fin like patterns in the peak location plot designate three distinct downstream movements of the peak source location. Although only the first hump is clearly visible in the spectrum, these movements suggest three different BBSN humps, occurring at (1) $0.66 < St < 1.51$ or 4.8 kHz $< f < 11$ kHz, (2) $1.66 < St < 2.40$ or 12 kHz $< f < 18$ kHz and (3) $2.65 < St < 3.23$ or 19 kHz $< f < 24$ kHz. In this case the first downstream movement (the lowest frequency hump) is produced at $4D < x < 7D$, the second downstream movement at $5D < x < 7D$, and the third at $6D < x < 7D$. Once again, the data are indicating that some of the same shocks that produce the first hump also produce the higher frequency humps.

Figures 193 to 237 show combined flow field and noise source location data obtained near the ideally-expanded operating condition for the SMC016 nozzle. Although the intent was to operate shock free, both the BOS and PIV data show some evidence of weak shocks in the flow. These weak shocks generated only a very slight oscillation in the flow along the jet centerline. Consequently, it was difficult to determine shock spacing from the wavelength of the oscillation, especially for the BOS data. The lone shock spacing curve shown in red was generated from the PIV data. Like the other operating conditions discussed above, the peak noise source location starts out moving toward the nozzle as frequency increases. In these figures, it reaches $x = 8D$ at $St = 0.53$, (Fig. 216) then starts moving downstream. It continues to move downstream until it reaches $x = 13D$ at $St = 1.15$, then it jumps back upstream. The flow field data indicate that $x = 13D$ is near the end of the shock train. The spectra show a small BBSN hump at $0.53 < St < 1.15$, the range corresponding to the first downstream movement of the peak noise source location. A second downstream movement occurs at $1.2 < St < 1.8$, indicating another BBSN hump, but it is not as identifiable in the spectra. The shark fin patterns suggest that BBSN is responsible for creating much of the jet noise for $0.55 < St < 1.9$ even though the shocks are very weak.

The supersonic jet phased array data presented above were acquired in 2011 to 2012 using the convergent-divergent SMC016 nozzle. It should be pointed out that supersonic jet data obtained with the convergent SMC000 nozzle in 2008 indicate that phased array results can vary depending on the external configuration of the test hardware. In particular, the acoustic "hardness" (i.e., ability to reflect noise) of the surfaces upstream of the nozzle exit tends to be important, at least in the case of screeching jets. The sound waves associated with screech tones propagate very strongly along the jet axis due to a feedback that occurs between noise produced in the jet and

noise reflecting back into the flow off of the upstream hardware. Consequently, making the upstream hardware softer (less reflective) can reduce the screech tones significantly. This is illustrated in Figures 238 to 317, which show phased array data obtained at setpoint 9010. Data are provided for two configurations of the external nozzle hardware: (1) hard (not covered with foam), and (2) soft (covered with foam). During the 2008 test, the nozzle extension employed in the 2011 to 2012 tests was not used. Consequently, the hardware just upstream of the nozzle exit had a wider diameter. Interestingly, the phased array data presented in Figures 238 to 317 indicate that reducing the amount of noise reflecting back into the jet may alter both the screech tones *and* the broadband noise. Not only was the broadband associated with the BBSN humps reduced, but also the broadband noise occurring at frequencies lower than the humps. In the above discussion it was postulated that this low frequency broadband noise was caused by turbulent mixing between the jet and ambient air since the peak source location tended to move upstream toward the nozzle as frequency increased, like in a subsonic jet. These data suggest that that may not always be the cause. In fact, they indicate that when screech occurs the reflectivity of the upstream surfaces can have a profound effect on both (1) the noise level over a wide frequency range and (2) the locations in the jet where the noise is generated. Consequently, care should be exercised when examining data associated with screeching jets – it is possible that different results would be obtained if the reflectivity of the upstream hardware changed.

Summary

Phased array noise source location and two types of flow field data, BOS and PIV, were presented for both one subsonic and three supersonic operating conditions. These data show:

1. BBSN is created in the downstream part of a shock train where the turbulent structures have grown to at least the size of the shock spacing.
2. At off-design operating conditions, BBSN can be created by the very weak shocks near the downstream end the shock train.
3. BBSN can also be generated by the very weak shocks occurring in jets operated at almost perfectly expanded conditions.
4. The axial location in the flow where the average size of the turbulent structures equals the shock spacing tends to be a hot spot for shock noise.
5. Some of the same shocks that help to generate the lowest frequency BBSN hump also help to generate the higher frequency humps.
6. The higher frequency noise in a BBSN hump tends to come from further downstream than the lower frequency noise within the same hump. The frequency of the noise generated increases as the turbulent structures move downstream because (a) the structures are growing in size and (b) the shocks are getting closer together.

In addition, phased array data were provided for an unheated supersonic jet with and without the upstream nozzle hardware covered with foam. These data show that with screeching jets, the acoustic reflectivity of the upstream nozzle hardware can impact the level of broadband noise produced. The reflectivity can impact not only the level of BBSN, but also the broadband level at frequencies lower than the BBSN.

References

1. Harper-Bourne, M., Fisher, M.J., "The noise from shock waves in supersonic jets," AGARD, 131, pp. 1–13.
2. Martens, S., and Spyropoulos, J.T. "Practical Jet Noise Reduction for Tactical Aircraft," ASME GT2010-23699. June 2010.
3. Mengle, V.G., Ganz, U.W., Nesbitt, E., Bultemeier, E.J., Thomas, R.H., "Flight Results for Uniquely Tailored Propulsion-Airframe Aeroacoustic Chevrons: Shockcell Noise," AIAA paper 2006-2439, May 2006.
4. Brown, C.A. and Bridges, J.E., "Small Hot Jet Acoustic Rig Validation," NASA/TM—2006-214234, April 2006.
5. Bridges, J. and Brown, C.A., "Parametric Testing of Chevrons on Single Flow Hot Jets," NASA/TM—2004-213107, AIAA paper 2004-2824.
6. Khavaran, A. and Bridges, J., "SHJAR Jet Noise Data and Power Spectral Laws," NASA/TM—2009-215608, March 2009.
7. Richard, H. and Raffle, M., "Principle and applications of the background oriented schlieren (BOS) method," Measurement Science and Technology, vol. 12, pp. 1576–1585, 2001.
8. Clem, M.M., Zaman, K.B.M.Q., and Fagan, A.F., "Background Oriented Schlieren Applied to Study Shock Spacing in a Screeching Circular Jet," AIAA paper 2012-0403, 2012.
9. Hargather, M.J. and Settles, G.S., "Recent Developments in Schlieren and Shadowgraph," AIAA–2010–4206, 2010.
10. Brown, C., and Wernet, M., "Jet-Surface Interaction Test: Flow Measurement Results," AIAA paper 2014–3198, June 2014.
11. Bridges, J. and Wernet, M.P., "Measurements of the Aeroacoustic Sound Source in Hot Jets," AIAA–2003–3130, May 2003.
12. Podboy, G., "Jet-Surface Interaction Test: Phased Array Noise Source Localization Results," ASME GT2012-69801, June 2012.
13. Tam, C.K.W., "Stochastic Model Theory of Broadband Shock Associated Noise from Supersonic Jets," Journal of Sound and Vibration, 116(2), pp. 265–302, 1987.
14. Miller, S.A.E., "The Prediction of Broadband Shock-Associated Noise Using Reynolds-Averaged Navier-Stokes Solutions," Ph. D. dissertation, Pennsylvania State University, December 2009.
15. Morris, P., email communication, 2012.

TABLE 1.—JET OPERATING CONDITIONS

Nozzle	Setpoint	NPR P_t/P_{amb}	TSR T_s/T_{amb}	M_a V/c_{amb}	M_j V/c_{local}
SMC000	7	1.86	0.835	0.90	0.98
SMC000	9010	3.18	0.74	1.18	1.40
SMC016	11606	2.75	0.76	1.13	1.29
SMC016	11610	3.67	0.72	1.31	1.50
SMC016	11617	4.32	0.76	1.41	1.61

Detector P
(36 mm x 2

1.4 m

0.5<h/D_j<5

1.4 m

nozzle
(D_j=50.8 mm)

Background
(0.9 m x 0.7 m)

0.6 m

10W LED
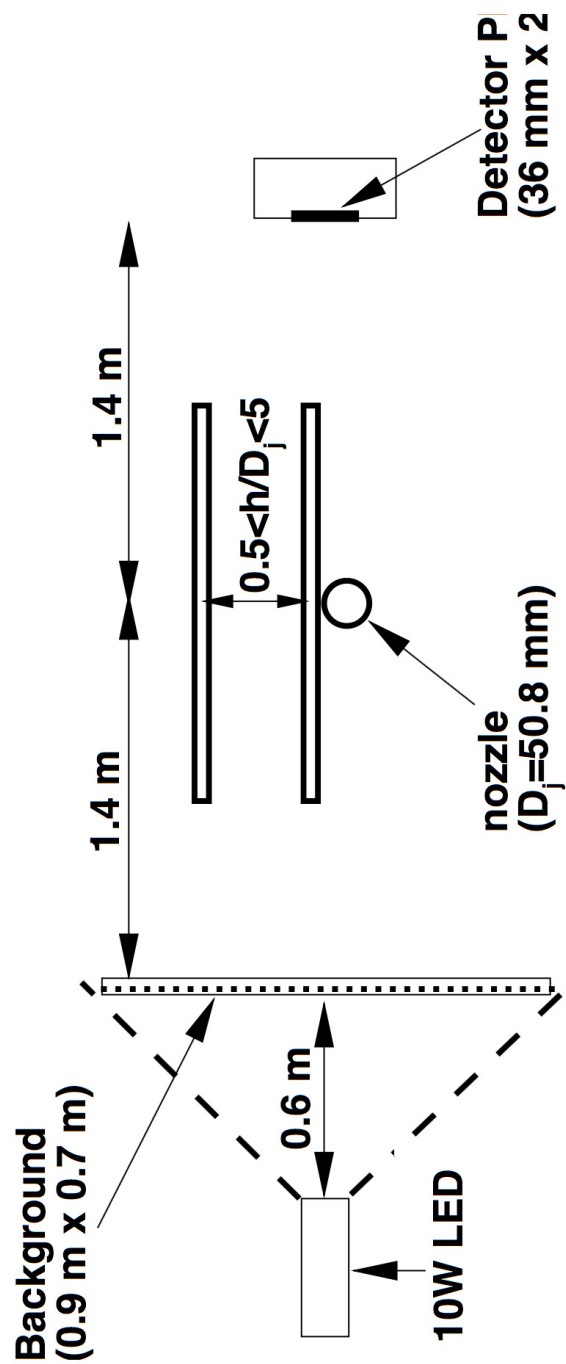
Figure 1.—Schematic of the BOS setup, looking upstream into the plane of the nozzle. Note that the random dot pattern, represented by the dotted line on the downstream edge of the background above, is printed on the flow side of the background.
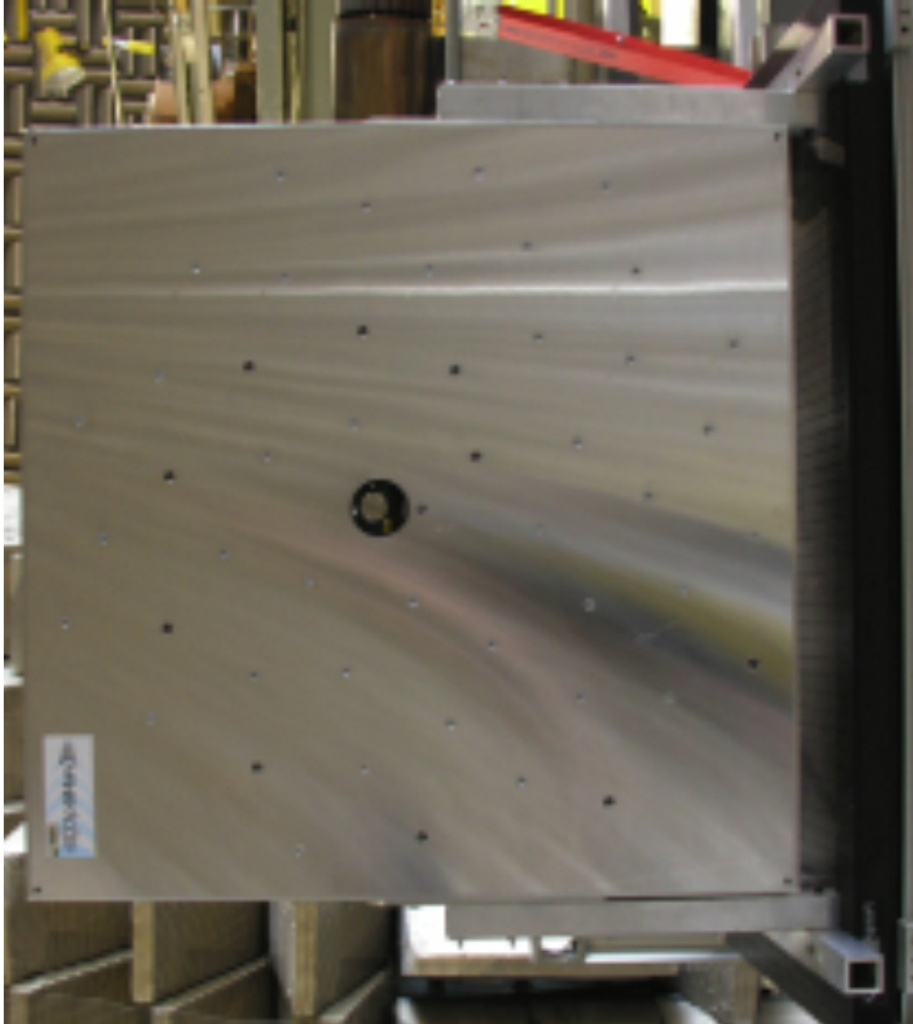
Figure 2.—Photo of the front of the Array48 microphone array.

Figure 3.—Photo of the back of the Array48 microphone array.
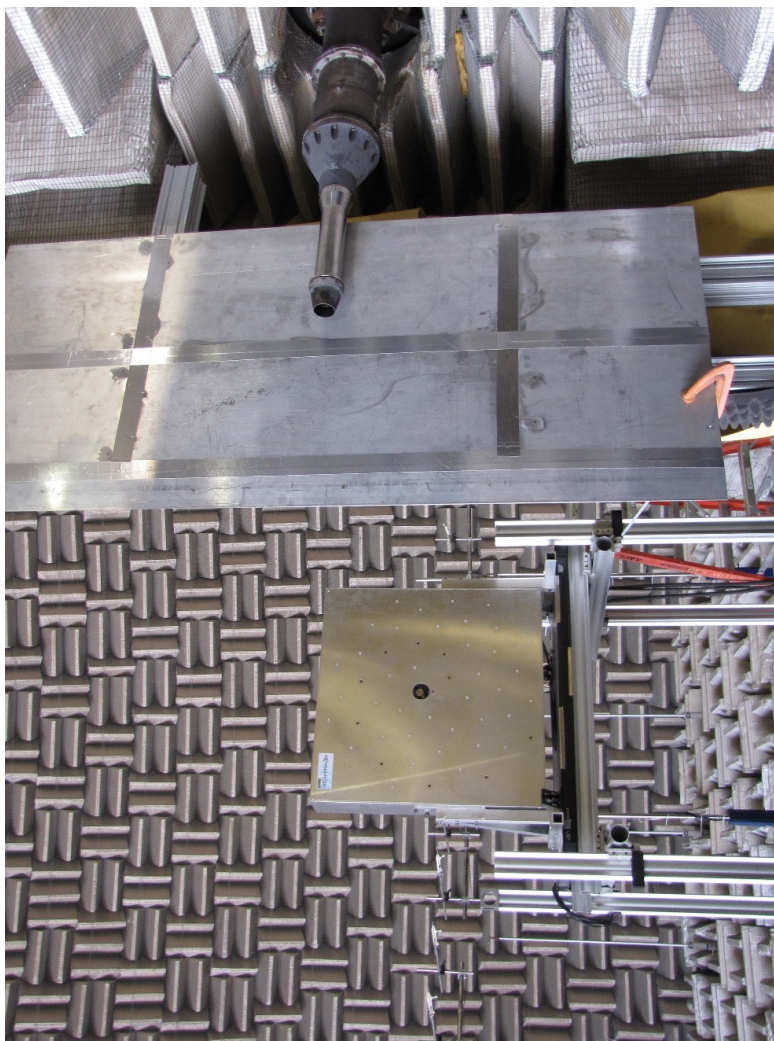
Figure 4.—Photo showing Arry48 setup at SHJAR during a jet-surface interaction test.
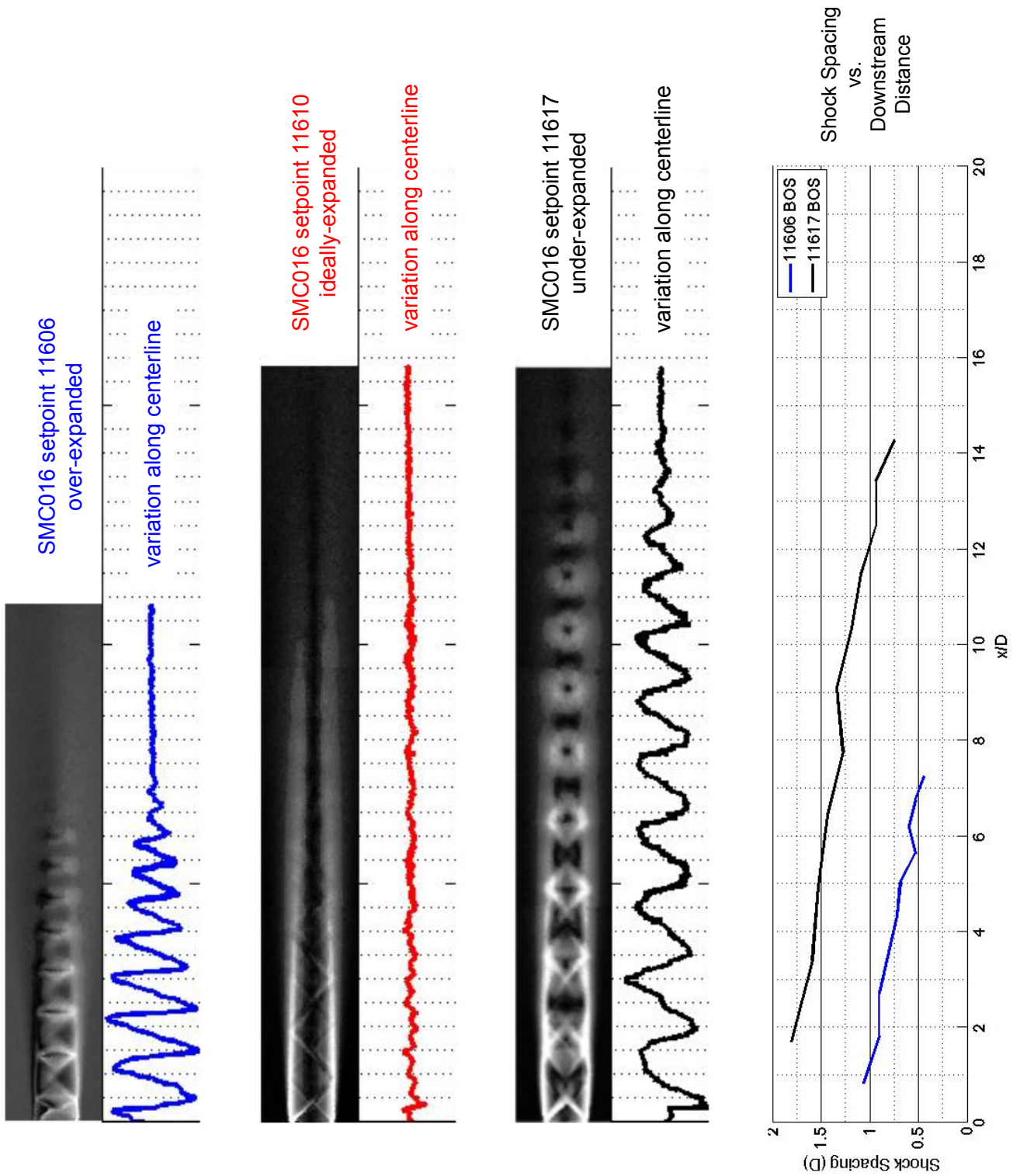
Figure 5.—BOS results obtained on the SMC016 nozzle at 3 supersonic setpoints. The gray-scale contours are BOS images.
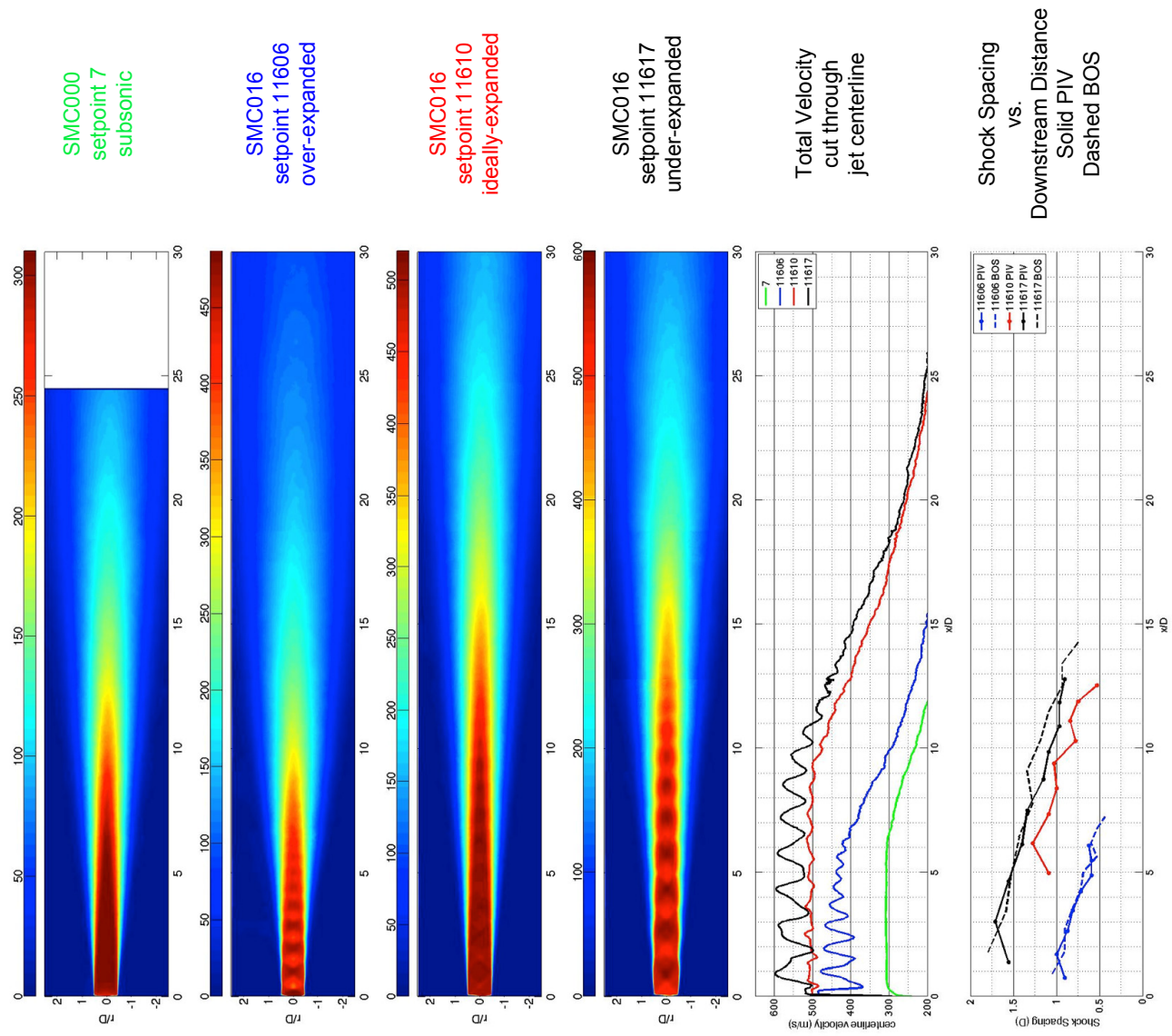
Figure 6.—PIV and BOS results obtained on the SMC000 and SMC026 nozzles. The color contours show total velocity (in m/s) measured with PIV.
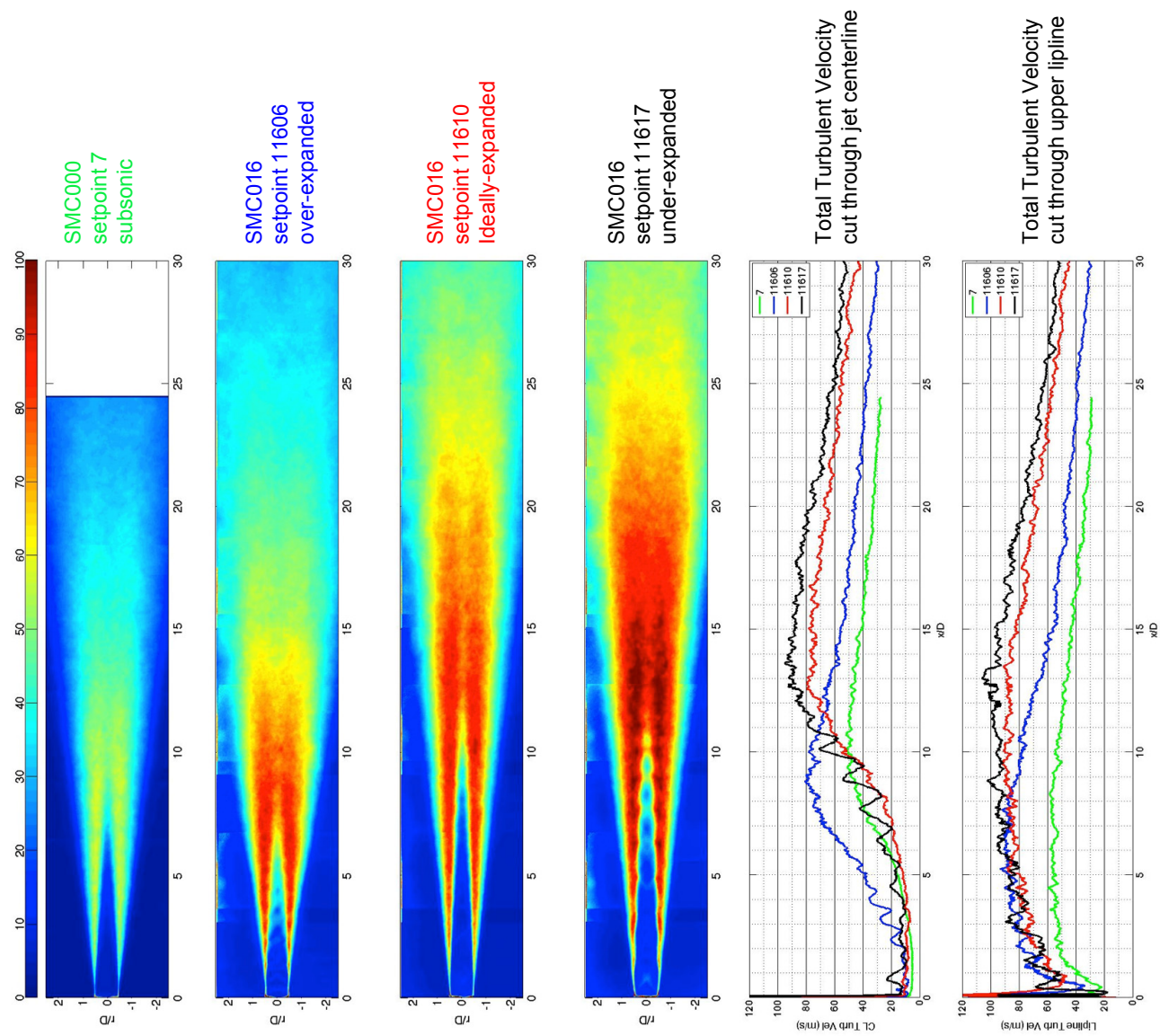
Figure 7.—PIV results obtained on the SMC000 and SMC026 nozzles. The color contours show total turbulent velocity (in m/s) measured with PIV.
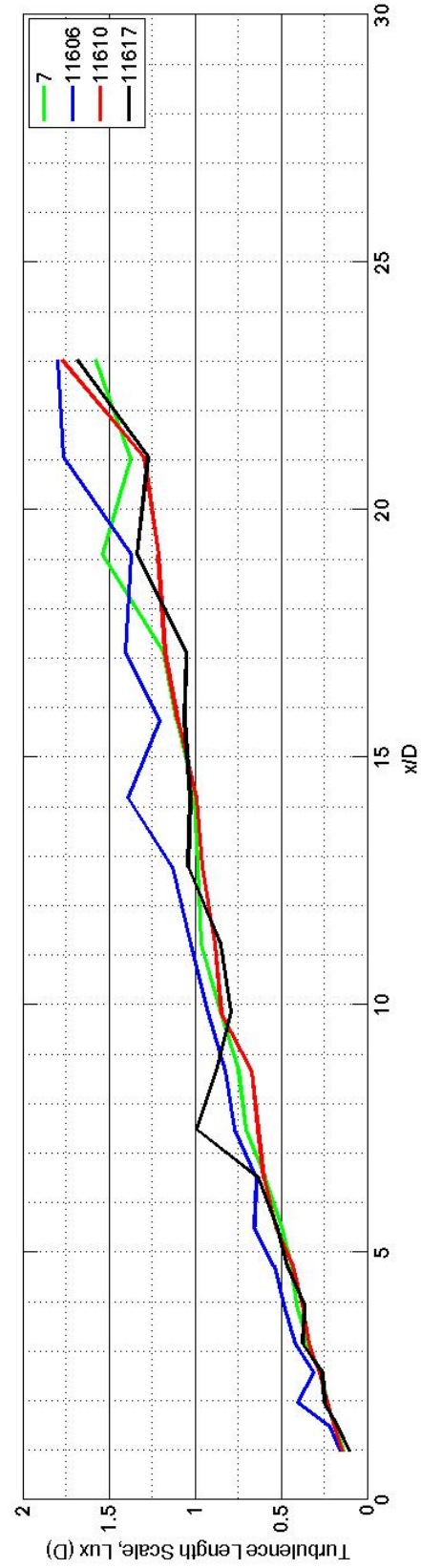
Figure 8.—Average of Lux Measured Along Upper and Lower Nozzle Liplines vs. x/D.
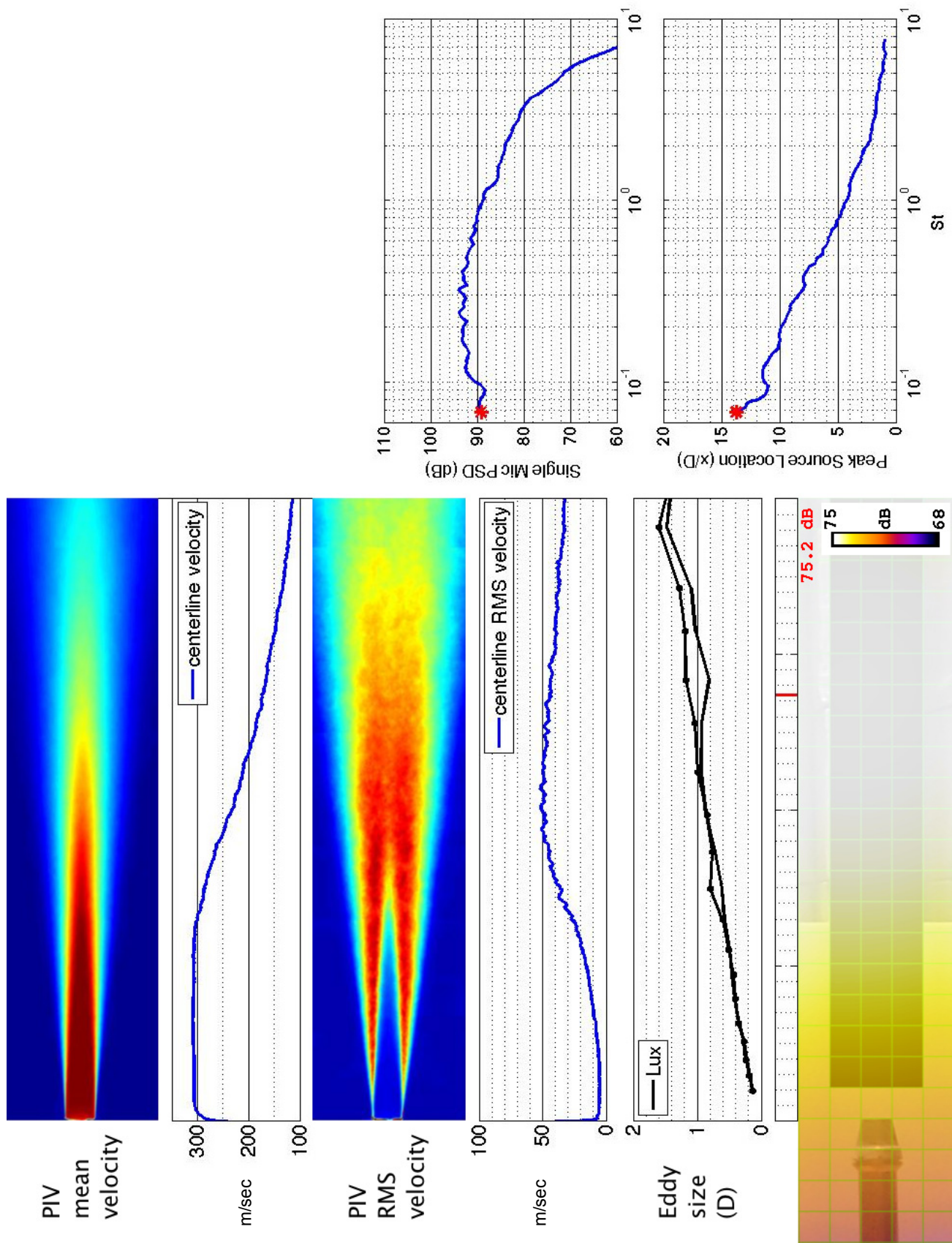
Figure 9.—SMC000; set point 7; Mj=0.98; St=0.068.
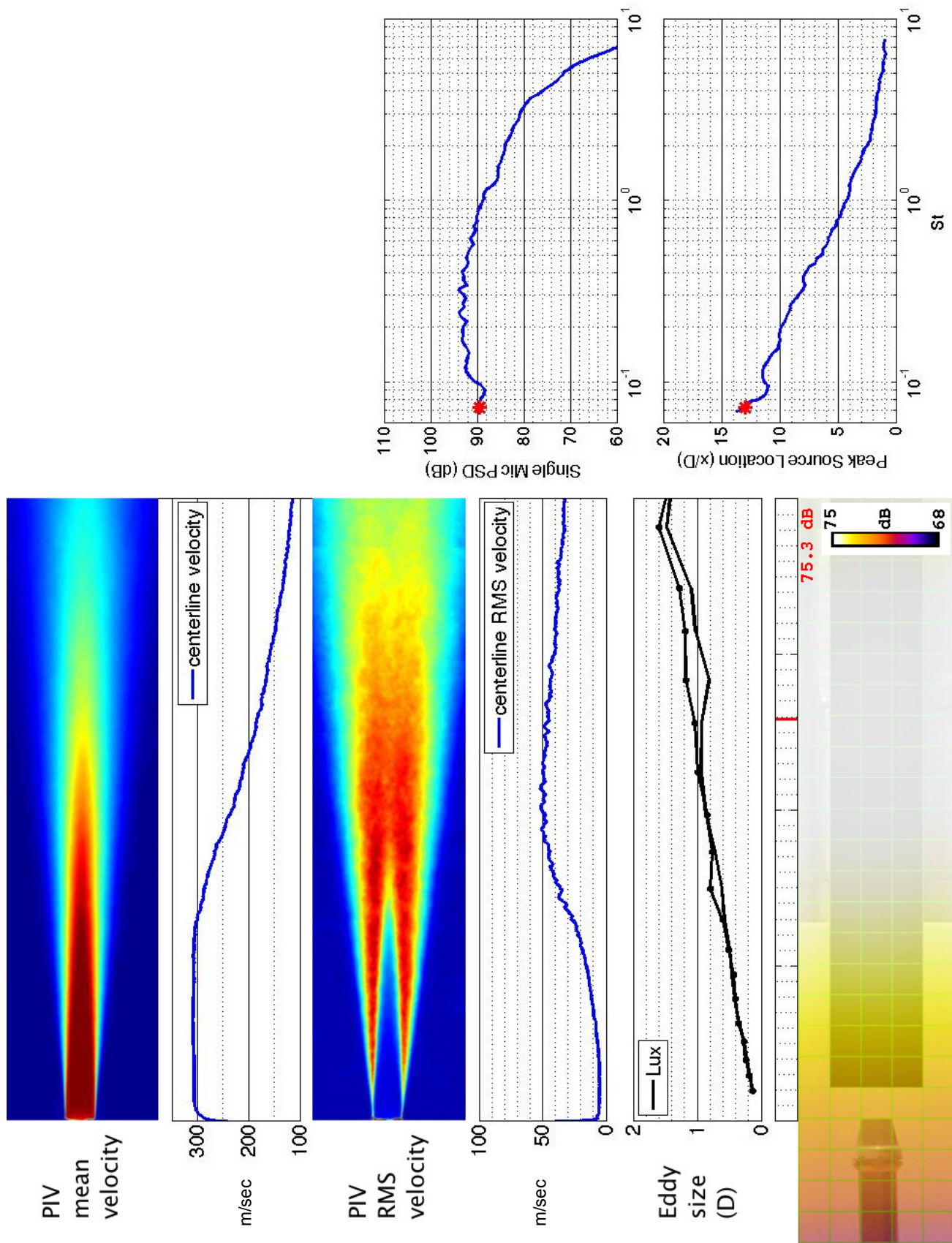
Figure 10.—SMC000; set point 7; Mj=0.98; St=0.072.
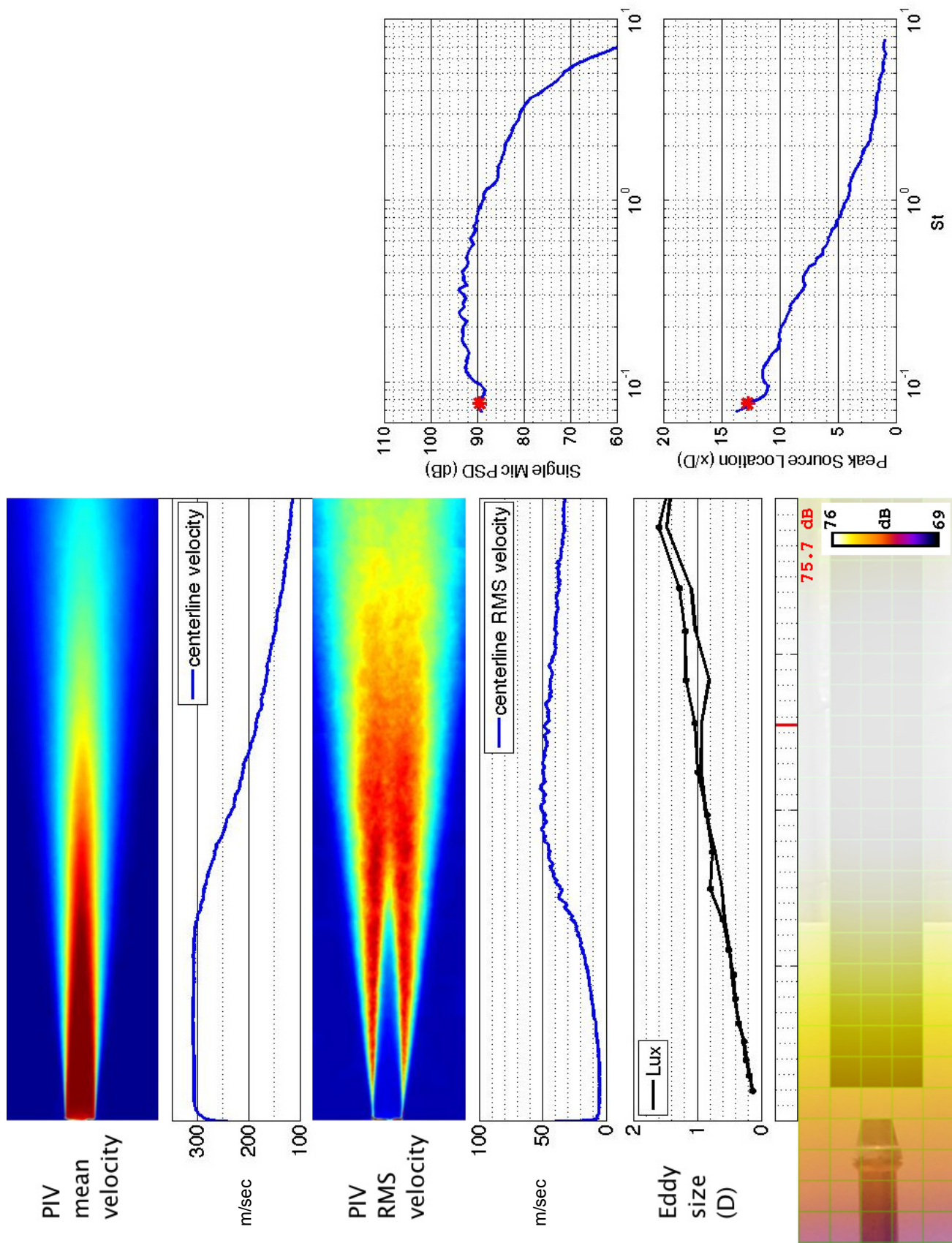
Figure 11.—SMC000; set point 7; Mj=0.98; St=0.076.
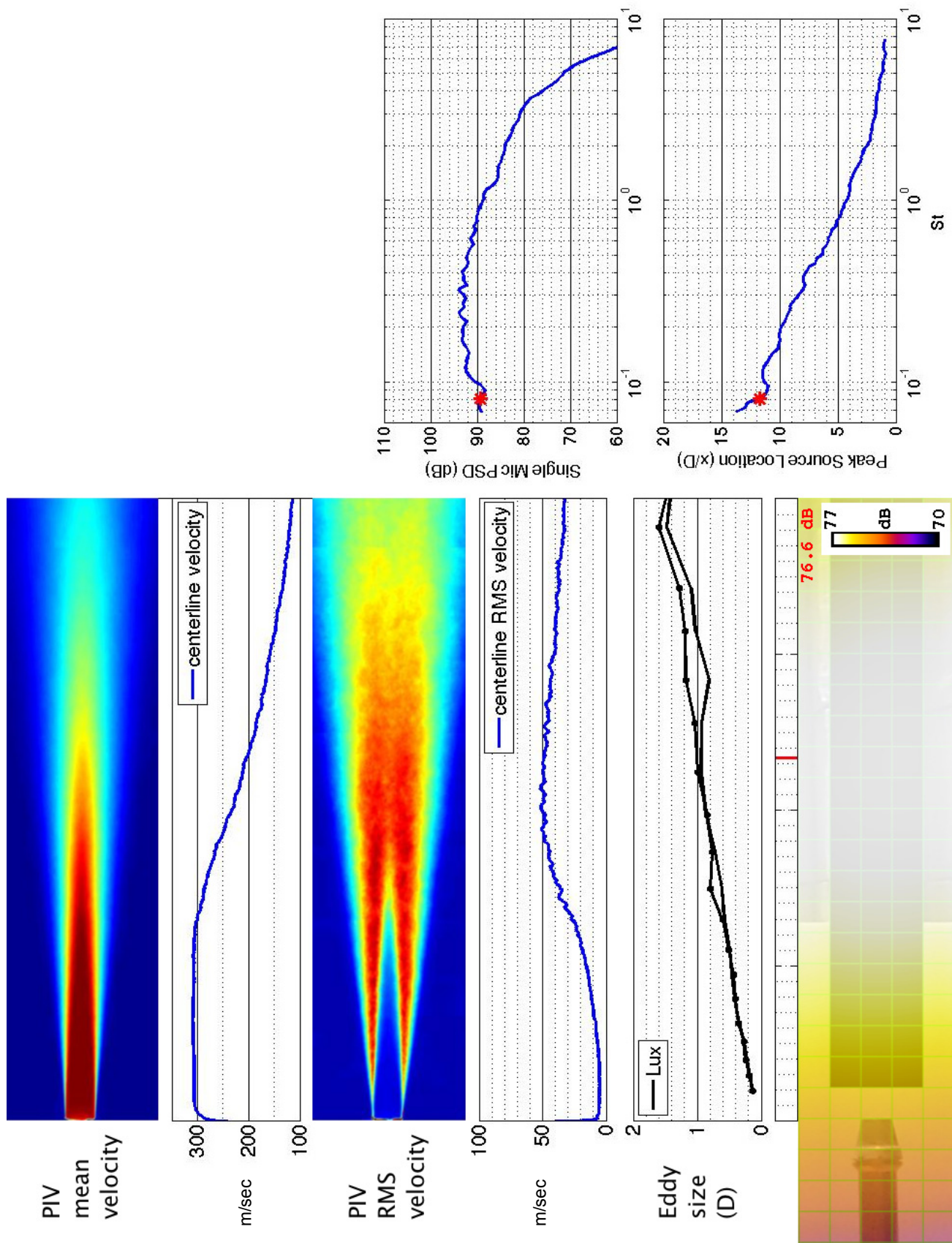
Figure 12.—SMC000; set point 7; Mj=0.98; St=0.081.
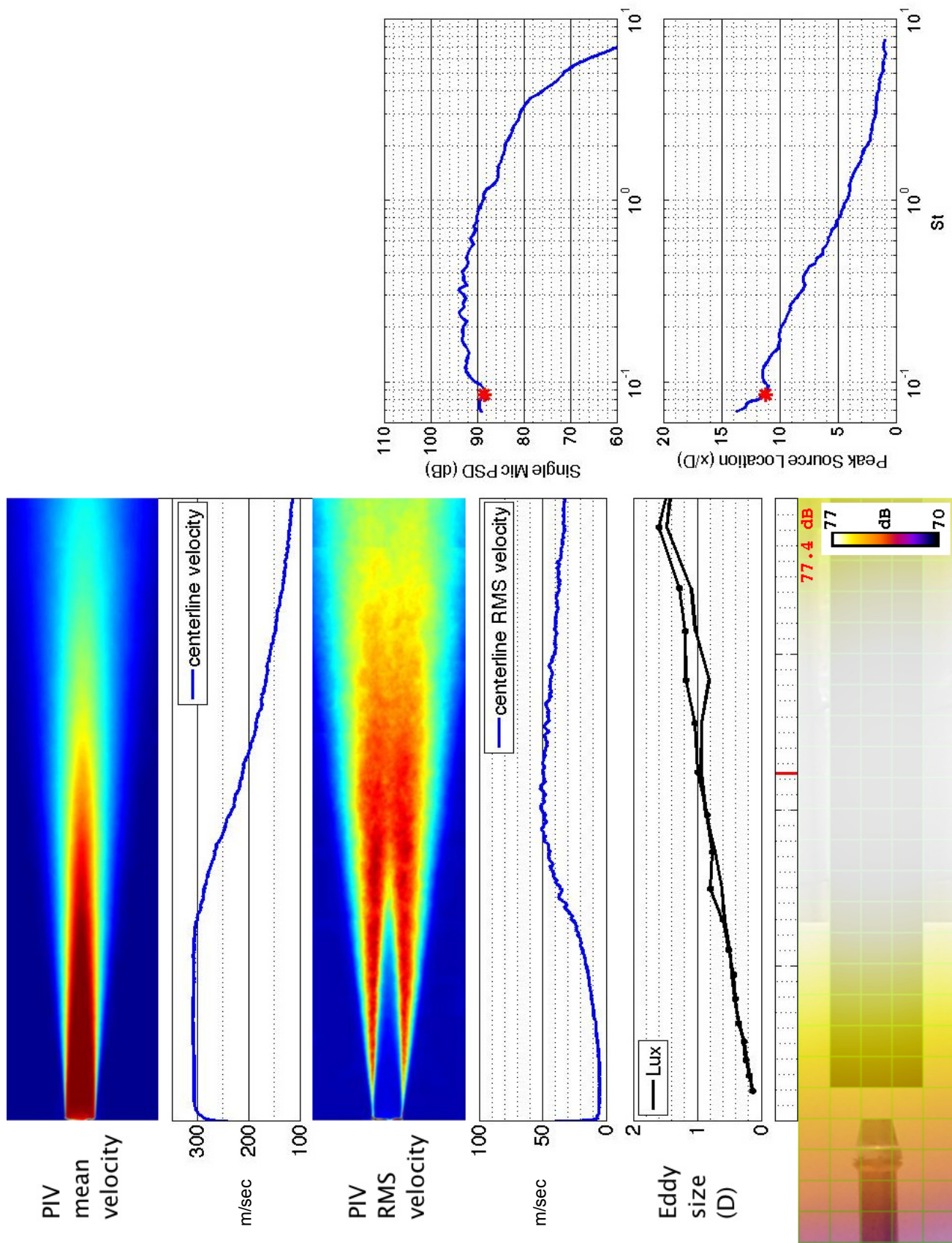
Figure 13.—SMC000; set point 7; Mj=0.98; St=0.086.
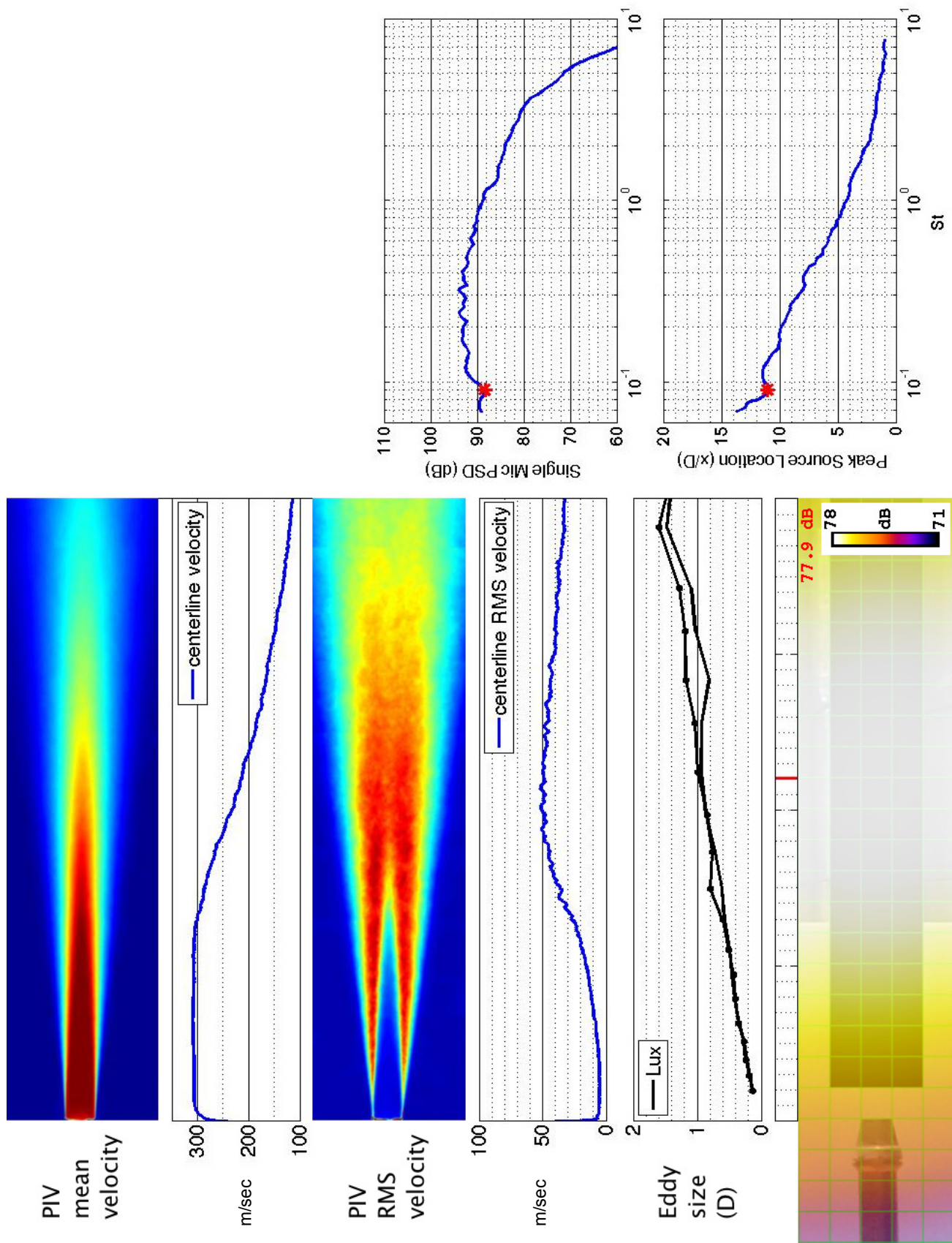
Figure 14.—SMC000; set point 7; Mj=0.98; St=0.091.
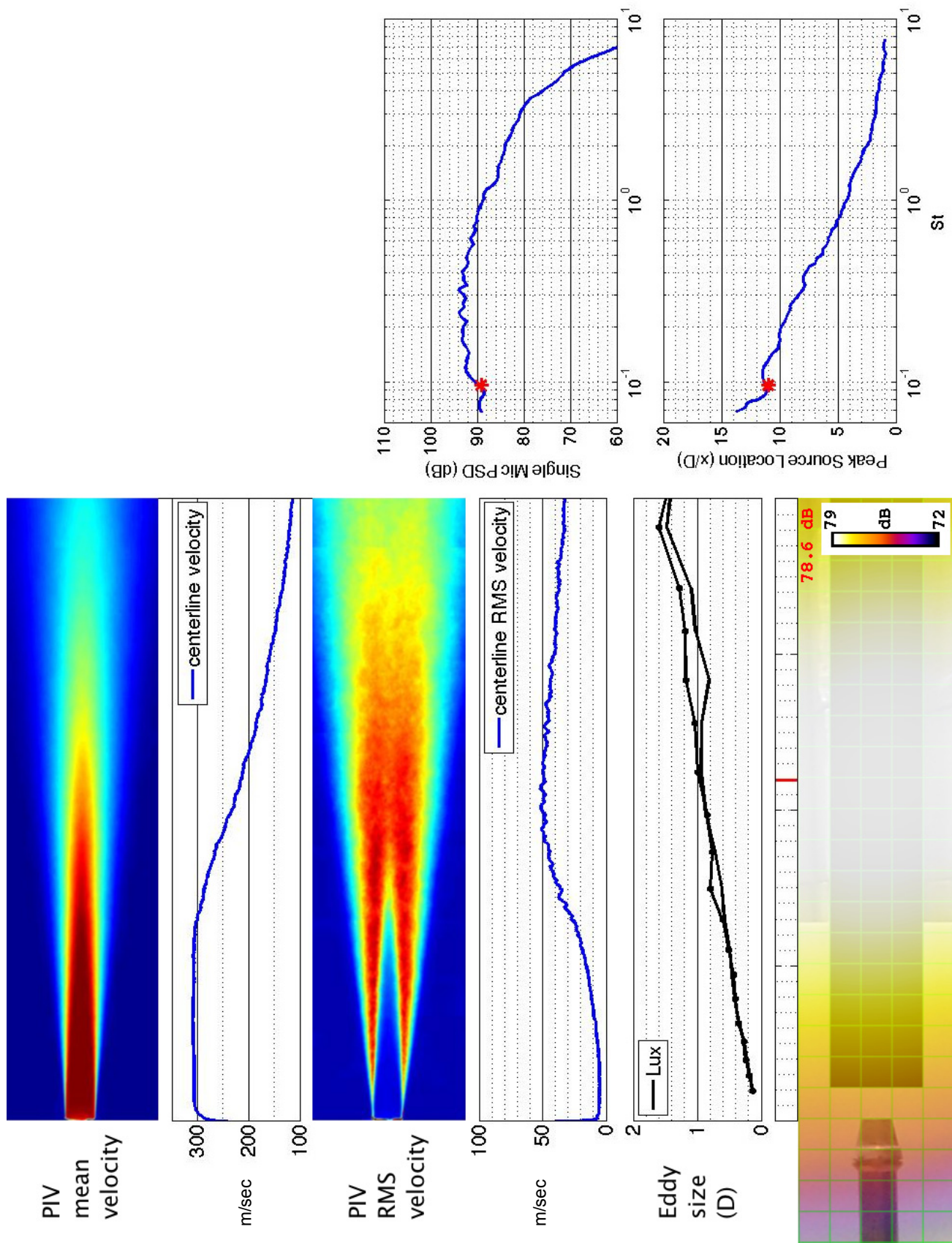
Figure 15.—SMC000; set point 7; Mj=0.98; St=0.096.
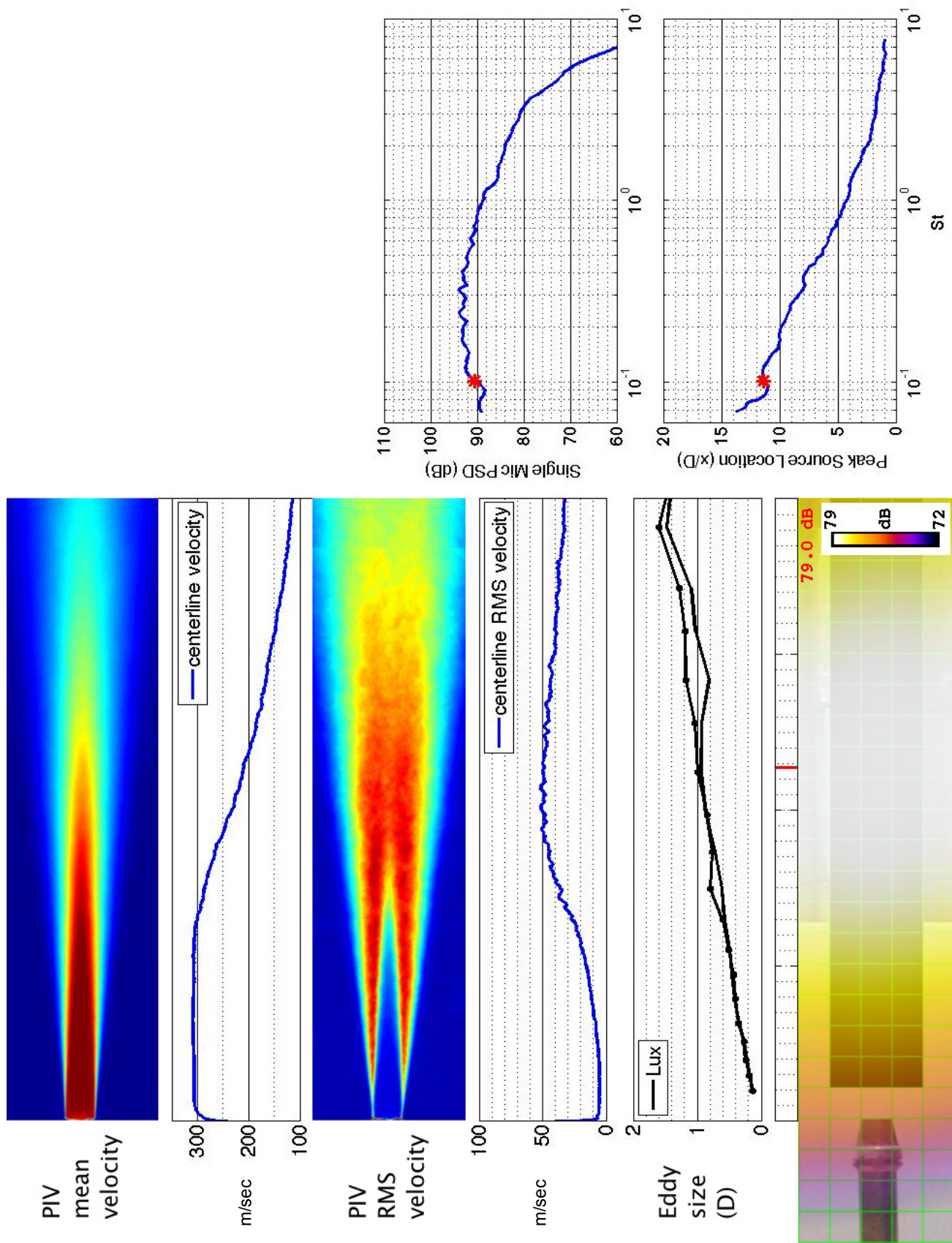
Figure 16.—SMC000; set point 7; Mj=0.98; St=0.102.
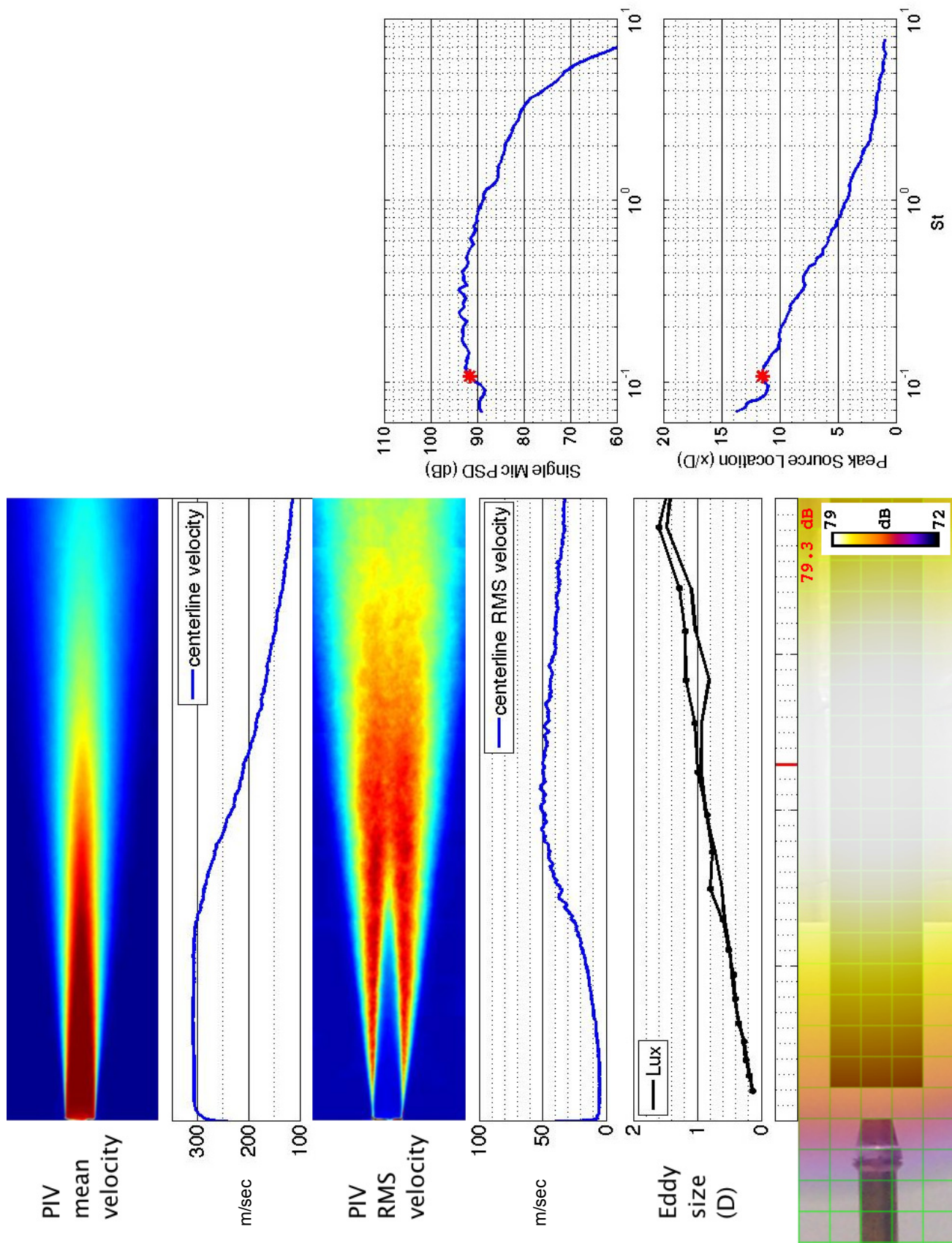
Figure 17.—SMC000; set point 7; Mj=0.98; St=0.106.
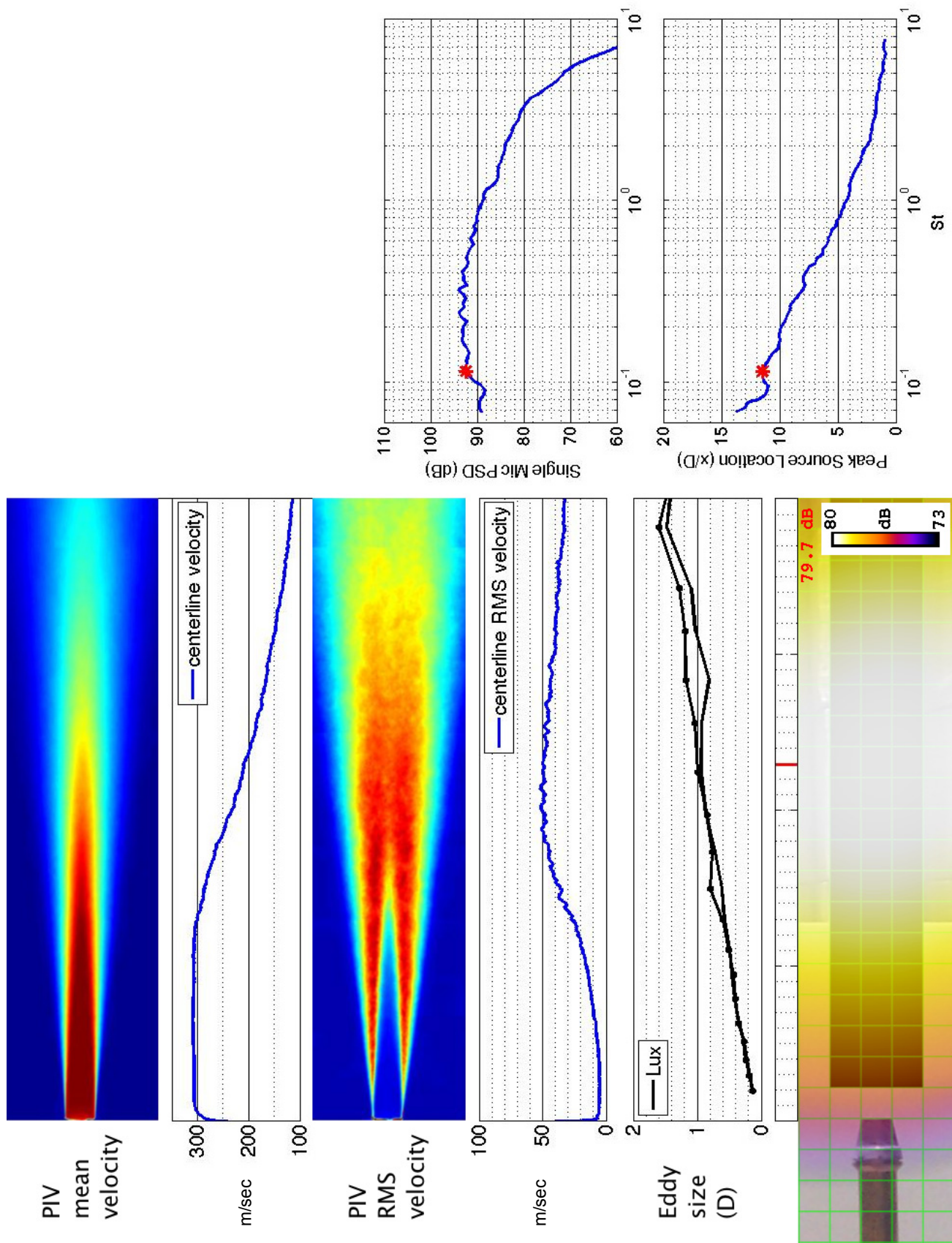
Figure 18.—SMC000; set point 7; Mj=0.98; St=0.114.
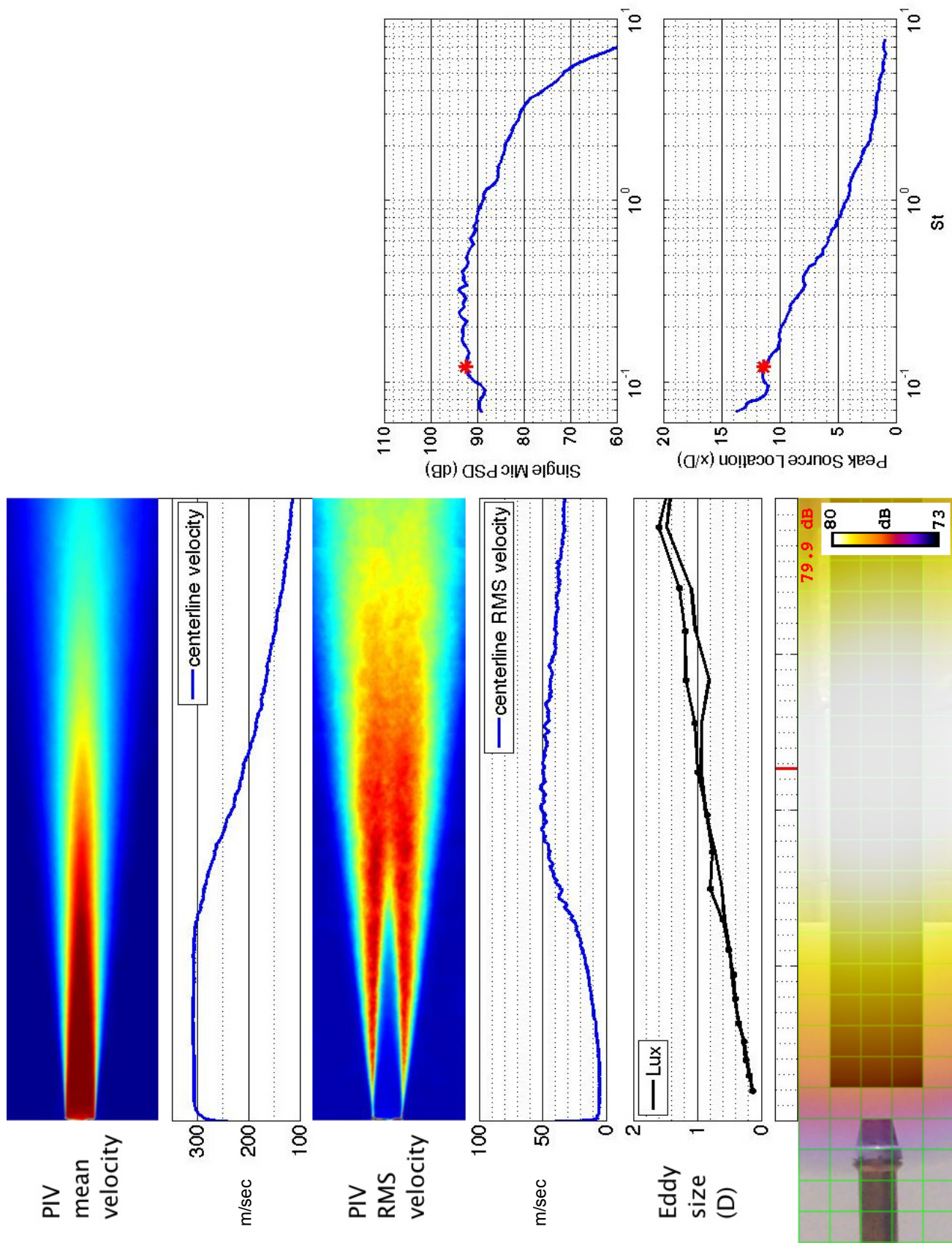
Figure 19.—SMC000; set point 7; Mj=0.98; St=0.121.
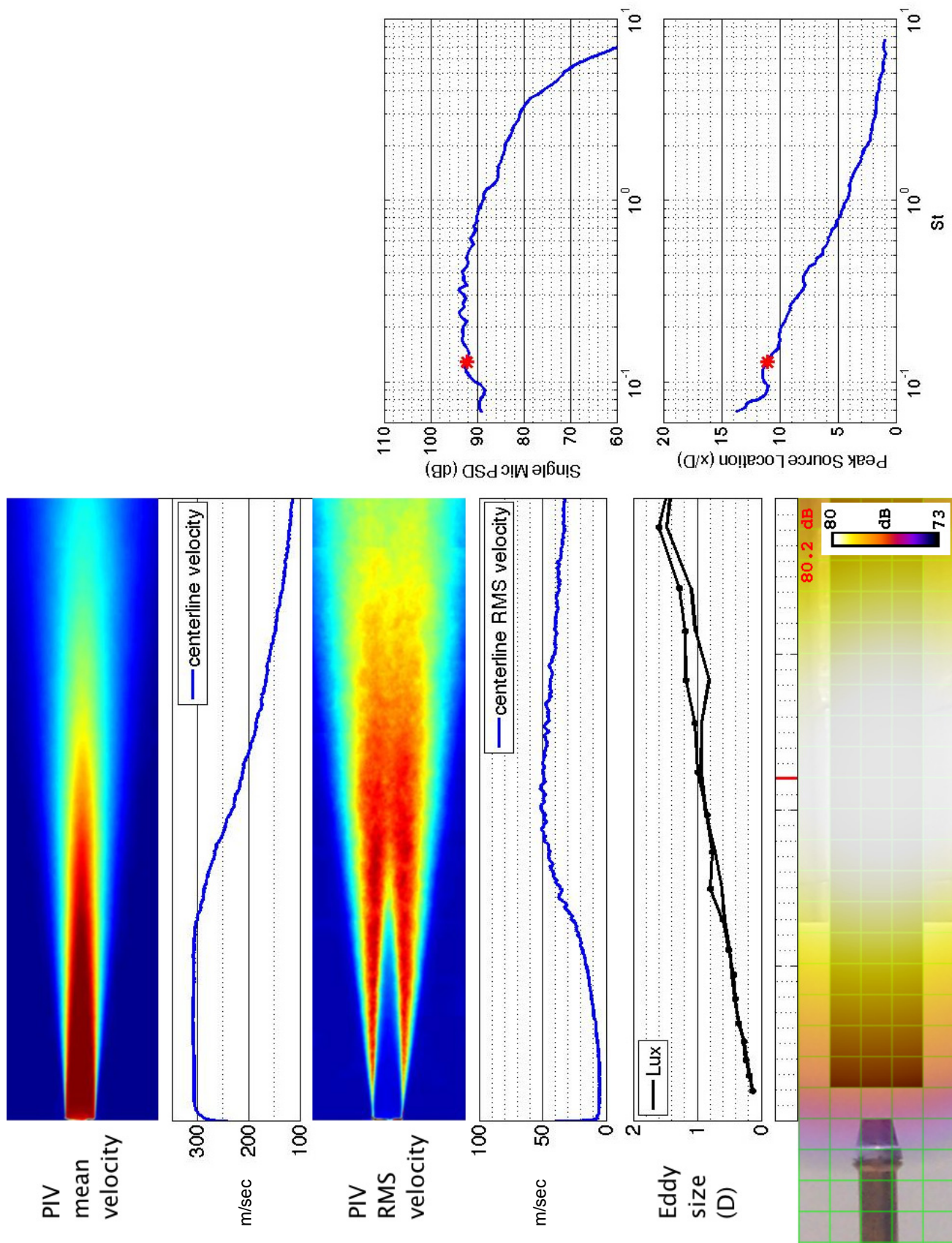
Figure 20.—SMC000; set point 7; Mj=0.98; St=0.129.
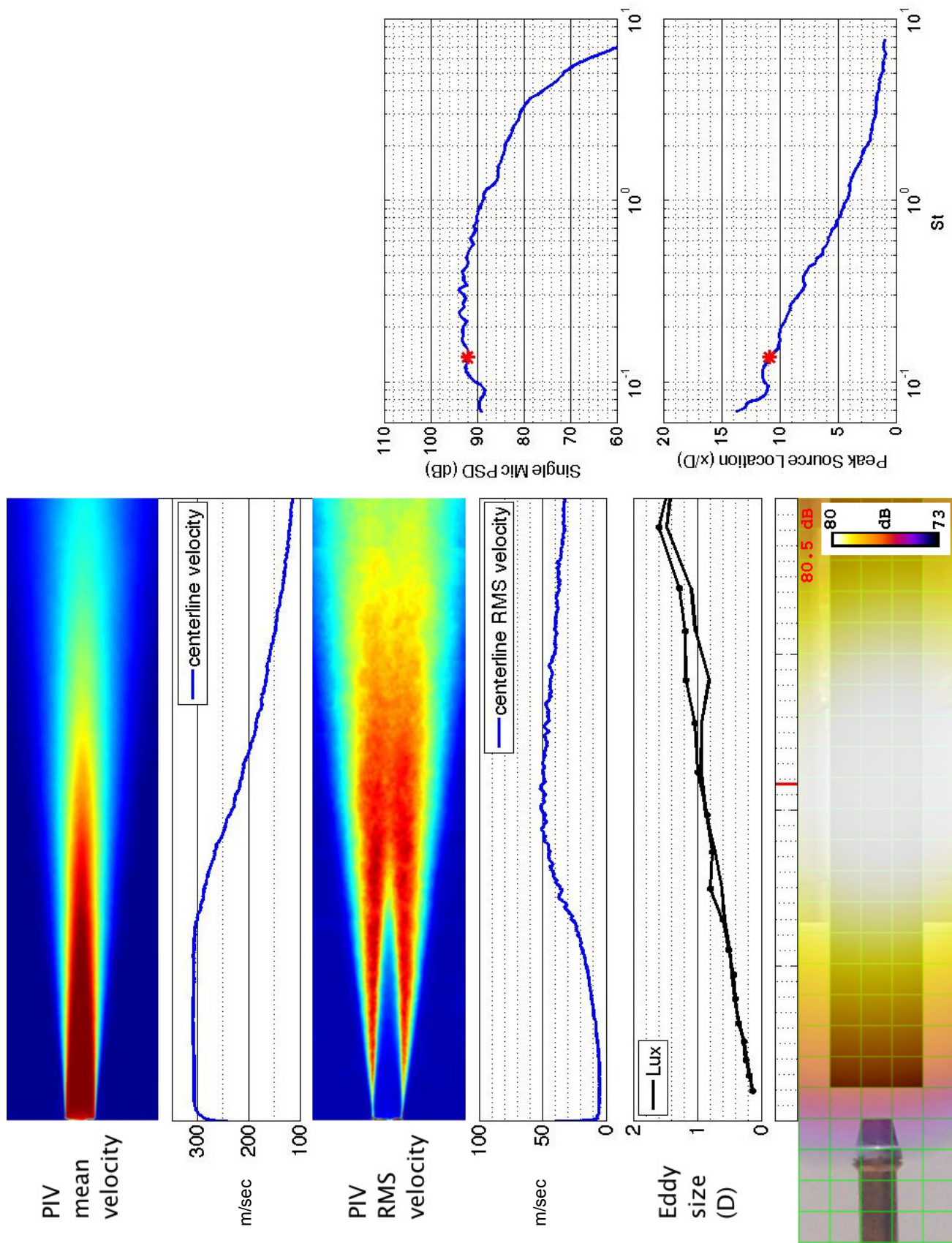
Figure 21.—SMC000; set point 7; Mj=0.98; St=0.137.
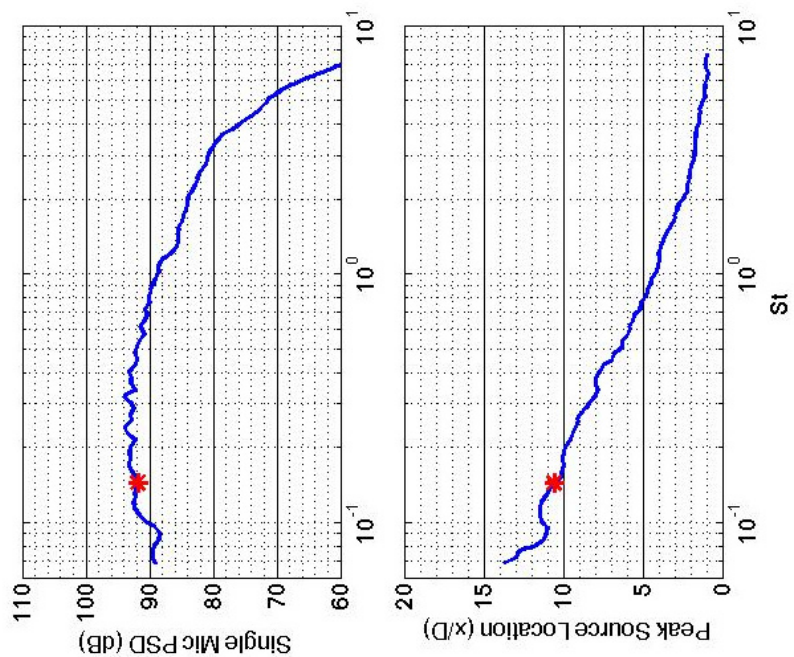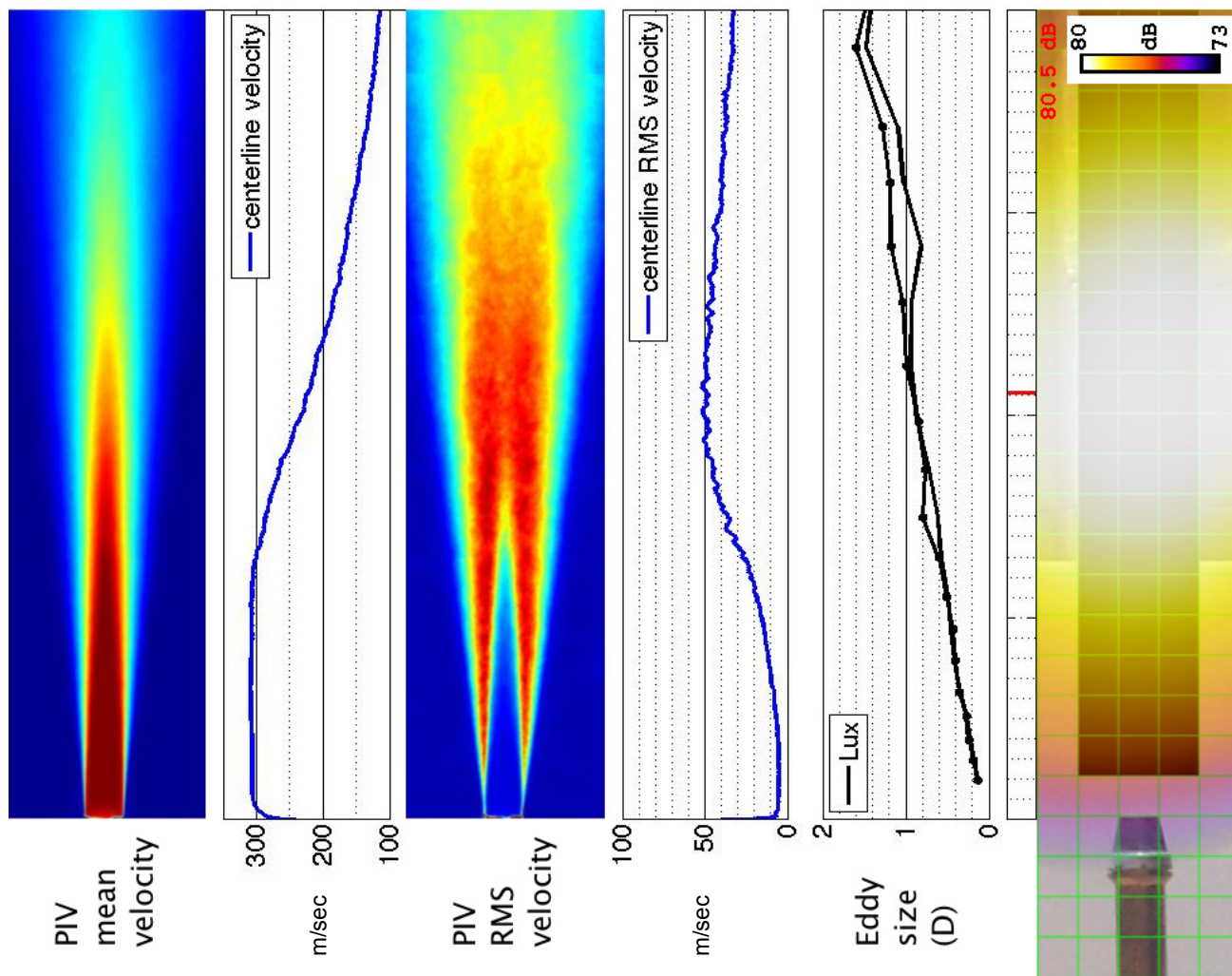
Figure 22.—SMC000; set point 7; Mj=0.98; St=0.145.
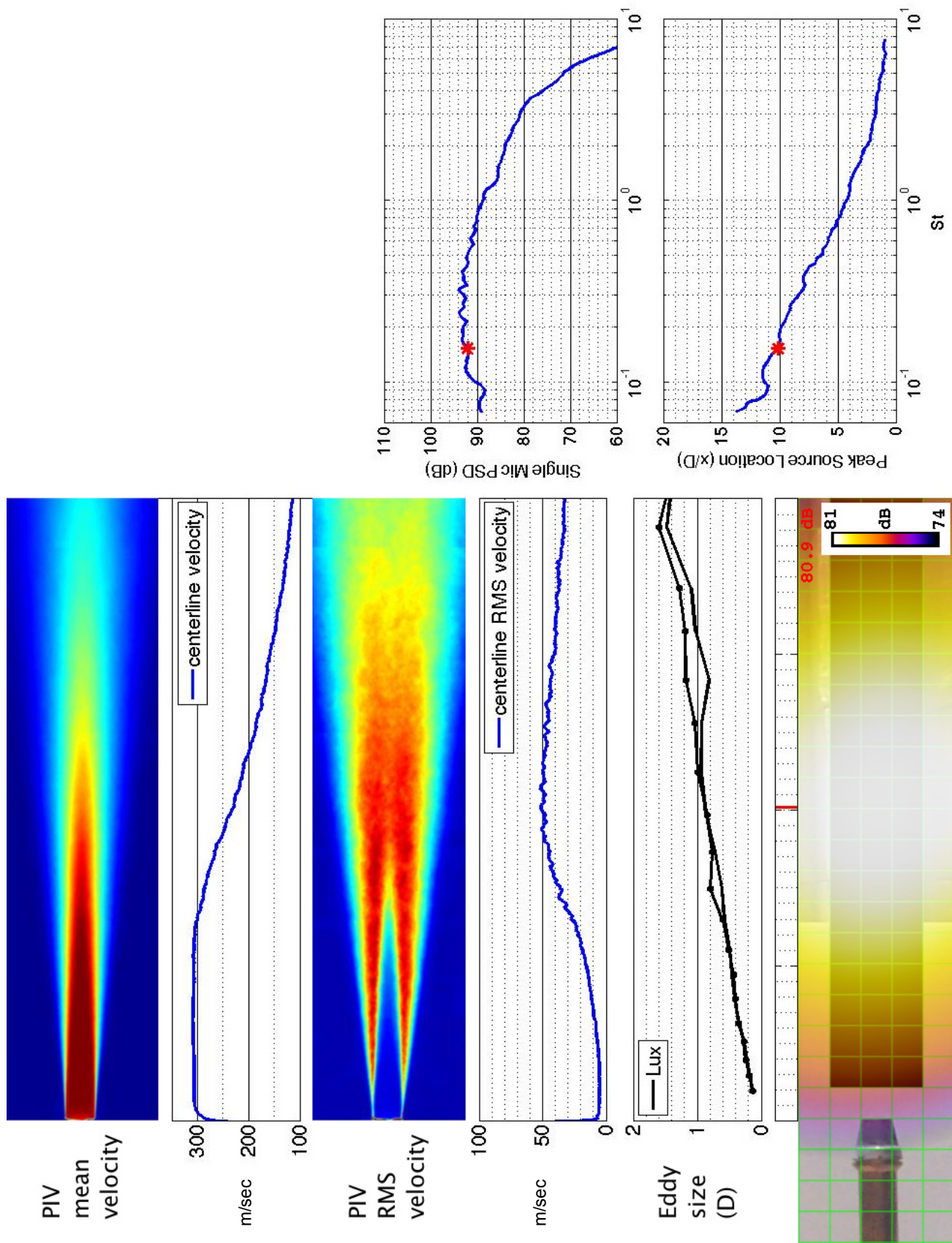
Figure 23.—SMC000; set point 7; Mj=0.98; St=0.153.
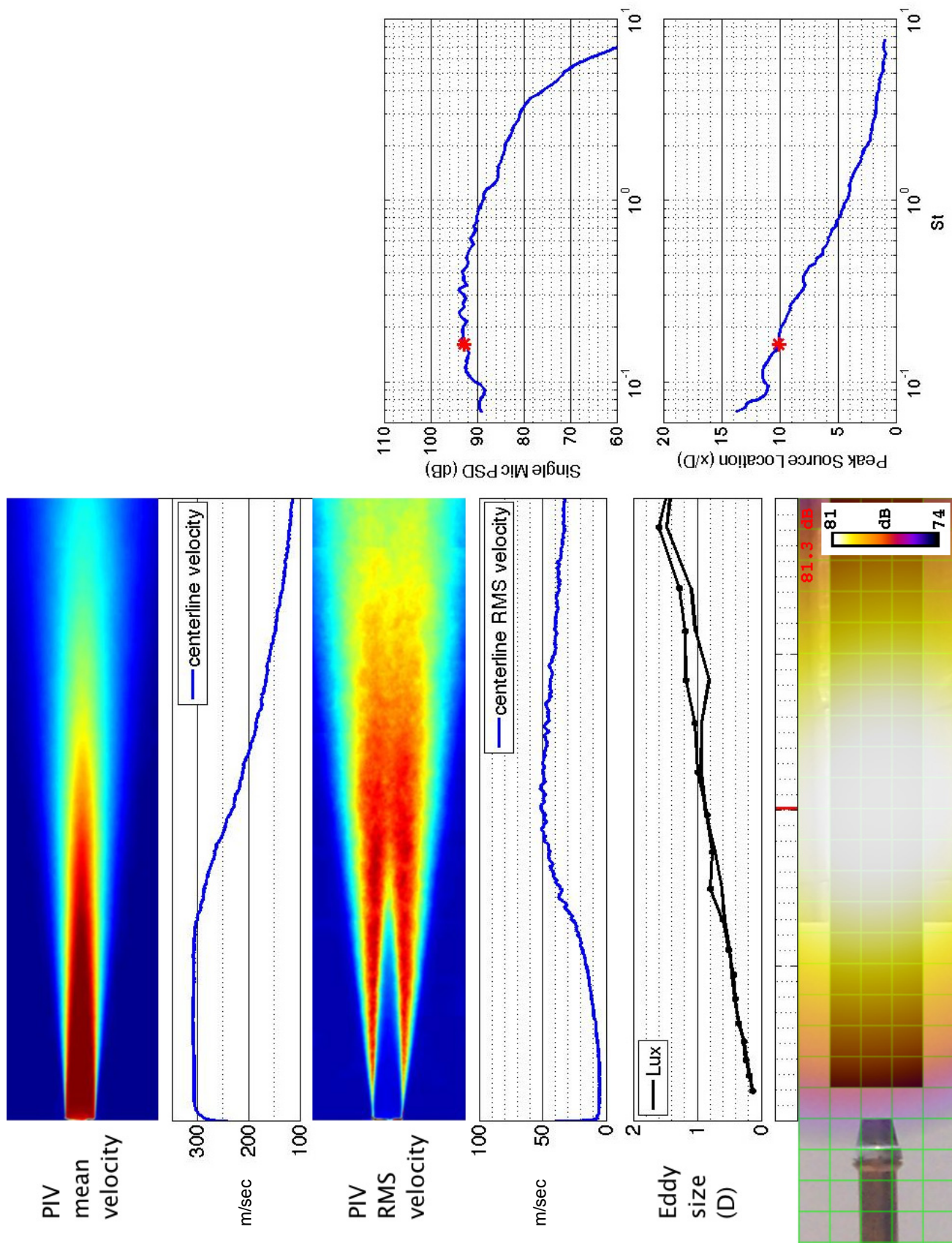
Figure 24.—SMC000; set point 7; Mj=0.98; St=0.162.
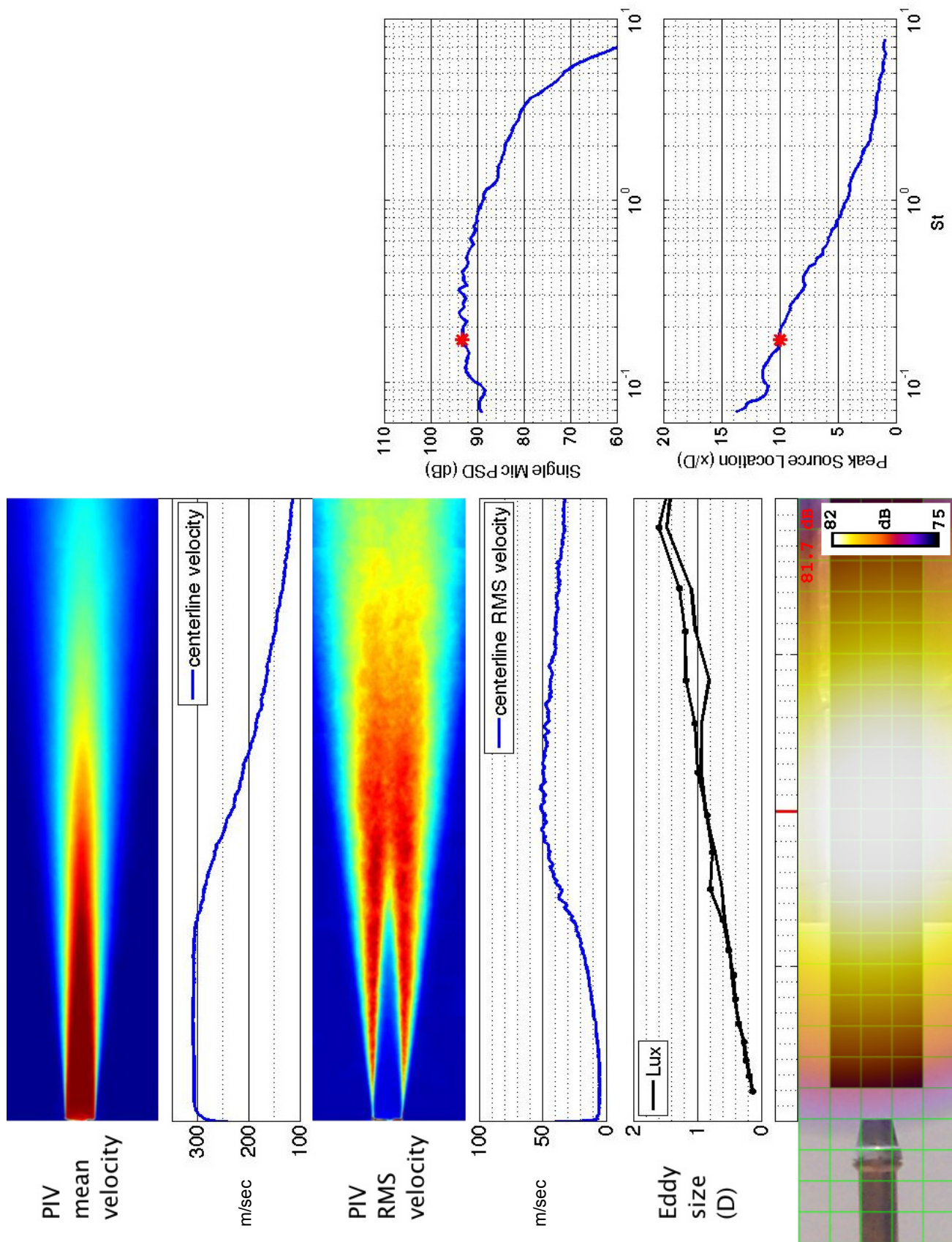
Figure 25.—SMC000; set point 7; Mj=0.98; St=0.171.
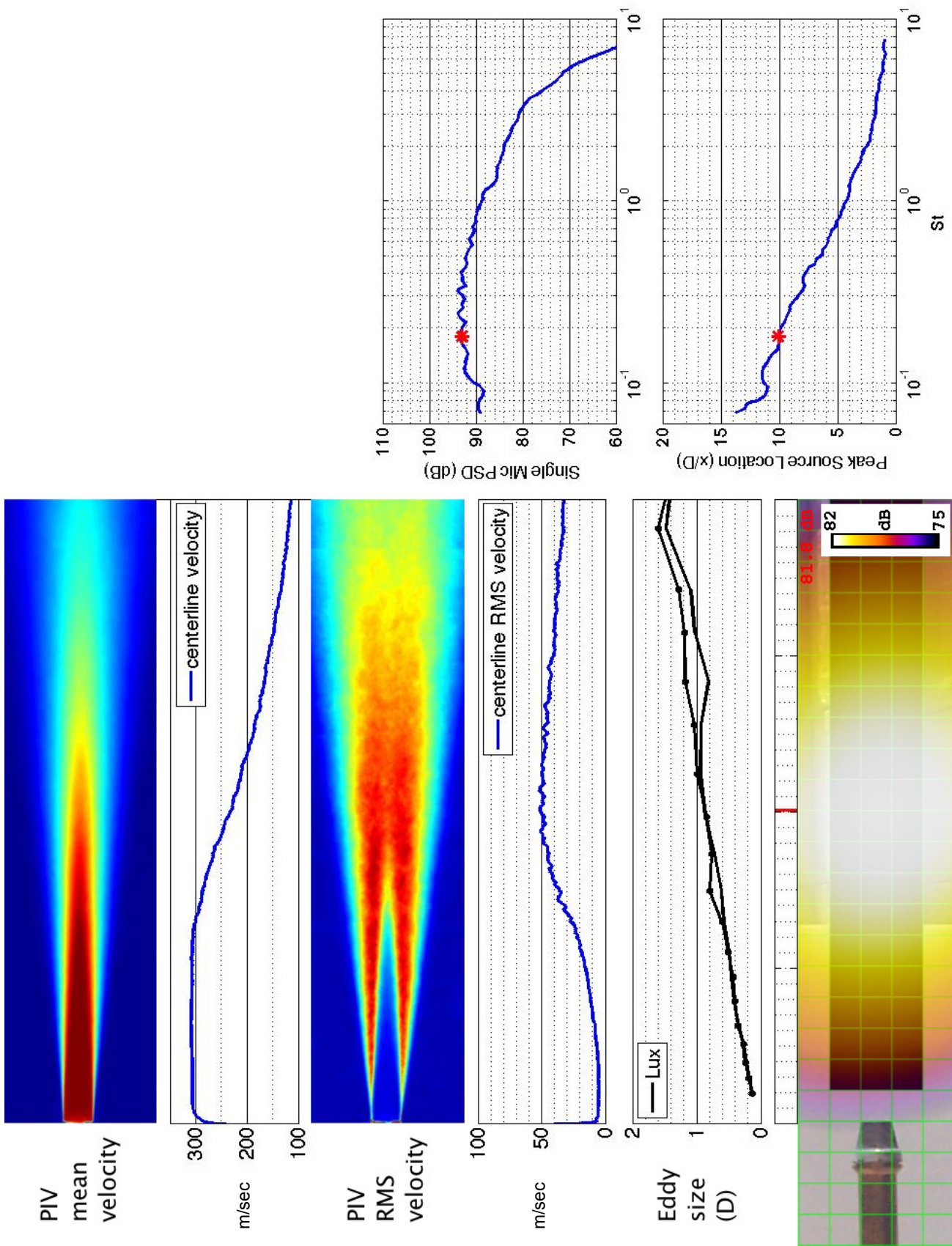
Figure 26.—SMC000; set point 7; Mj=0.98; St=0.181.
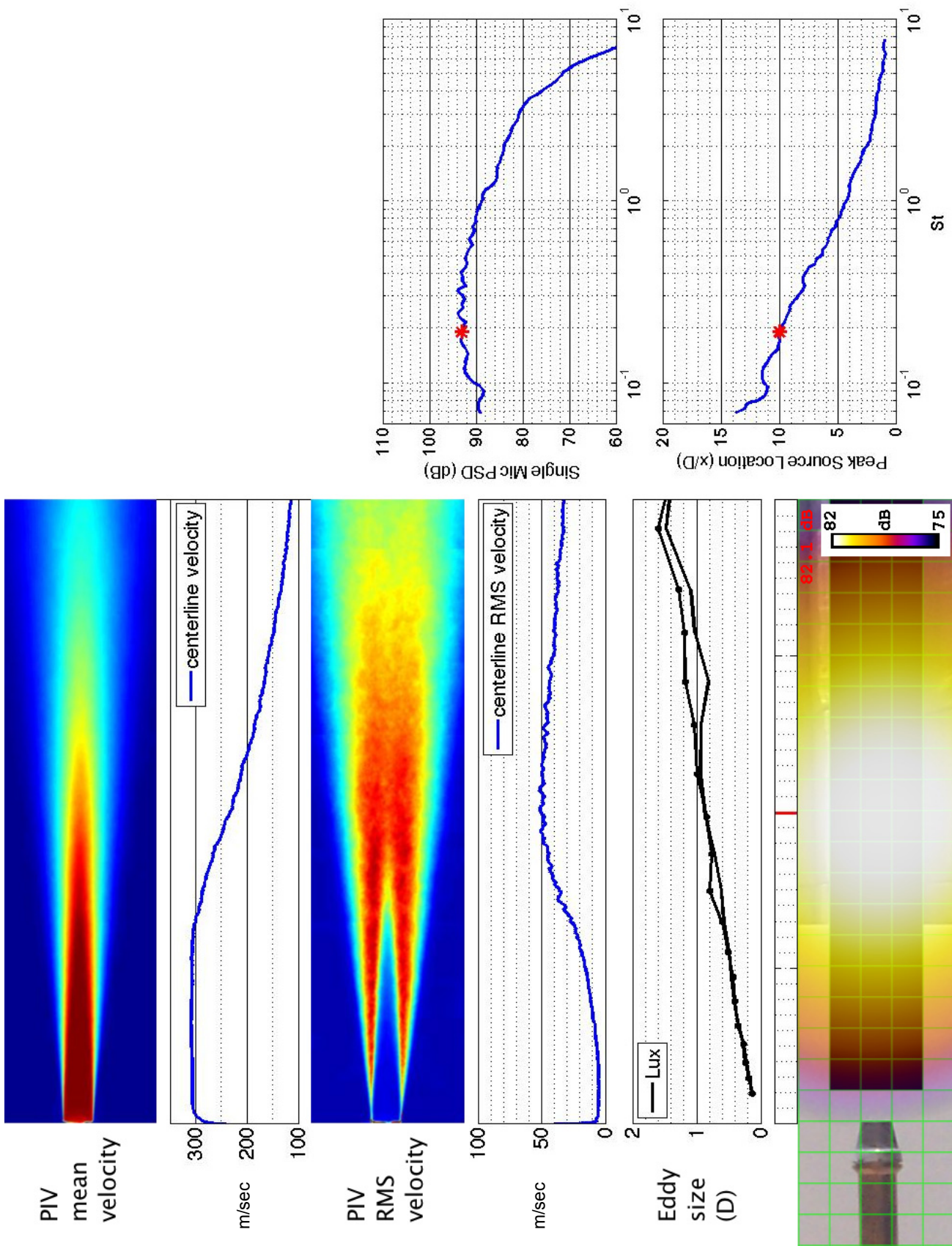
Figure 27.—SMC000; set point 7; Mj=0.98; St=0.191.
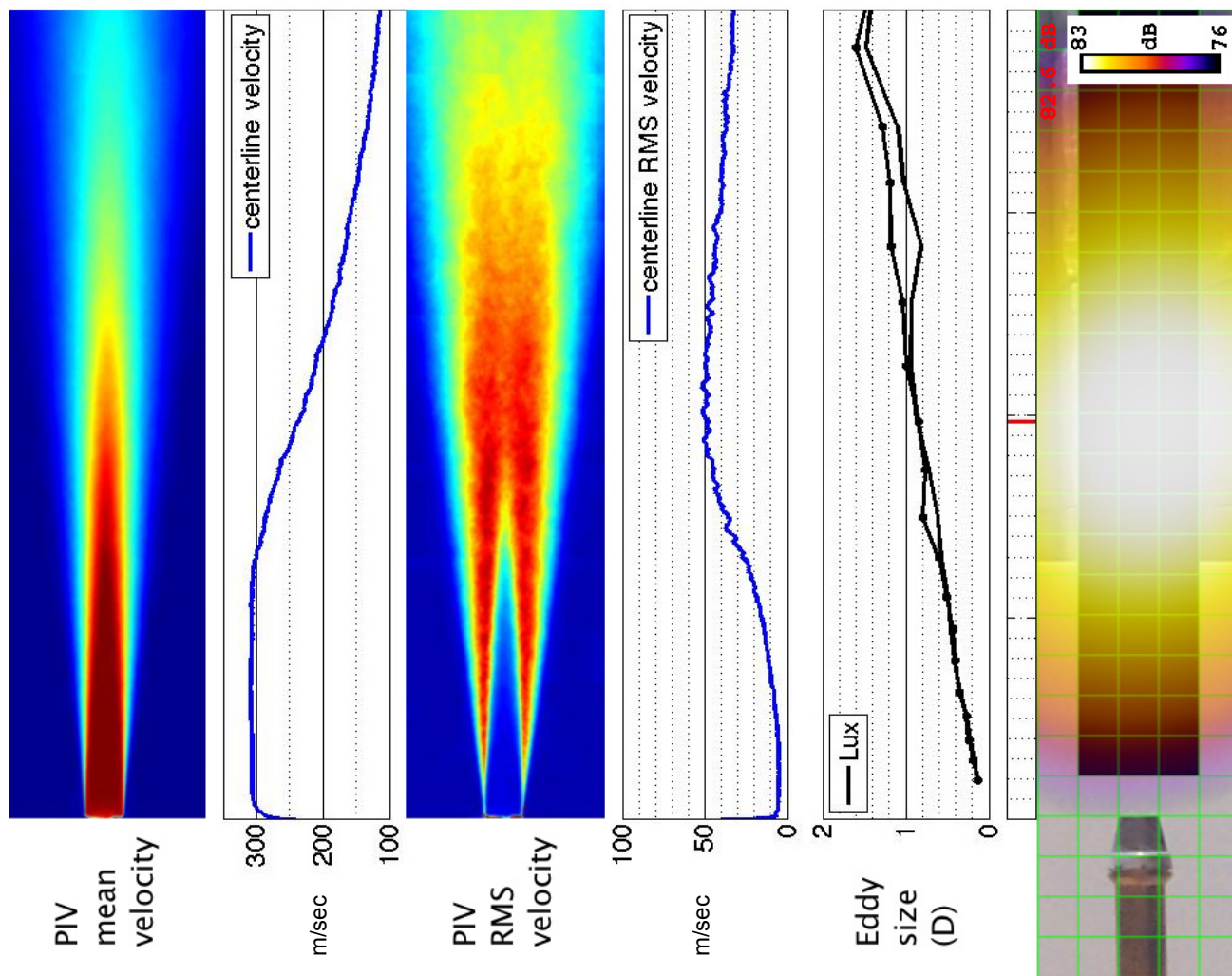
Figure 28.—SMC000; set point 7; Mj=0.98; St=0.202.
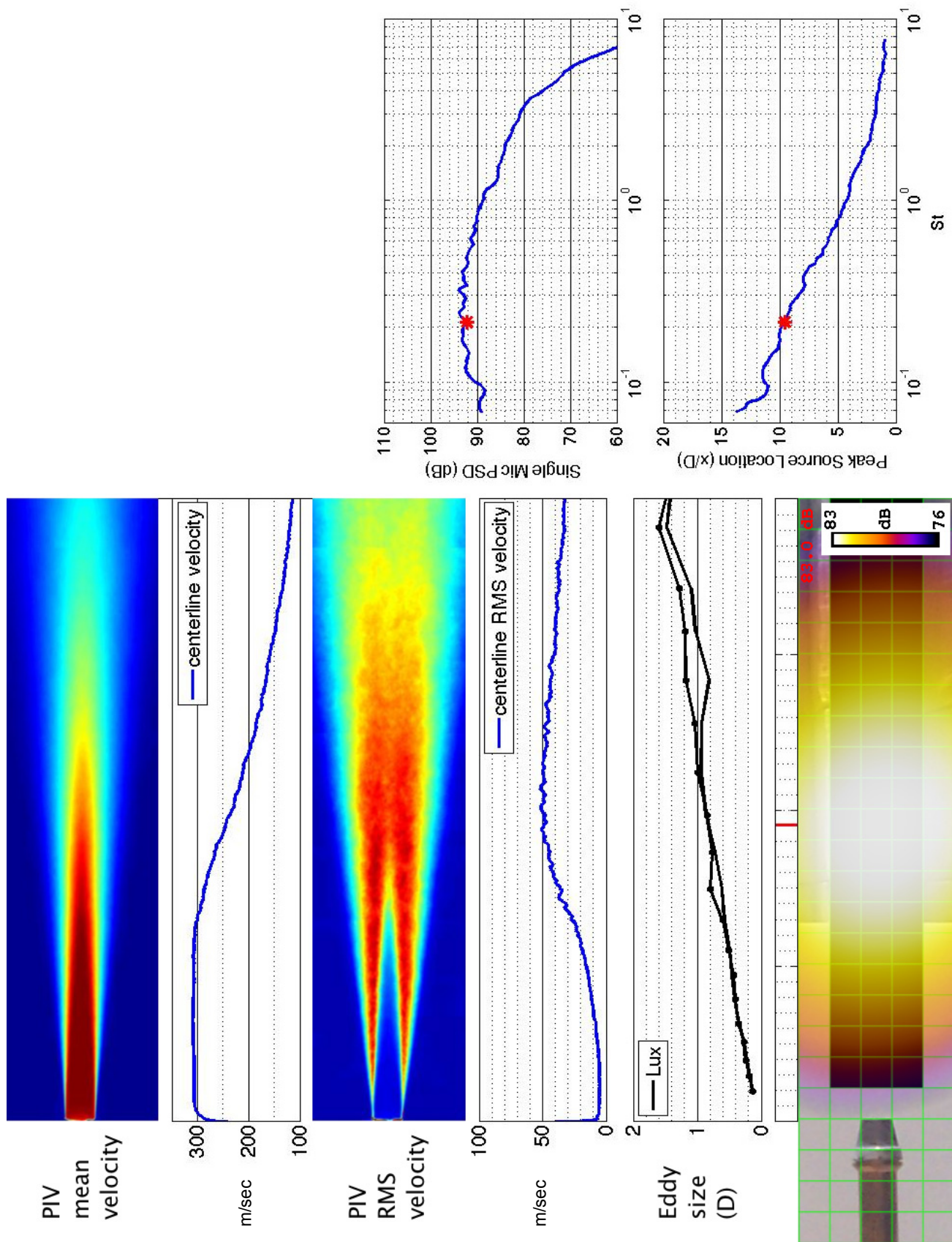
Figure 29.—SMC000; set point 7; Mj=0.98; St=0.214.
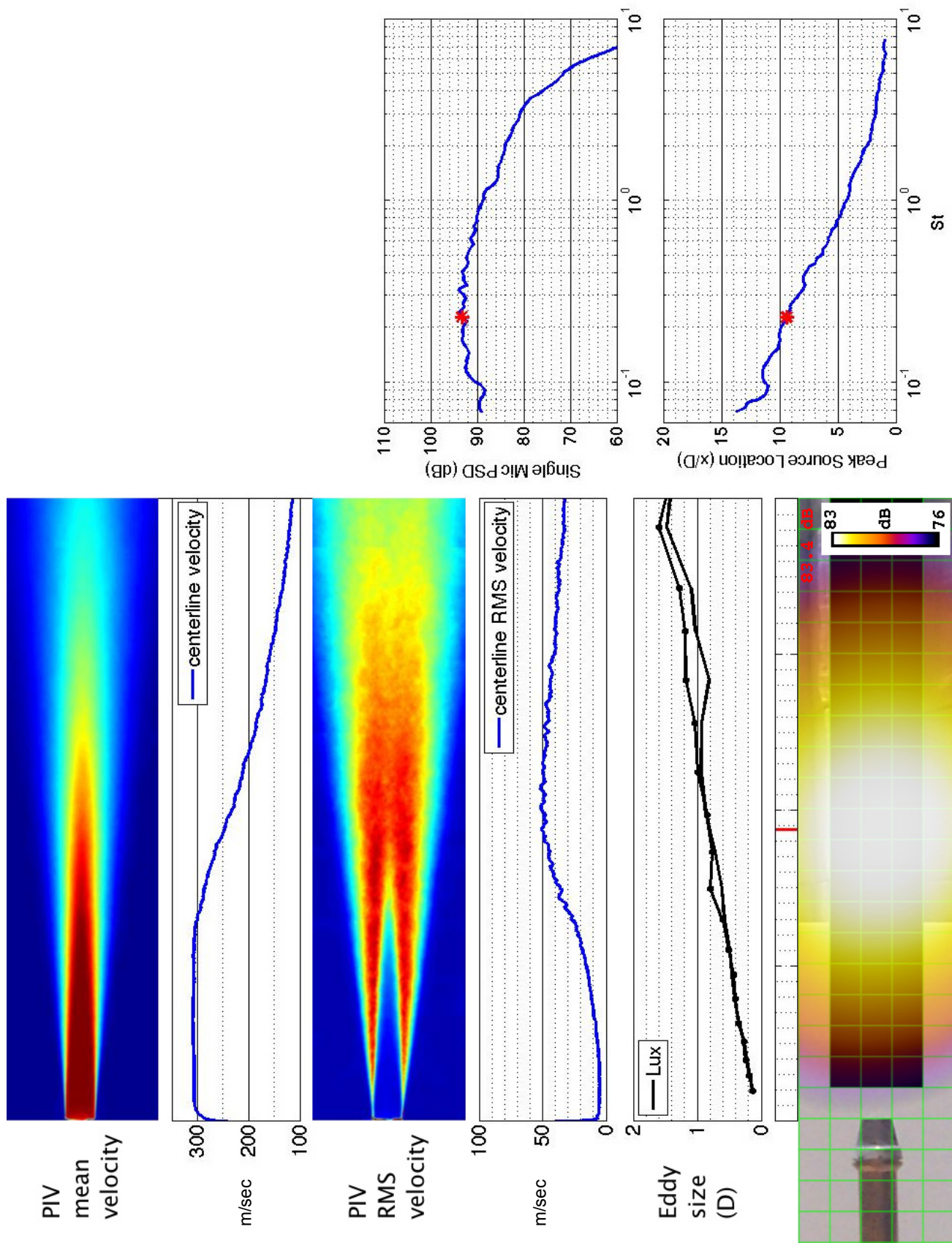
Figure 30.—SMC000; set point 7; Mj=0.98; St=0.227.
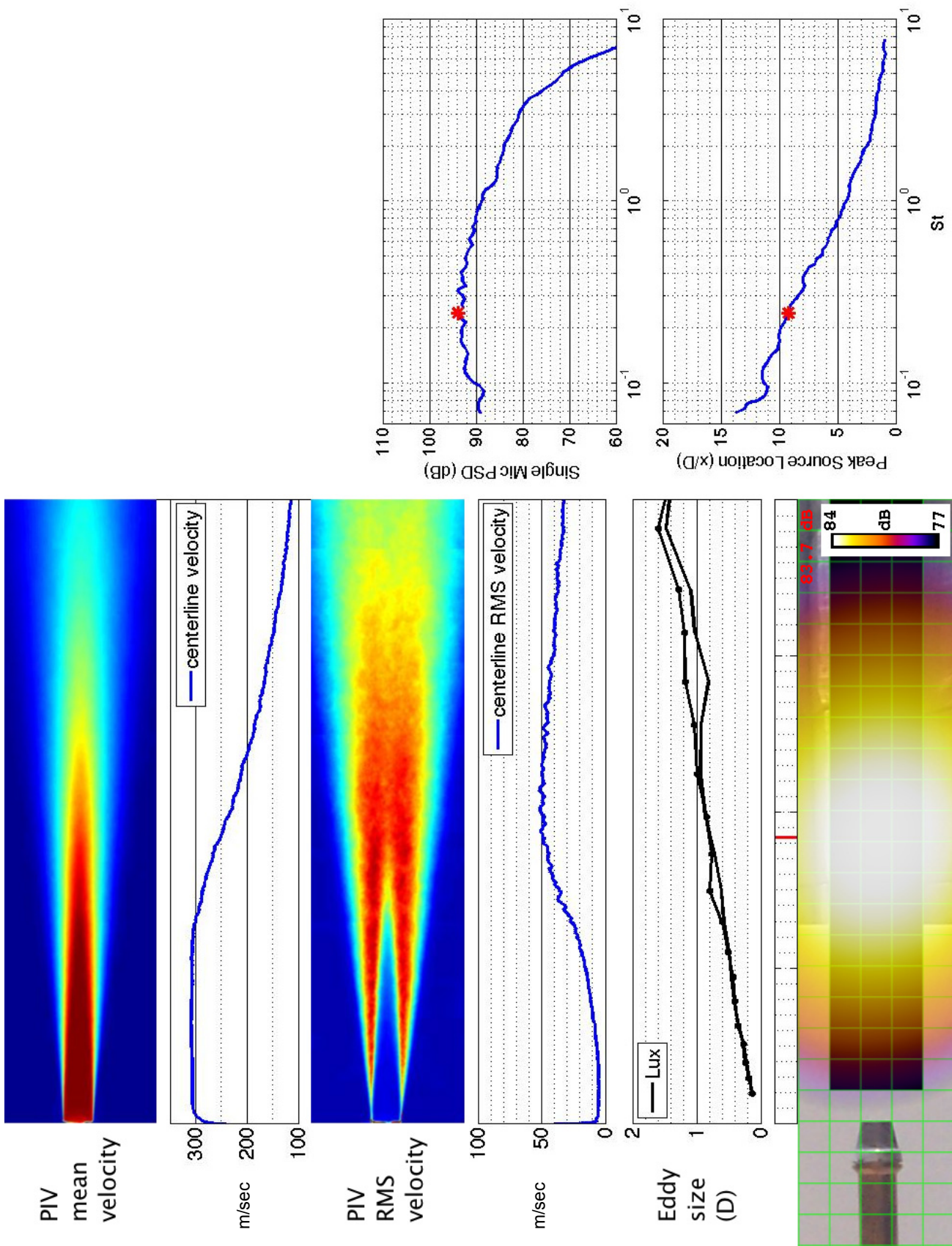
Figure 31.—SMC000; set point 7; Mj=0.98; St=0.242.
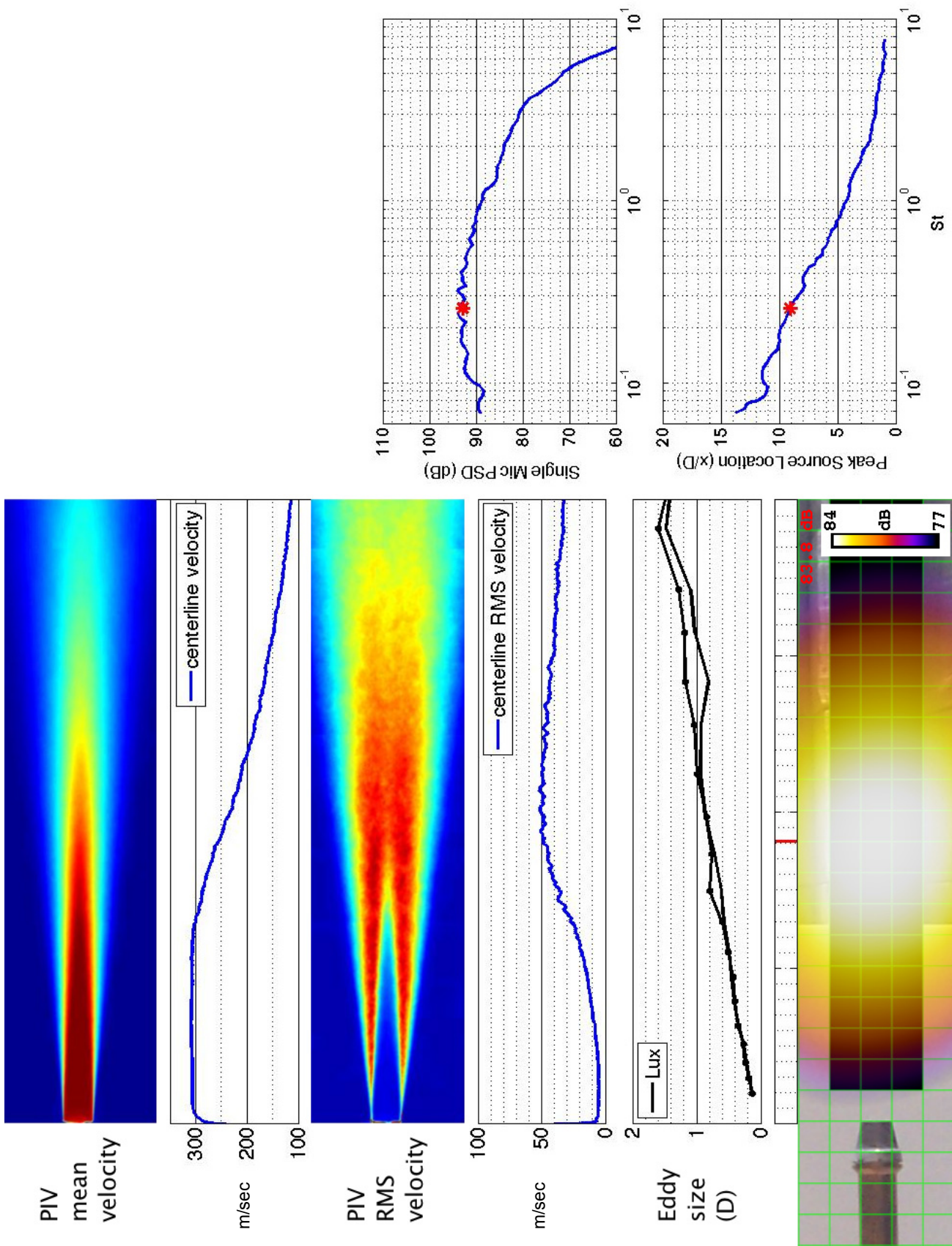
Figure 32.—SMC000; set point 7; Mj=0.98; St=0.257.
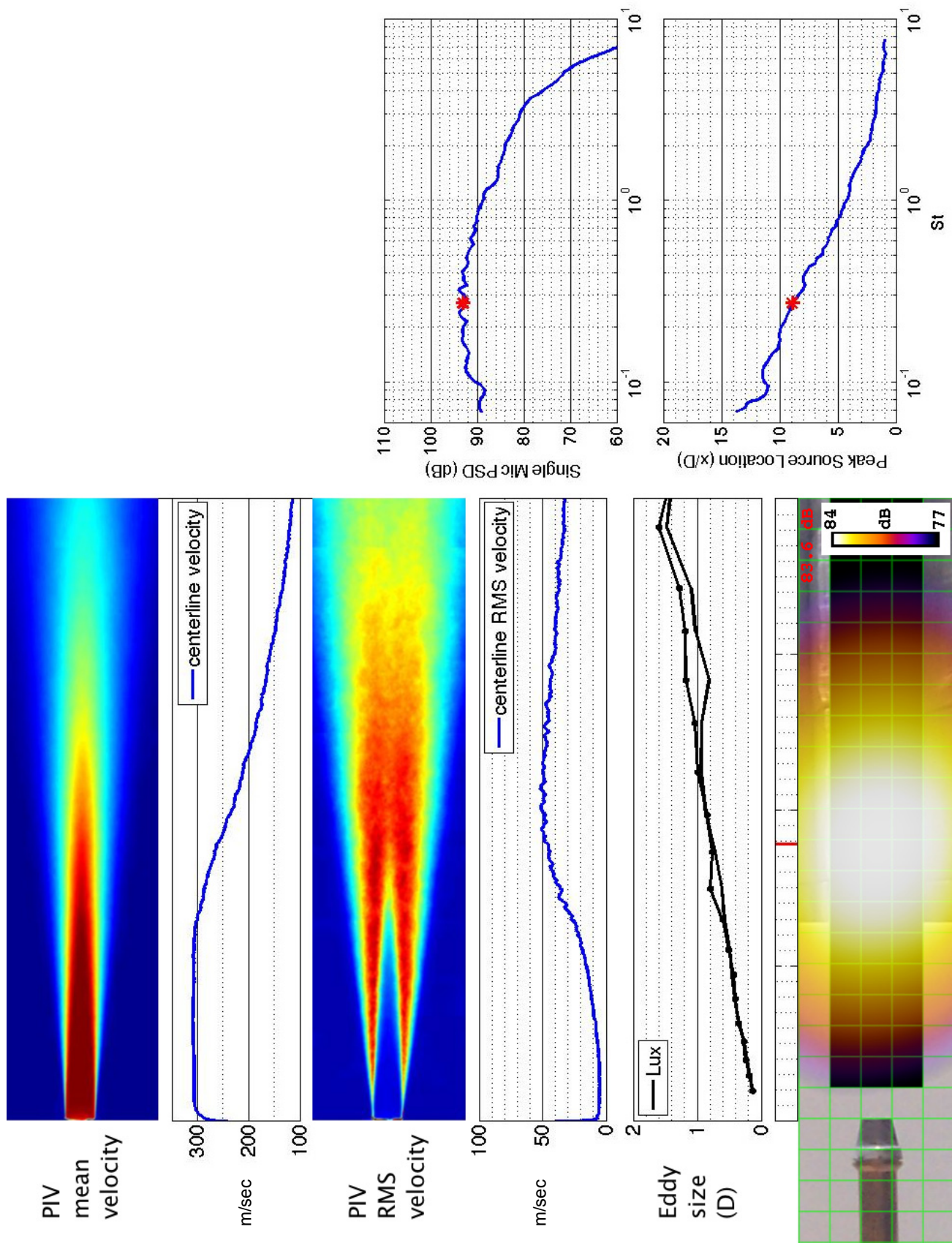
Figure 33.—SMC000; set point 7; Mj=0.98; St=0.273.
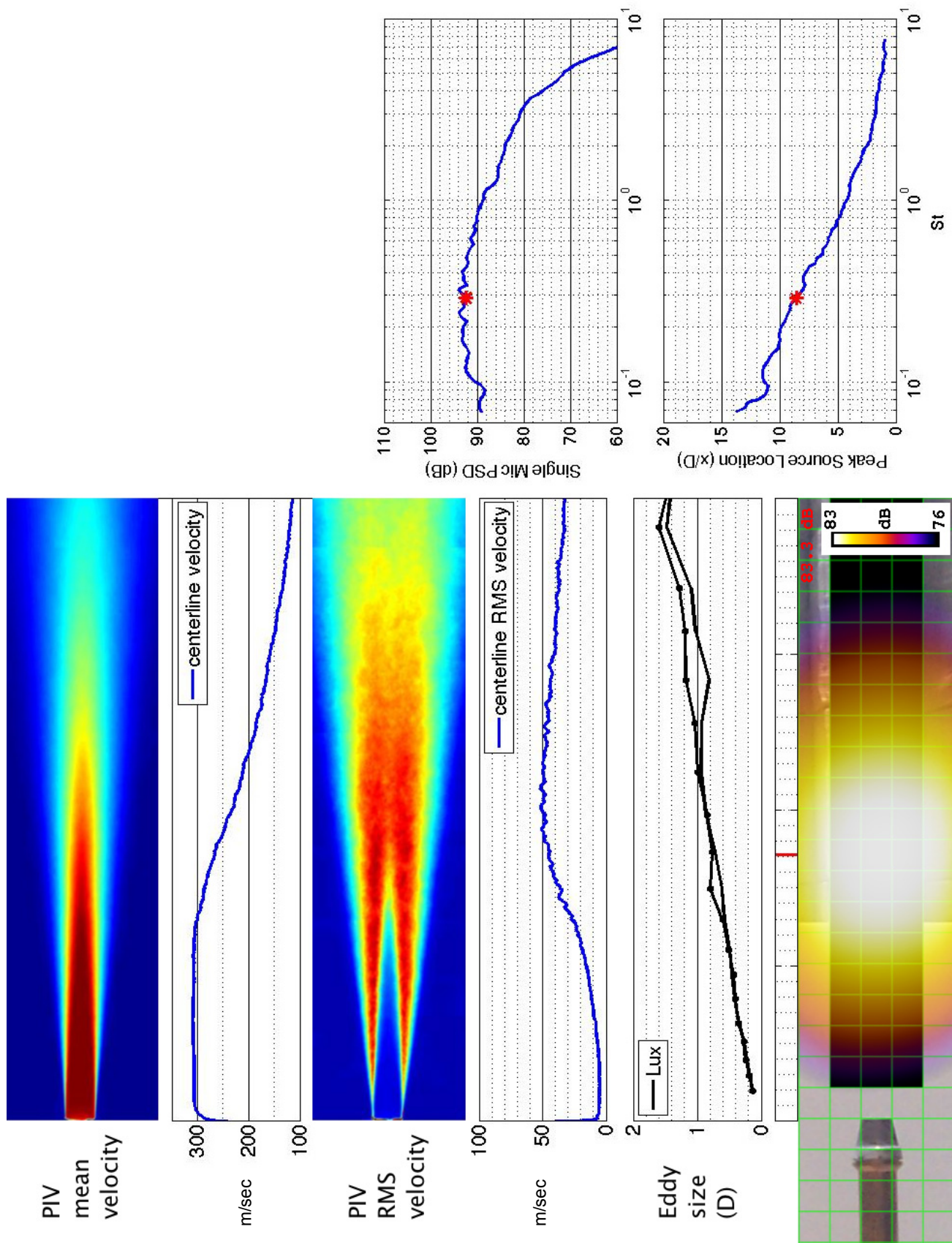
Figure 34.—SMC000; set point 7; Mj=0.98; St=0.289.
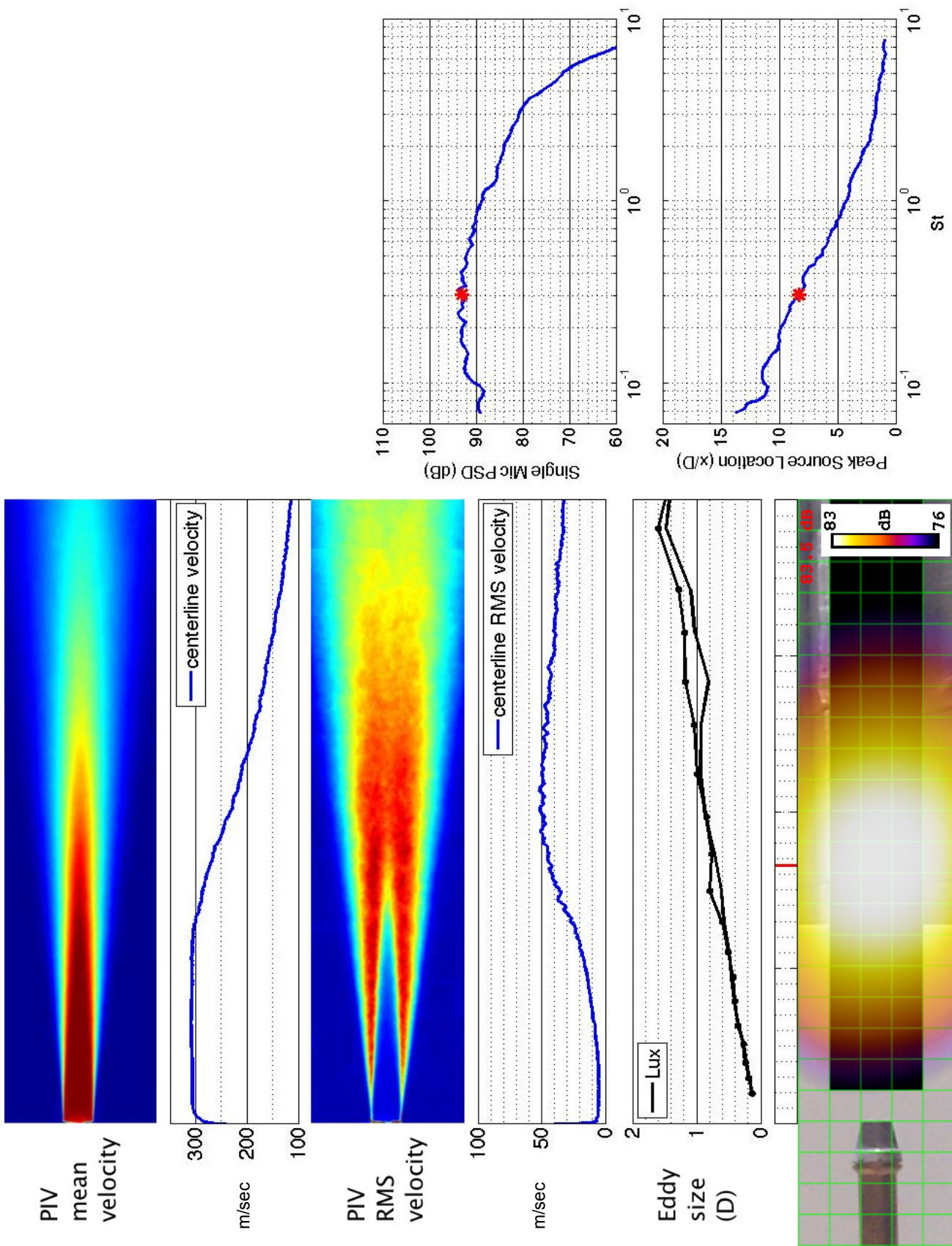
Figure 35.—SMC000; set point 7; Mj=0.98; St=0.306.
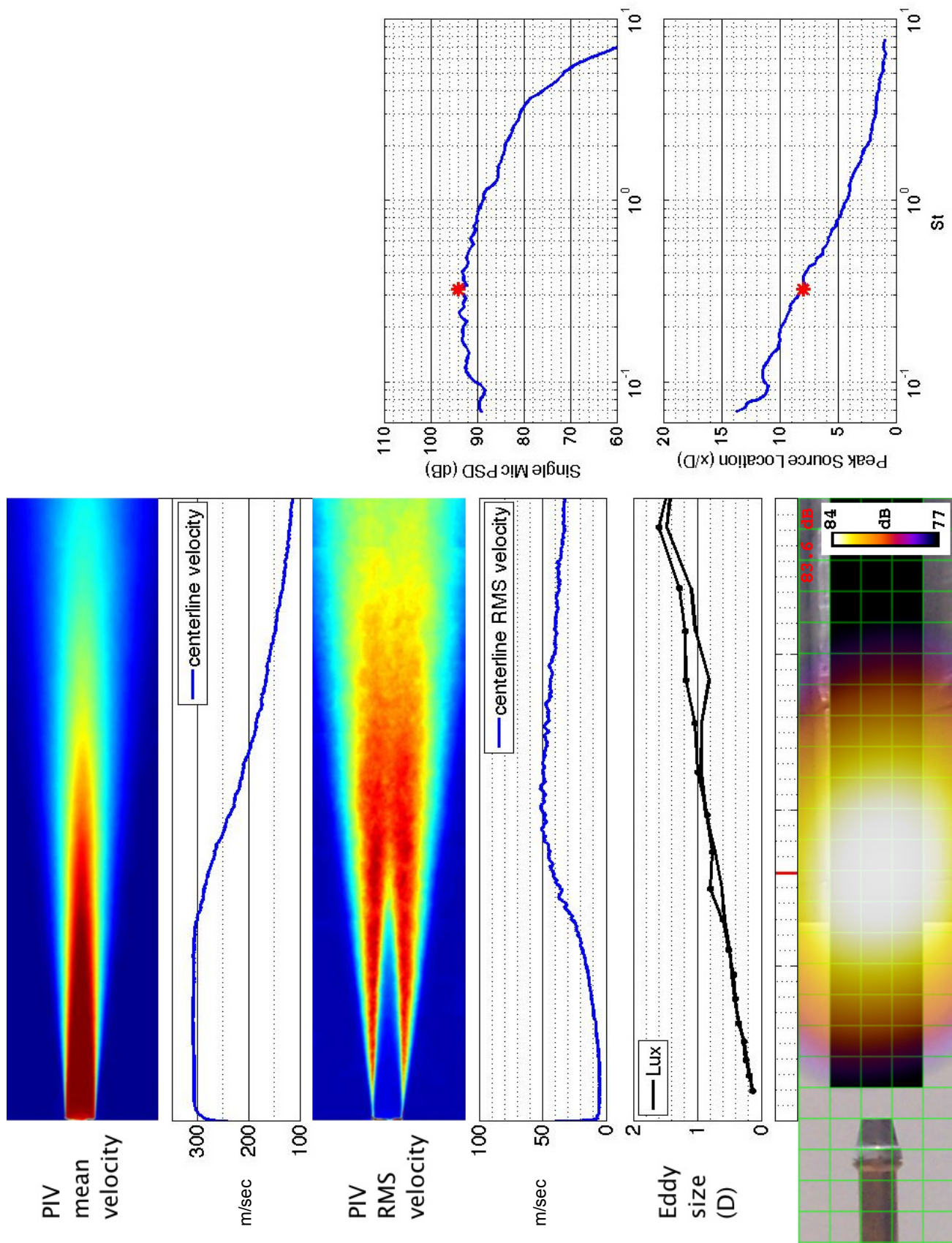
Figure 36.—SMC000; set point 7; Mj=0.98; St=0.323.
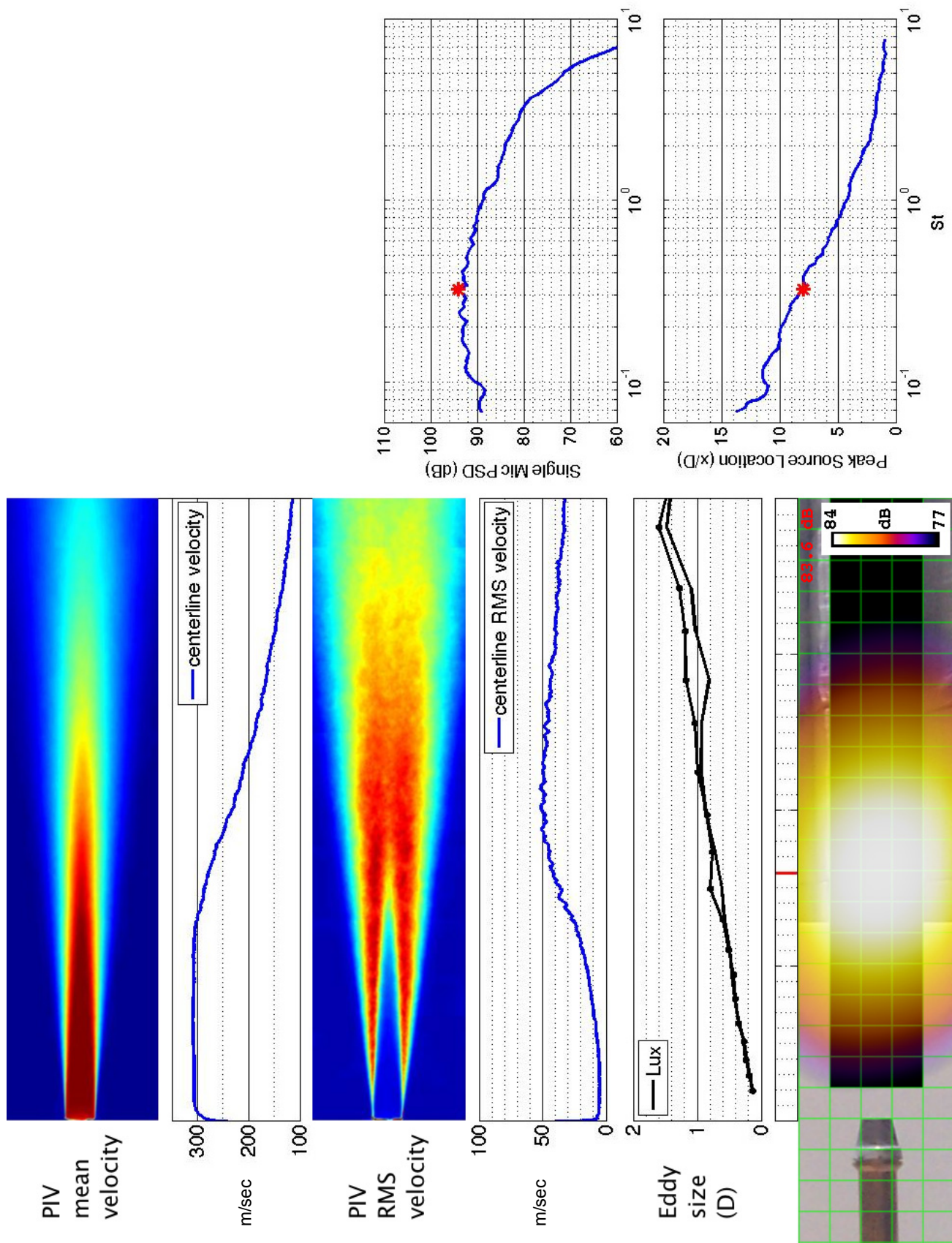
Figure 37.—SMC000; set point 7; Mj=0.98; St=0.342.
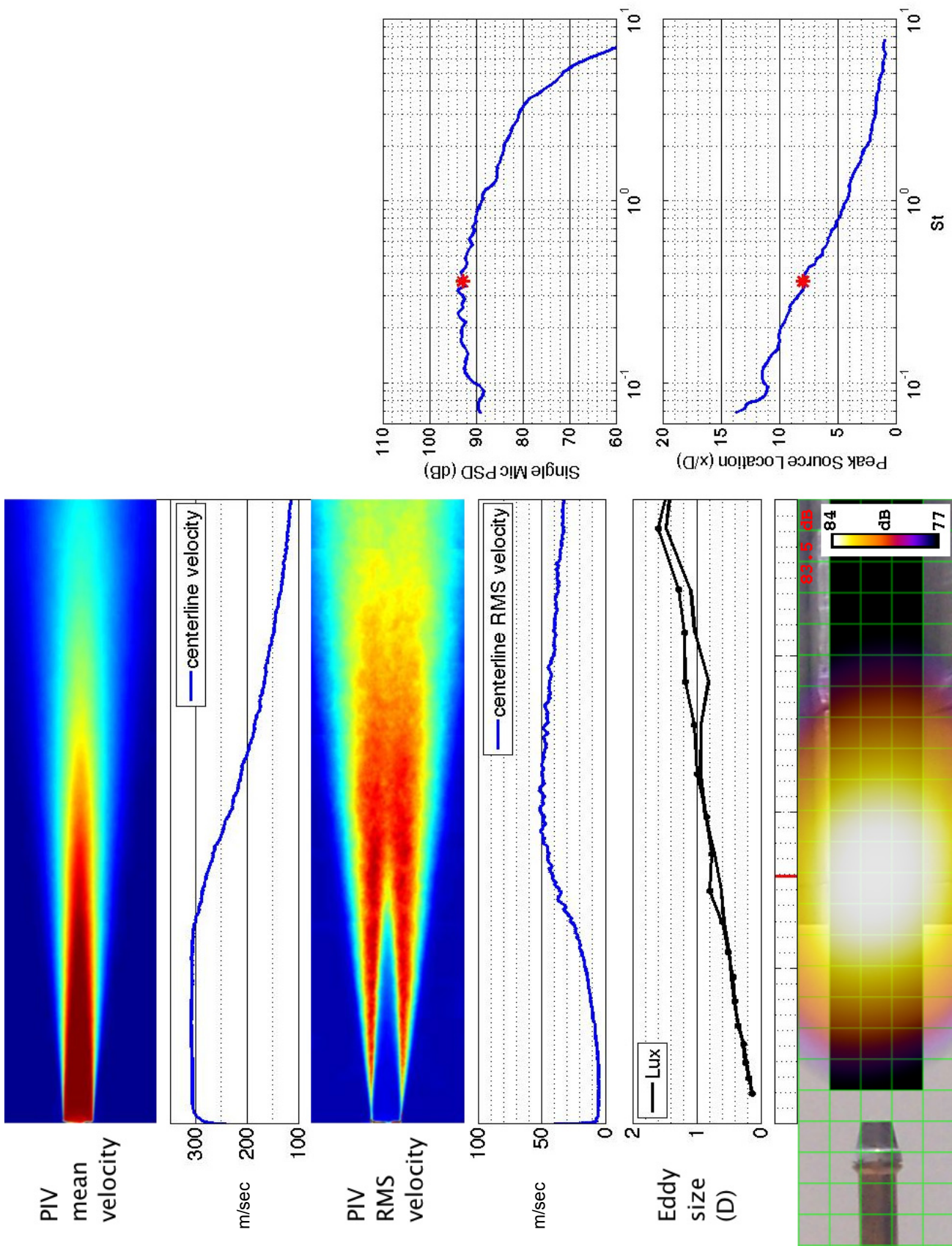
Figure 38.—SMC000; set point 7; Mj=0.98; St=0.361.
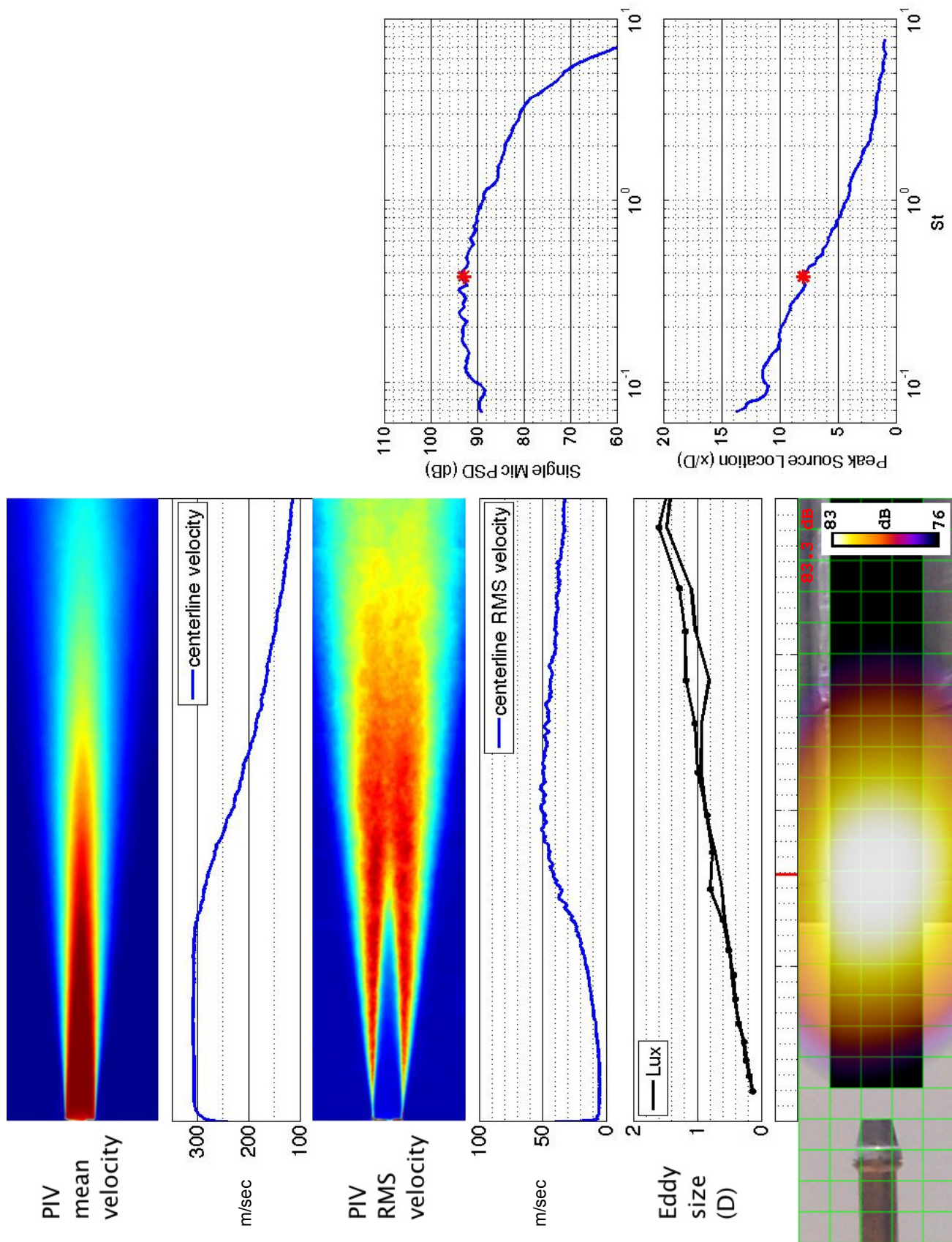
Figure 39.—SMC000; set point 7; Mj=0.98; St=0.382.
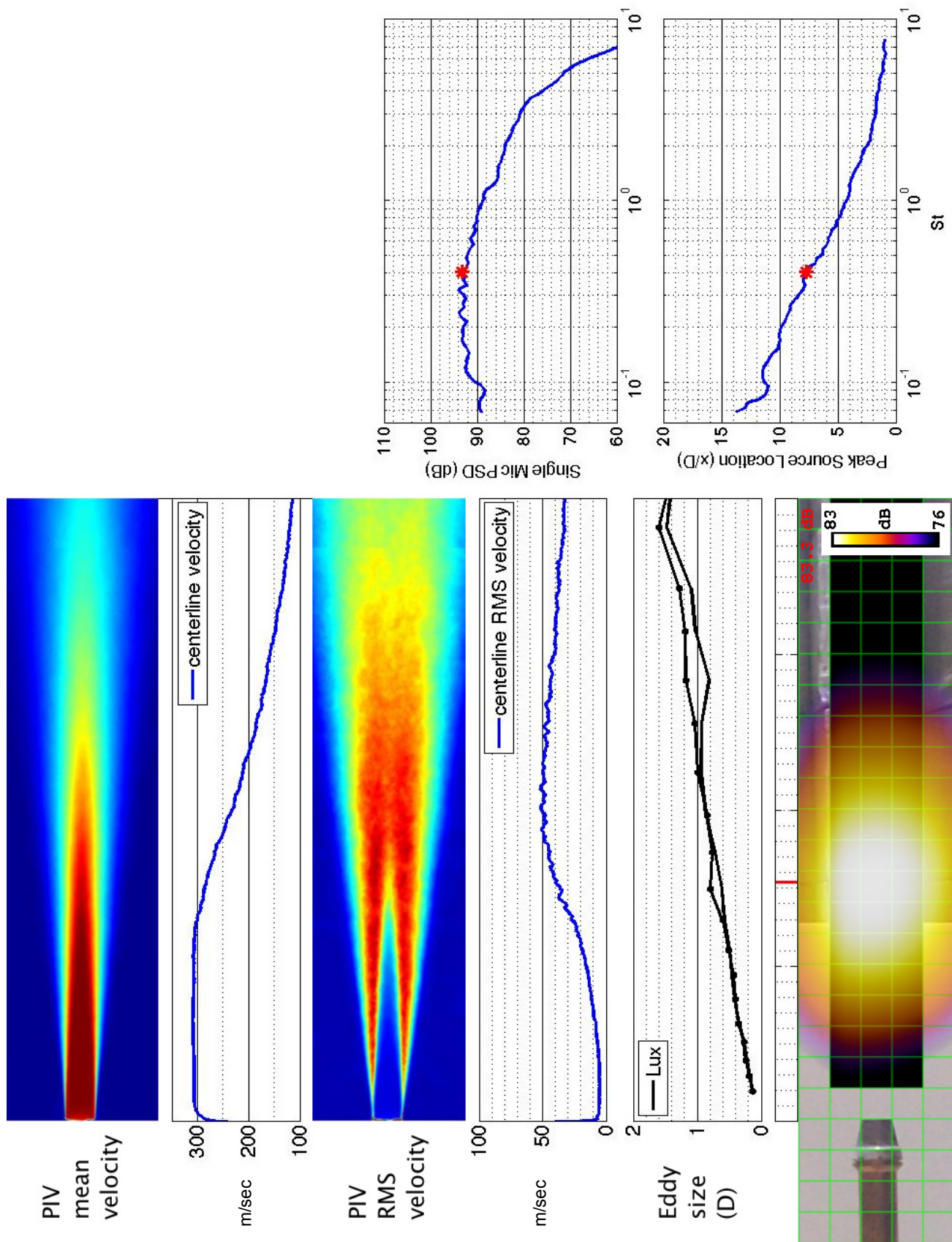
Figure 40.—SMC000; set point 7; Mj=0.98; St=0.404.
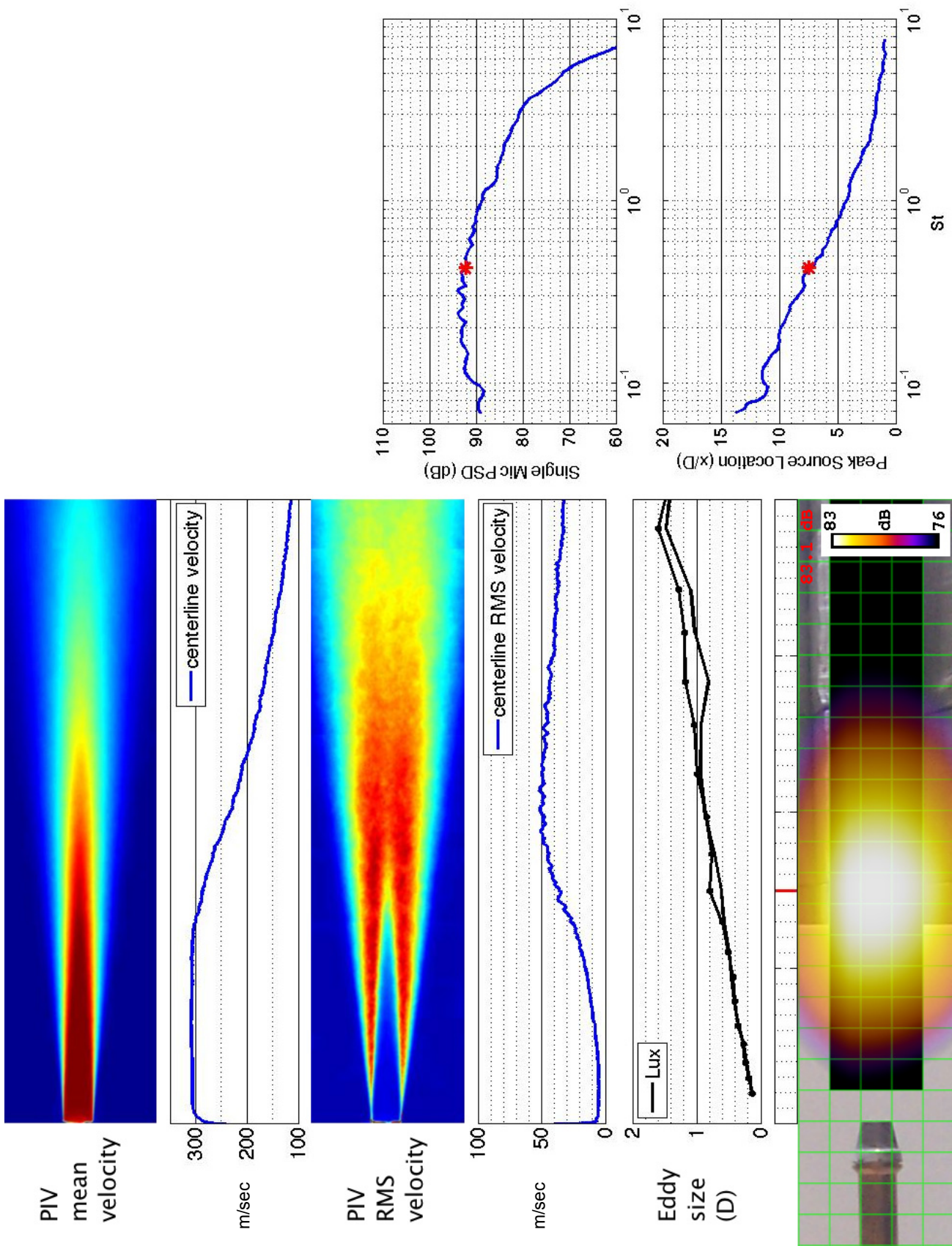
Figure 41.—SMC000; set point 7; Mj=0.98; St=0.427.
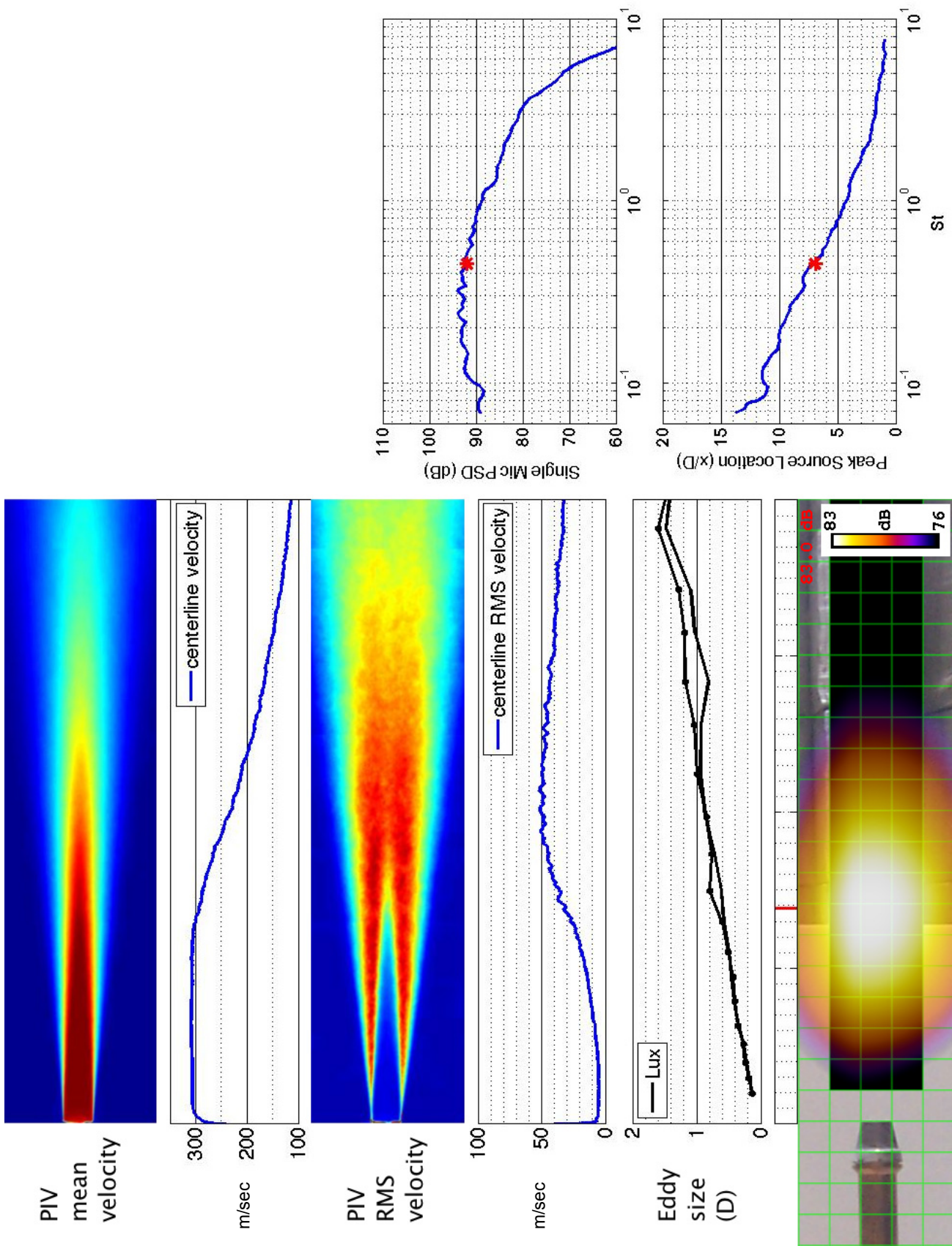
Figure 42.—SMC000; set point 7; Mj=0.98; St=0.453.
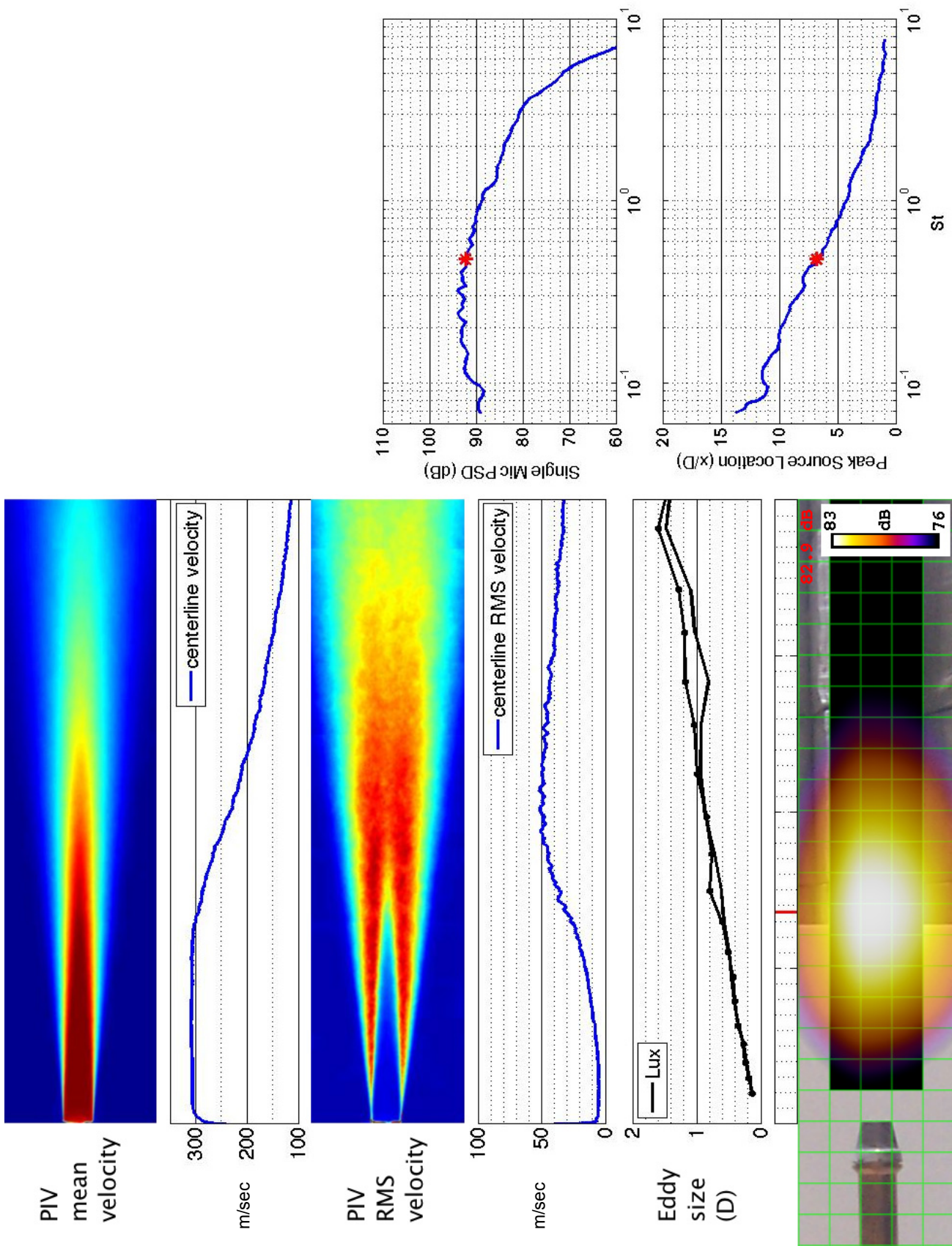
Figure 43.—SMC000; set point 7; Mj=0.98; St=0.480.
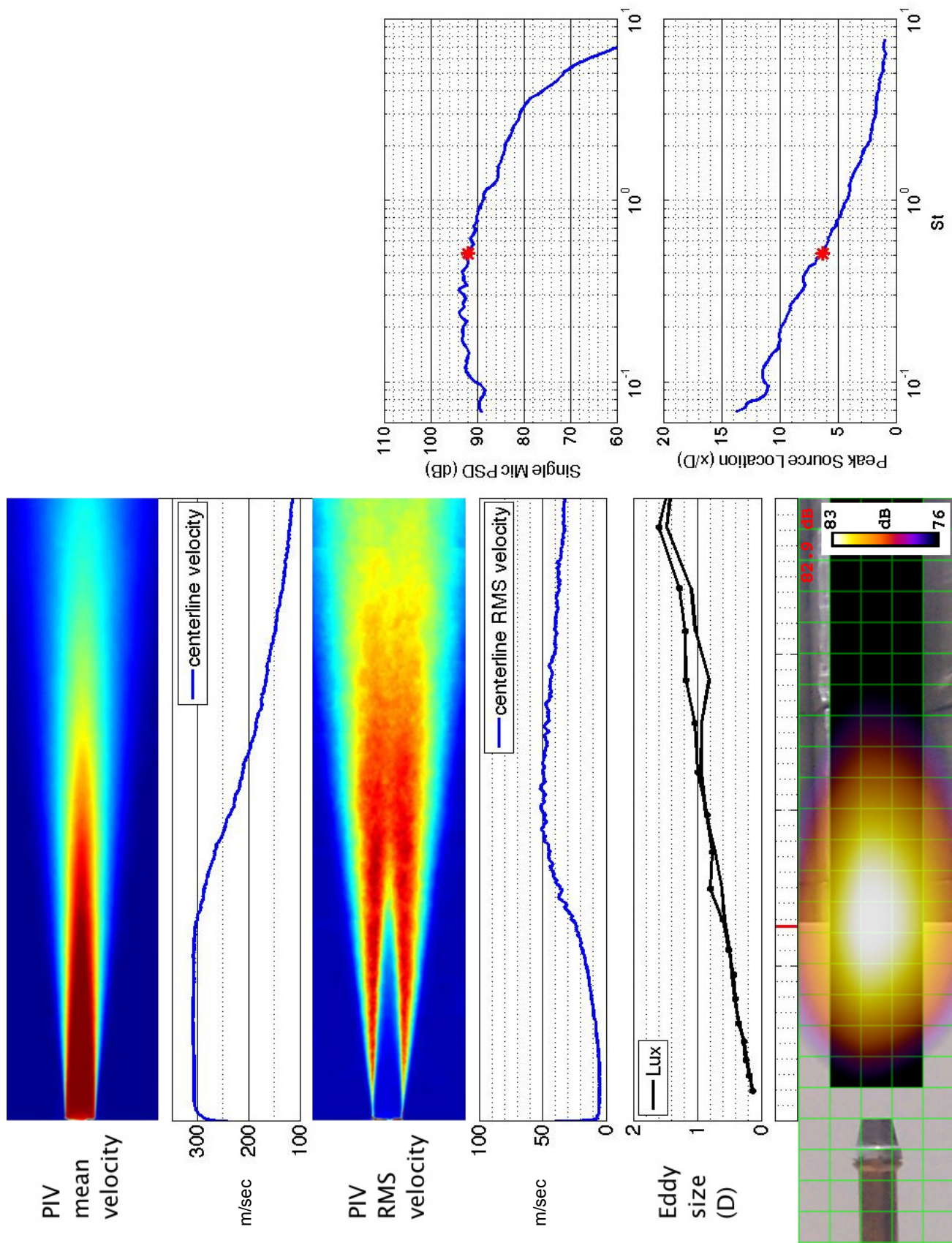
Figure 44.—SMC000; set point 7; Mj=0.98; St=0.508.
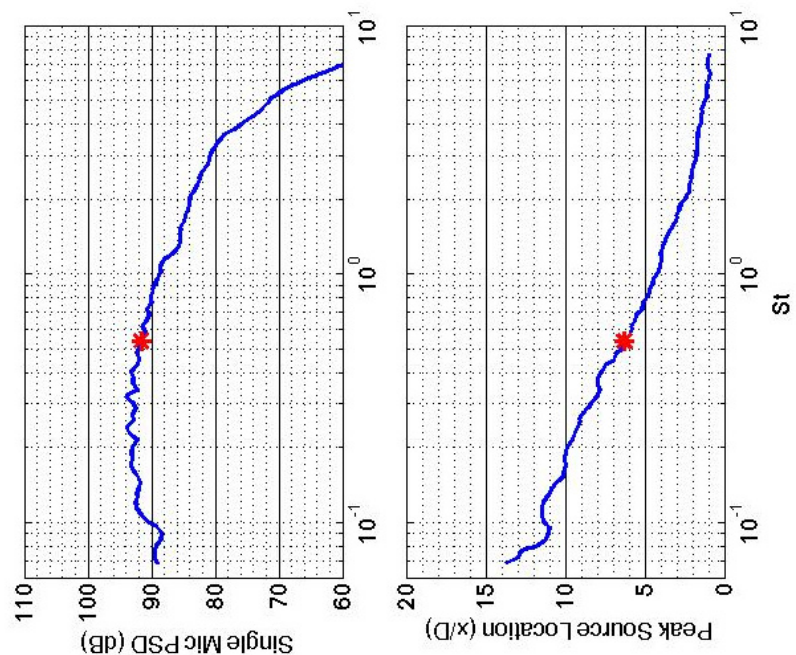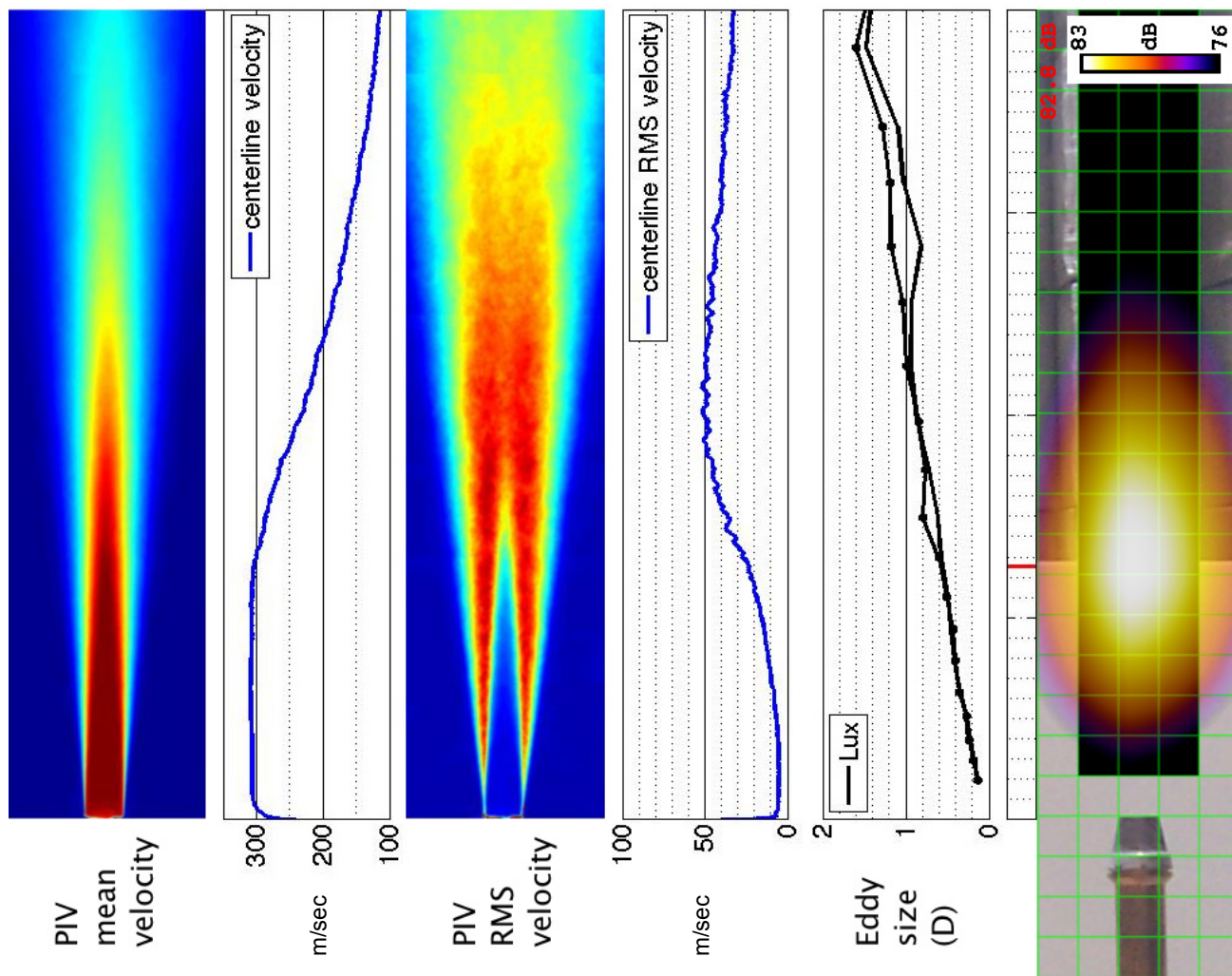
Figure 45.—SMC000; set point 7; Mj=0.98; St=0.538.
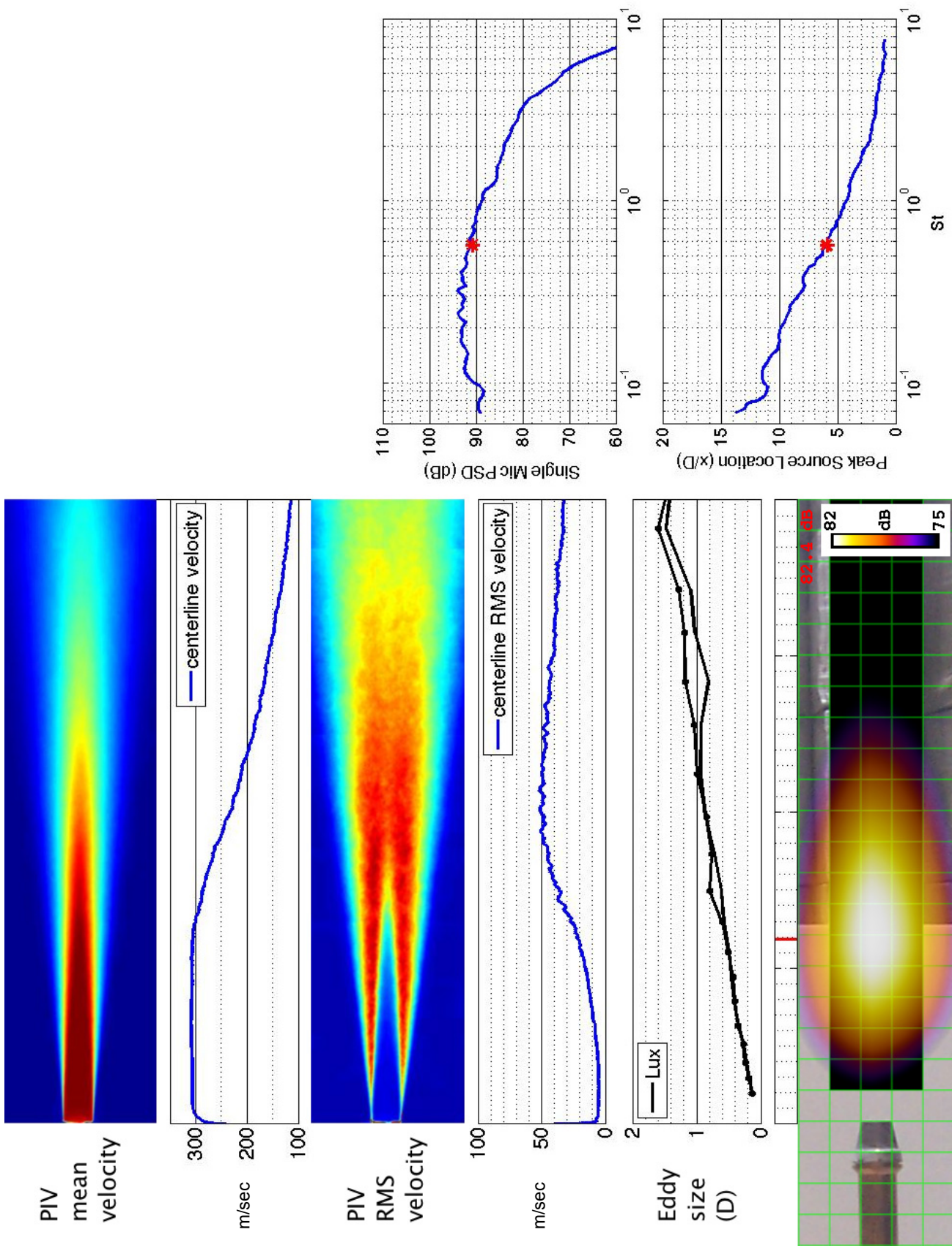
Figure 46.—SMC000; set point 7; Mj=0.98; St=0.571.
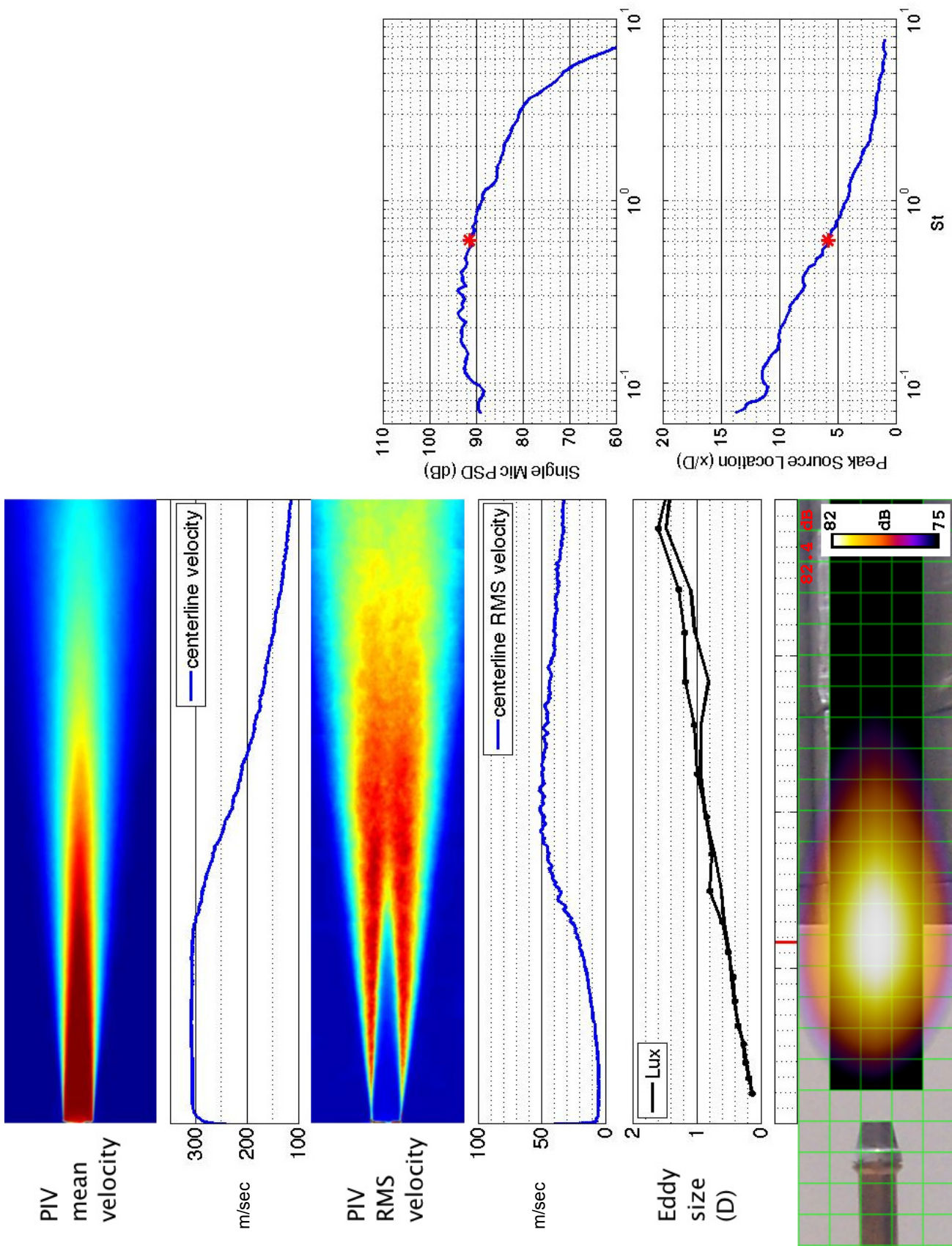
Figure 47.—SMC000; set point 7; Mj=0.98; St=0.607.
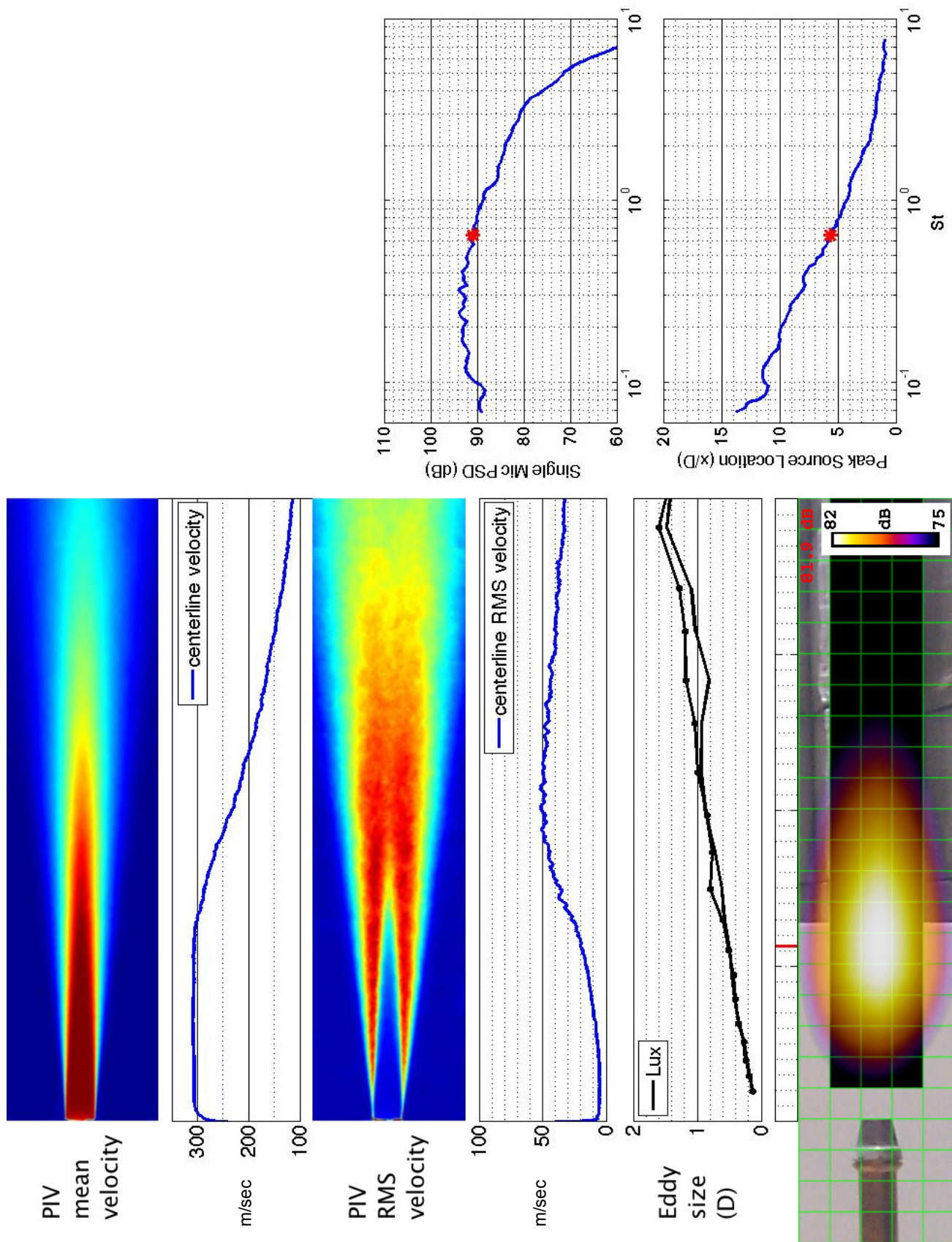
Figure 48.—SMC000; set point 7; Mj=0.98; St=0.644.
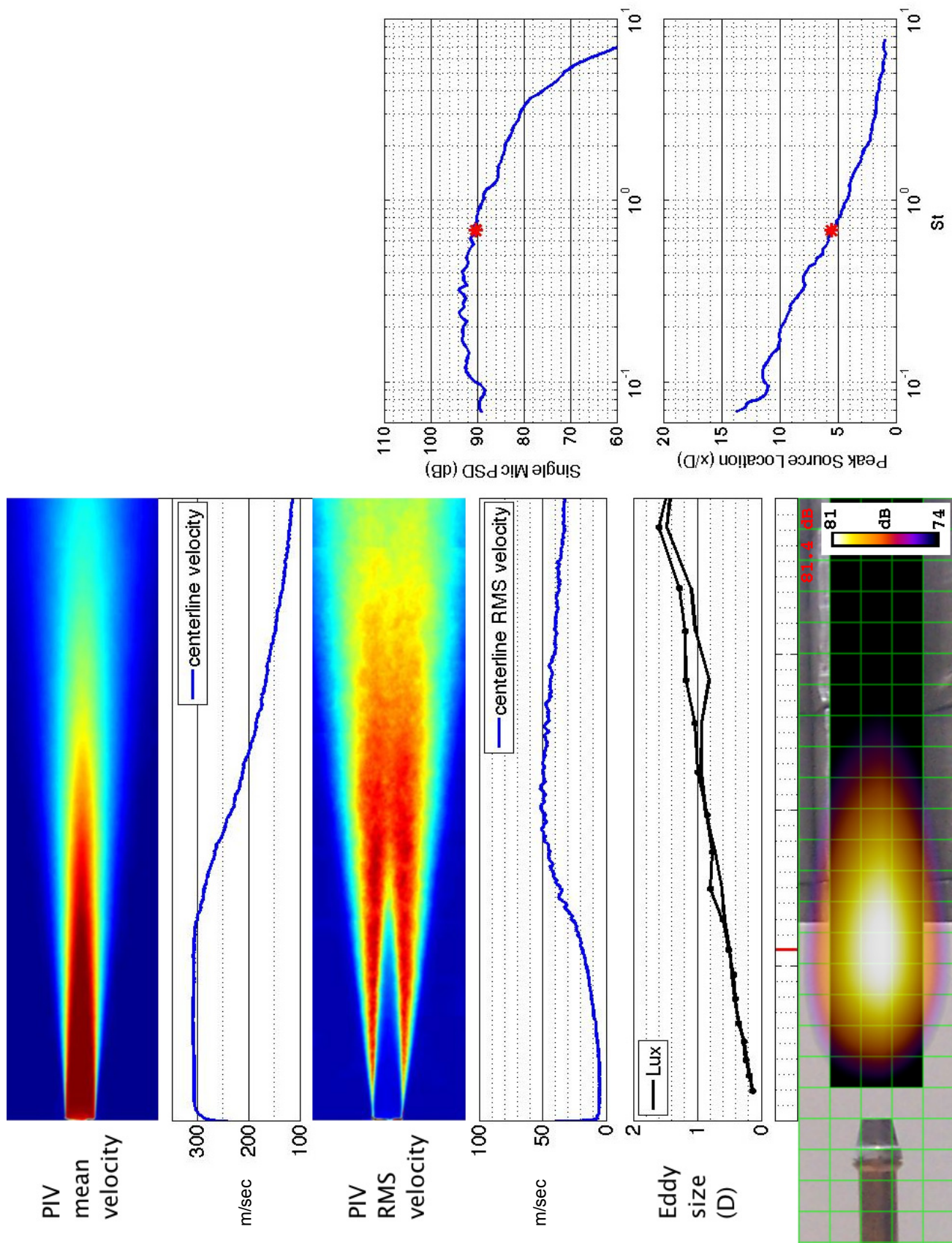
Figure 49.—SMC000; set point 7; Mj=0.98; St=0.683.
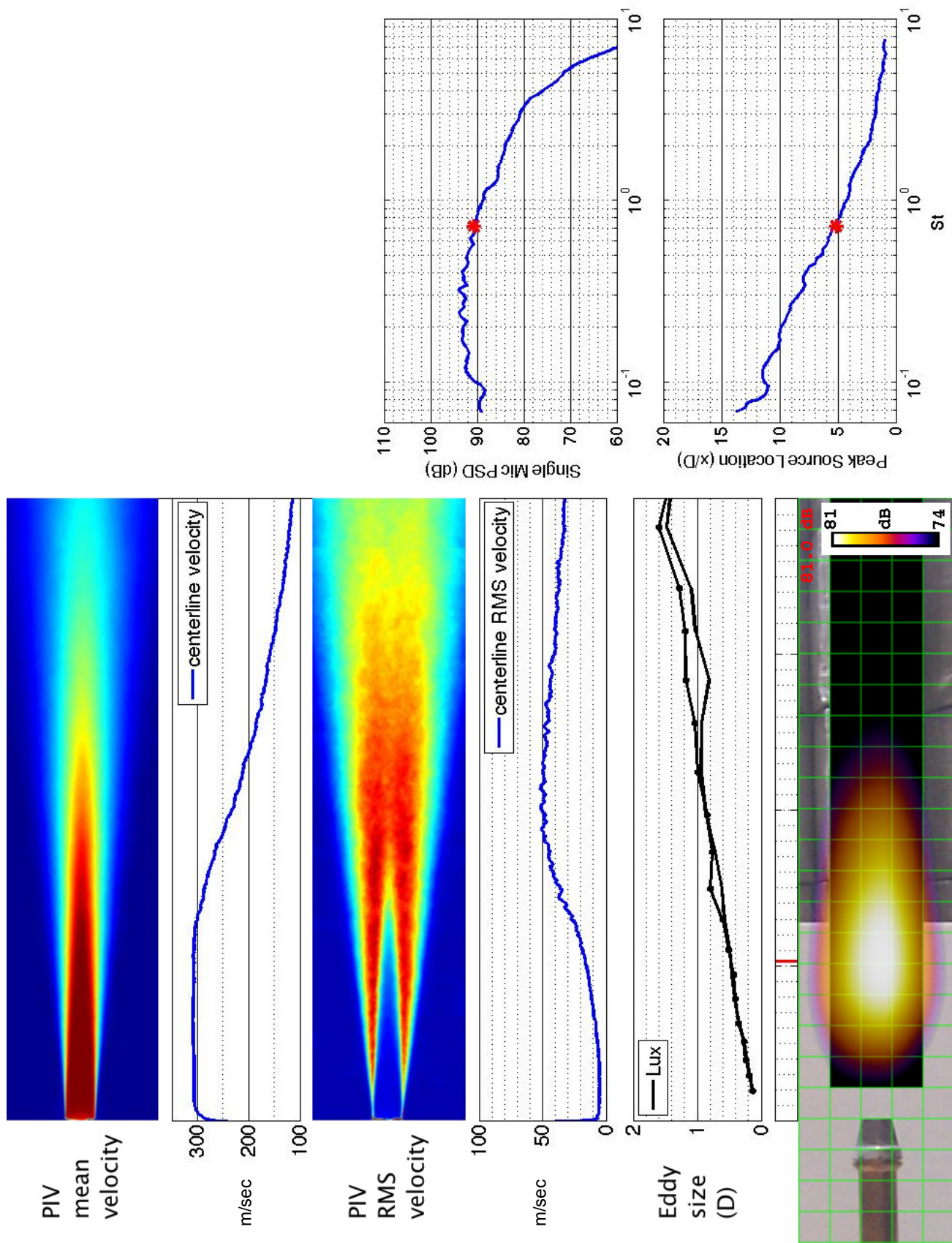
Figure 50.—SMC000; set point 7; Mj=0.98; St=0.723.
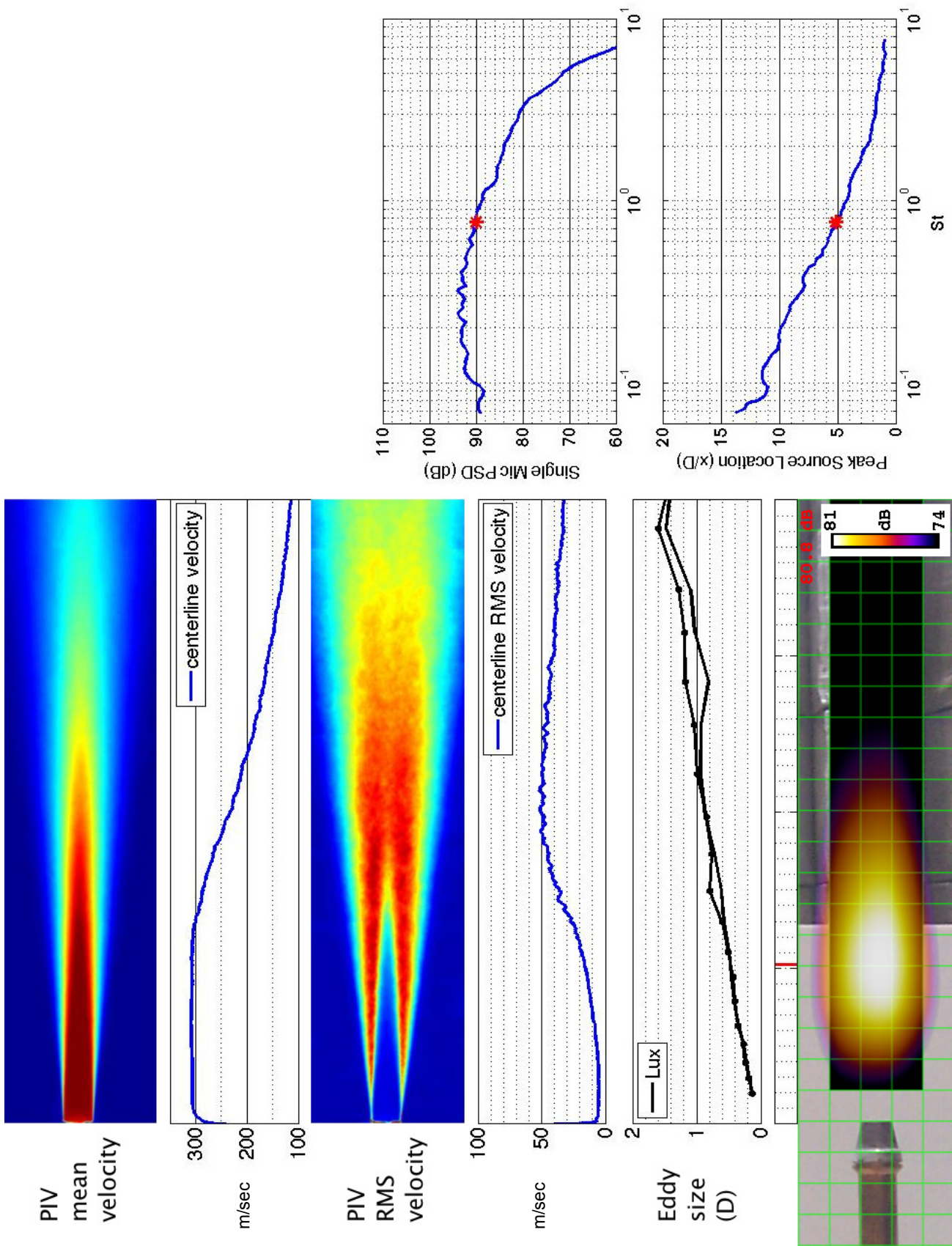
Figure 51.—SMC000; set point 7; Mj=0.98; St=0.764.
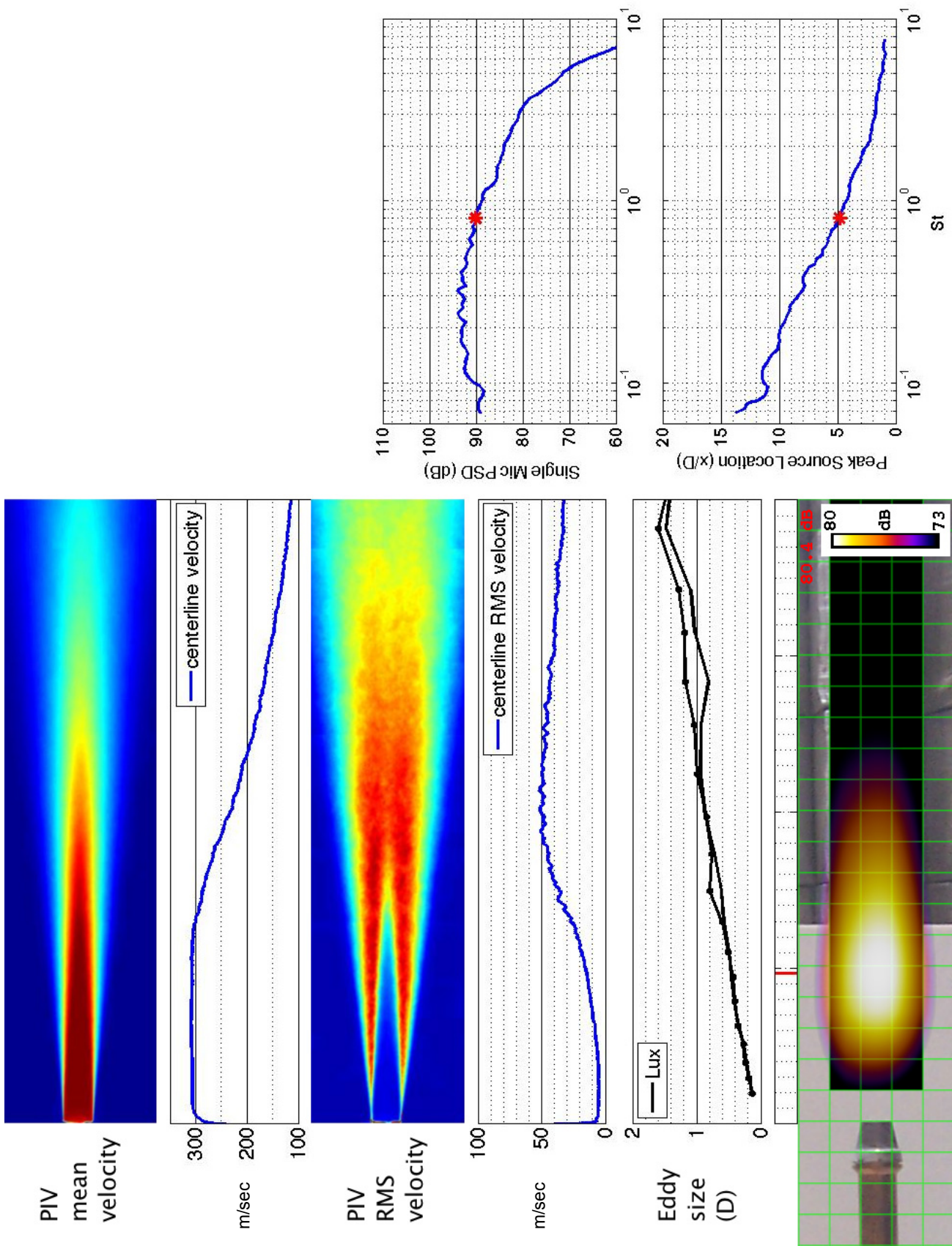
Figure 52.—SMC000; set point 7; Mj=0.98; St=0.808.
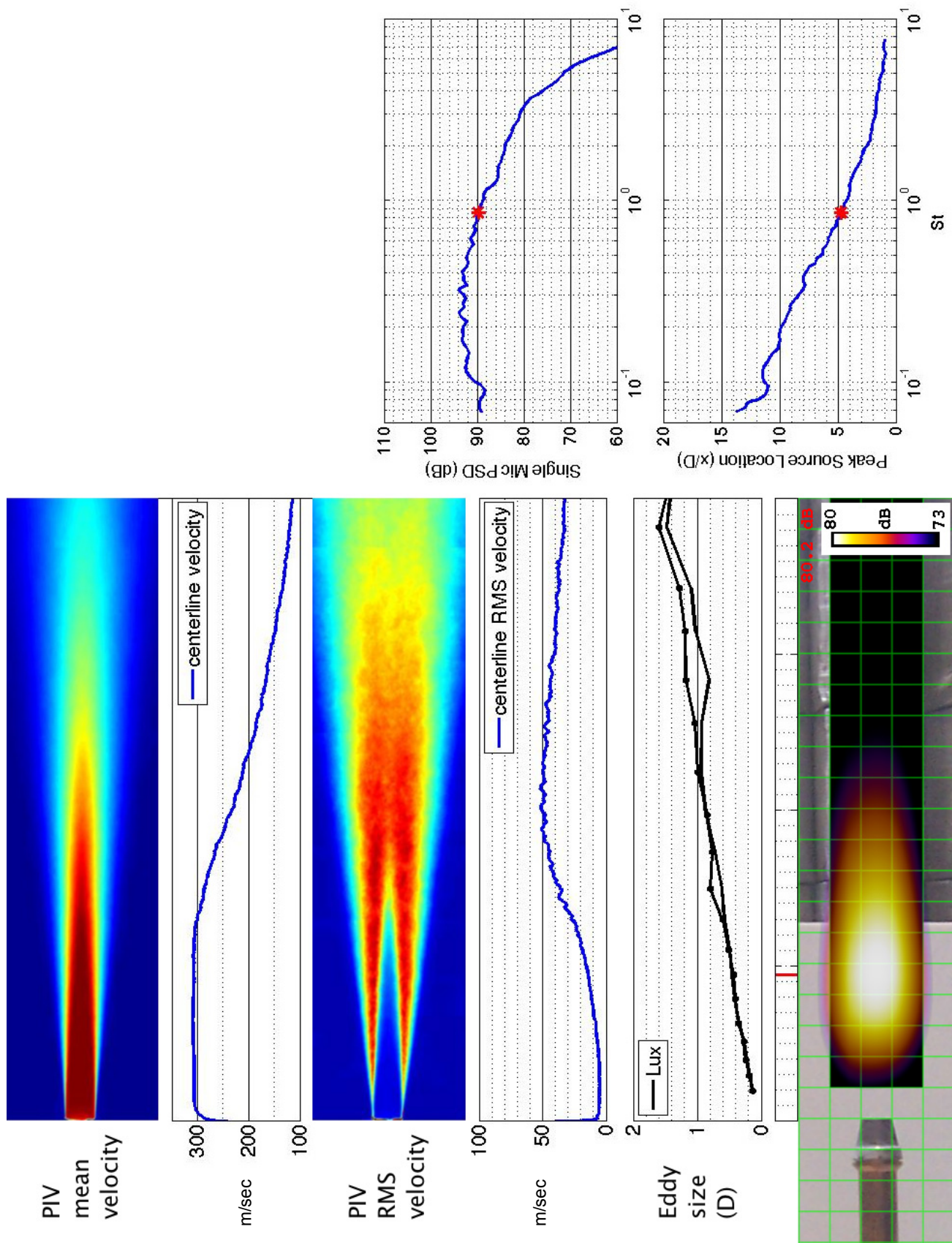
Figure 53.—SMC000; set point 7; Mj=0.98; St=0.855.
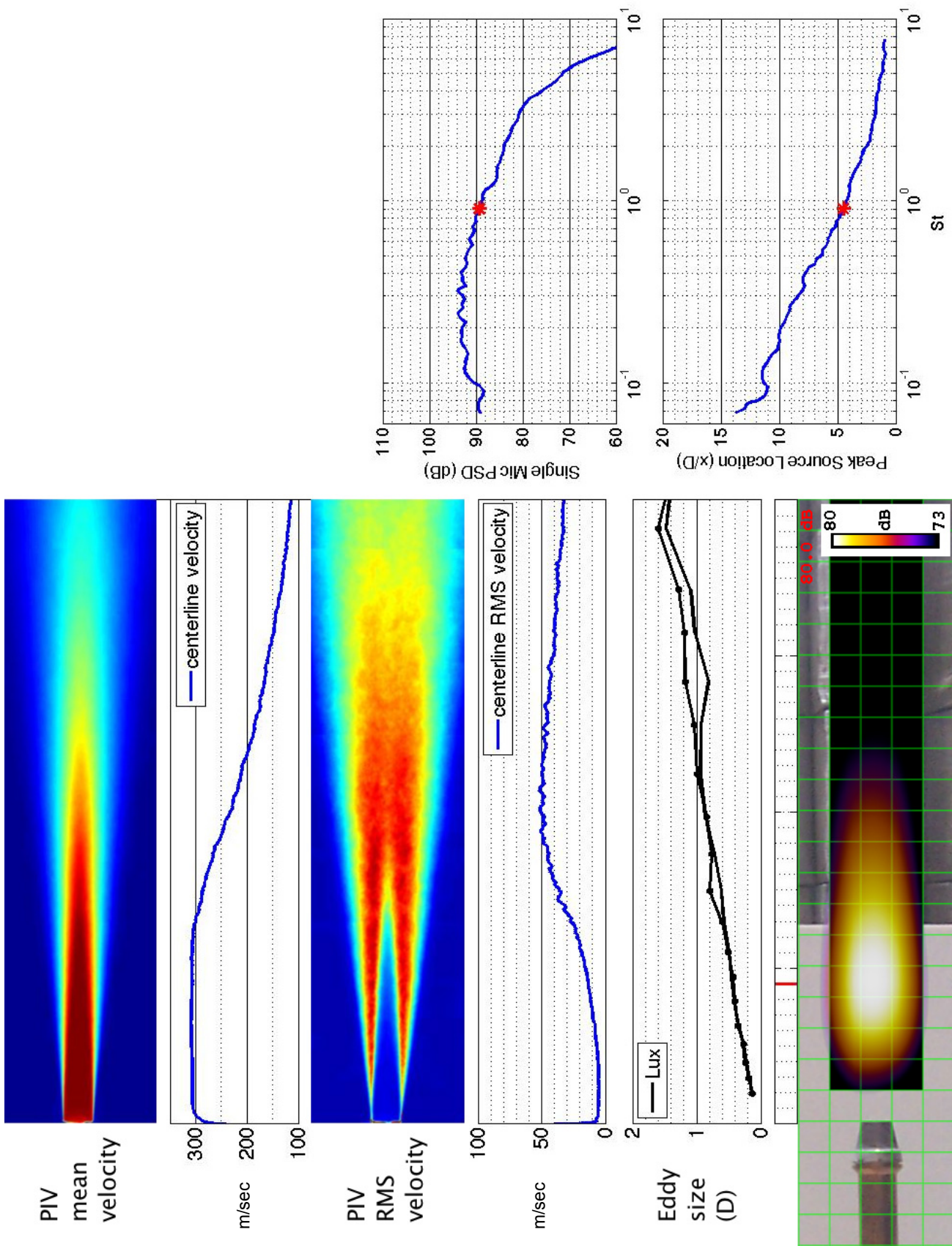
Figure 54.—SMC000; set point 7; Mj=0.98; St=0.905.
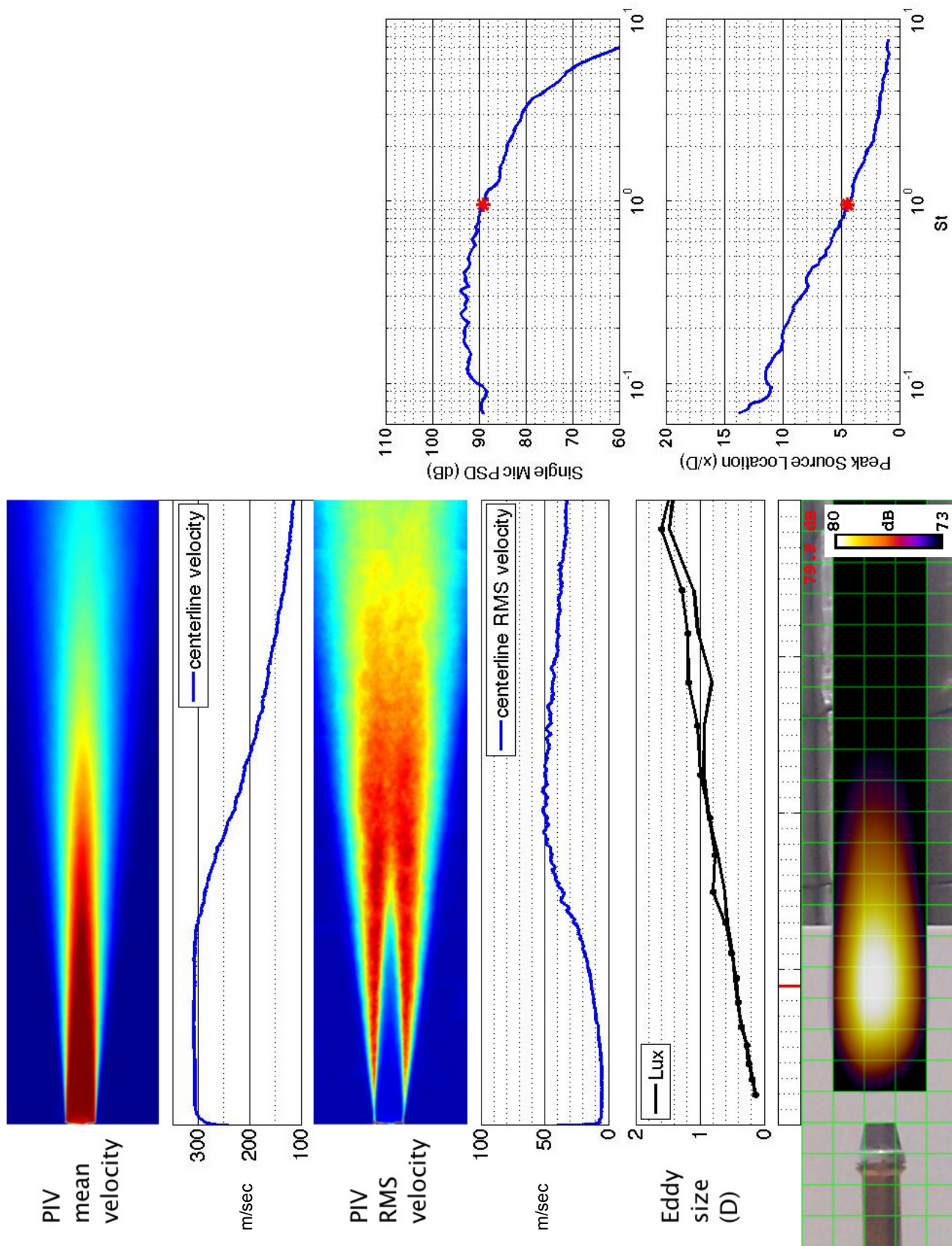
Figure 55.—SMC000; set point 7; Mj=0.98; St=0.959.
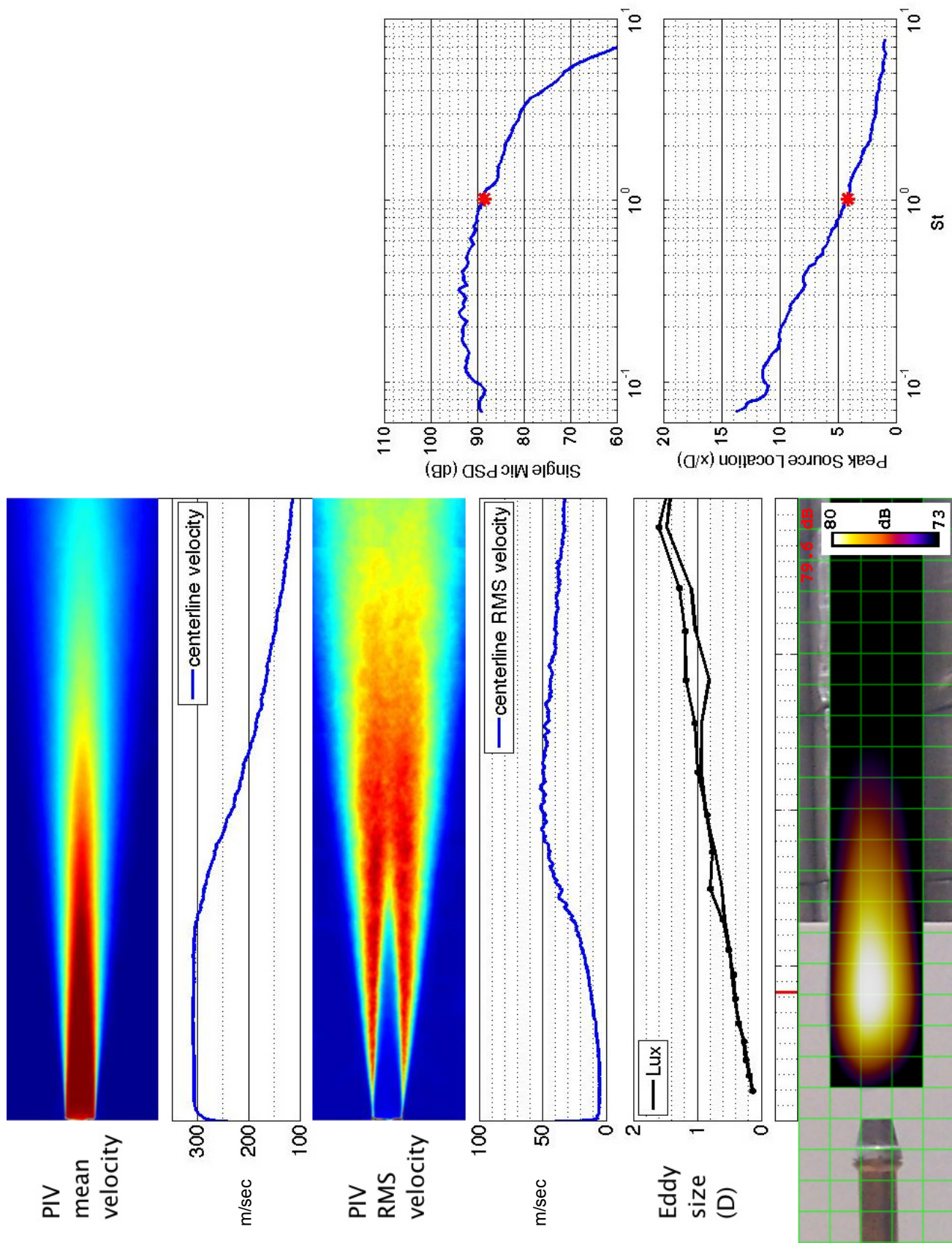
Figure 56.—SMC000; set point 7; Mj=0.98; St=1.02.
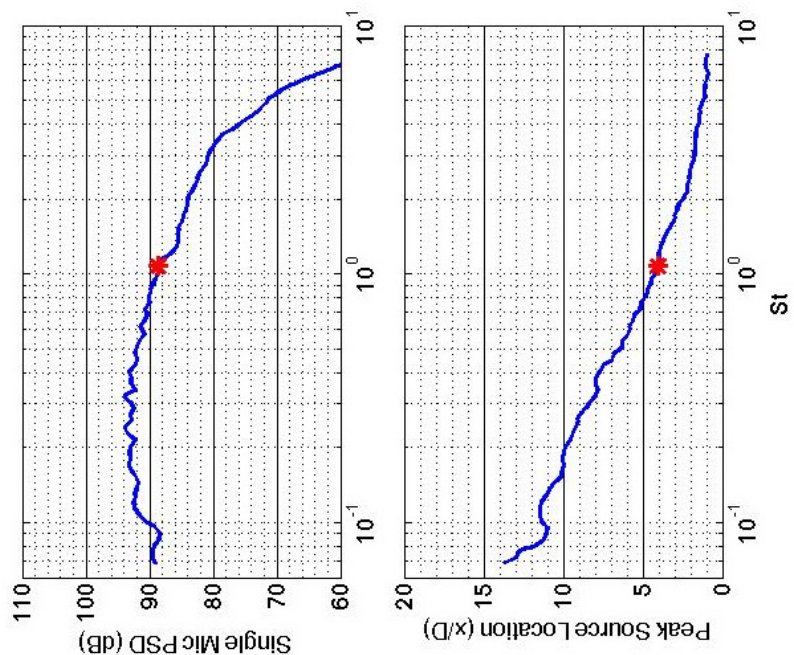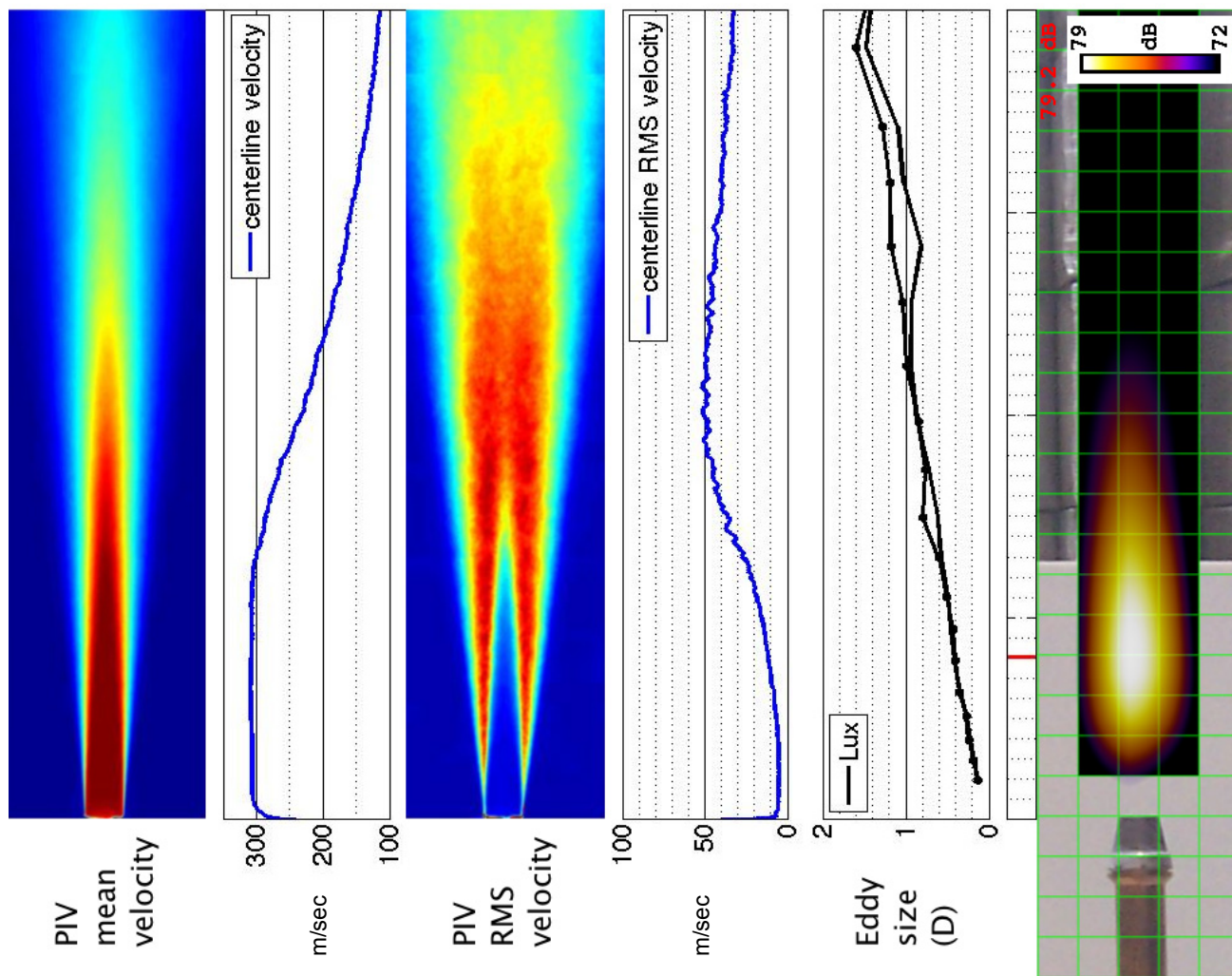
Figure 57.—SMC000; set point 7; Mj=0.98; St=1.08.
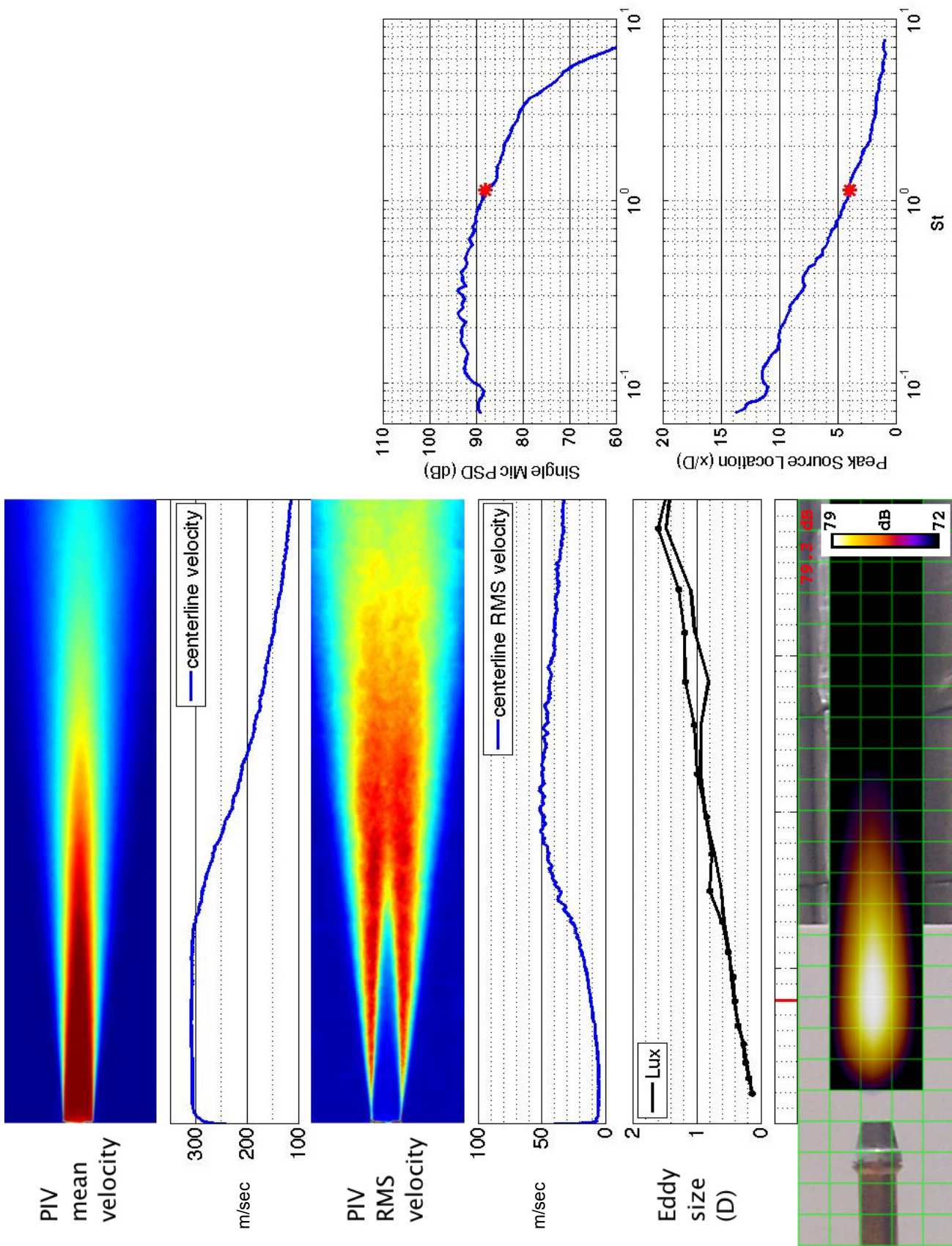
Figure 58.—SMC000; set point 7; Mj=0.98; St=1.14.
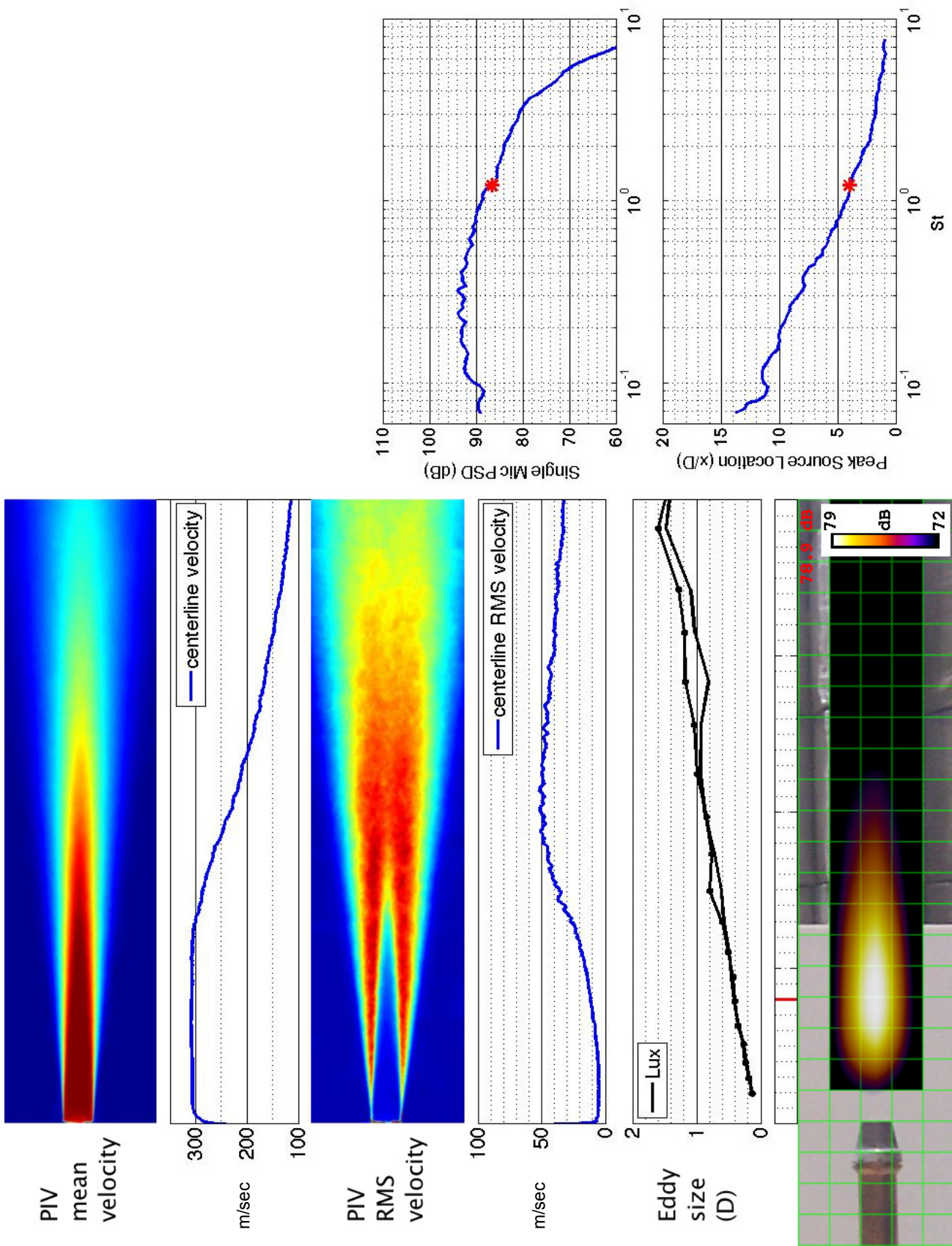
Figure 59.—SMC000; set point 7; Mj=0.98; St=1.21.
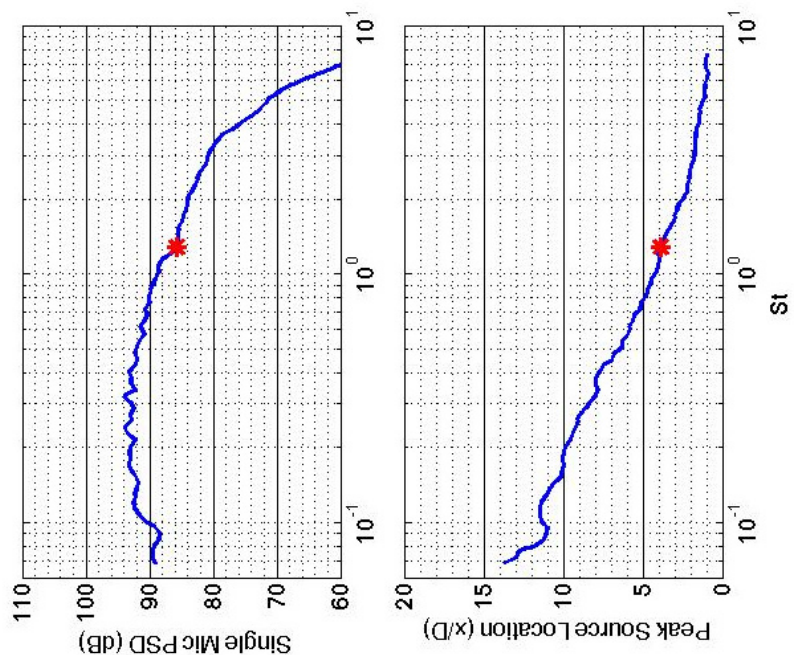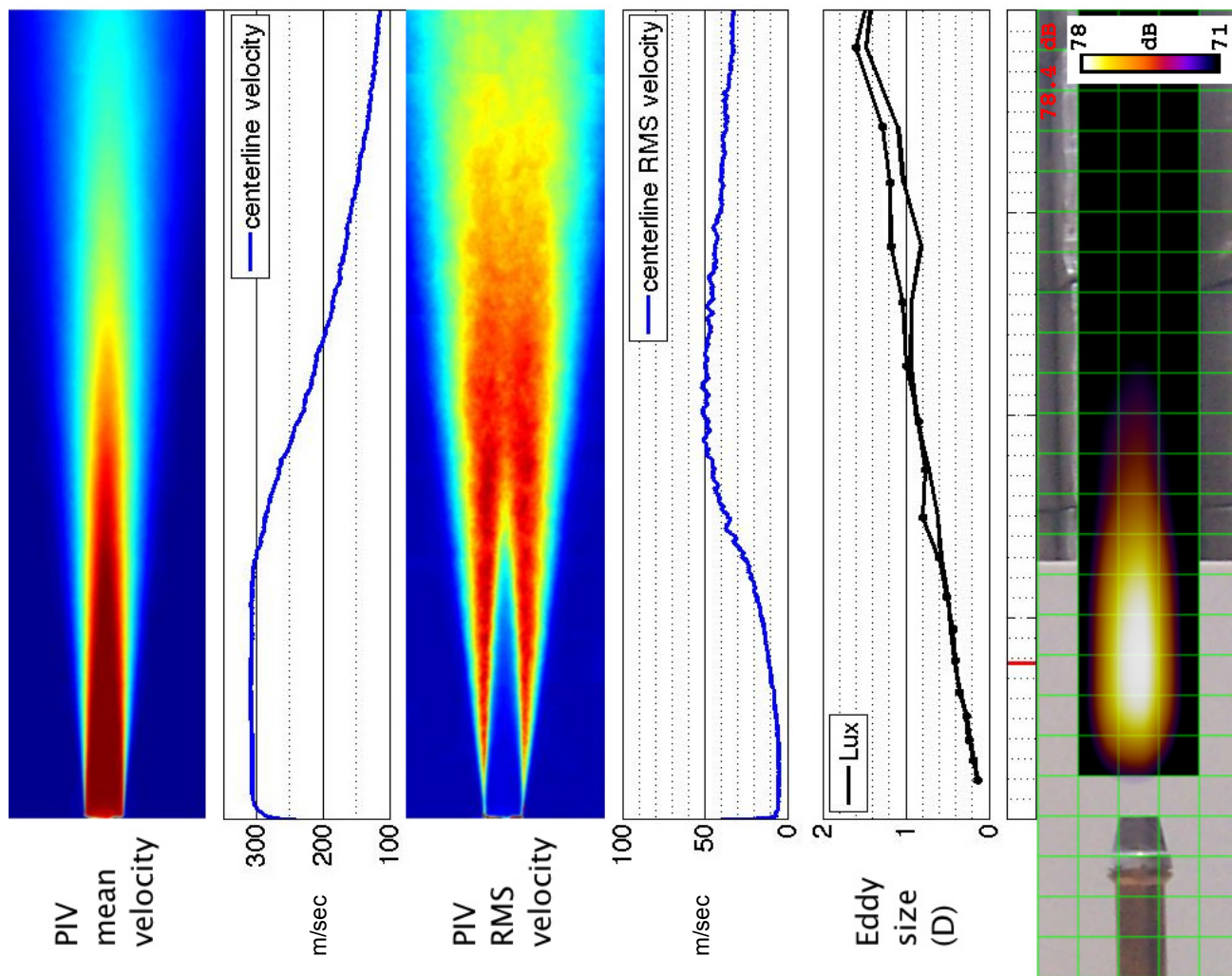
Figure 60.—SMC000; set point 7; Mj=0.98; St=1.29.
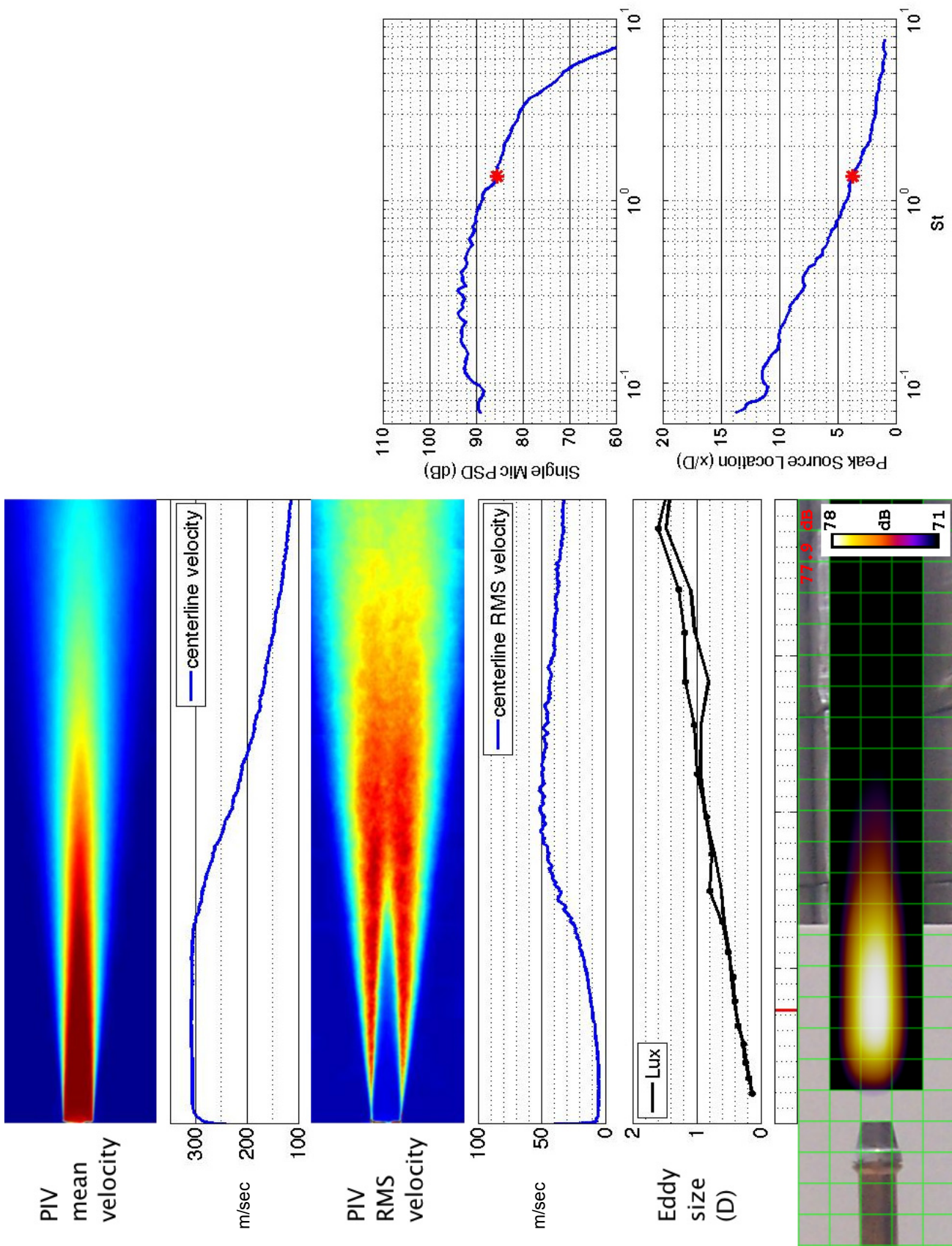
Figure 61.—SMC000; set point 7; Mj=0.98; St=1.37.
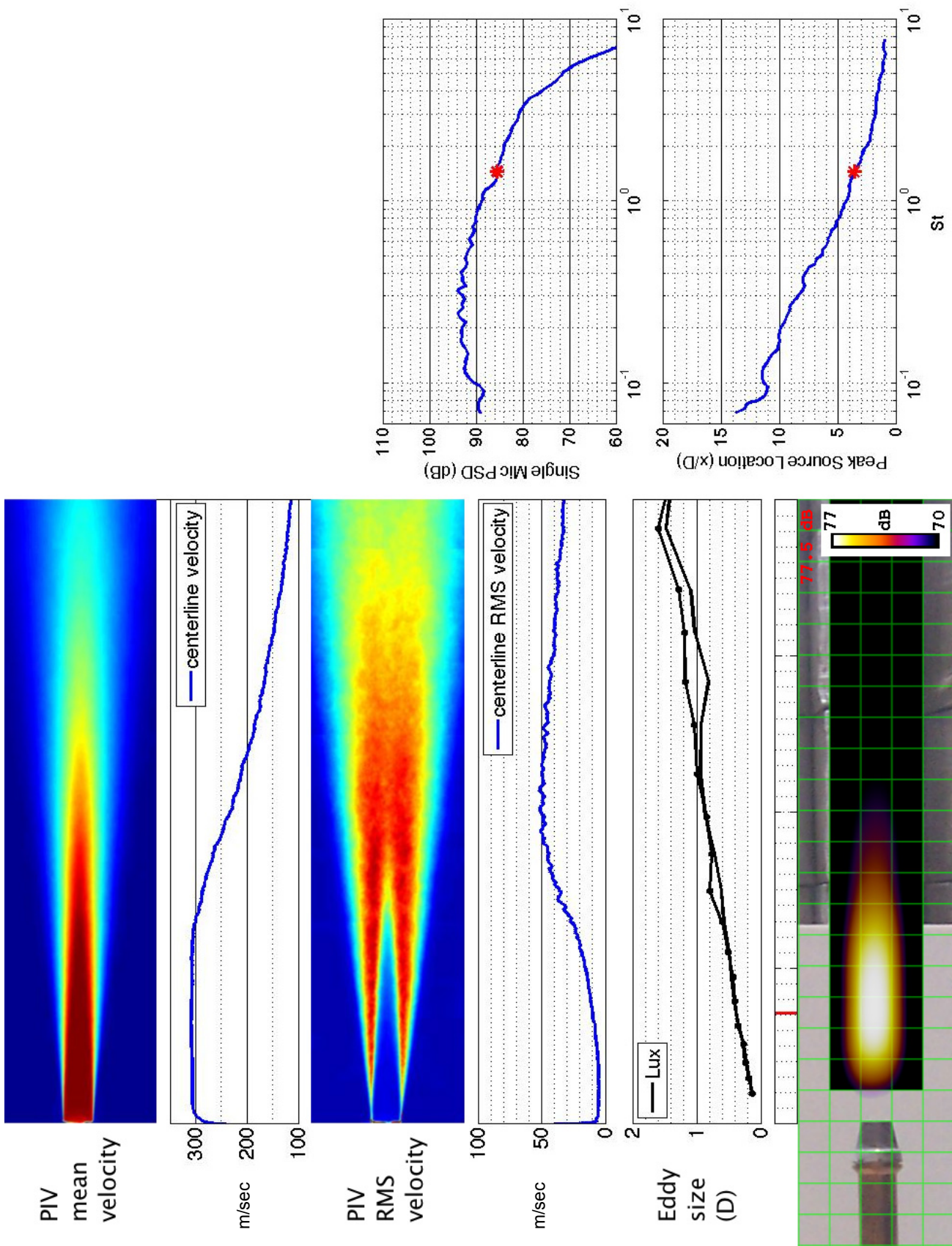
Figure 62.—SMC000; set point 7; Mj=0.98; St=1.45.
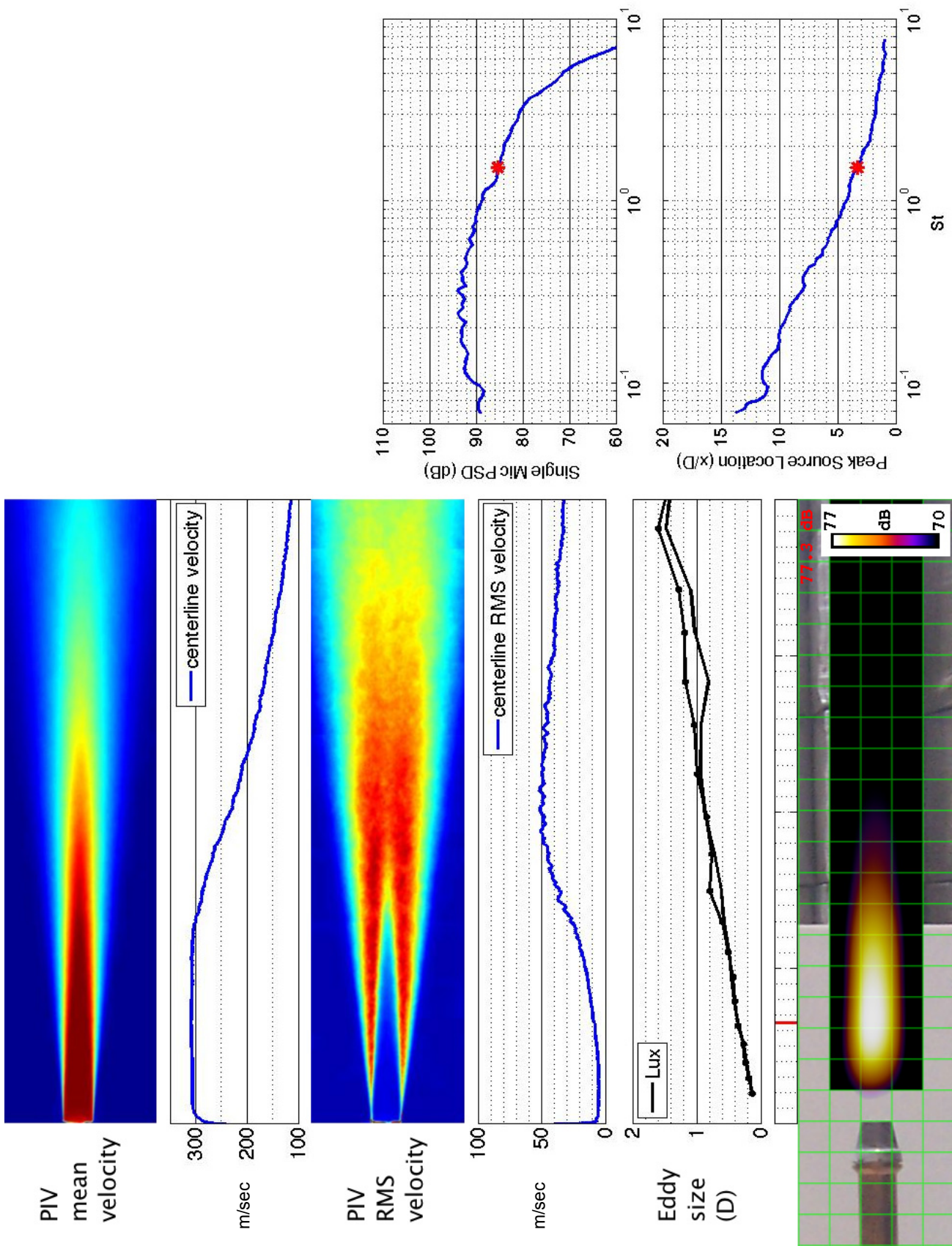
Figure 63.—SMC000; set point 7; Mj=0.98; St=1.53.
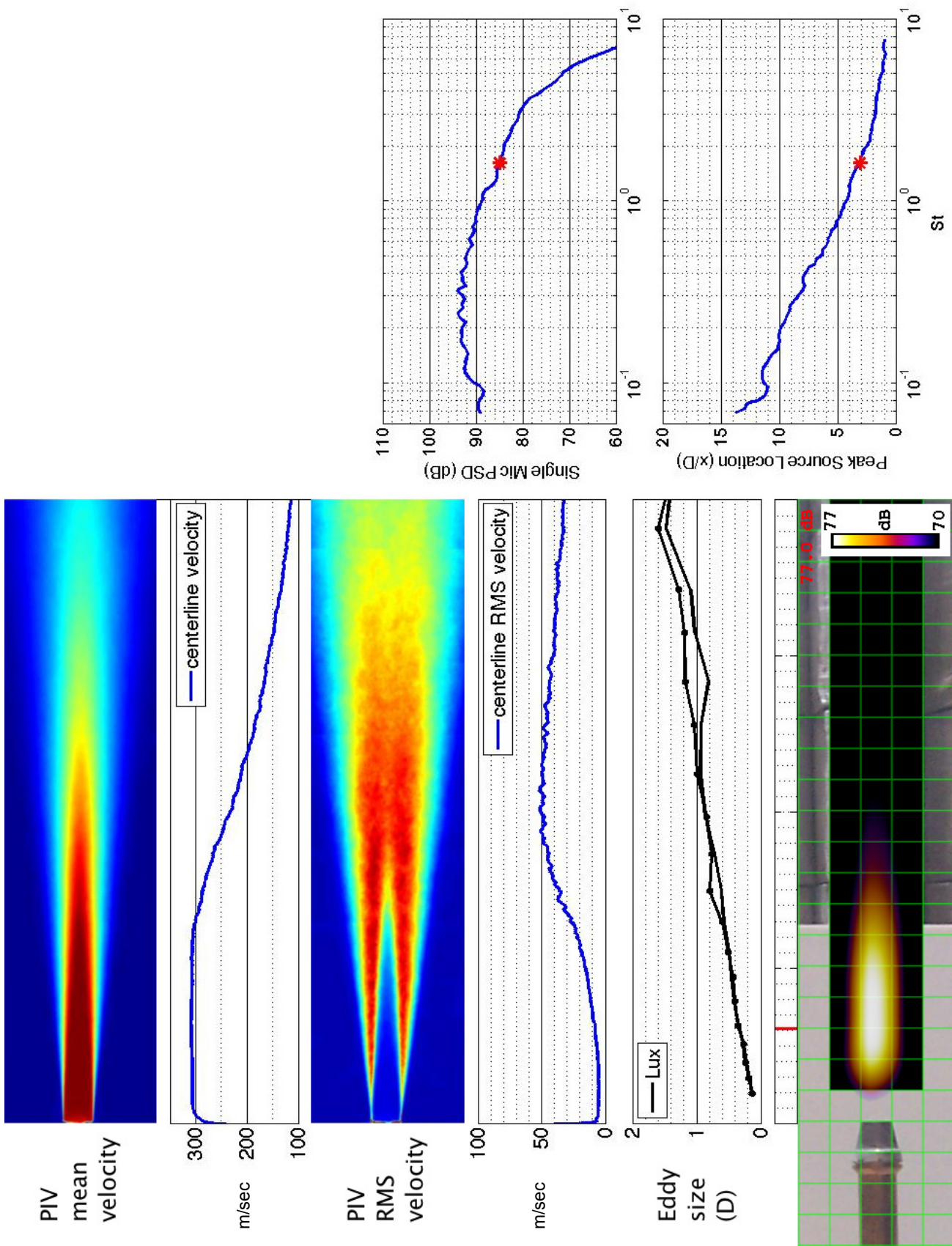
Figure 64.—SMC000; set point 7; Mj=0.98; St=1.62.
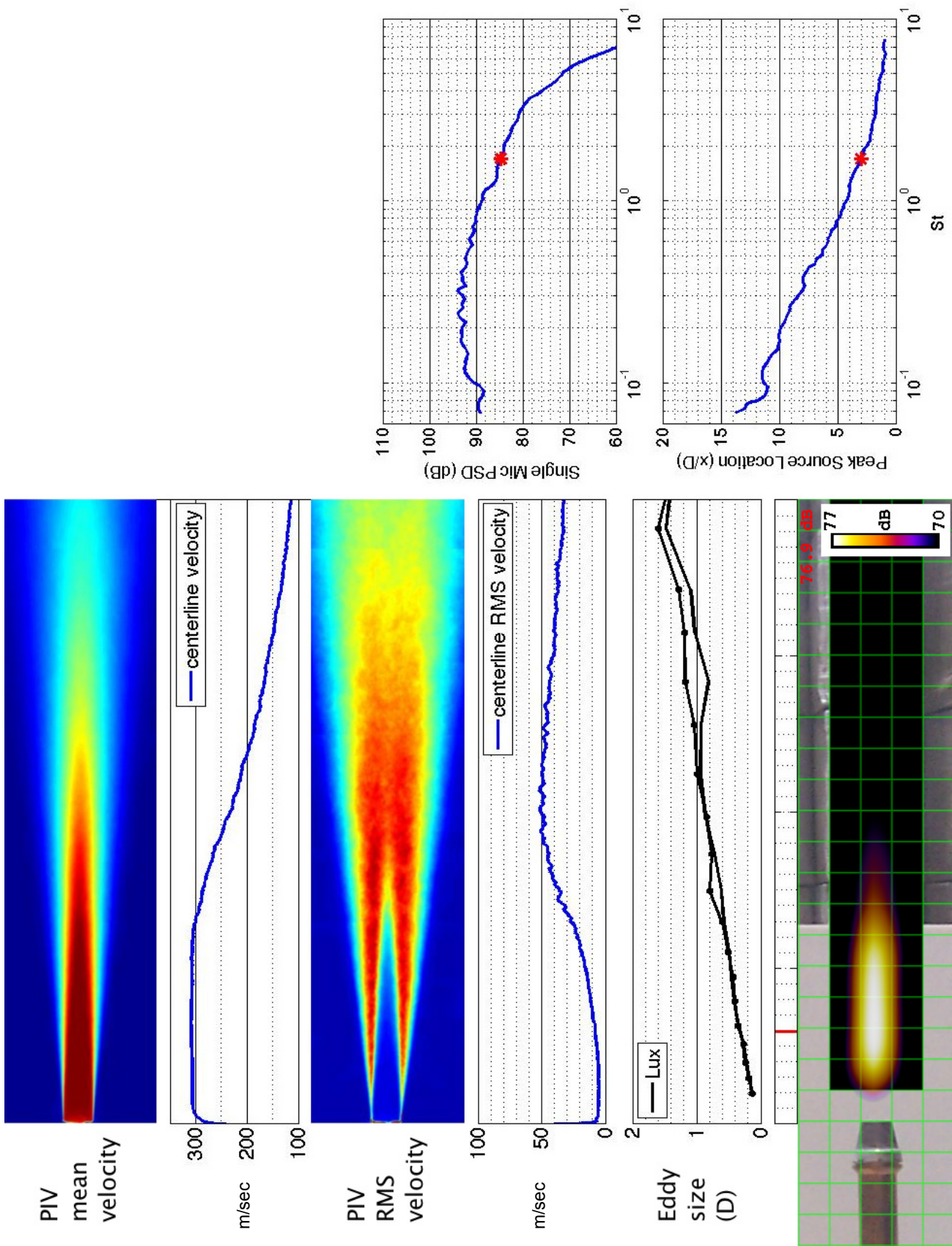
Figure 65.—SMC000; set point 7; Mj=0.98; St=1.71.
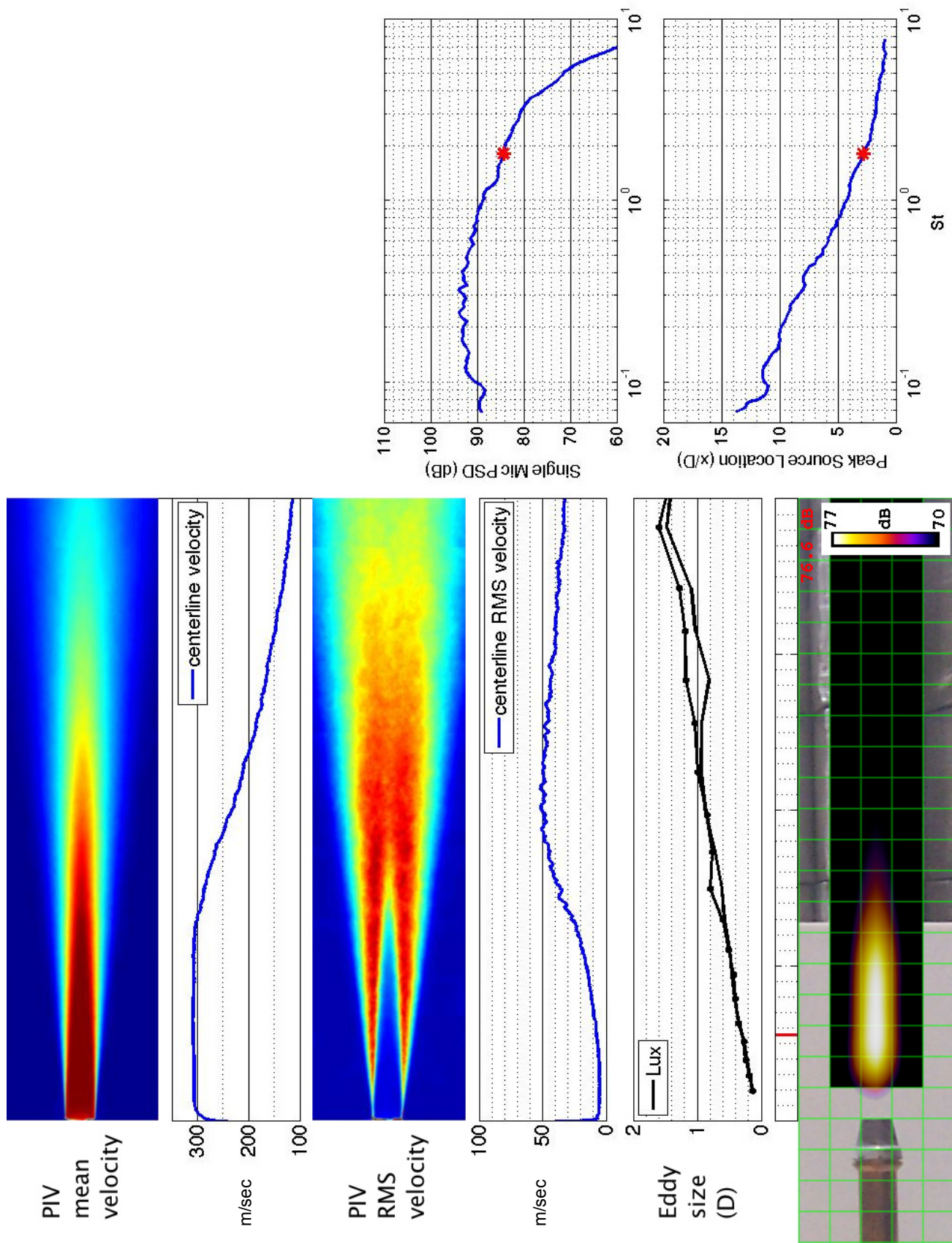
Figure 66.—SMC000; set point 7; Mj=0.98; St=1.81.
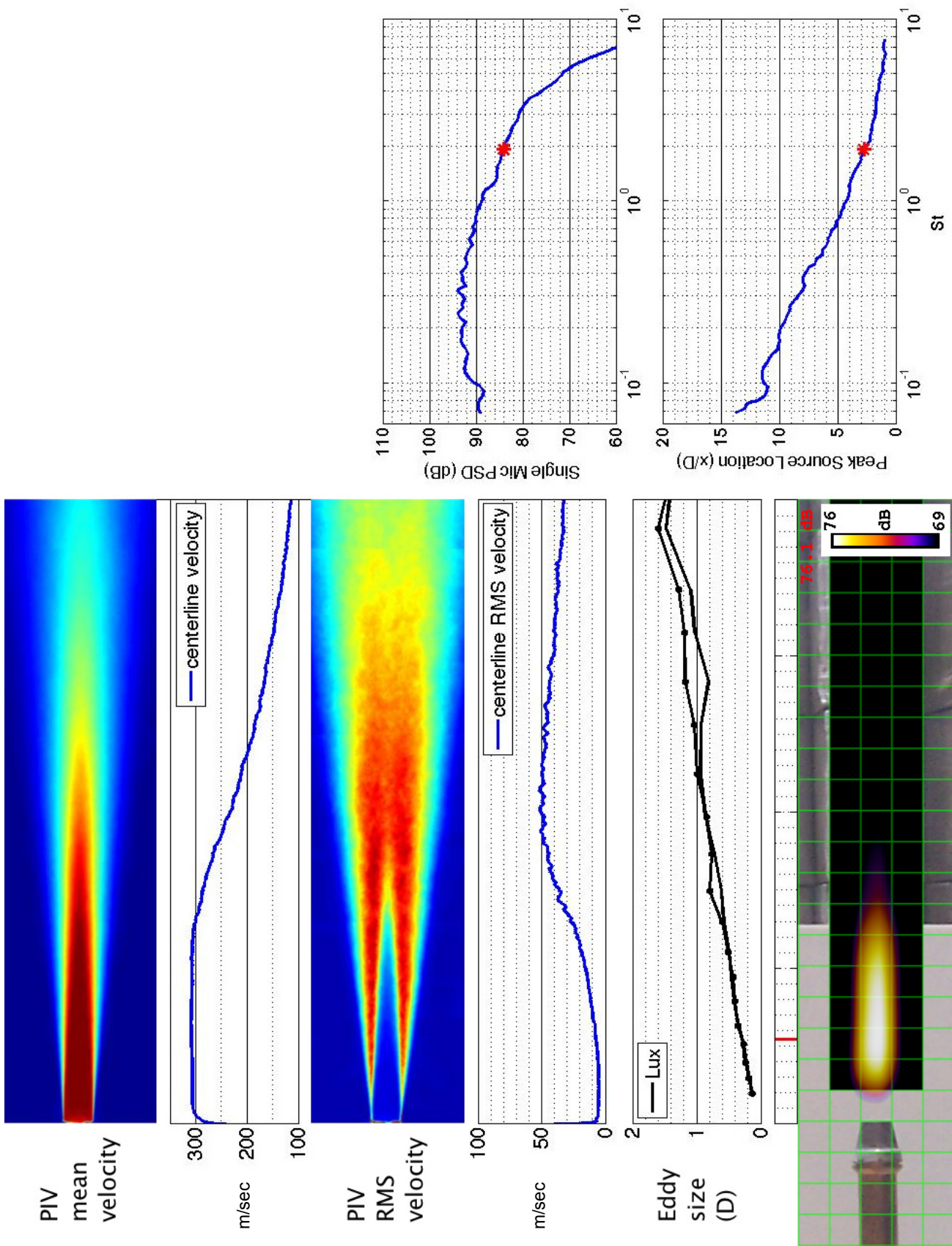
Figure 67.—SMC000; set point 7; Mj=0.98; St=1.91.
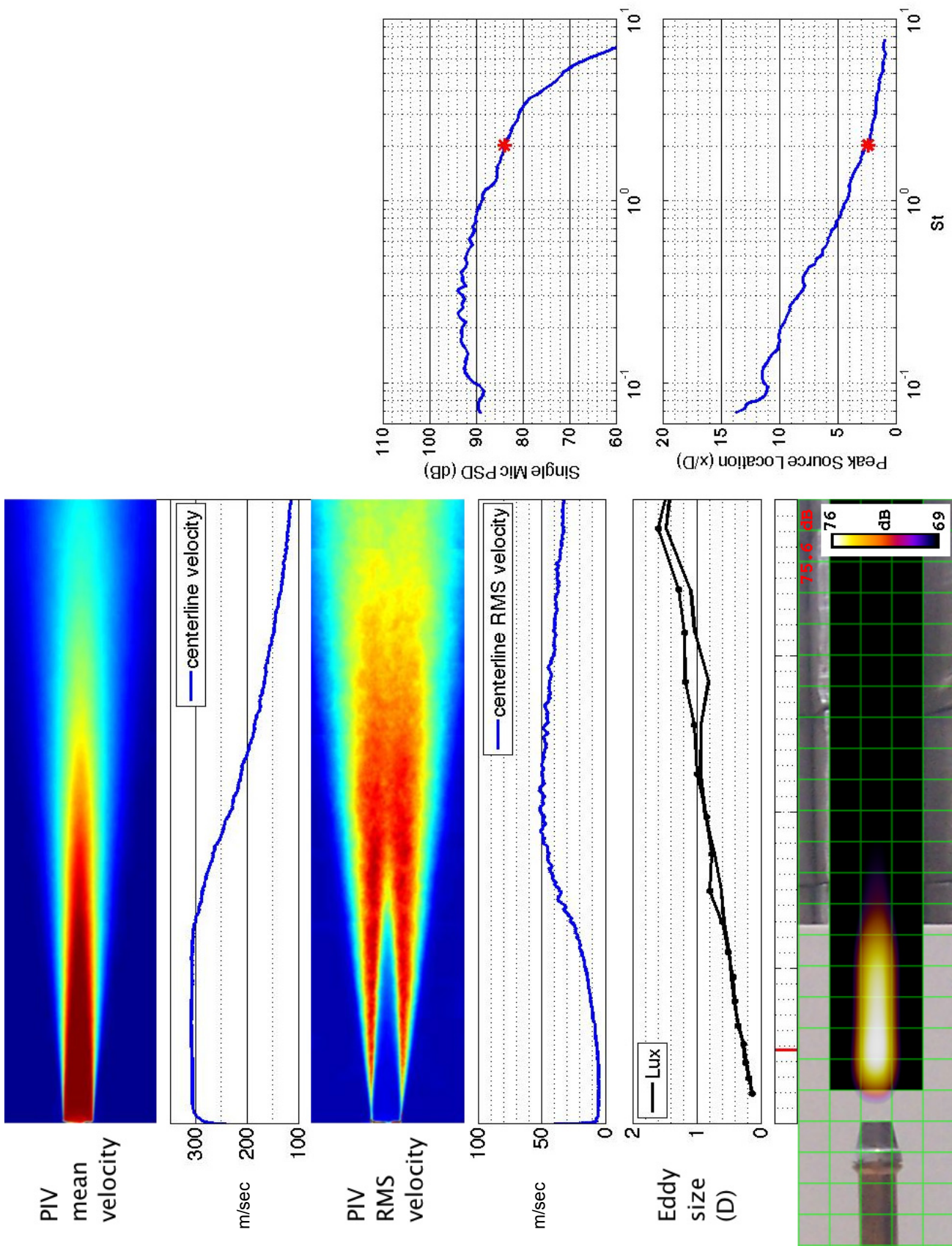
Figure 68.—SMC000; set point 7; Mj=0.98; St=2.02.
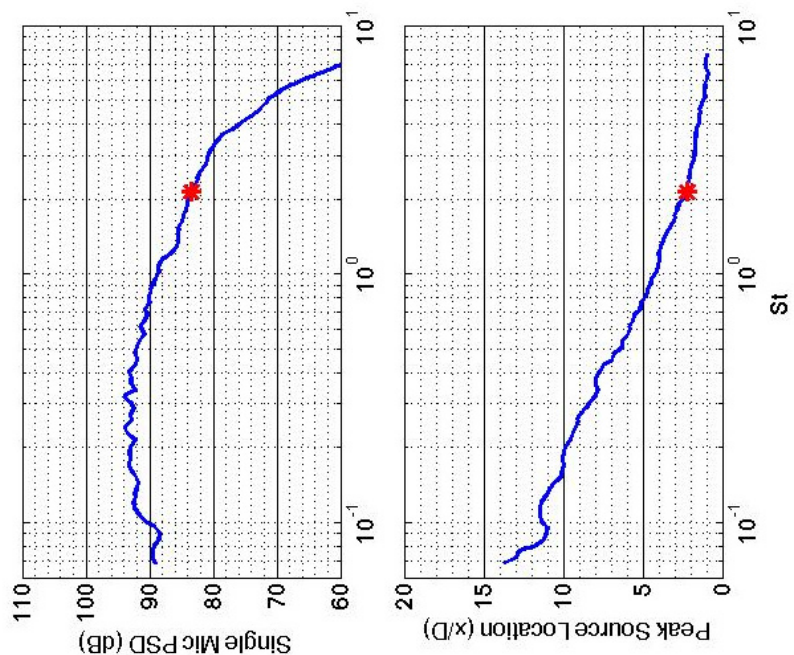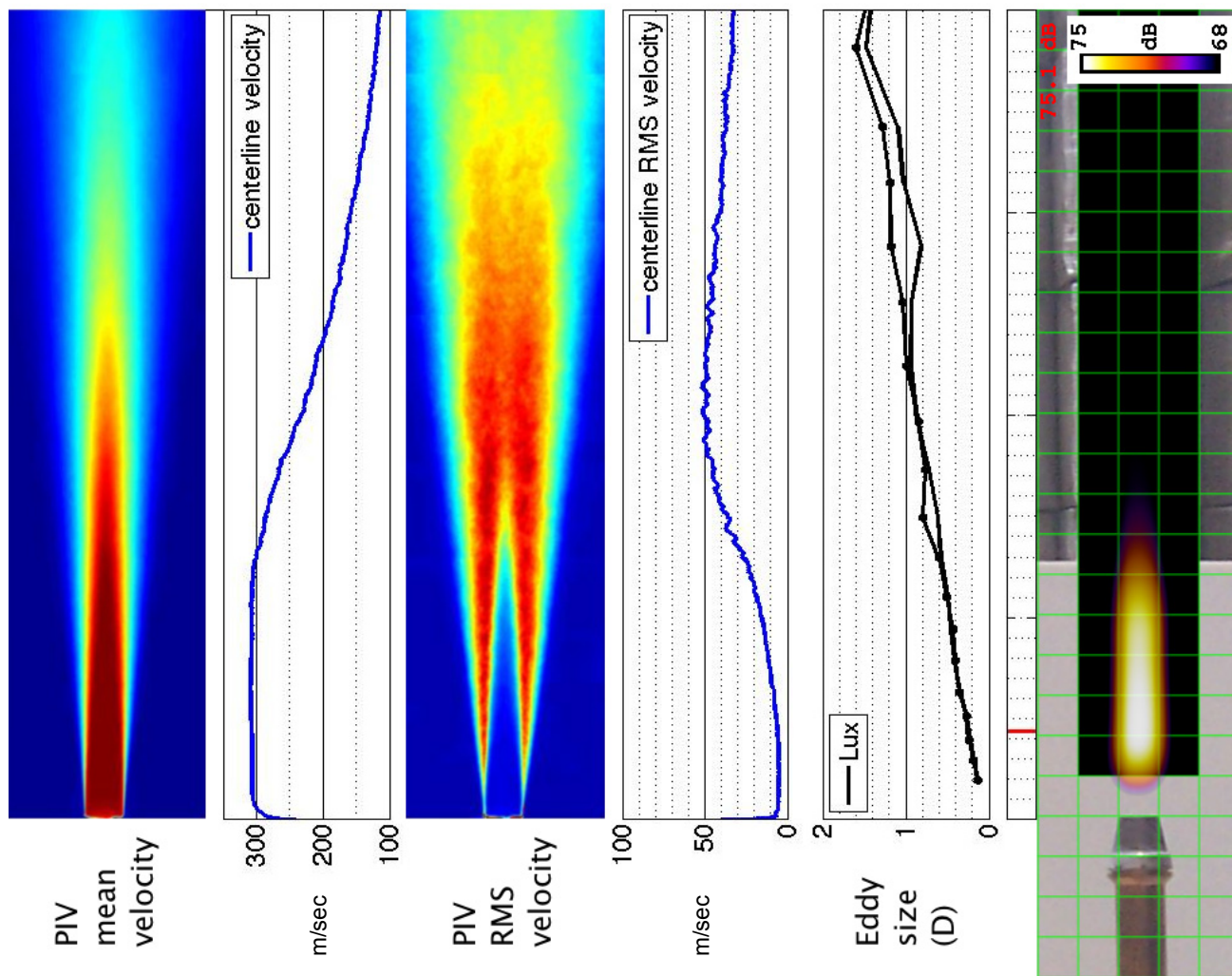
Figure 69.—SMC000; set point 7; Mj=0.98; St=2.14.
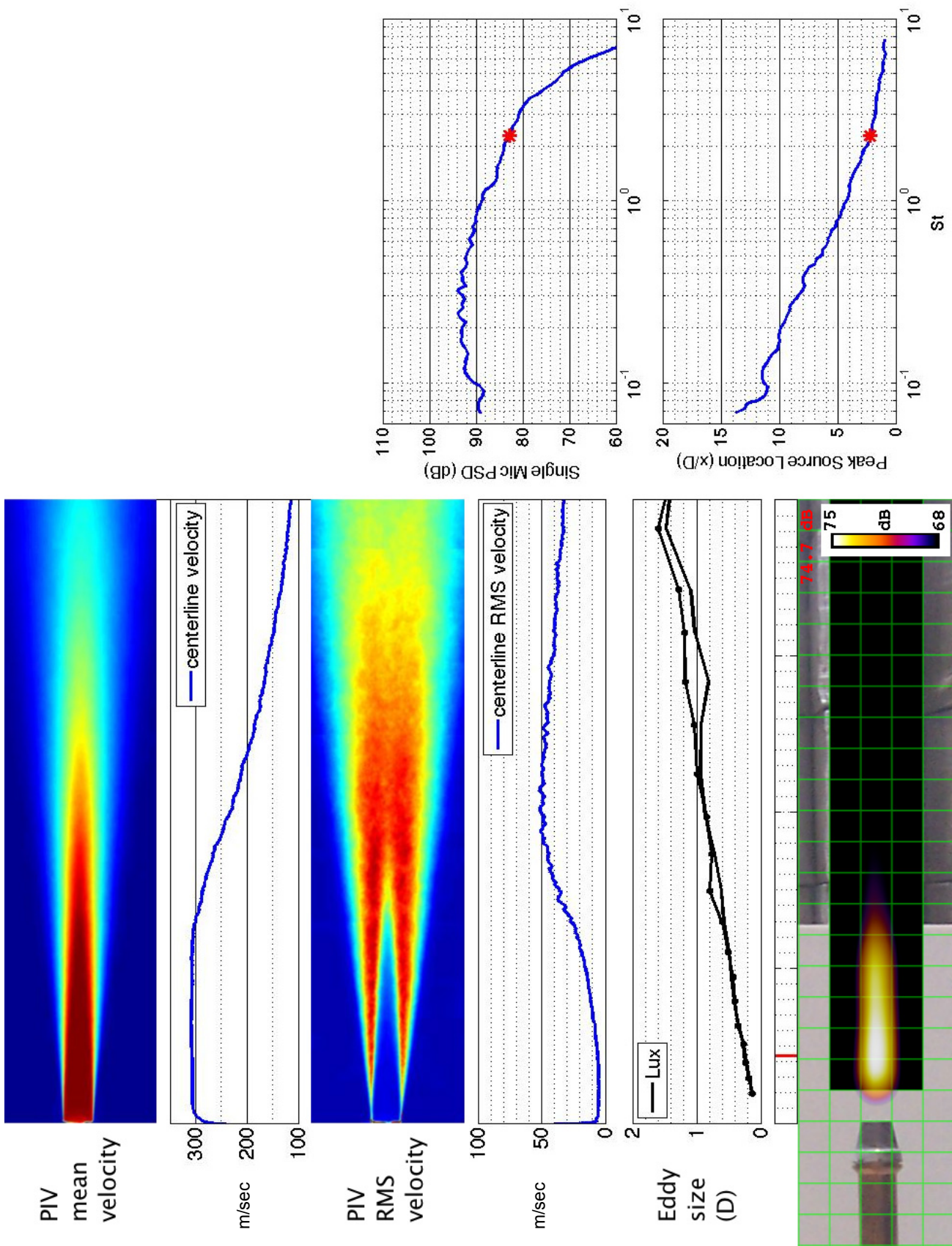
Figure 70.—SMC000; set point 7; Mj=0.98; St=2.27.
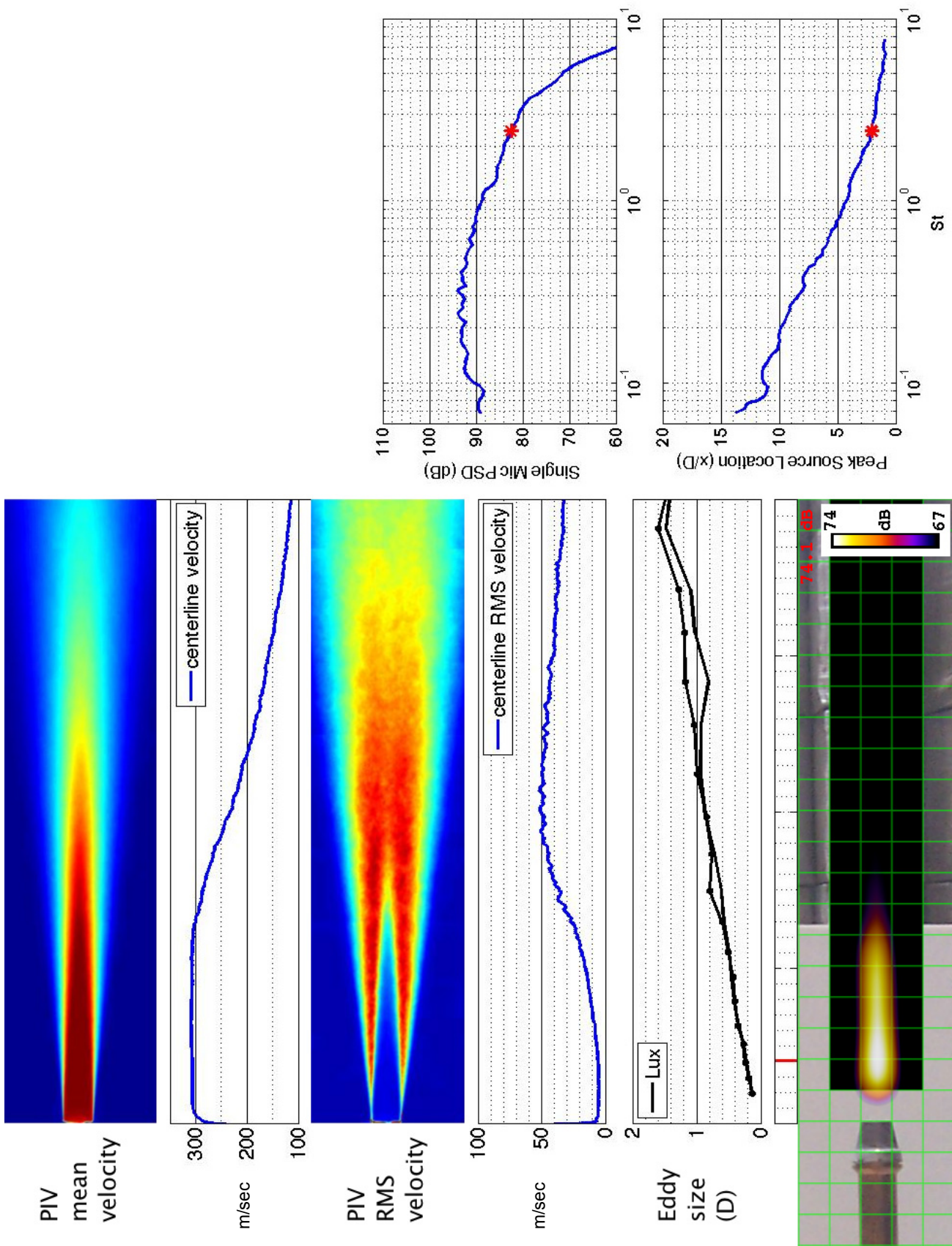
Figure 71.—SMC000; set point 7; Mj=0.98; St=2.42.
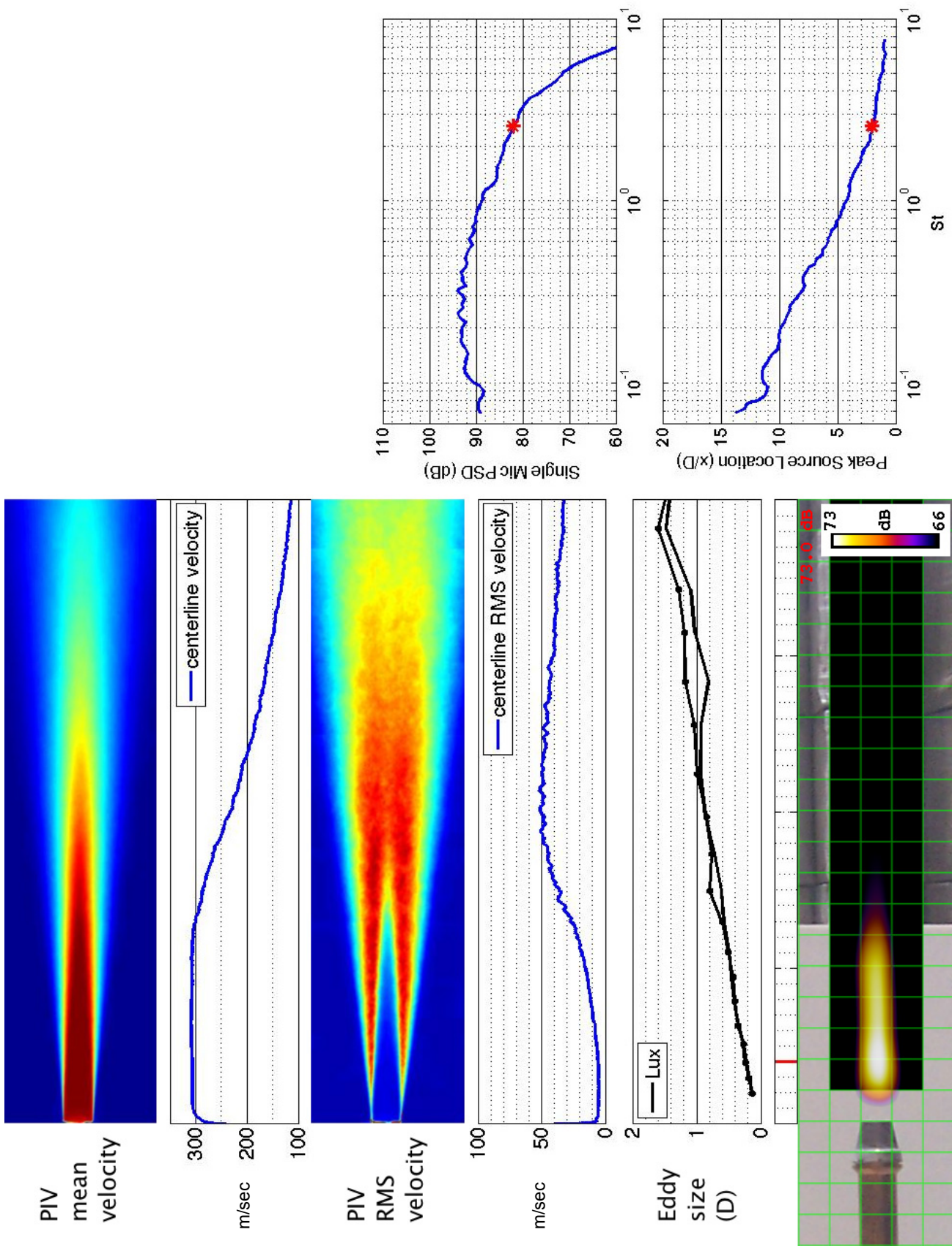
Figure 72.—SMC000; set point 7; Mj=0.98; St=2.57.
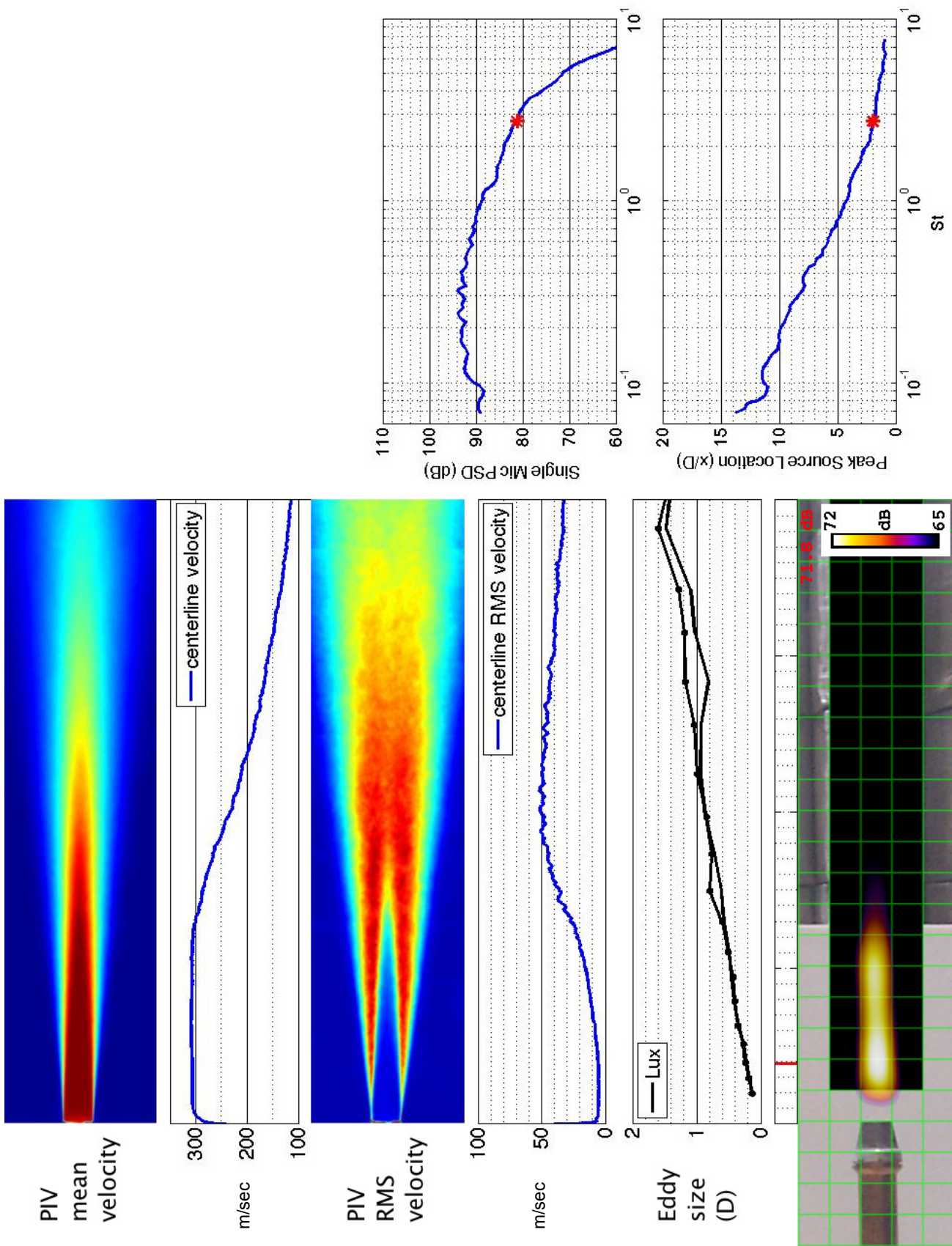
Figure 73.—SMC000; set point 7; Mj=0.98; St=2.73.
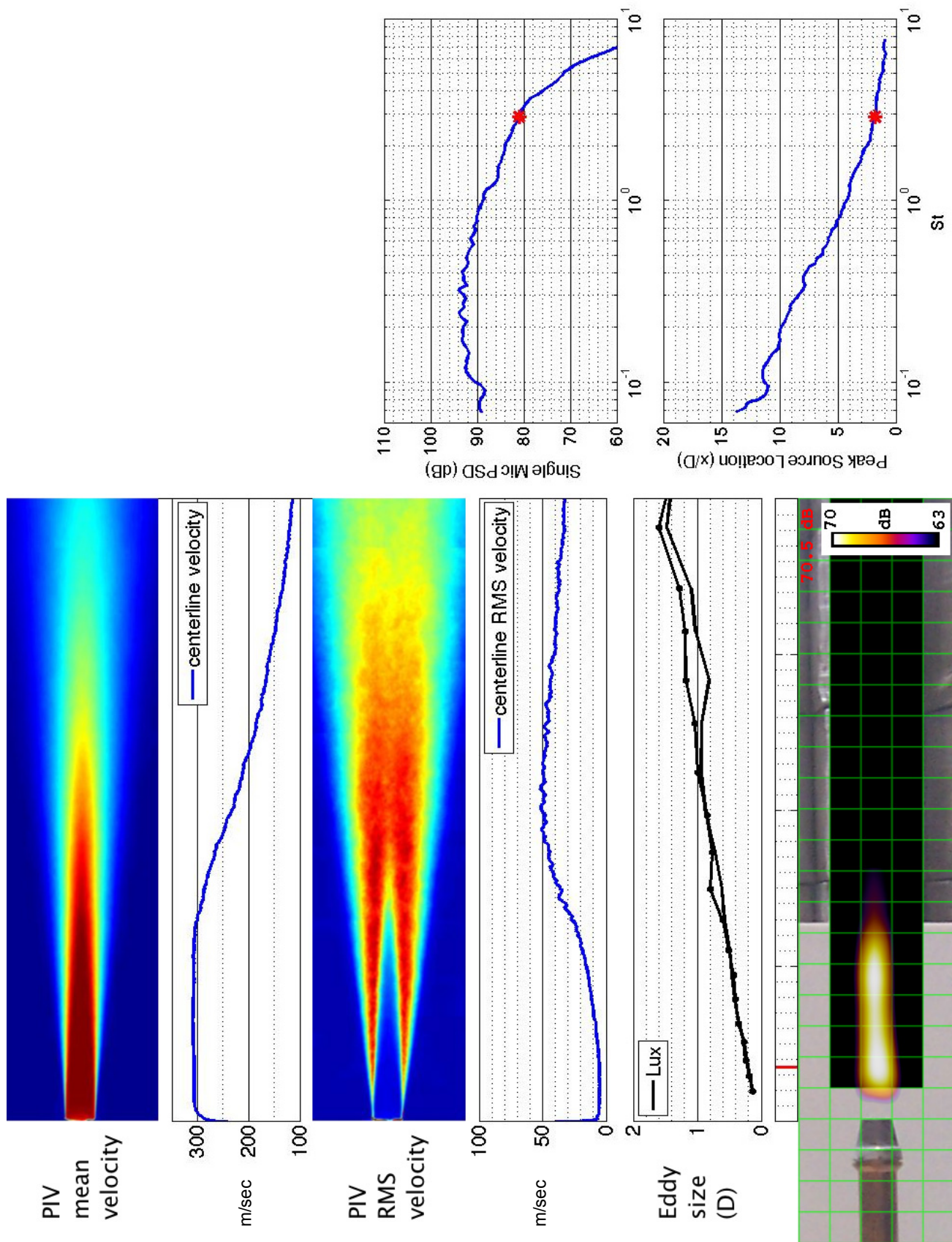
Figure 74.—SMC000; set point 7; Mj=0.98; St=2.89.
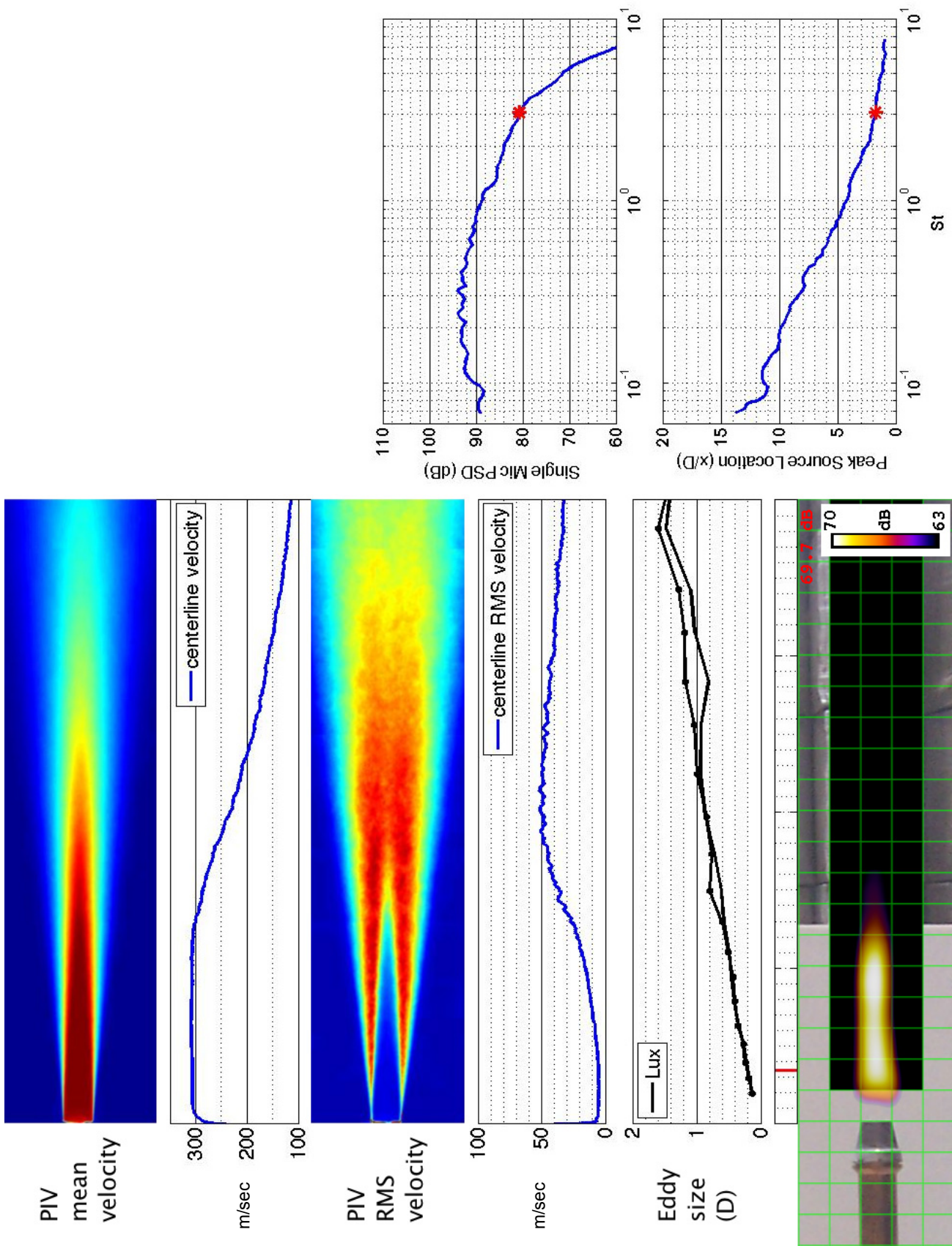
Figure 75.—SMC000; set point 7; Mj=0.98; St=3.06.
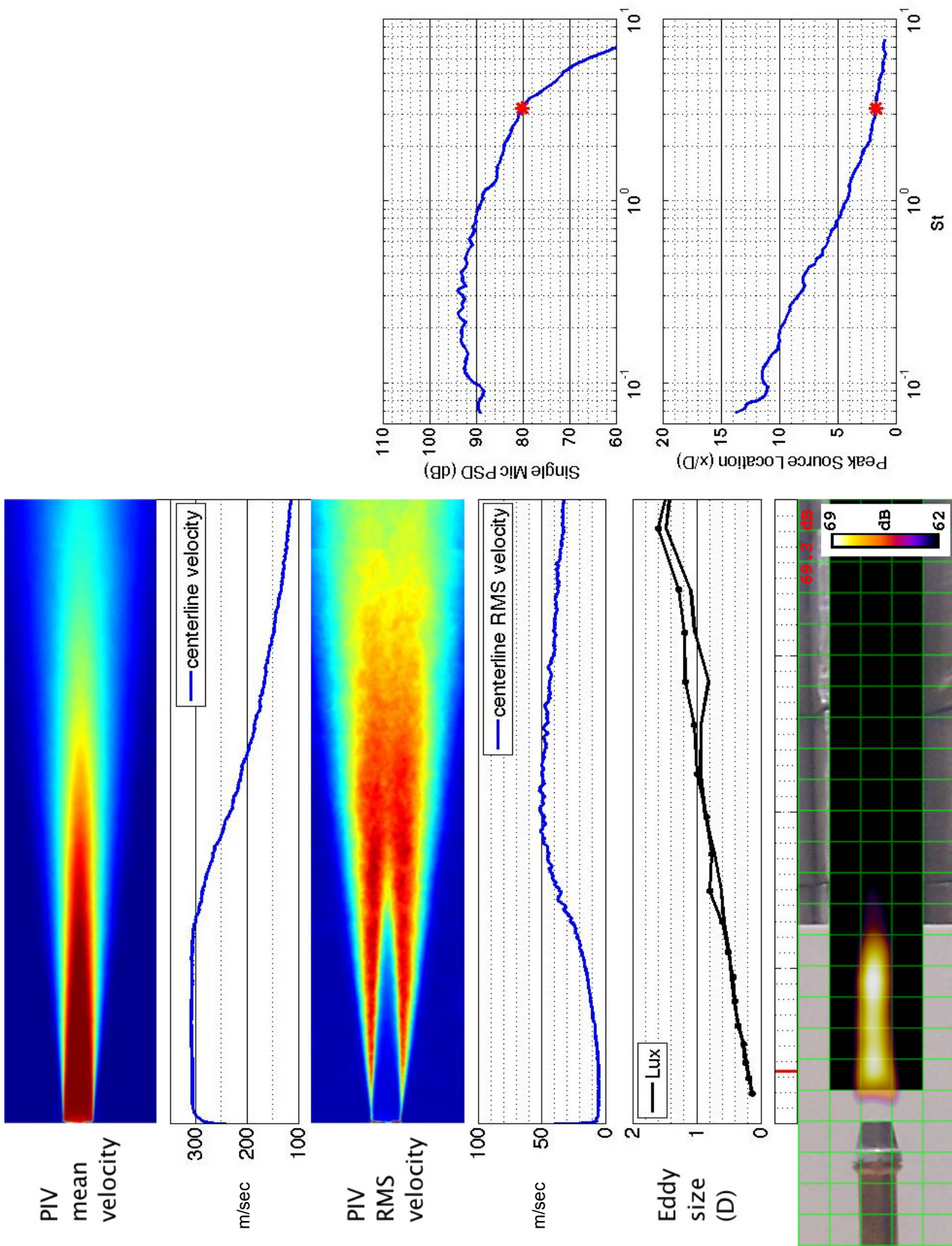
Figure 76.—SMC000; set point 7; Mj=0.98; St=3.23.
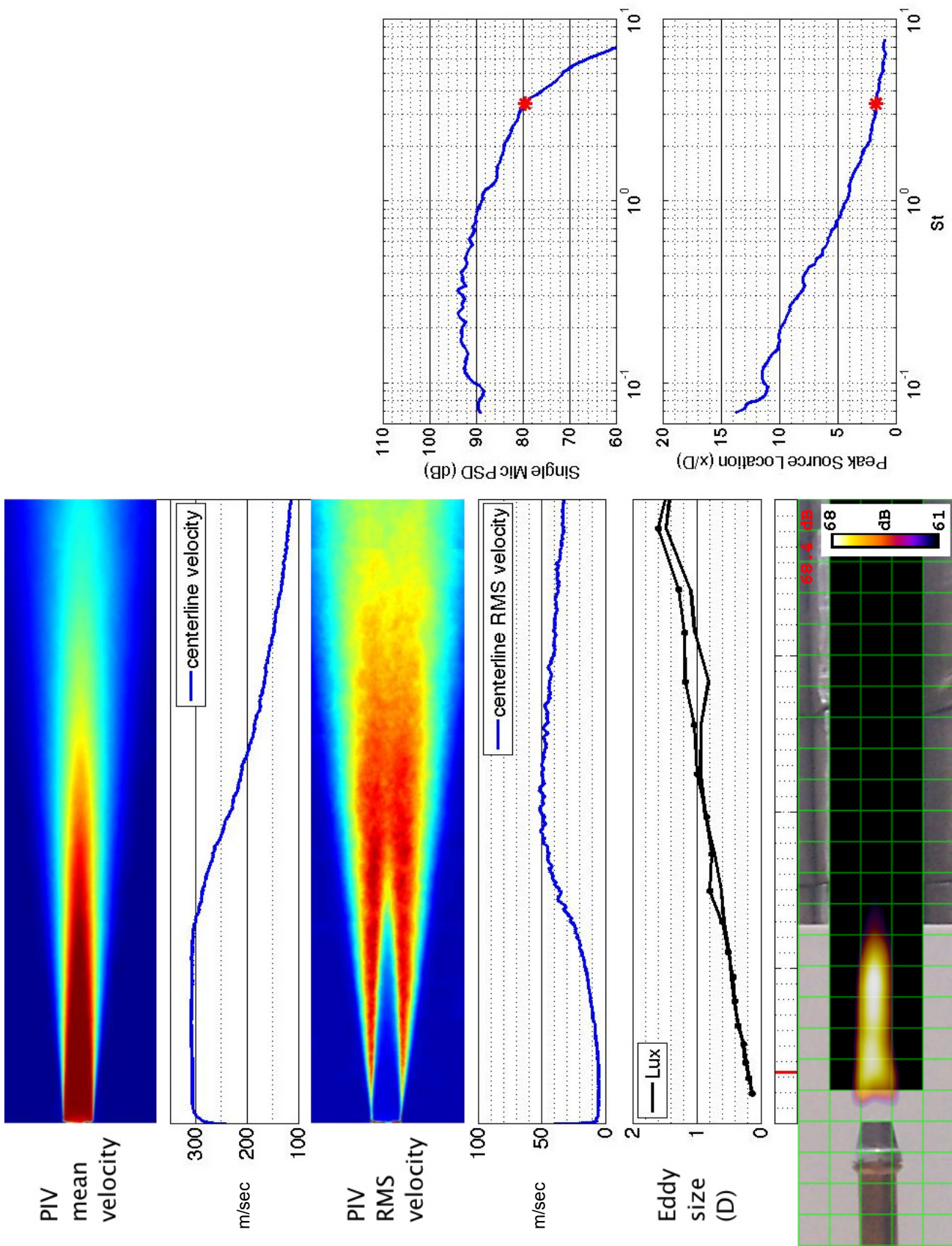
Figure 77.—SMC000; set point 7; Mj=0.98; St=3.42.
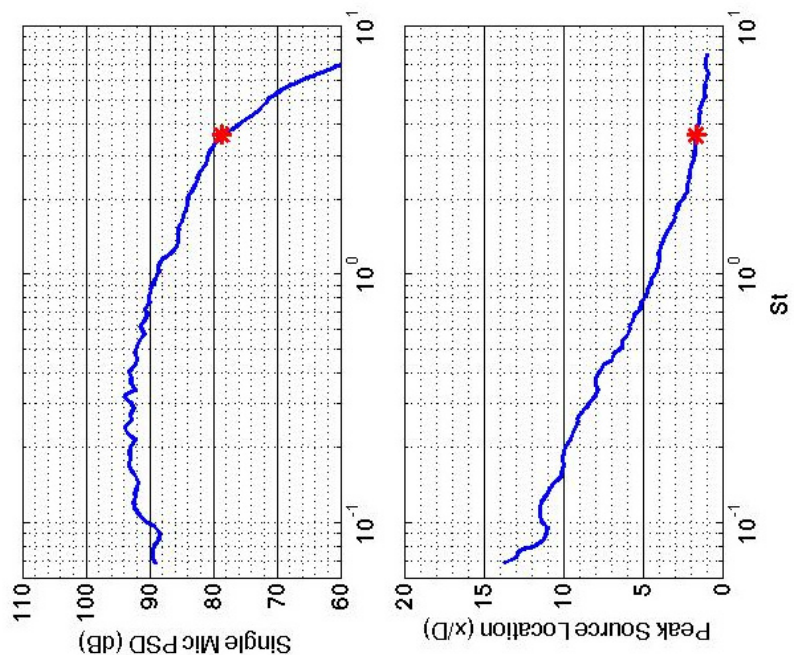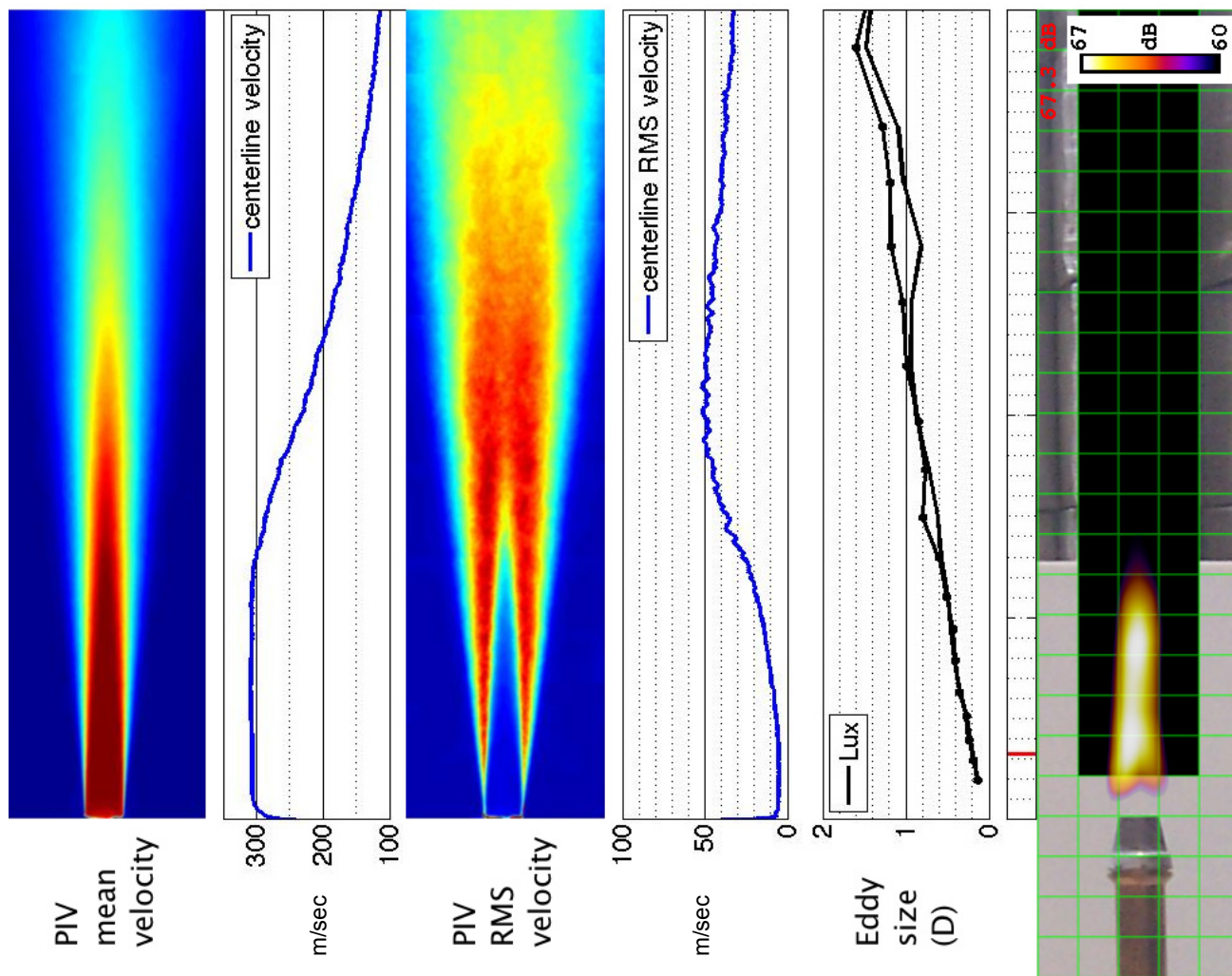
Figure 78.—SMC000; set point 7; Mj=0.98; St=3.61.
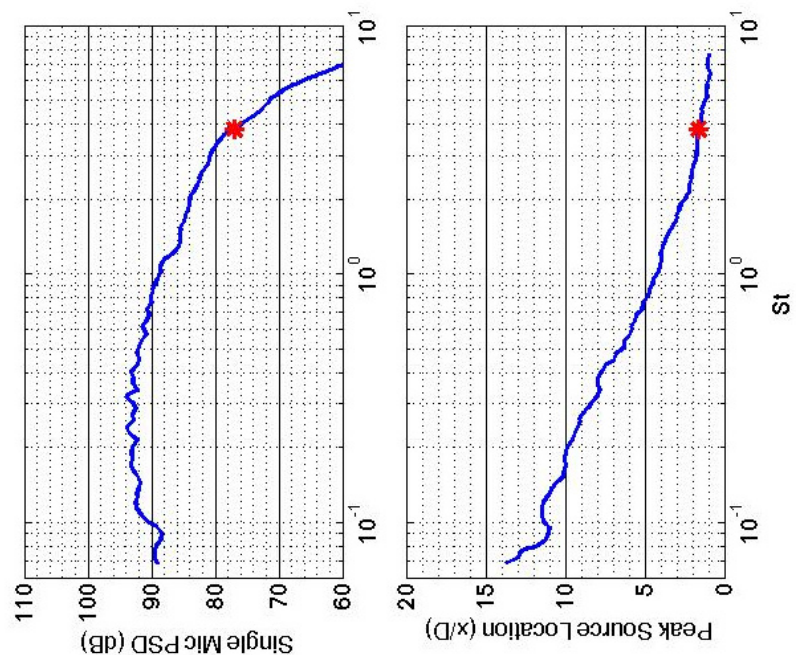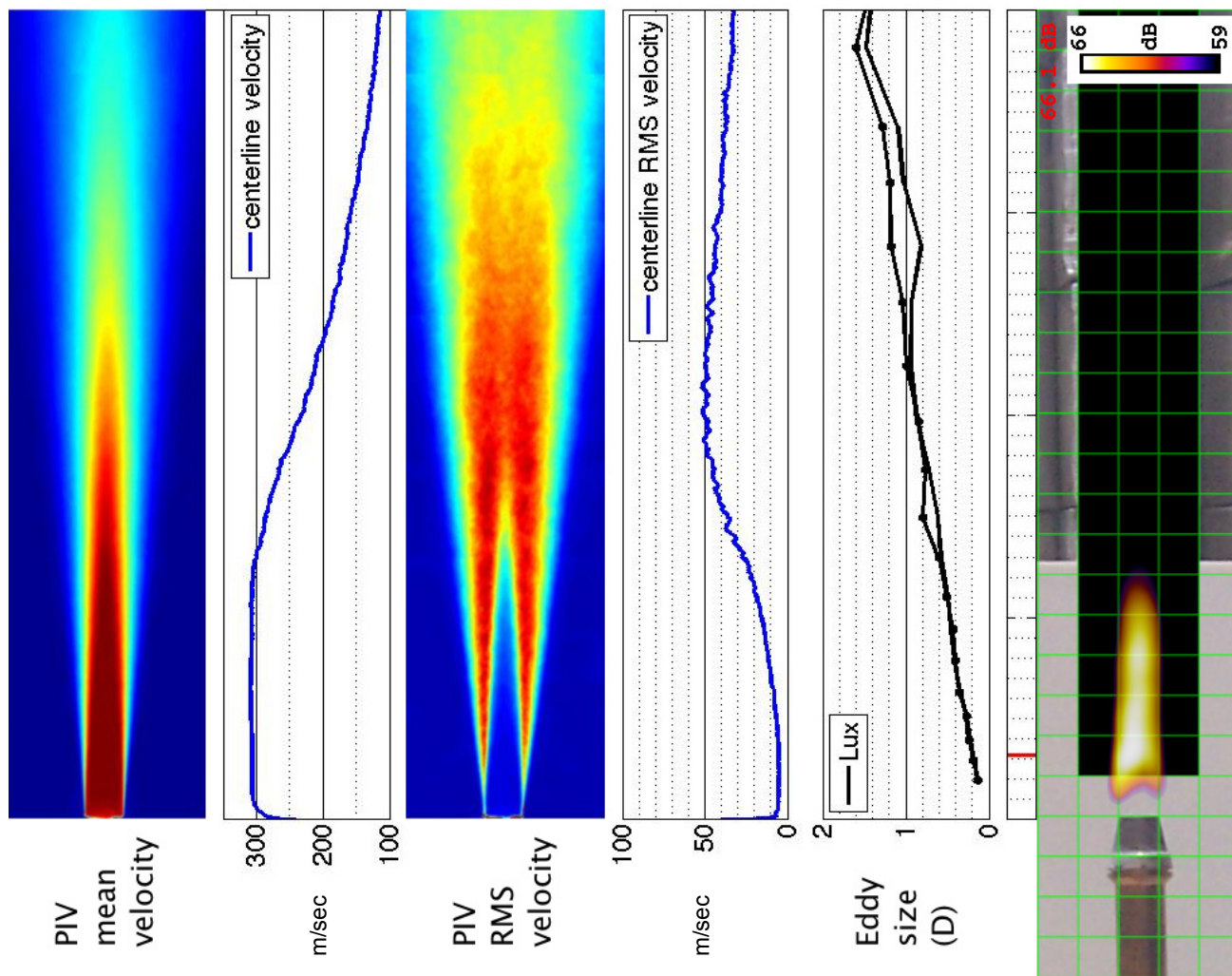
Figure 79.—SMC000; set point 7; Mj=0.98; St=3.82.
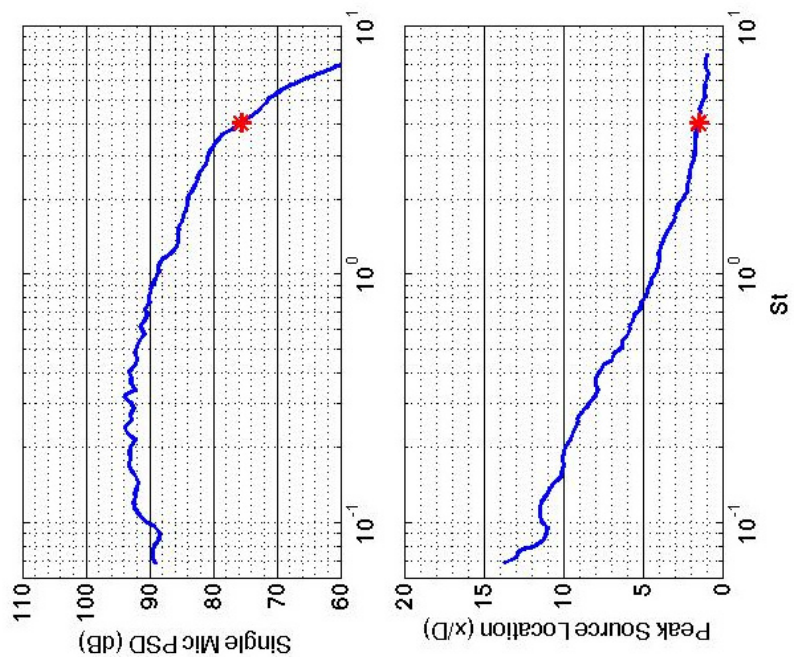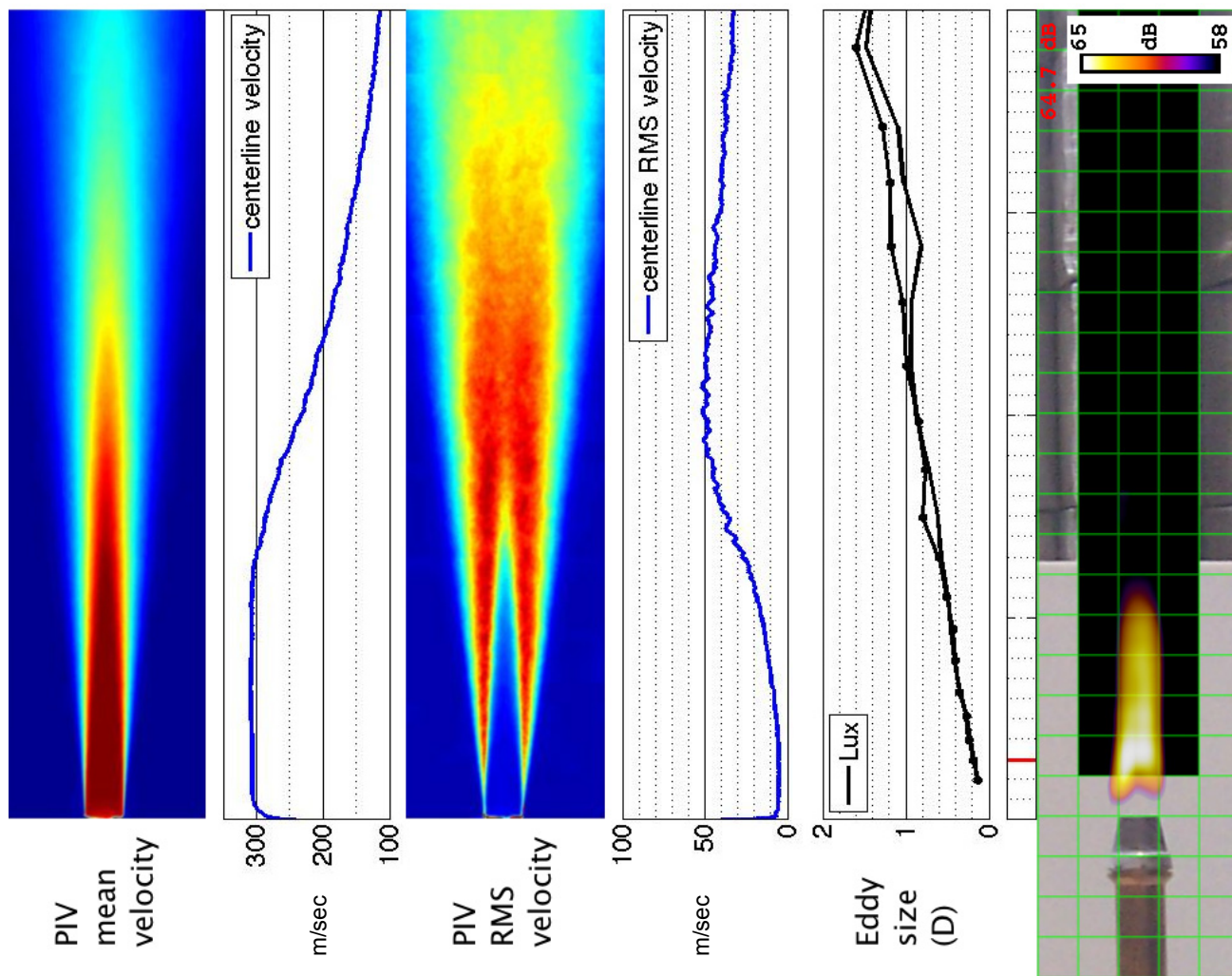
Figure 80.—SMC000; set point 7; Mj=0.98; St=4.04.
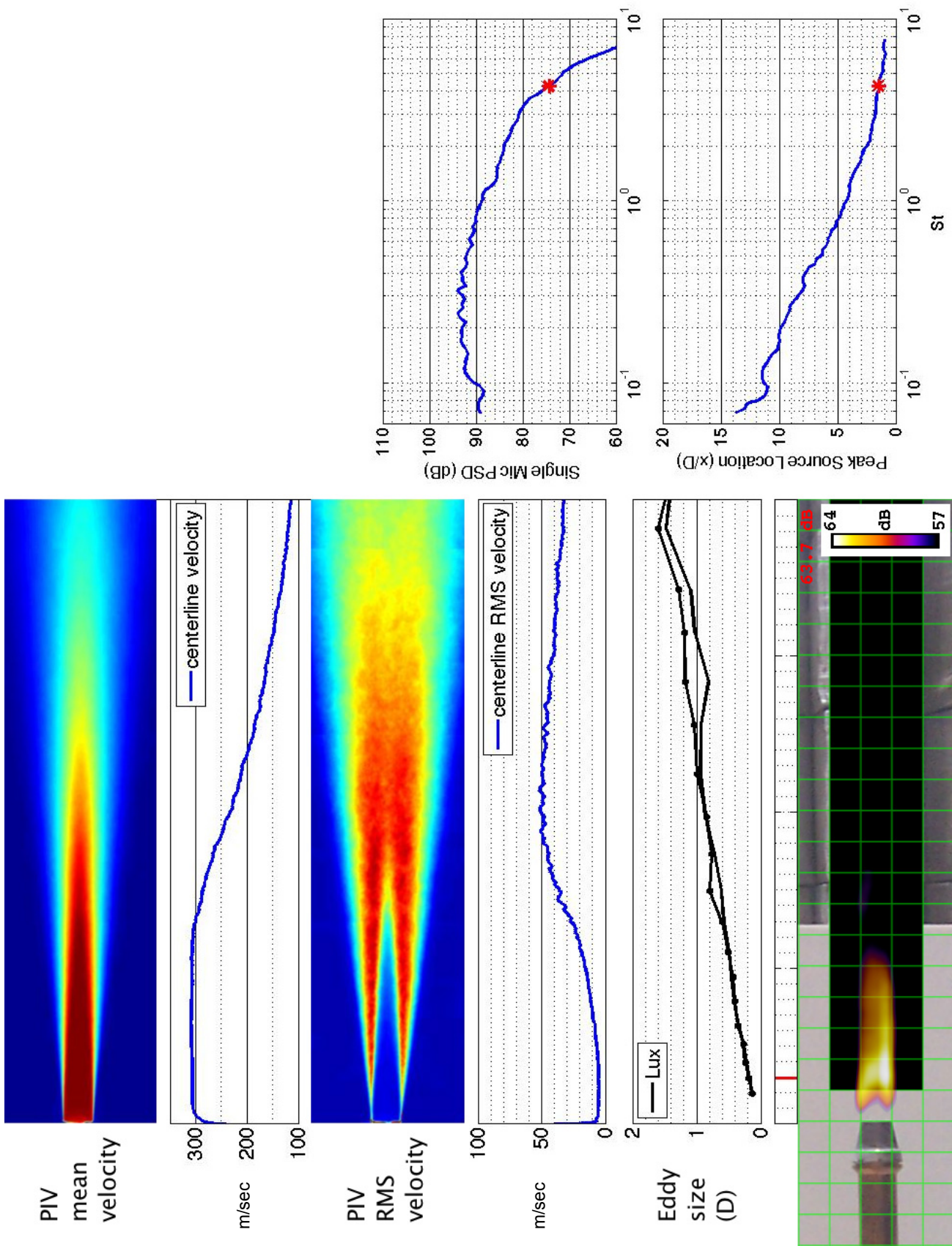
Figure 81.—SMC000; set point 7; Mj=0.98; St=4.28.
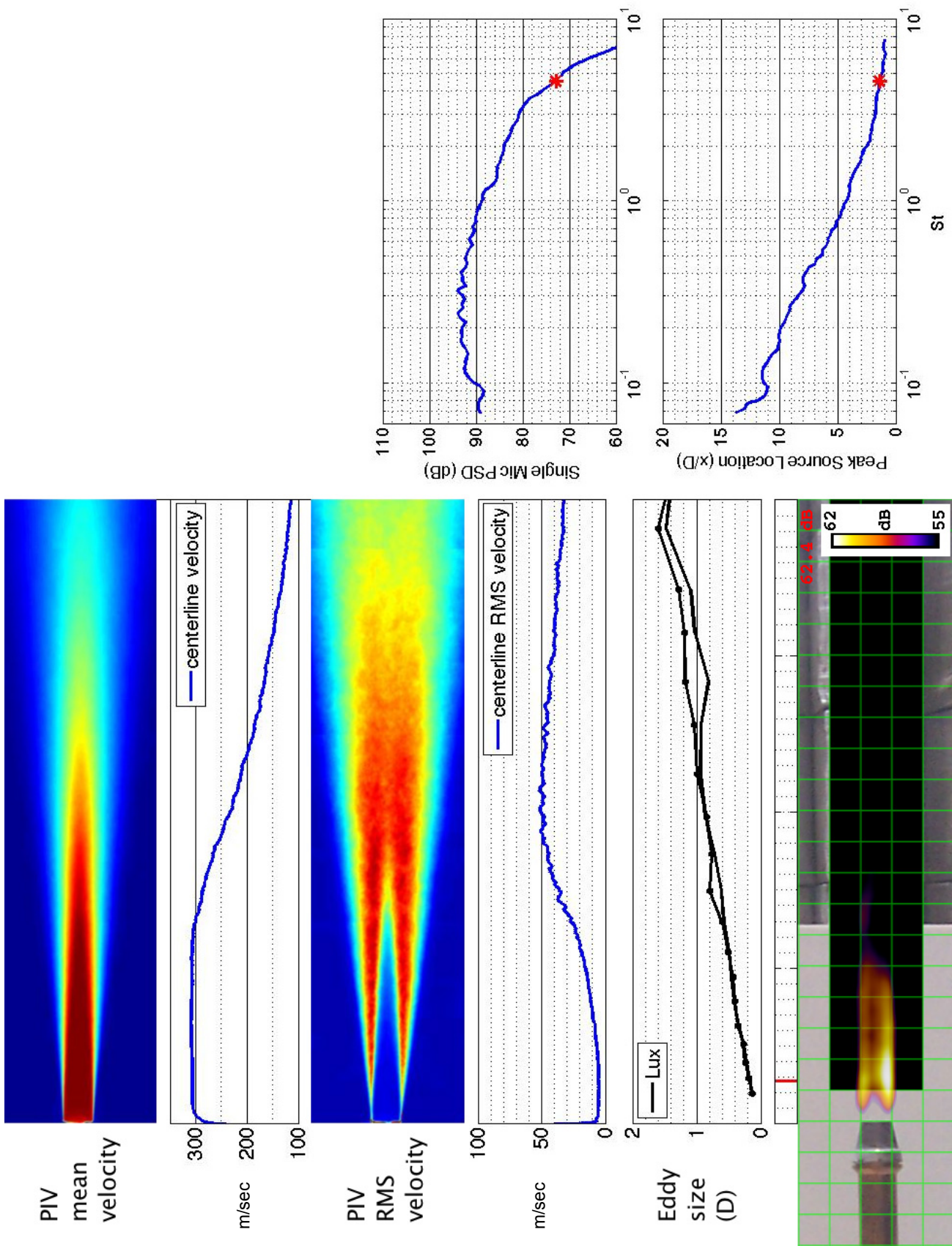
Figure 82.—SMC000; set point 7; Mj=0.98; St=4.54.
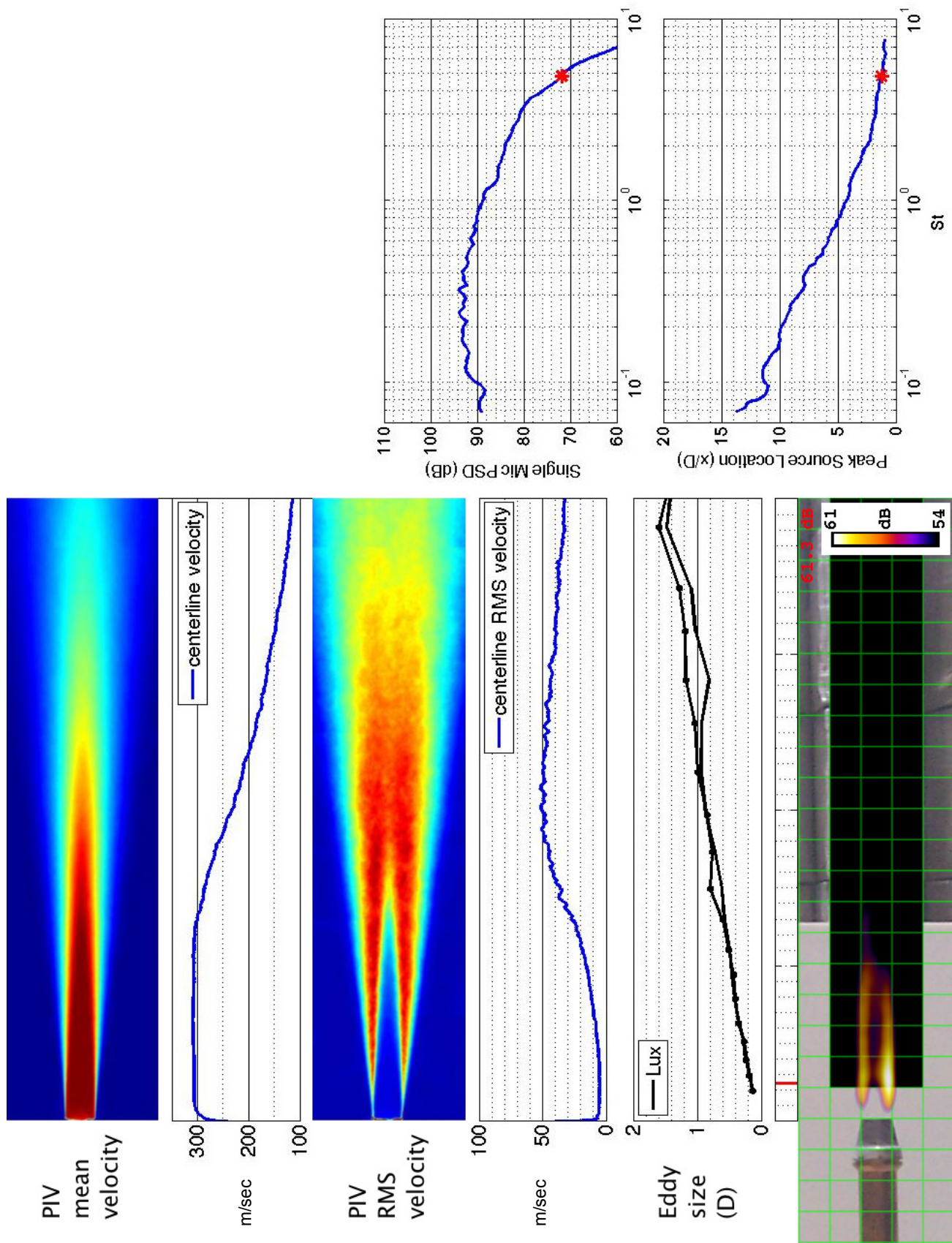
Figure 83.—SMC000; set point 7; Mj=0.98; St=4.83.
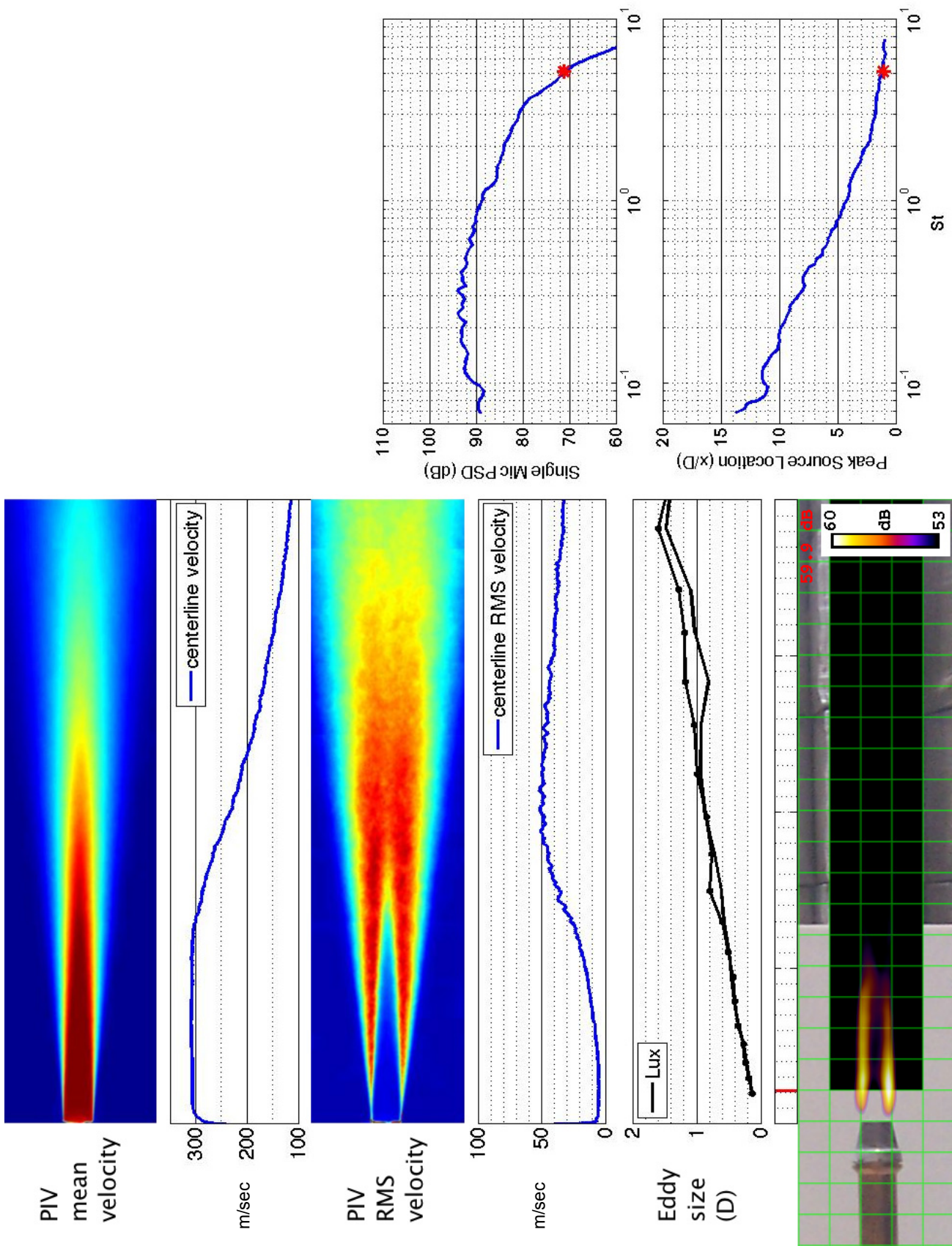
Figure 84.—SMC000; set point 7; Mj=0.98; St=5.14.
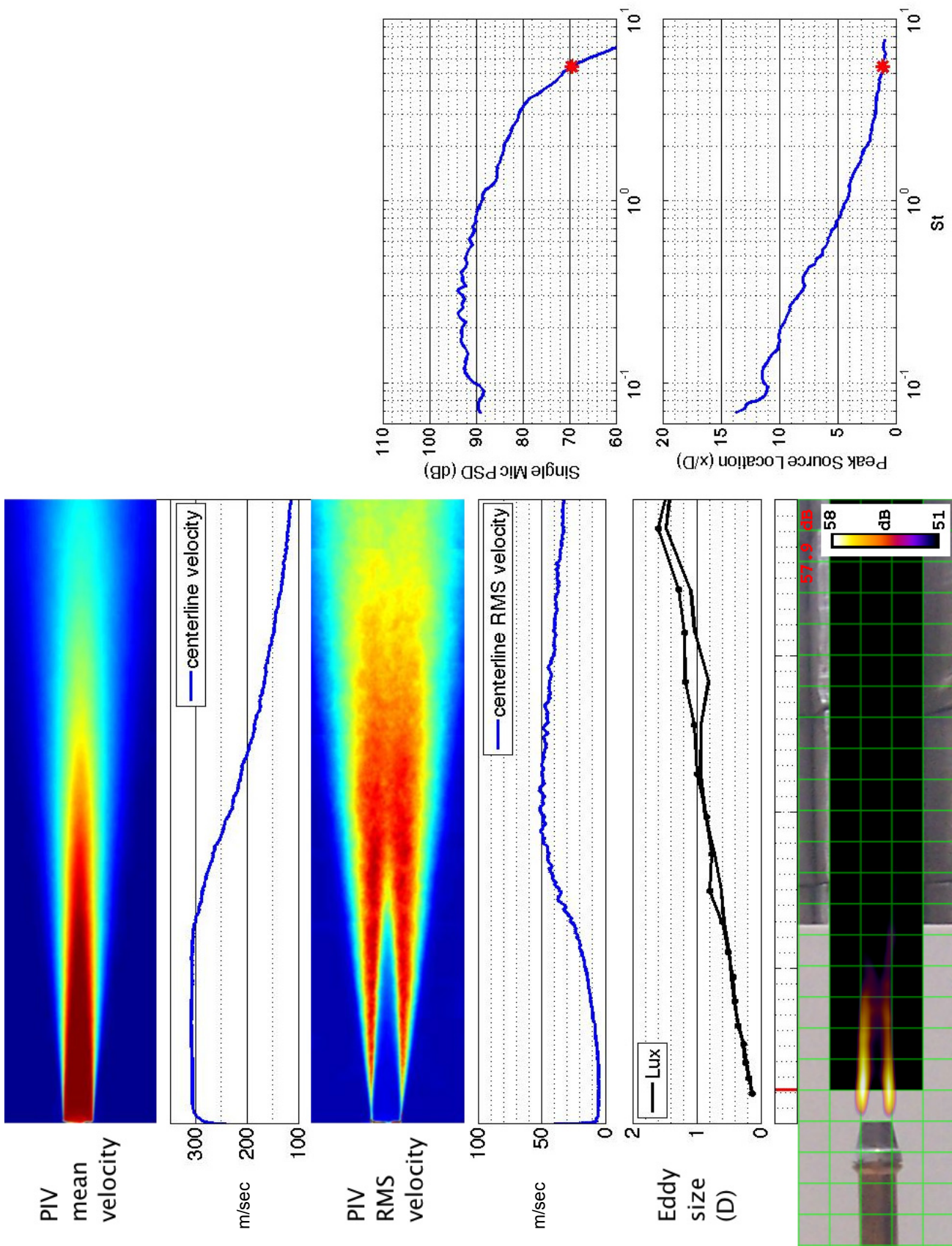
Figure 85.—SMC000; set point 7; Mj=0.98; St=5.46.
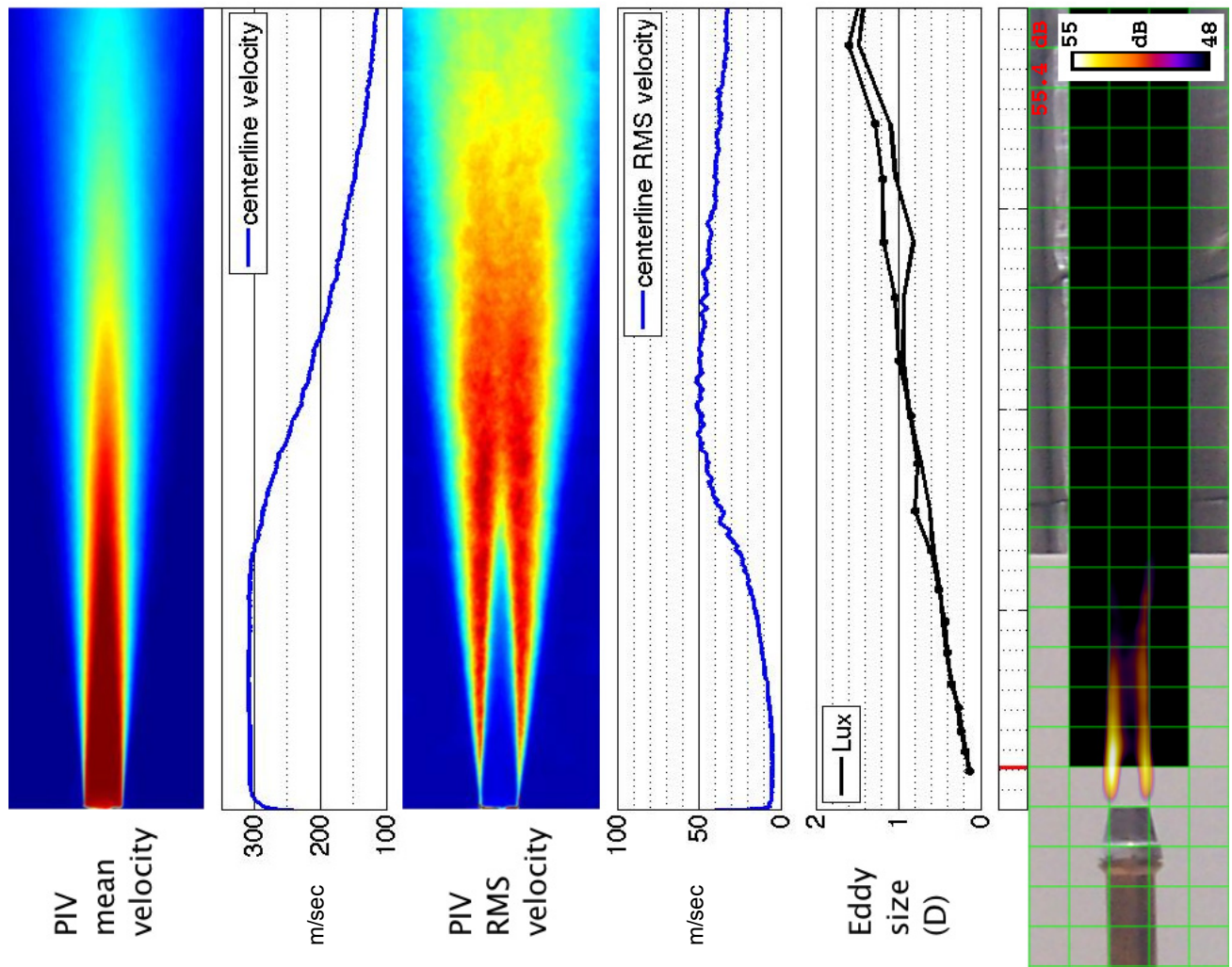
Figure 86.—SMC000; set point 7; Mj=0.98; St=5.78.
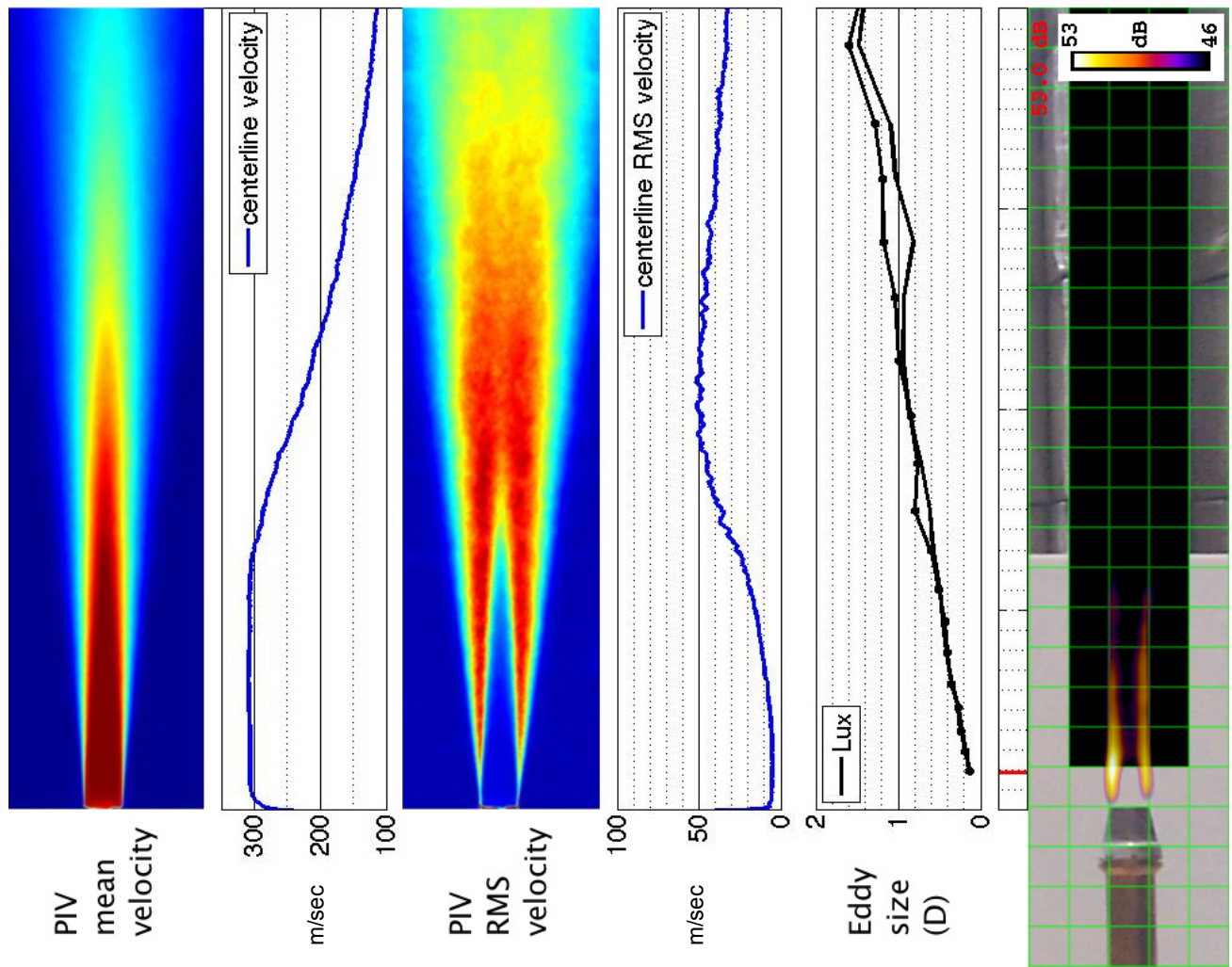
Figure 87.—SMC000; set point 7; Mj=0.98; St=6.11.
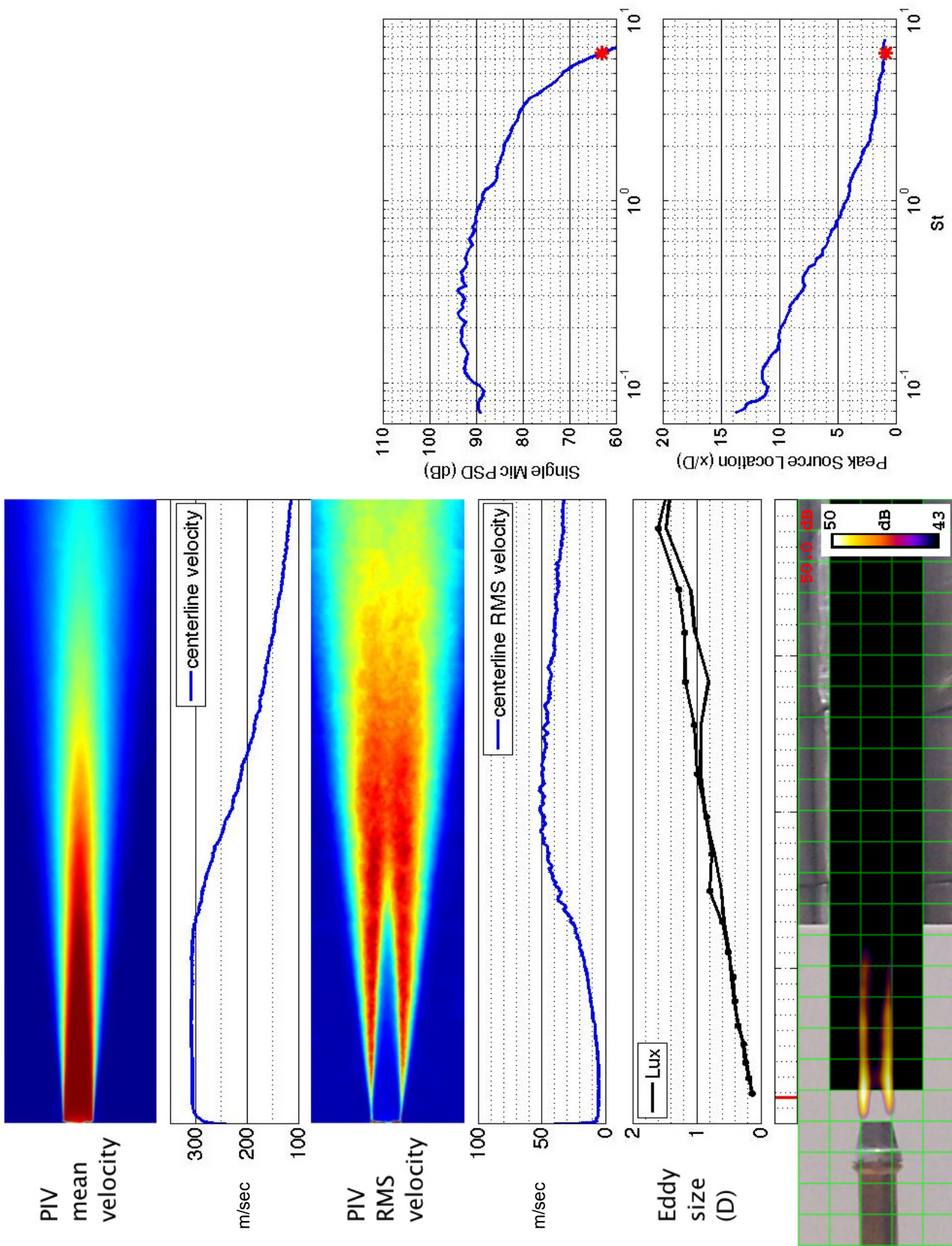
Figure 88.—SMC000; set point 7; Mj=0.98; St=6.46.
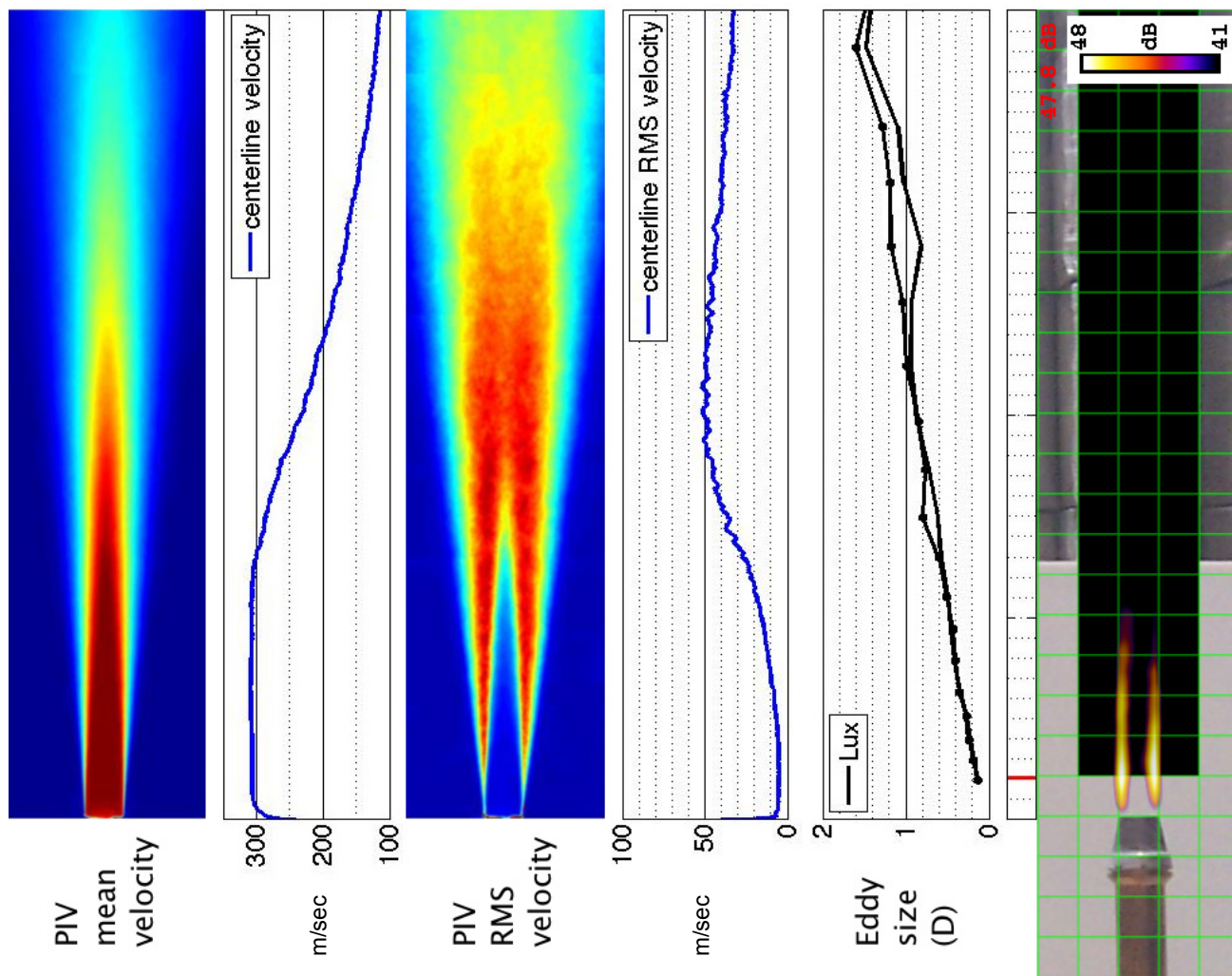
Figure 89.—SMC000; set point 7; Mj=0.98; St=6.83.
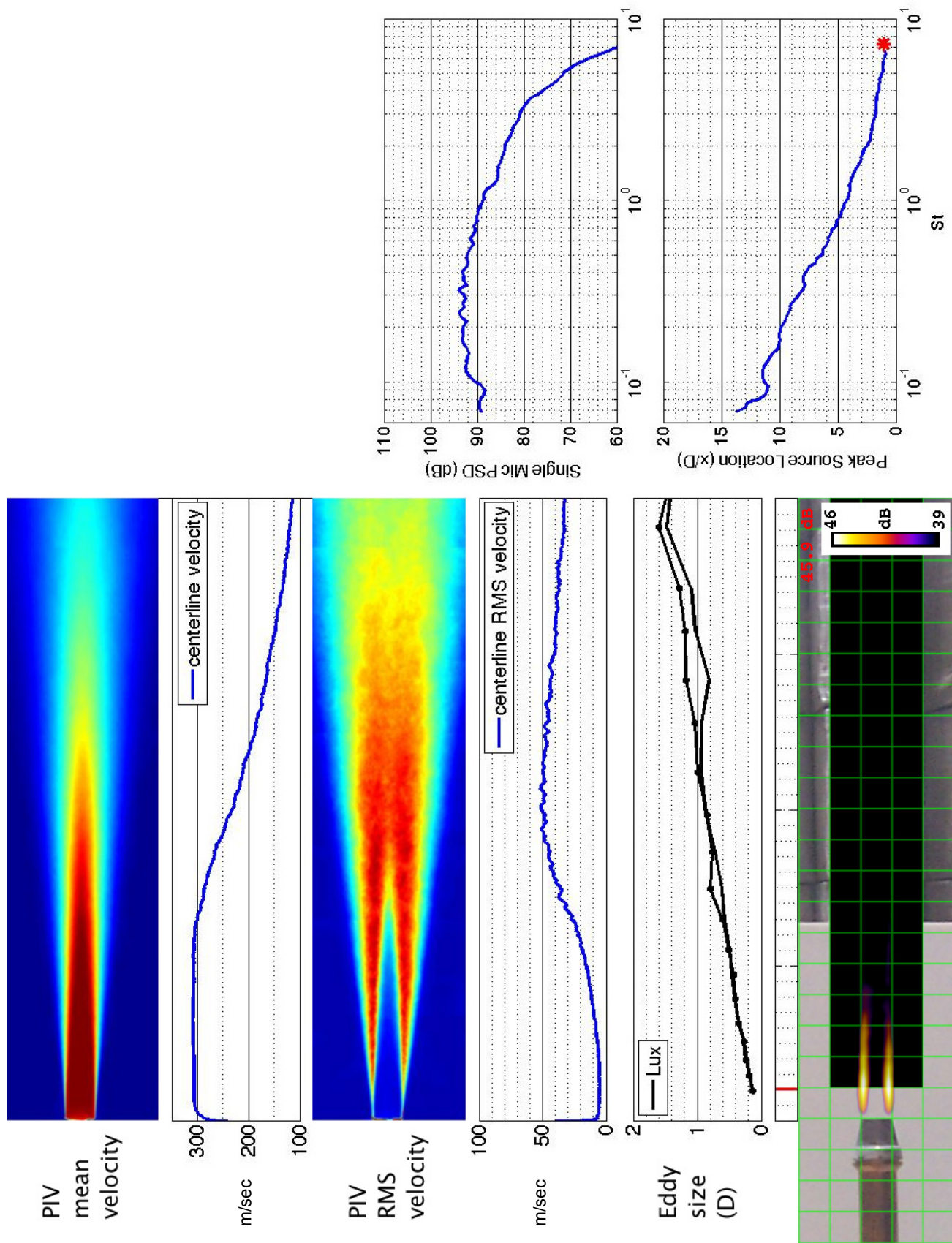
Figure 90.—SMC000; set point 7; Mj=0.98; St=7.23.
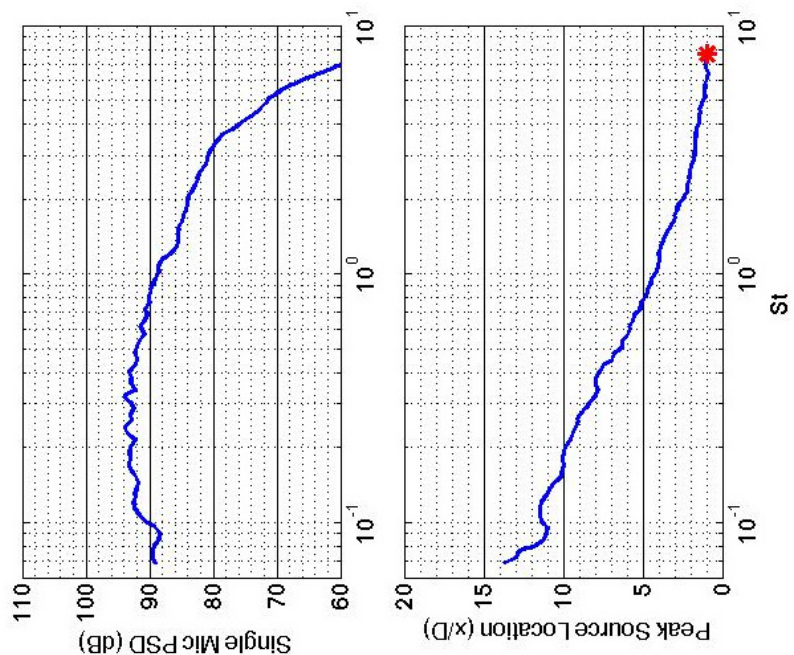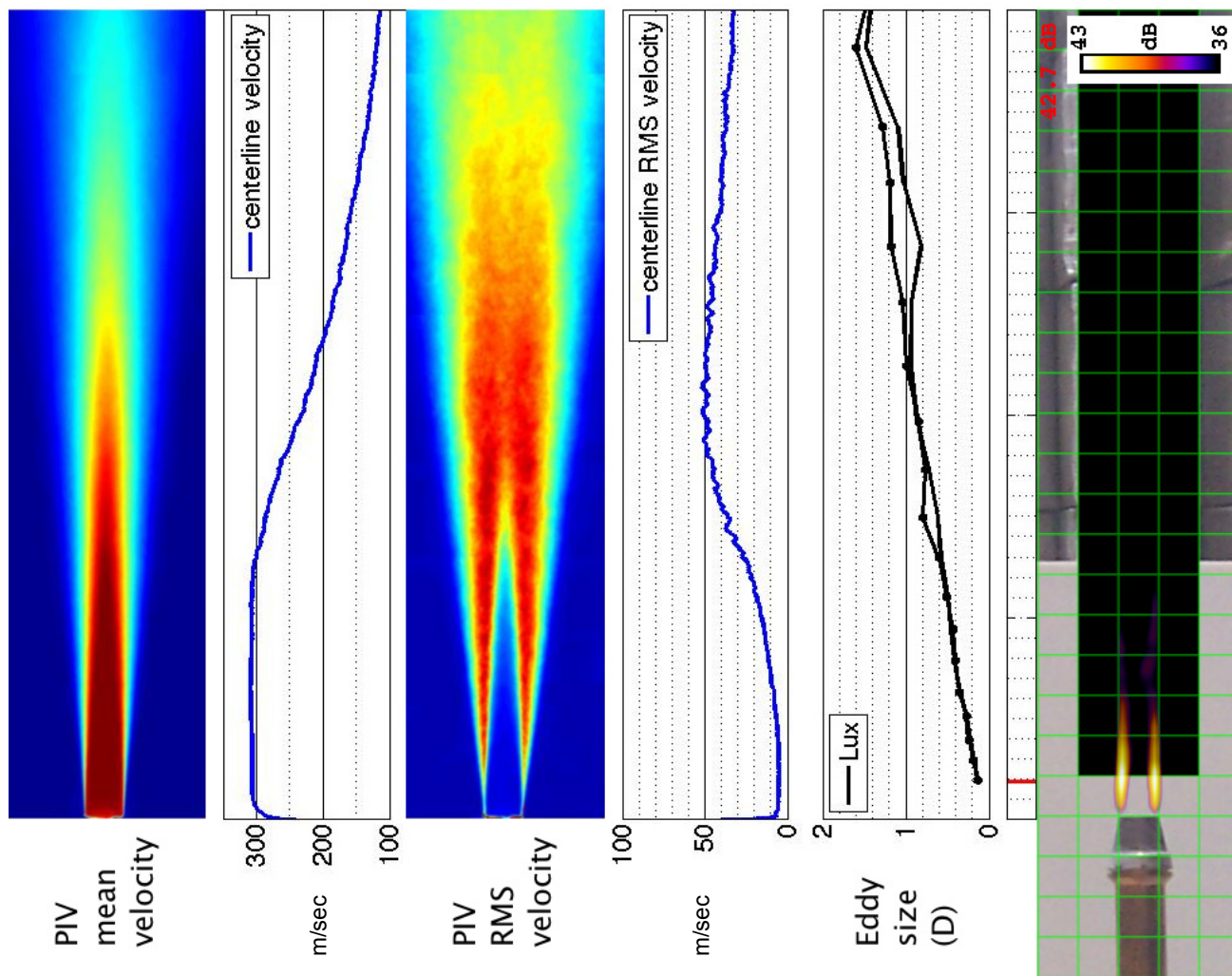
Figure 91.—SMC000; set point 7; Mj=0.98; St=7.64.
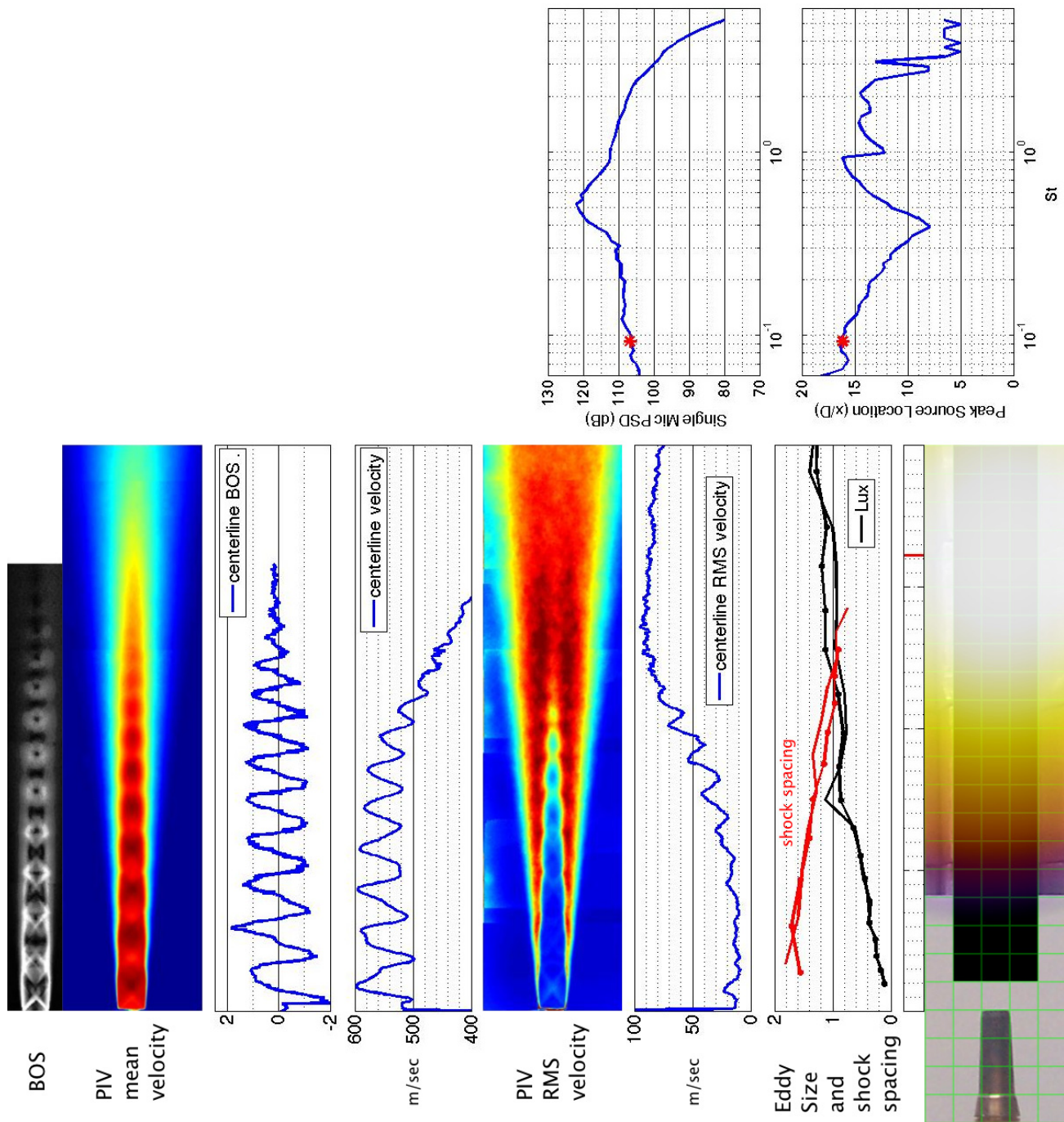
Figure 92.—SMC016; under-expanded; set point 11617; Mj=1.61; Mjdesign=1.50; St=0.093.
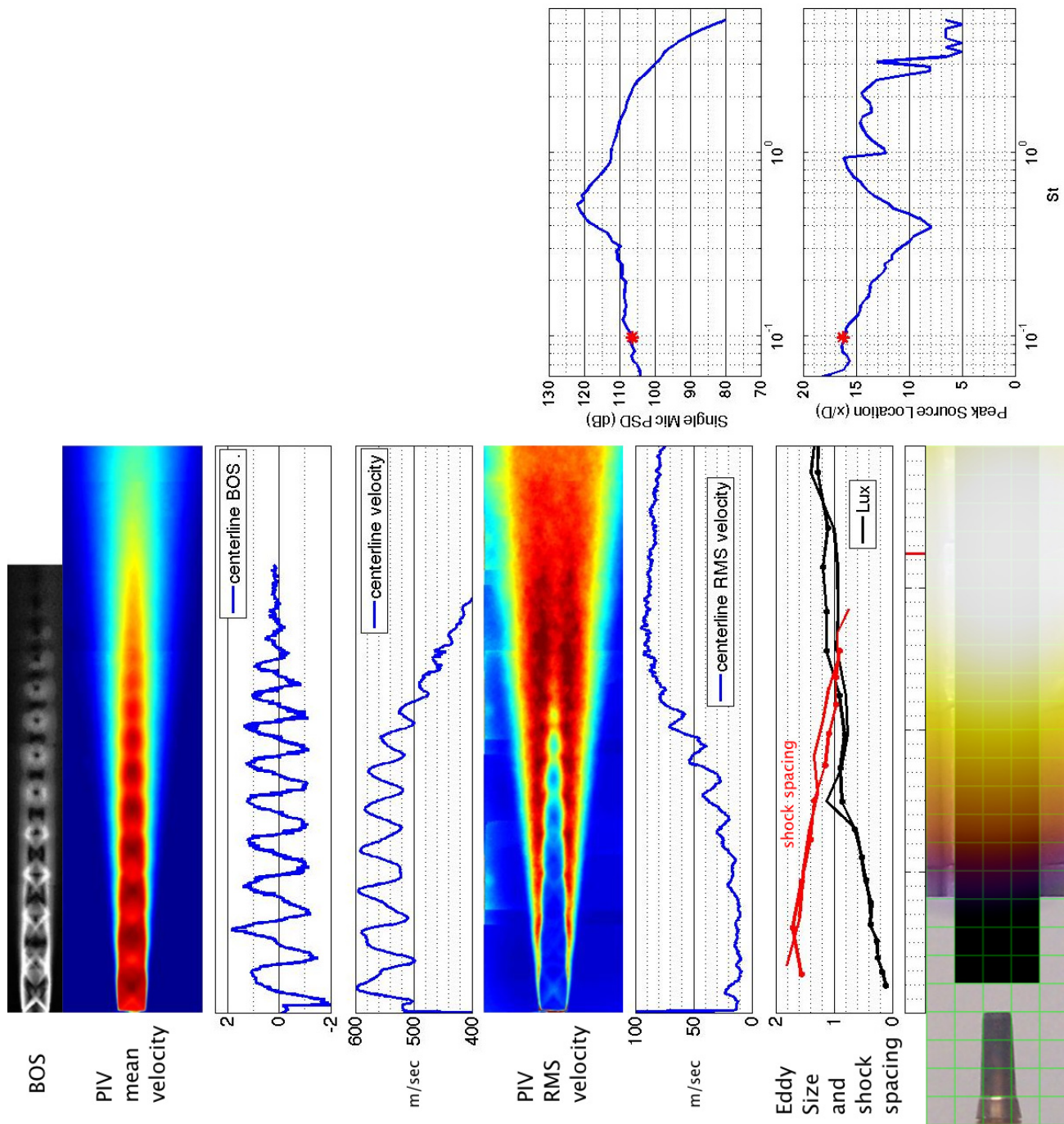
Figure 93.—SMC016; under-expanded; set point 11617; Mj=1.61; Mjdesign=1.50; St=0.099.
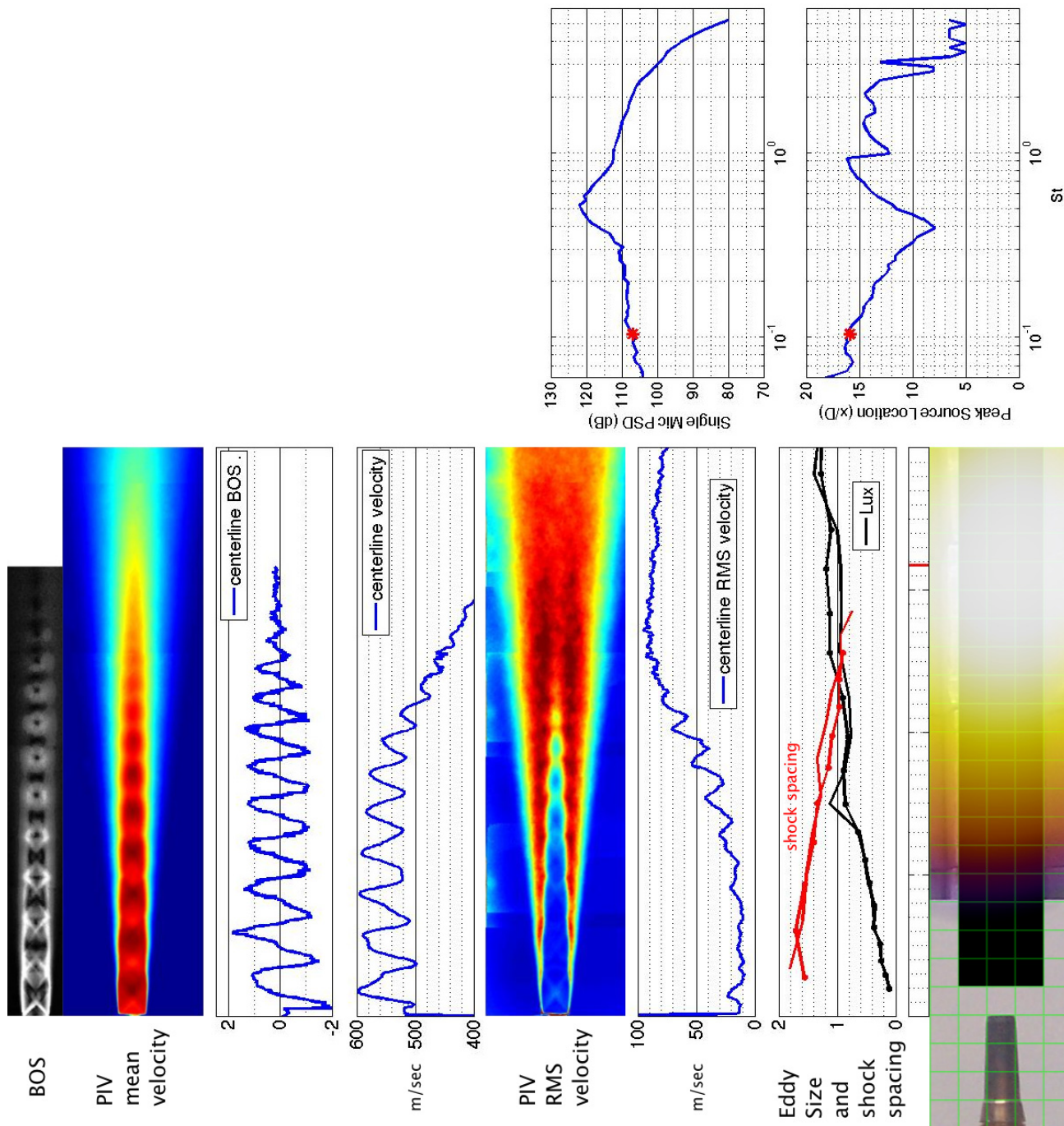
Figure 94.—SMC016; under-expanded; set point 11617; Mj=1.61; Mjdesign=1.50; St=0.104.
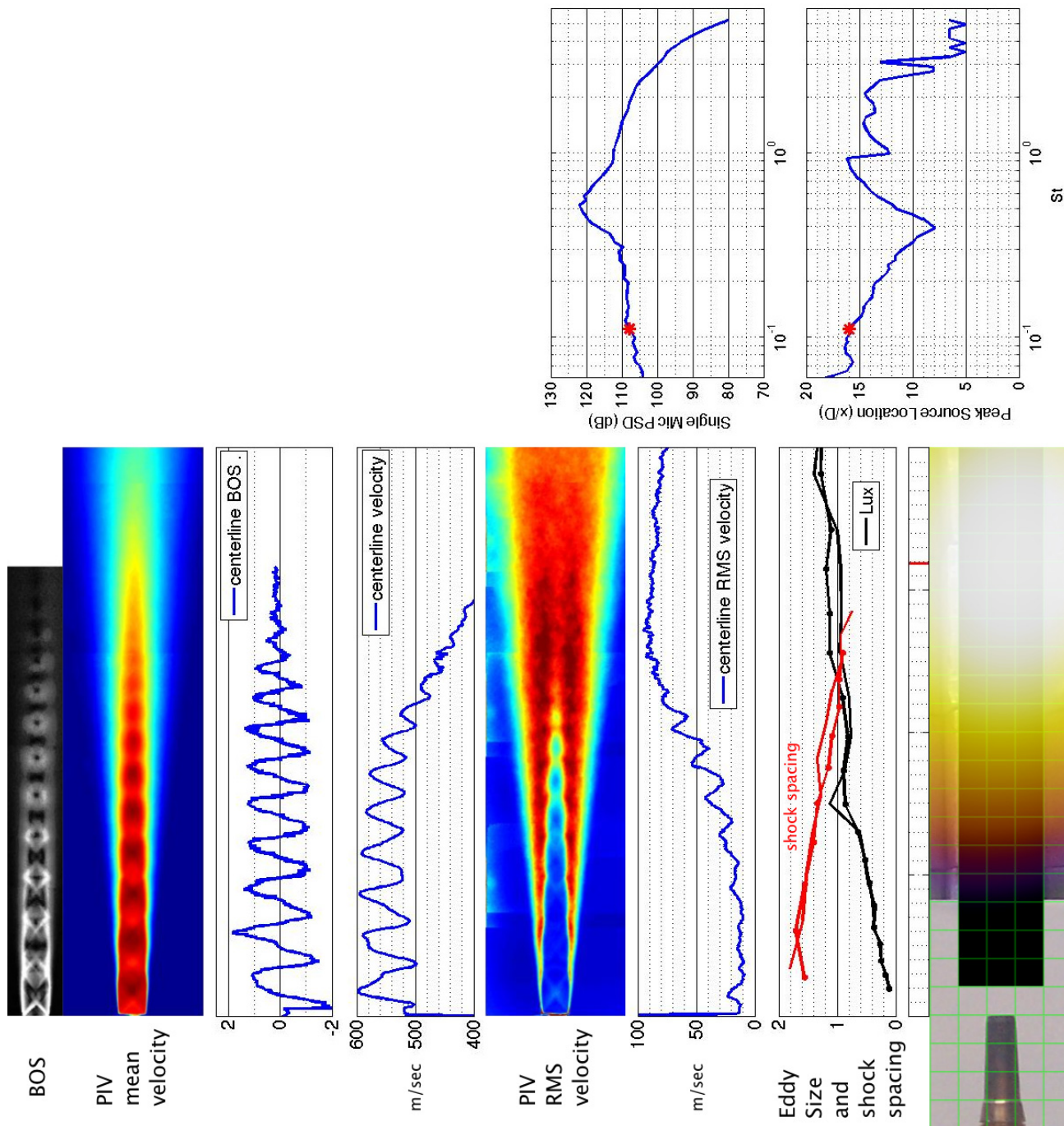
Figure 95.—SMC016; under-expanded; set point 11617; Mj=1.61; Mjdesign=1.50; St=0.110.
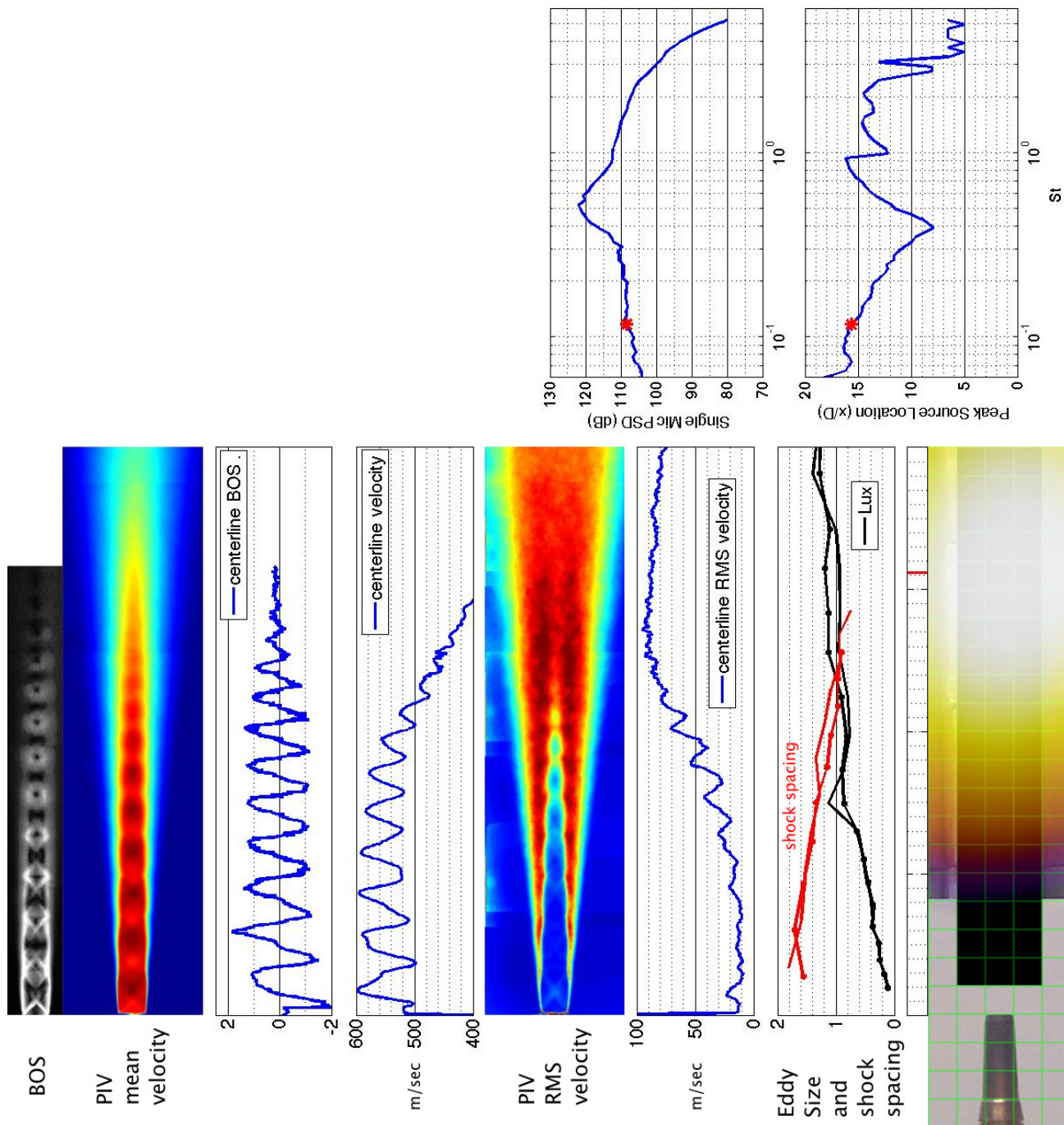
Figure 96.—SMC016; under-expanded; set point 11617; Mj=1.61; Mjdesign=1.50; St=0.116.
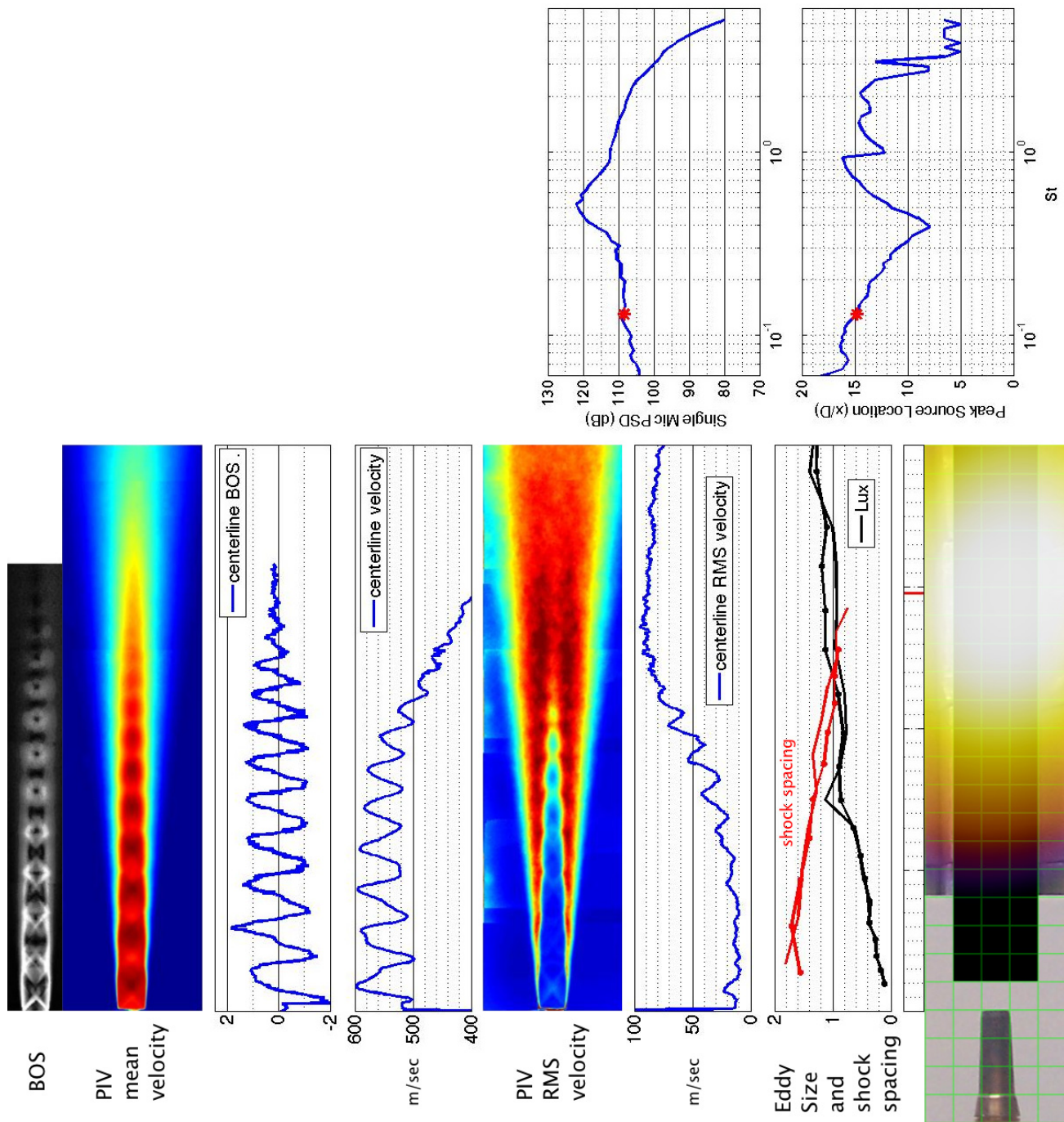
Figure 97.—SMC016; under-expanded; set point 11617; Mj=1.61; Mjdesign=1.50; St=0.130.
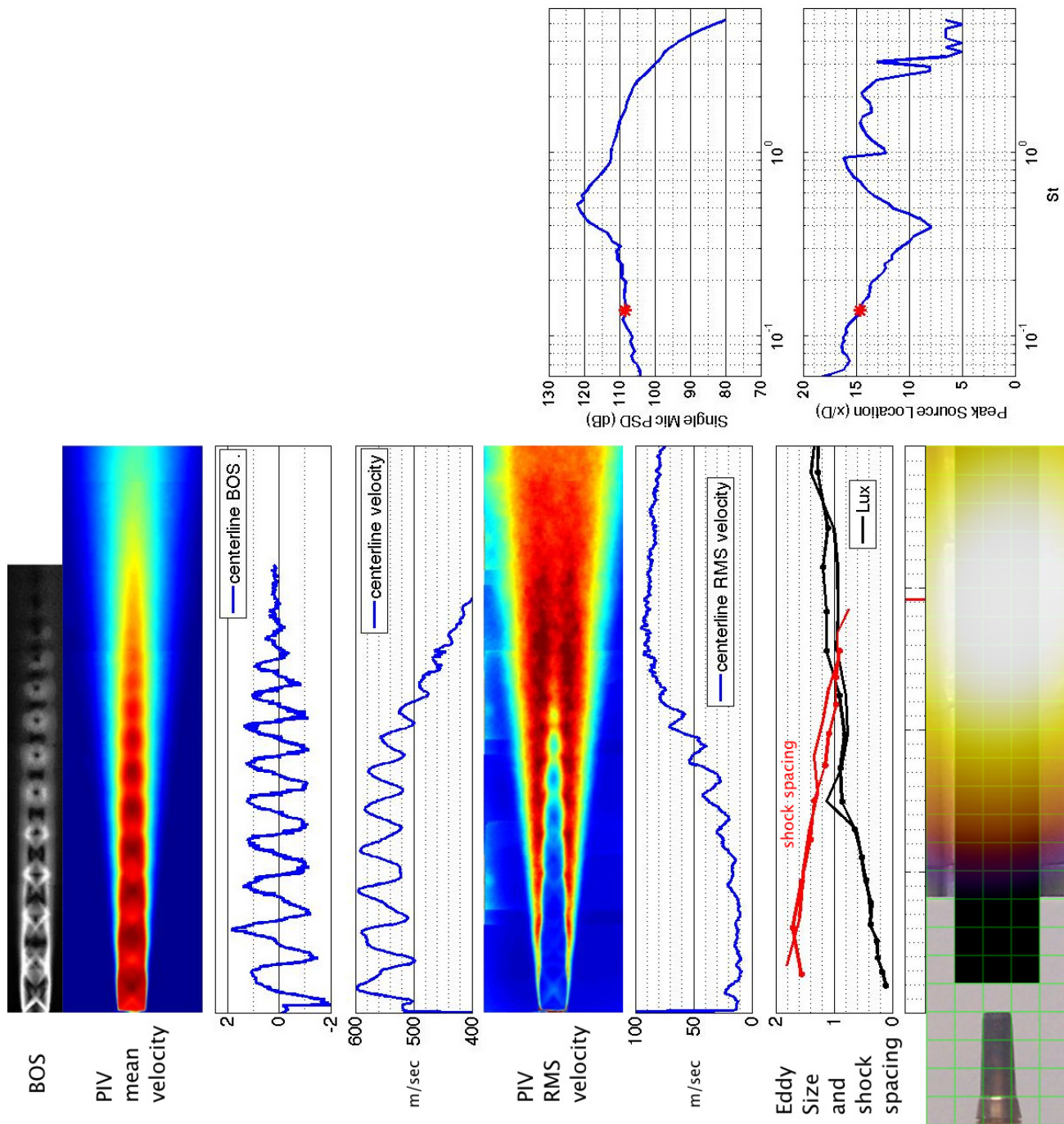
Figure 98.—SMC016; under-expanded; set point 11617; Mj=1.61; Mjdesign=1.50; St=0.138.
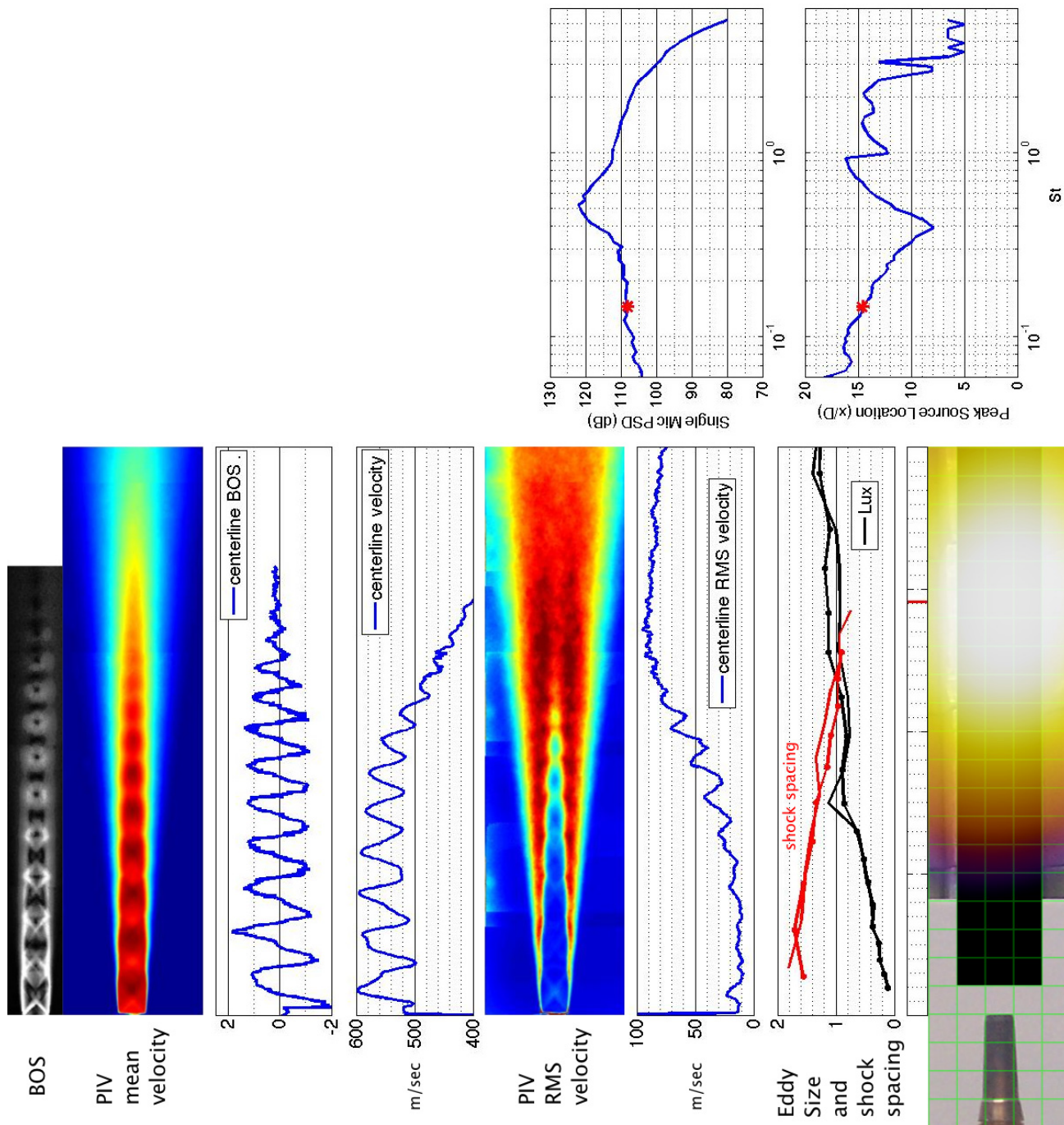
Figure 99.—SMC016; under-expanded; set point 11617; Mj=1.61; Mjdesign=1.50; St=0.146.
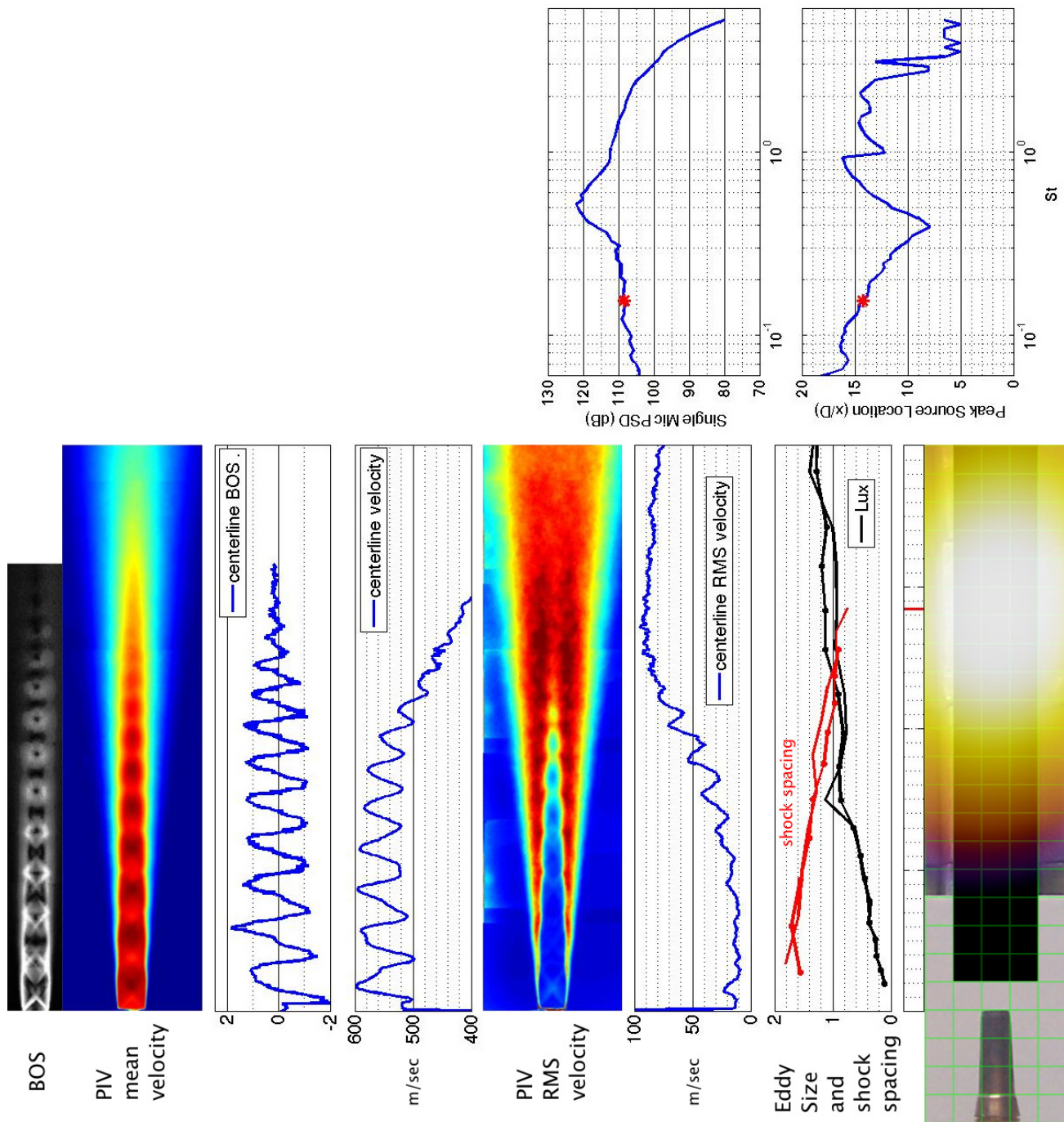
Figure 100.—SMC016; under-expanded; set point 11617; Mj=1.61; Mjdesign=1.50; St=0.155.
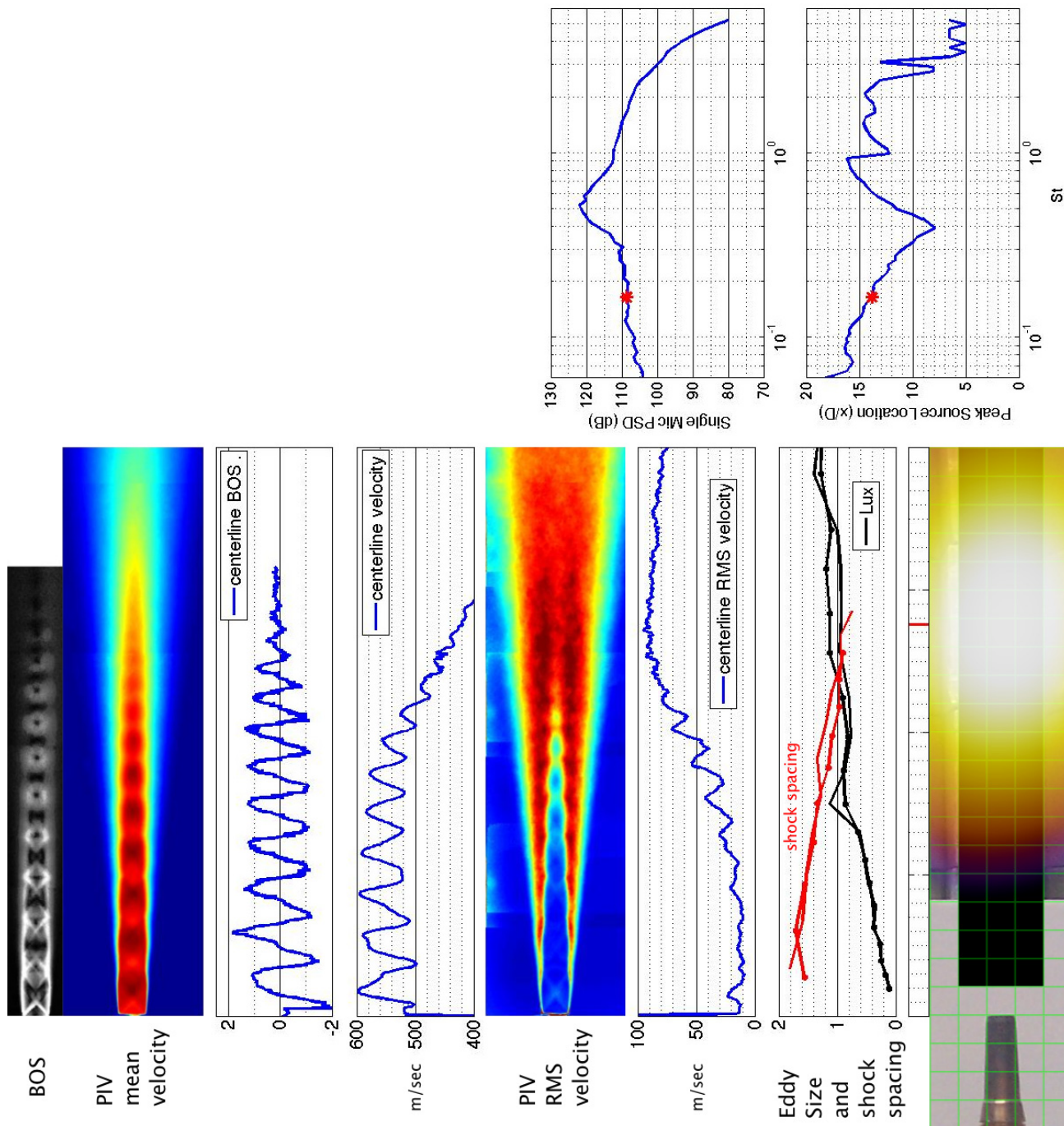
Figure 101.—SMC016; under-expanded; set point 11617; Mj=1.61; Mjdesign=1.50; St=0.165.
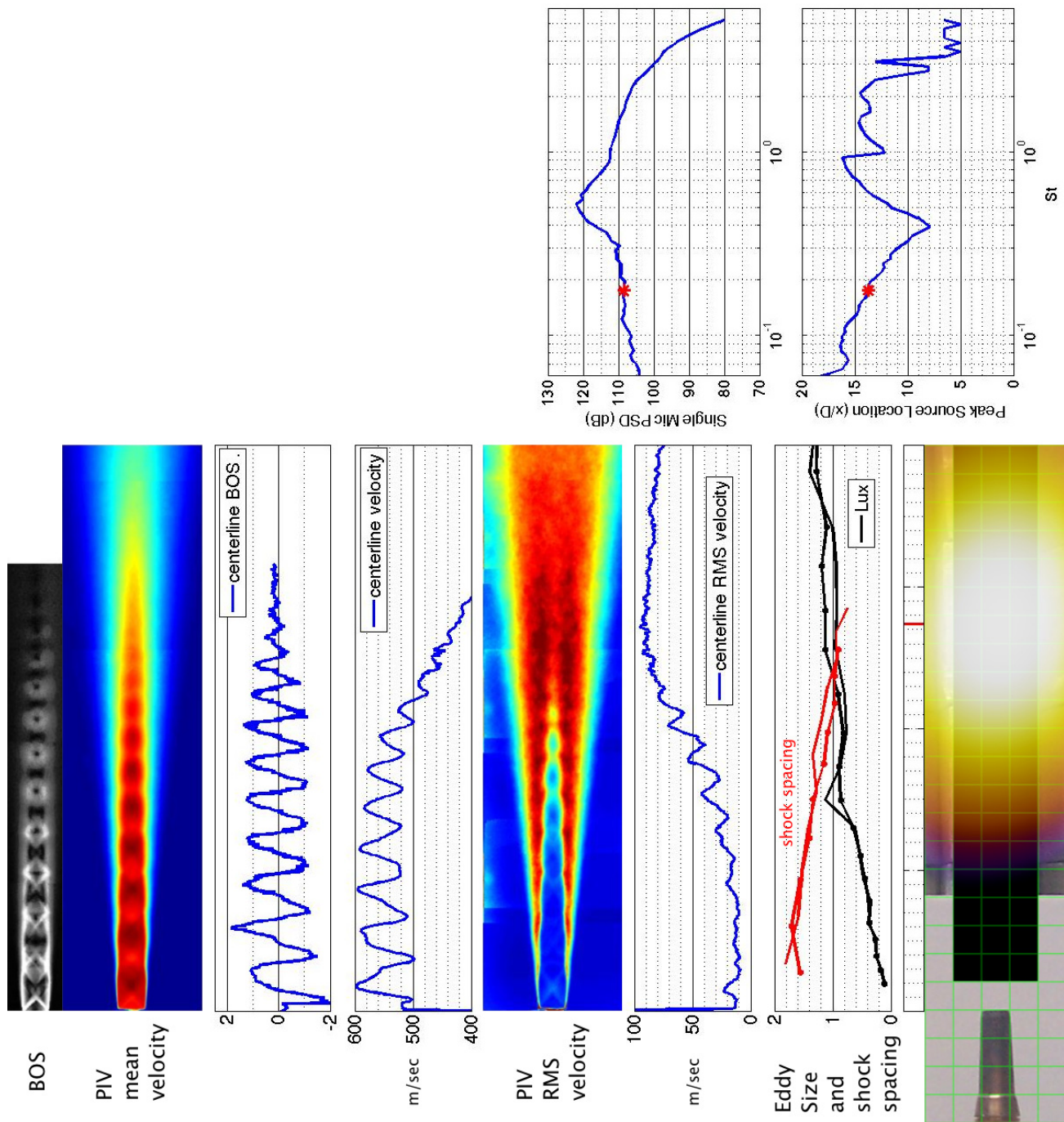
Figure 102.—SMC016; under-expanded; set point 11617; Mj=1.61; Mjdesign=1.50; St=0.175.
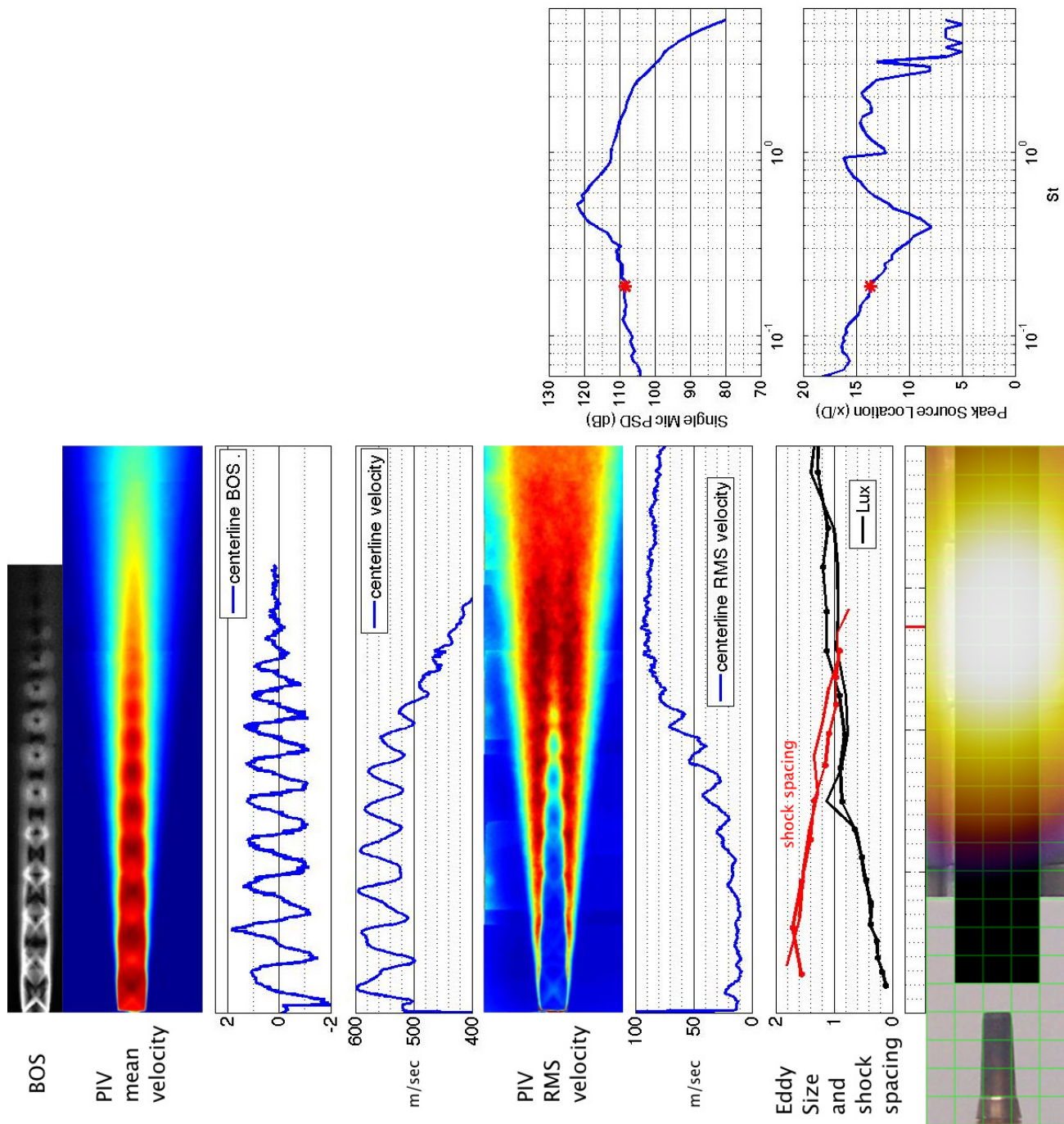
Figure 103.—SMC016; under-expanded; set point 11617; Mj=1.61; Mjdesign=1.50; St=0.186.
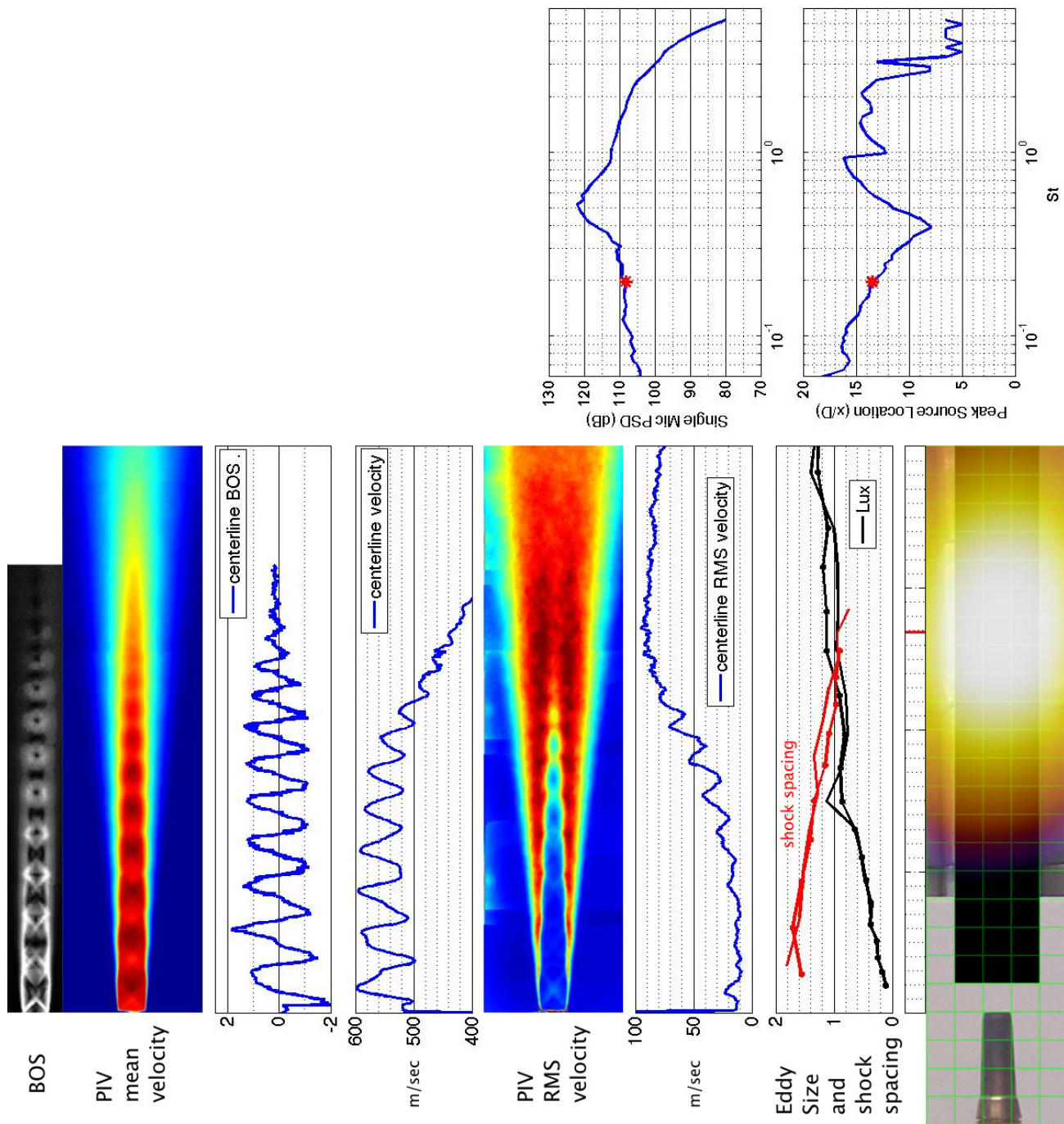
Figure 104.—SMC016; under-expanded; set point 11617; Mj=1.61; Mjdesign=1.50; St=0.197.
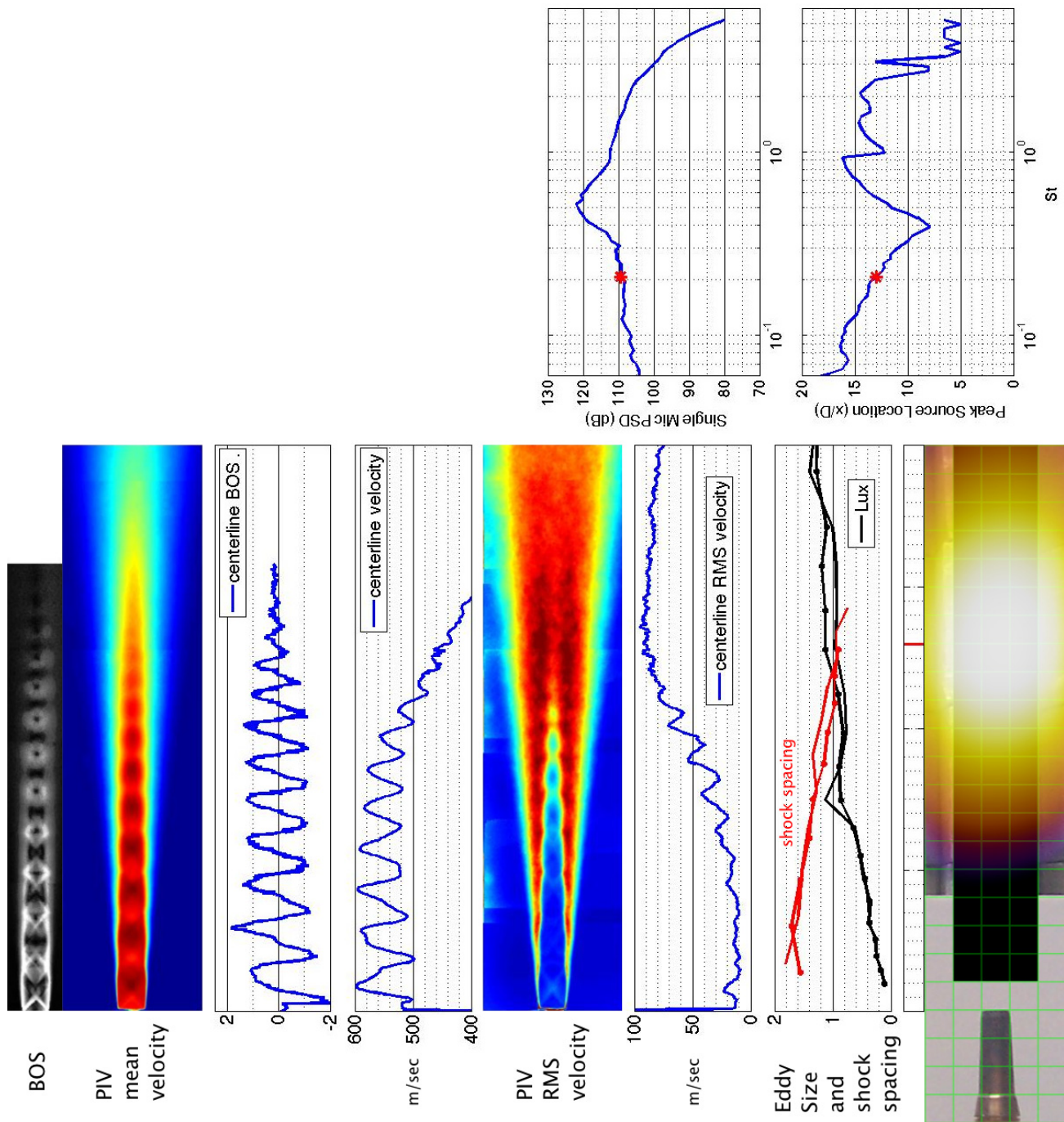
Figure 105.—SMC016; under-expanded; set point 11617; Mj=1.61; Mjdesign=1.50; St=0.208.
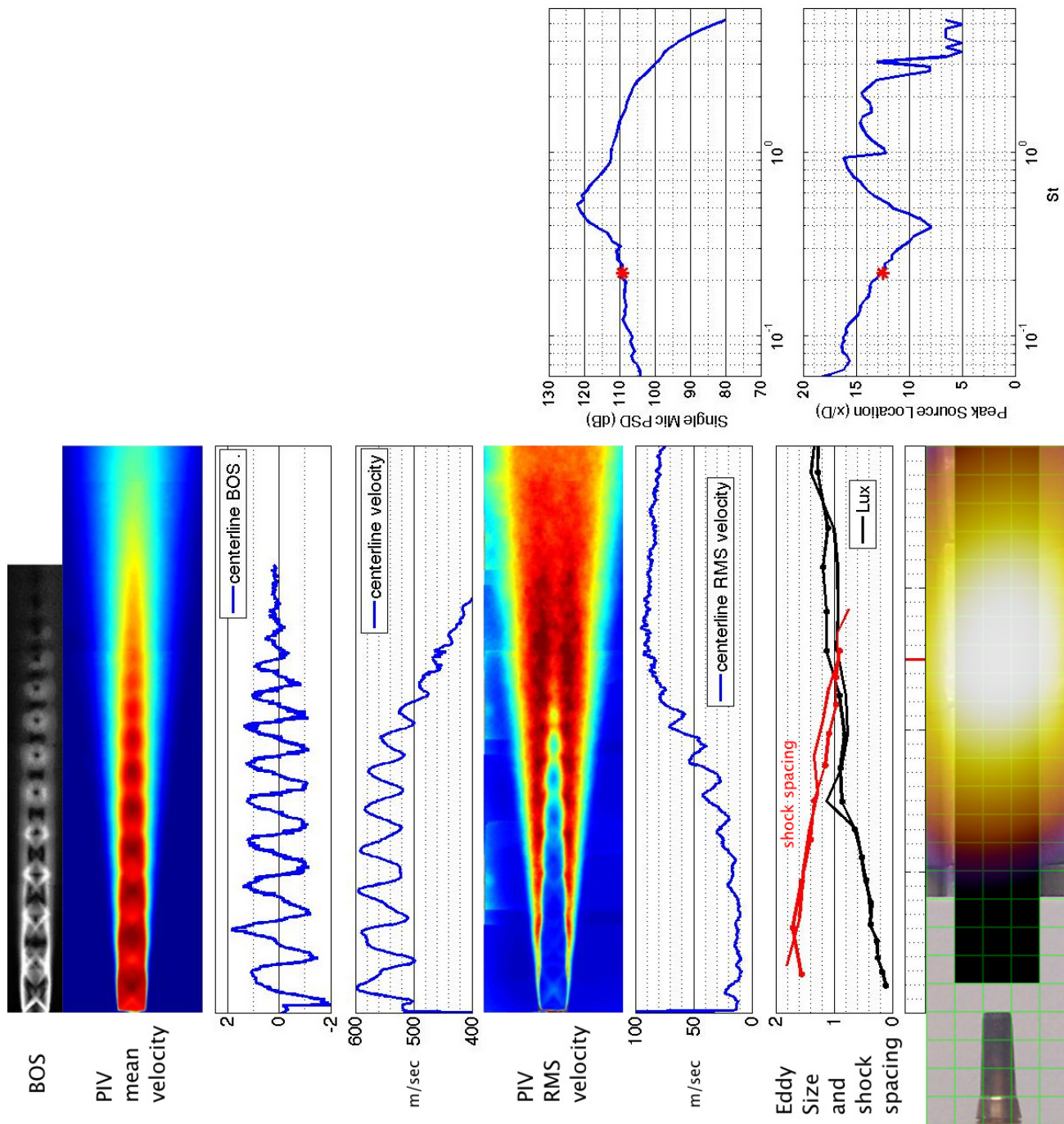
Figure 106.—SMC016; under-expanded; set point 11617; Mj=1.61; Mjdesign=1.50; St=0.220.
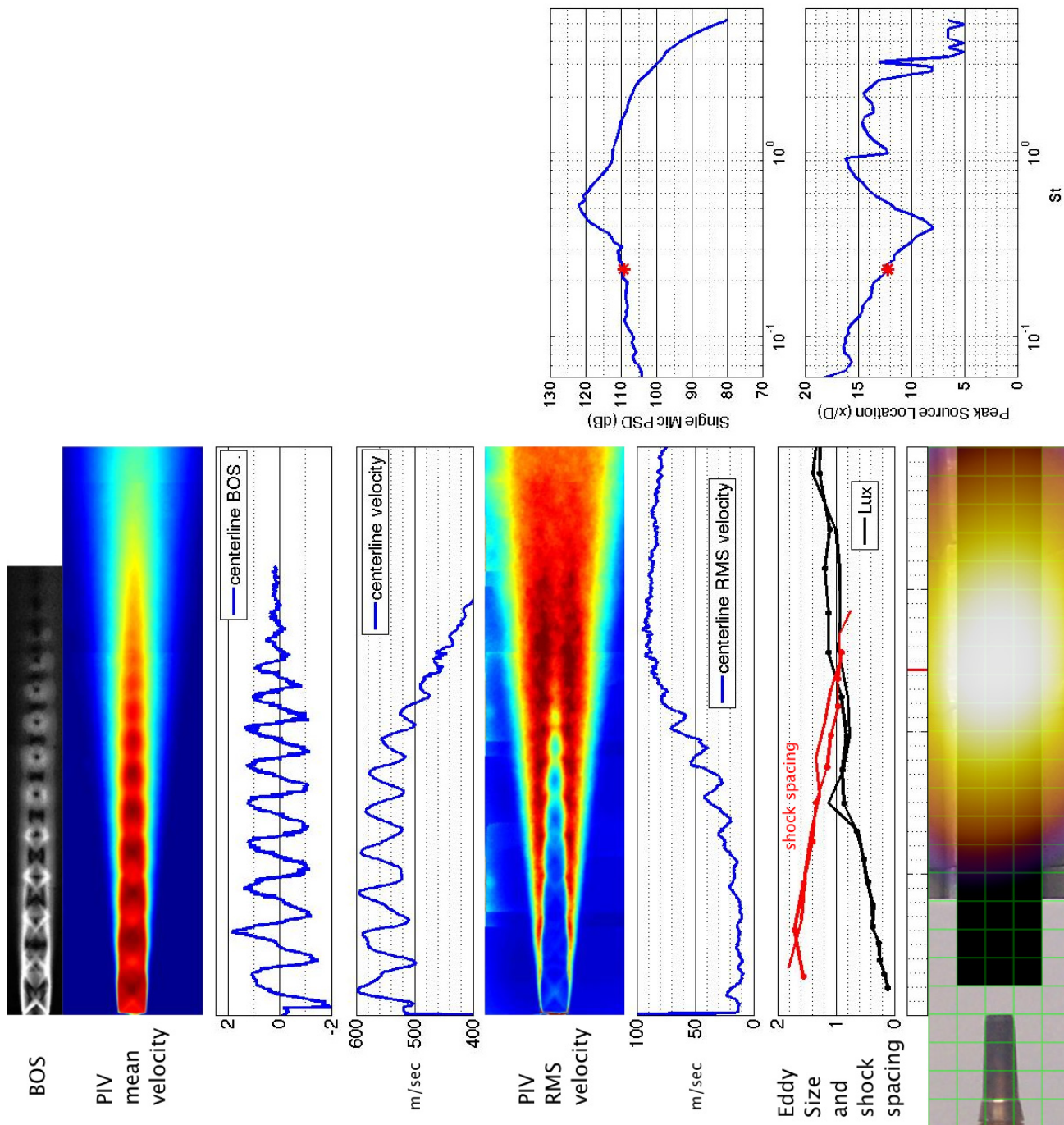
Figure 107.—SMC016; under-expanded; set point 11617; Mj=1.61; Mjdesign=1.50; St=0.233.
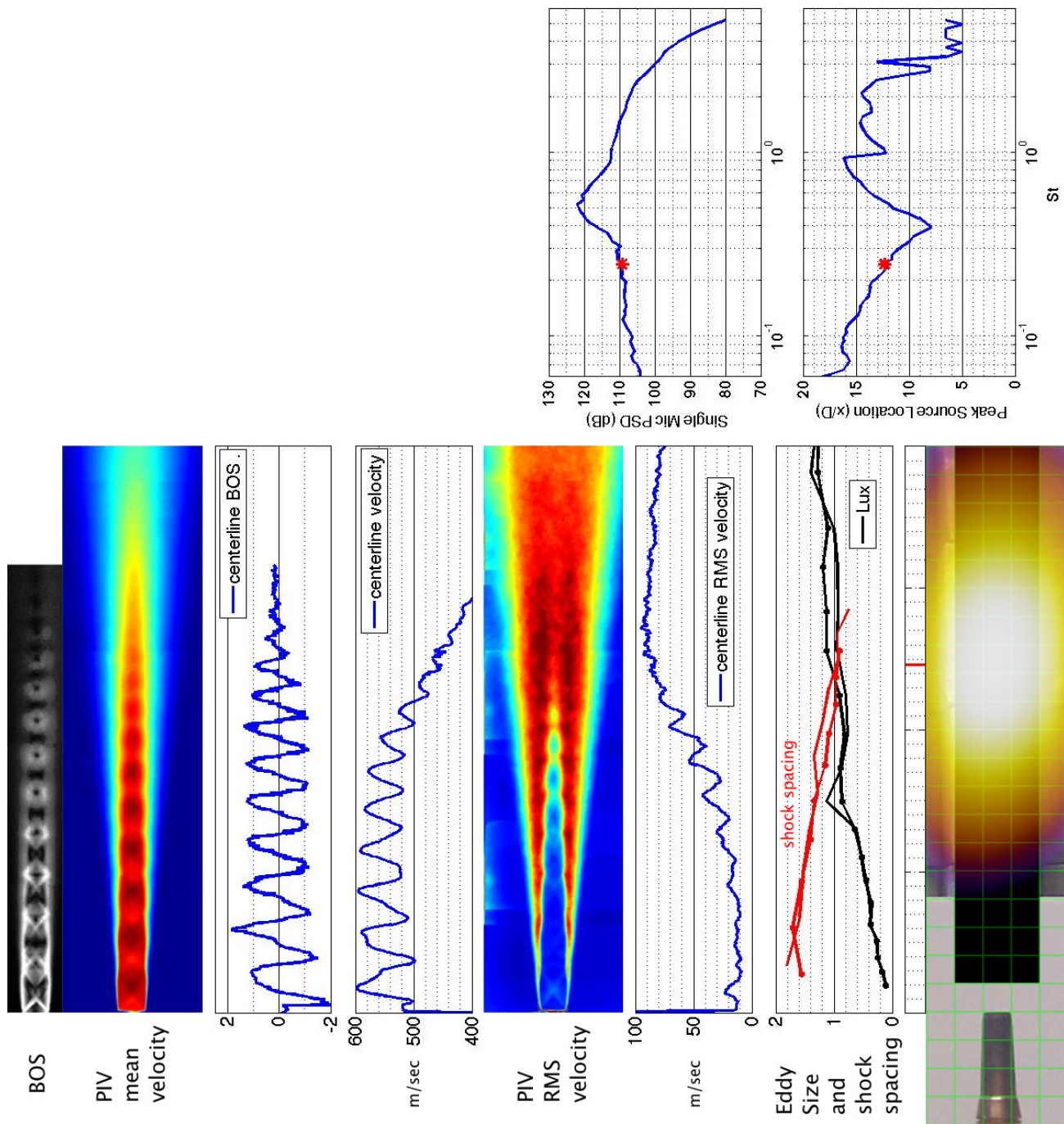
Figure 108.—SMC016; under-expanded; set point 11617; Mj=1.61; Mjdesign=1.50; St=0.246.
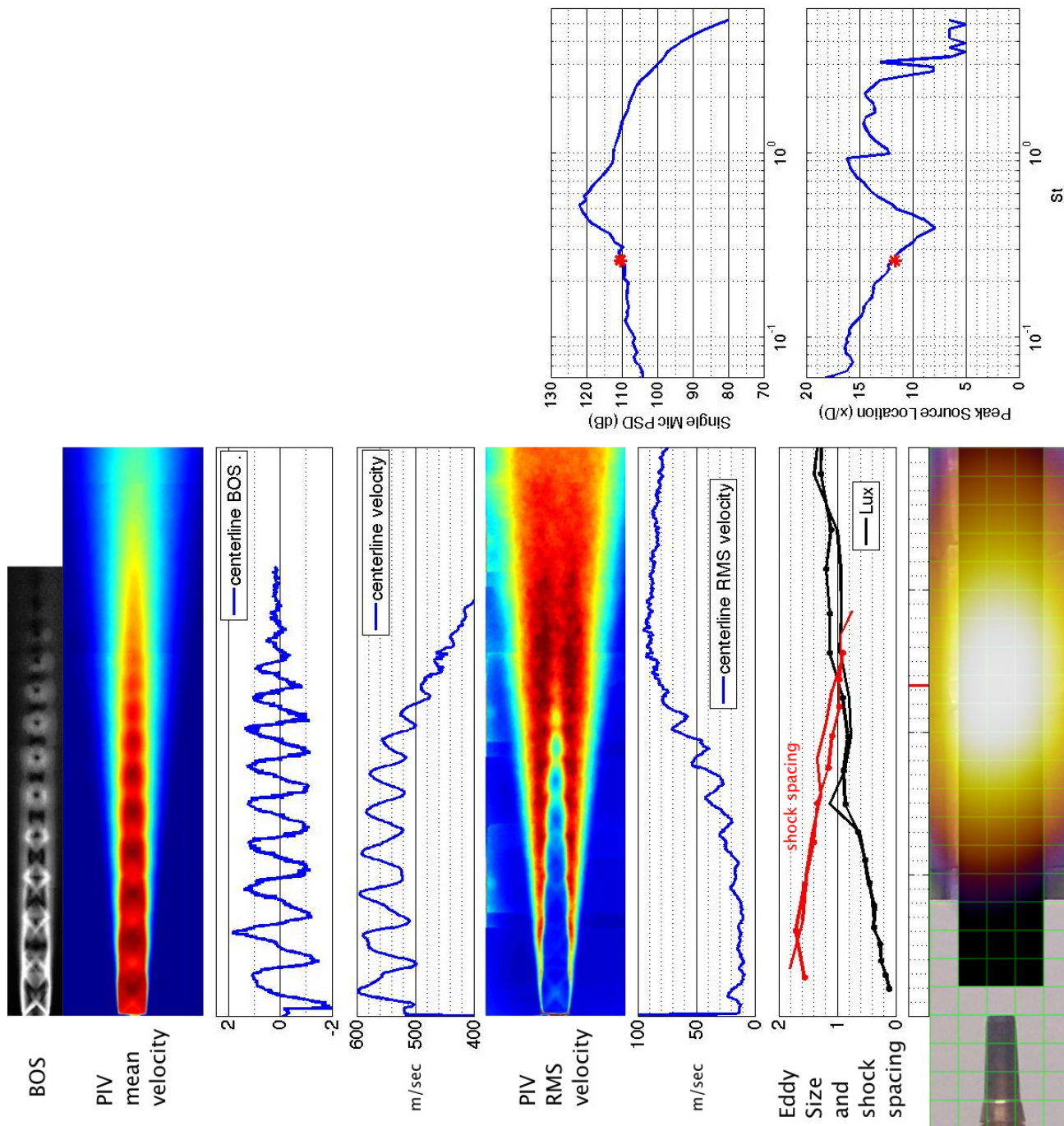
Figure 109.—SMC016; under-expanded; set point 11617; Mj=1.61; Mjdesign=1.50; St=0.260.
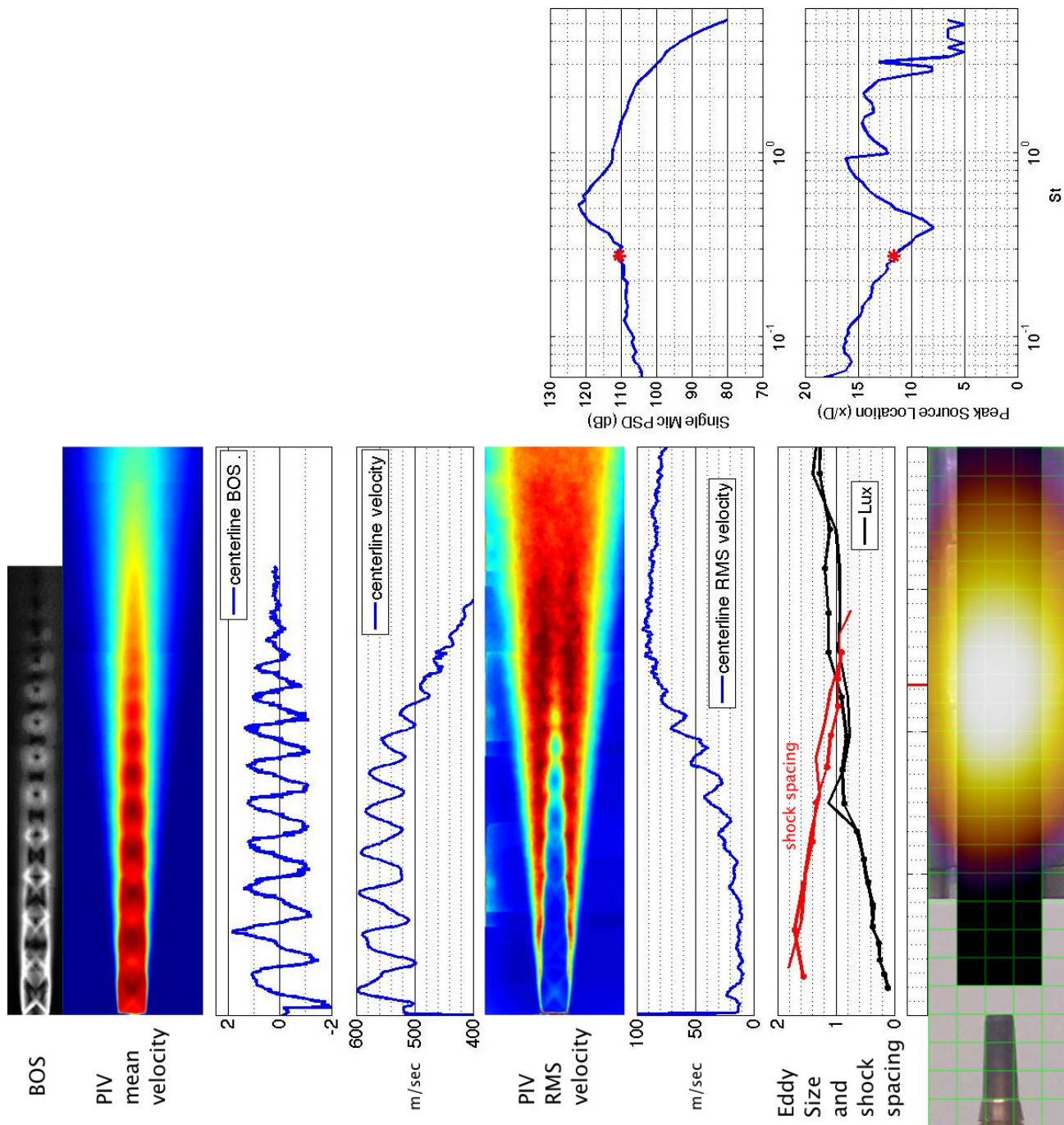
Figure 110.—SMC016; under-expanded; set point 11617; Mj=1.61; Mjdesign=1.50; St=0.275.
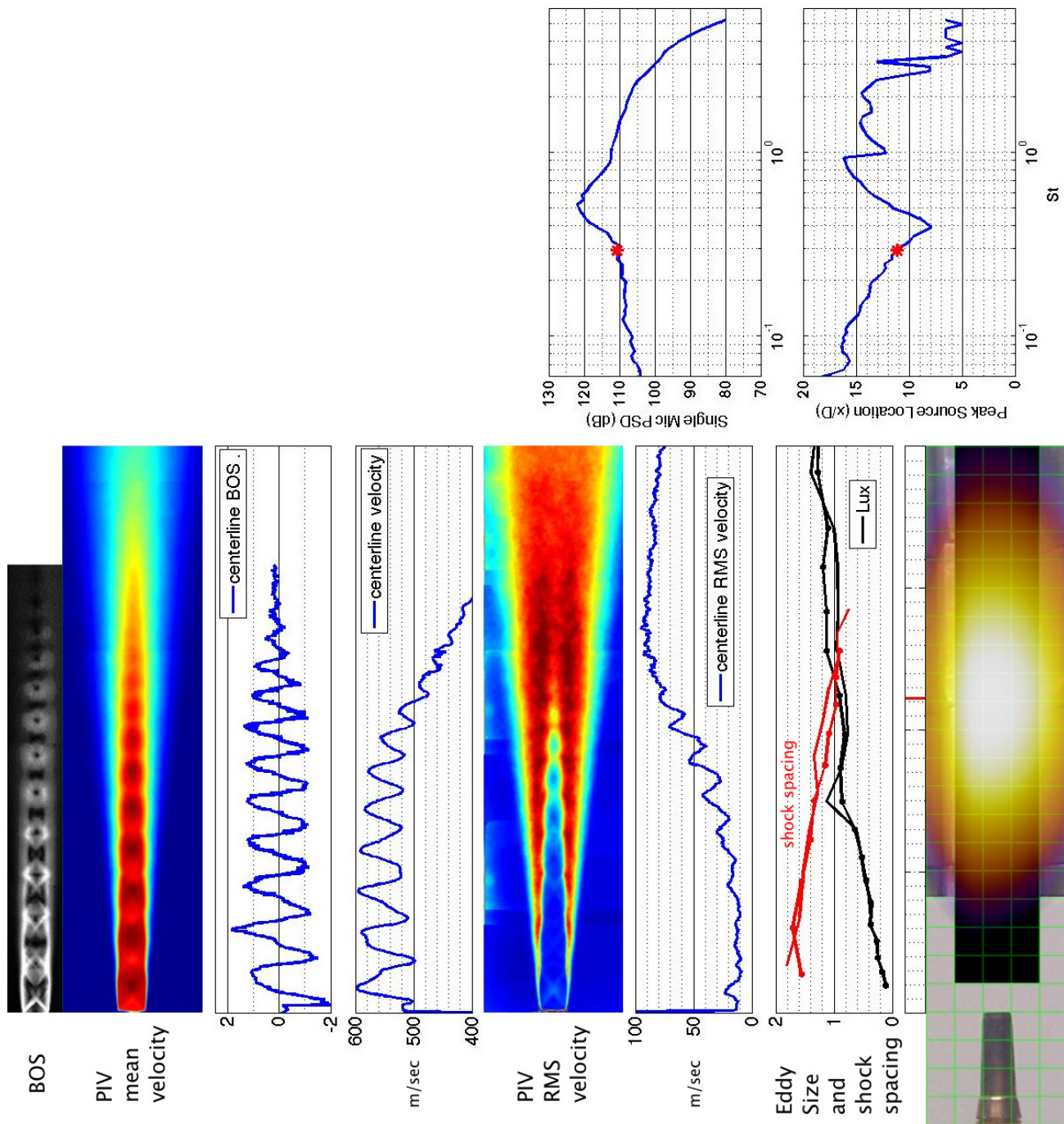
Figure 111.—SMC016; under-expanded; set point 11617; Mj=1.61; Mjdesign=1.50; St=0.291.
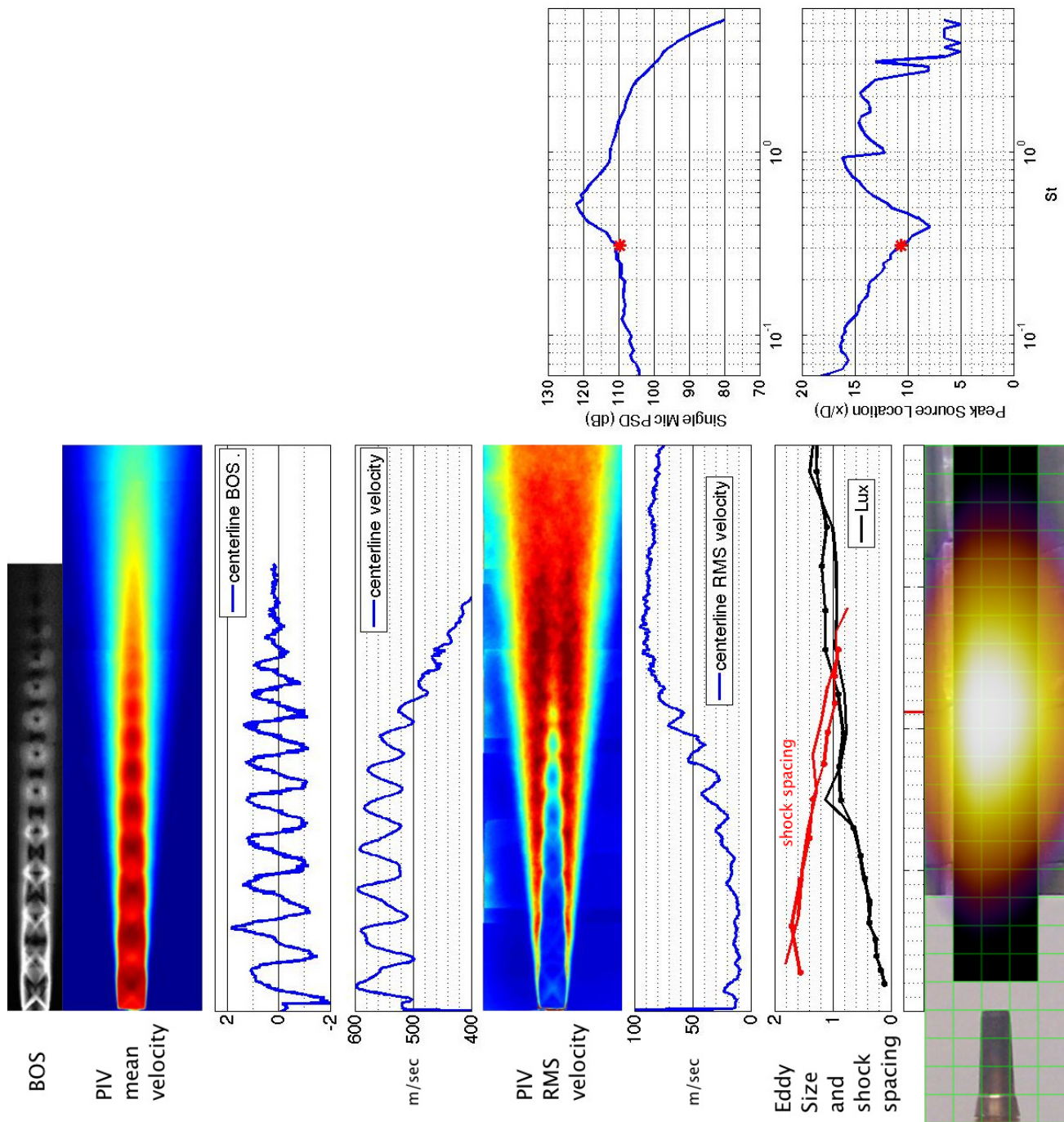
Figure 112.—SMC016; under-expanded; set point 11617; Mj=1.61; Mjdesign=1.50; St=0.309.
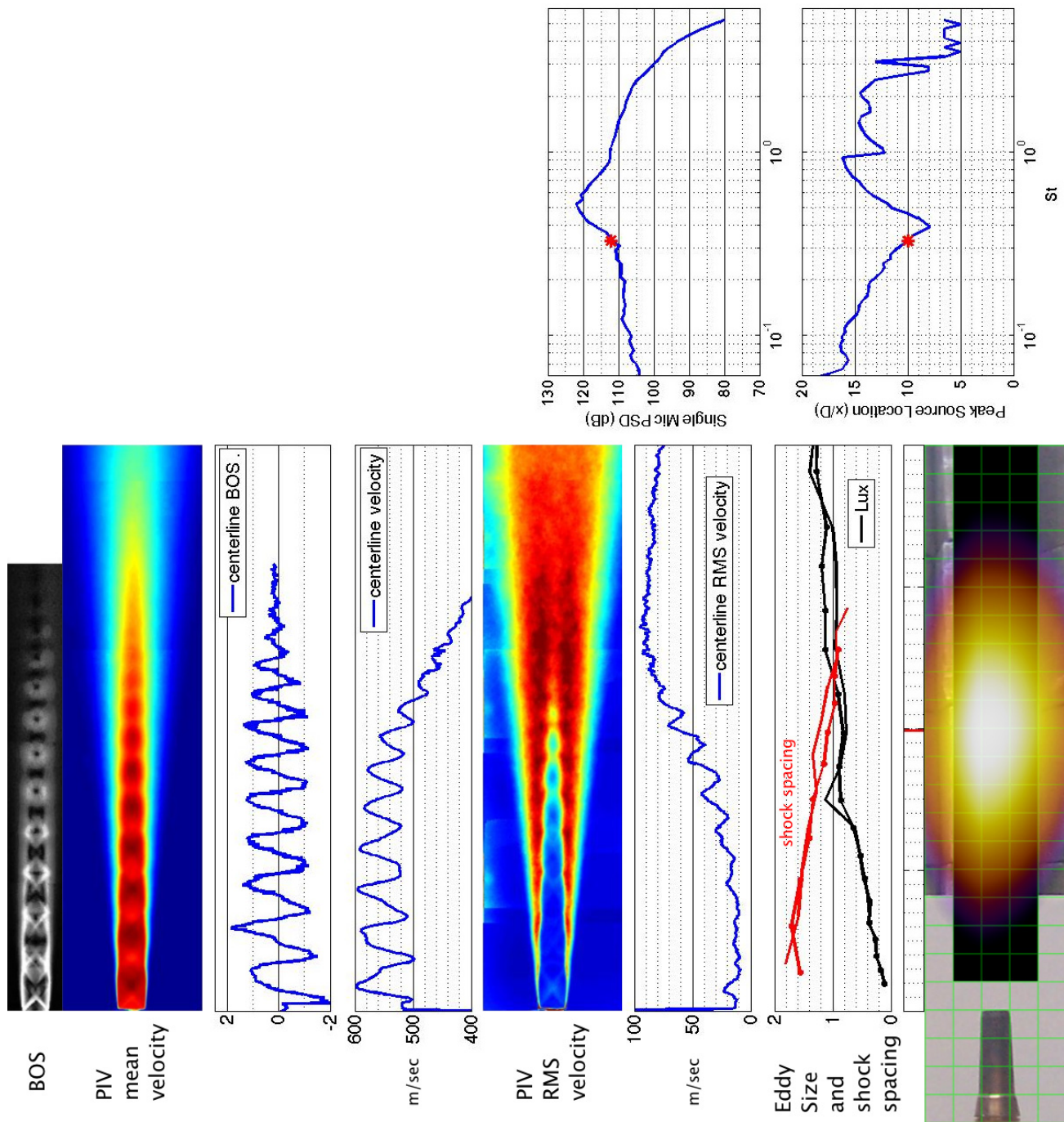
Figure 113.—SMC016; under-expanded; set point 11617; Mj=1.61; Mjdesign=1.50; St=0.327.
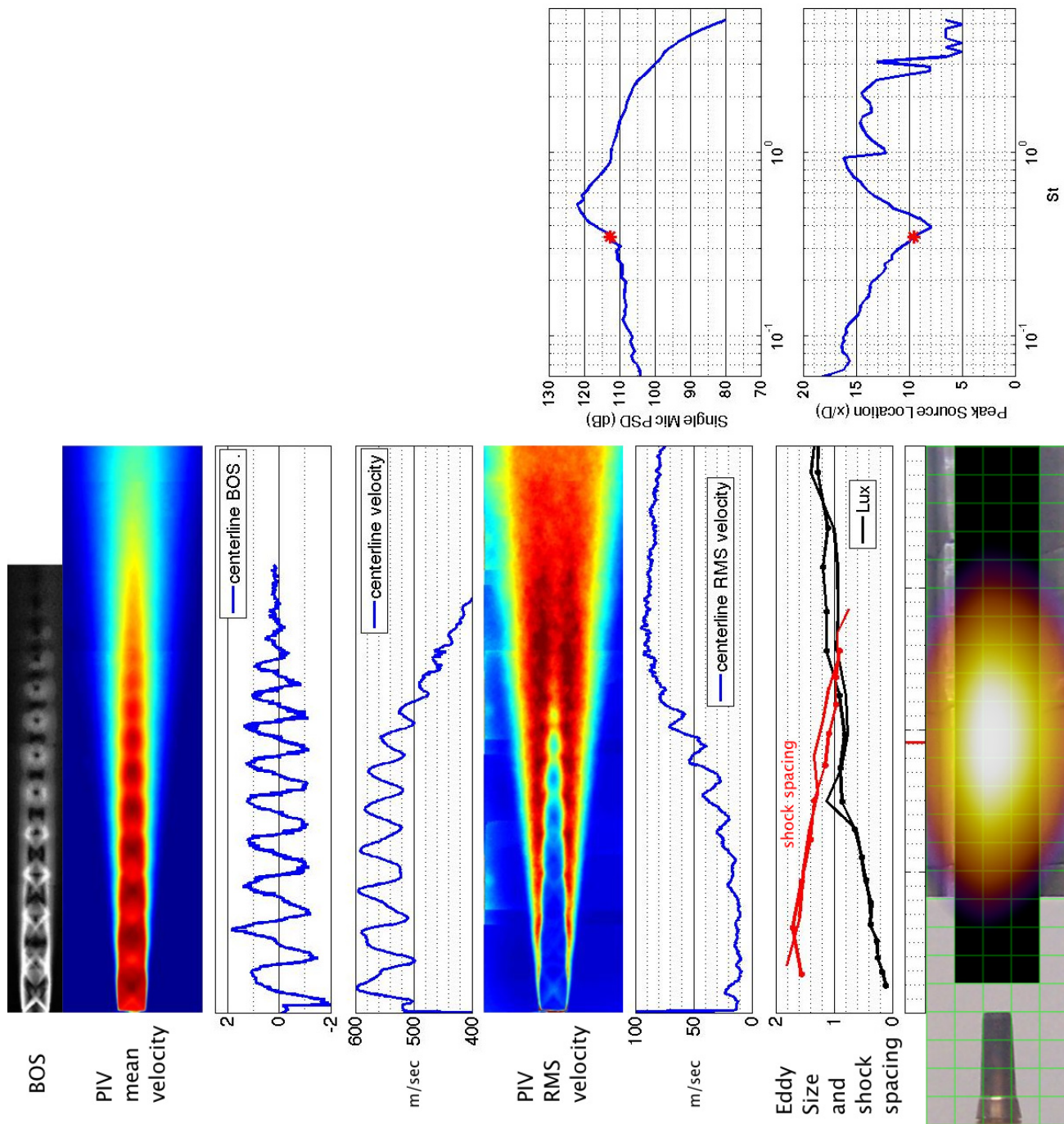
Figure 114.—SMC016; under-expanded; set point 11617; Mj=1.61; Mjdesign=1.50; St=0.346.
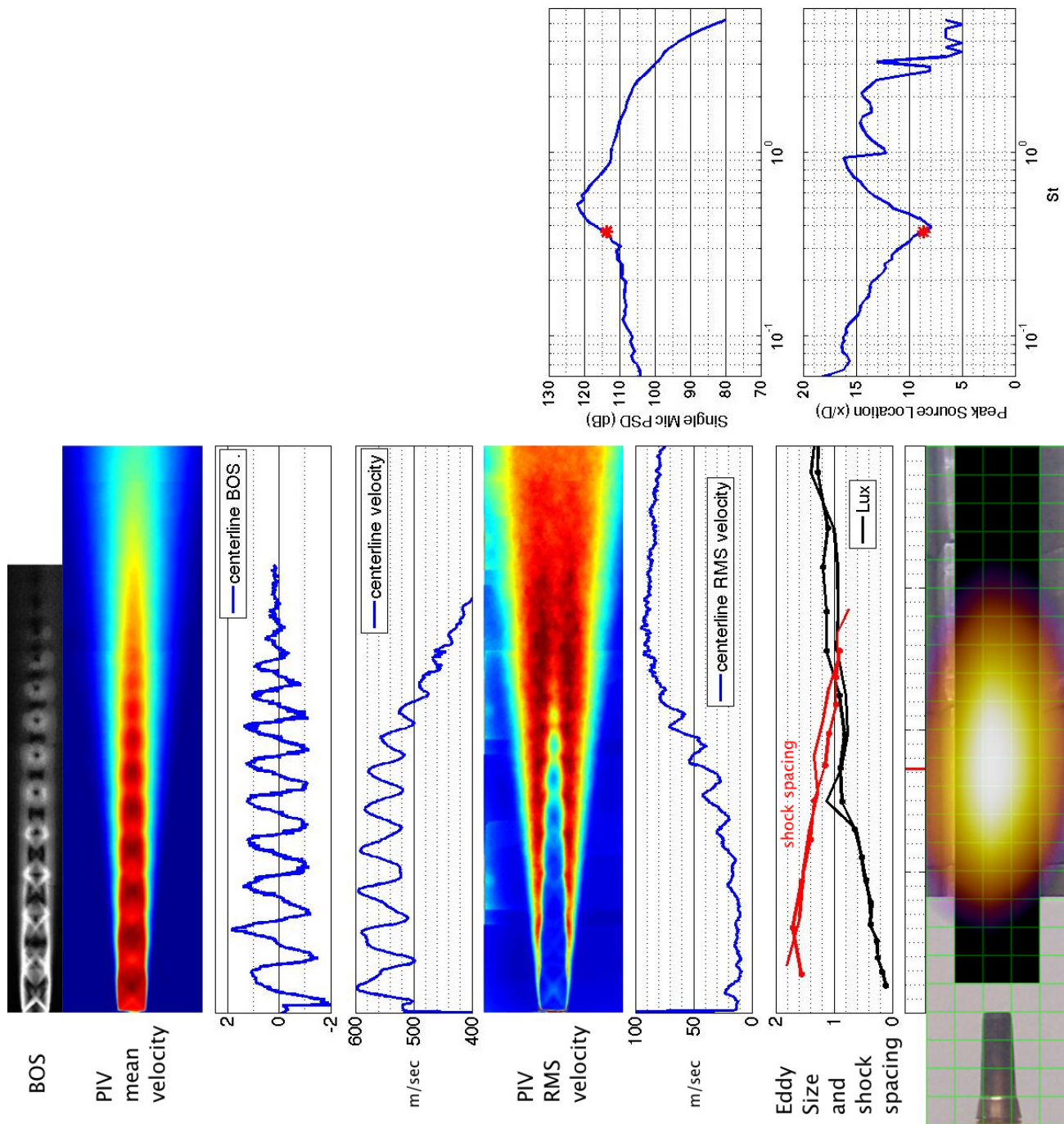
Figure 115.—SMC016; under-expanded; set point 11617; Mj=1.61; Mjdesign=1.50; St=0.367.
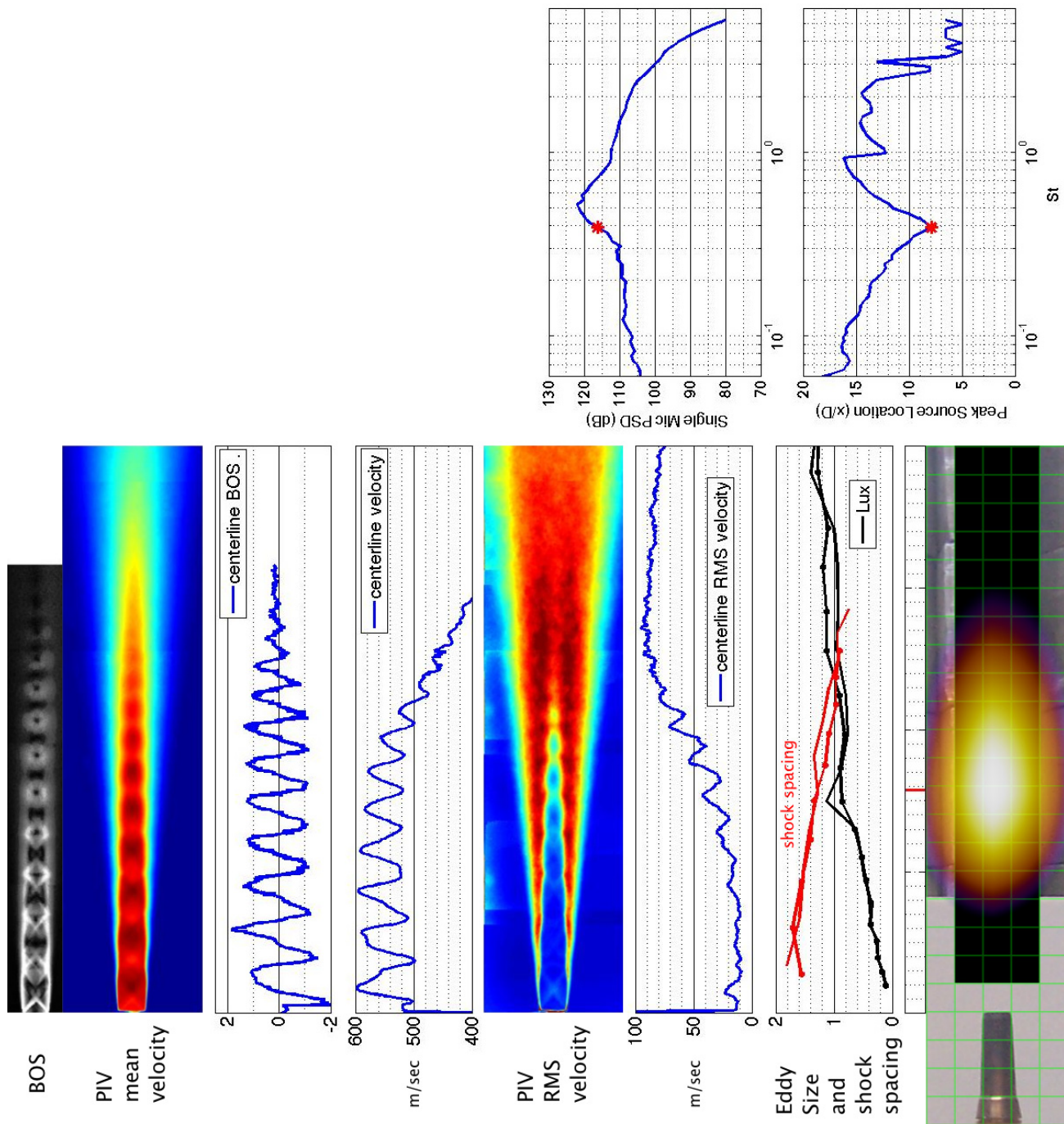
Figure 116.—SMC016; under-expanded; set point 11617; Mj=1.61; Mjdesign=1.50; St=0.390.
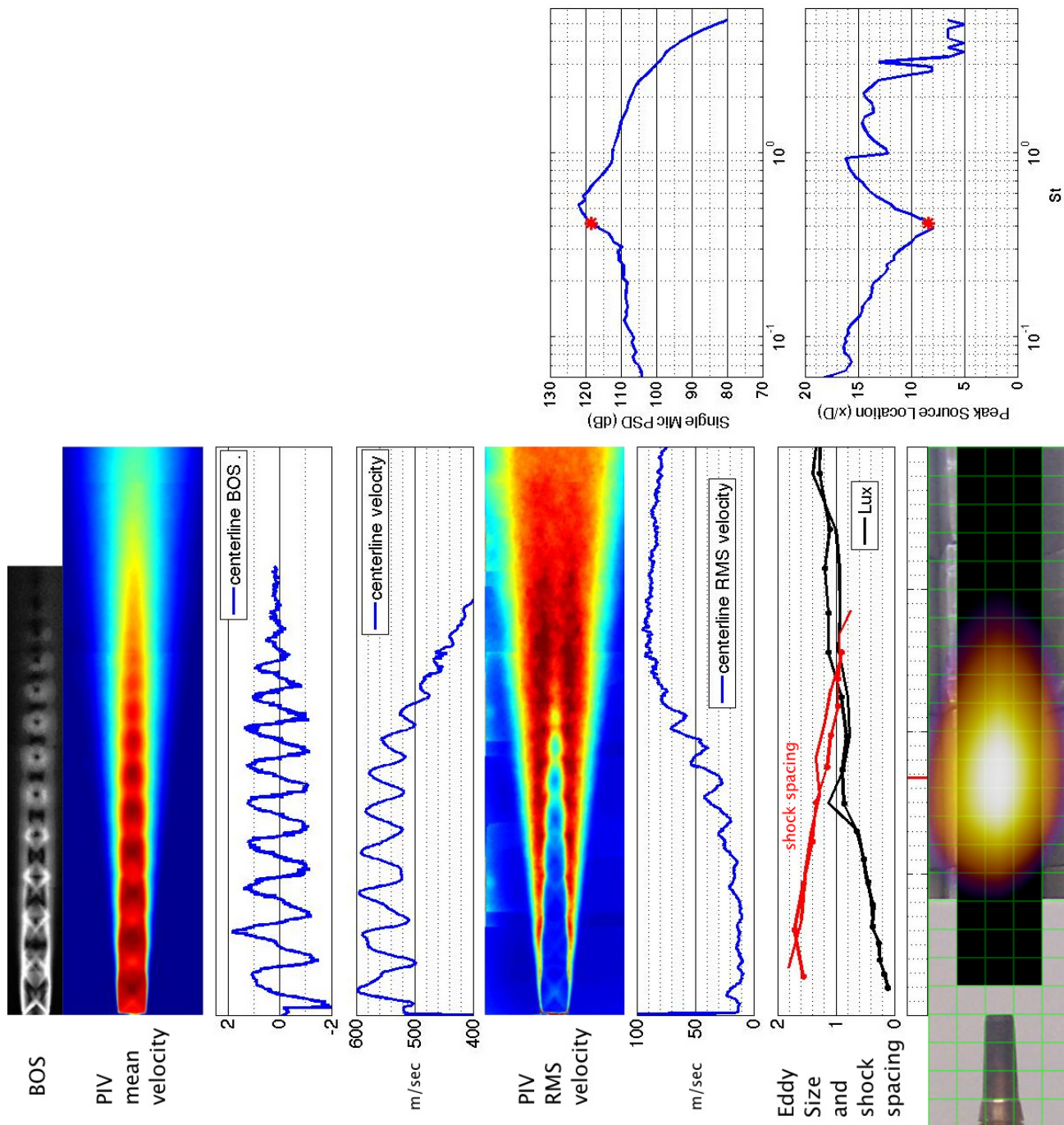
Figure 117.—SMC016; under-expanded; set point 11617; Mj=1.61; Mjdesign=1.50; St=0.414.
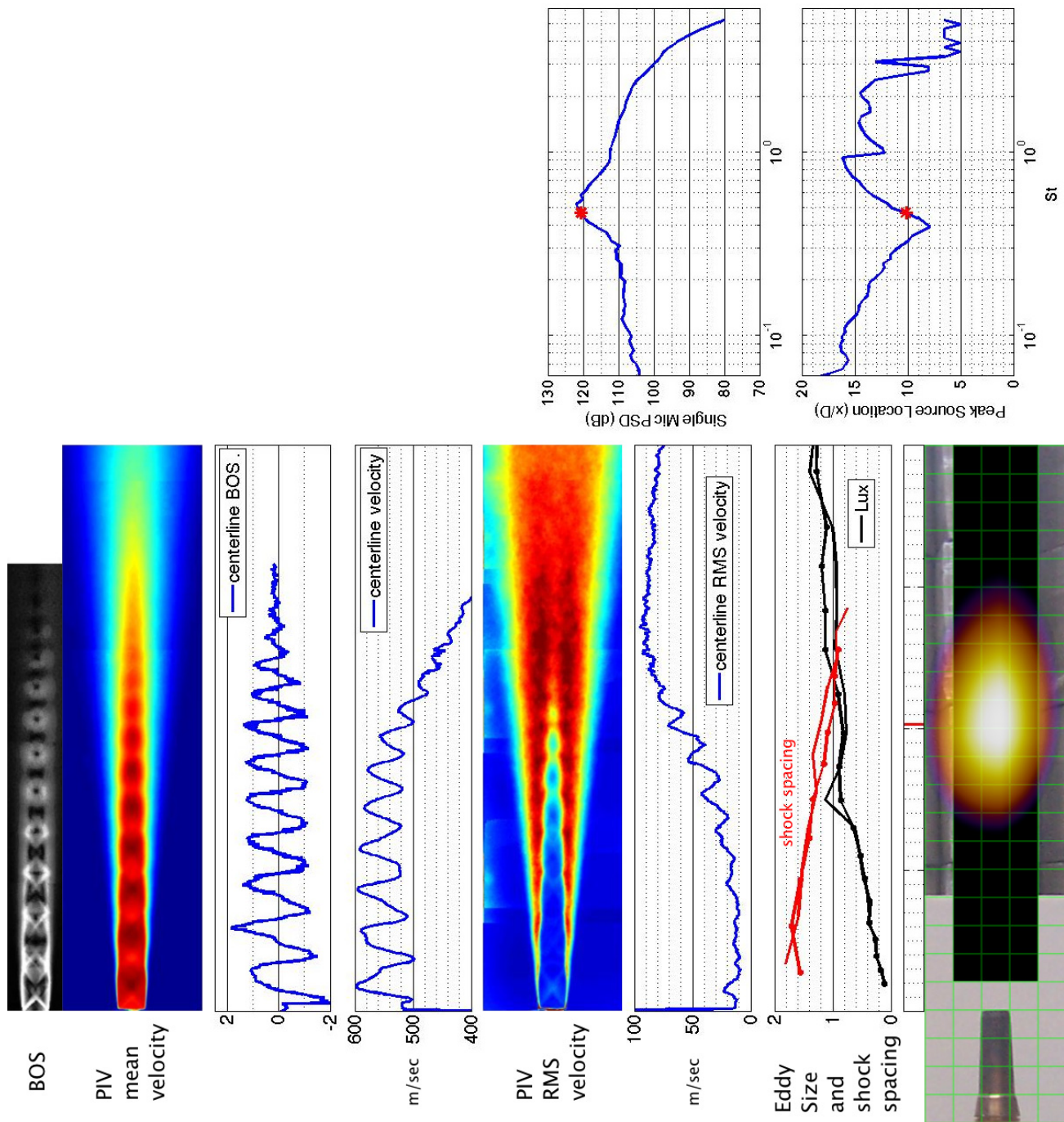
Figure 118.—SMC016; under-expanded; set point 11617; Mj=1.61; Mjdesign=1.50; St=0.466.
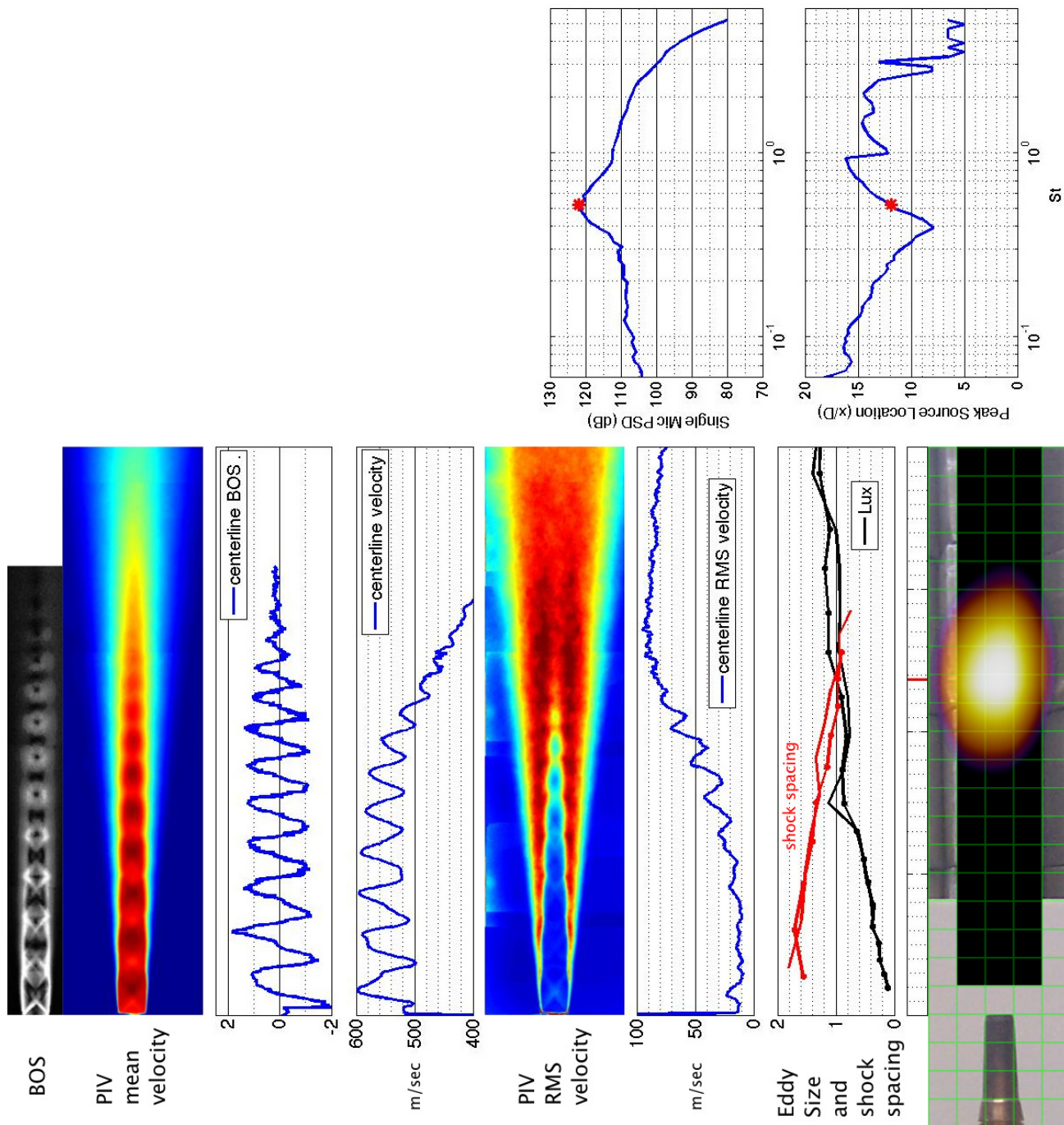
Figure 119.—SMC016; under-expanded; set point 11617; Mj=1.61; Mjdesign=1.50; St=0.521.
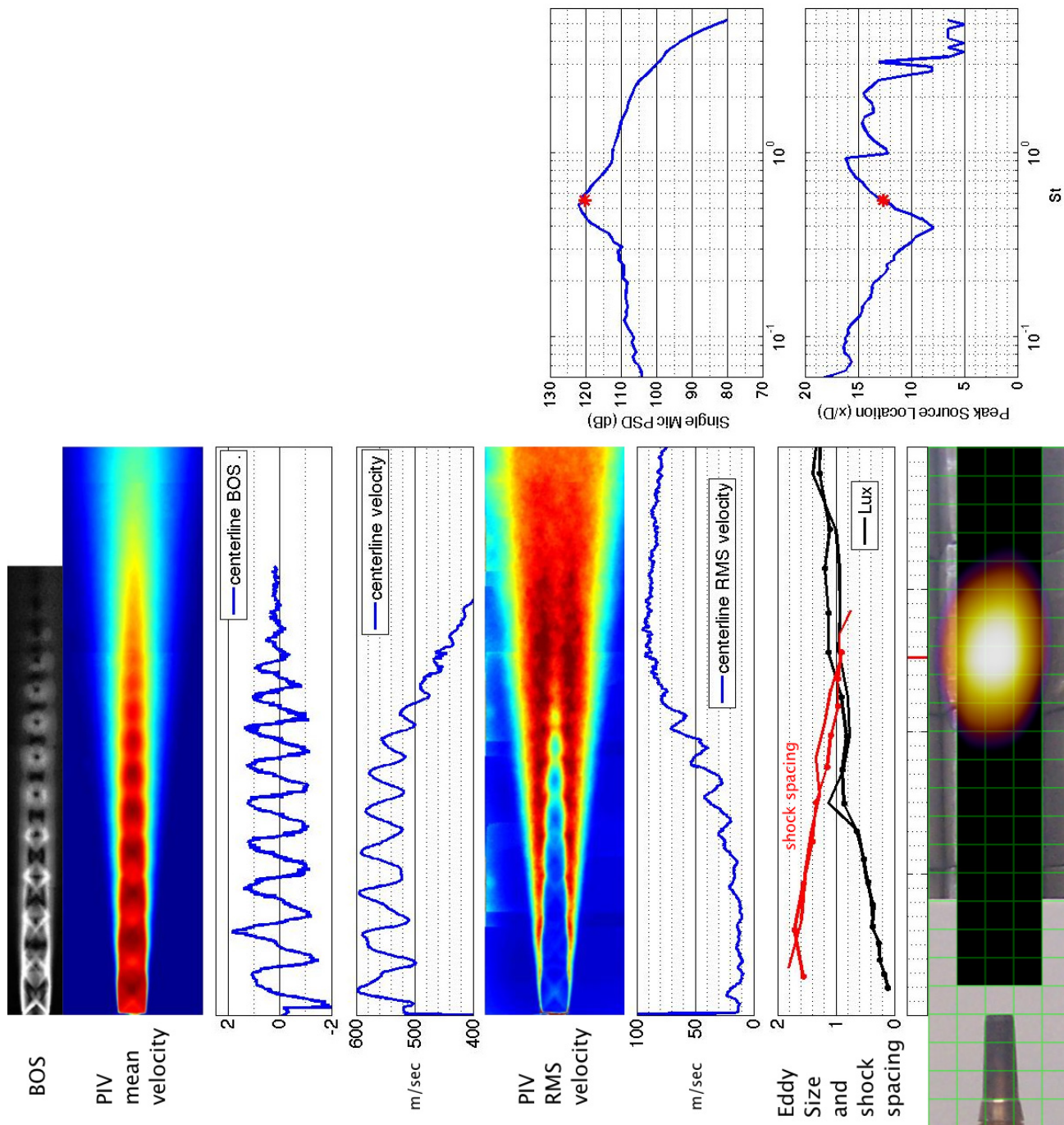
Figure 120.—SMC016; under-expanded; set point 11617; Mj=1.61; Mjdesign=1.50; St=0.551.
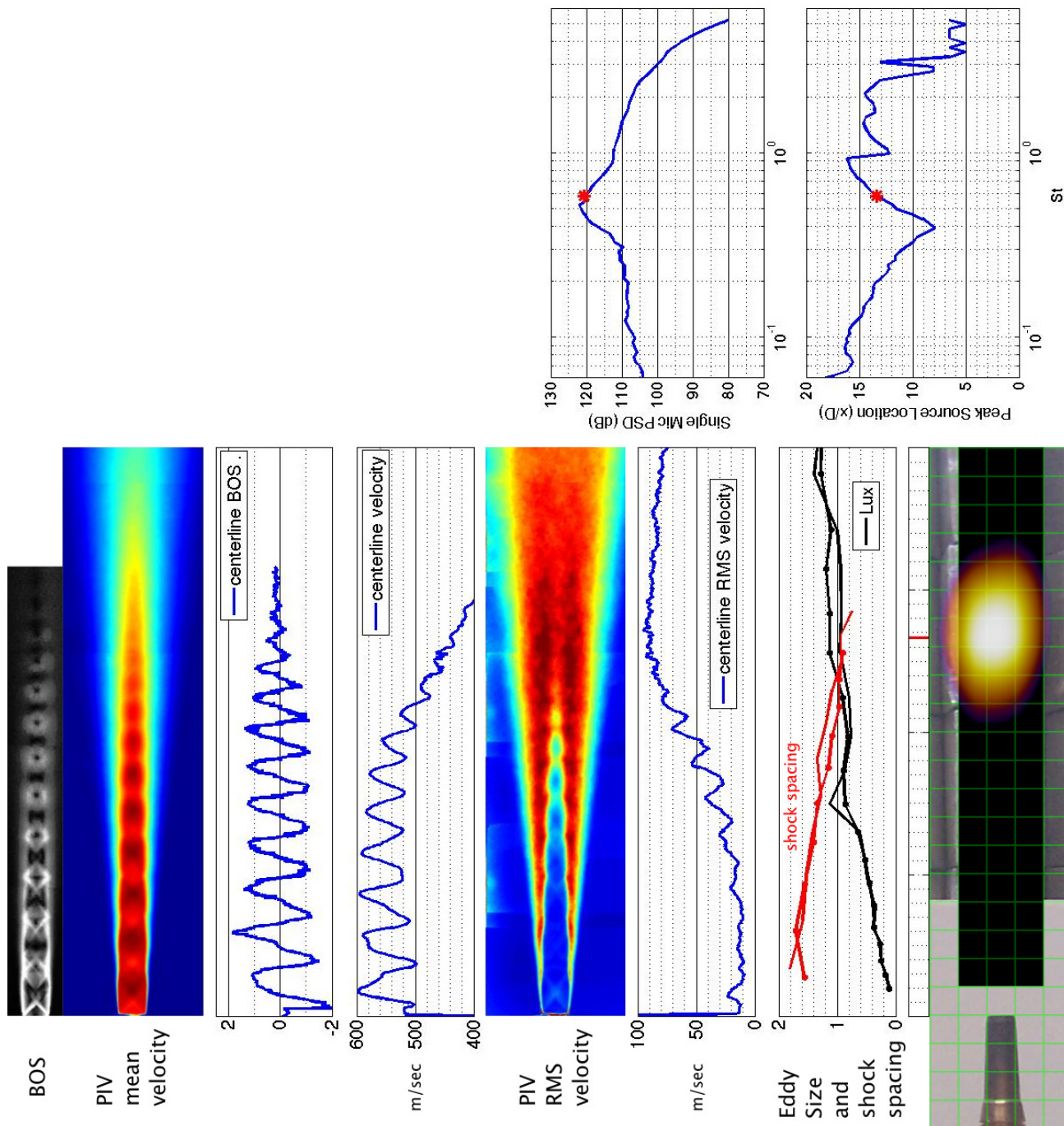
Figure 121.—SMC016; under-expanded; set point 11617; Mj=1.61; Mjdesign=1.50; St=0.583.
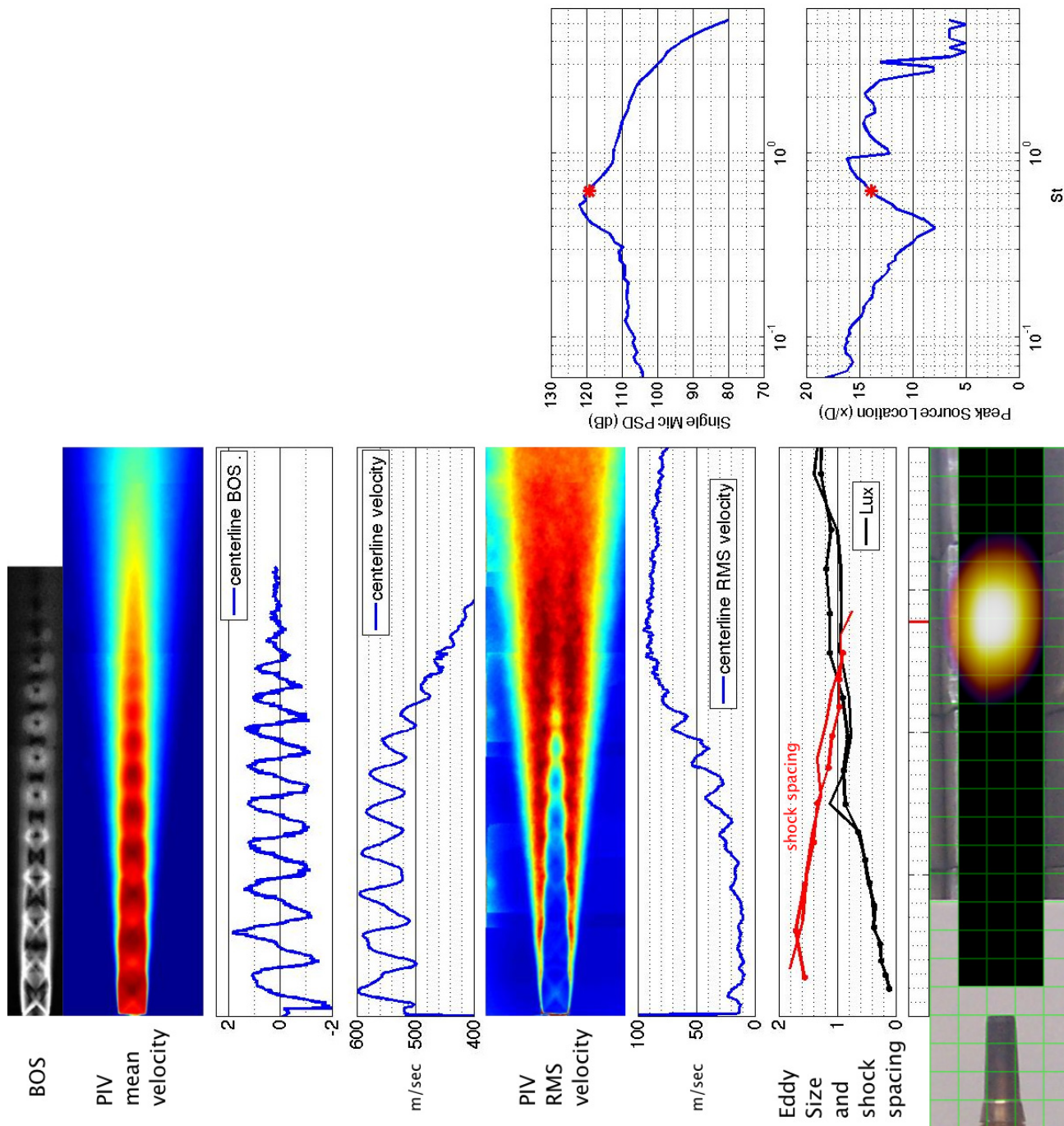
Figure 122.—SMC016; under-expanded; set point 11617; Mj=1.61; Mjdesign=1.50; St=0.617.
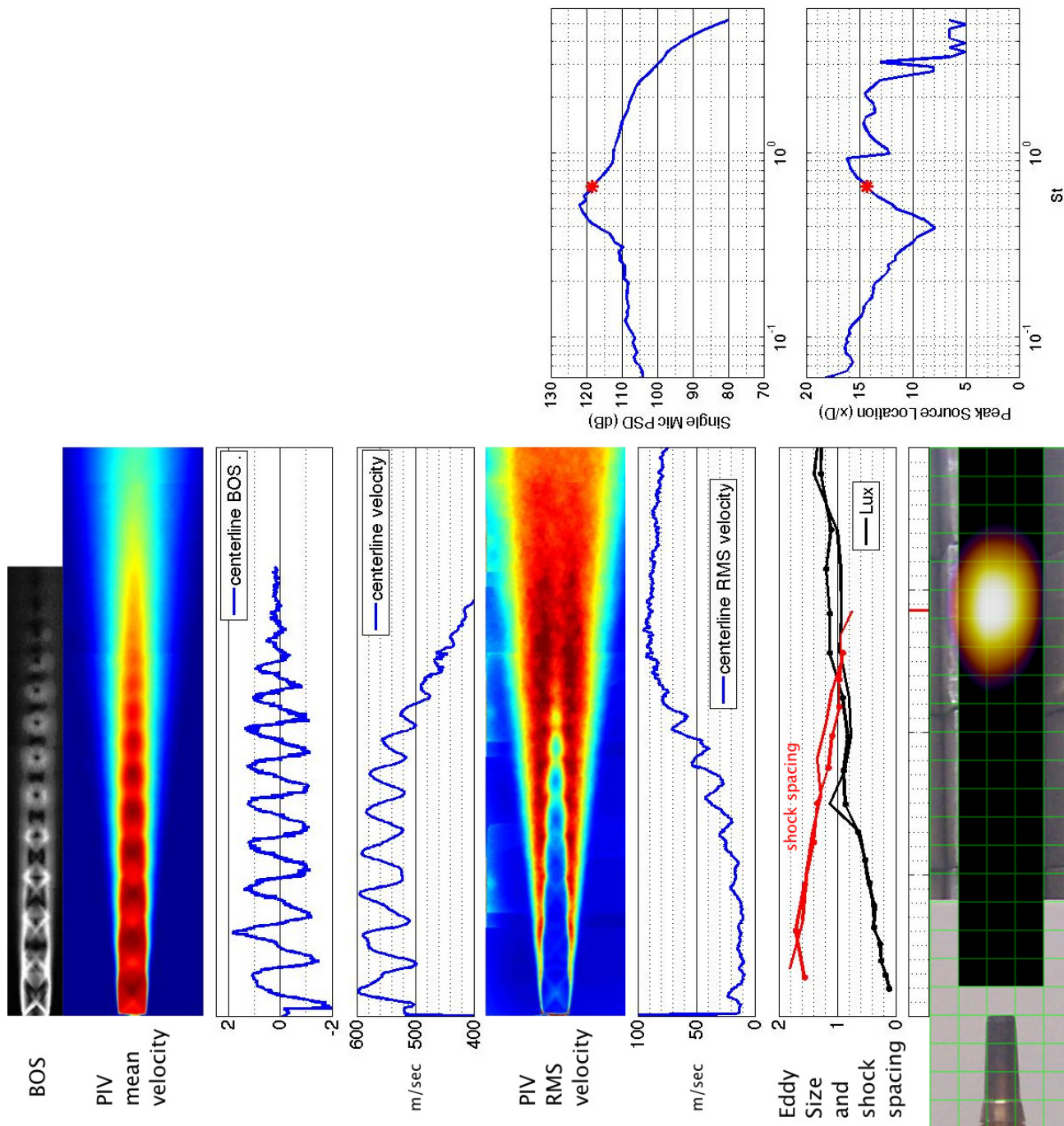
Figure 123.—SMC016; under-expanded; set point 11617; Mj=1.61; Mjdesign=1.50; St=0.654.
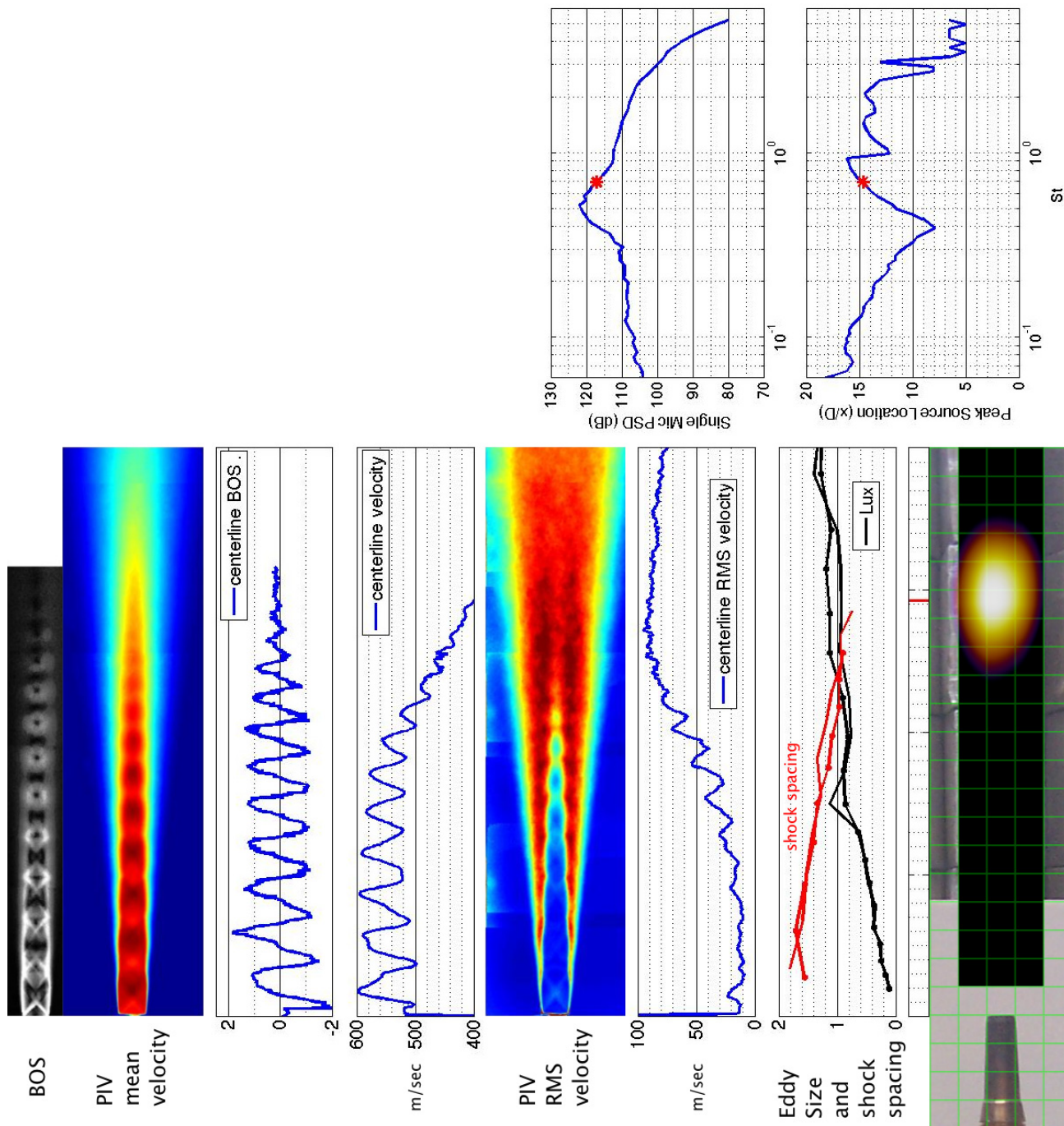
Figure 124.—SMC016; under-expanded; set point 11617; Mj=1.61; Mjdesign=1.50; St=0.693.
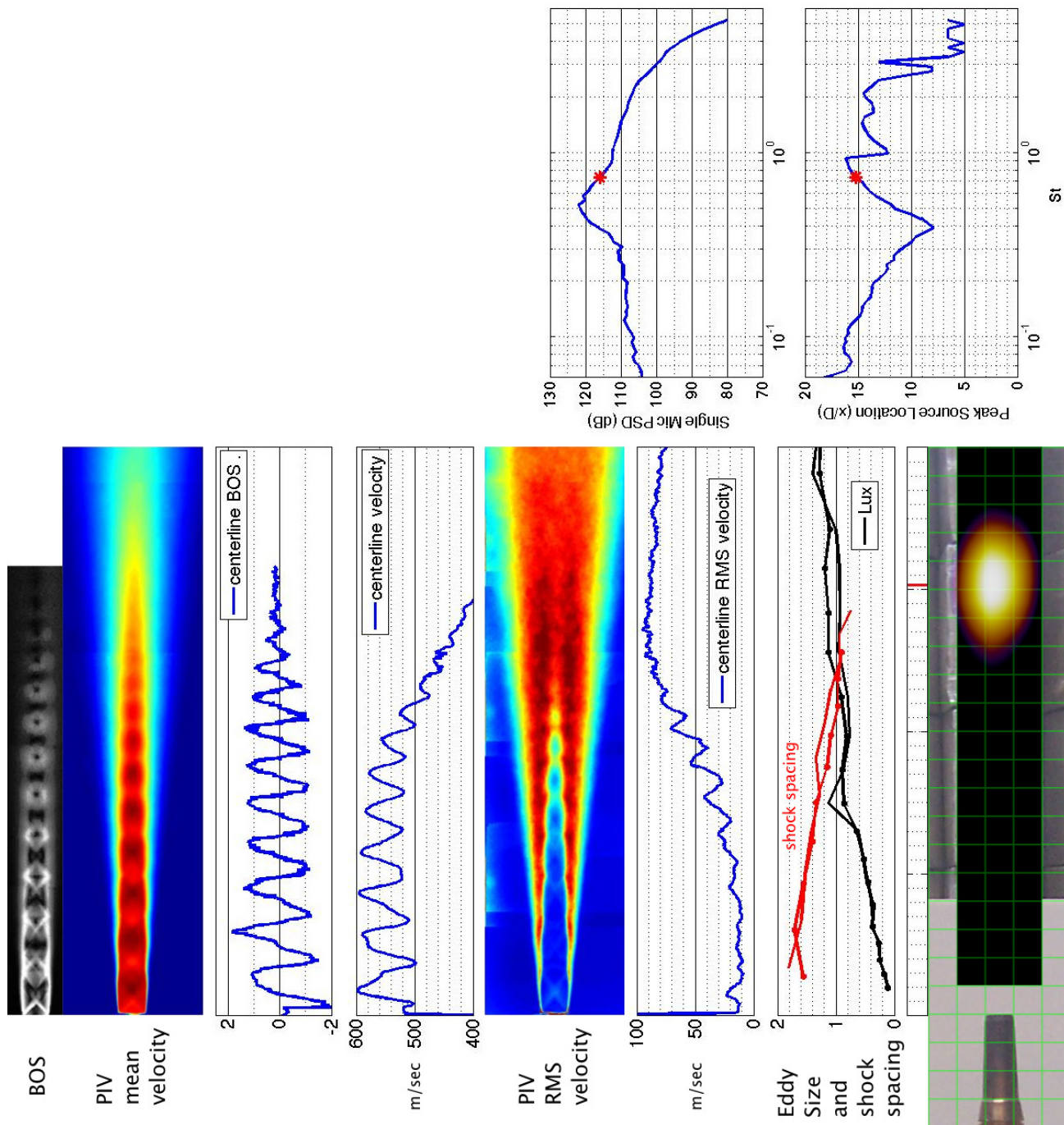
Figure 125.—SMC016; under-expanded; set point 11617; Mj=1.61; Mjdesign=1.50; St=0.734.
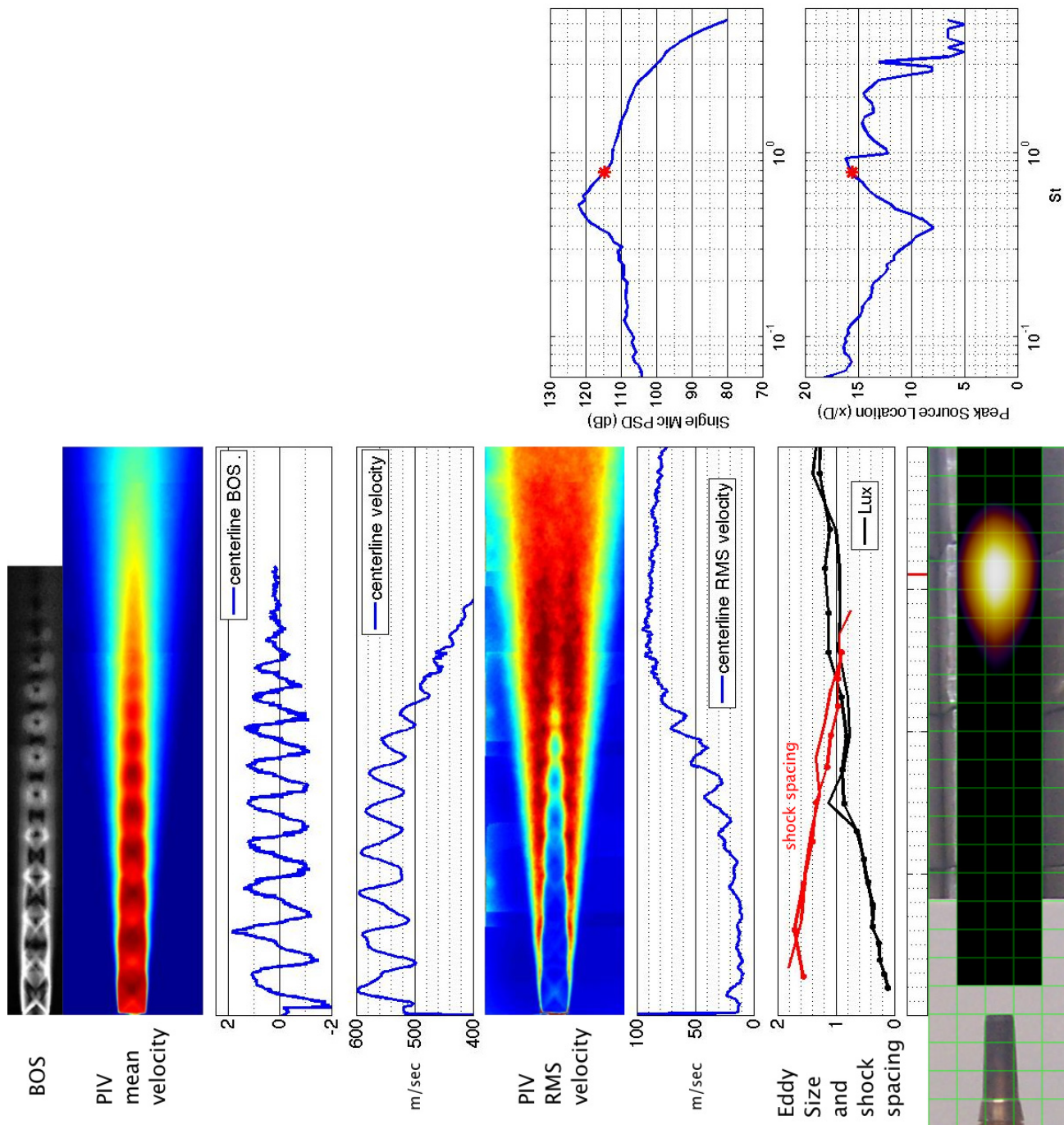
Figure 126.—SMC016; under-expanded; set point 11617; Mj=1.61; Mjdesign=1.50; St=0.779.
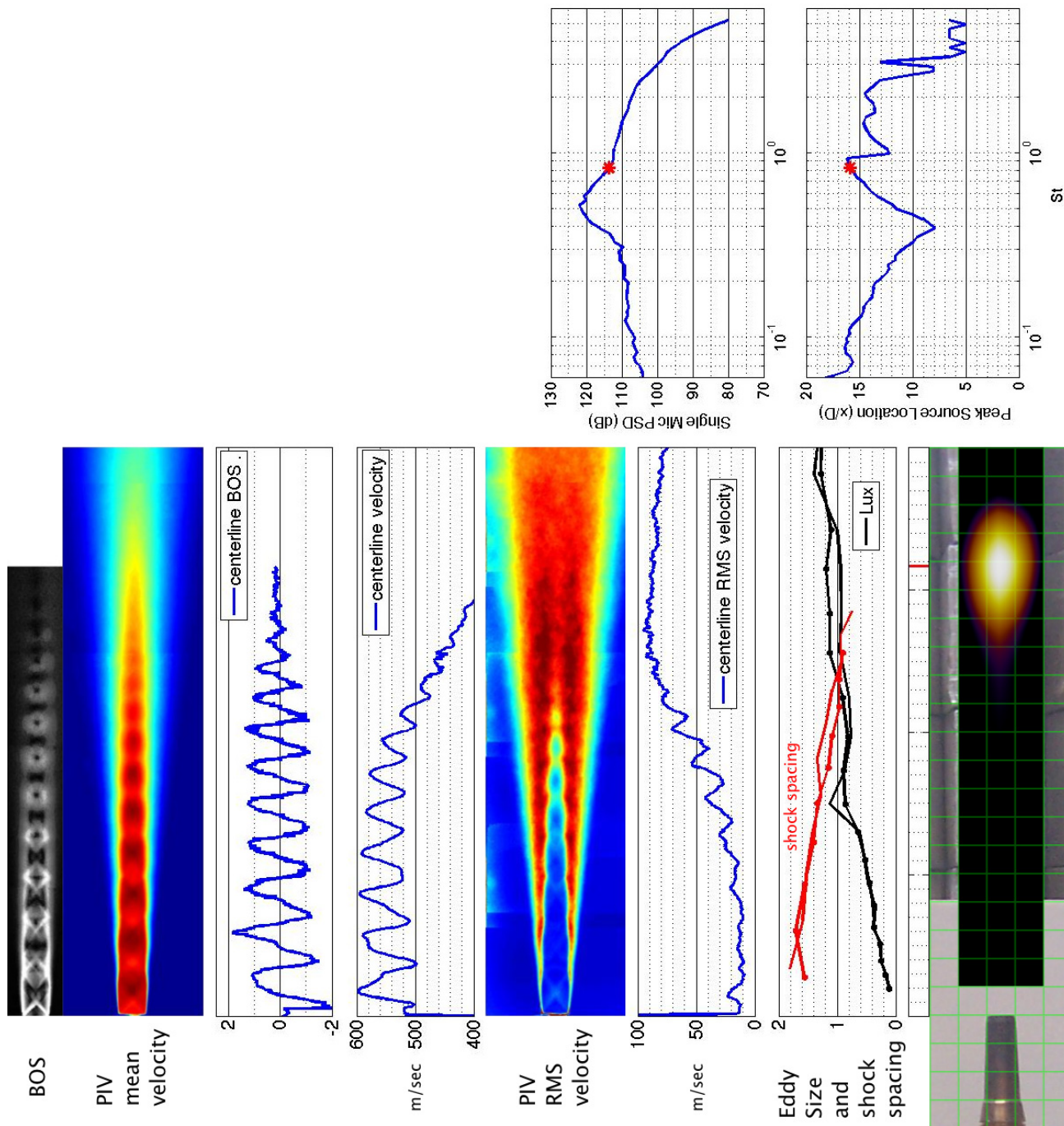
Figure 127.—SMC016; under-expanded; set point 11617; Mj=1.61; Mjdesign=1.50; St=0.827.
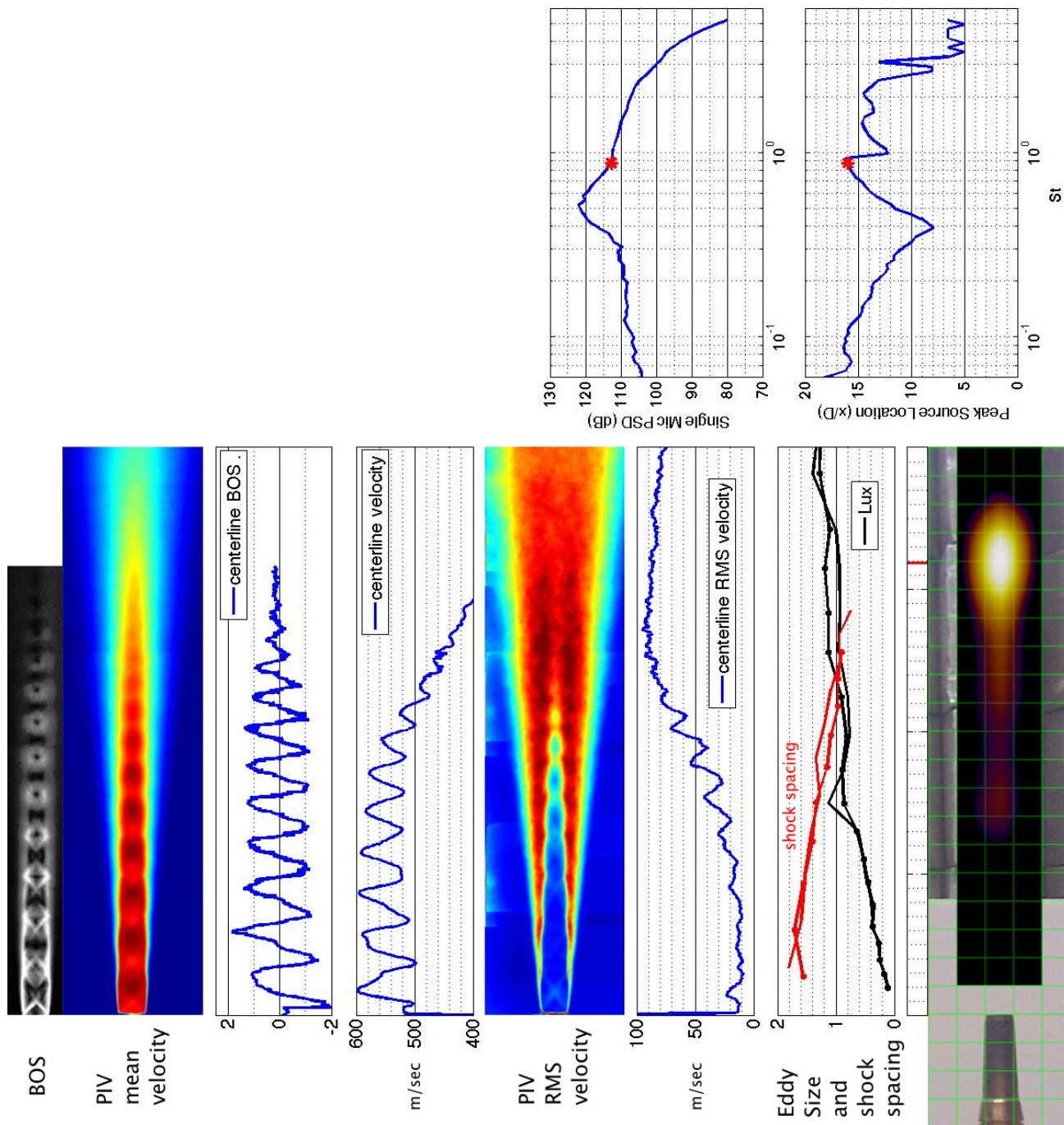
Figure 128.—SMC016; under-expanded; set point 11617; Mj=1.61; Mjdesign=1.50; St=0.878.

Figure 129.—SMC016; under-expanded; set point 11617; Mj=1.61; Mjdesign=1.50; St=0.931.
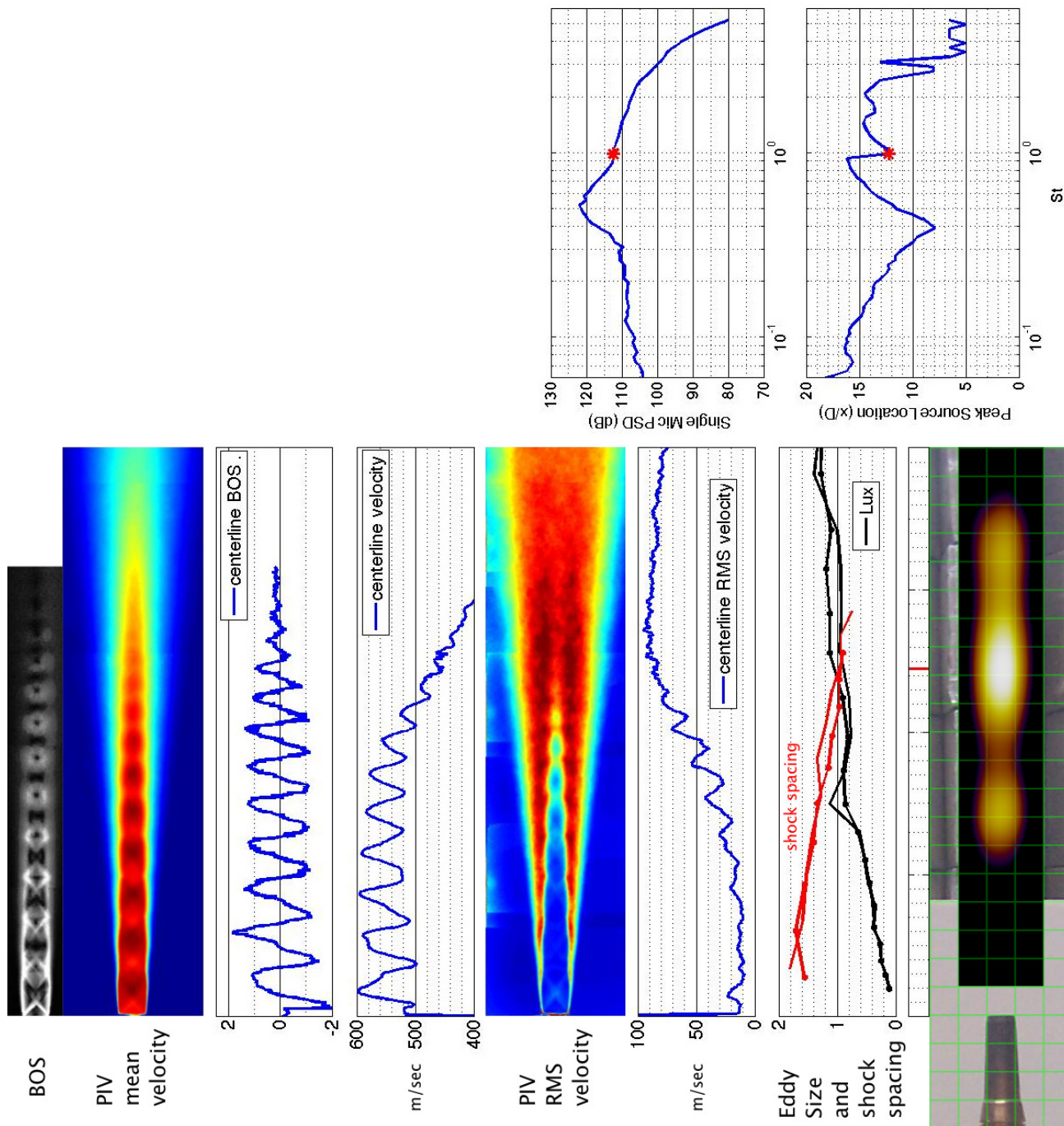
Figure 130.—SMC016; under-expanded; set point 11617; Mj=1.61; Mjdesign=1.50; St=0.985.
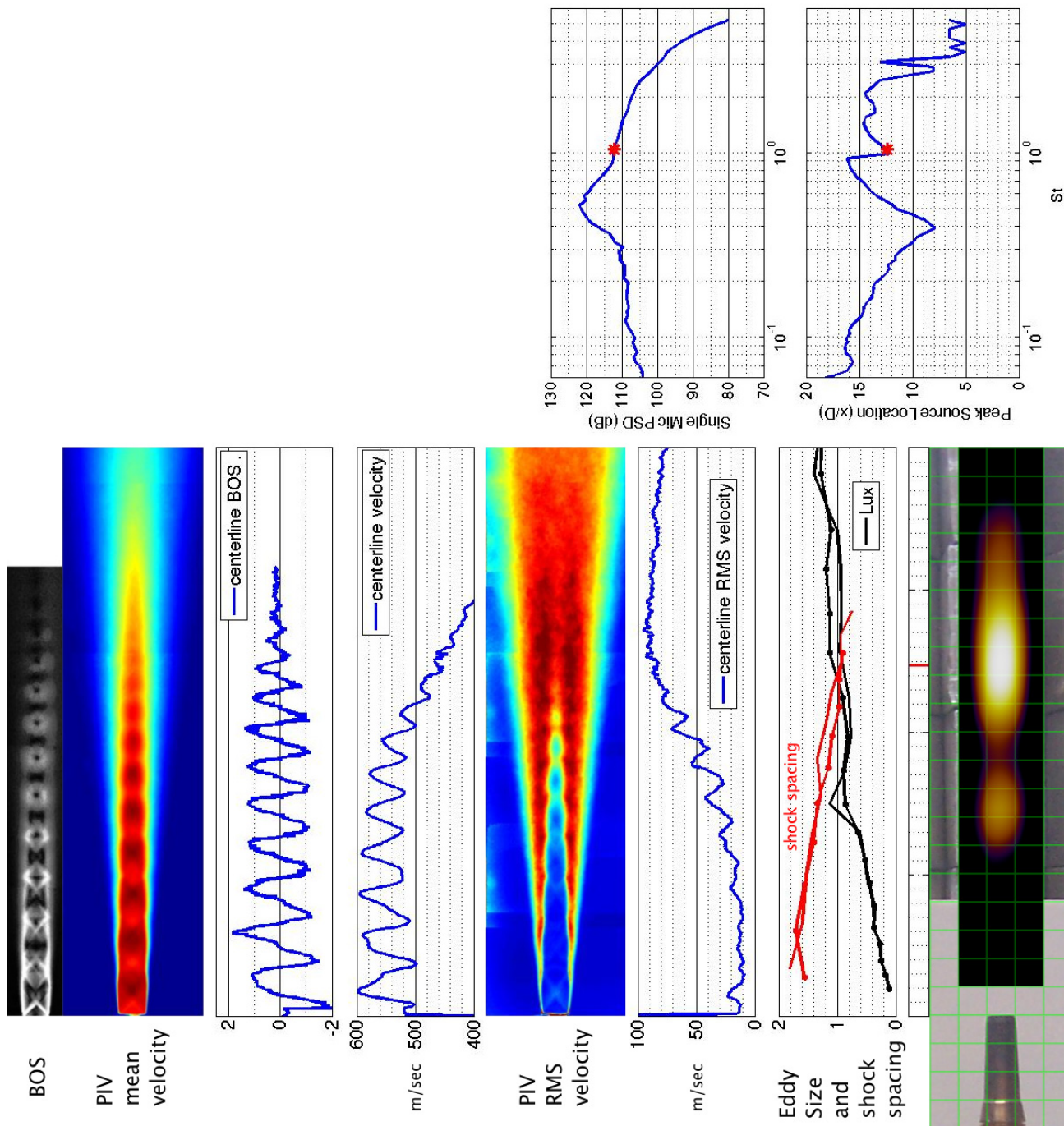
Figure 131.—SMC016; under-expanded; set point 11617; Mj=1.61; Mjdesign=1.50; St=1.042.
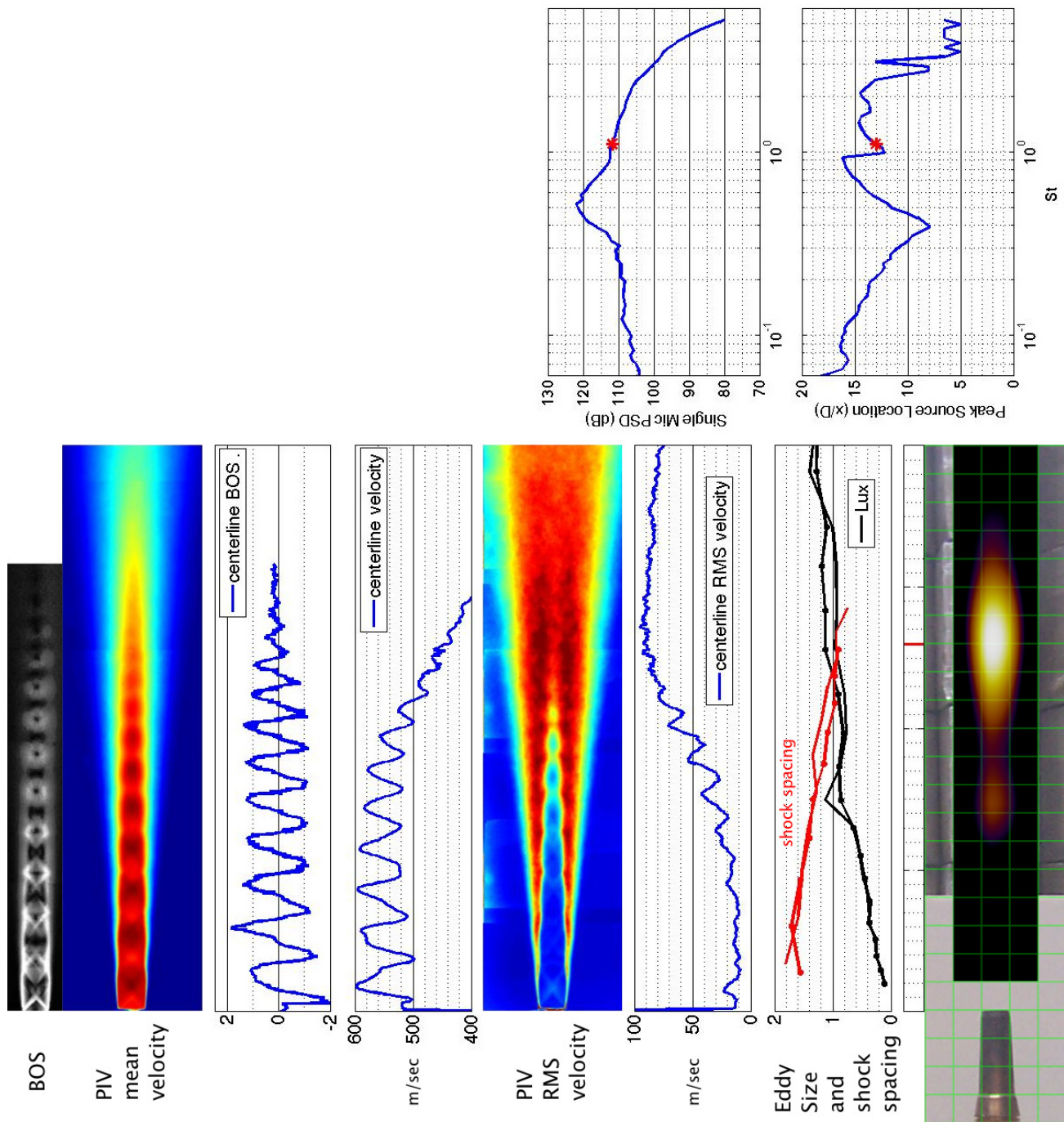
Figure 132.—SMC016; under-expanded; set point 11617; Mj=1.61; Mjdesign=1.50; St=1.102.
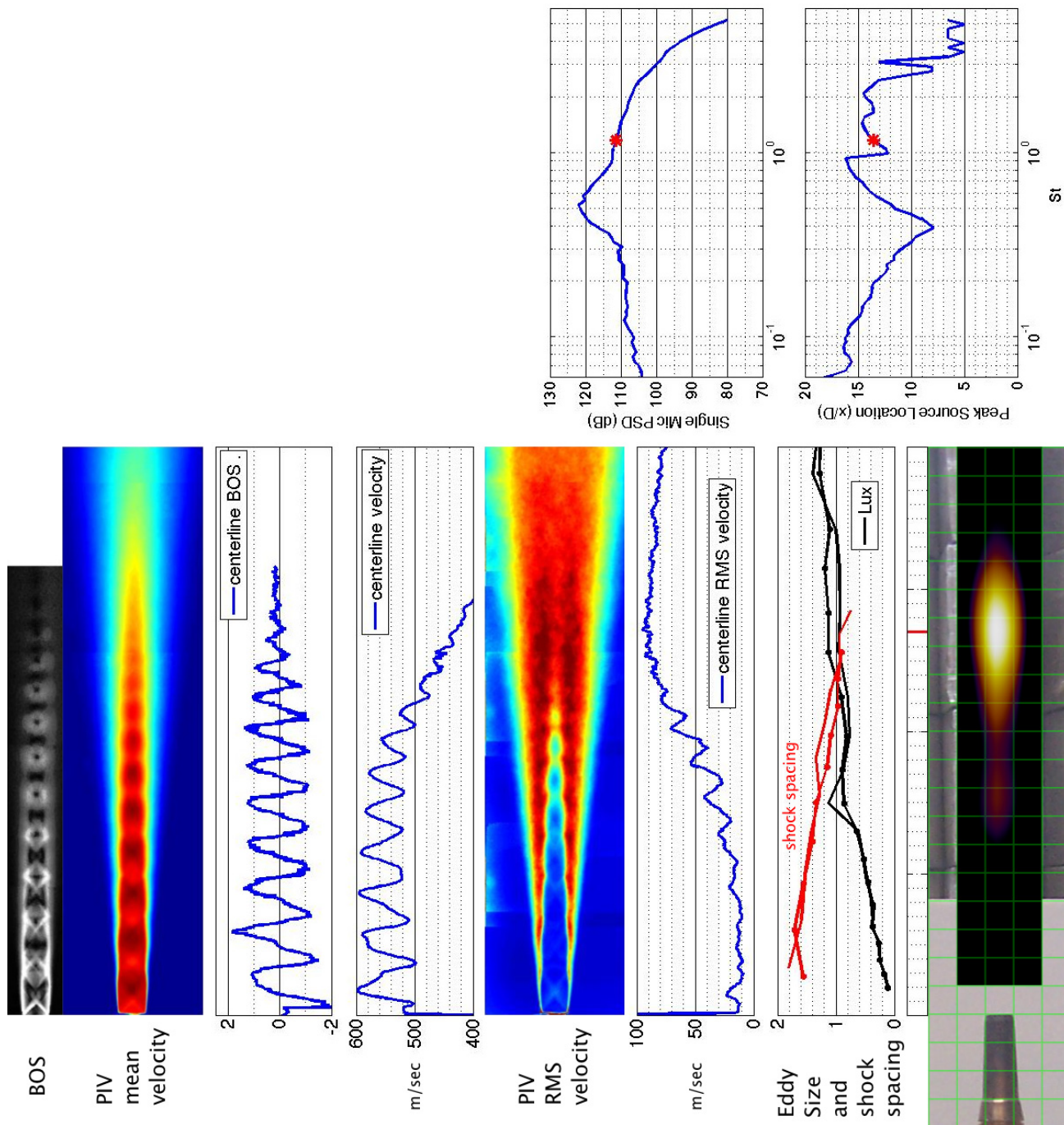
Figure 133.—SMC016; under-expanded; set point 11617; Mj=1.61; Mjdesign=1.50; St=1.165.
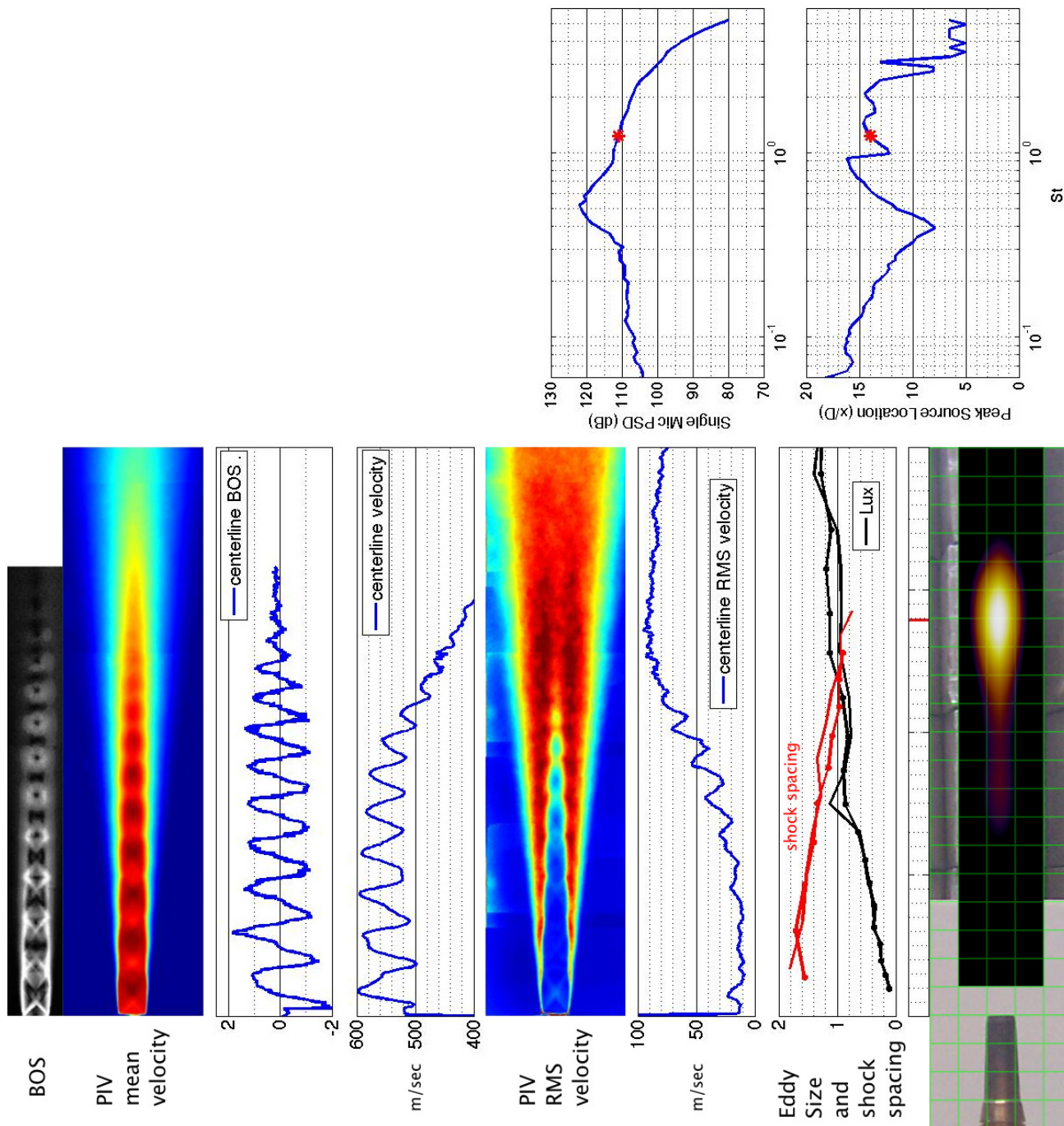
Figure 134.—SMC016; under-expanded; set point 11617; Mj=1.61; Mjdesign=1.50; St=1.232.
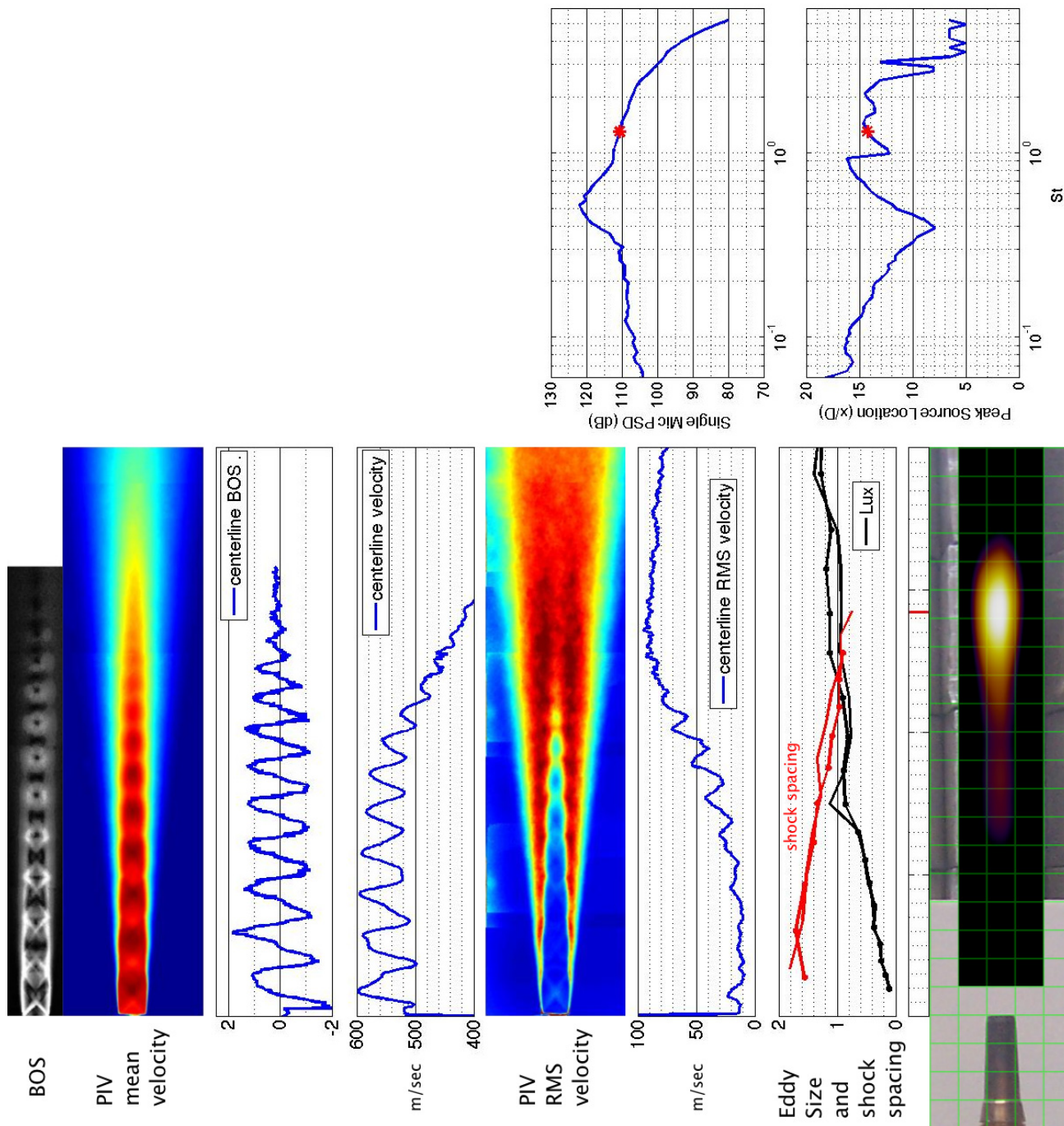
Figure 135.—SMC016; under-expanded; set point 11617; Mj=1.61; Mjdesign=1.50; St=1.302.
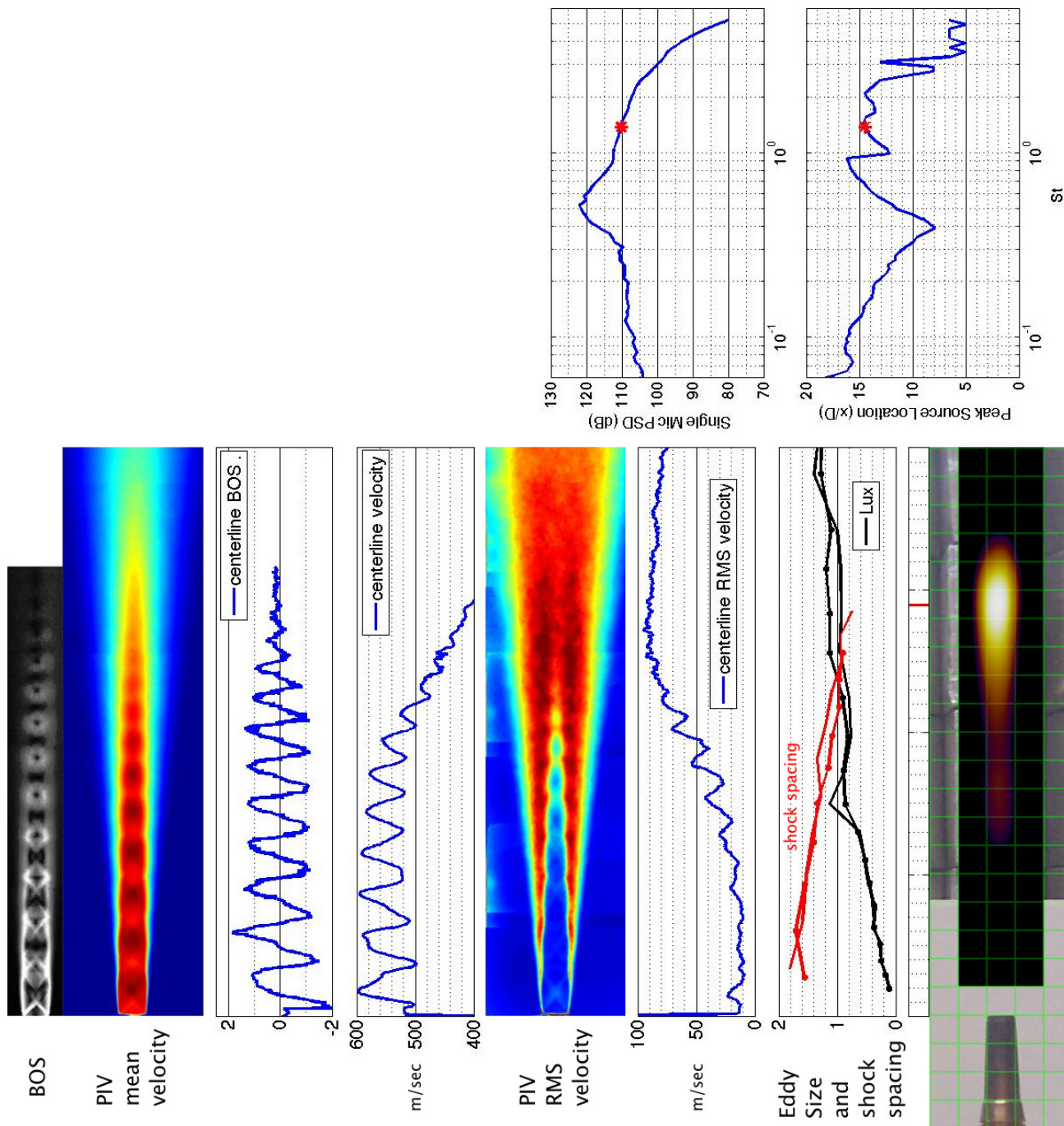
Figure 136.—SMC016; under-expanded; set point 11617; Mj=1.61; Mjdesign=1.50; St=1.377.
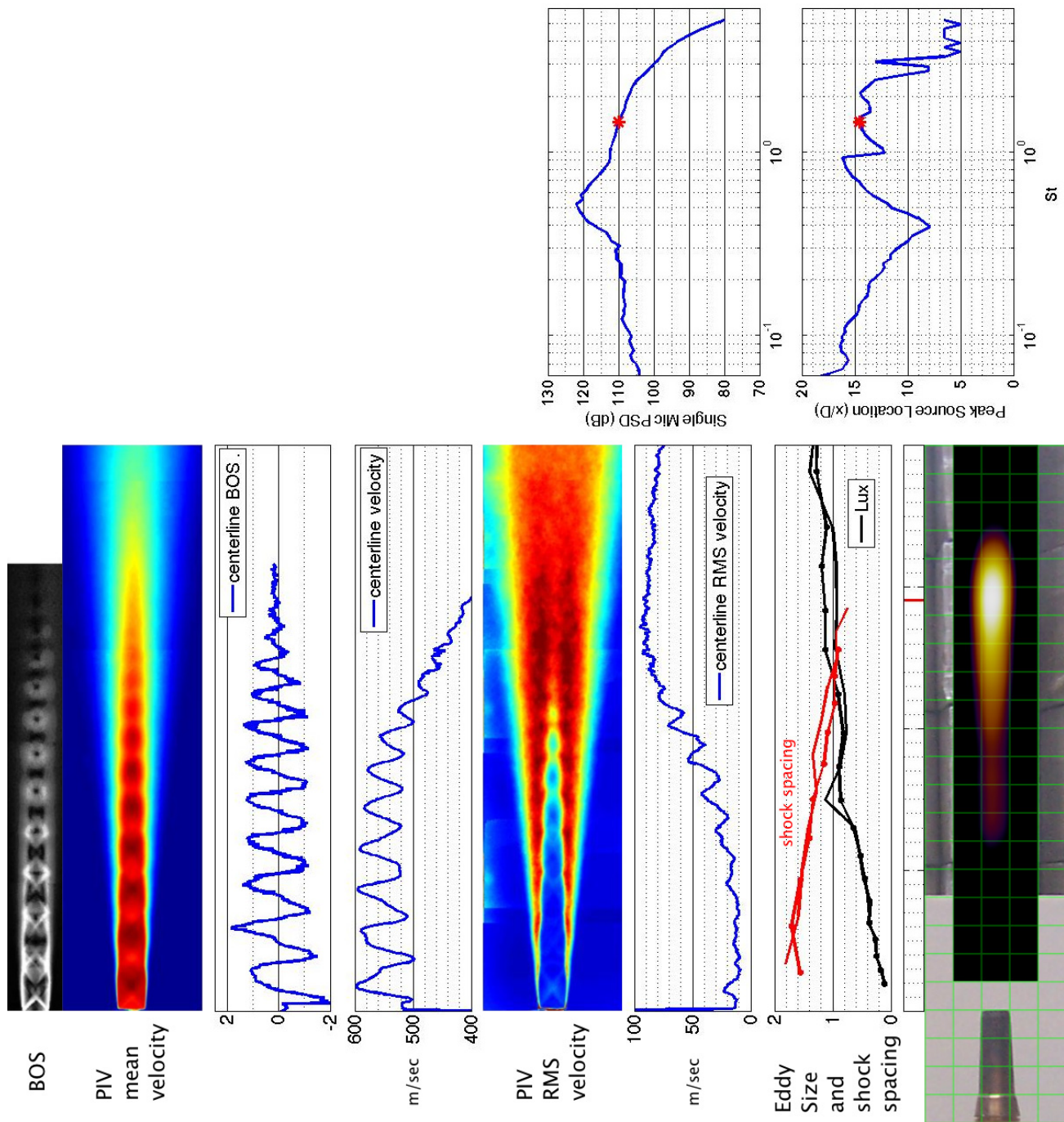
Figure 137.—SMC016; under-expanded; set point 11617; Mj=1.61; Mjdesign=1.50; St=1.458.
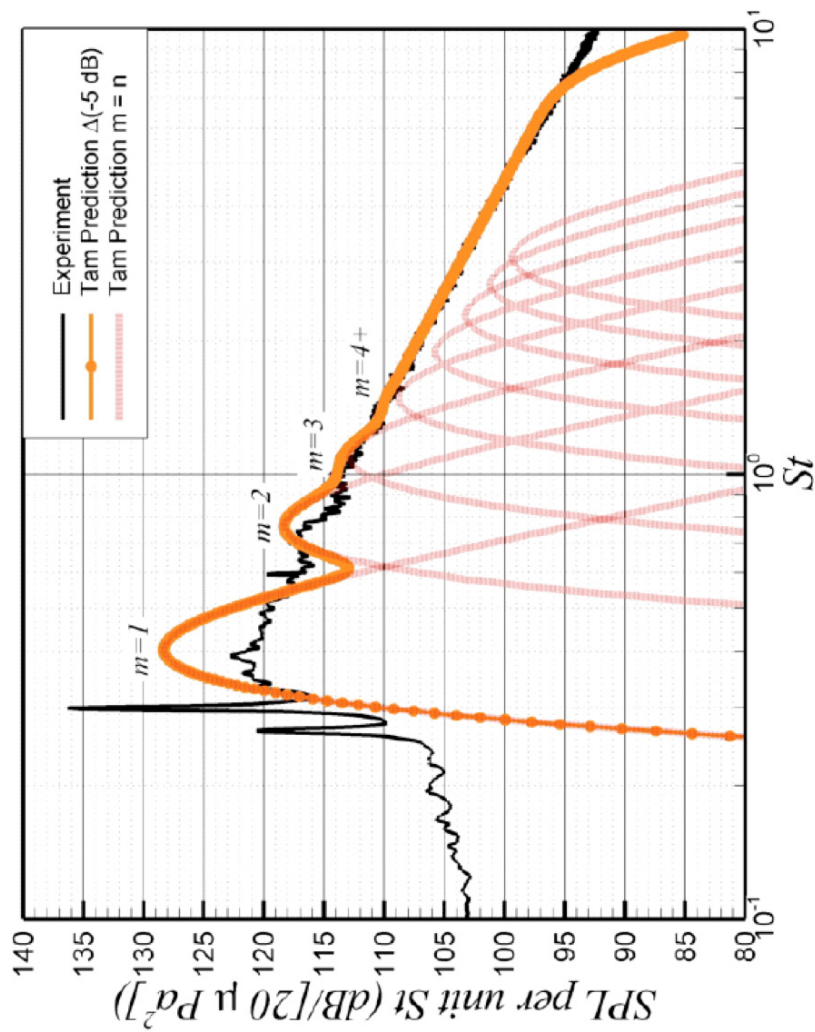
Figure 138.—Experimental results (in black) compared with a prediction of BBSN based on Tam's model (in orange). (Figure taken from Miller, S.A.E., "The Prediction of Broadband Shock-Associated Noise Using Reynolds-Averaged Navier-Stokes Solutions," Ph. D. dissertation, Pennsylvania State University, December 2009. Used with permission).
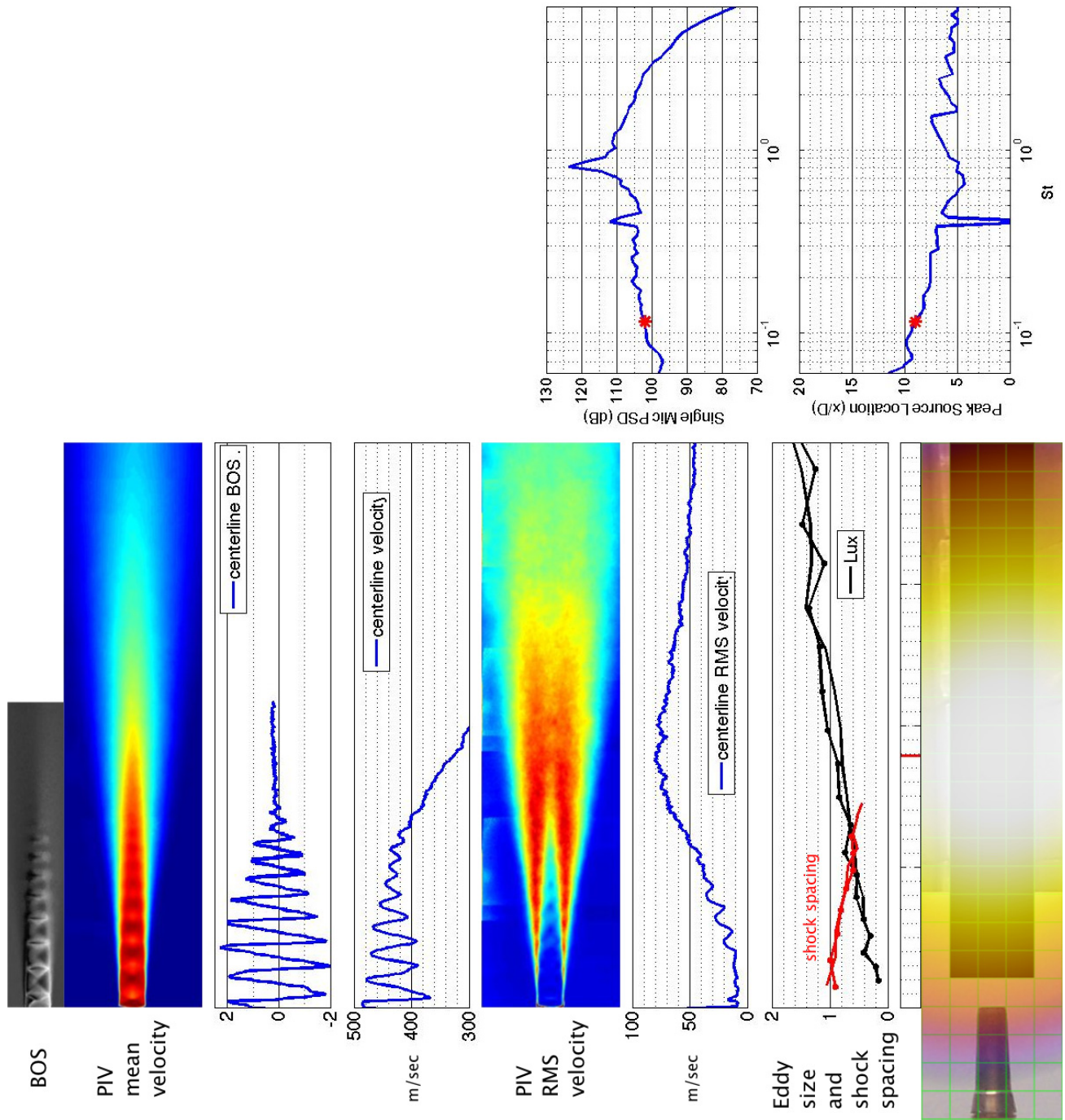
Figure 139.—SMC016; over-expanded; set point 11606; Mj=1.29; Mjdesign=1.50; St=0.115.
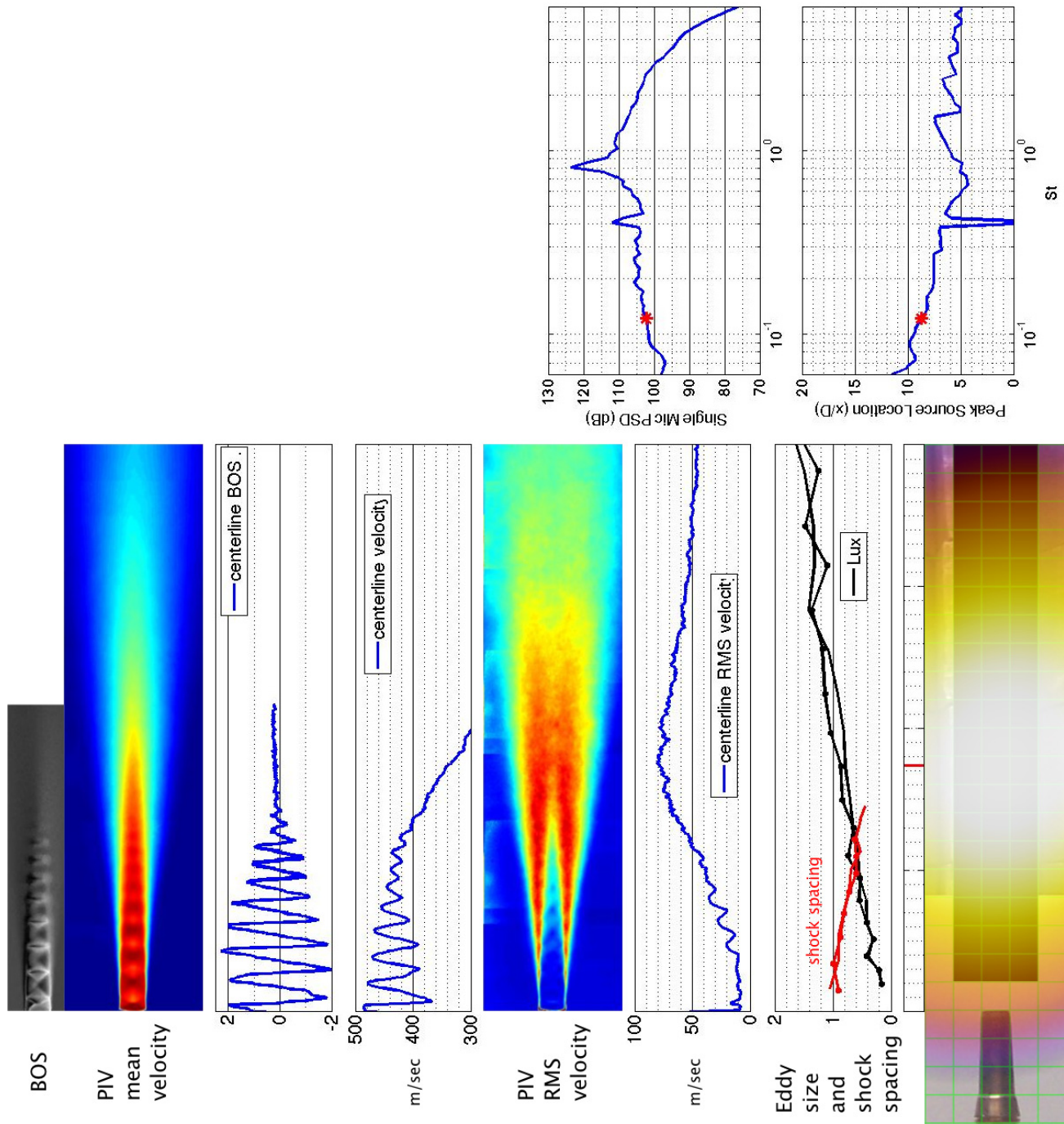
Figure 140.—SMC016; under-expanded; set point 11617; Mj=1.61; Mjdesign=1.50; St=0.122.
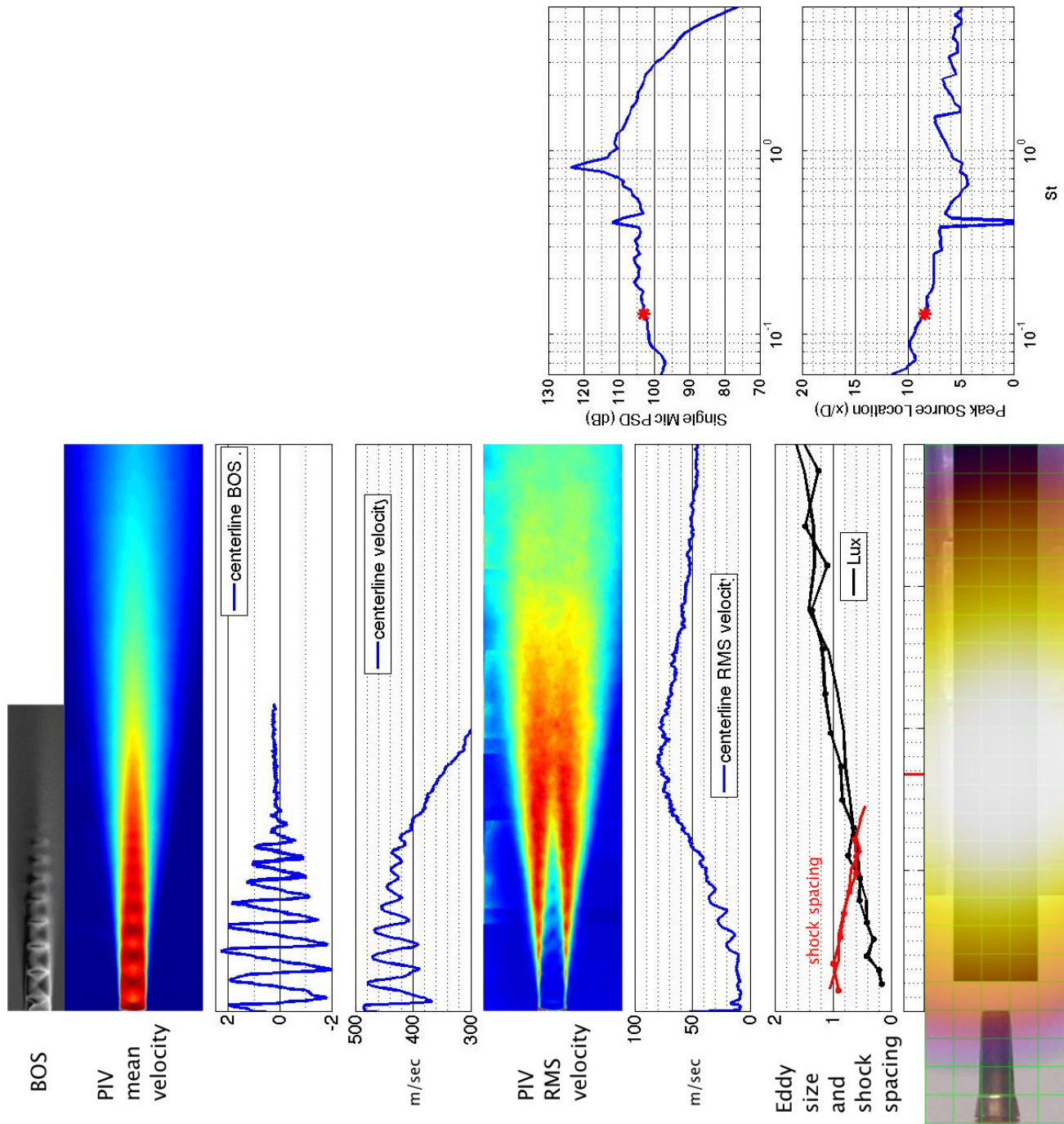
Figure 141.—SMC016; under-expanded; set point 11617; Mj=1.61; Mjdesign=1.50; St=0.129.
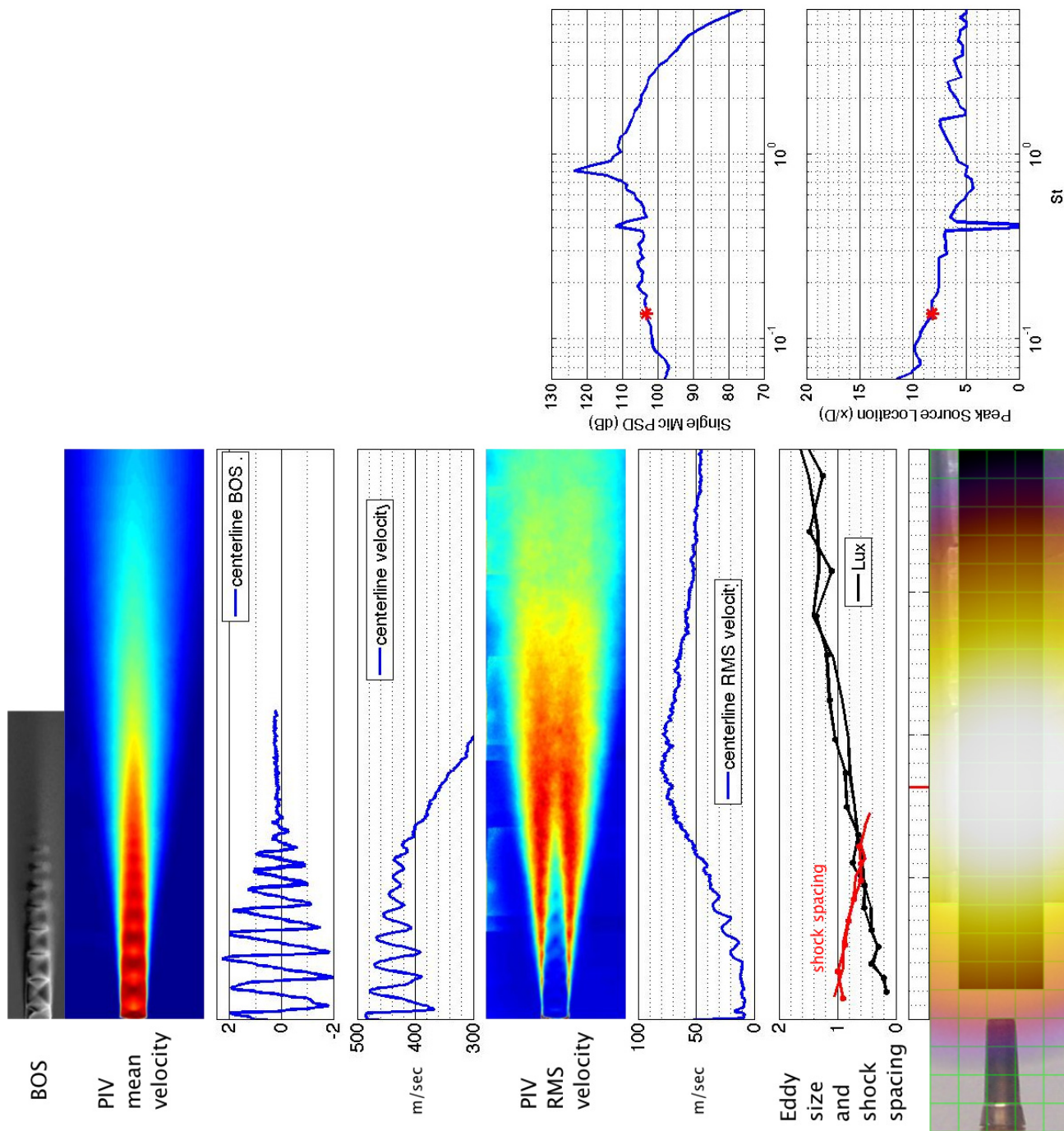
Figure 142.—SMC016; under-expanded; set point 11617; Mj=1.61; Mjdesign=1.50; St=0.136.
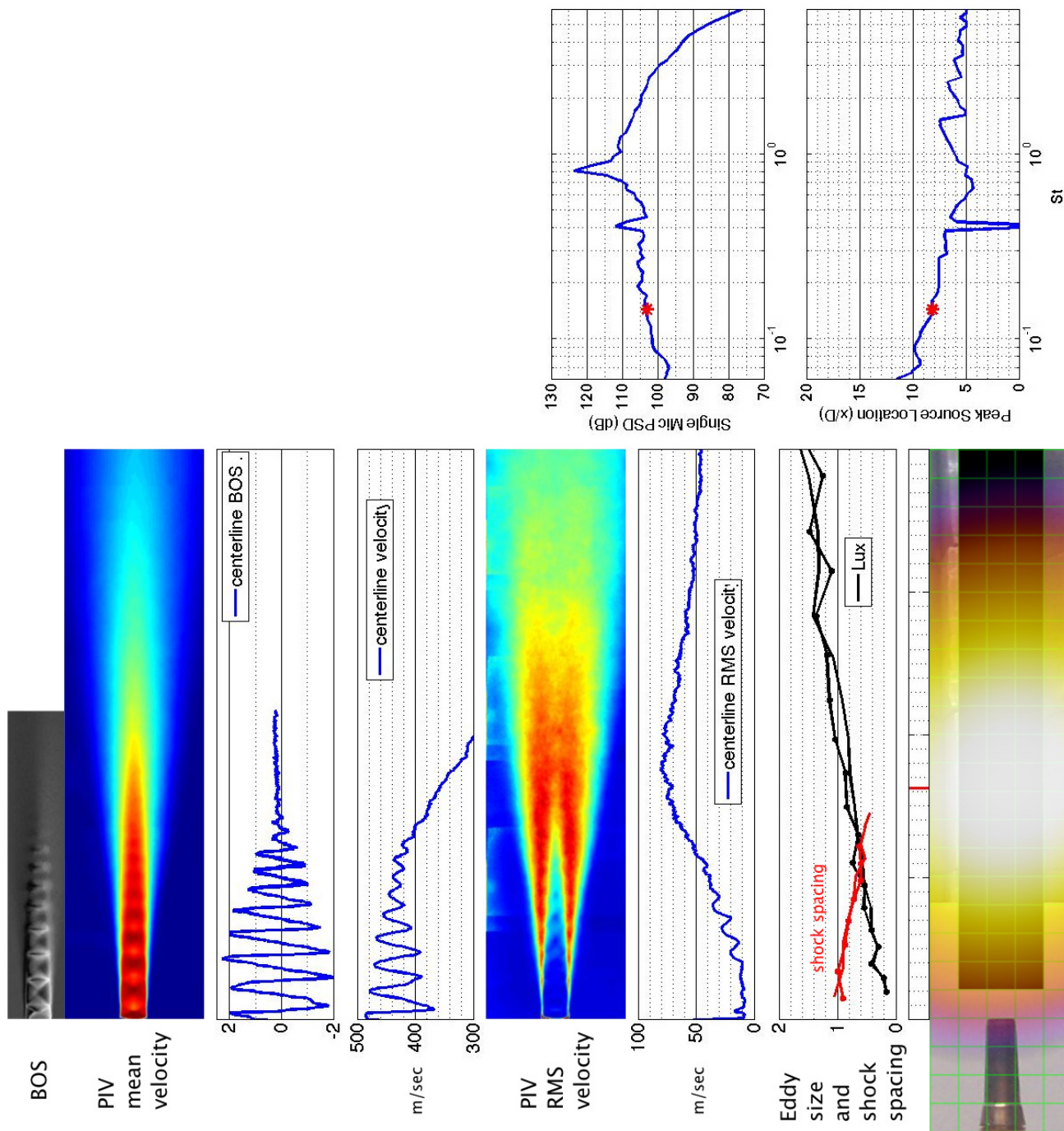
Figure 143.—SMC016; under-expanded; set point 11617; Mj=1.61; Mjdesign=1.50; St=0.144.
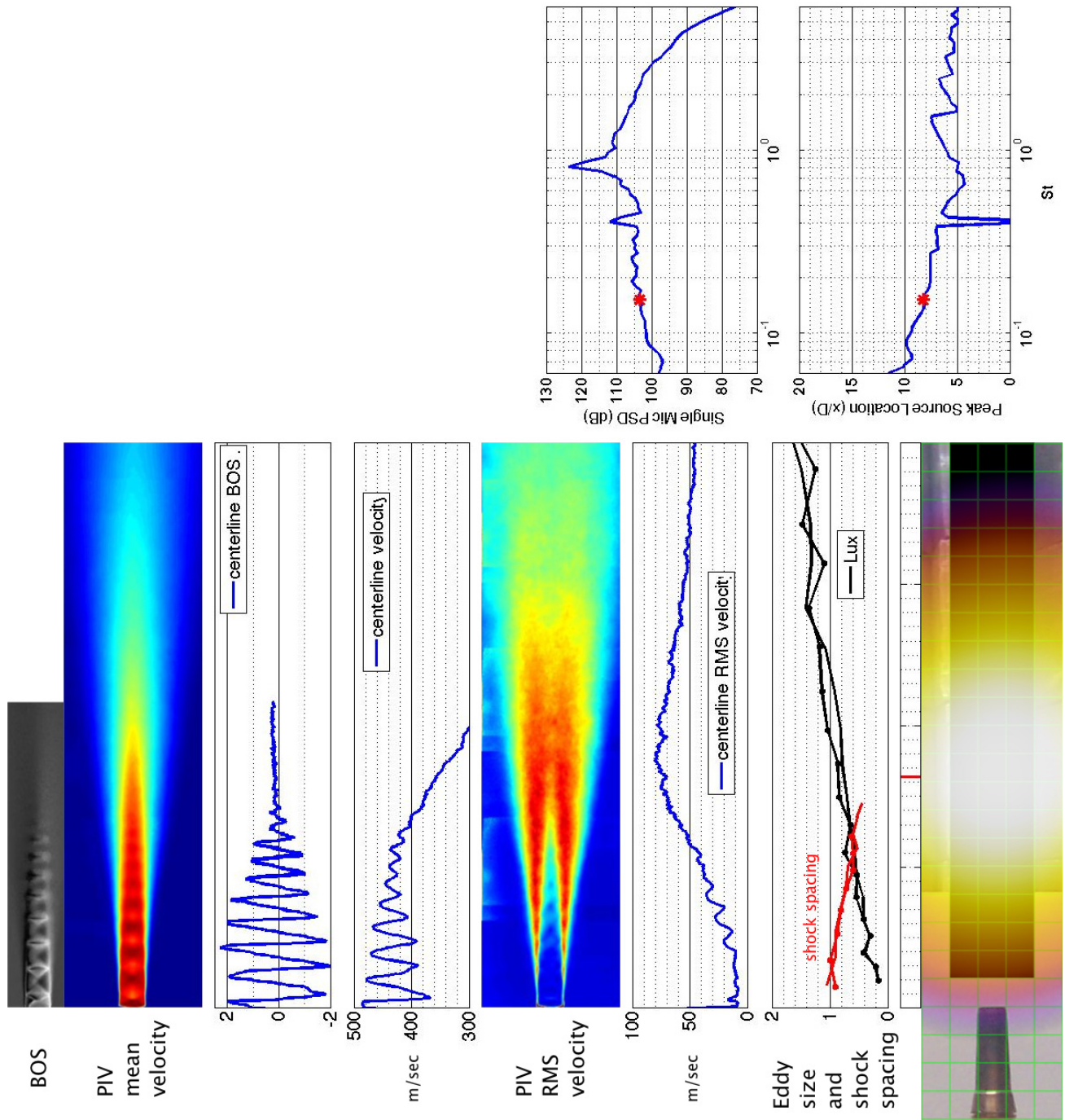
Figure 144.—SMC016; under-expanded; set point 11617; Mj=1.61; Mjdesign=1.50; St=0.153.
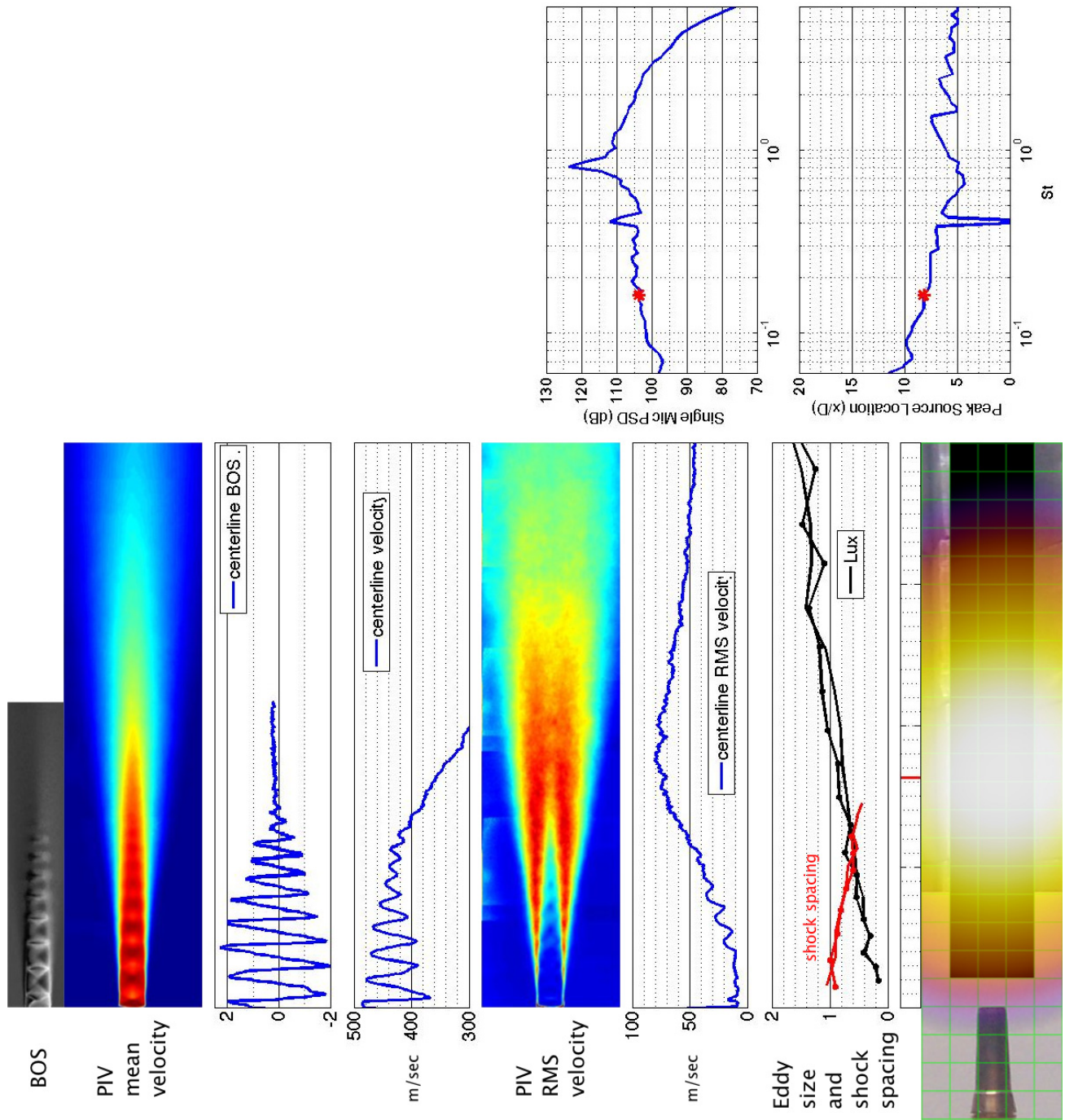
Figure 145.—SMC016; under-expanded; set point 11617; Mj=1.61; Mjdesign=1.50; St=0.161.
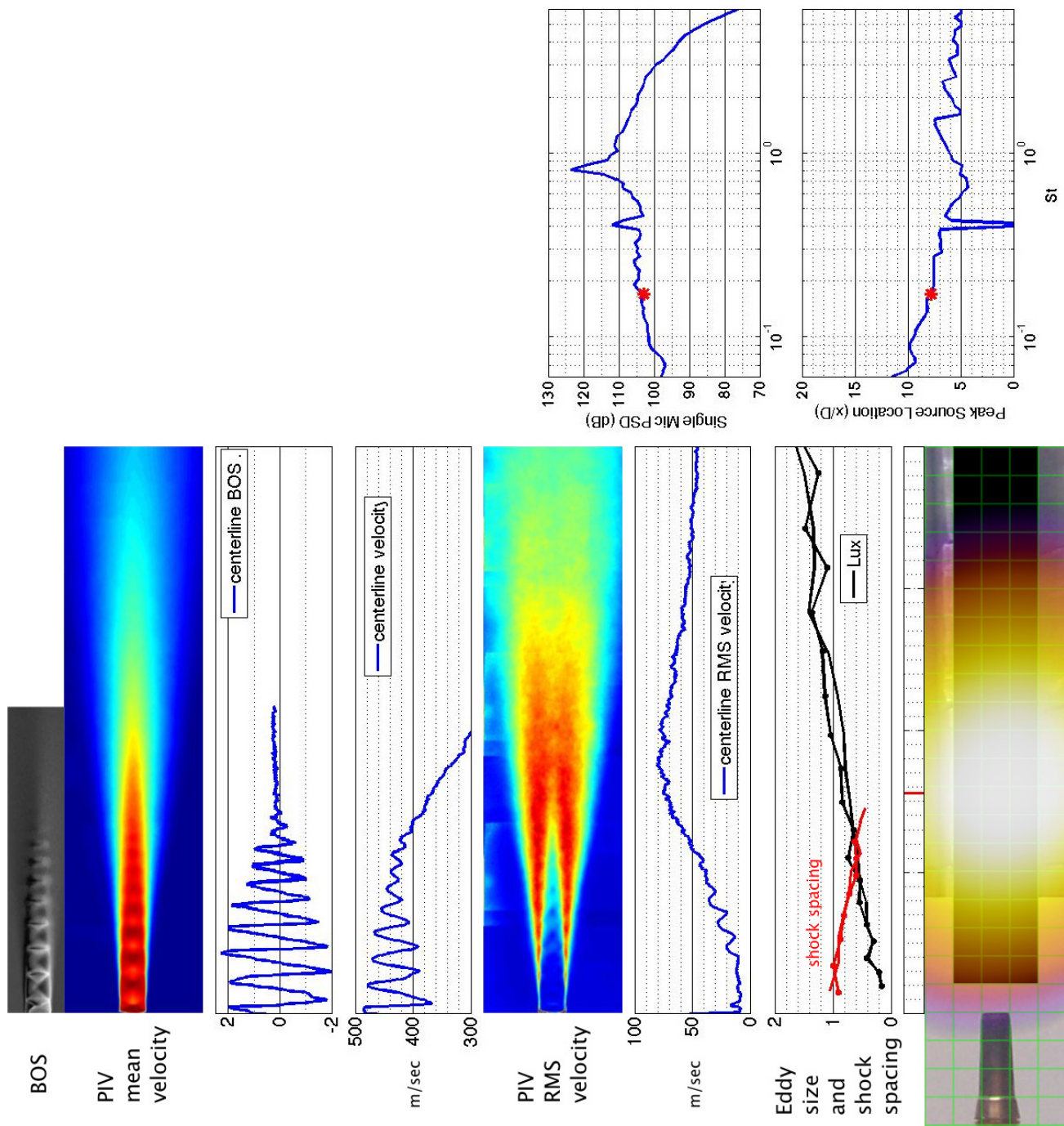
Figure 146.—SMC016; under-expanded; set point 11617; Mj=1.61; Mjdesign=1.50; St=0.171.
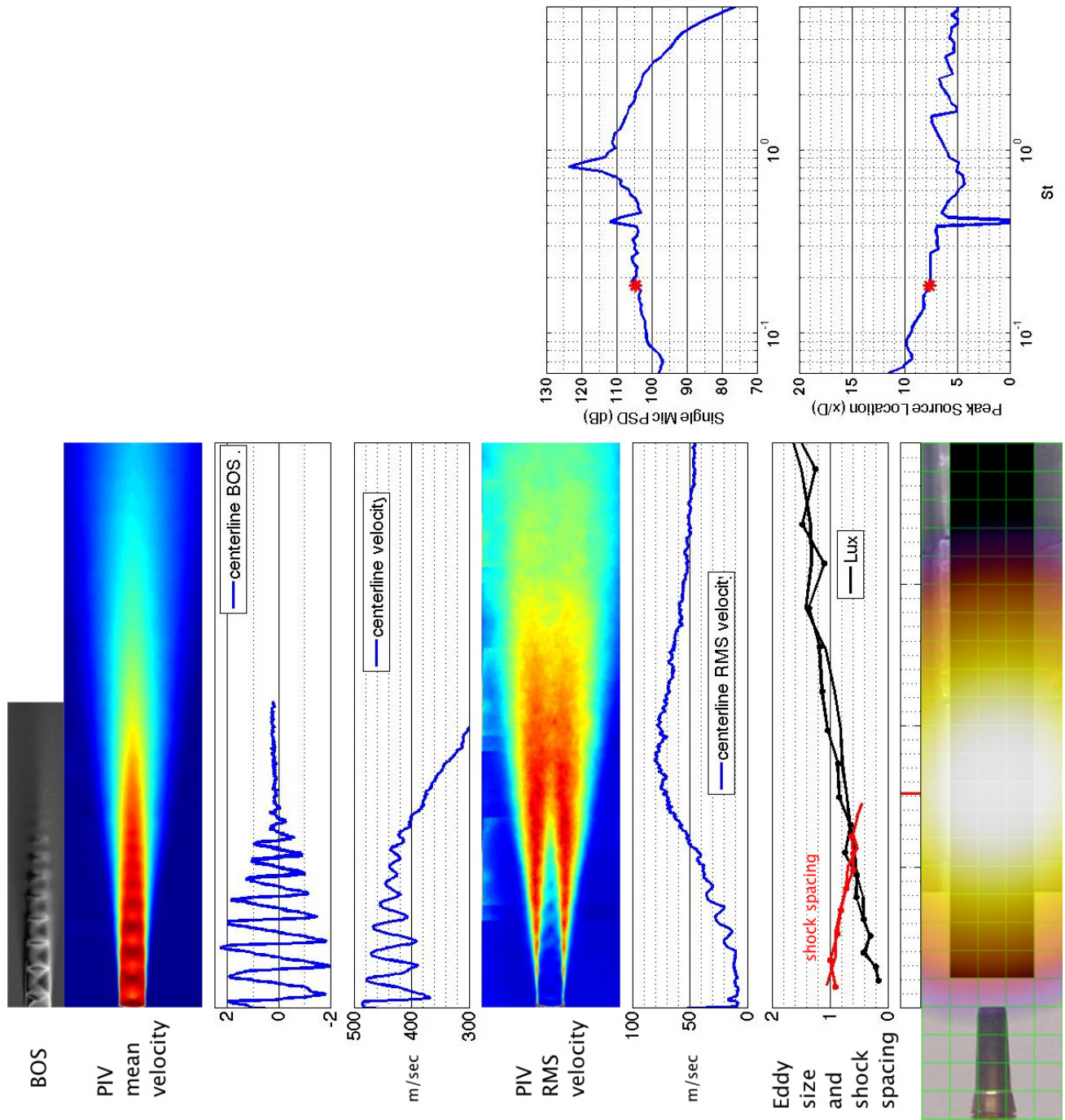
Figure 147.—SMC016; under-expanded; set point 11617; Mj=1.61; Mjdesign=1.50; St=0.181.
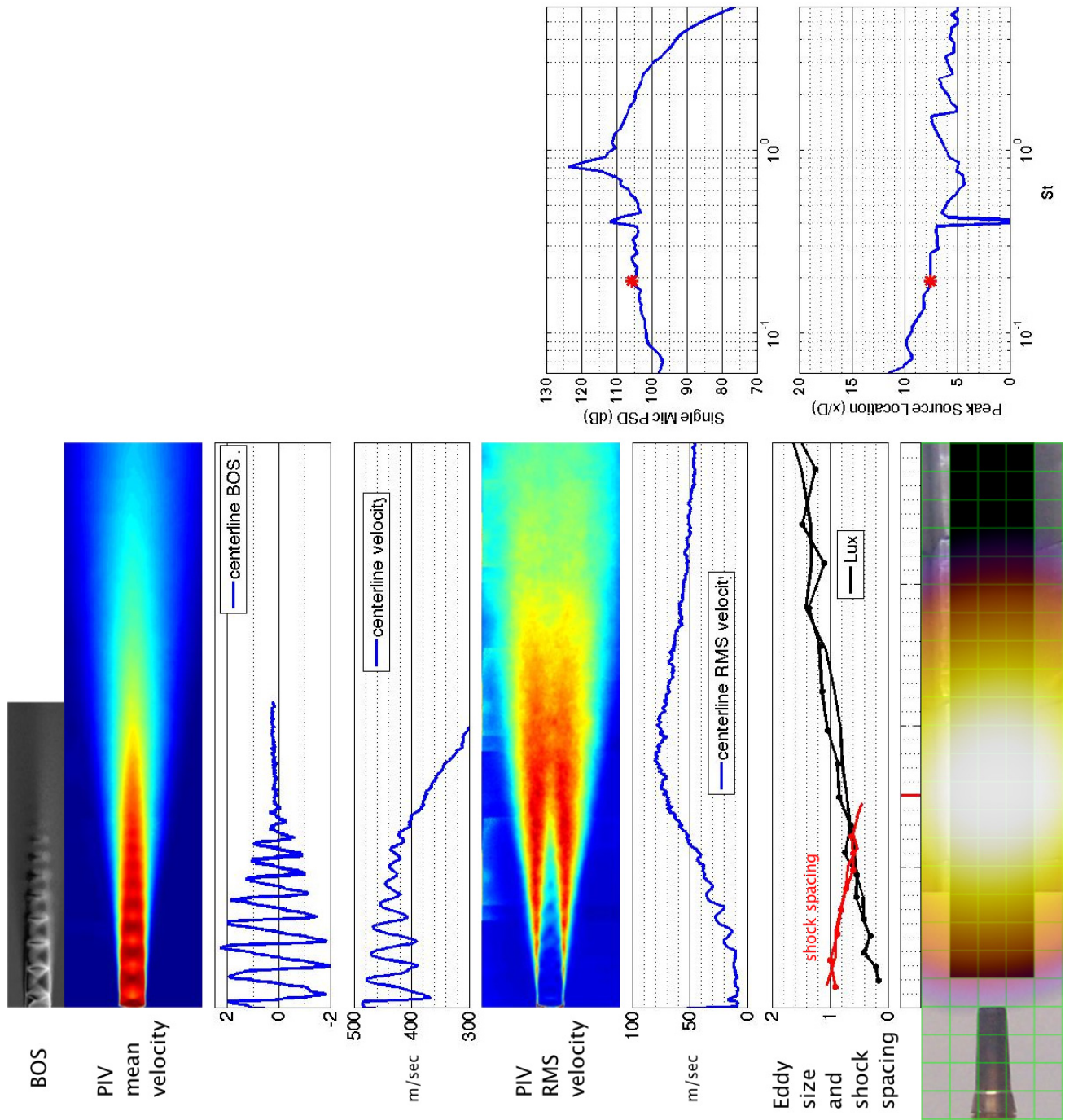
Figure 148.—SMC016; under-expanded; set point 11617; Mj=1.61; Mjdesign=1.50; St=0.193.
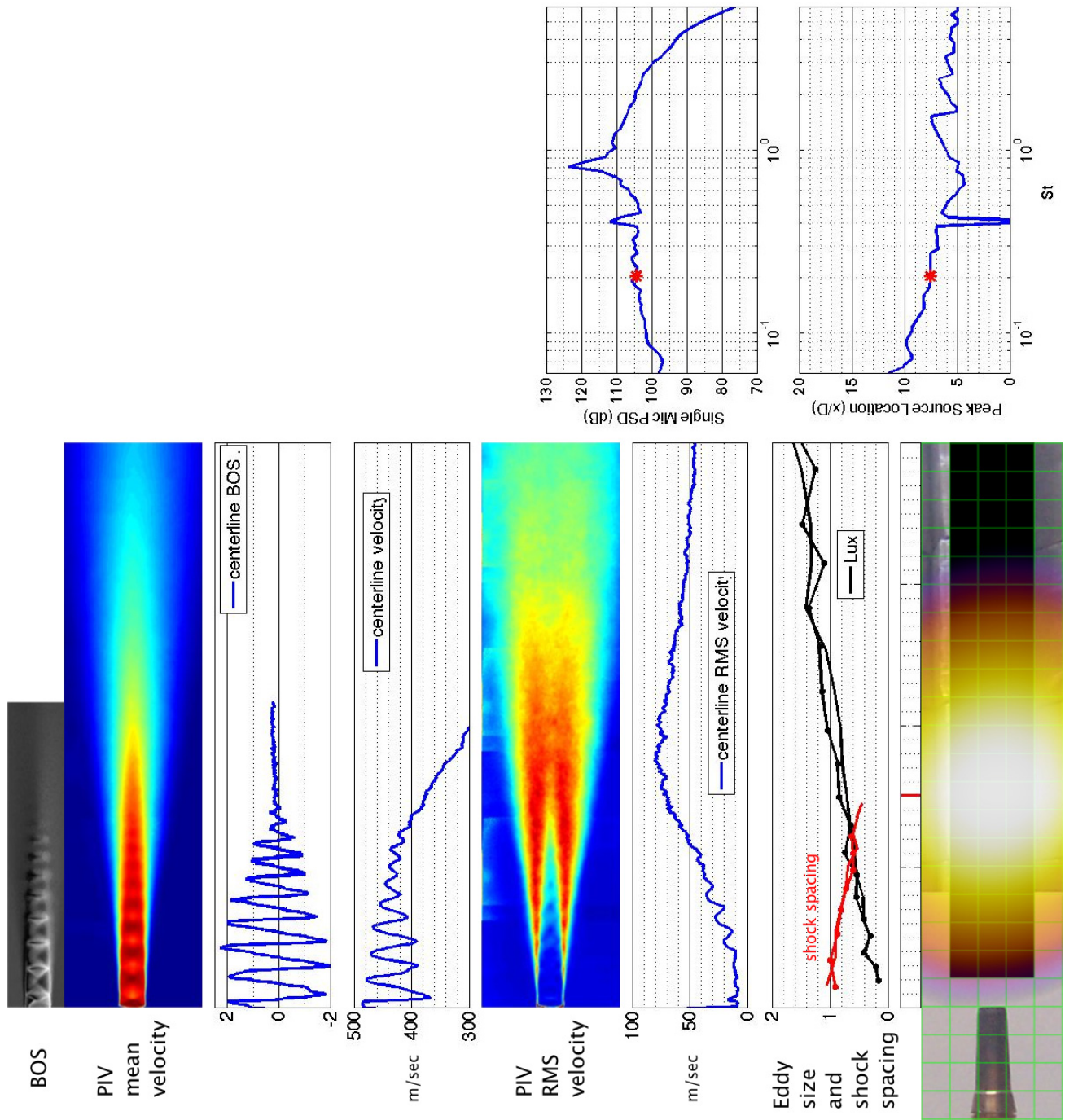
Figure 149.—SMC016; under-expanded; set point 11617; Mj=1.61; Mjdesign=1.50; St=0.205.
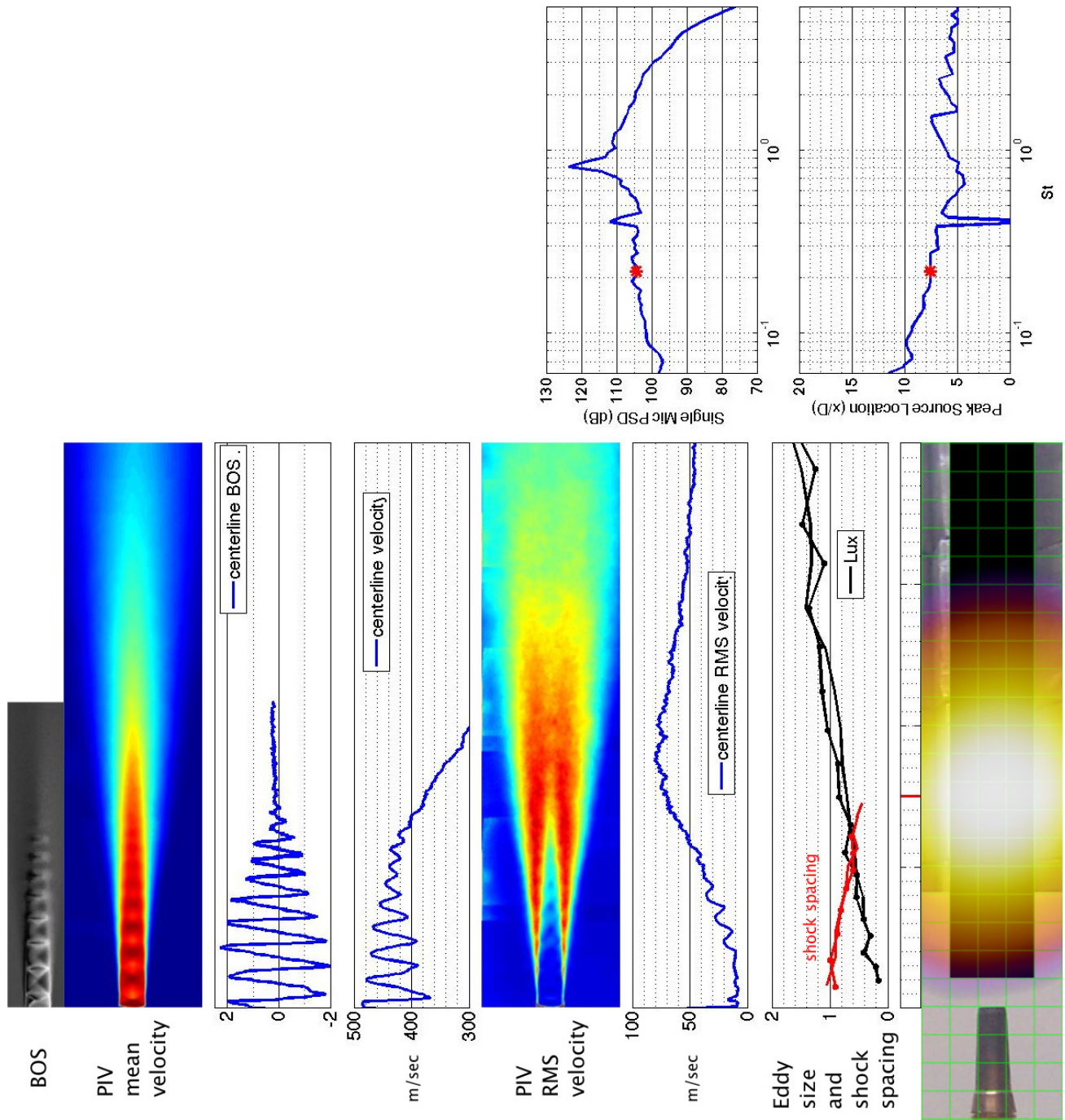
Figure 150.—SMC016; under-expanded; set point 11617; Mj=1.61; Mjdesign=1.50; St=0.218.
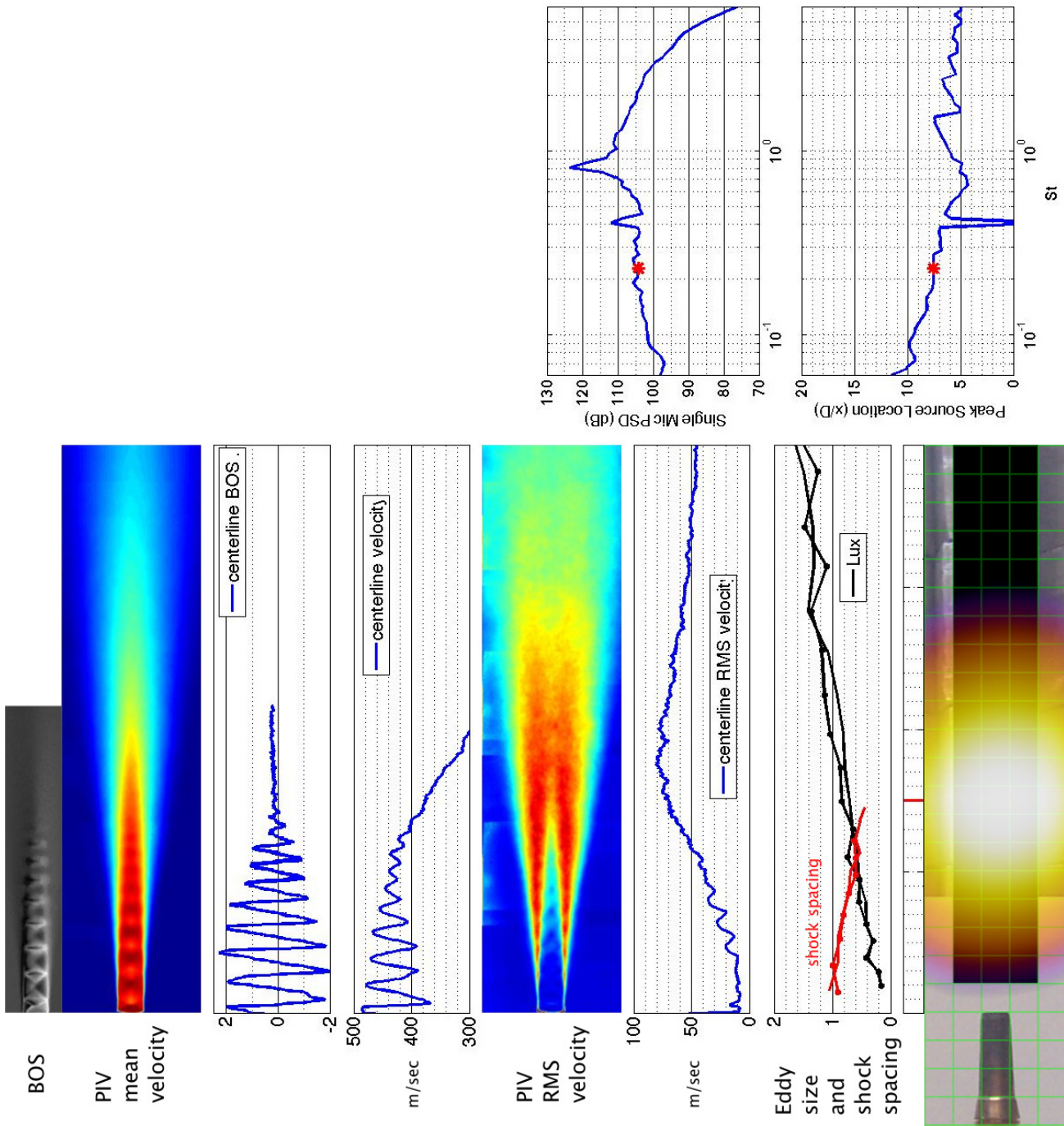
Figure 151.—SMC016; under-expanded; set point 11617; Mj=1.61; Mjdesign=1.50; St=0.231.
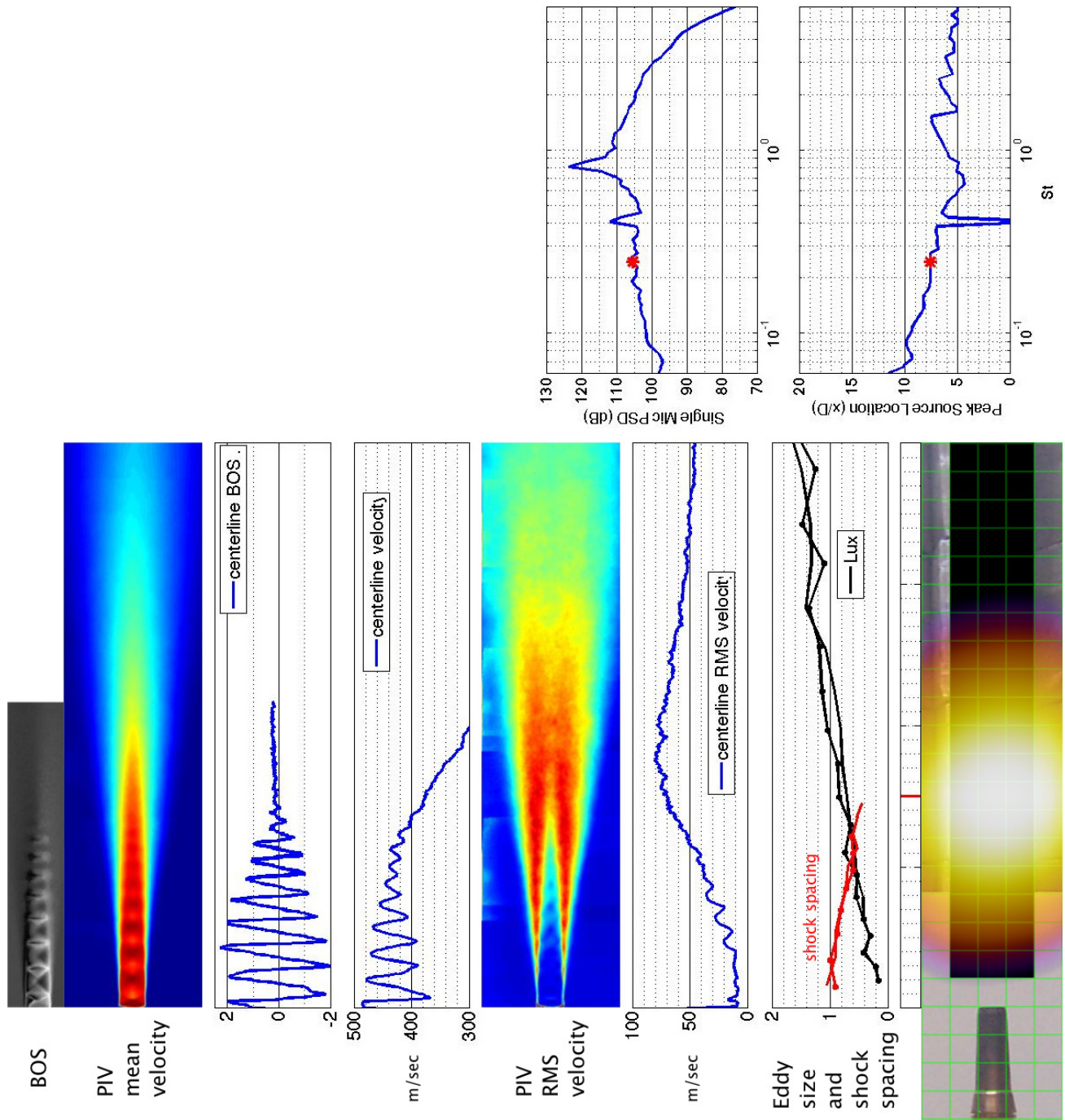
Figure 152.—SMC016; under-expanded; set point 11617; Mj=1.61; MJdesign=1.50; St=0.244.
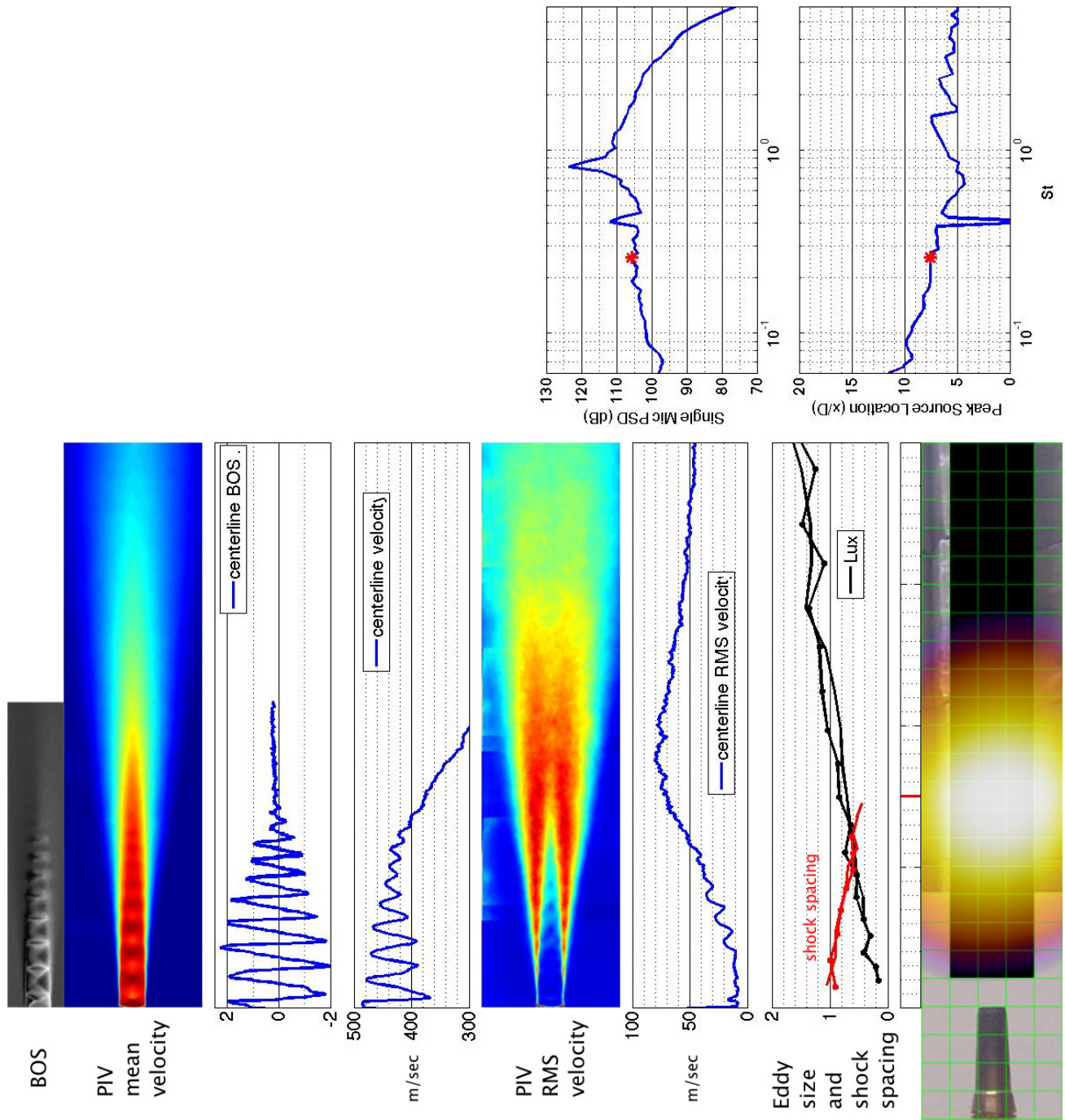
Figure 153.—SMC016; under-expanded; set point 11617; Mj=1.61; Mjdesign=1.50; St=0.258.
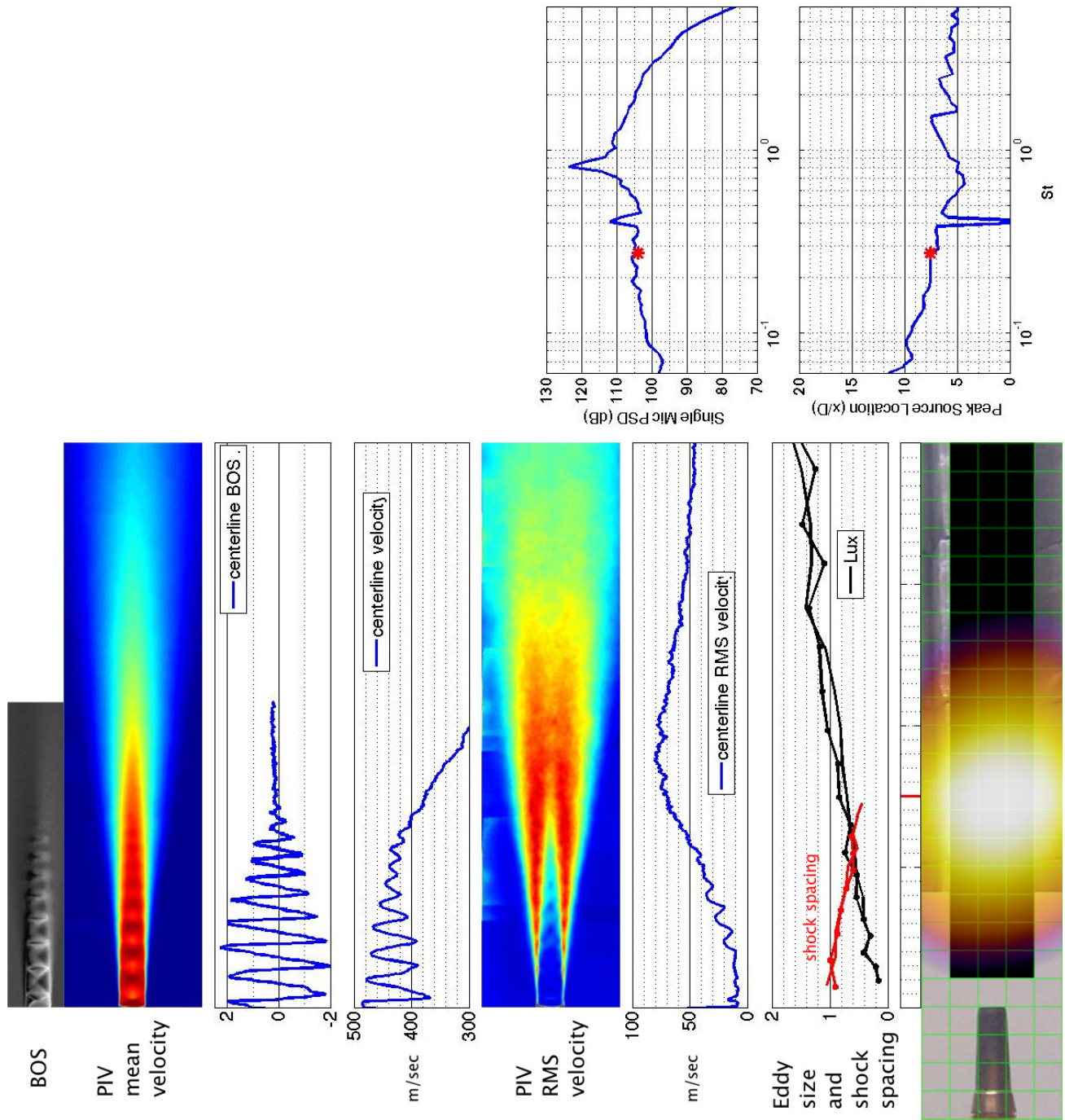
Figure 154.—SMC016; under-expanded; set point 11617; Mj=1.61; Mjdesign=1.50; St=0.273.
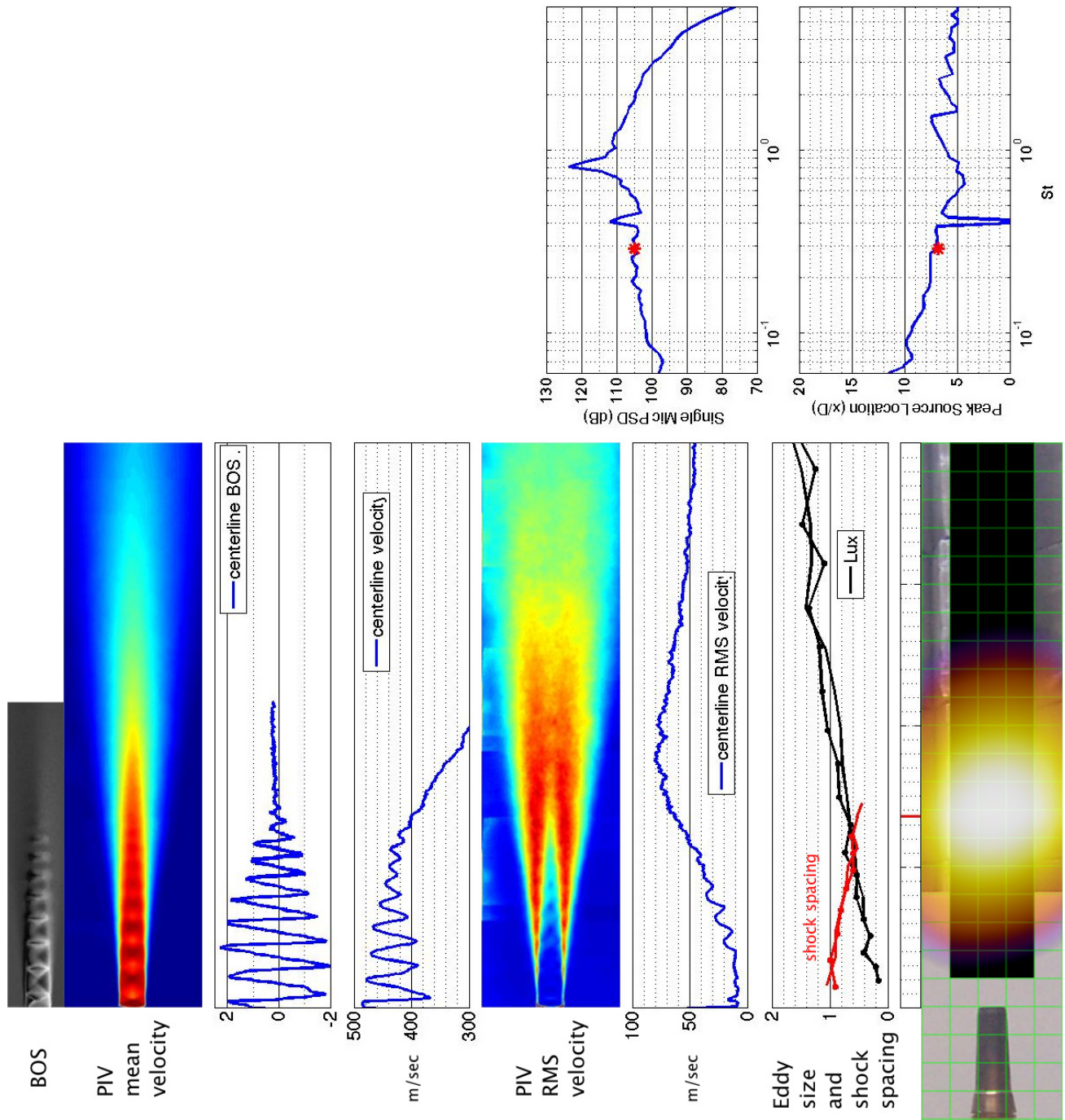
Figure 155.—SMC016; under-expanded; set point 11617; Mj=1.61; Mjdesign=1.50; St=0.288.
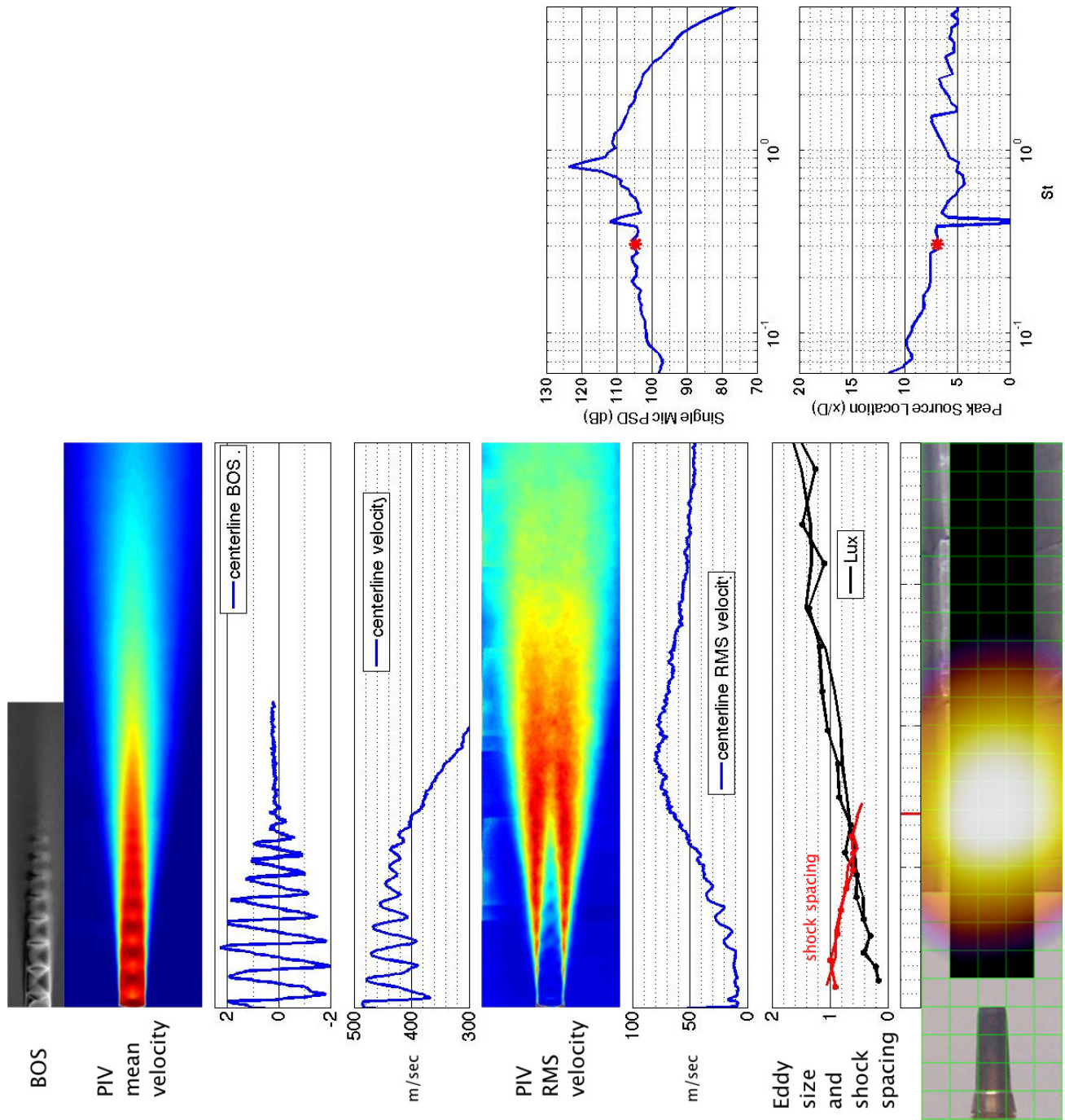
Figure 156.—SMC016; under-expanded; set point 11617; Mj=1.61; Mjdesign=1.50; St=0.305.
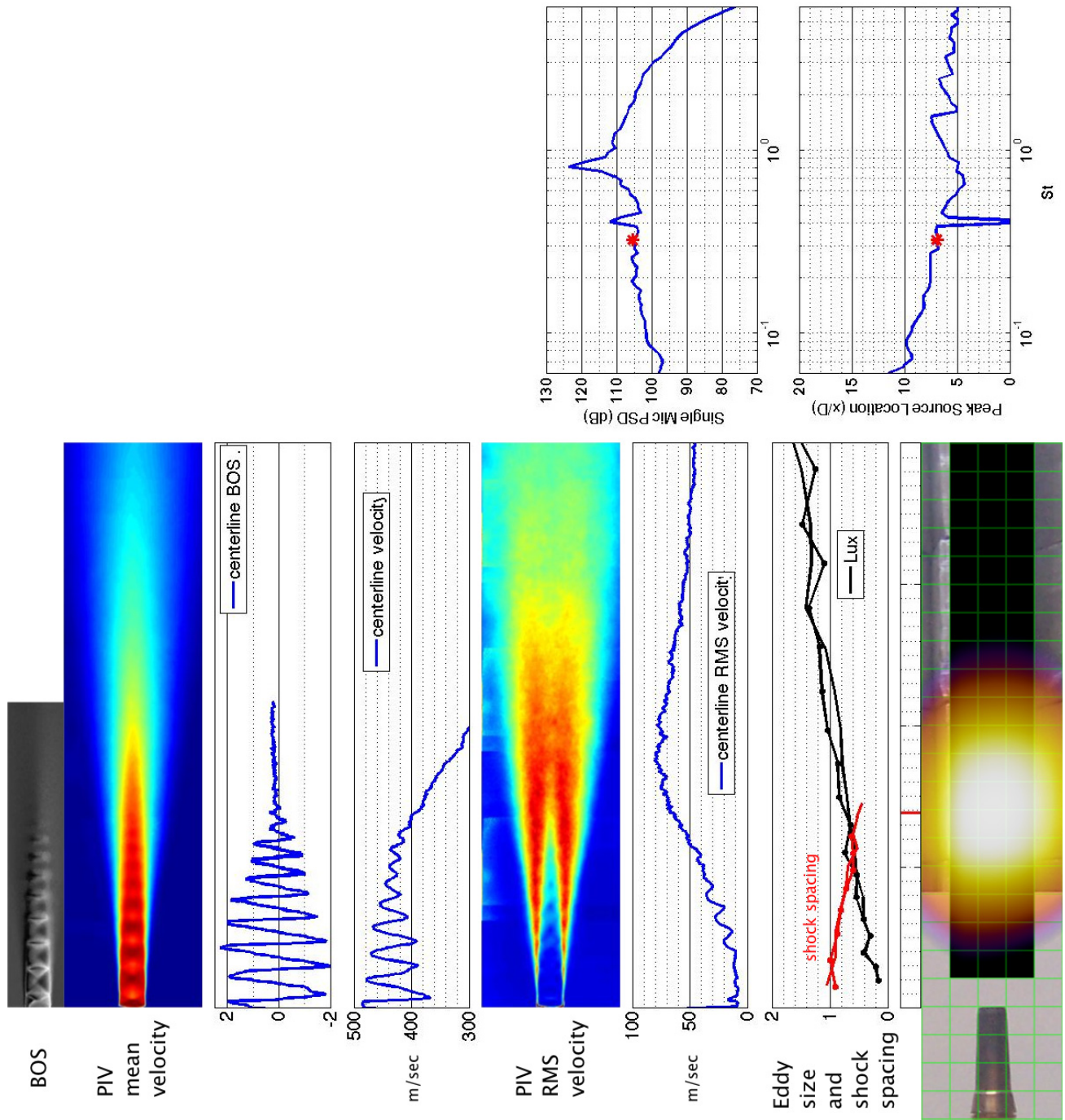
Figure 157.—SMC016; under-expanded; set point 11617; Mj=1.61; Mjdesign=1.50; St=0.323.
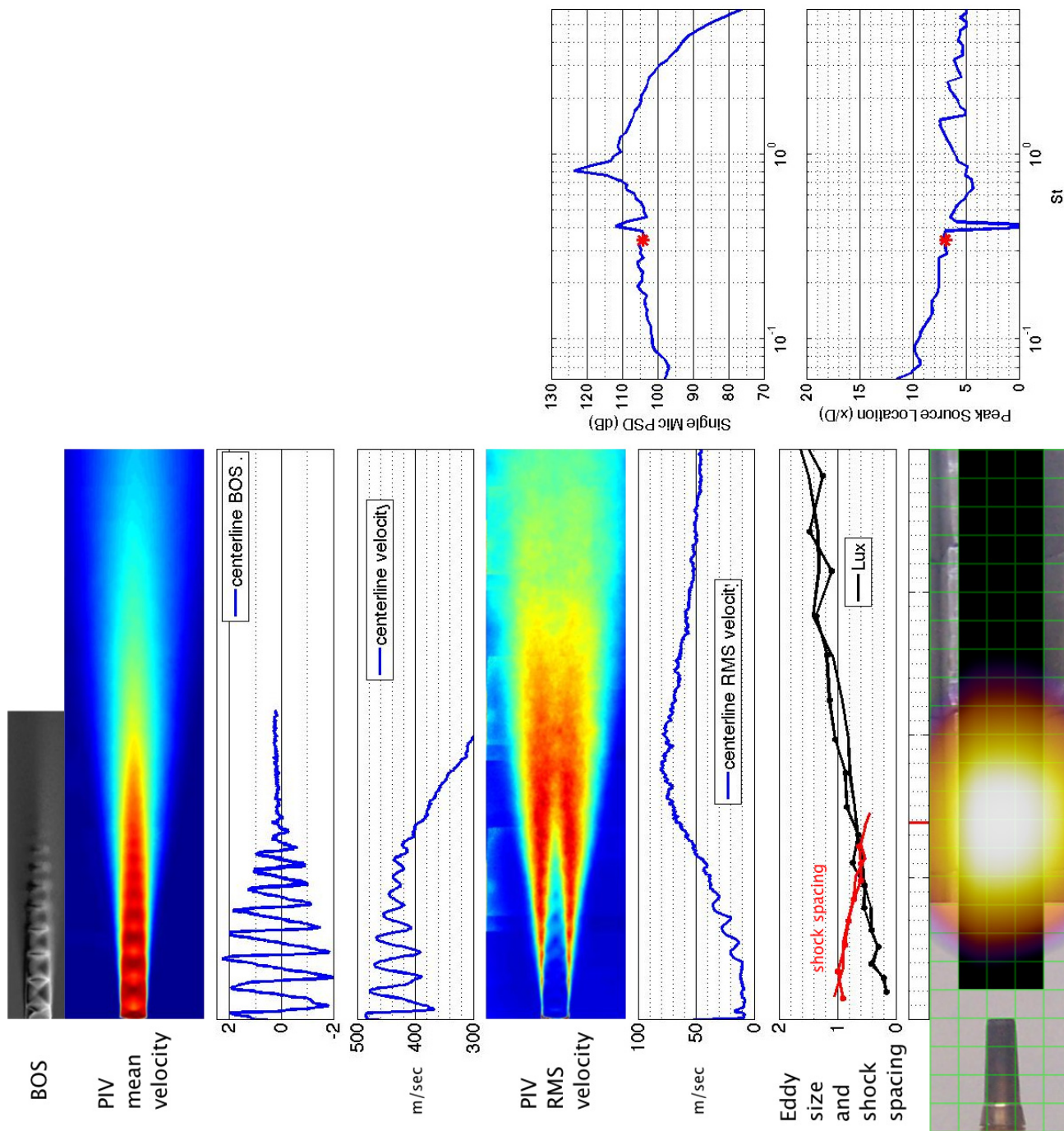
Figure 158.—SMC016; under-expanded; set point 11617; Mj=1.61; Mjdesign=1.50; St=0.341.

BOS

PIV
mean
velocity

centerline BOS .

centerline velocity

2

0

-2

PIV
RMS
velocity

centerline velocity

500

m/sec 400

300

centerline RMS velocity

100

m/sec 50

0

Eddy
size
and
shock
spacing

Lux

shock spacing

2

1

0

Single Mic PSD (dB)

130
120
110
100
90
80
70

10^{-1} 10^{0}

Peak Source Location (x/D)

20

15

10

5

0

10^{-1} 10^{0}

St
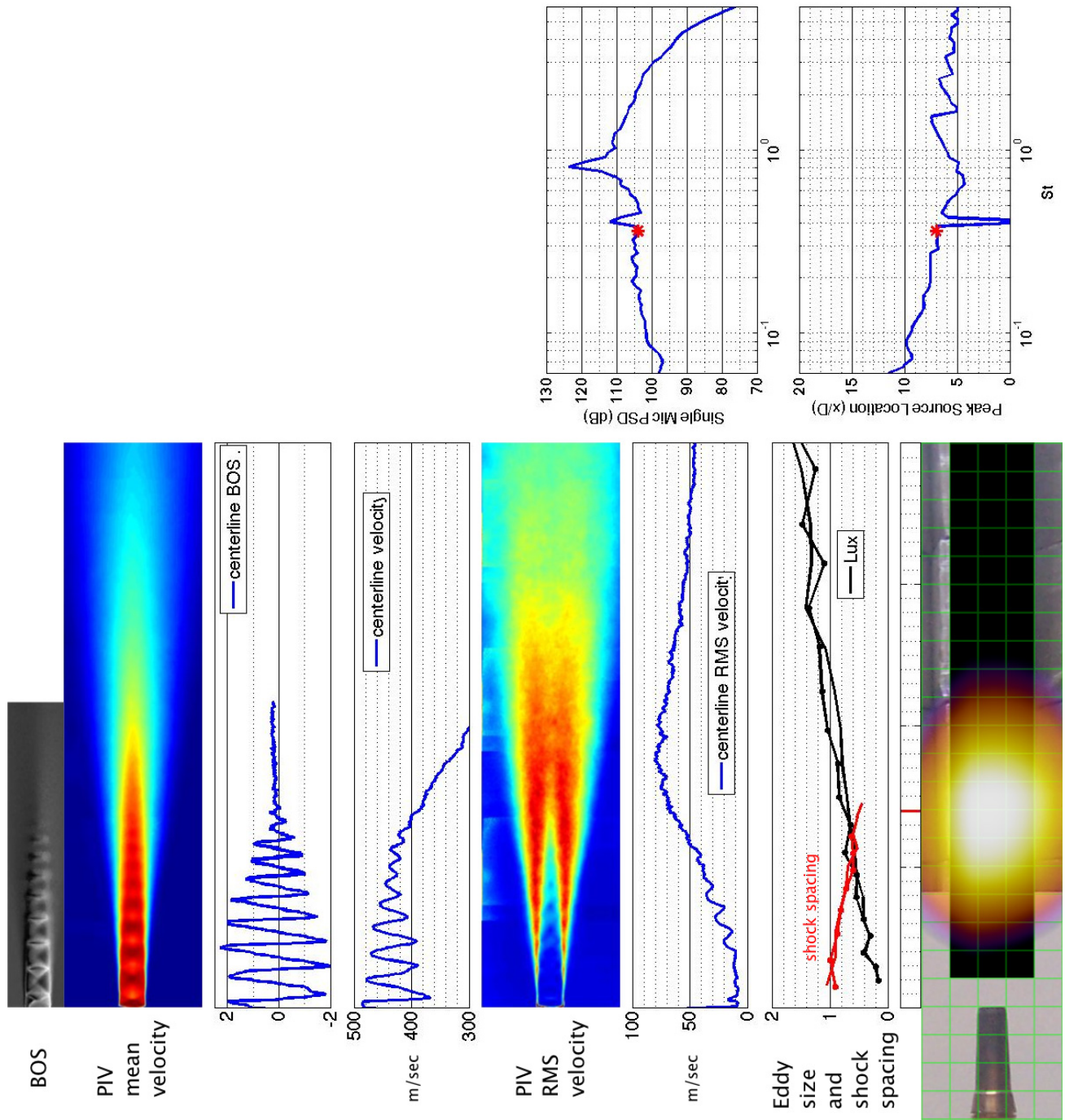
Figure 159.—SMC016; under-expanded; set point 11617; Mj=1.61; Mjdesign=1.50; St=0.361.
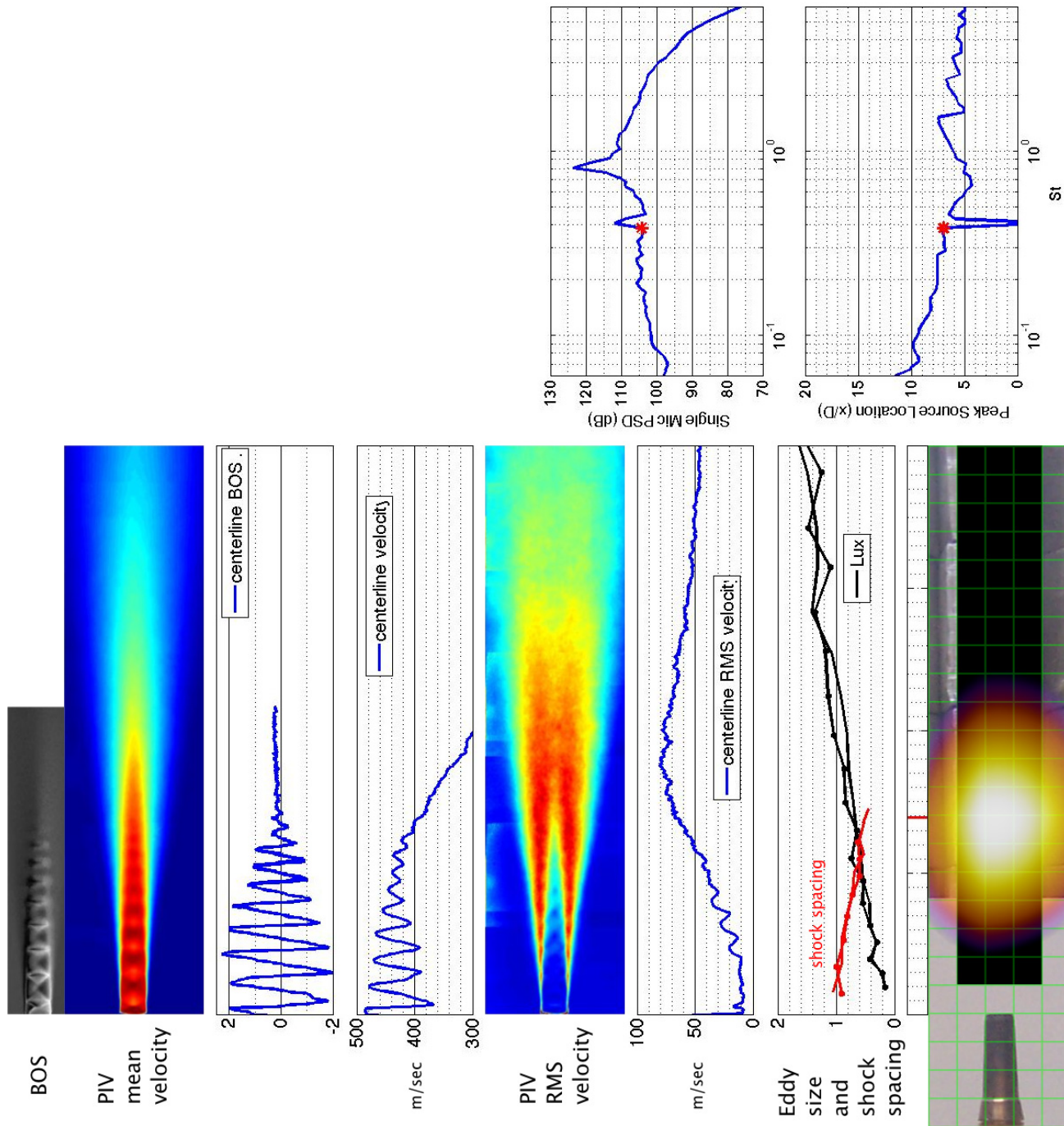
Figure 160.—SMC016; under-expanded; set point 11617; Mj=1.61; Mjdesign=1.50; St=0.383.
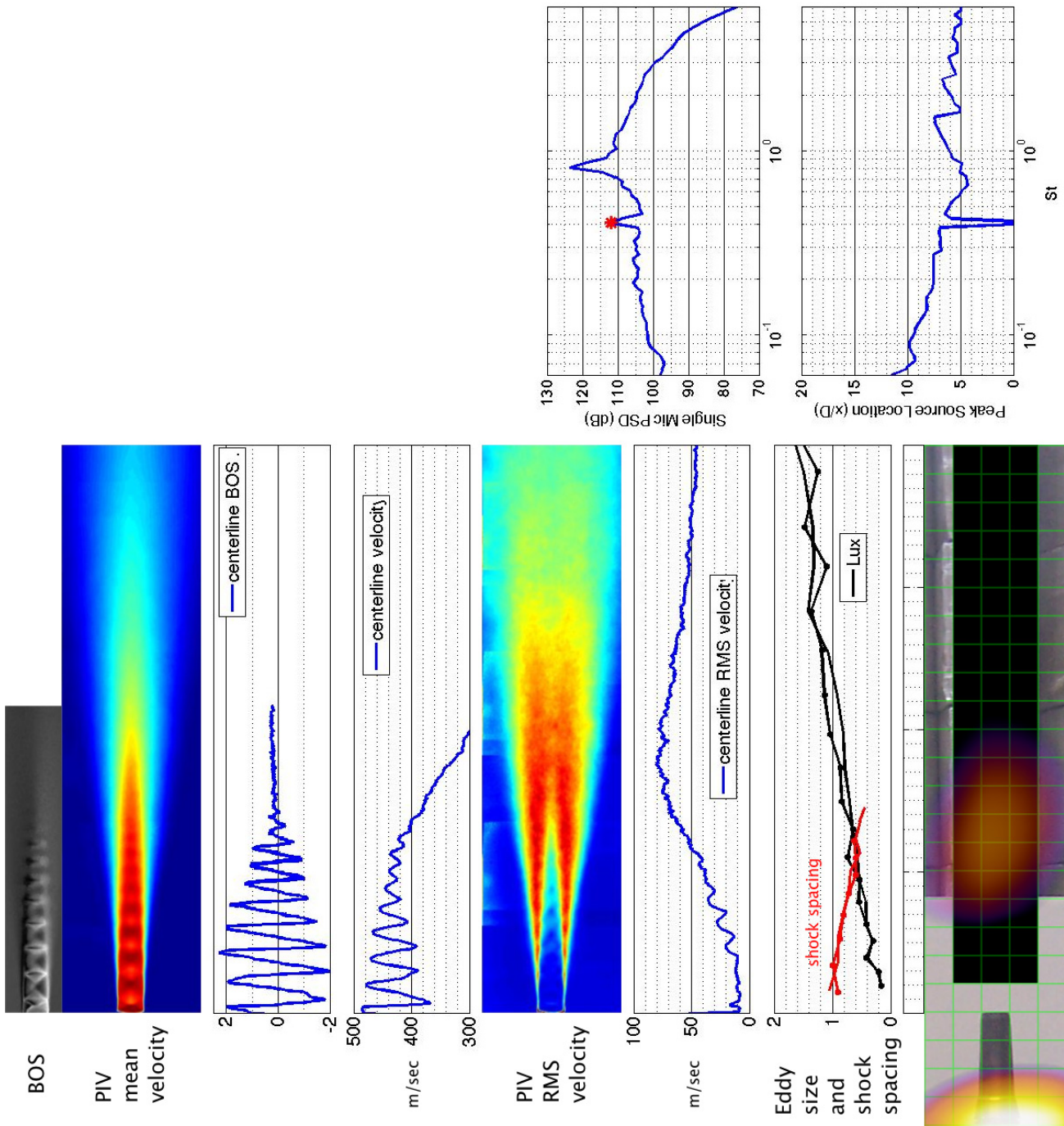
Figure 161.—SMC016; under-expanded; set point 11617; Mj=1.61; Mjdesign=1.50; St=0.406.
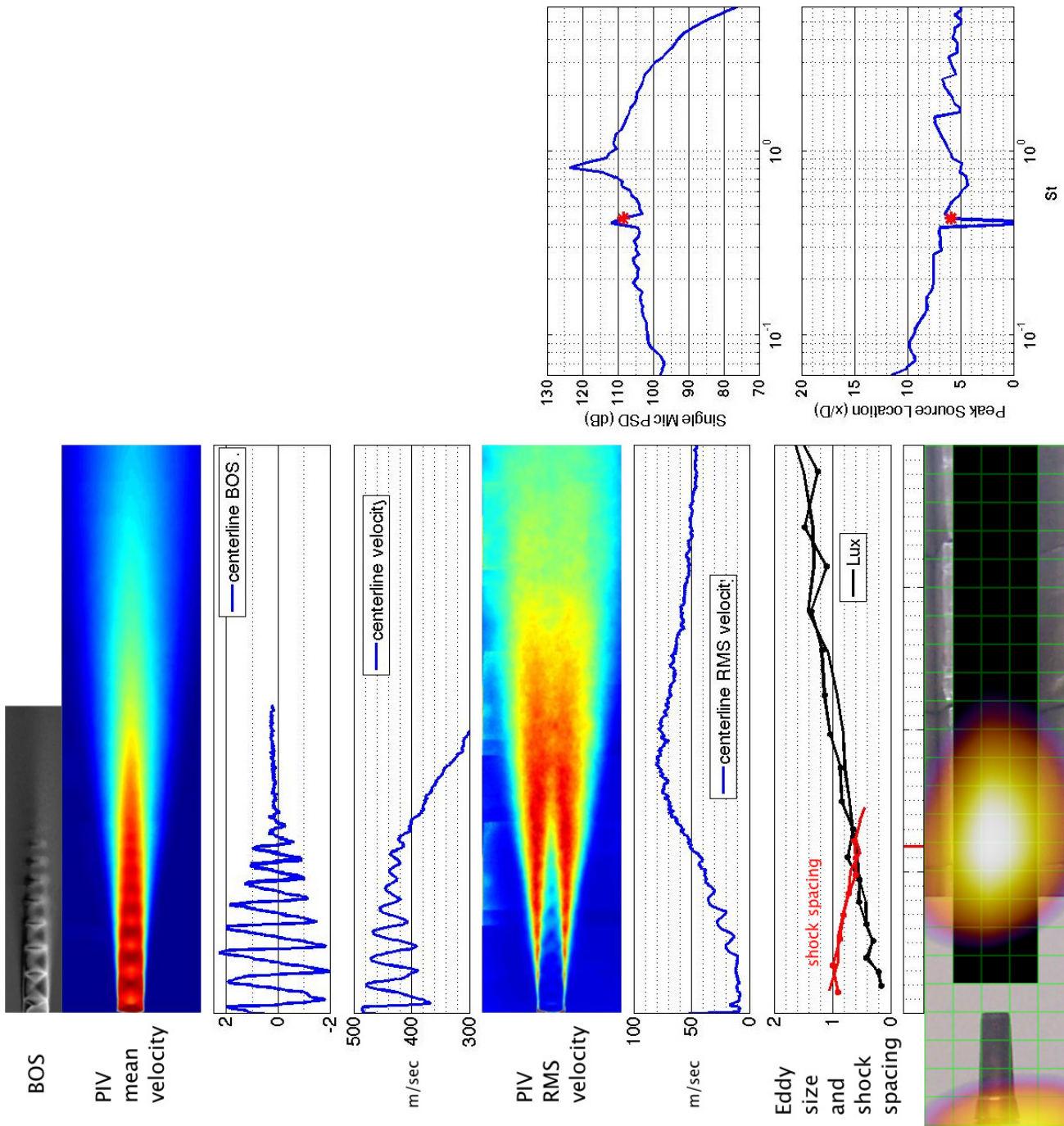
Figure 162.—SMC016; under-expanded; set point 11617; Mj=1.61; Mjdesign=1.50; St=0.430.
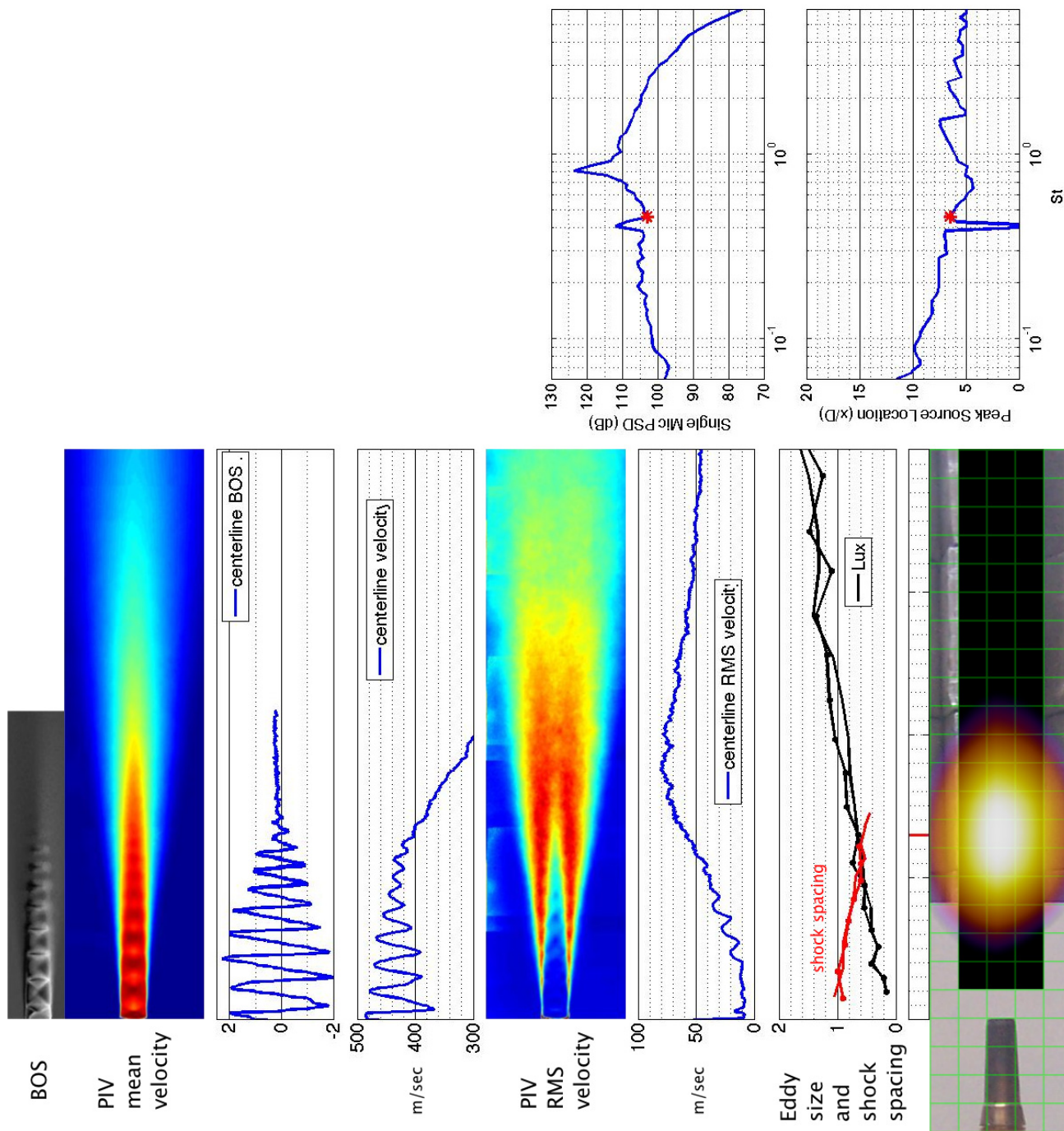
Figure 163.—SMC016; under-expanded; set point 11617; Mj=1.61; Mjdesign=1.50; St=0.456.
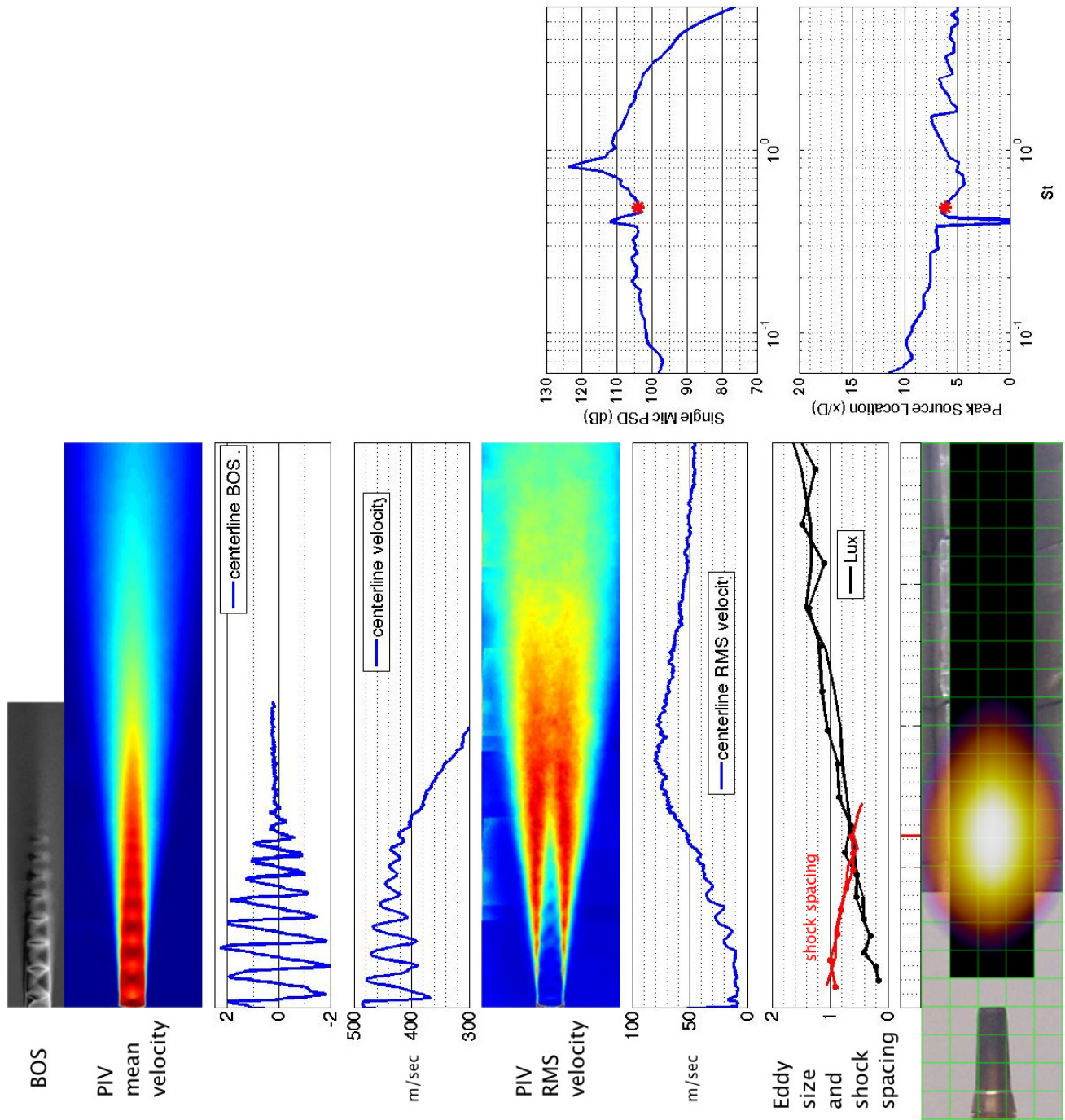
Figure 164.—SMC016; under-expanded; set point 11617; Mj=1.61; Mjdesign=1.50; St=0.484.
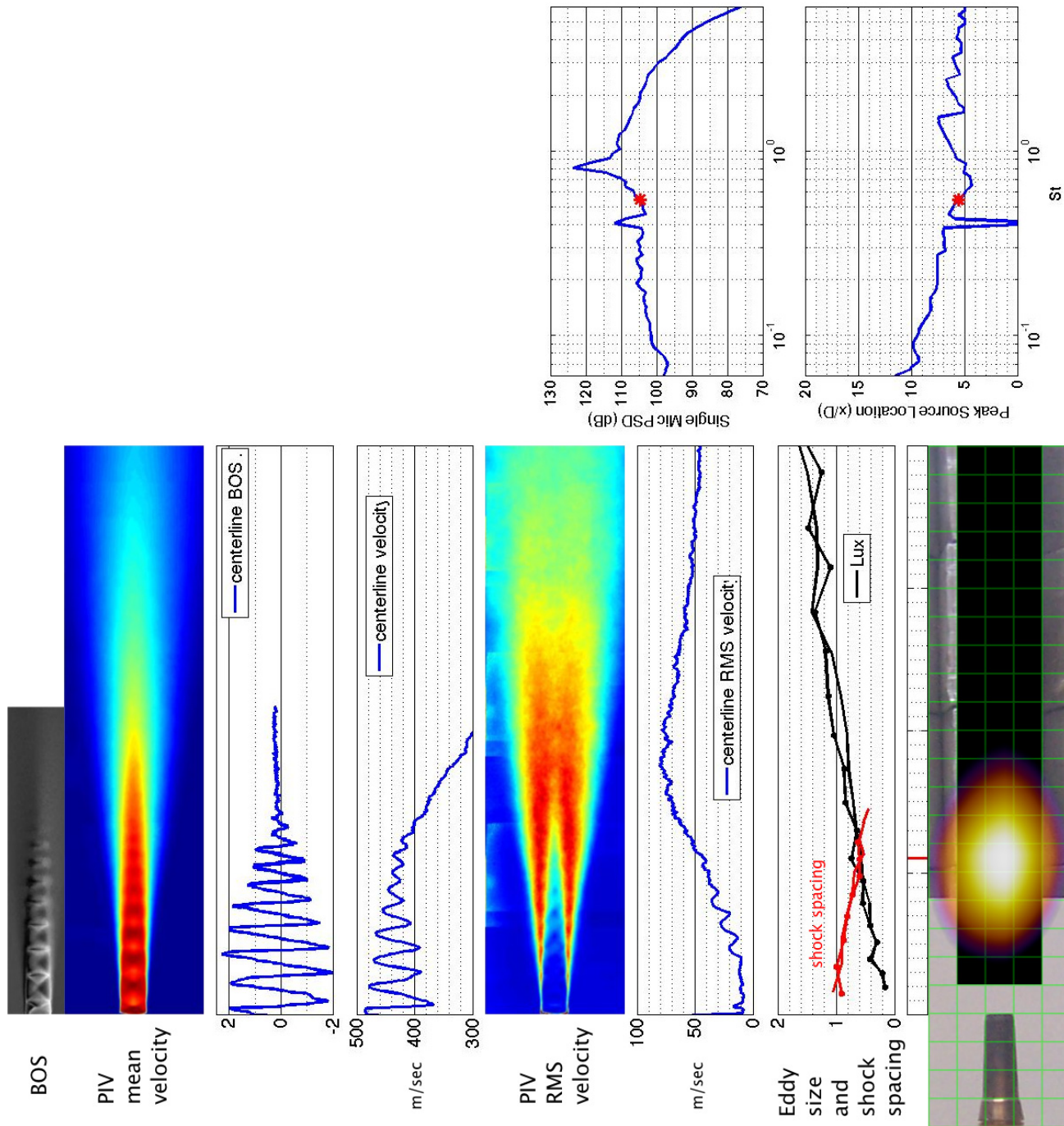
Figure 165.—SMC016; under-expanded; set point 11617; Mj=1.61; Mjdesign=1.50; St=0.545.
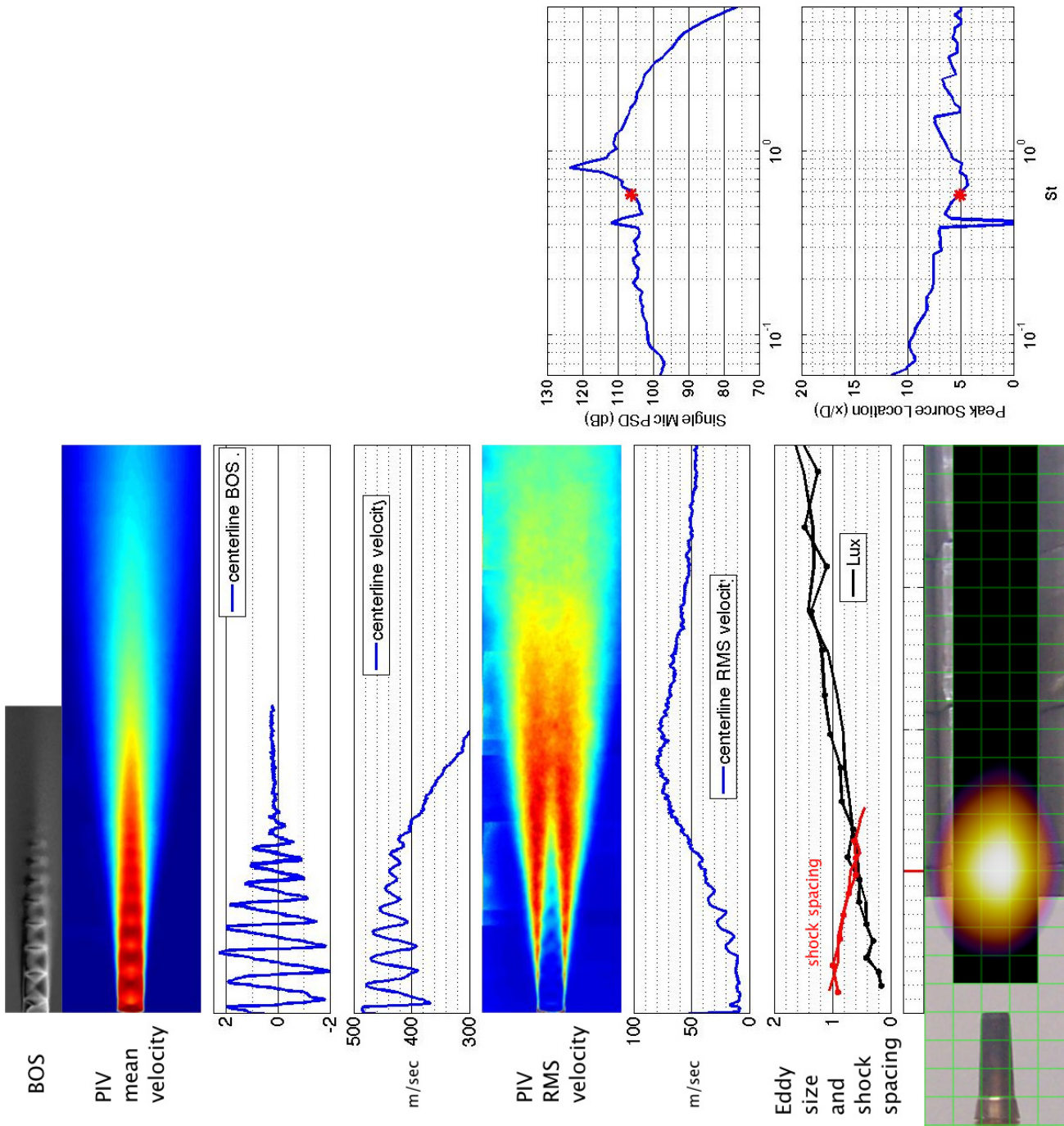
Figure 166.—SMC016; under-expanded; set point 11617; Mj=1.61; Mjdesign=1.50; St=0.577.
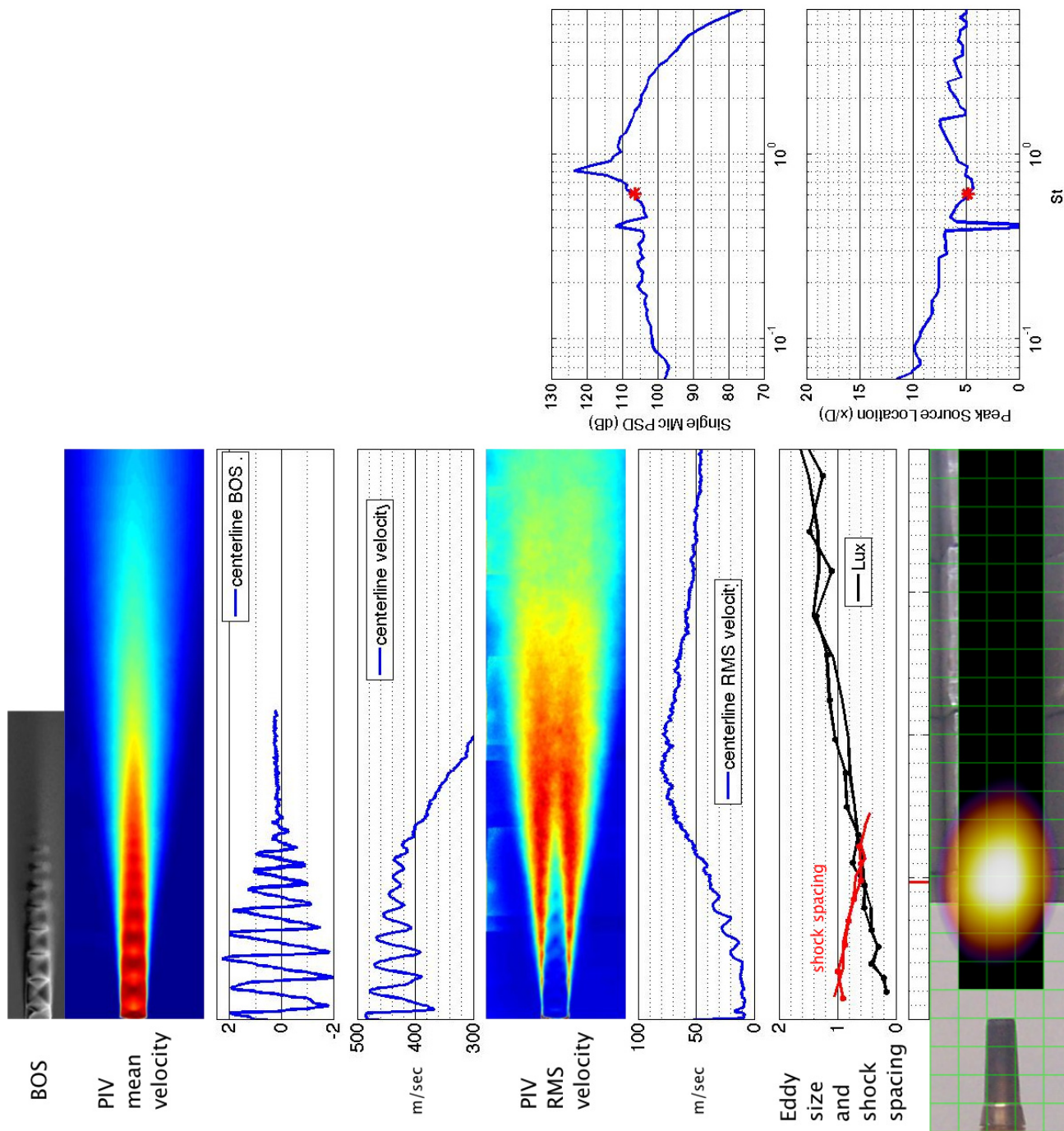
Figure 167.—SMC016; under-expanded; set point 11617; Mj=1.61; Mjdesign=1.50; St=0.610.
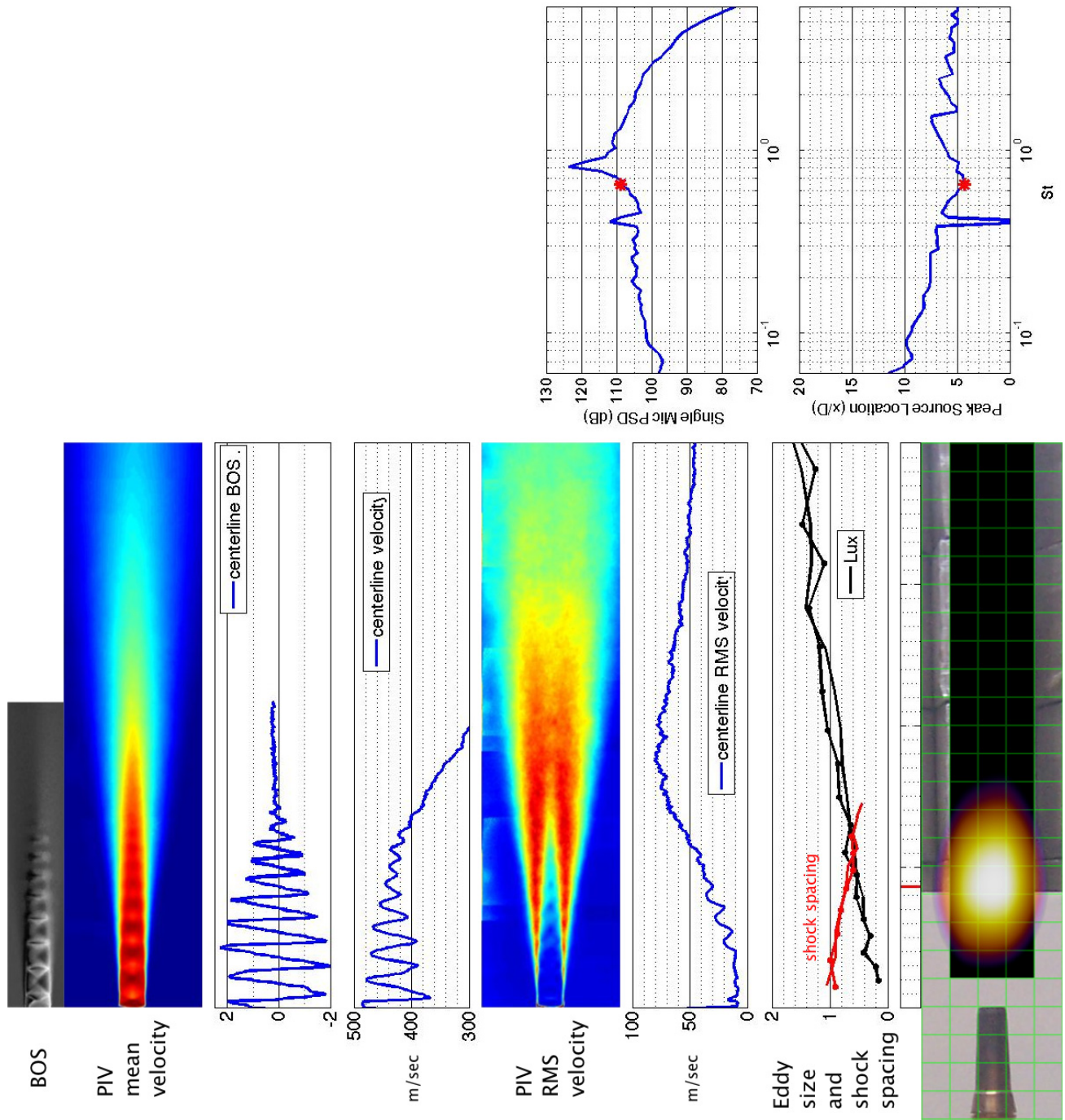
Figure 168.—SMC016; under-expanded; set point 11617; Mj=1.61; Mjdesign=1.50; St=0.645.
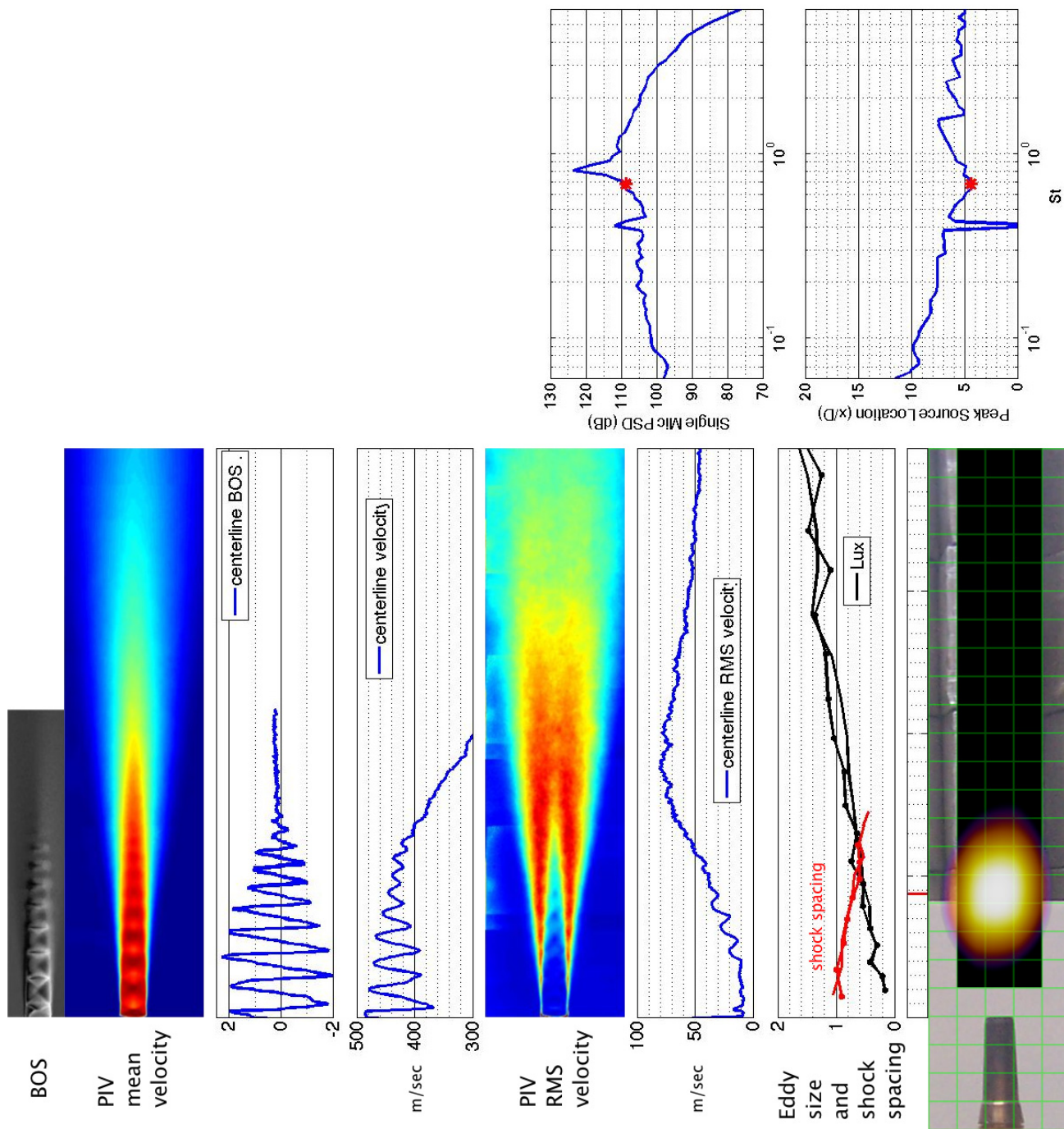
Figure 169.—SMC016; under-expanded; set point 11617; Mj=1.61; Mjdesign=1.50; St=0.682.
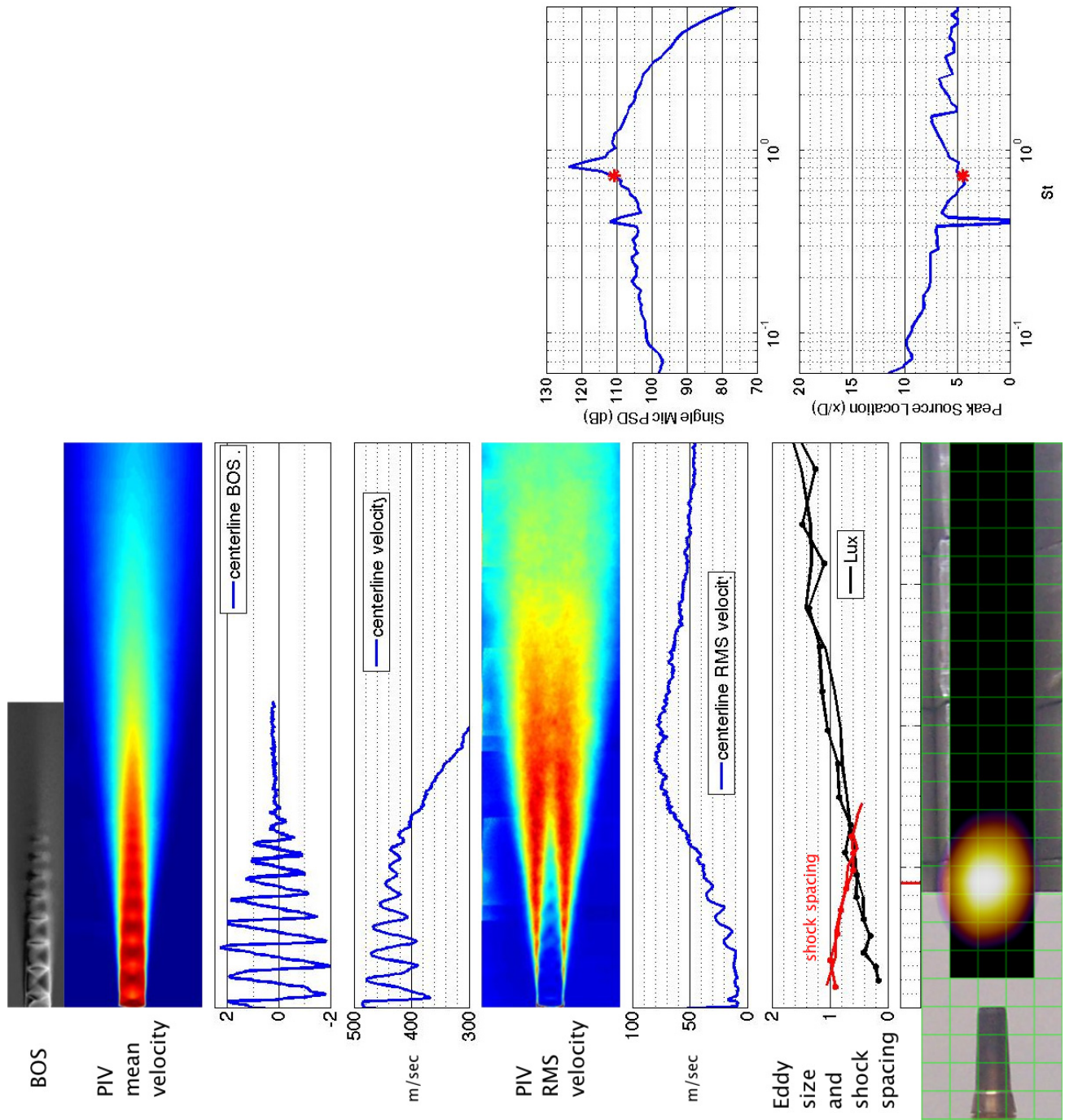
Figure 170.—SMC016; under-expanded; set point 11617; Mj=1.61; Mjdesign=1.50; St=0.723.
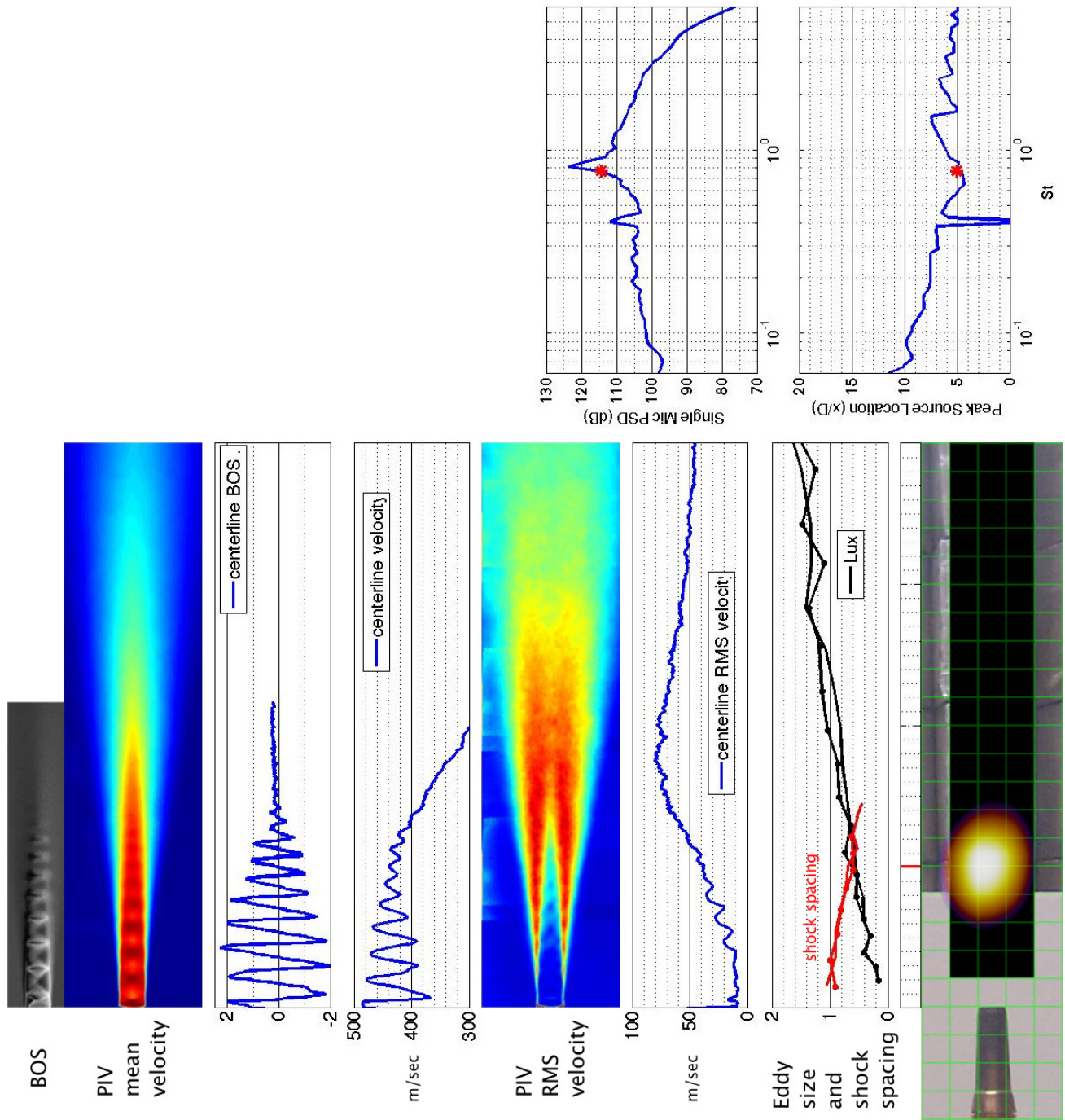
Figure 171.—SMC016; under-expanded; set point 11617; Mj=1.61; Mjdesign=1.50; St=0.766.
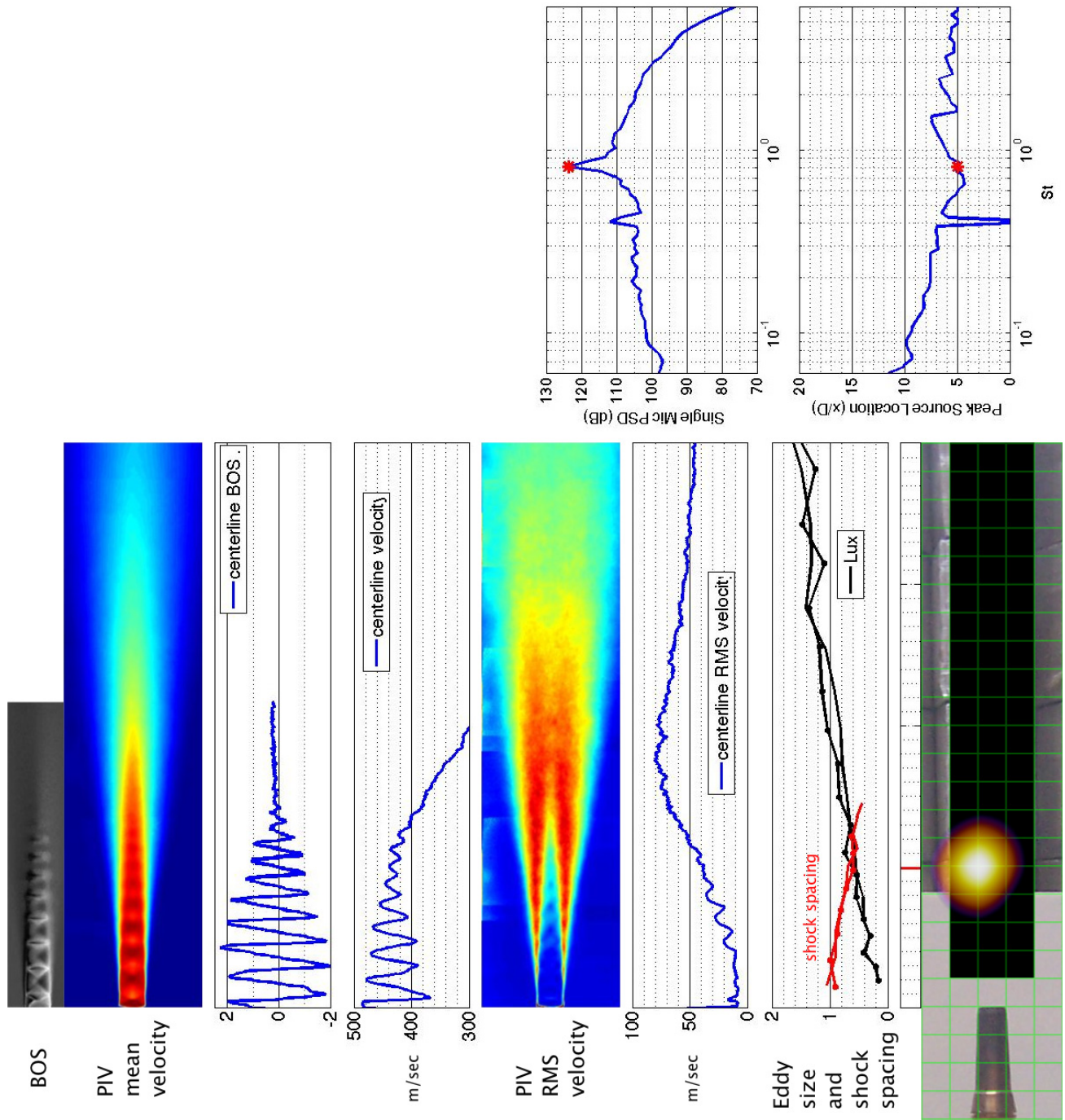
Figure 172.—SMC016; under-expanded; set point 11617; Mj=1.61; Mjdesign=1.50; St=0.811.
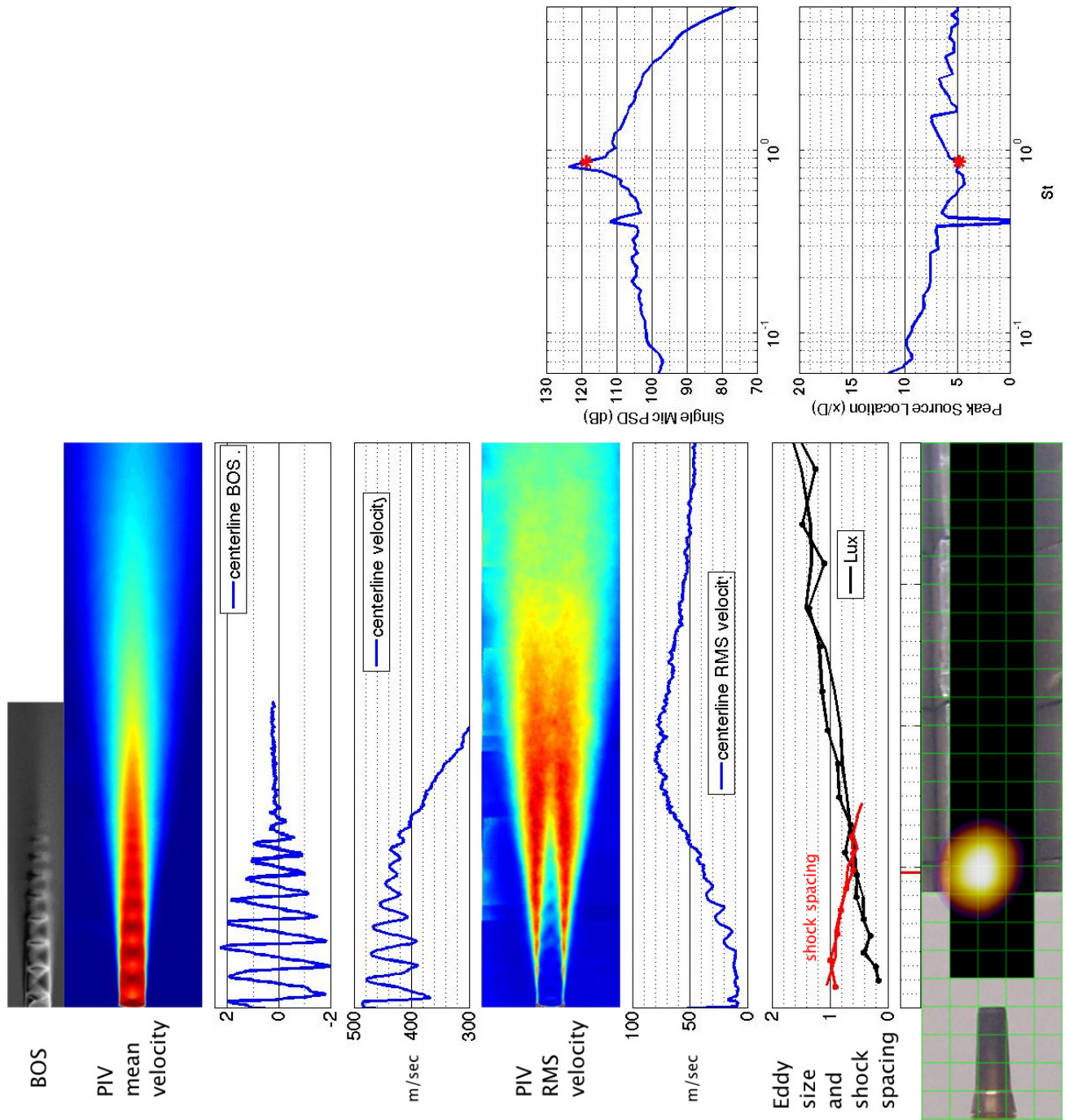
Figure 173.—SMC016; under-expanded; set point 11617; Mj=1.61; Mjdesign=1.50; St=0.860.
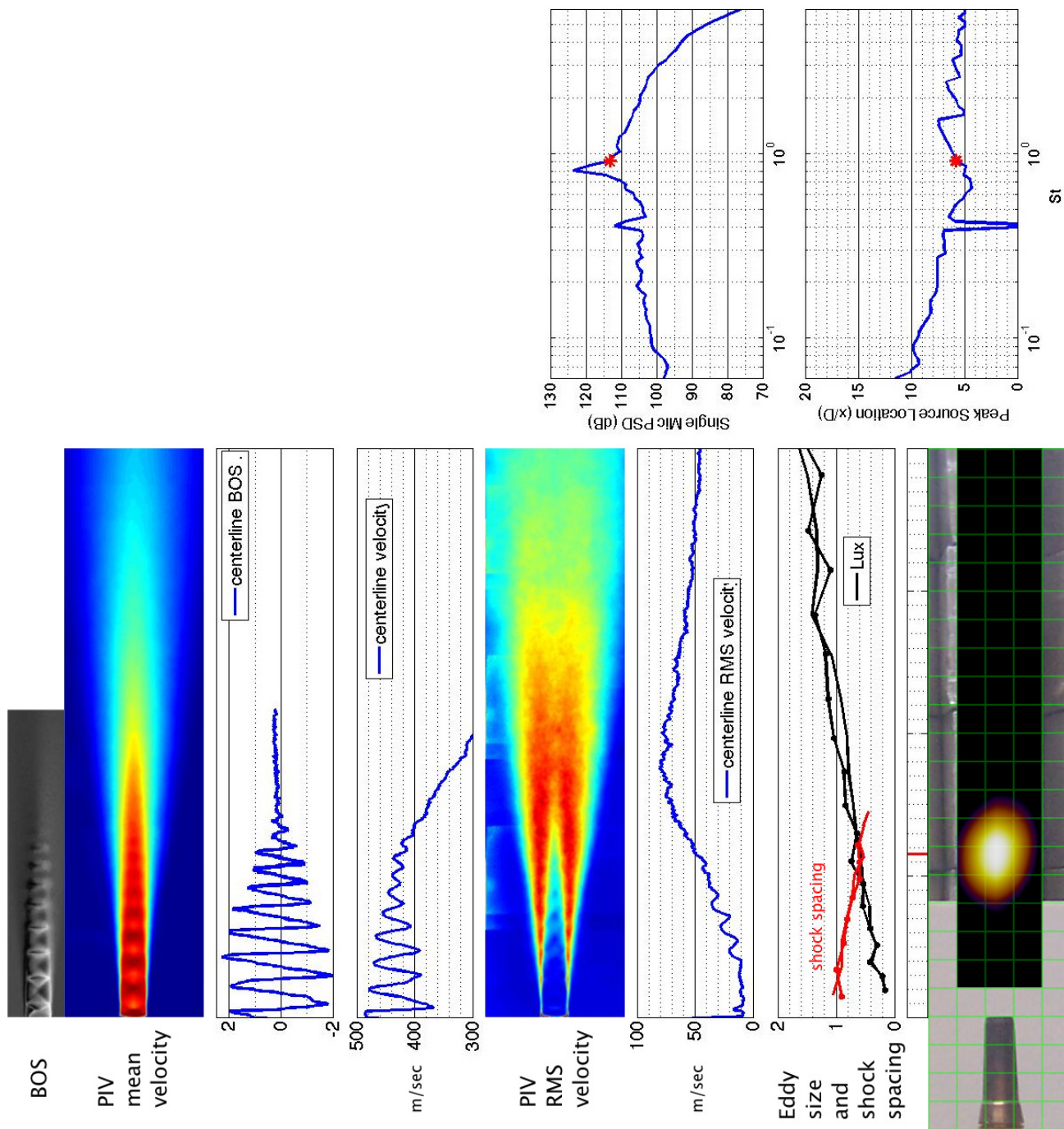
Figure 174.—SMC016; under-expanded; set point 11617; Mj=1.61; Mjdesign=1.50; St=0.912.
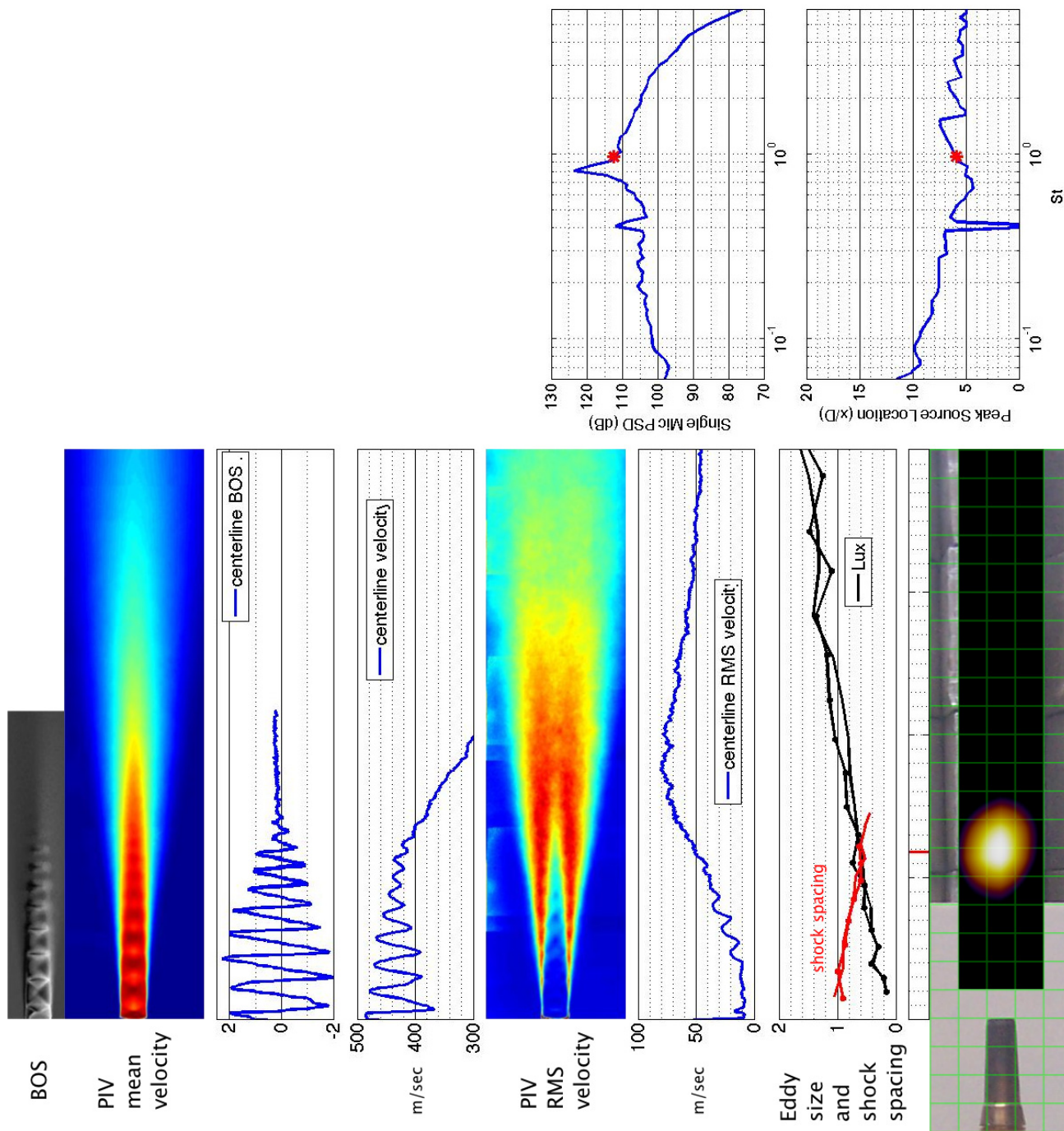
Figure 175.—SMC016; under-expanded; set point 11617; Mj=1.61; Mjdesign=1.50; St=0.968.
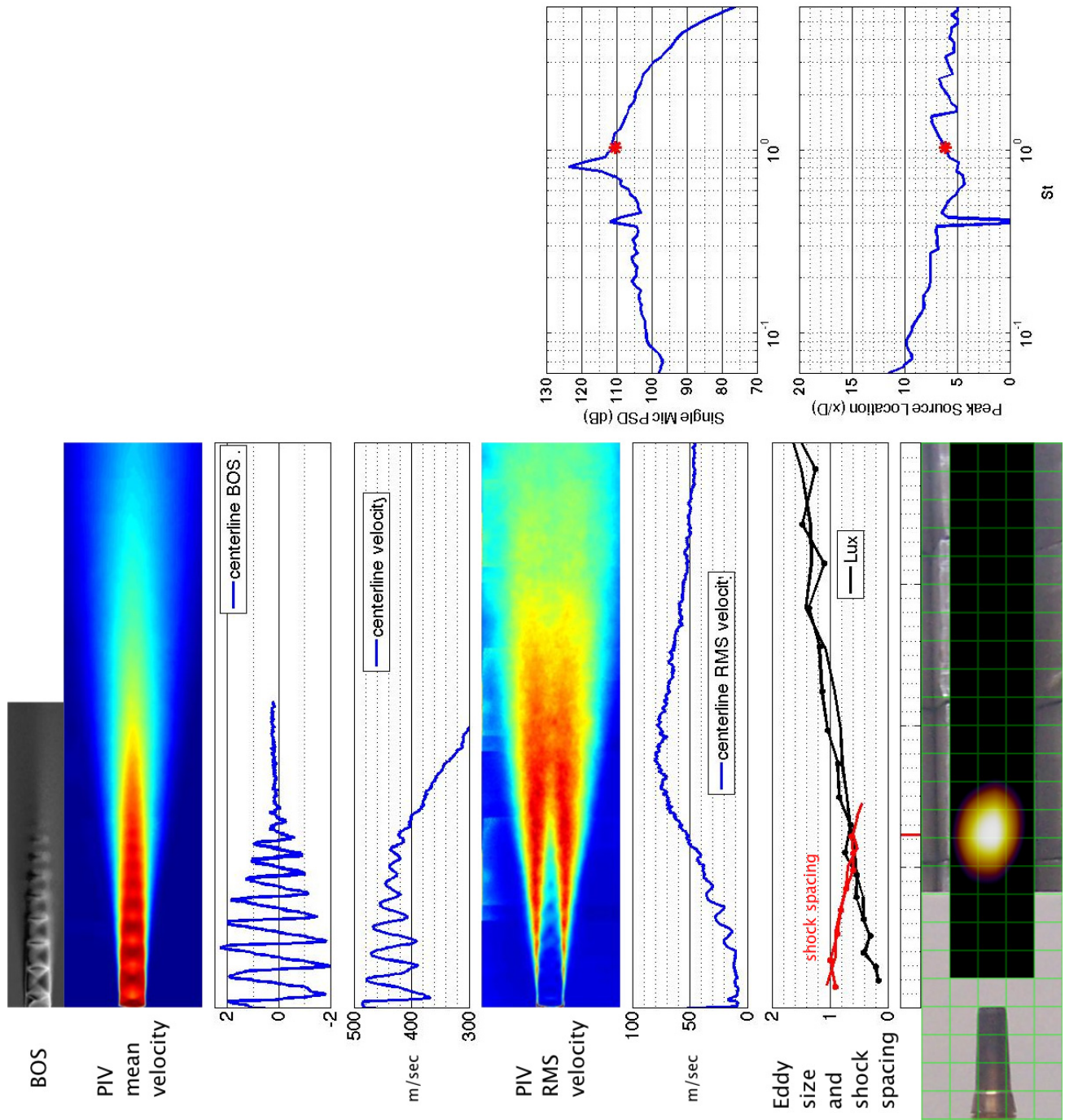
Figure 176.—SMC016; under-expanded; set point 11617; Mj=1.61; Mjdesign=1.50; St=1.028.
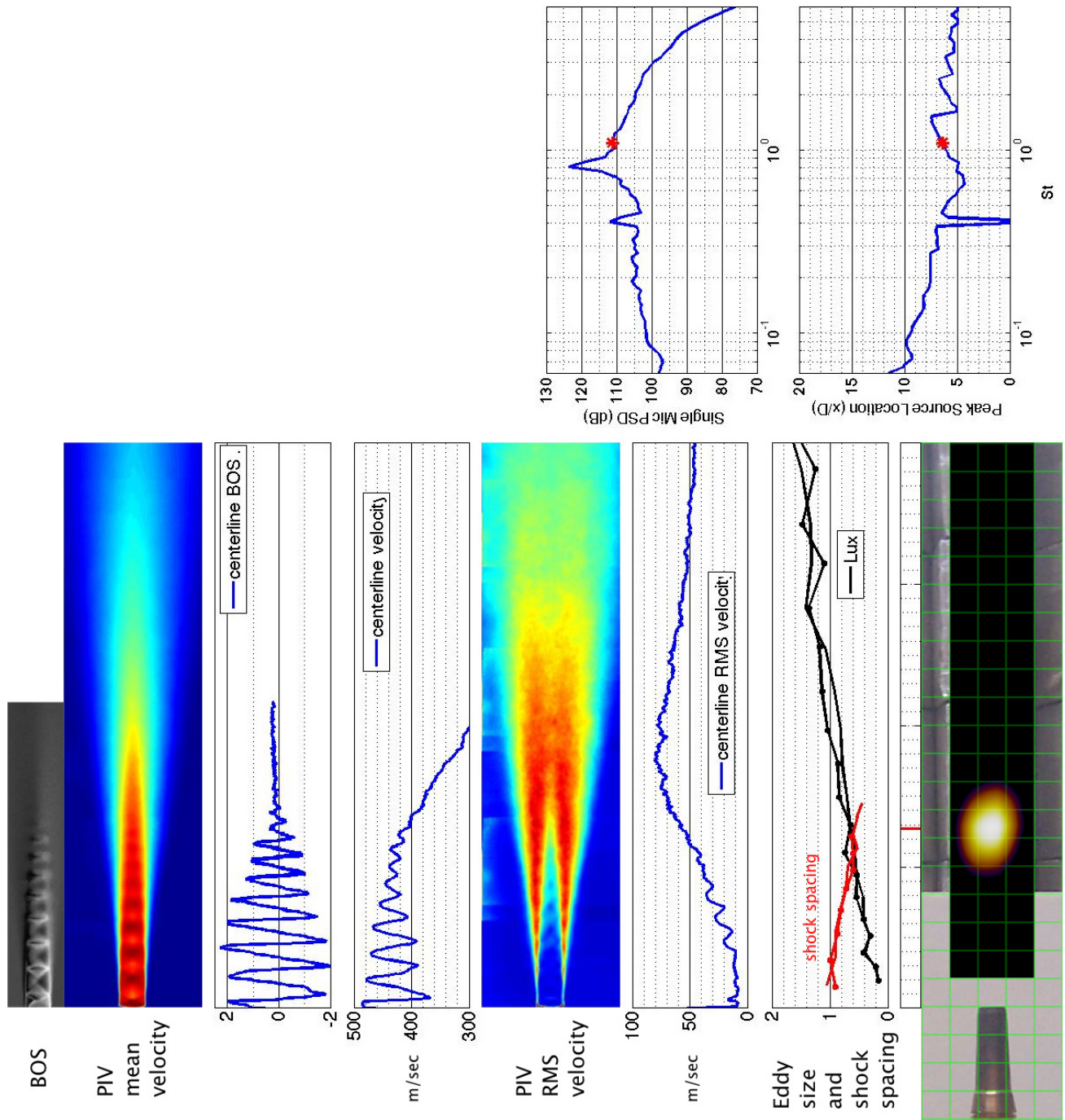
Figure 177.—SMC016; under-expanded; set point 11617; Mj=1.61; Mjdesign=1.50; St=1.090.
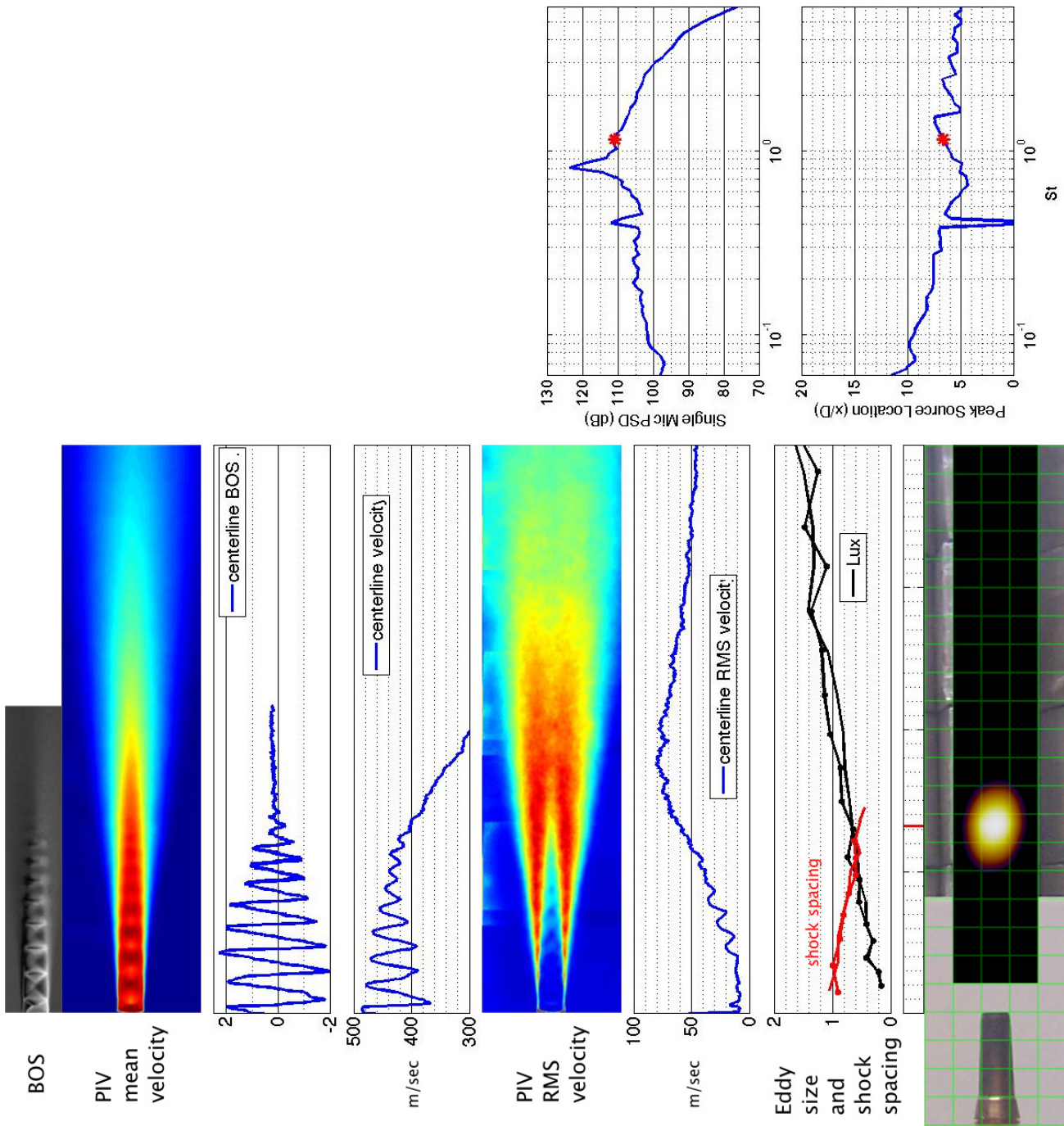
Figure 178.—SMC016; under-expanded; set point 11617; Mj=1.61; Mjdesign=1.50; St=1.154.
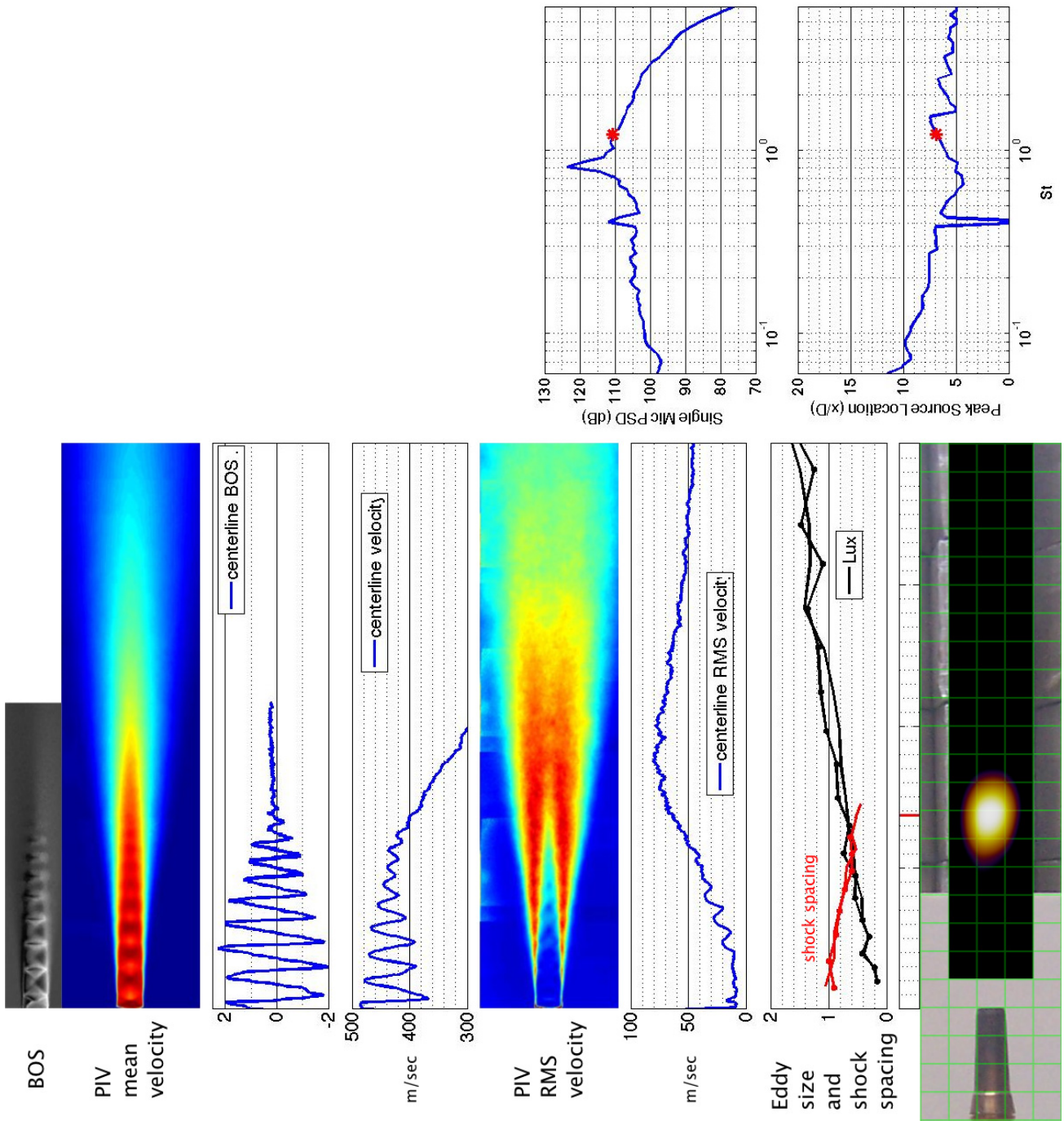
Figure 179.—SMC016; under-expanded; set point 11617; Mj=1.61; Mjdesign=1.50; St=1.220.
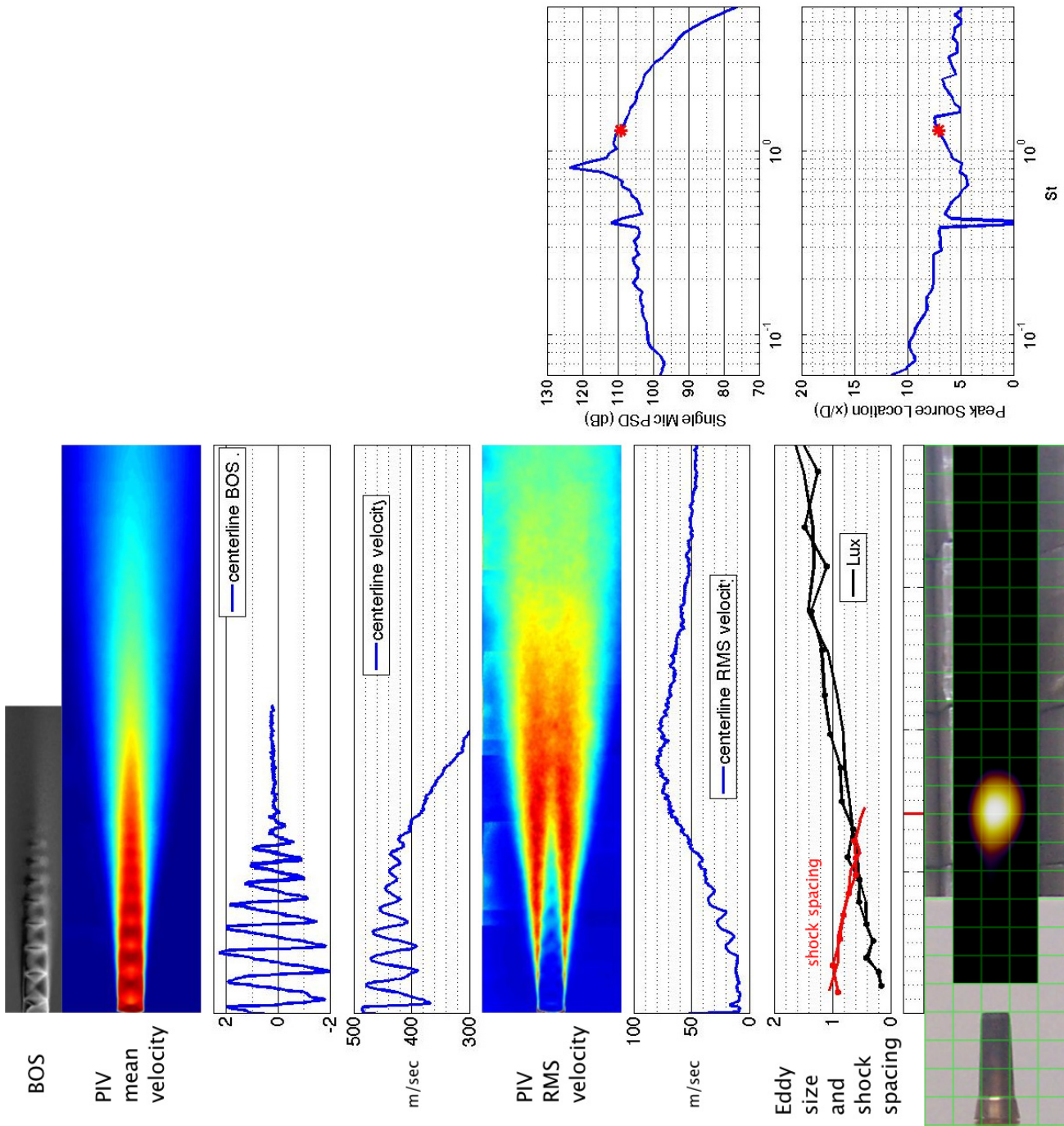
Figure 180.—SMC016; under-expanded; set point 11617; Mj=1.61; Mjdesign=1.50; St=1.290.

BOS

PIV
mean
velocity

centerline BOS .

centerline velocity

2

0

−2

PIV
RMS
velocity

500

m/sec 400

300

centerline RMS velocity

100

m/sec 50

0

Eddy
size
and
shock
spacing

Lux

shock spacing

2

1

0

Single Mic PSD (dB)

130

120

110

100

90

80

70

Peak Source Location (x/D)

20

15

10

5

0

10^{-1} 10^{0}

St
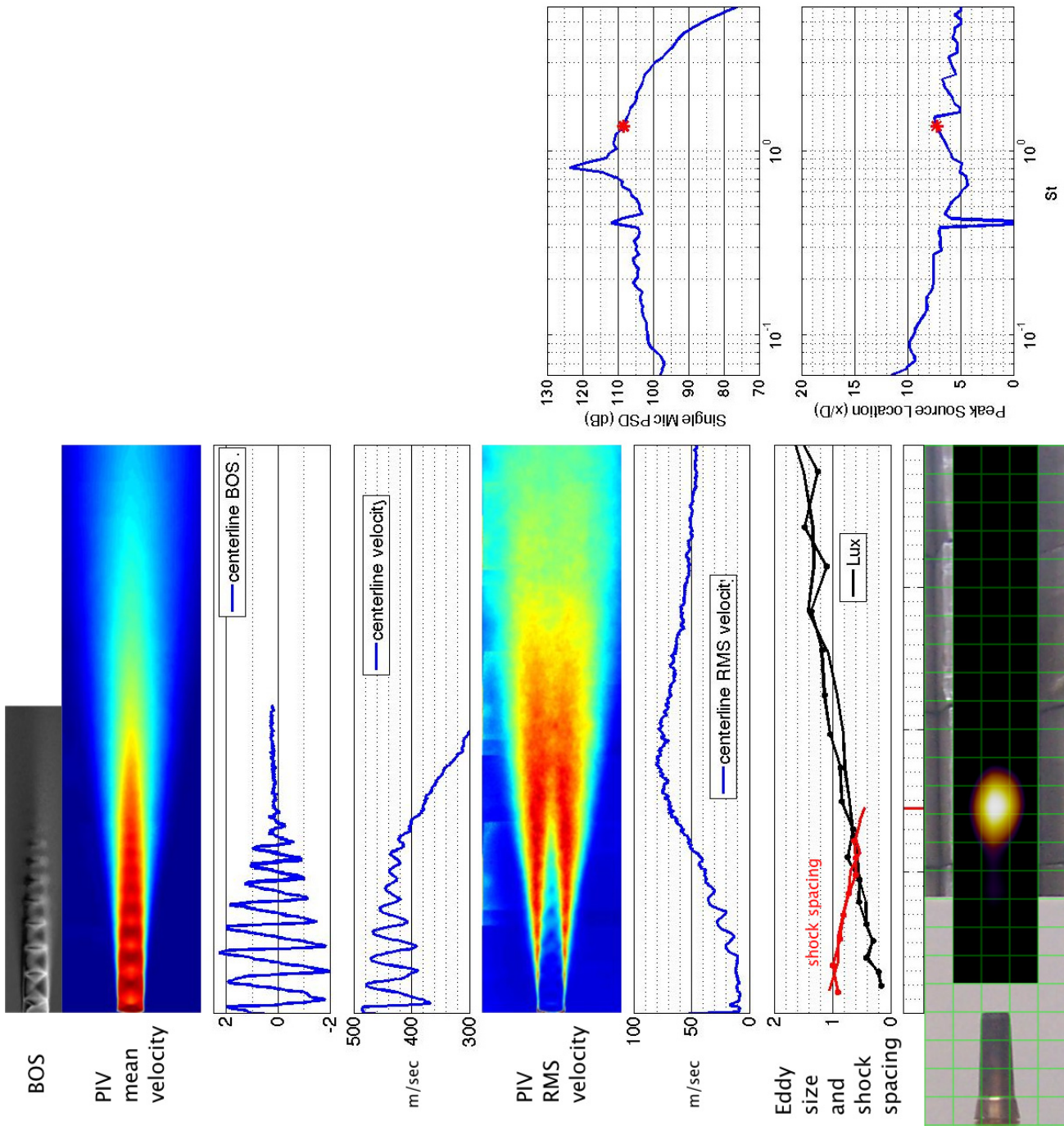
Figure 181.—SMC016; under-expanded; set point 11617; Mj=1.61; Mjdesign=1.50; St=1.364.
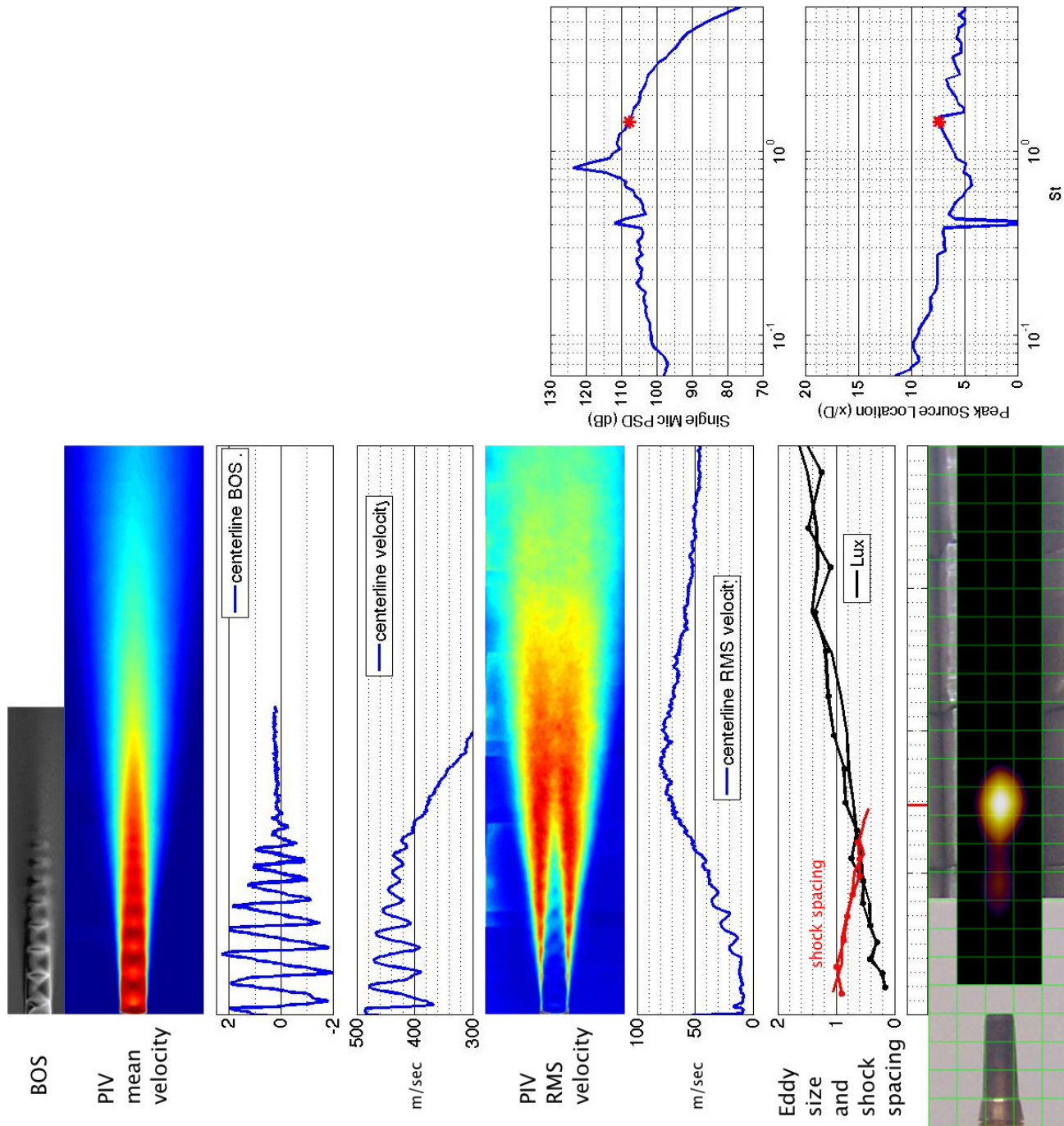
Figure 182.—SMC016; under-expanded; set point 11617; Mj=1.61; Mjdesign=1.50; St=1.442.
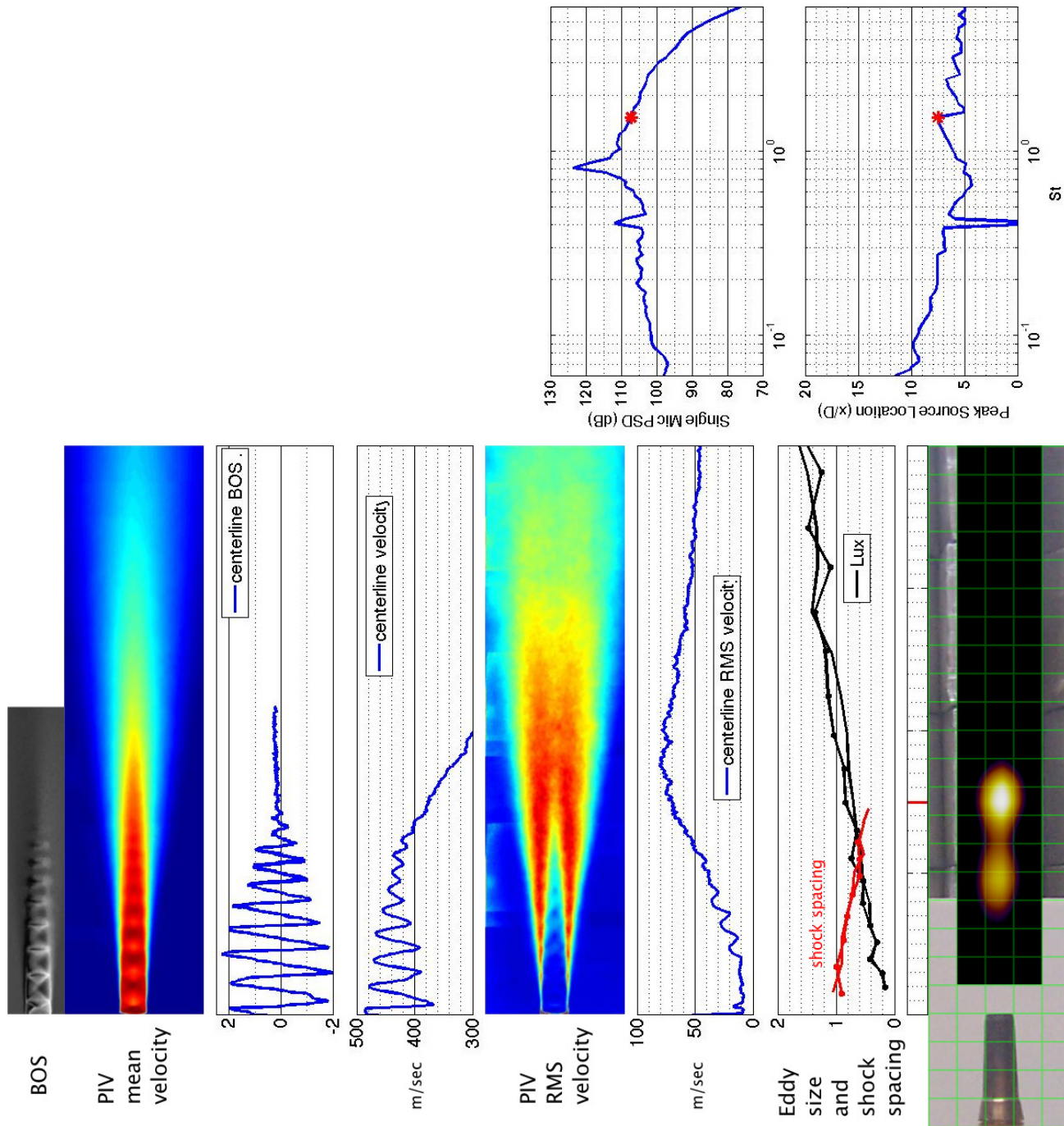
Figure 183.—SMC016; under-expanded; set point 11617; Mj=1.61; Mjdesign=1.50; St=1.525.
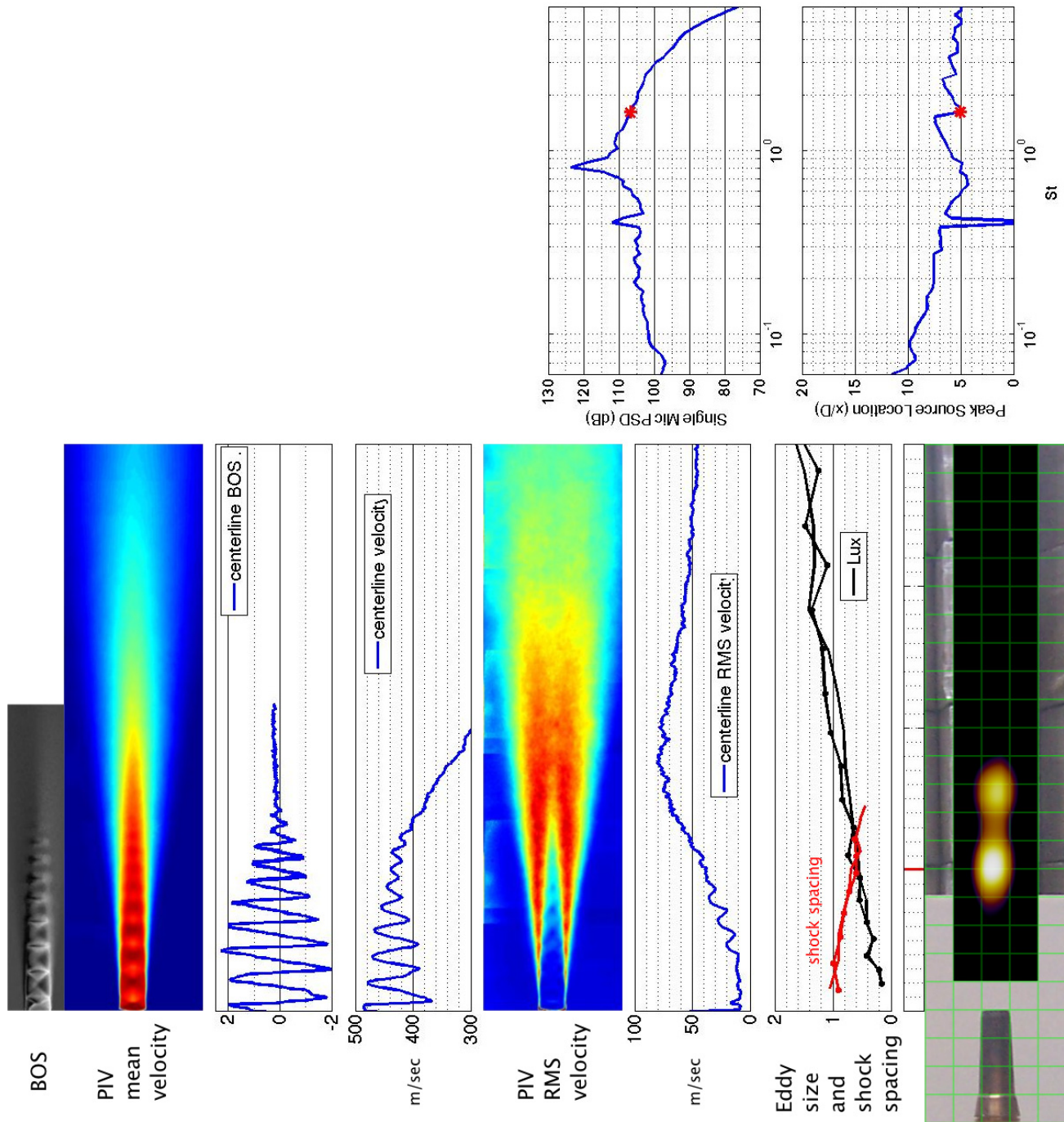
Figure 184.—SMC016; under-expanded; set point 11617; Mj=1.61; Mjdesign=1.50; St=1.613.
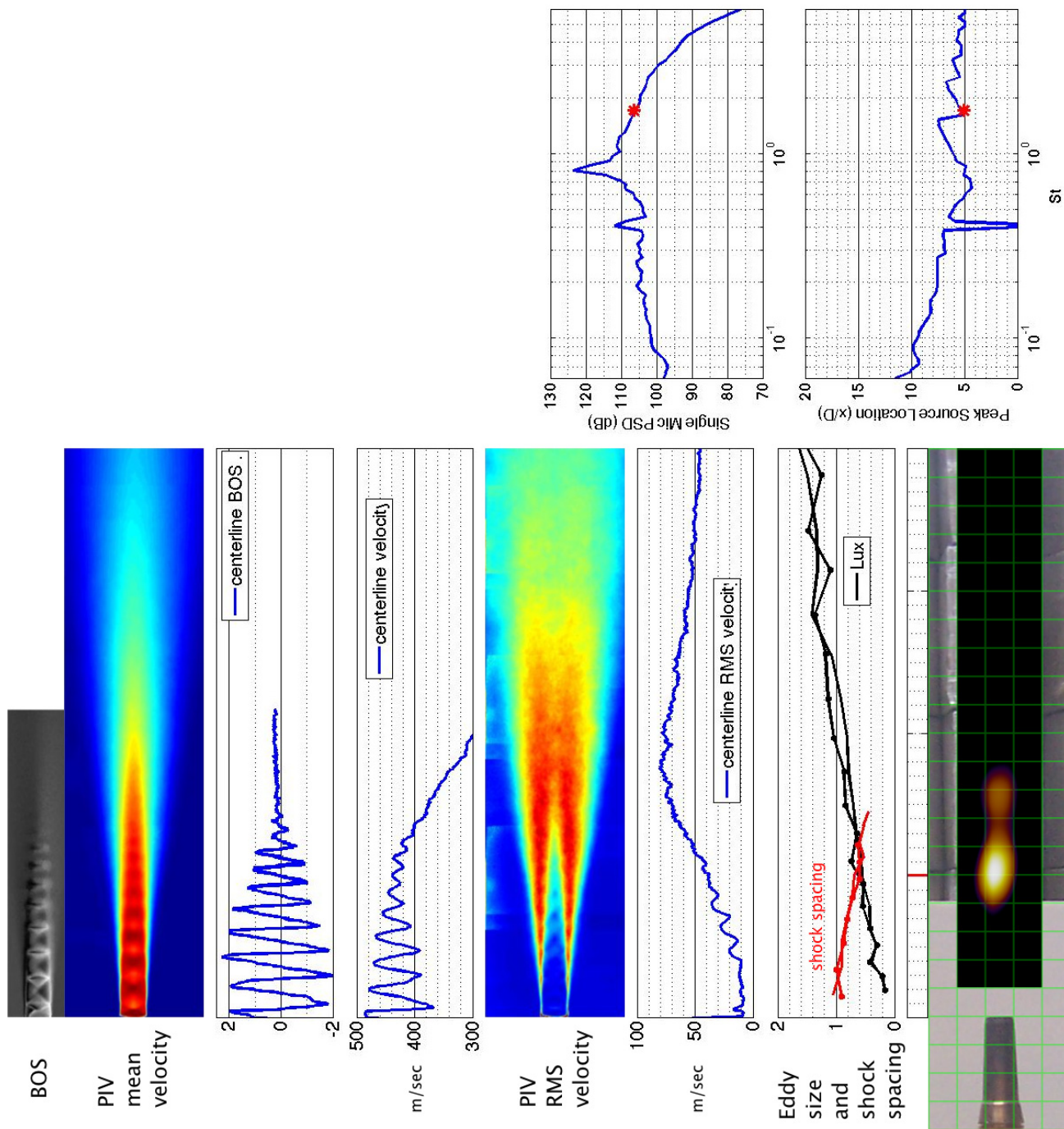
Figure 185.—SMC016; under-expanded; set point 11617; Mj=1.61; Mjdesign=1.50; St=1.708.
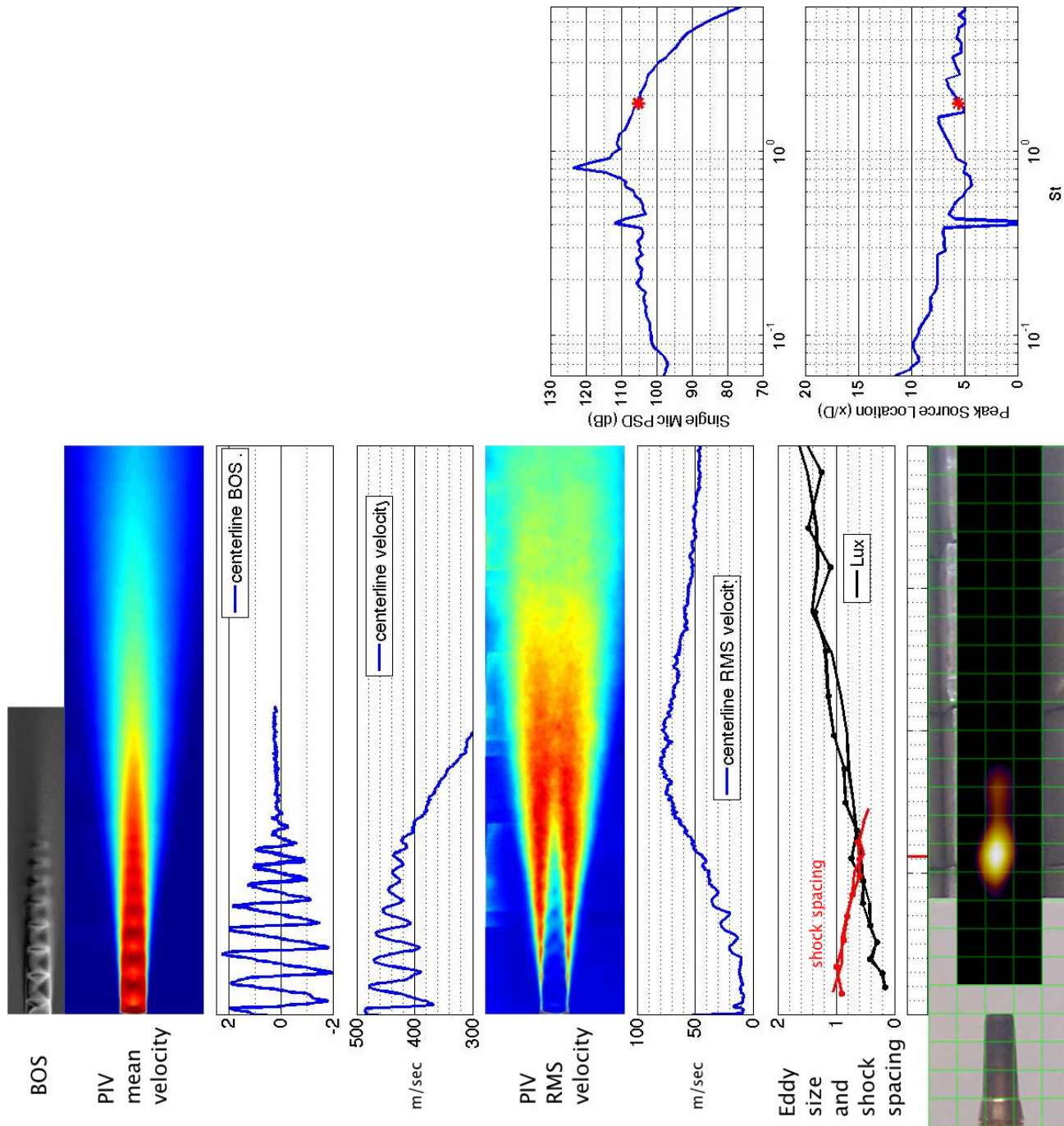
Figure 186.—SMC016; under-expanded; set point 11617; Mj=1.61; Mjdesign=1.50; St=1.814.
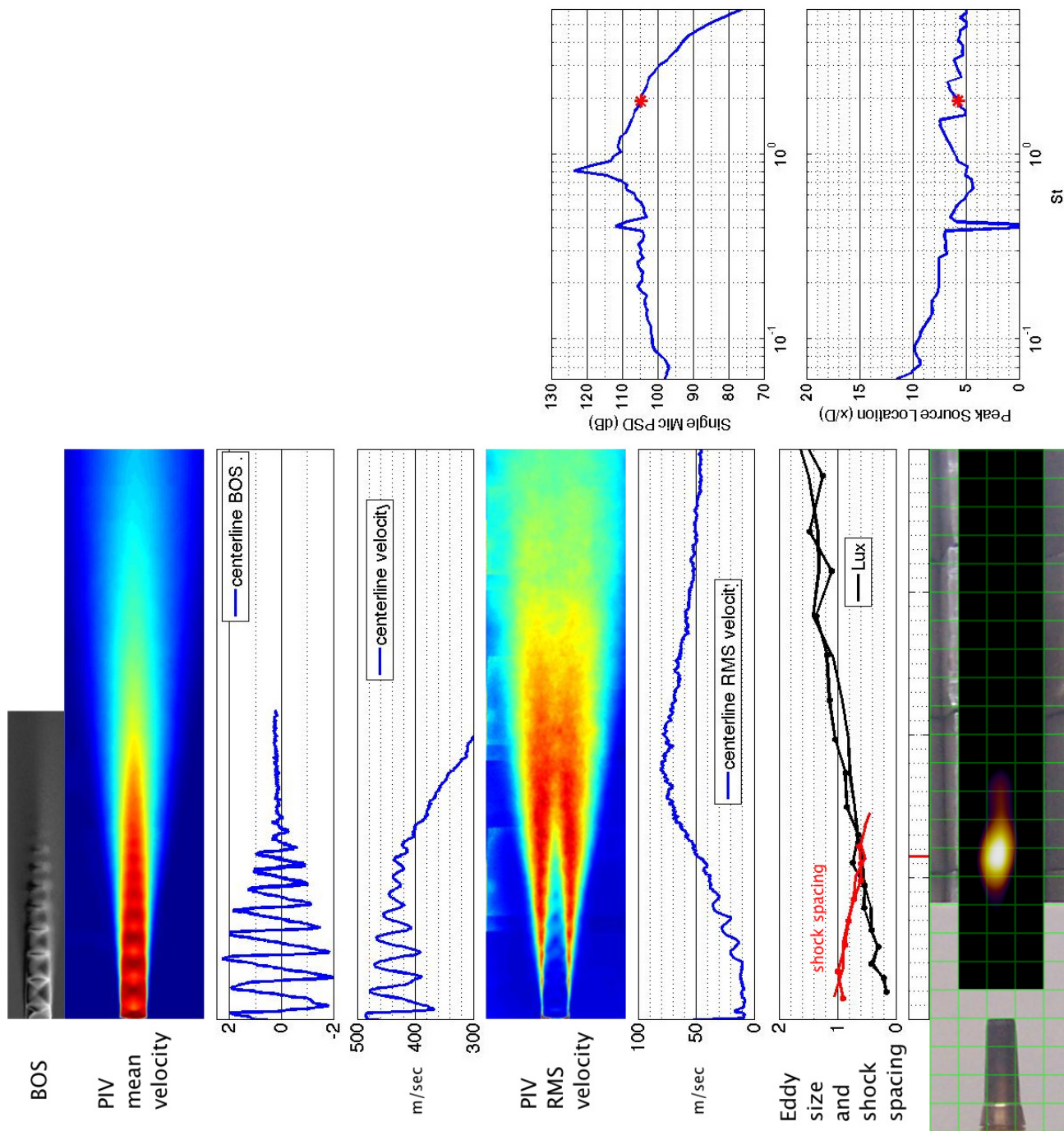
Figure 187.—SMC016; under-expanded; set point 11617; Mj=1.61; Mjdesign=1.50; St=1.929.
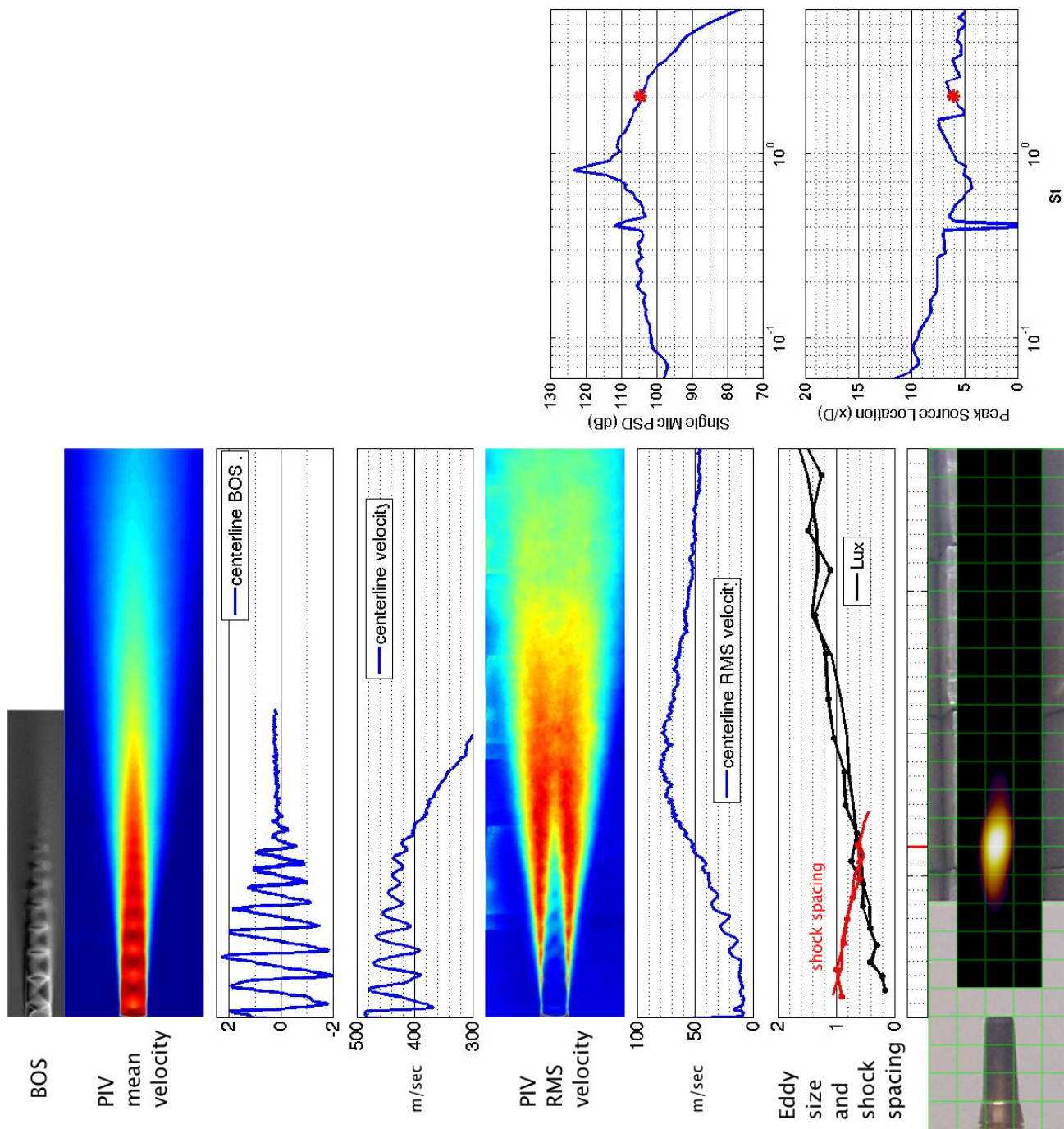
Figure 188.—SMC016; under-expanded; set point 11617; Mj=1.61; Mjdesign=1.50; St=2.052.
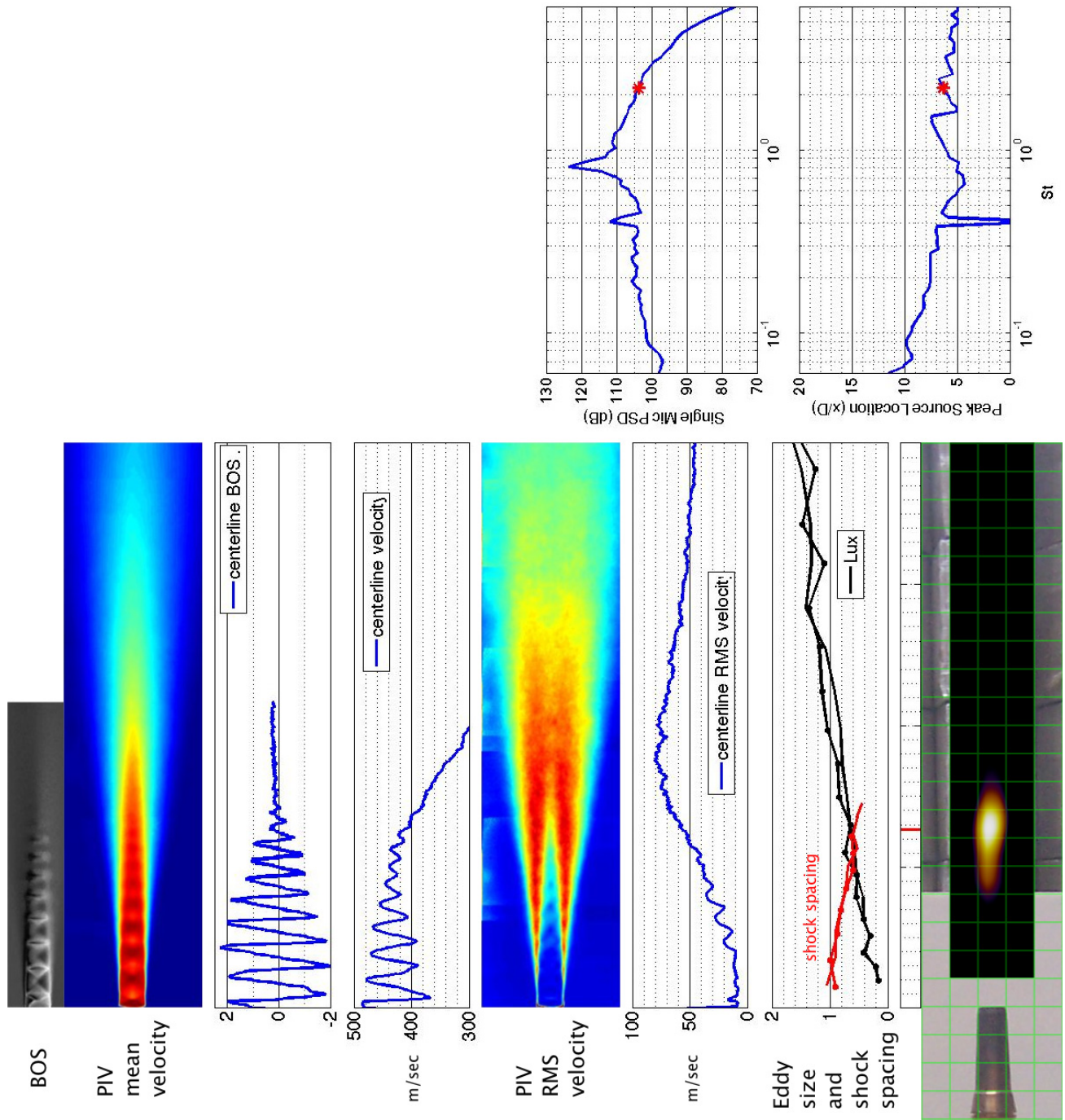
Figure 189.—SMC016; under-expanded; set point 11617; Mj=1.61; Mjdesign=1.50; St=2.179.
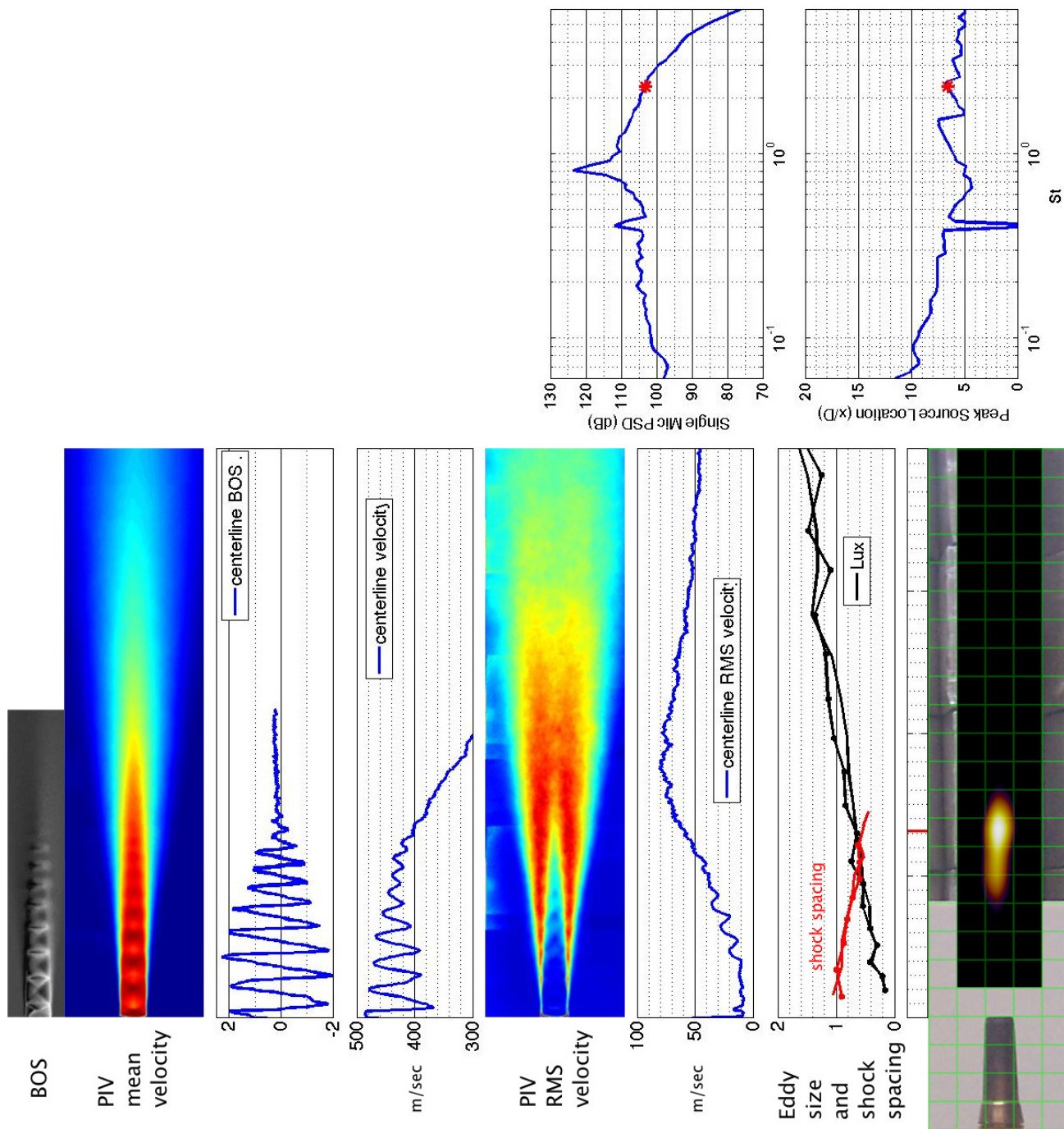
Figure 190.—SMC016; under-expanded; set point 11617; Mj=1.61; Mjdesign=1.50; St=2.308.
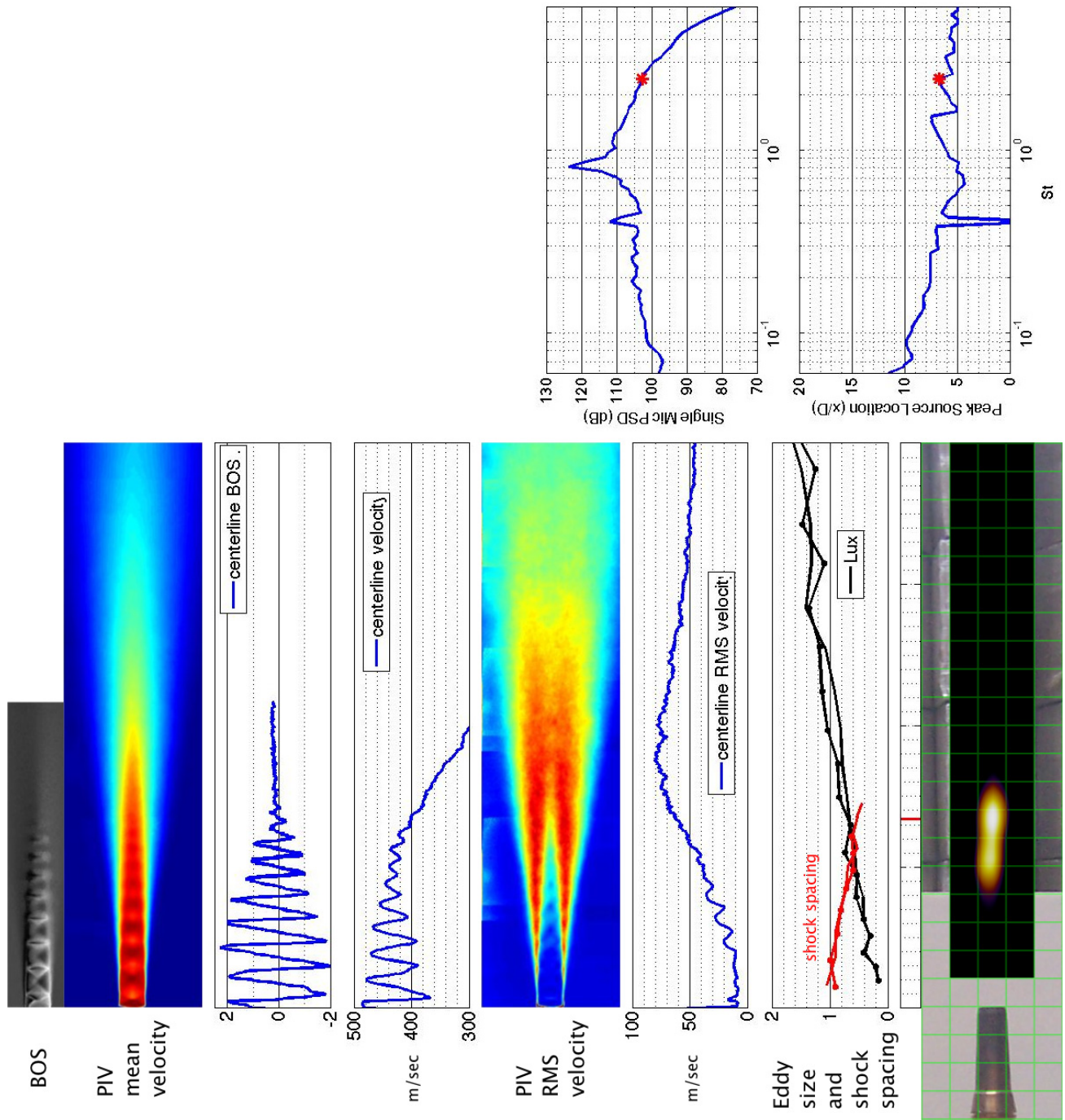
Figure 191.—SMC016; under-expanded; set point 11617; Mj=1.61; Mjdesign=1.50; St=2.440.
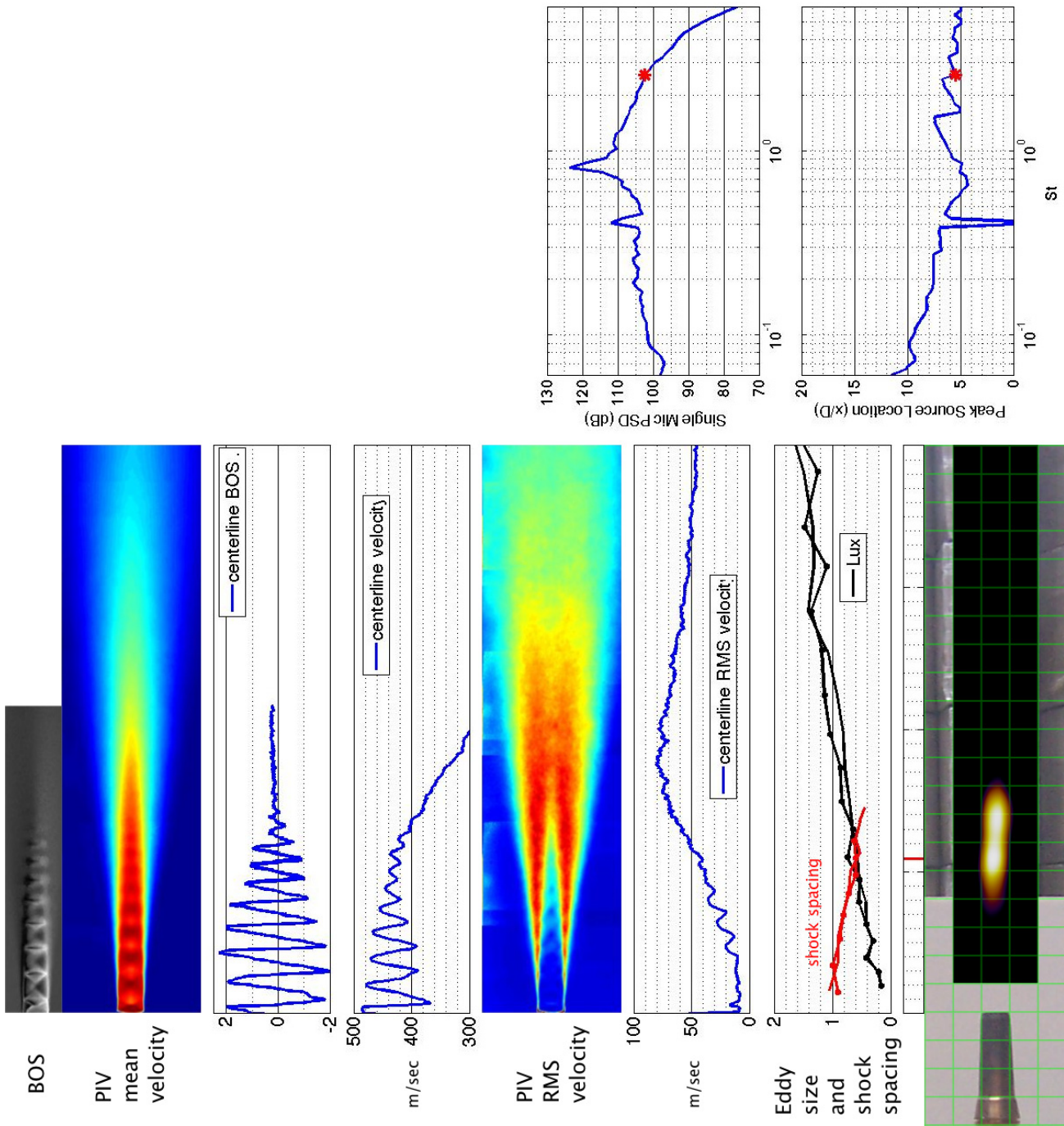
Figure 192.—SMC016; under-expanded; set point 11617; Mj=1.61; Mjdesign=1.50; St=2.580.
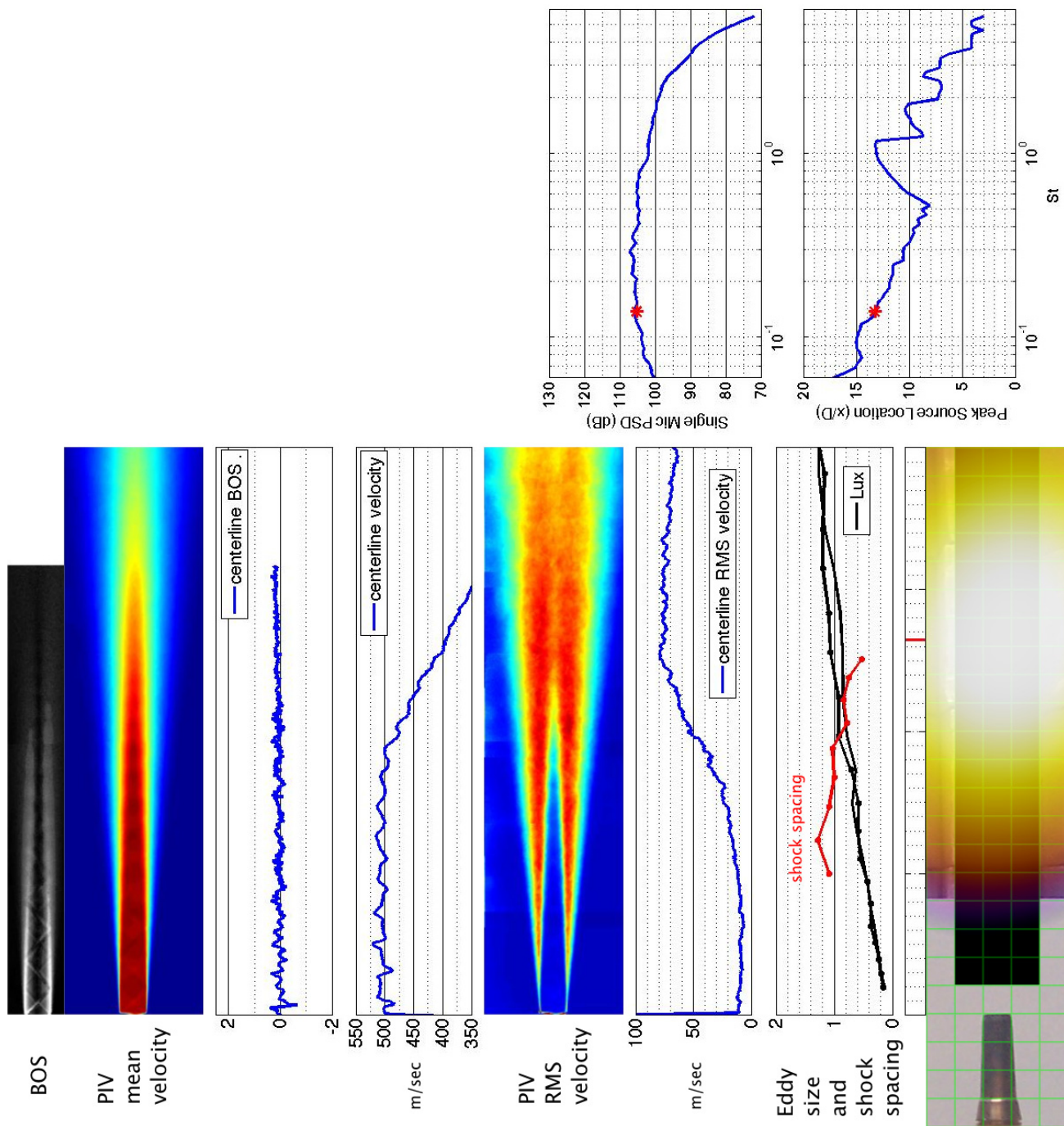
Figure 193.—SMC016; ideally-expanded; set point 11610; Mj=1.50; Mjdesign=1.50; St=0.137.

BOS

PIV
mean
velocity

centerline BOS.

centerline velocity

550
500
450
400
350
m/sec

PIV
RMS
velocity

centerline RMS velocity

100

50

0
m/sec

Eddy
size
and
shock
spacing

Lux

shock spacing

130
120
110
100
90
80
70
Single Mic PSD (dB)

20
15
10
5
0
Peak Source Location (x/D)

10^0

10^{-1}

St
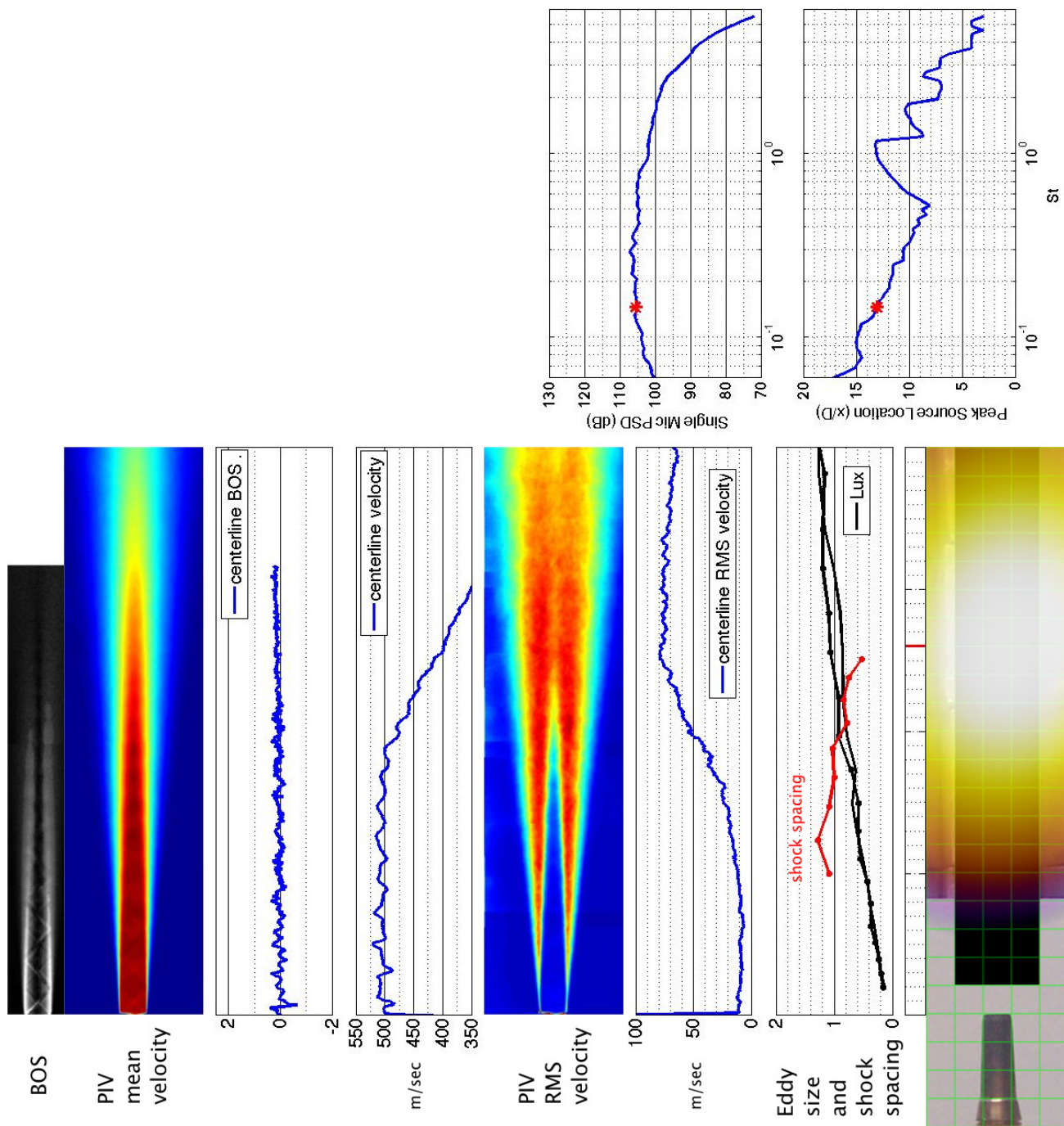
Figure 194.—SMC016; ideally-expanded; set point 11610; Mj=1.50; Mjdesign=1.50; St=0.145.
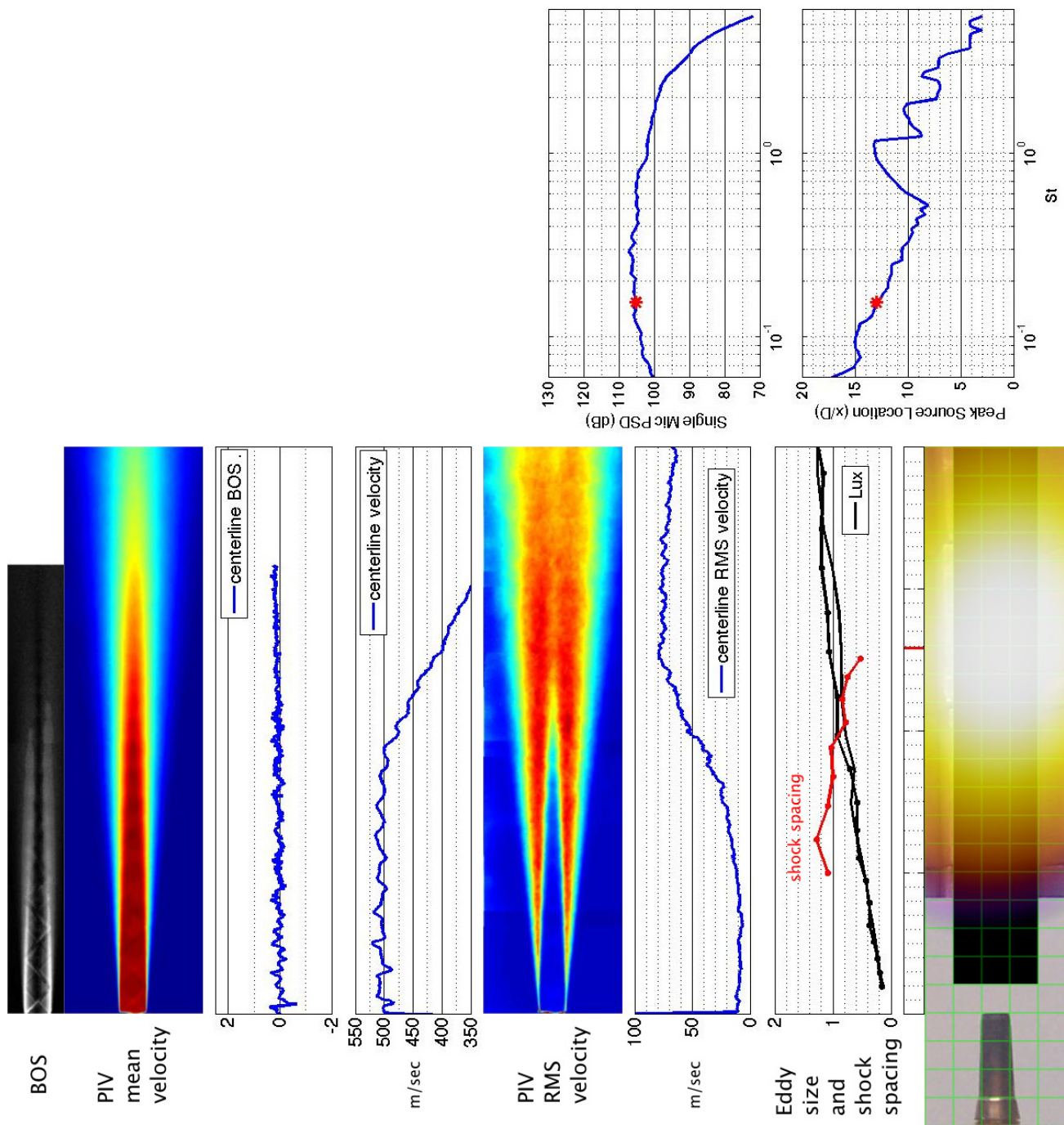
Figure 195.—SMC016; ideally-expanded; set point 11610; Mj=1.50; Mjdesign=1.50; St=0.154.
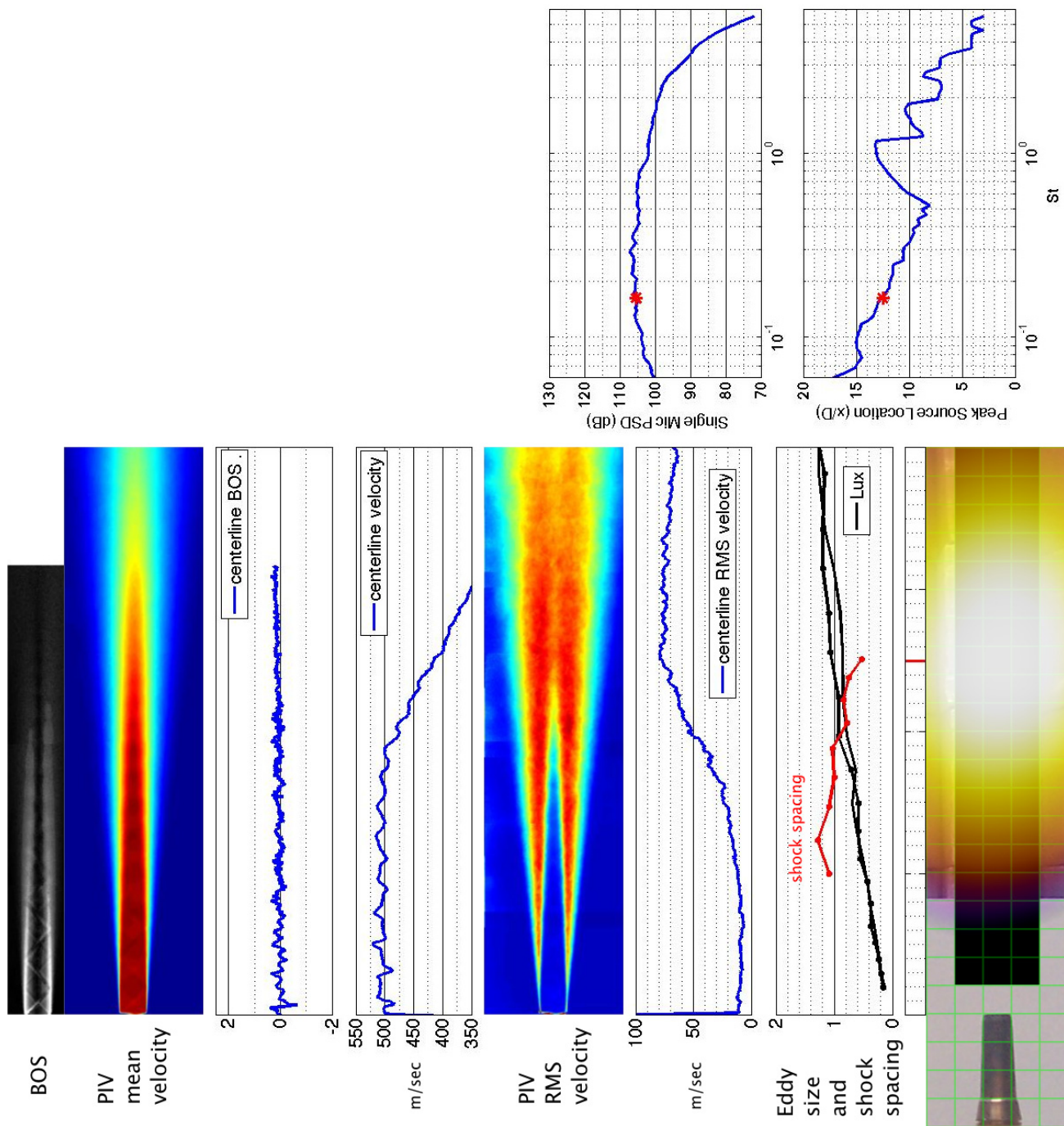
Figure 196.—SMC016; ideally-expanded; set point 11610; Mj=1.50; Mjdesign=1.50; St=0.164.
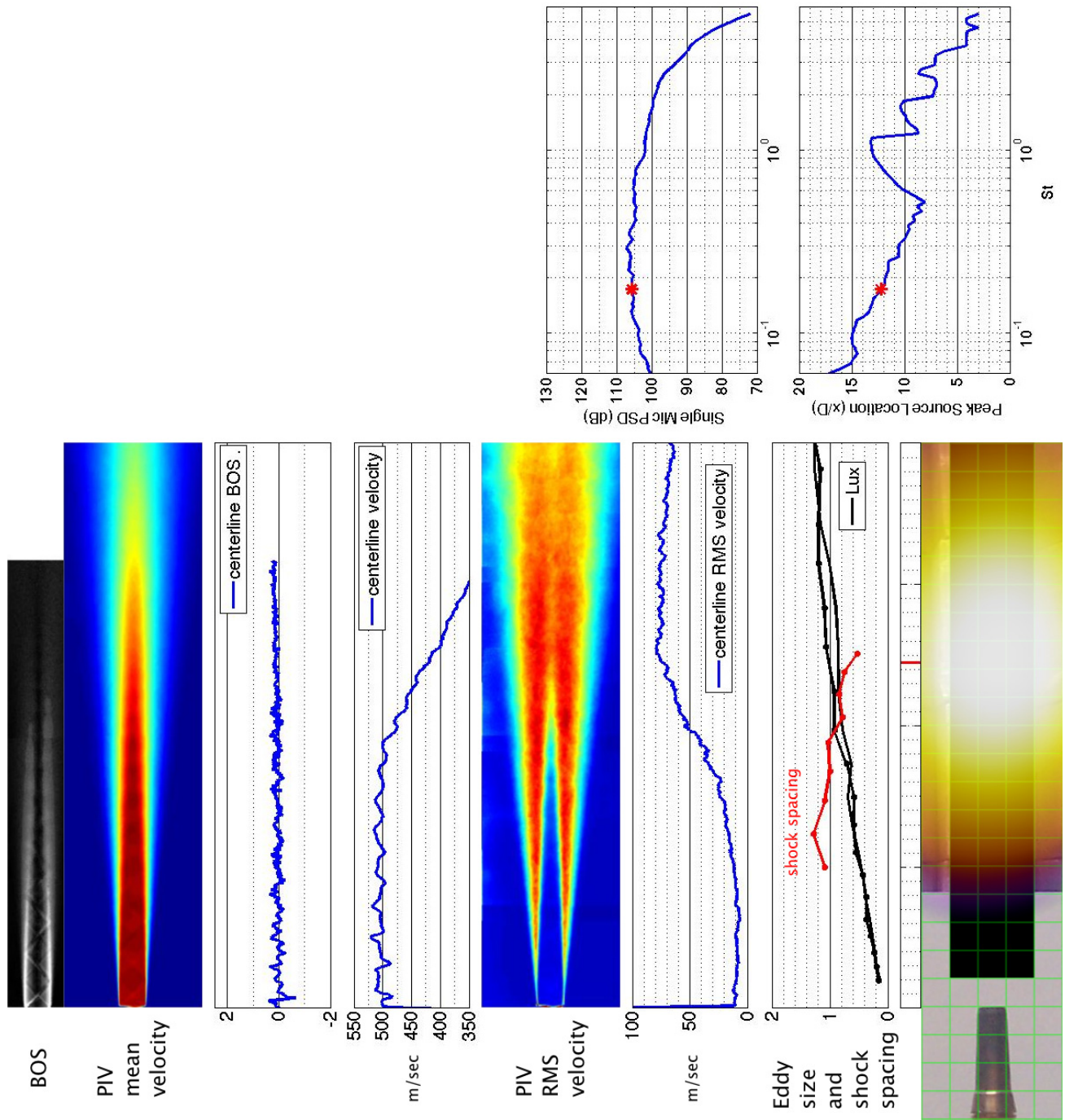
Figure 197.—SMC016; ideally-expanded; set point 11610; Mj=1.50; Mjdesign=1.50; St=0.174.
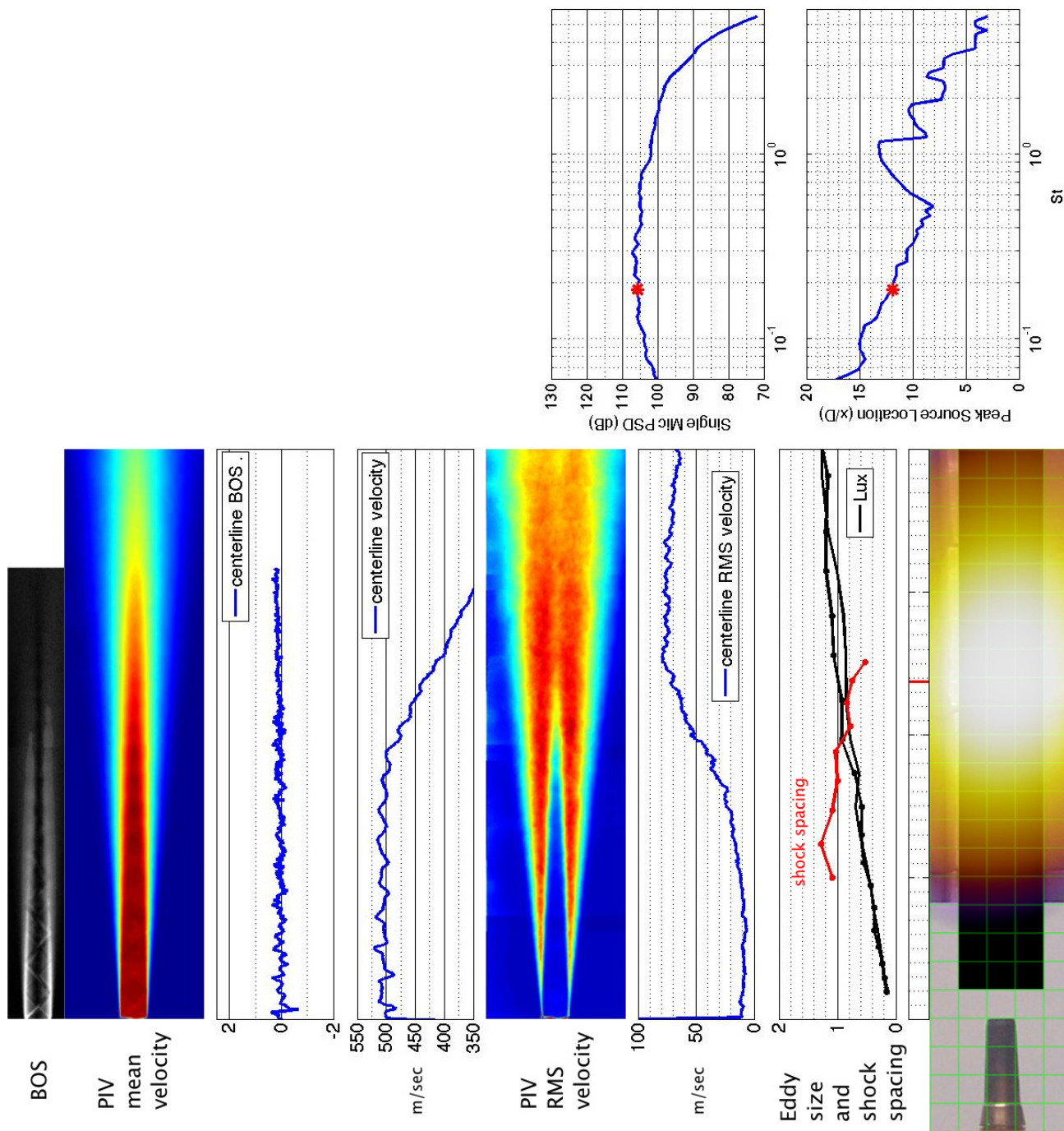
Figure 198.—SMC016; ideally-expanded; set point 11610; Mj=1.50; Mjdesign=1.50; St=0.185.
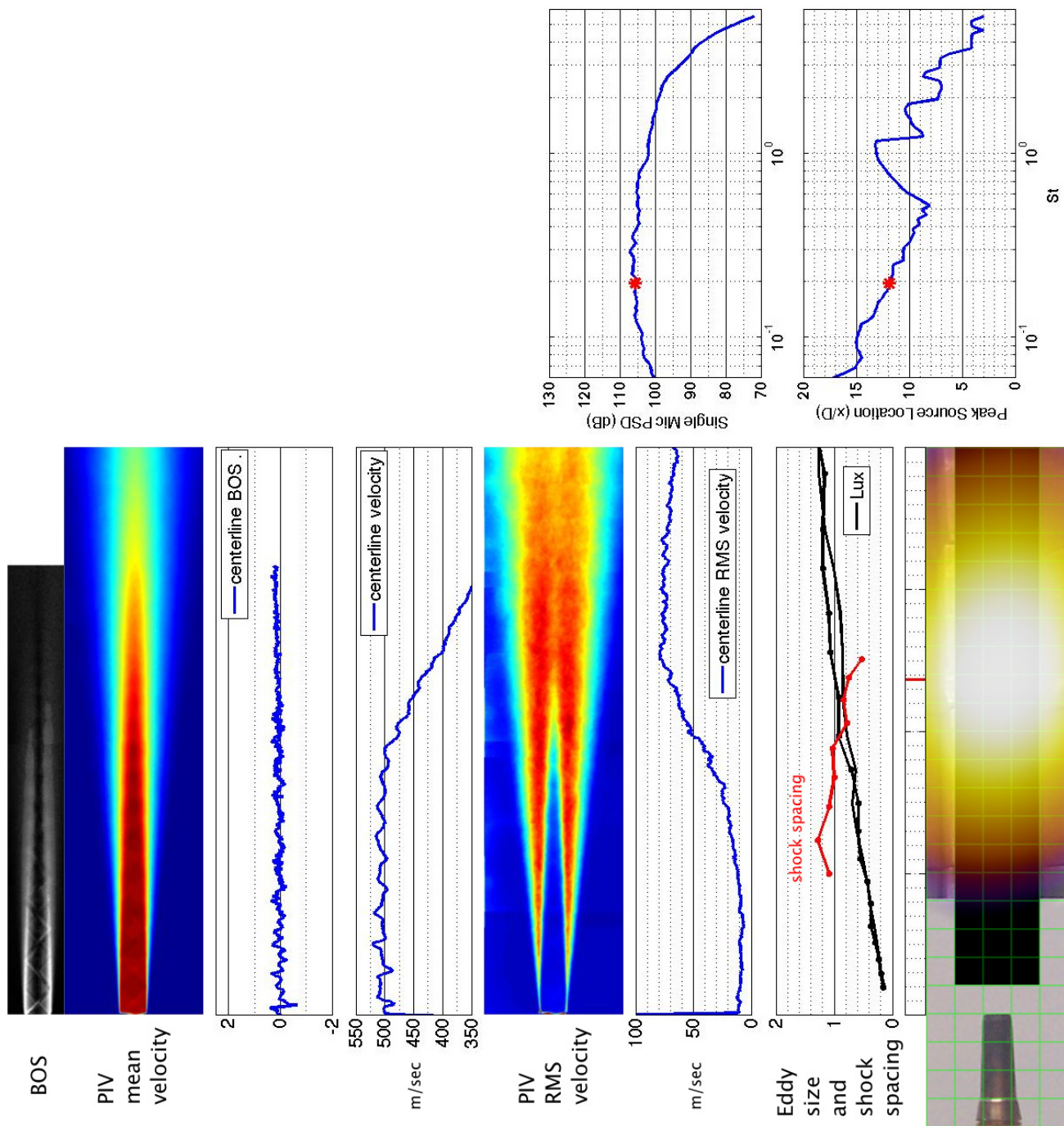
Figure 199.—SMC016; ideally-expanded; set point 11610; Mj=1.50; Mjdesign=1.50; St=0.196.
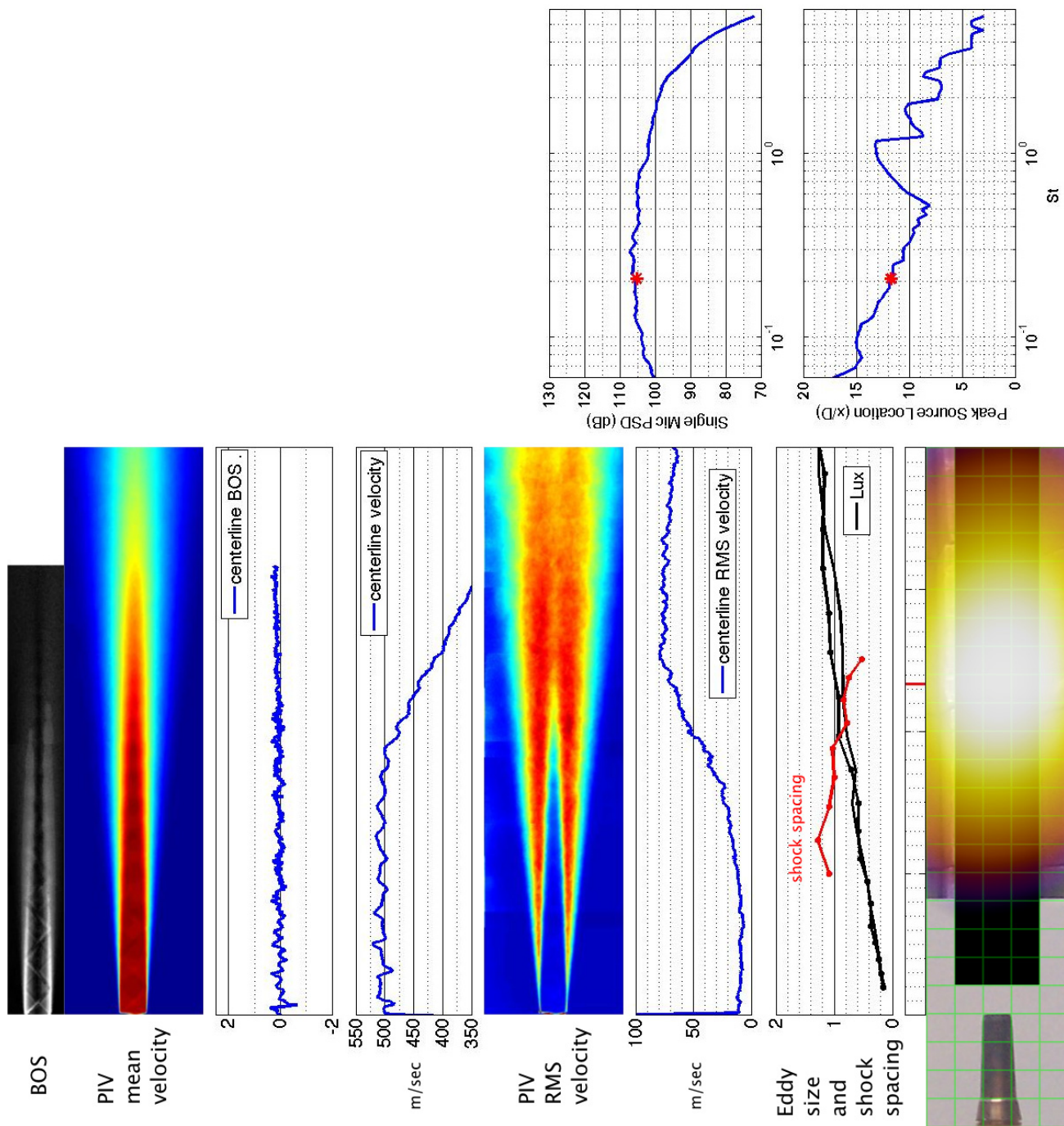
Figure 200.—SMC016; ideally-expanded; set point 11610; Mj=1.50; Mjdesign=1.50; St=0.208.
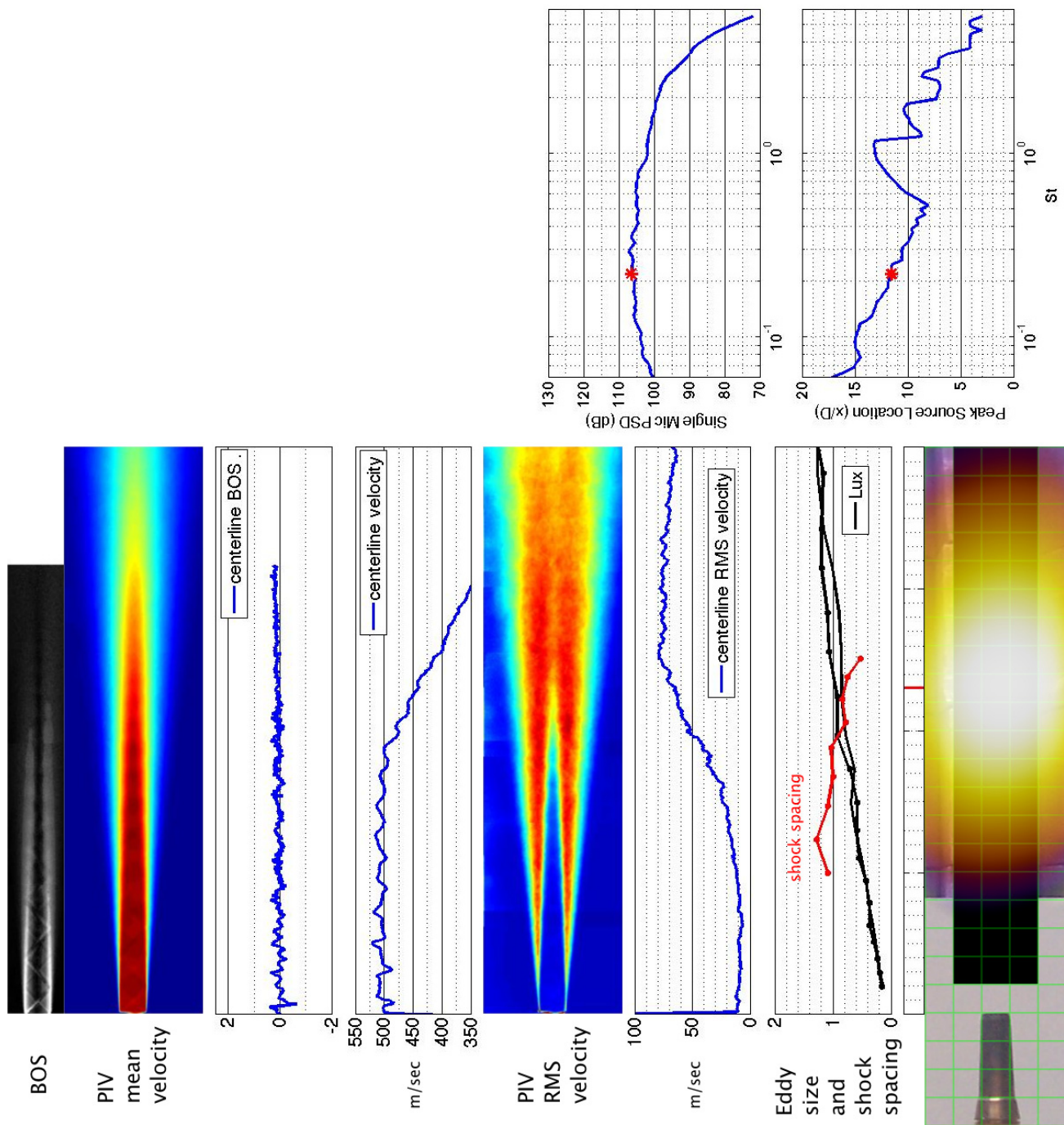
Figure 201.—SMC016; ideally-expanded; set point 11610; Mj=1.50; Mjdesign=1.50; St=0.220.
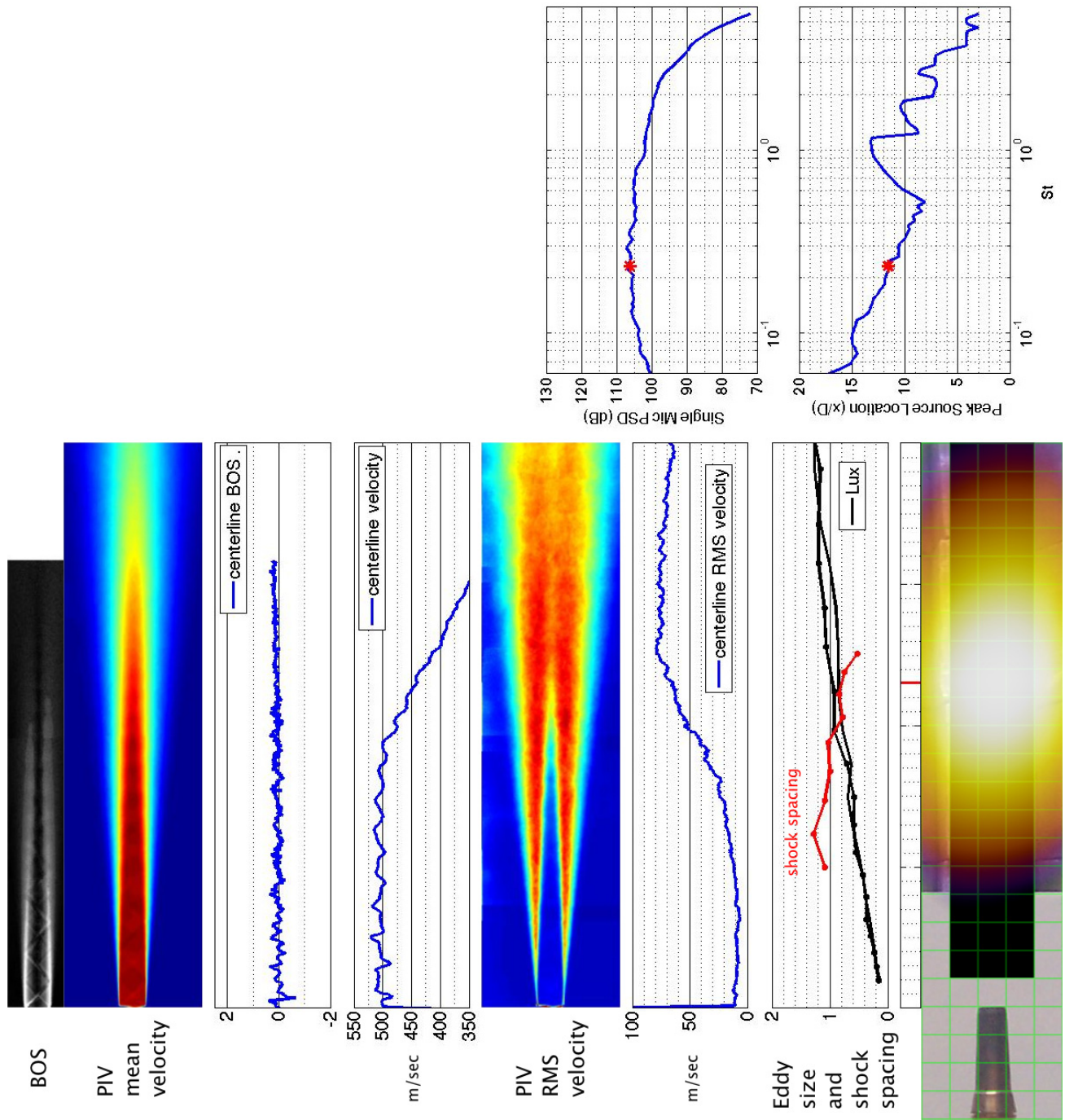
Figure 202.—SMC016; ideally-expanded; set point 11610; Mj=1.50; Mjdesign=1.50; St=0.223.
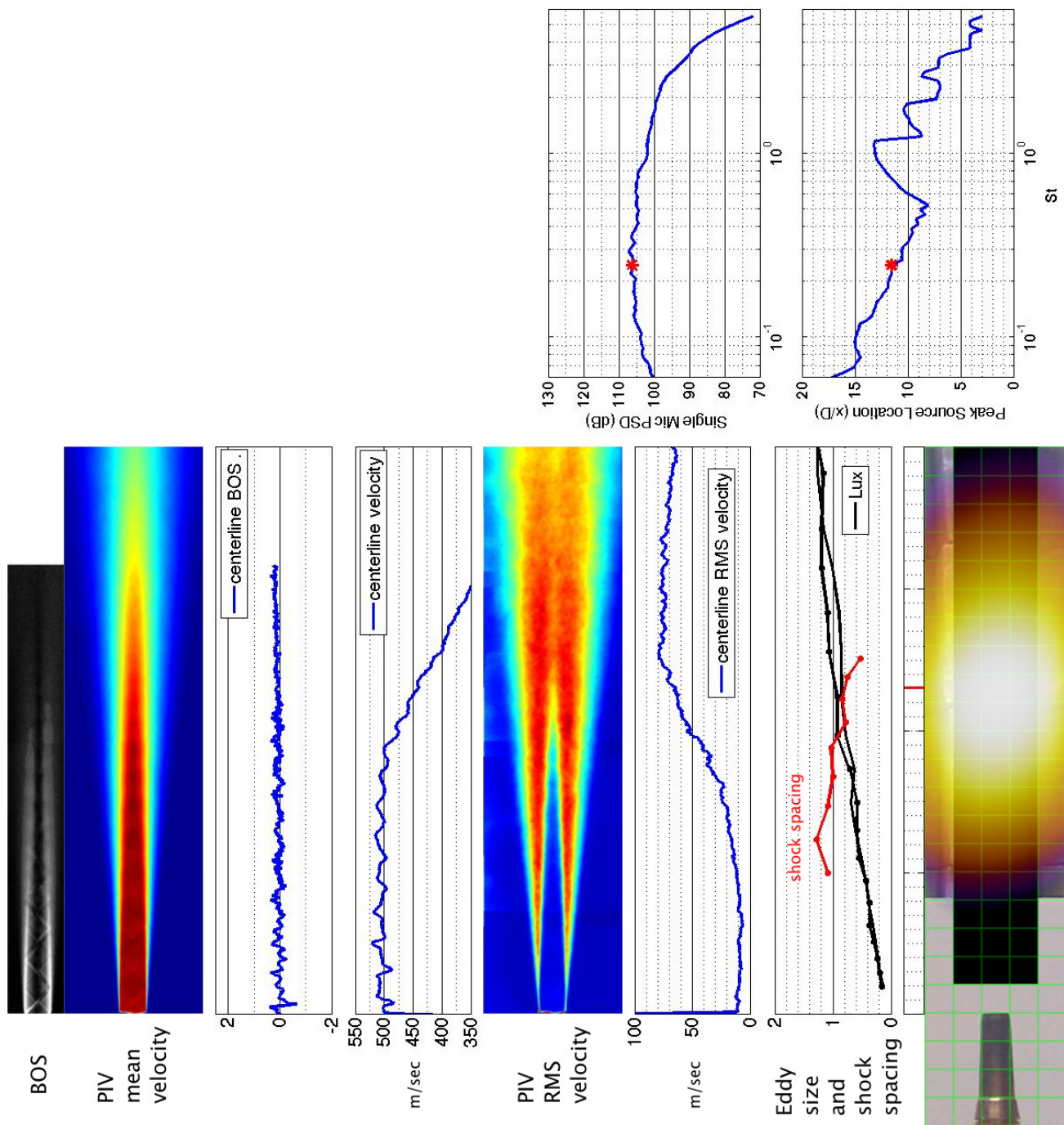
Figure 203.—SMC016; ideally-expanded; set point 11610; Mj=1.50; Mjdesign=1.50; St=0.246.
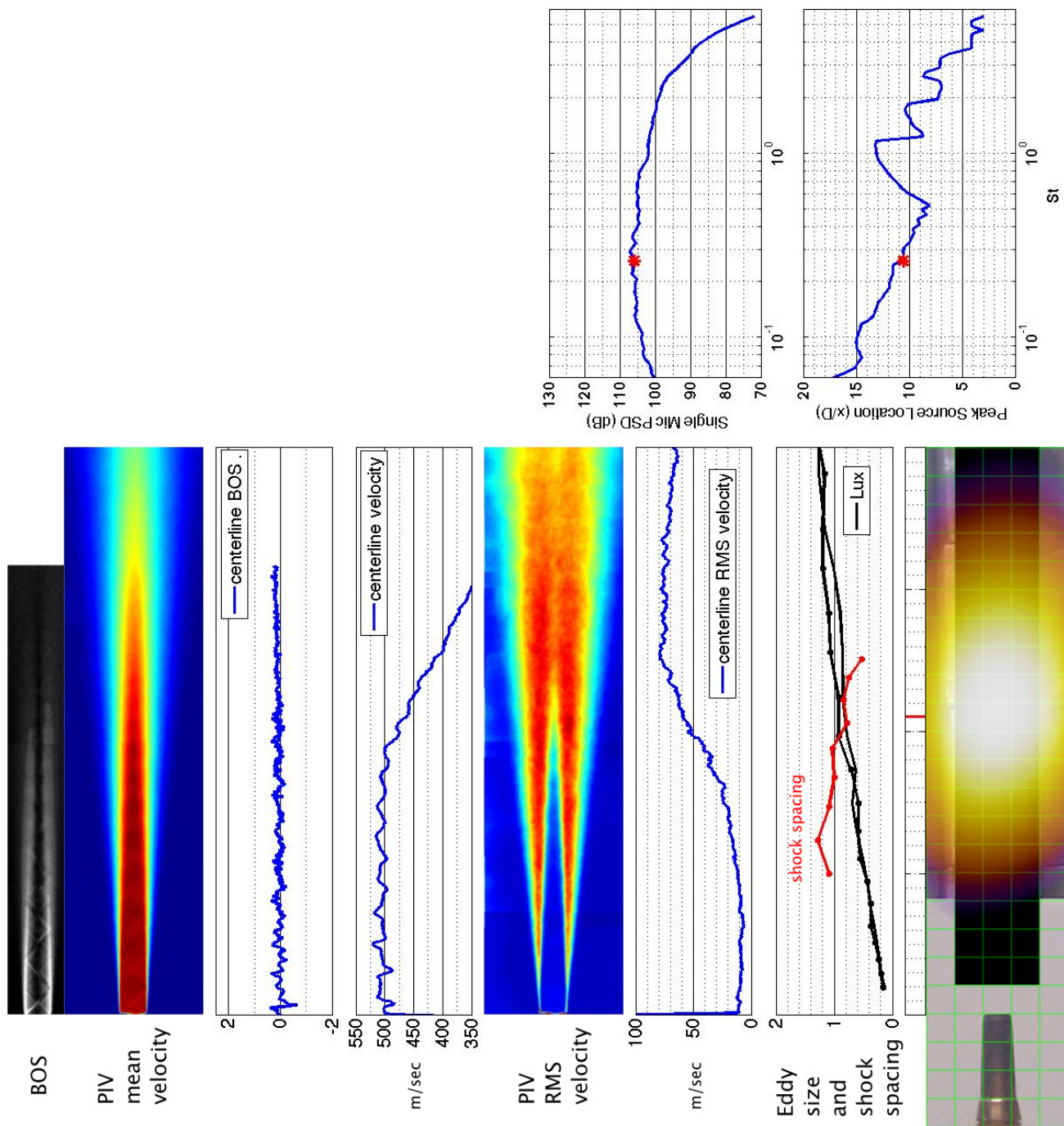
Figure 204.—SMC016; ideally-expanded; set point 11610; Mj=1.50; Mjdesign=1.50; St=0.260.
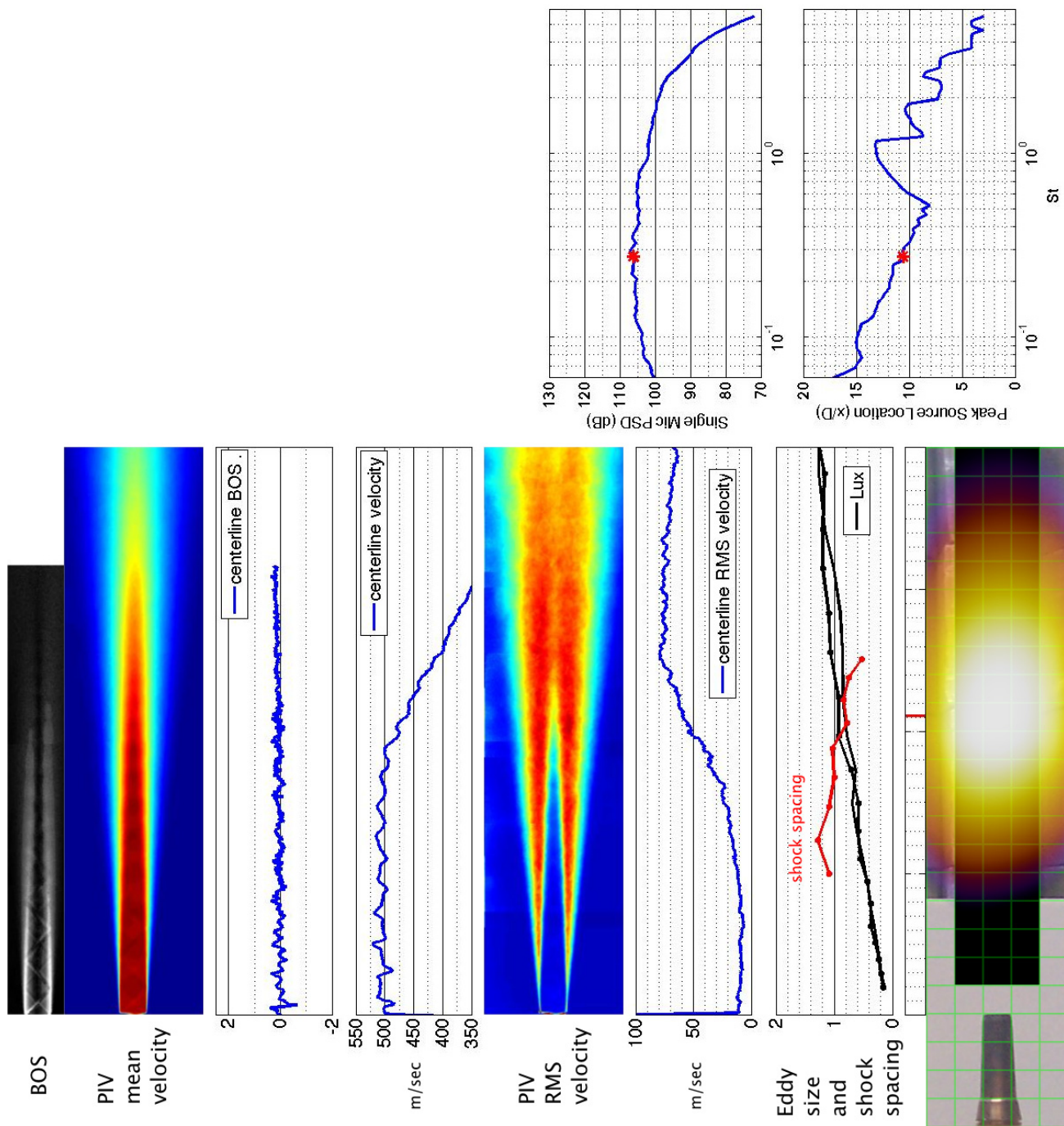
Figure 205.—SMC016; ideally-expanded; set point 11610; Mj=1.50; Mjdesign=1.50; St=0.275.
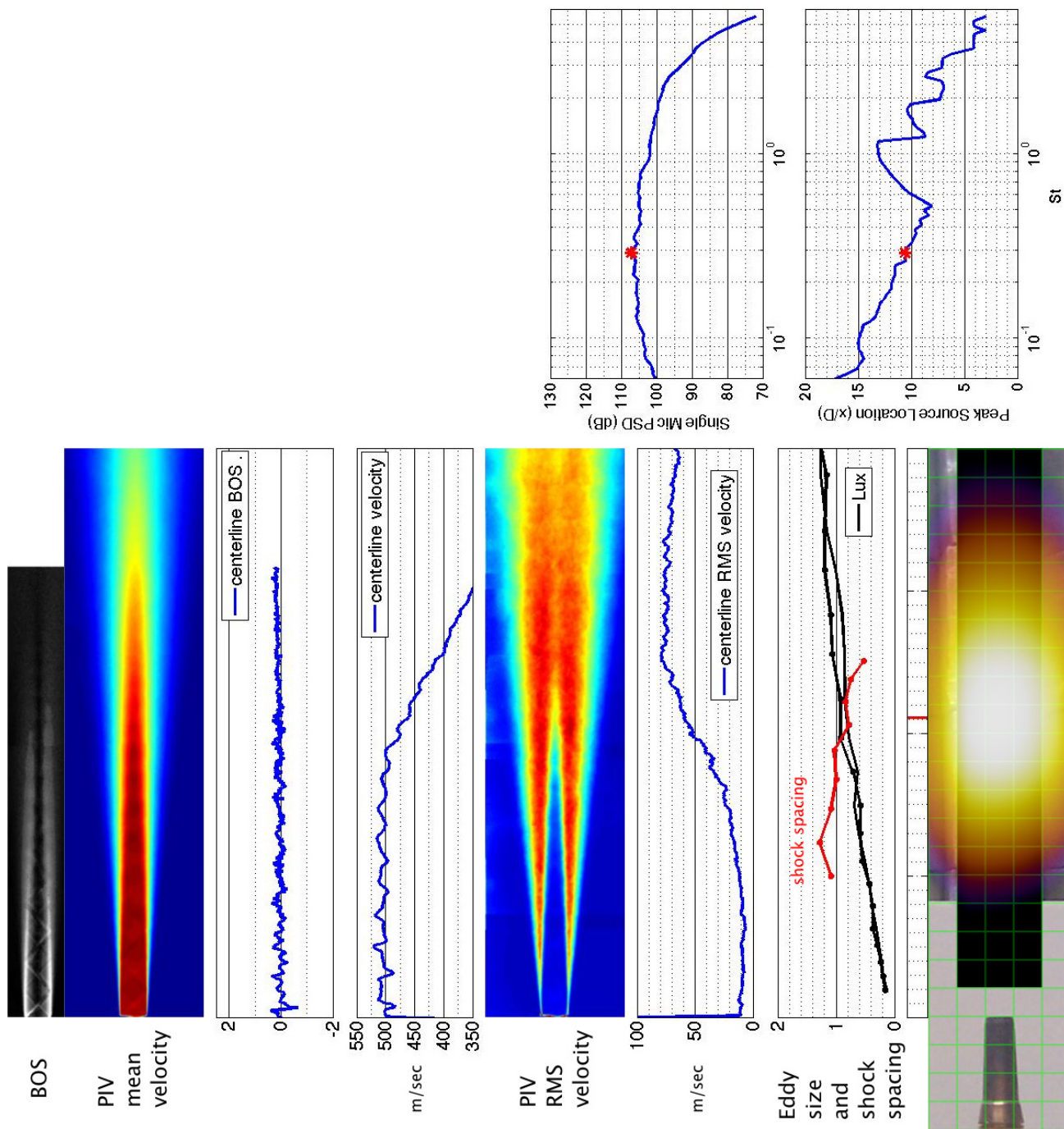
Figure 206.—SMC016; ideally-expanded; set point 11610; Mj=1.50; Mjdesign=1.50; St=0.291.
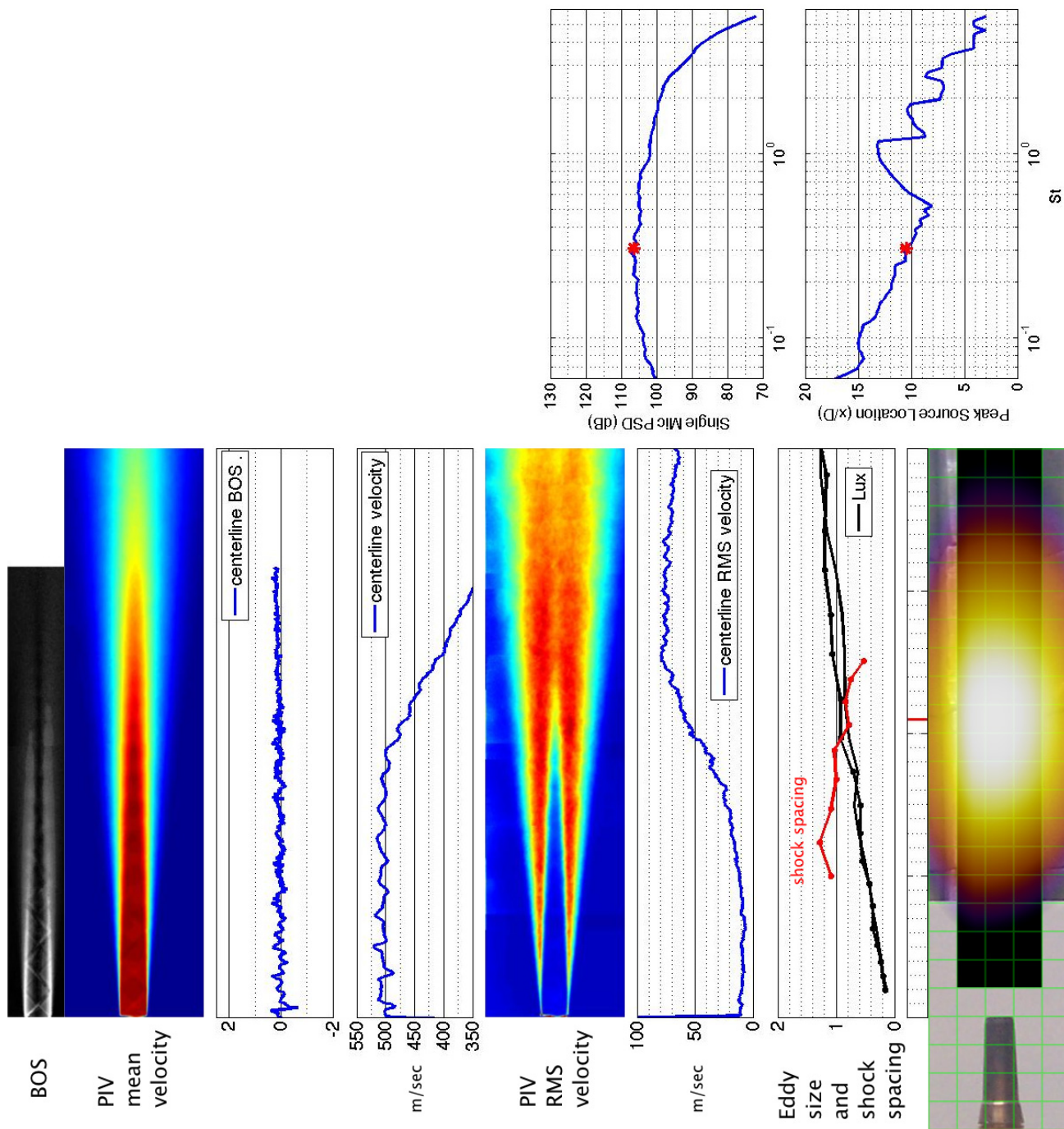
Figure 207.—SMC016; ideally-expanded; set point 11610; Mj=1.50; Mjdesign=1.50; St=0.308.
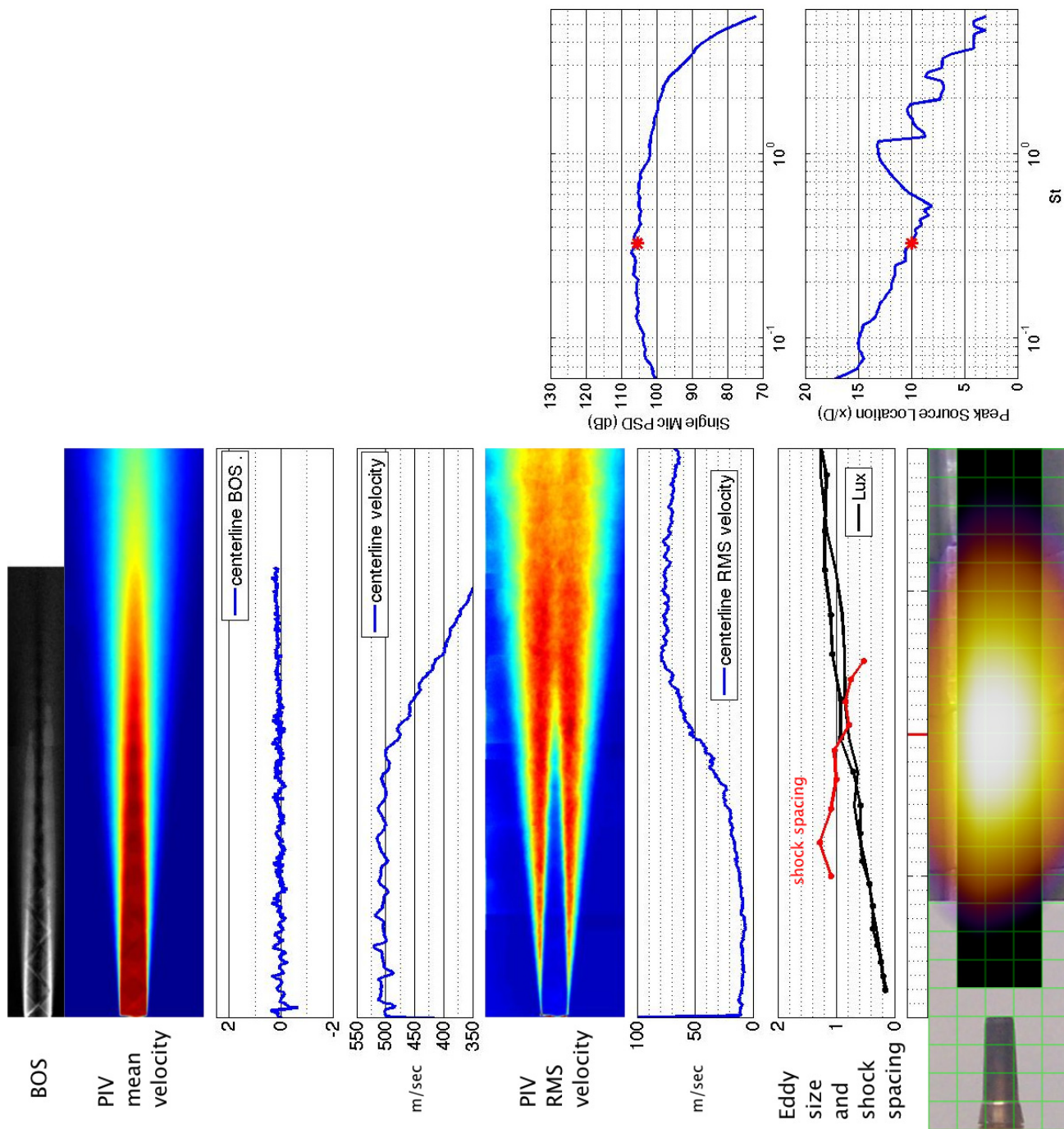
Figure 208.—SMC016; ideally-expanded; set point 11610; Mj=1.50; Mjdesign=1.50; St=0.326.
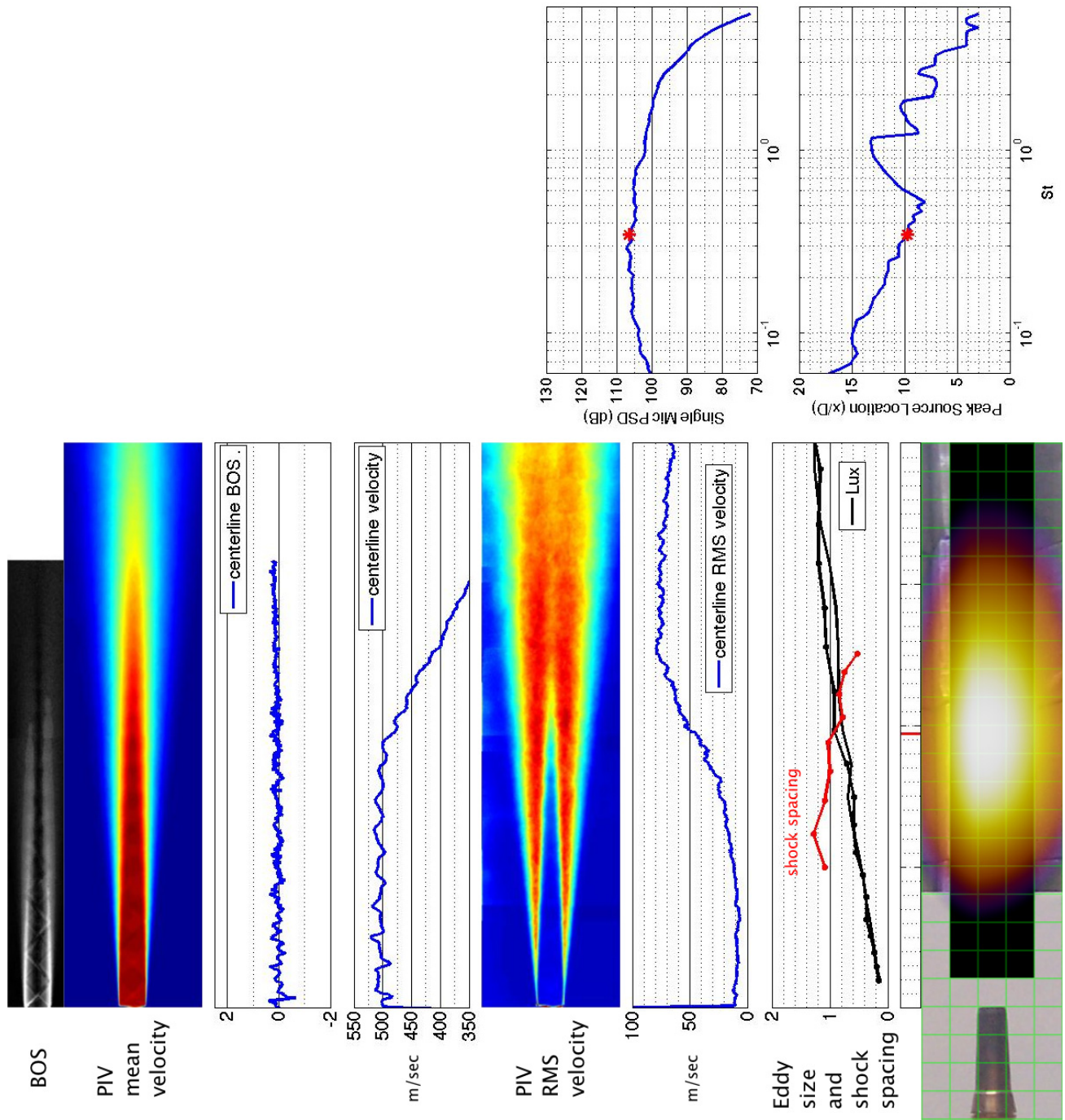
Figure 209.—SMC016; ideally-expanded; set point 11610; Mj=1.50; Mjdesign=1.50; St=0.345.
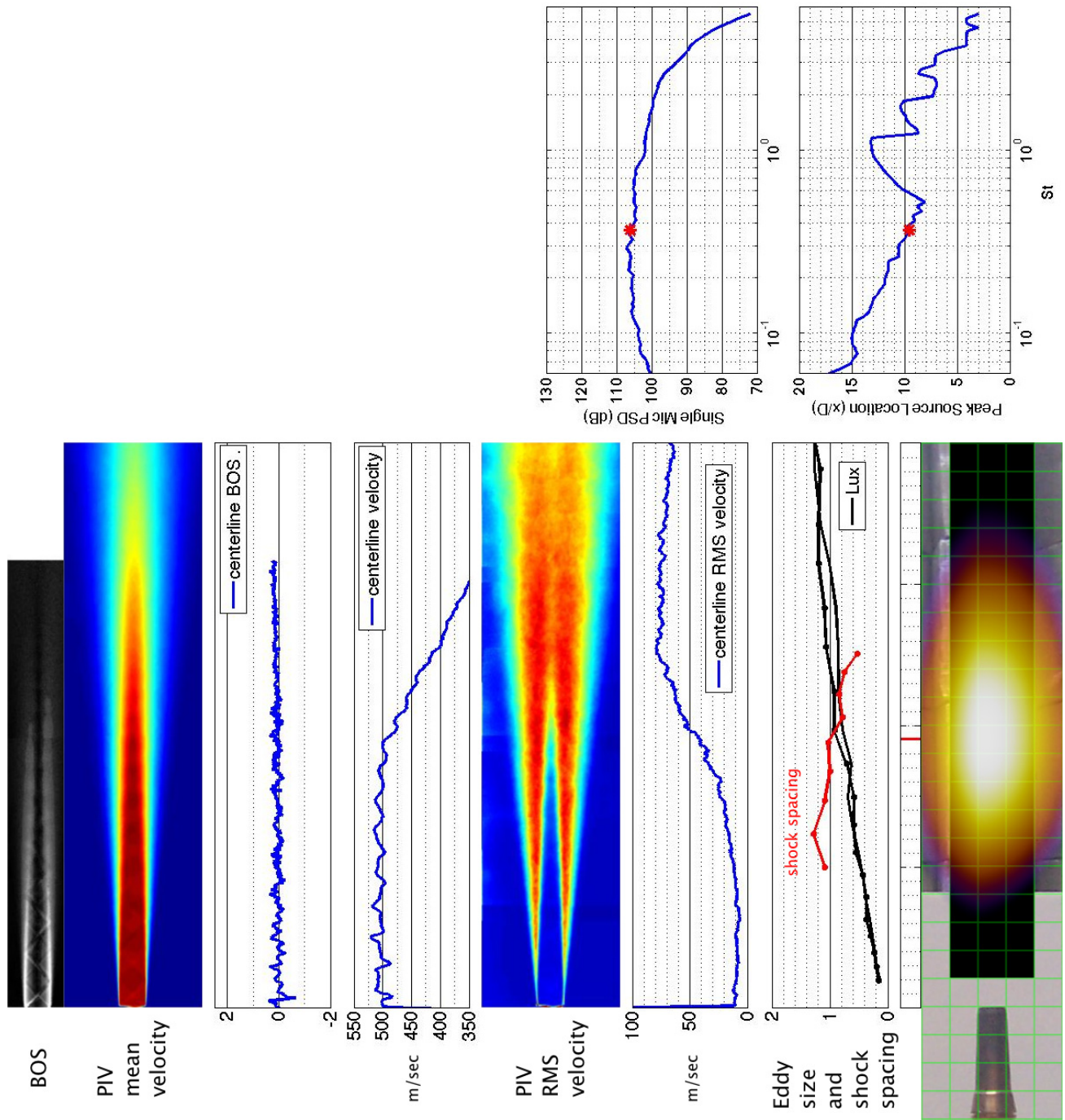
Figure 210.—SMC016; ideally-expanded; set point 11610; Mj=1.50; Mjdesign=1.50; St=0.366.
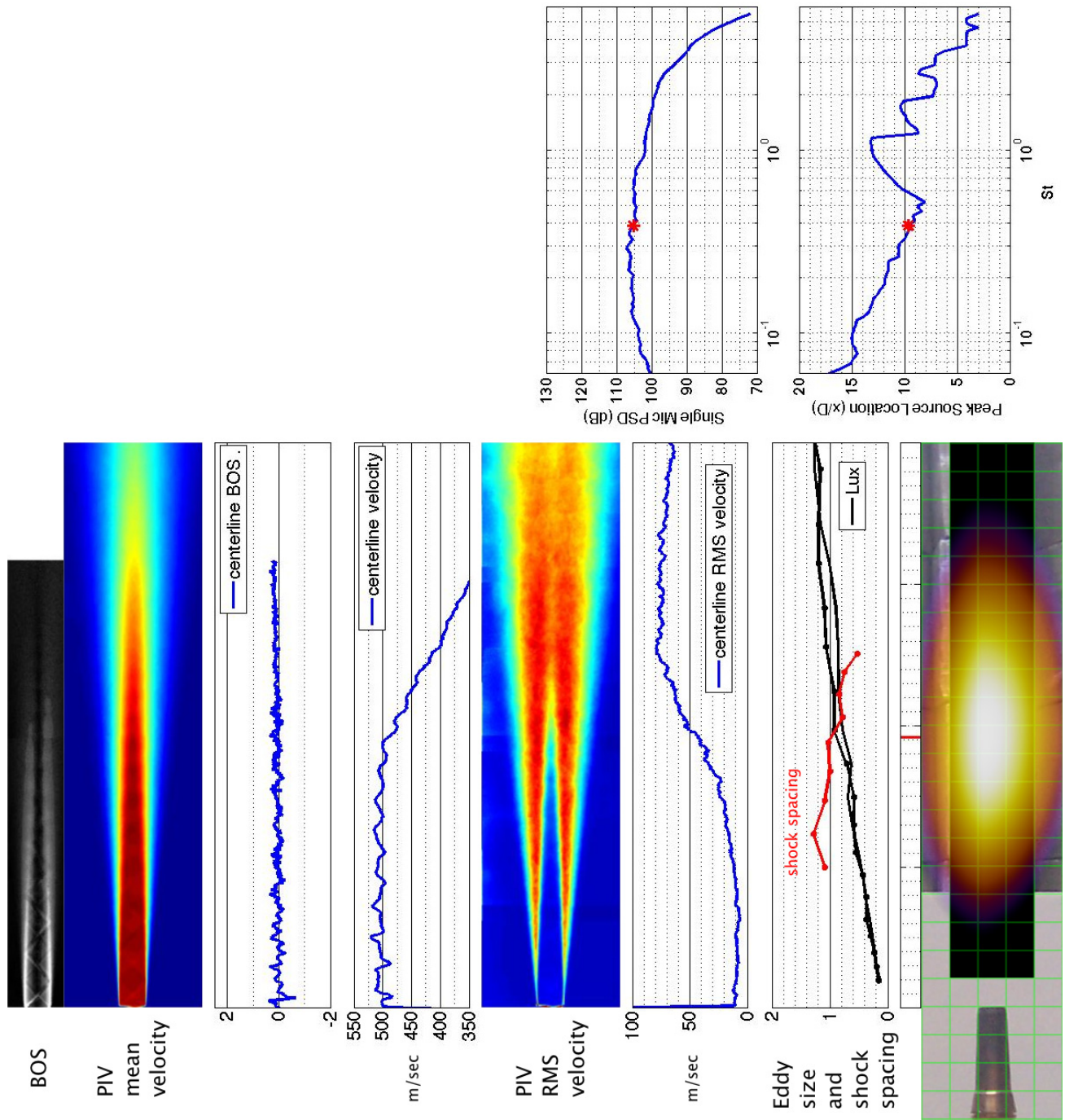
Figure 211.—SMC016; ideally-expanded; set point 11610; Mj=1.50; Mjdesign=1.50; St=0.388.
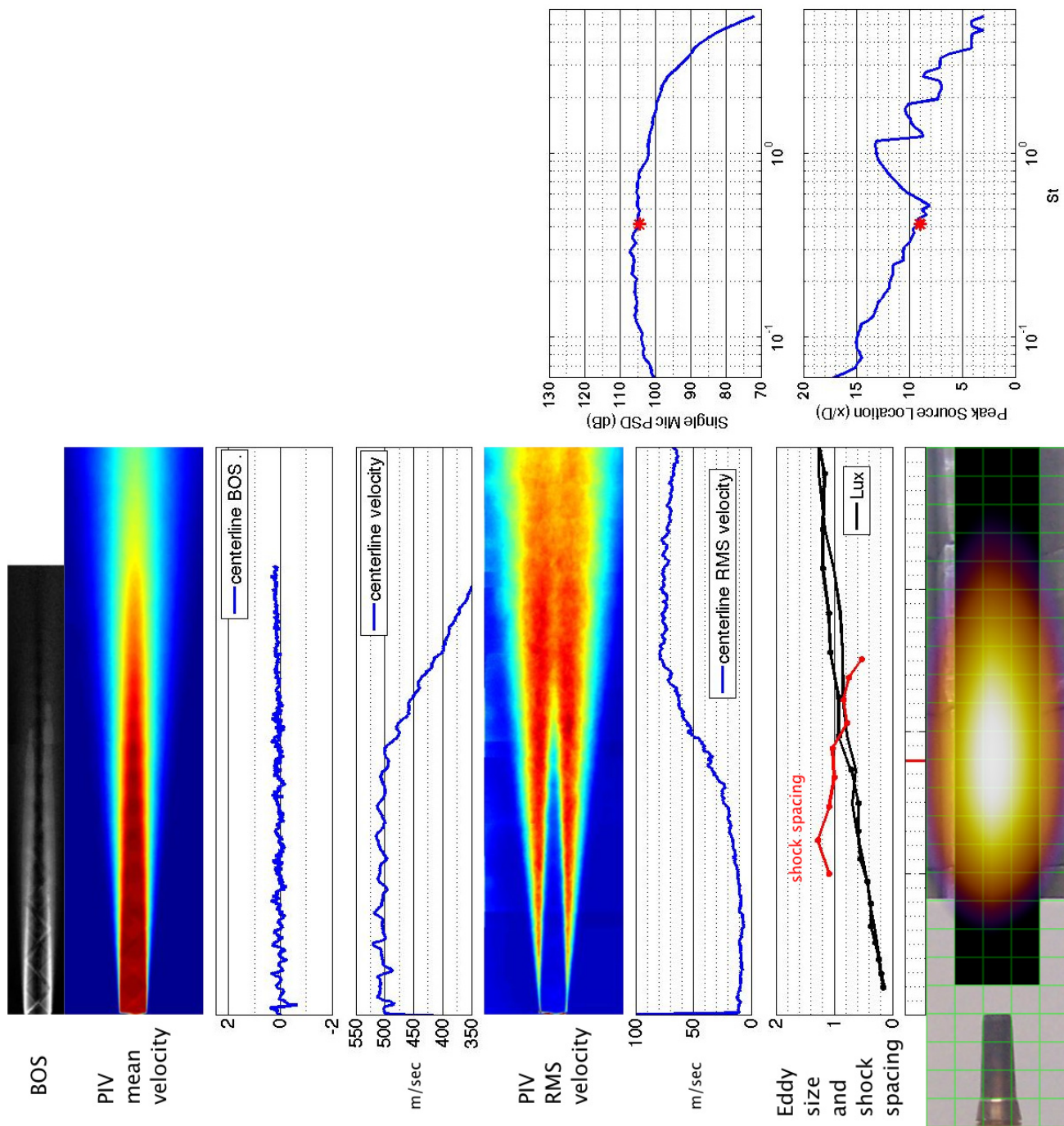
Figure 212.—SMC016; ideally-expanded; set point 11610; Mj=1.50; Mjdesign=1.50; St=0.411.
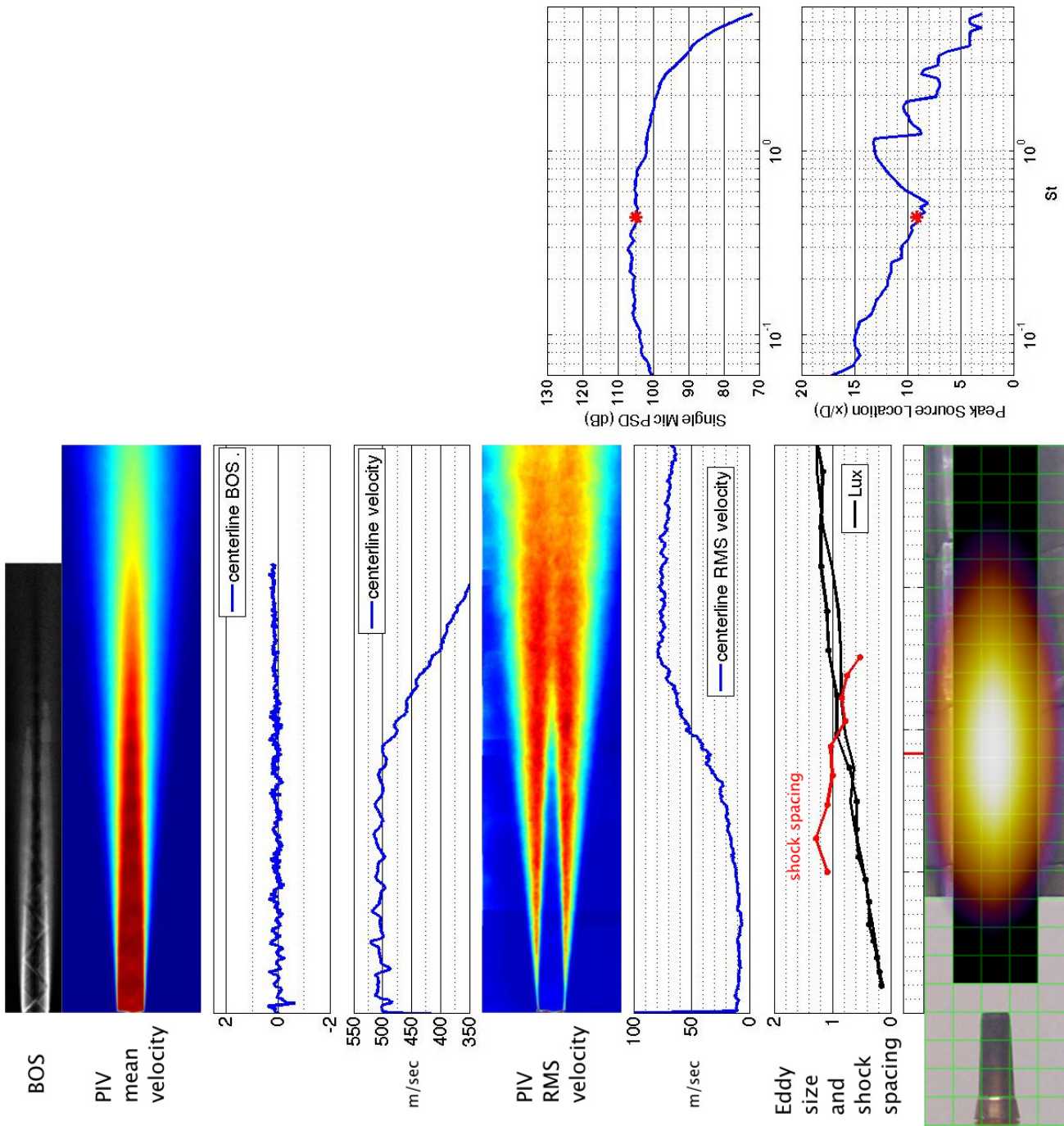
Figure 213.—SMC016; ideally-expanded; set point 11610; Mj=1.50; Mjdesign=1.50; St=0.437.
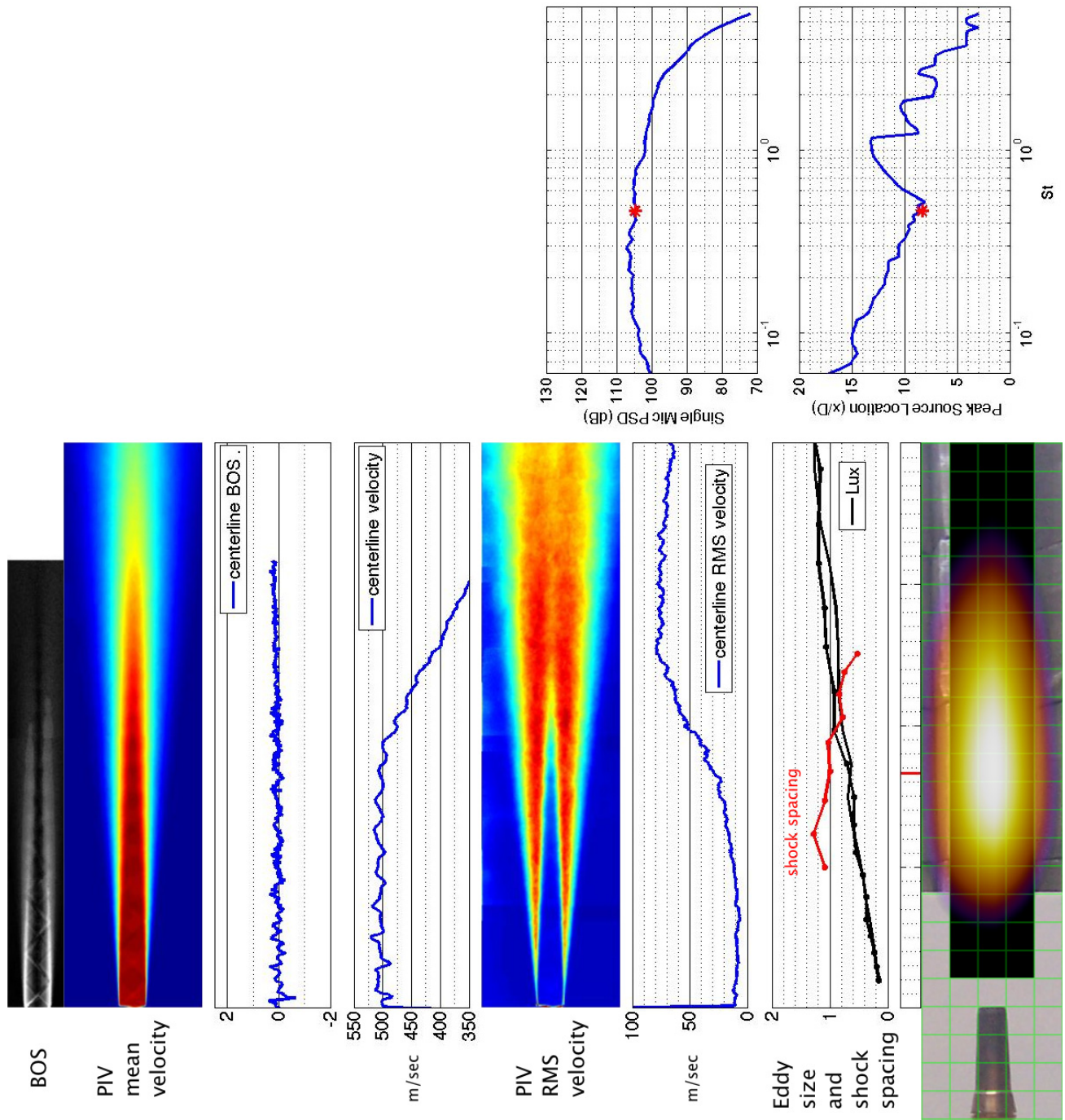
Figure 214.—SMC016; ideally-expanded; set point 11610; Mj=1.50; Mjdesign=1.50; St=0.463.
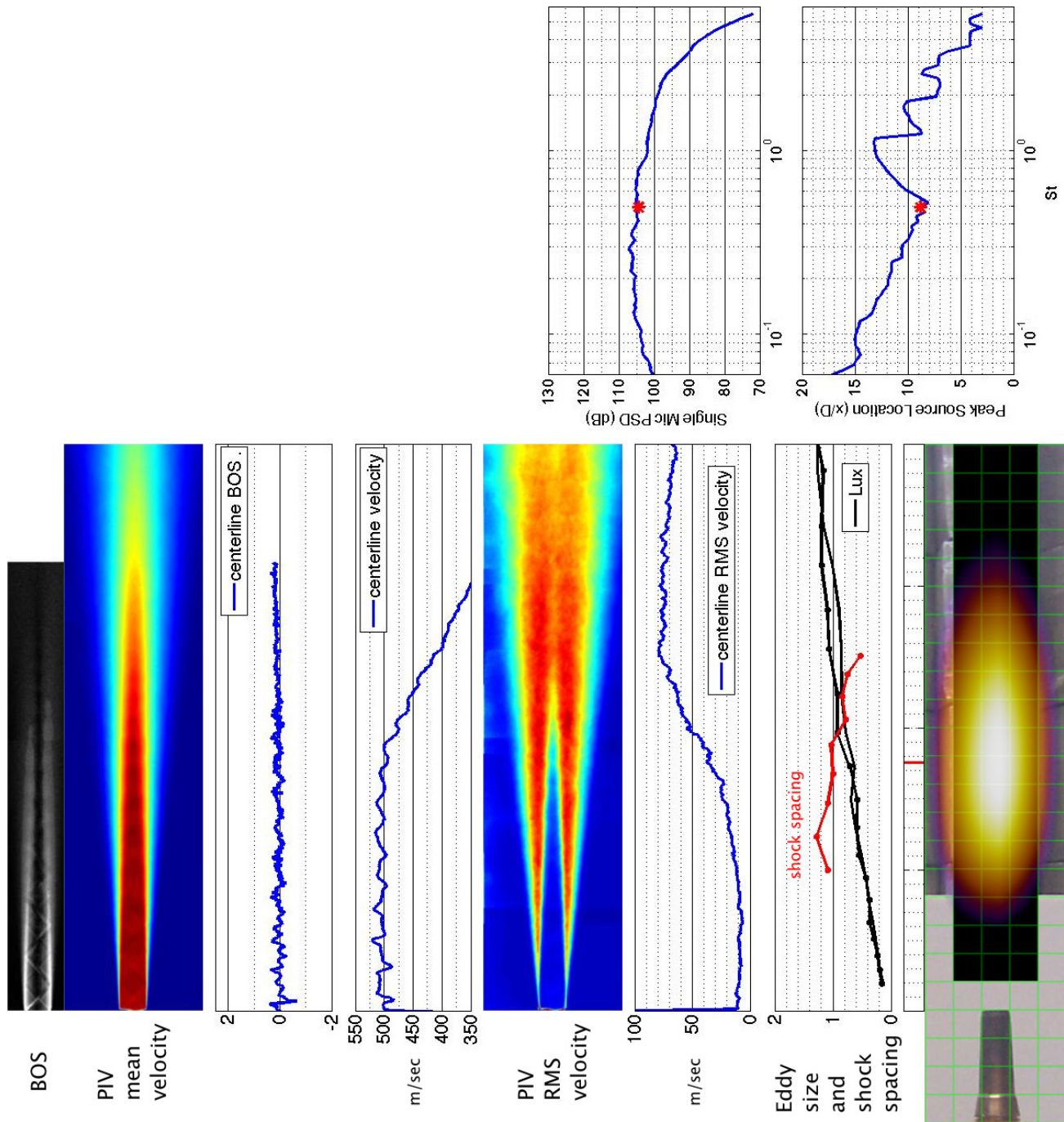
Figure 215.—SMC016; ideally-expanded; set point 11610; Mj=1.50; Mjdesign=1.50; St=0.491.
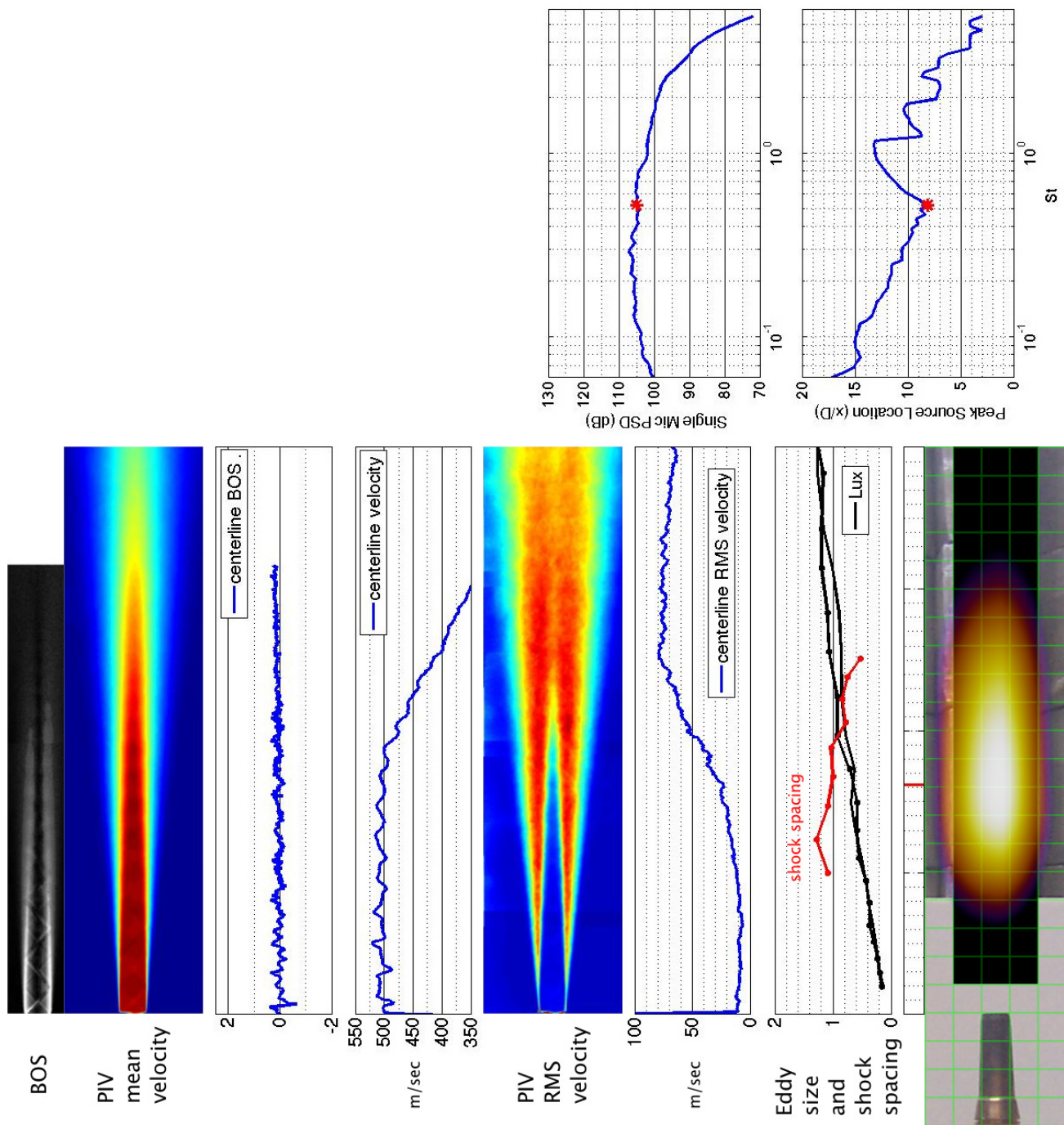
Figure 216.—SMC016; ideally-expanded; set point 11610; Mj=1.50; Mjdesign=1.50; St=0.520.
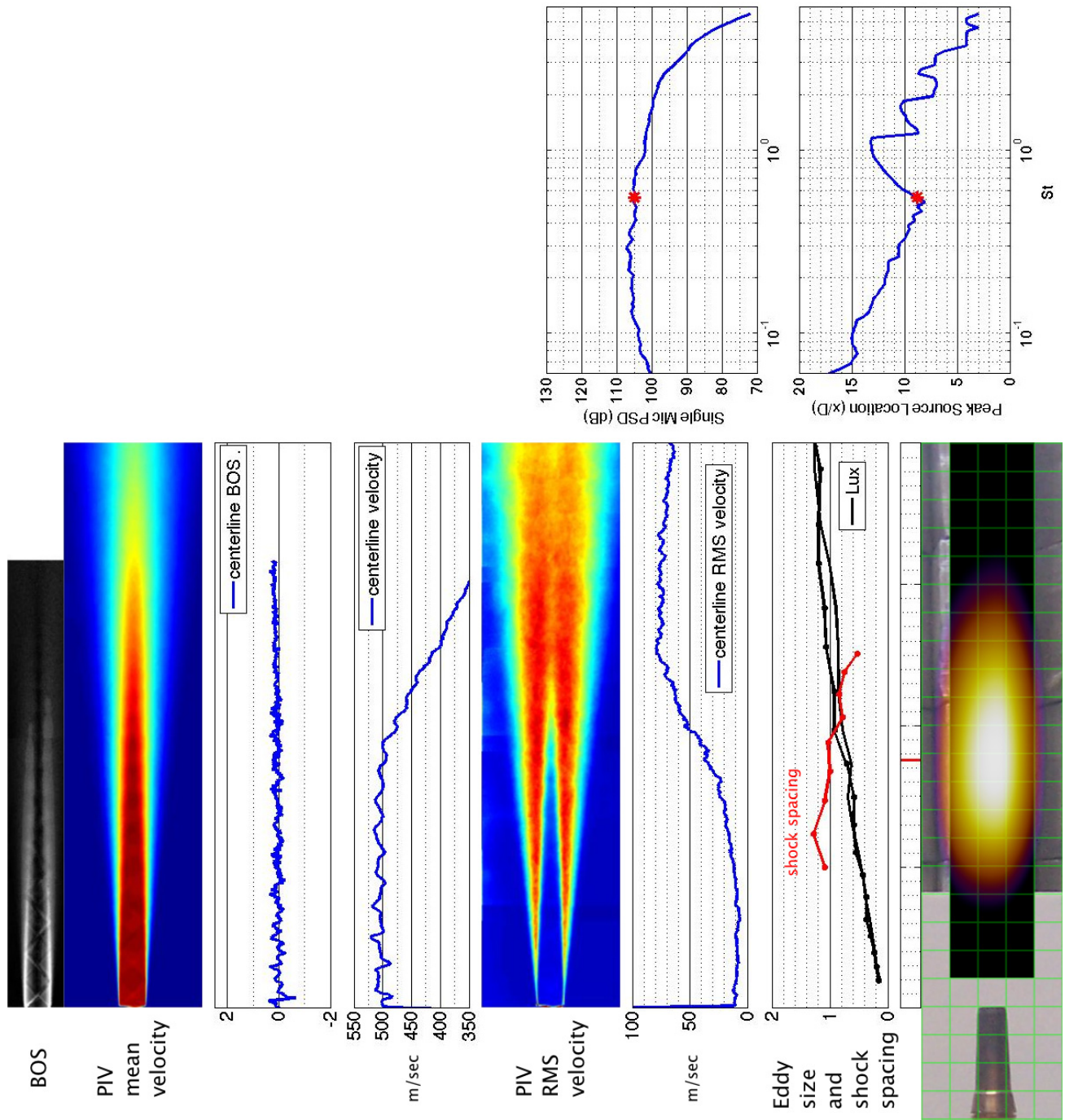
Figure 217.—SMC016; ideally-expanded; set point 11610; Mj=1.50; Mjdesign=1.50; St=0.550.
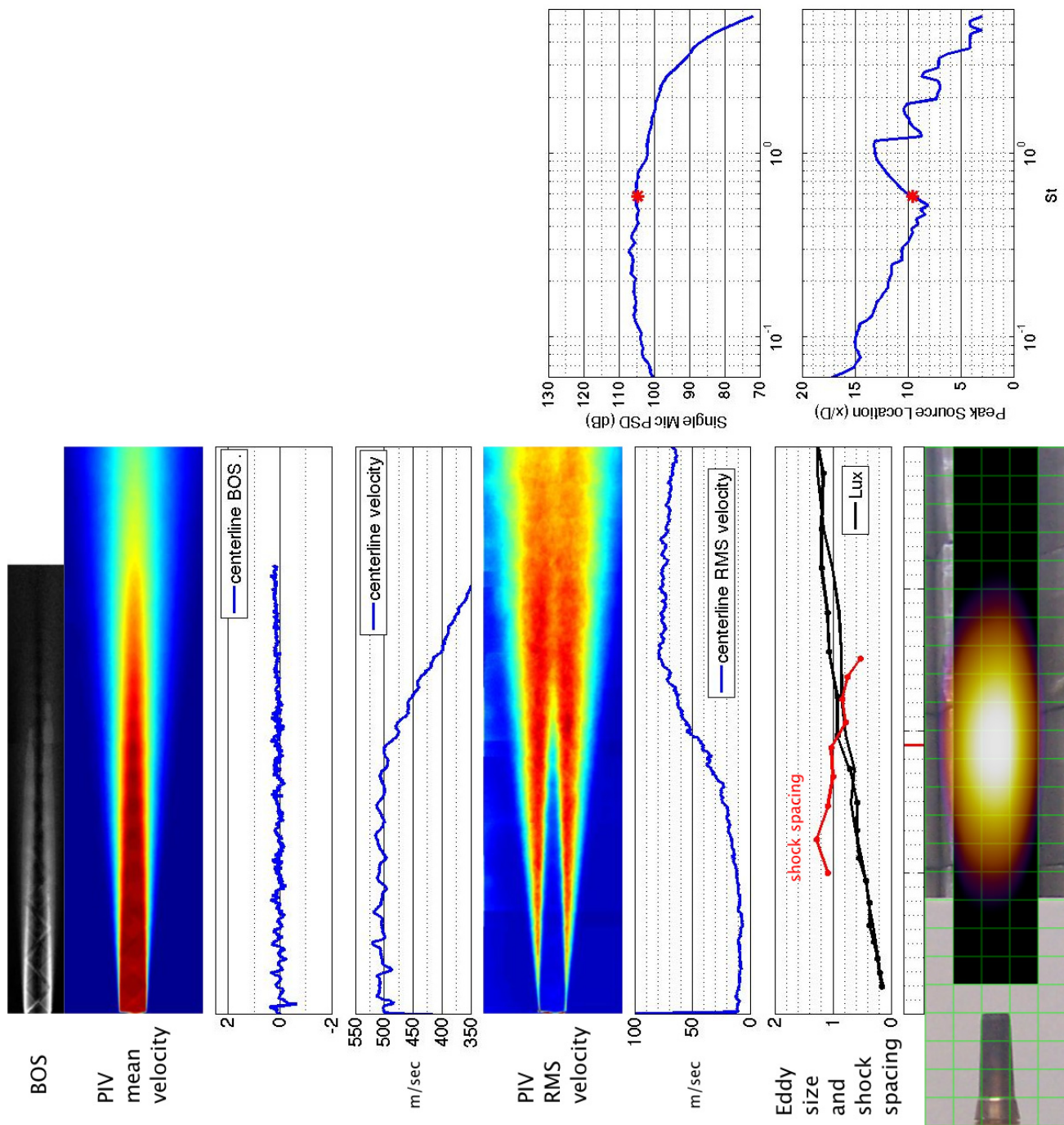
Figure 218.—SMC016; ideally-expanded; set point 11610; Mj=1.50; Mjdesign=1.50; St=0.582.
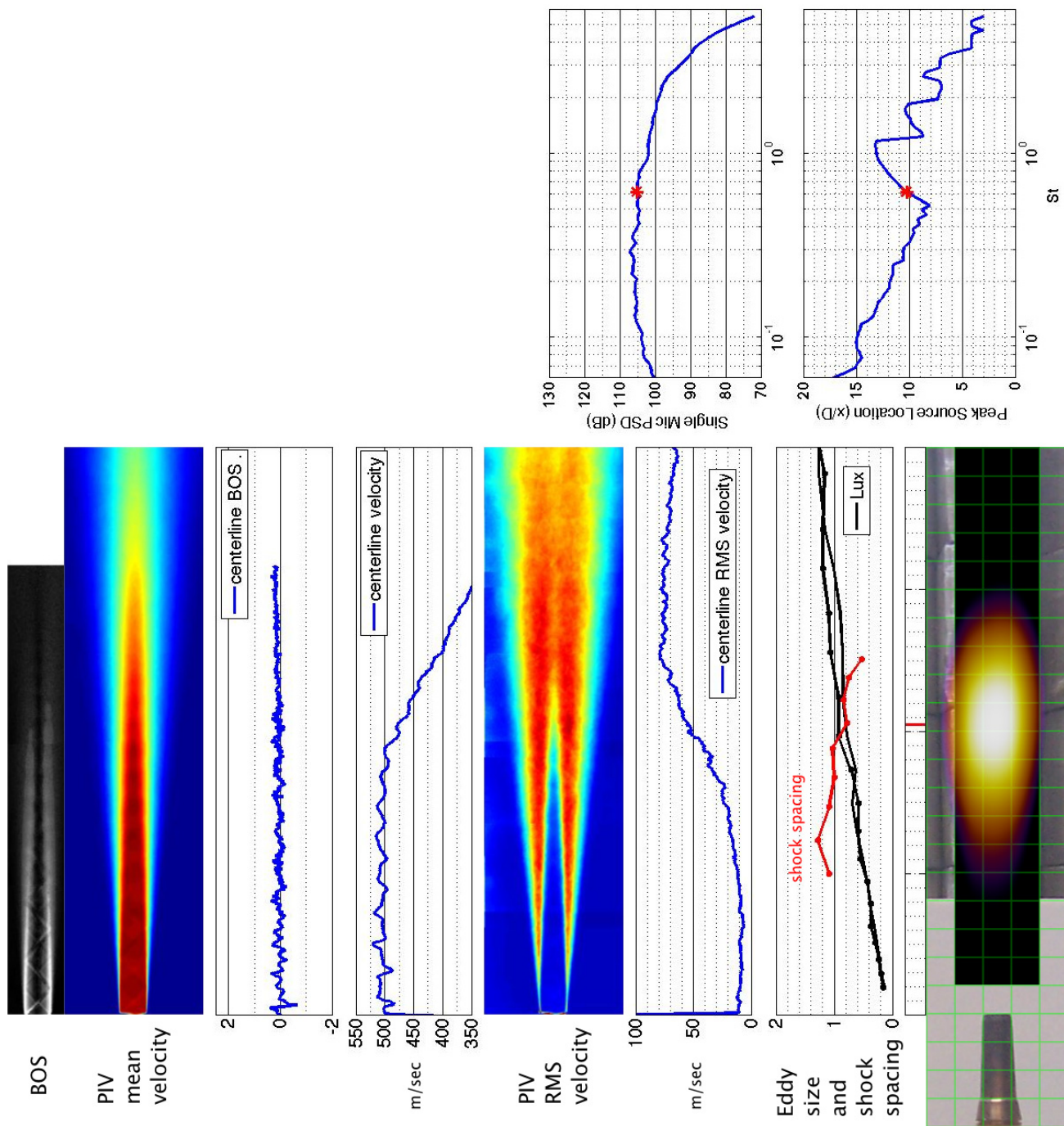
Figure 219.—SMC016; ideally-expanded; set point 11610; Mj=1.50; Mjdesign=1.50; St=0.615.
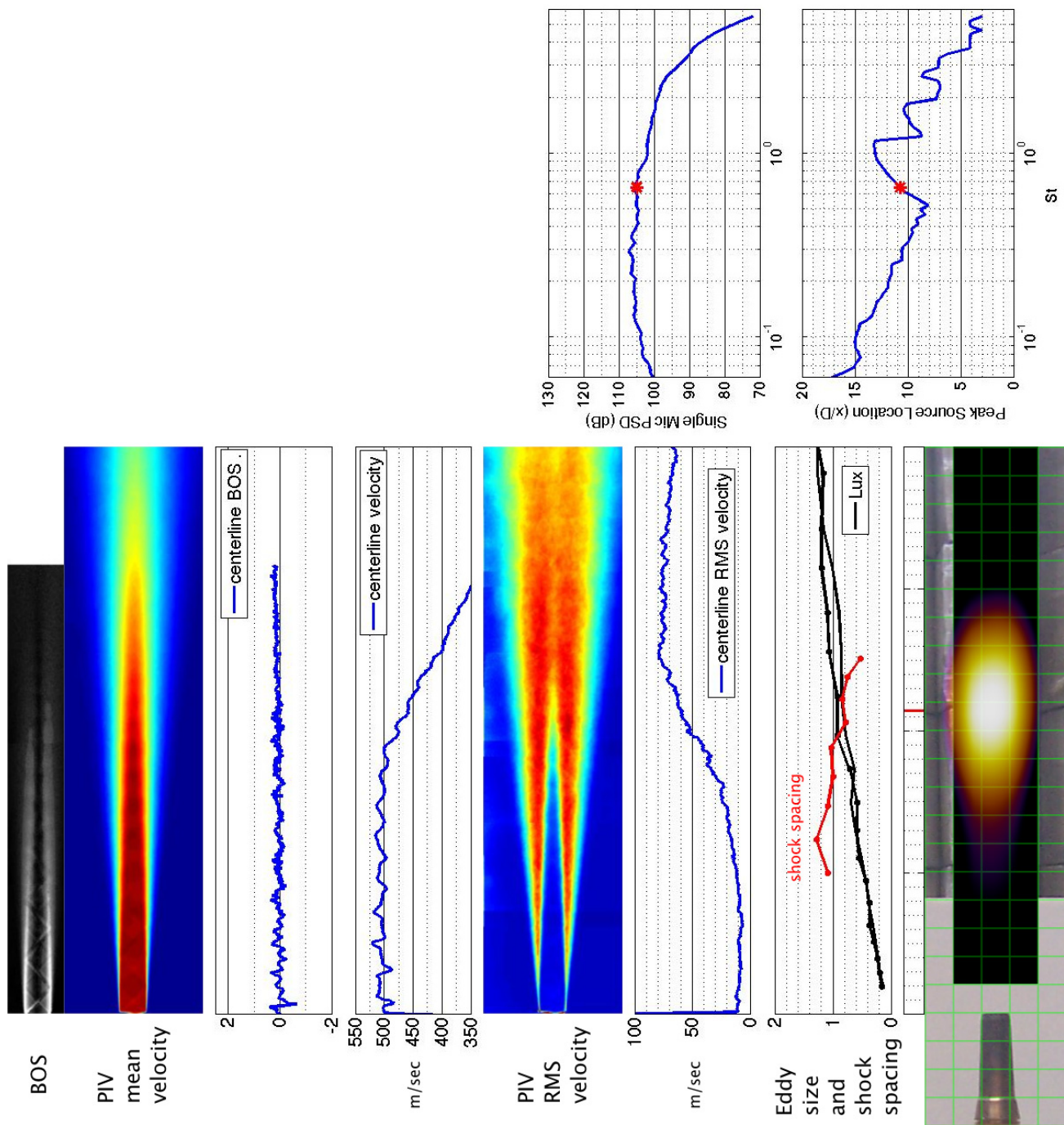
Figure 220.—SMC016; ideally-expanded; set point 11610; Mj=1.50; Mjdesign=1.50; St=0.651.
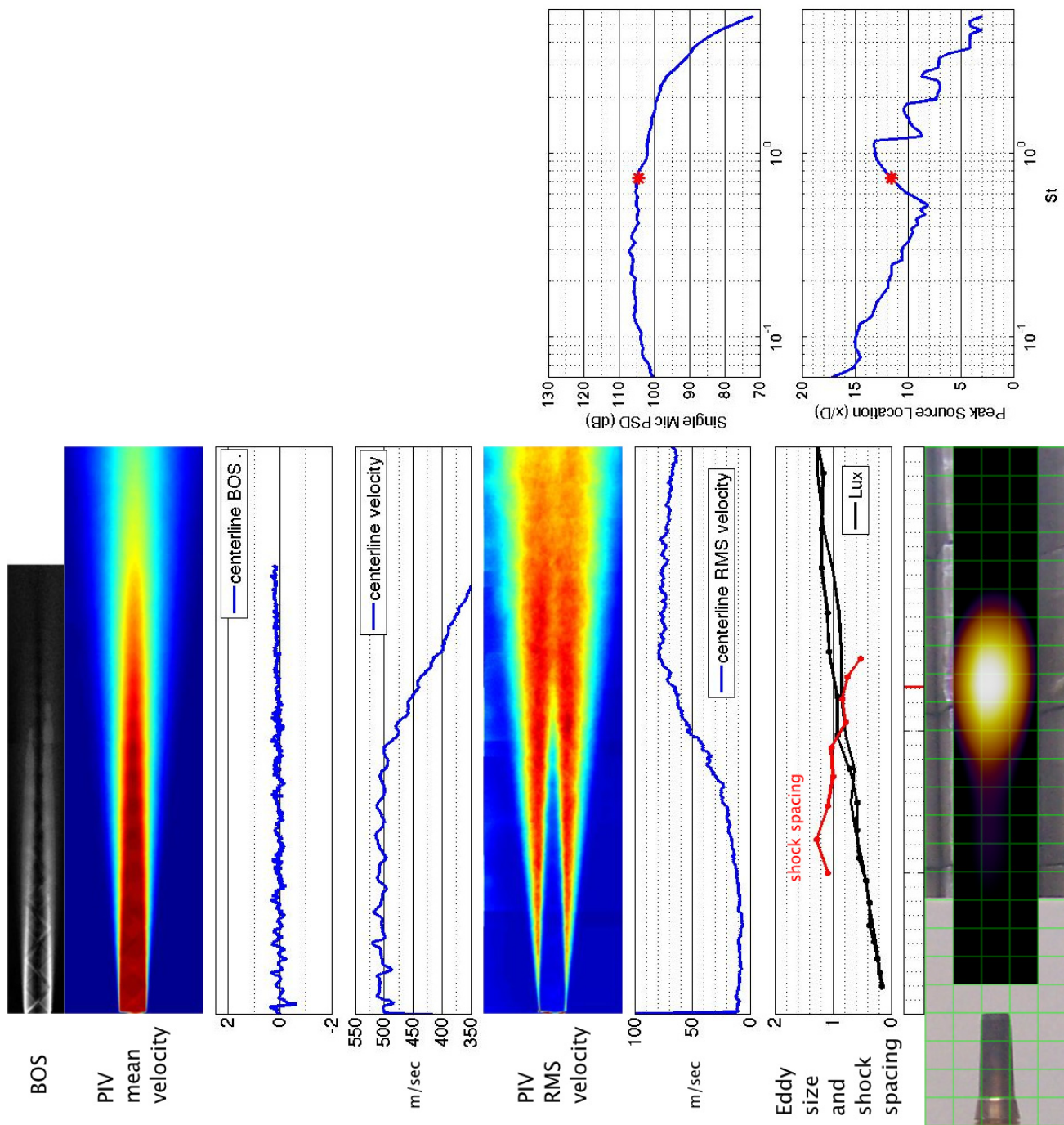
Figure 221.—SMC016; ideally-expanded; set point 11610; Mj=1.50; Mjdesign=1.50; St=0.731.
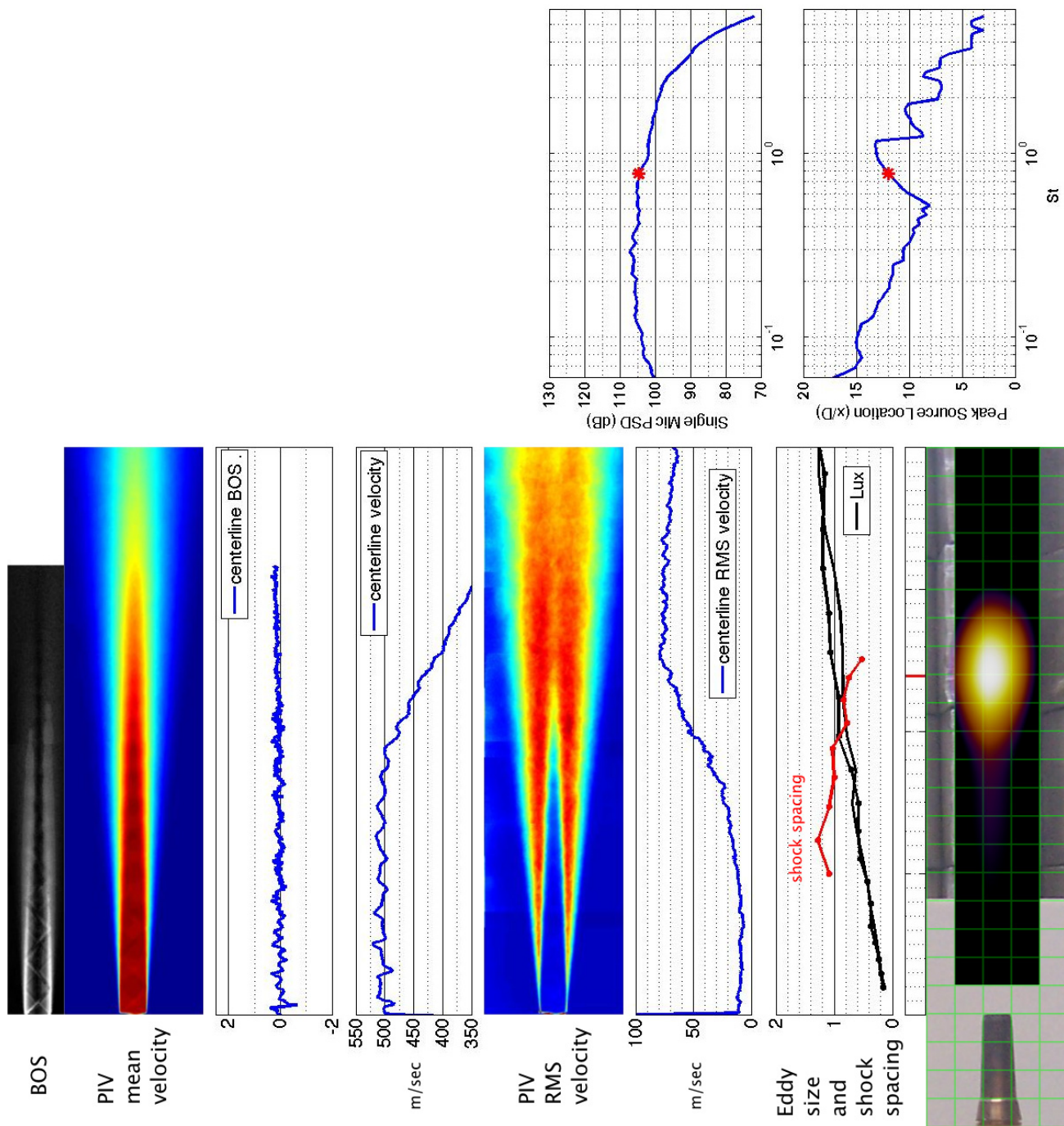
Figure 222.—SMC016; ideally-expanded; set point 11610; Mj=1.50; Mjdesign=1.50; St=0.775.
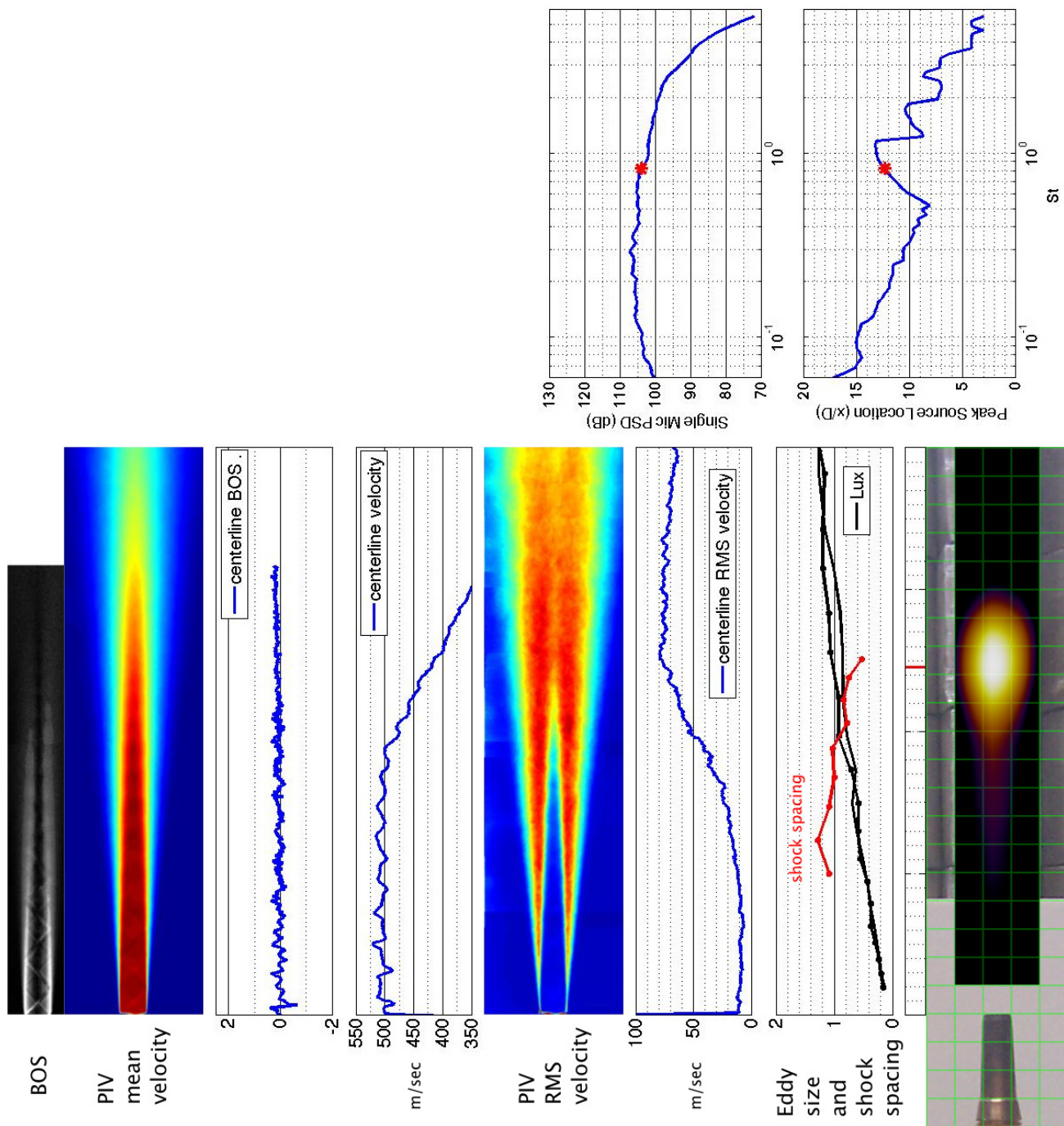
Figure 223.—SMC016; ideally-expanded; set point 11610; Mj=1.50; Mjdesign=1.50; St=0.822.
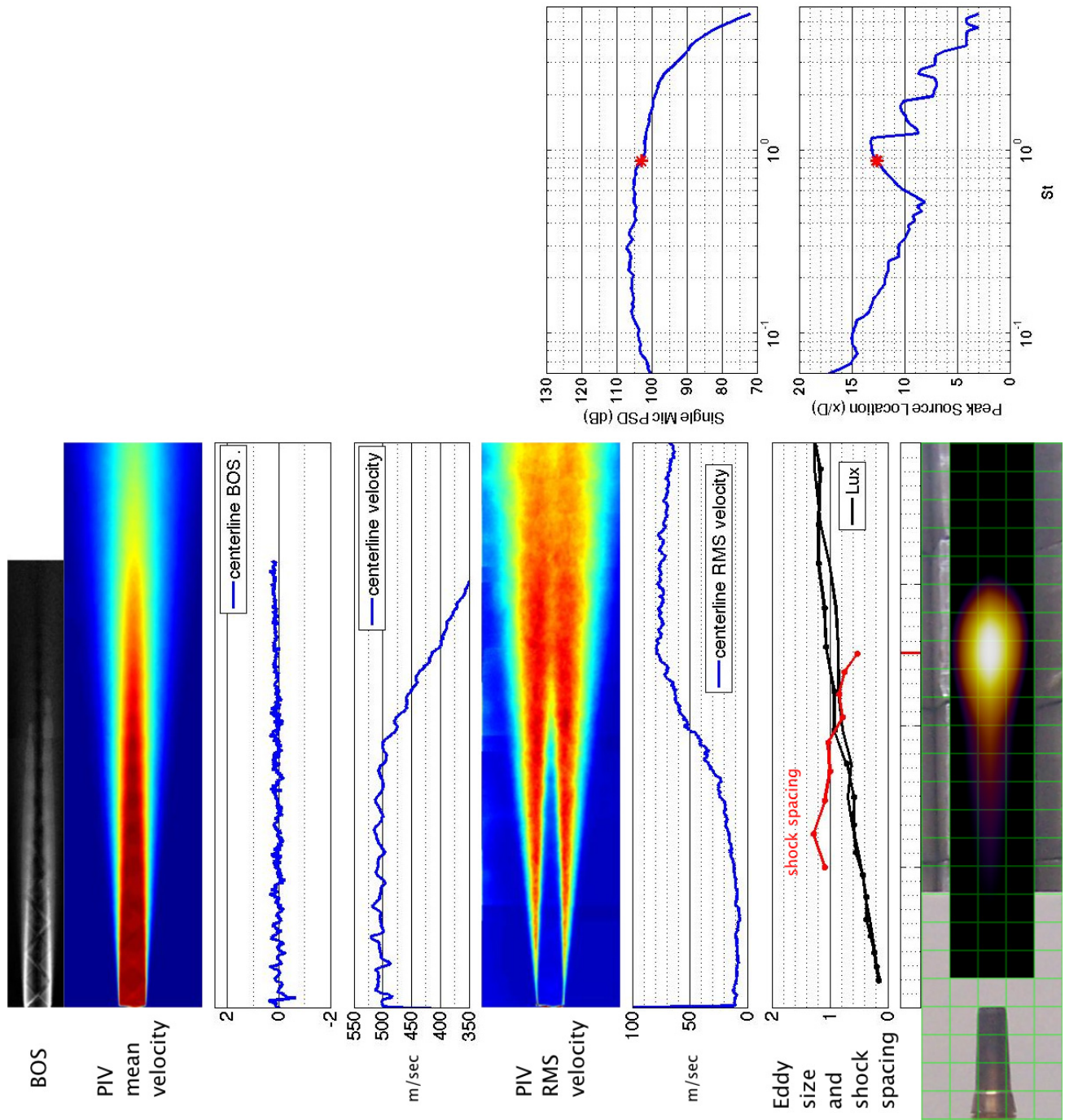
Figure 224.—SMC016; ideally-expanded; set point 11610; Mj=1.50; Mjdesign=1.50; St=0.873.
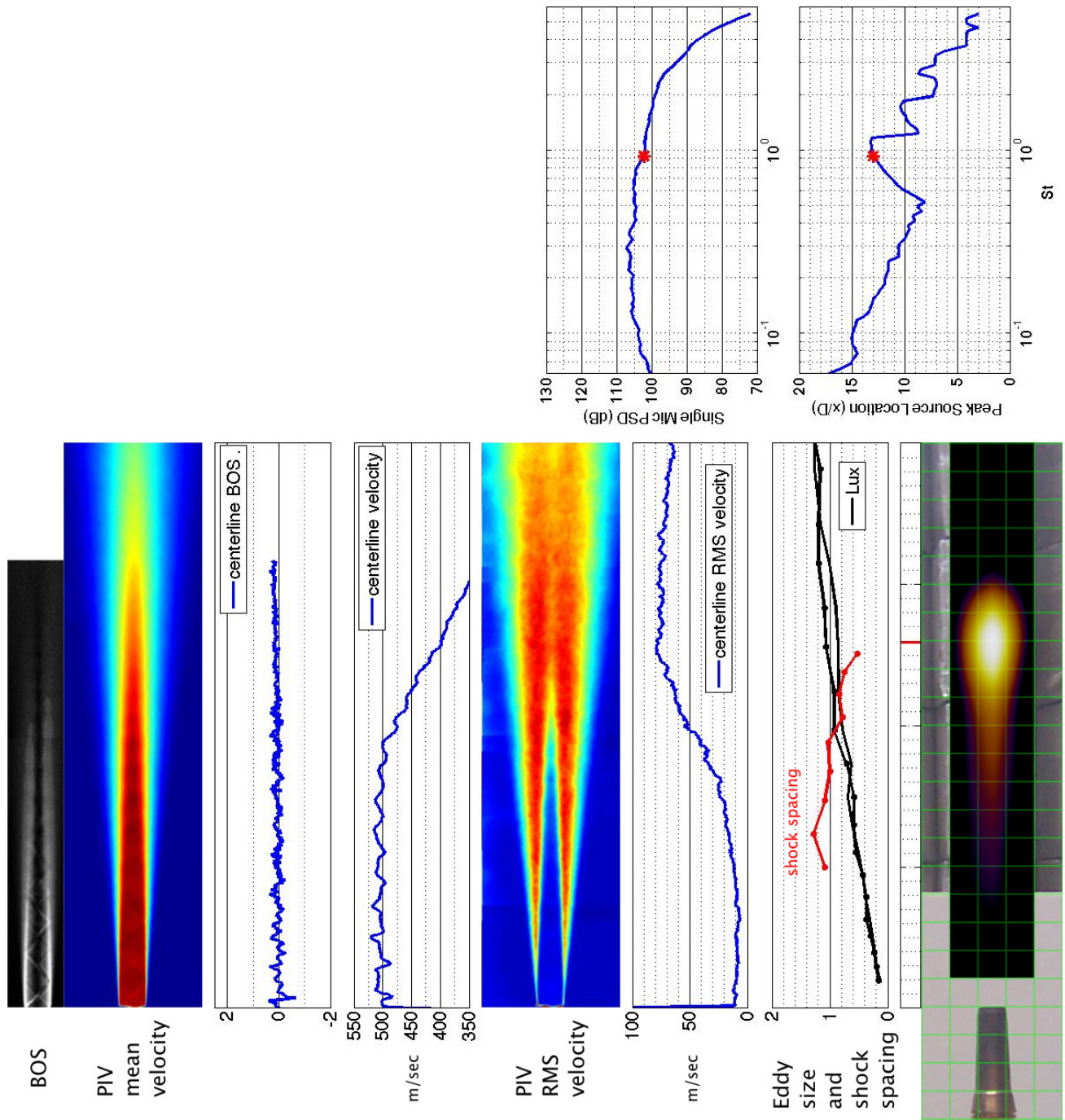
Figure 225.—SMC016; ideally-expanded; set point 11610; Mj=1.50; Mjdesign=1.50; St=0.927.
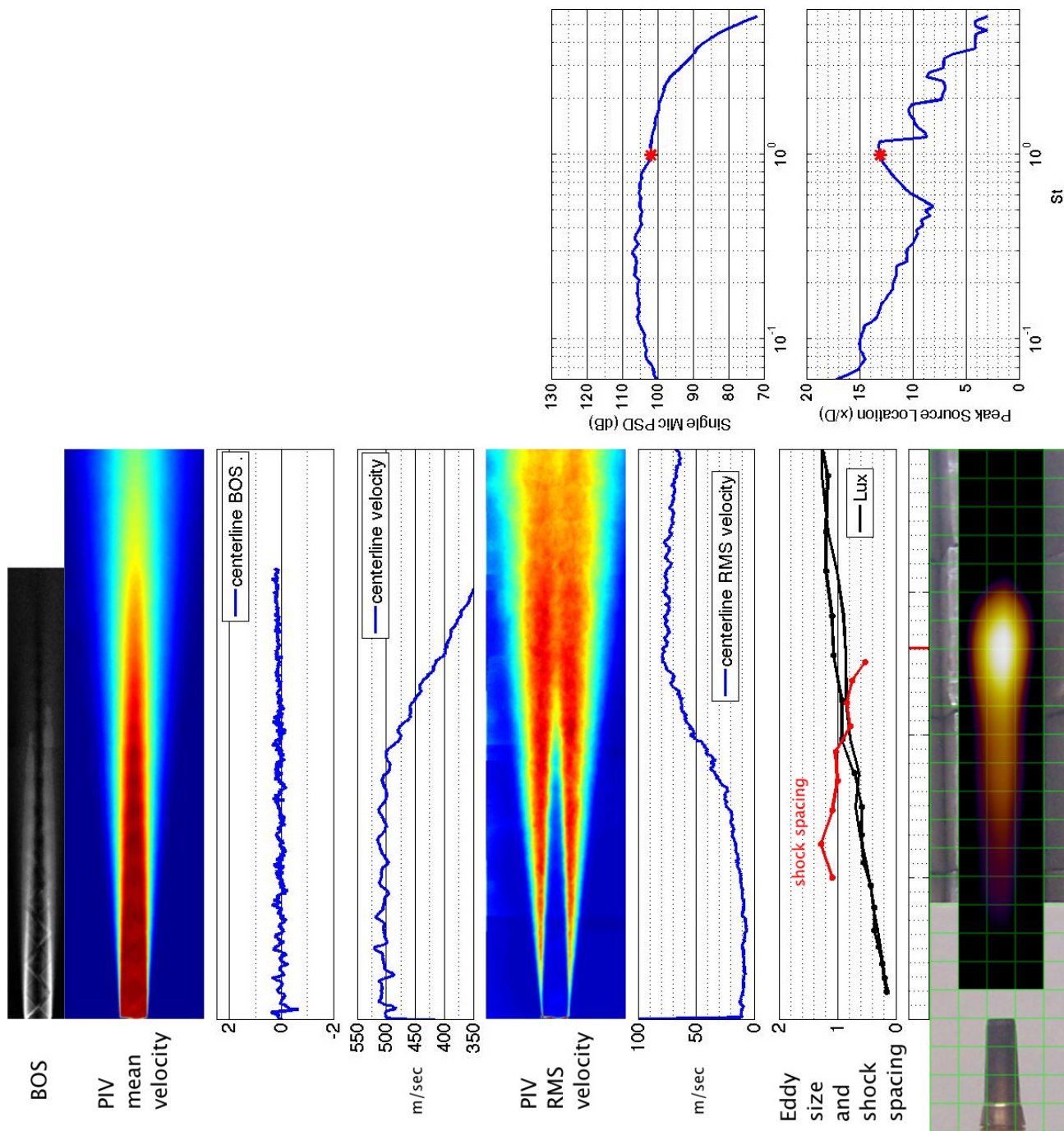
Figure 226.—SMC016; ideally-expanded; set point 11610; Mj=1.50; Mjdesign=1.50; St=0.983.
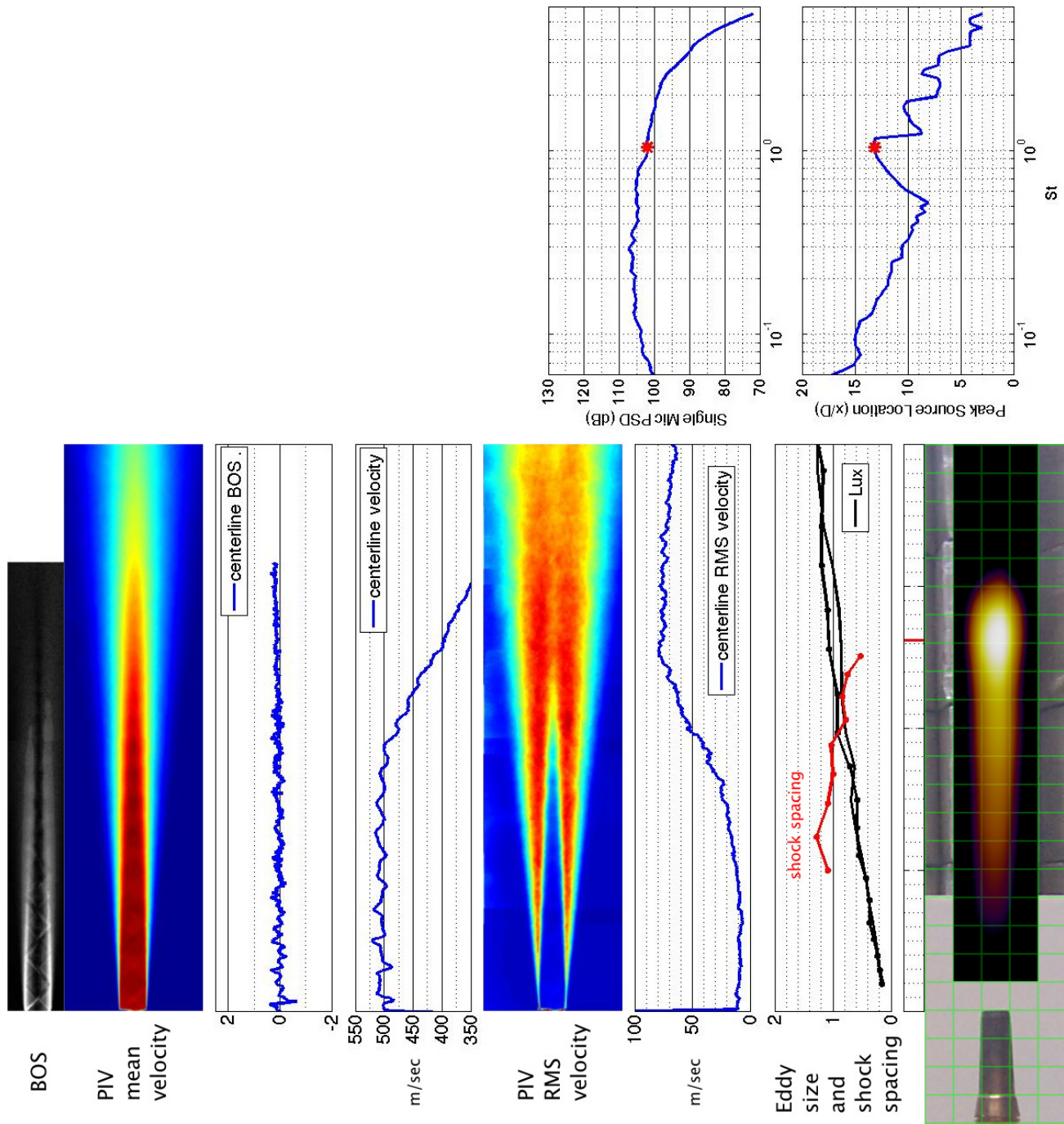
Figure 227.—SMC016; ideally-expanded; set point 11610; Mj=1.50; Mjdesign=1.50; St=1.040.
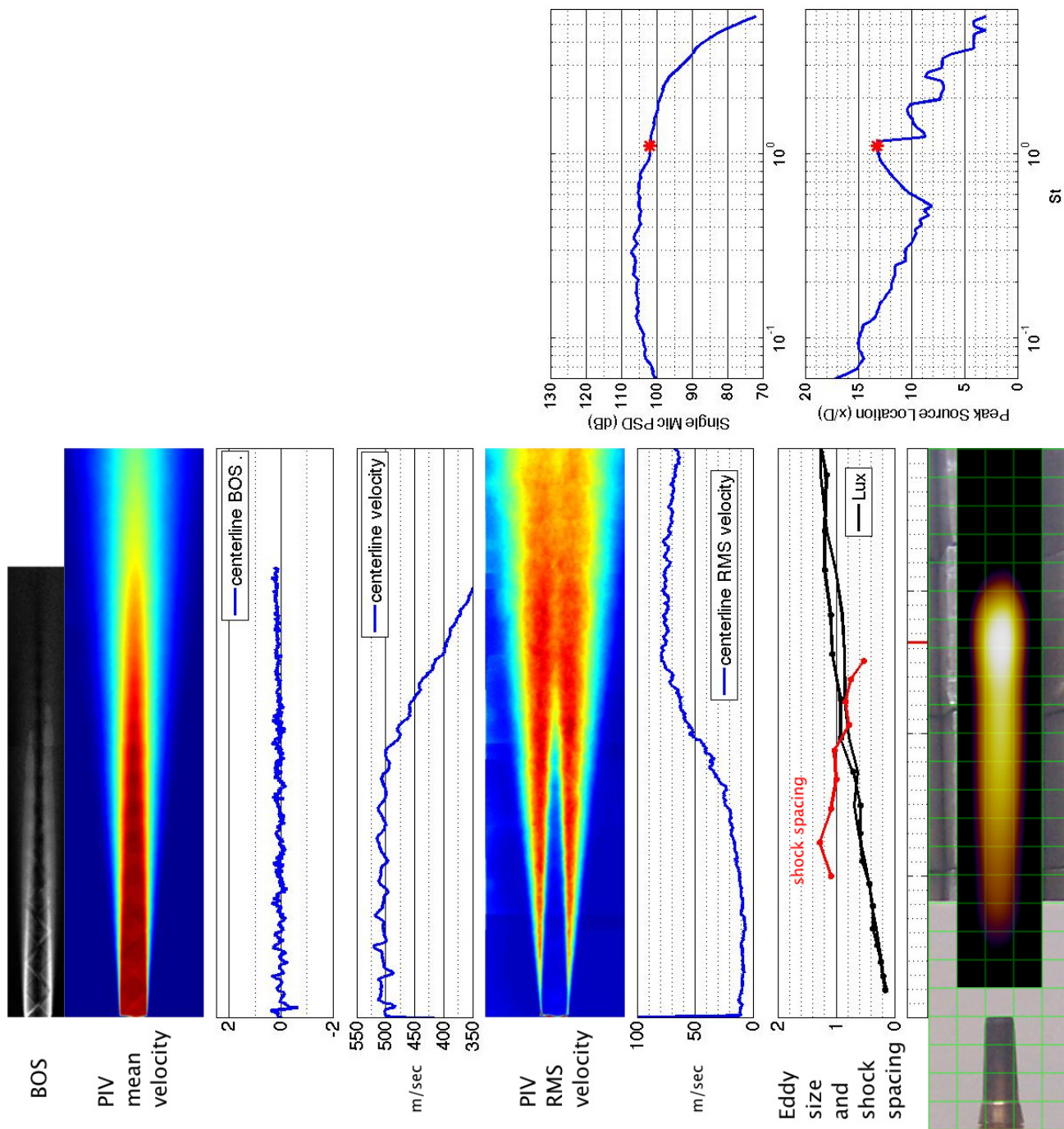
Figure 228.—SMC016; ideally-expanded; set point 11610; Mj=1.50; Mjdesign=1.50; St=1.100.
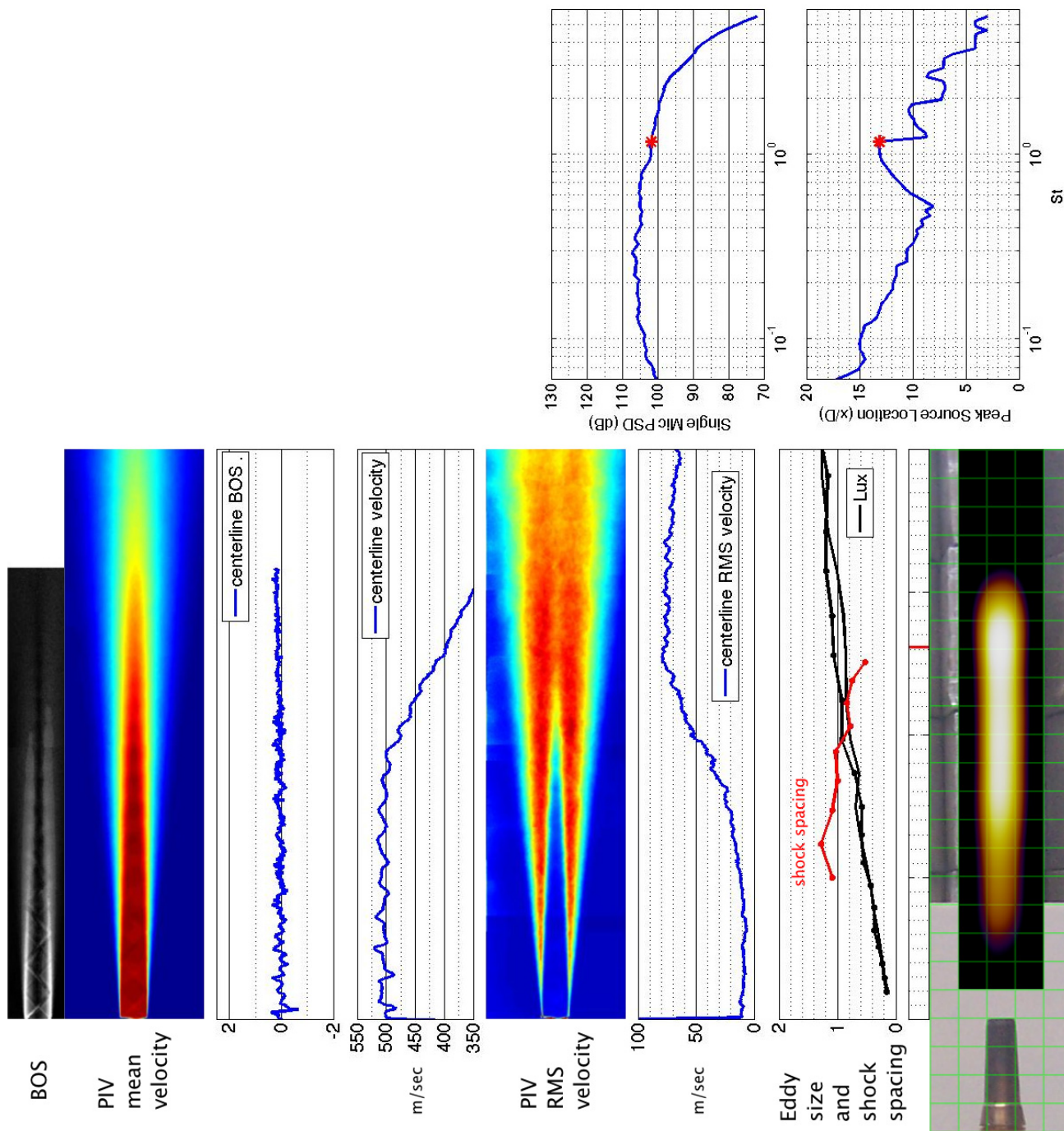
Figure 229.—SMC016; ideally-expanded; set point 11610; Mj=1.50; Mjdesign=1.50; St=1.163.
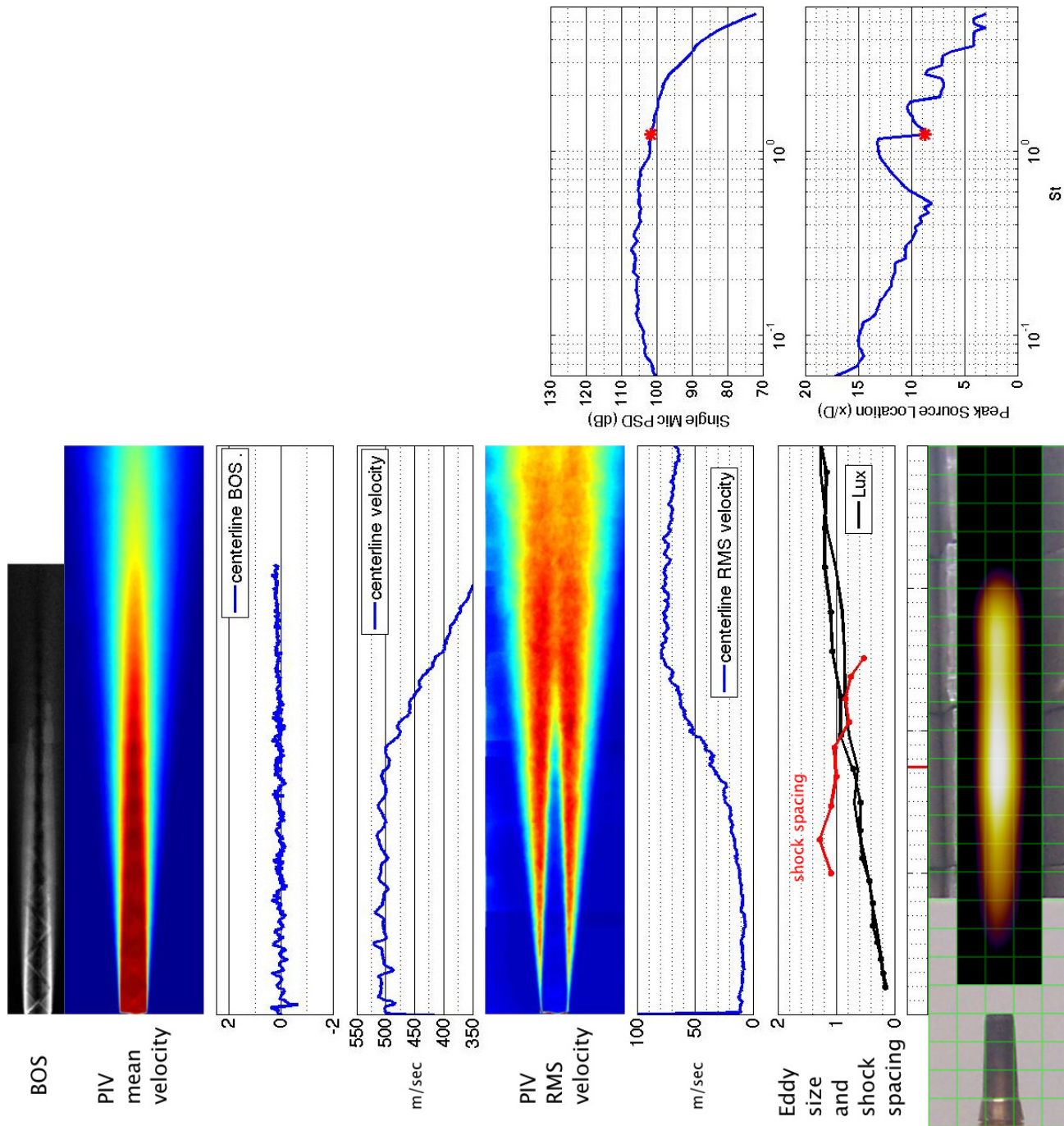
Figure 230.—SMC016; ideally-expanded; set point 11610; Mj=1.50; Mjdesign=1.50; St=1.230.
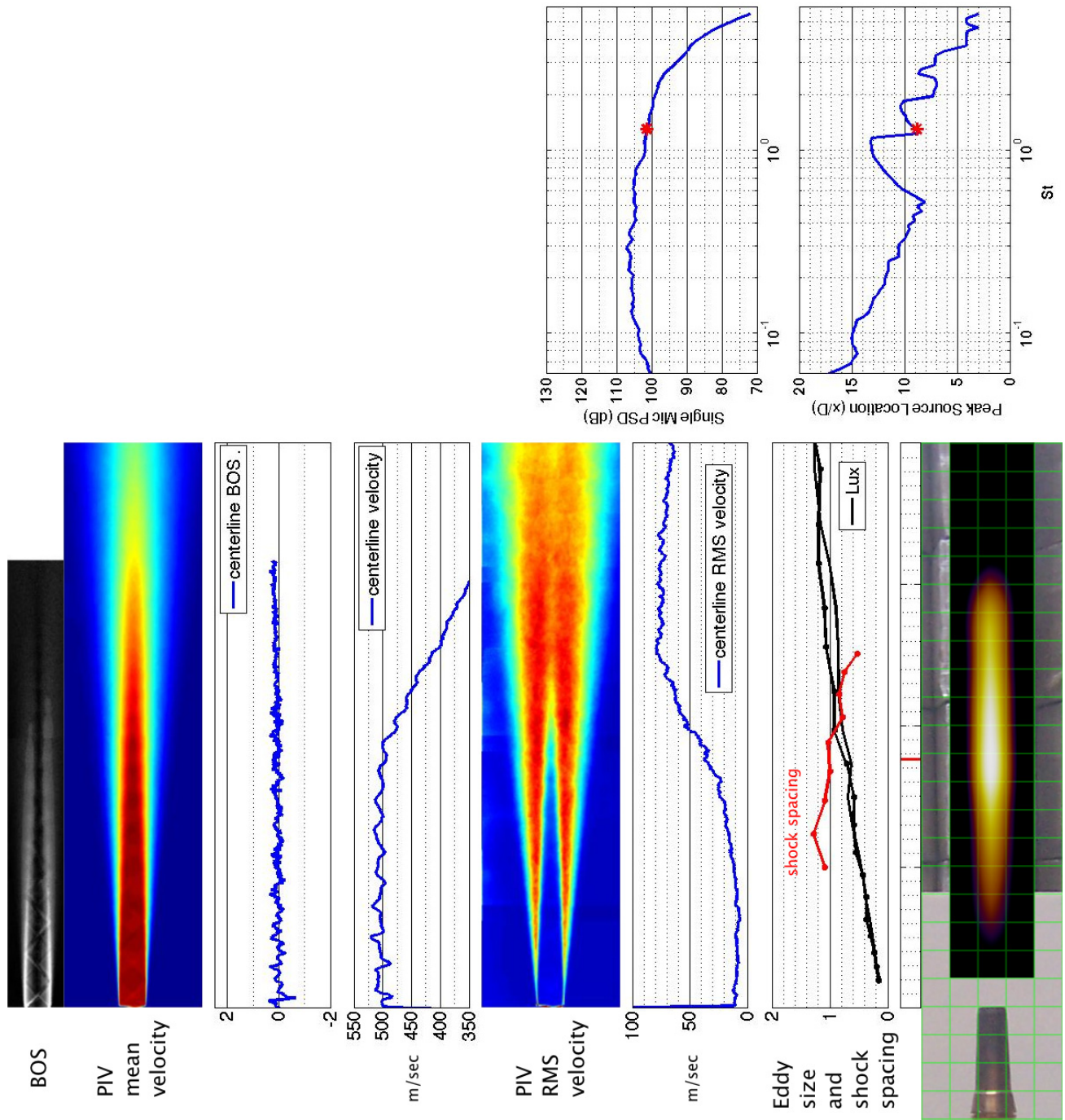
Figure 231.—SMC016; ideally-expanded; set point 11610; Mj=1.50; Mjdesign=1.50; St=1.300.
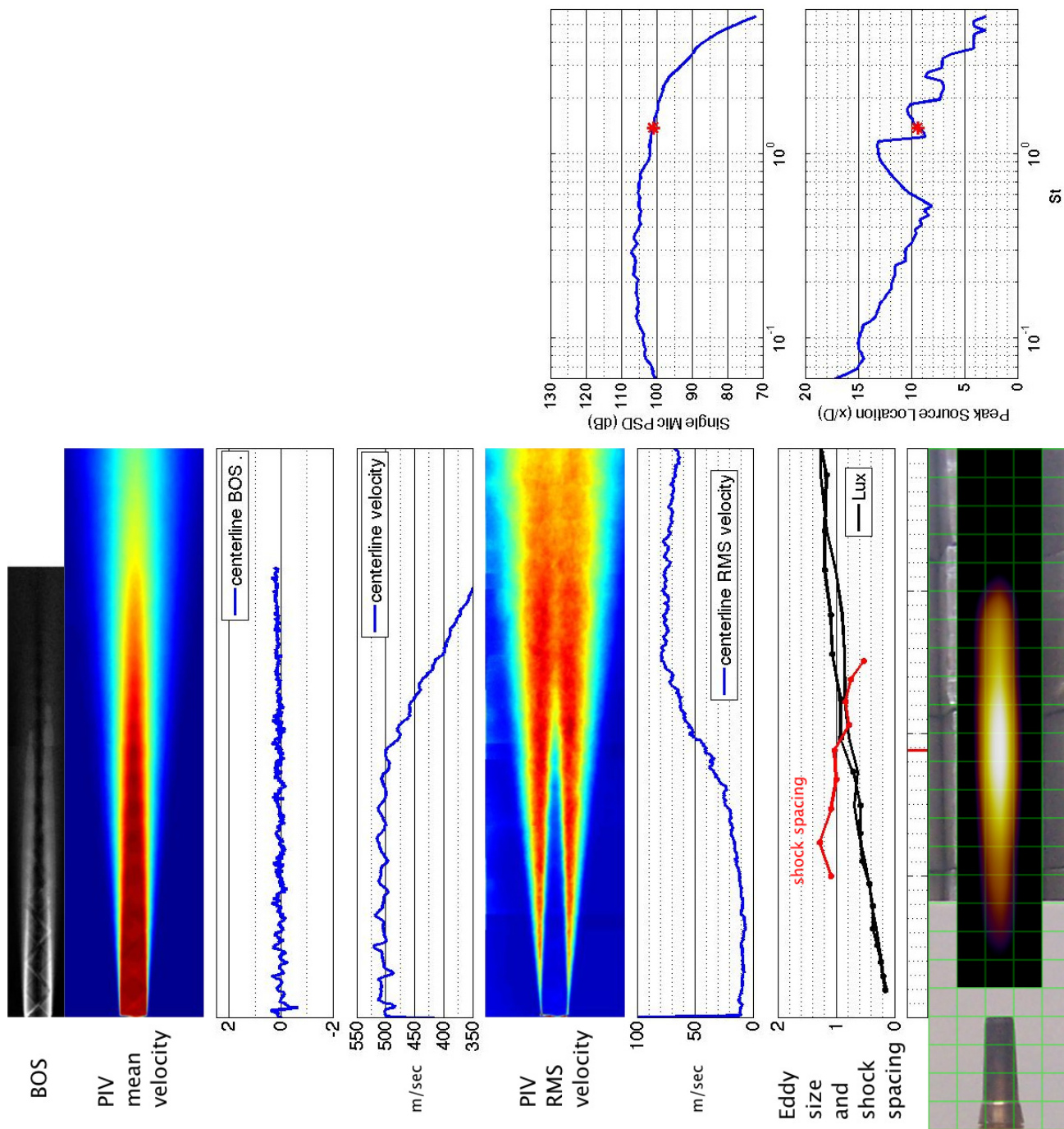
Figure 232.—SMC016; ideally-expanded; set point 11610; Mj=1.50; Mjdesign=1.50; St=1.375.
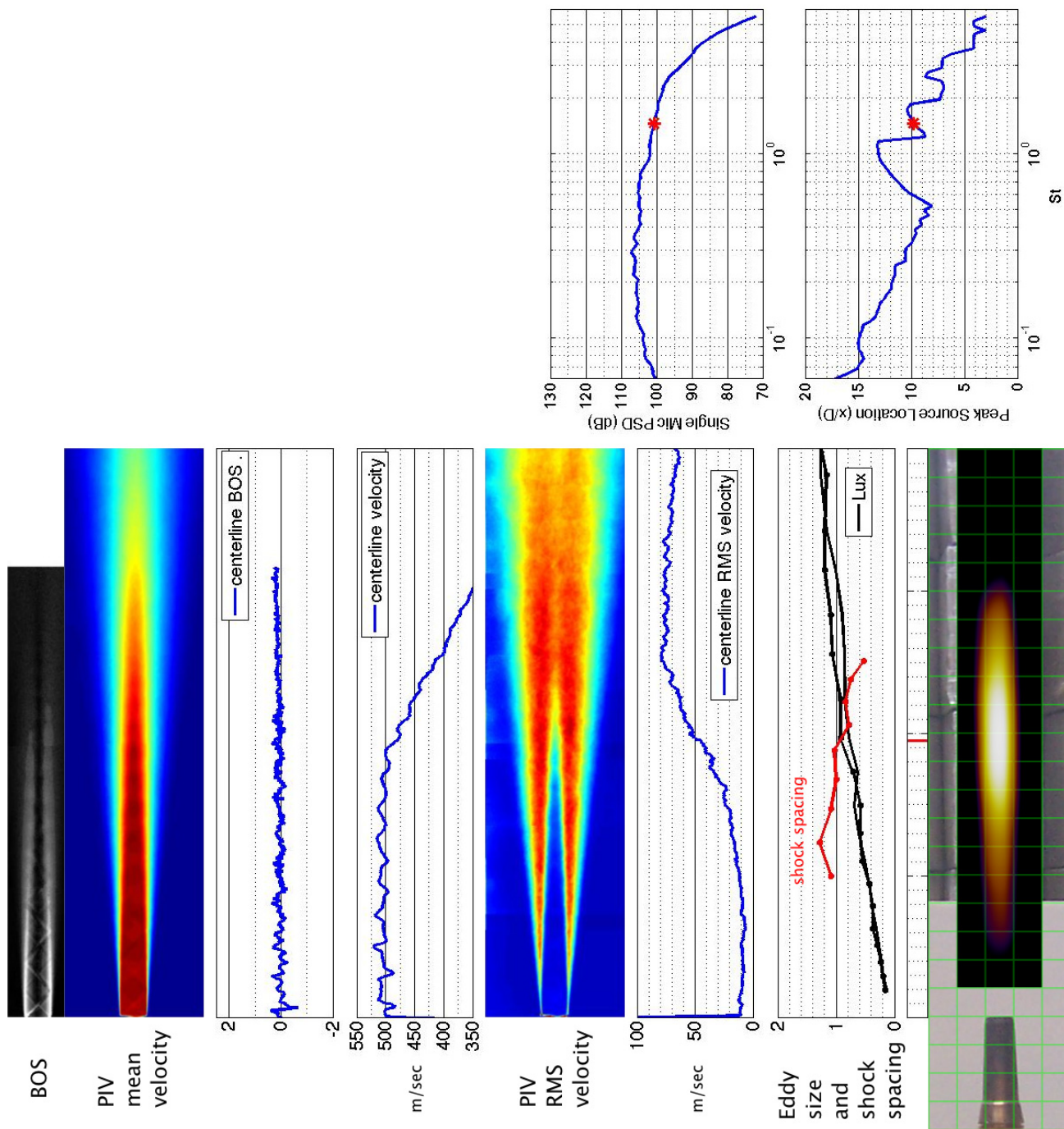
Figure 233.—SMC016; ideally-expanded; set point 11610; Mj=1.50; Mjdesign=1.50; St=1.454.
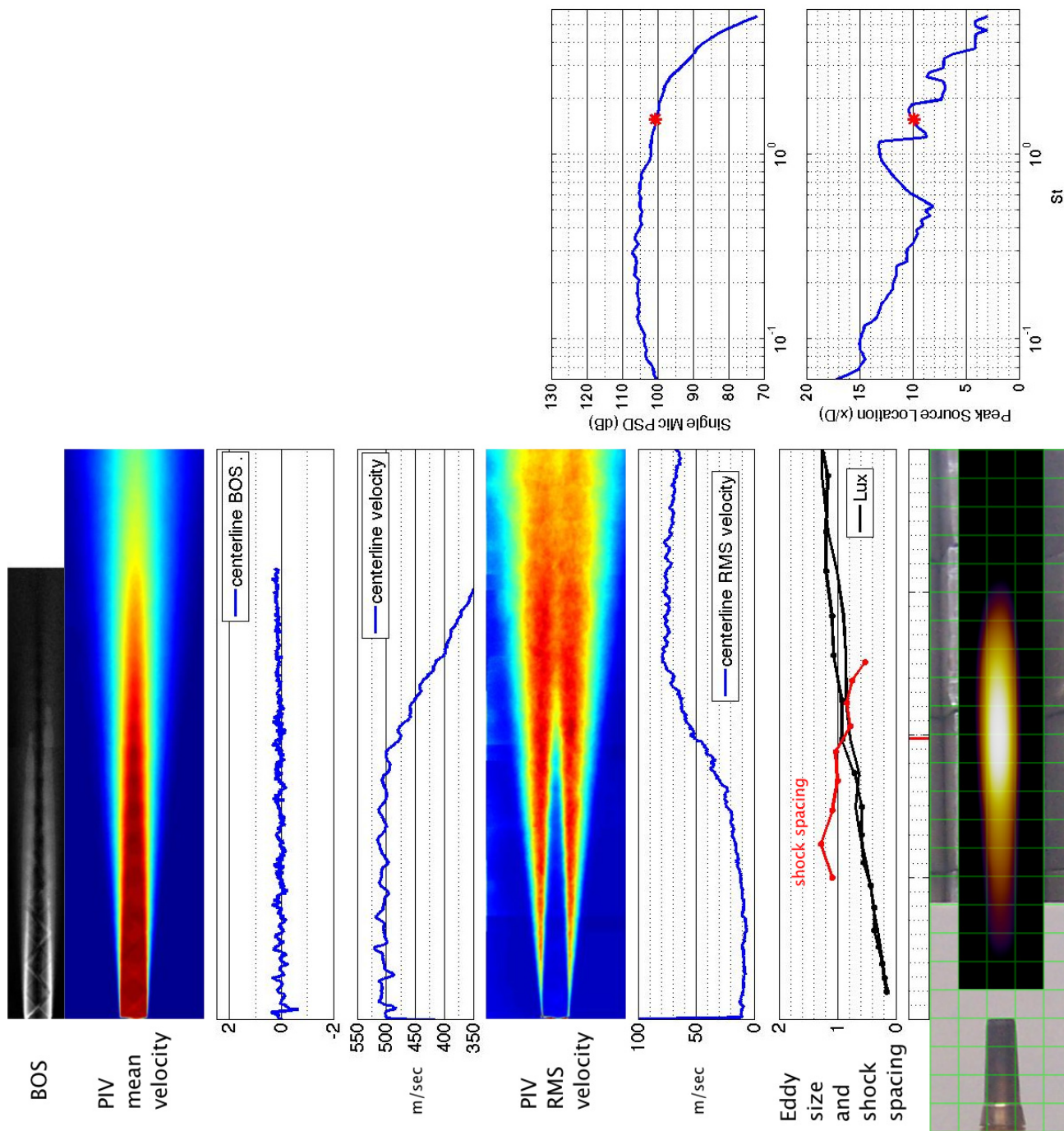
Figure 234.—SMC016; ideally-expanded; set point 11610; Mj=1.50; Mjdesign=1.50; St=1.540.
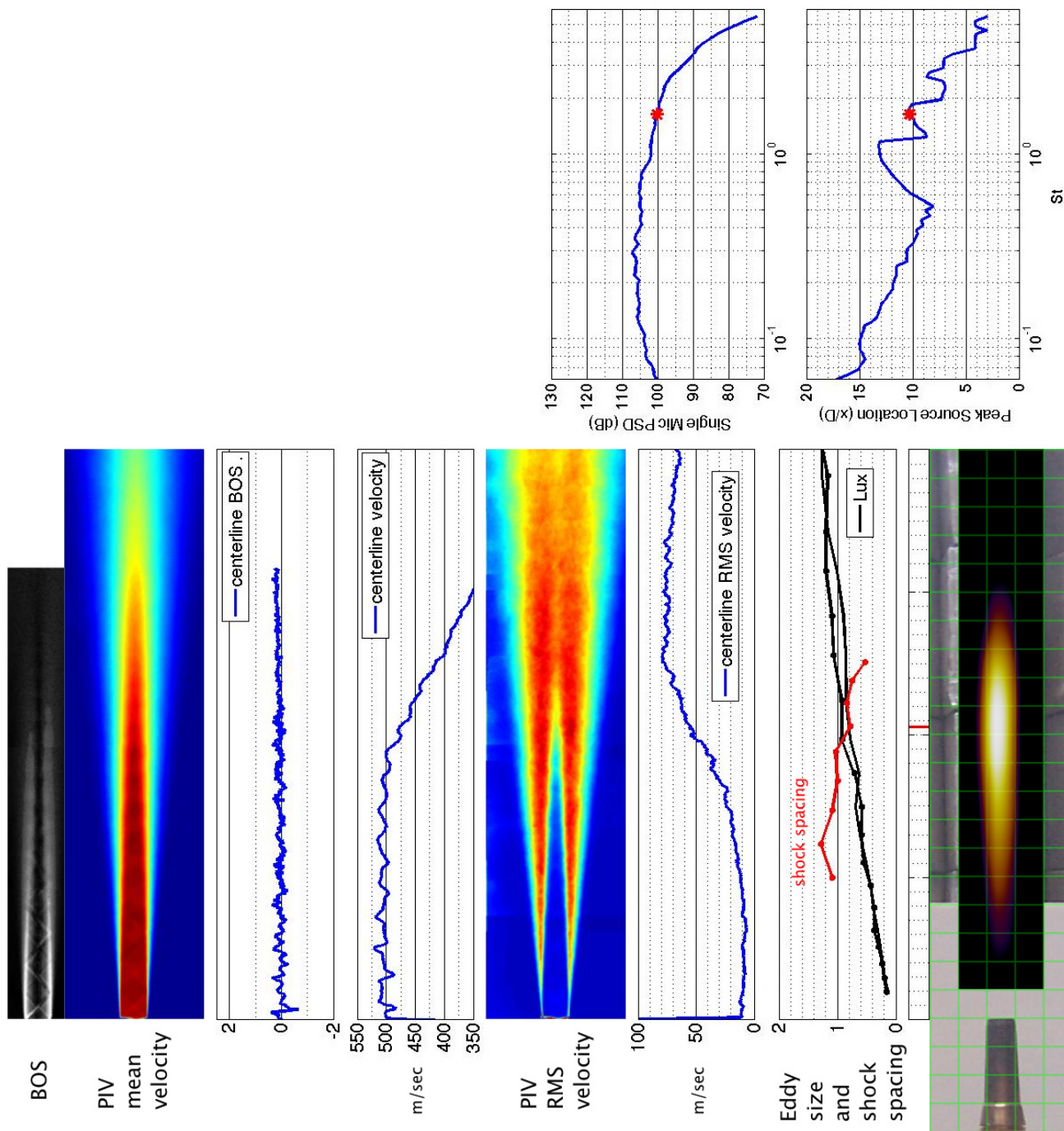
Figure 235.—SMC016; ideally-expanded; set point 11610; Mj=1.50; Mjdesign=1.50; St=1.635.
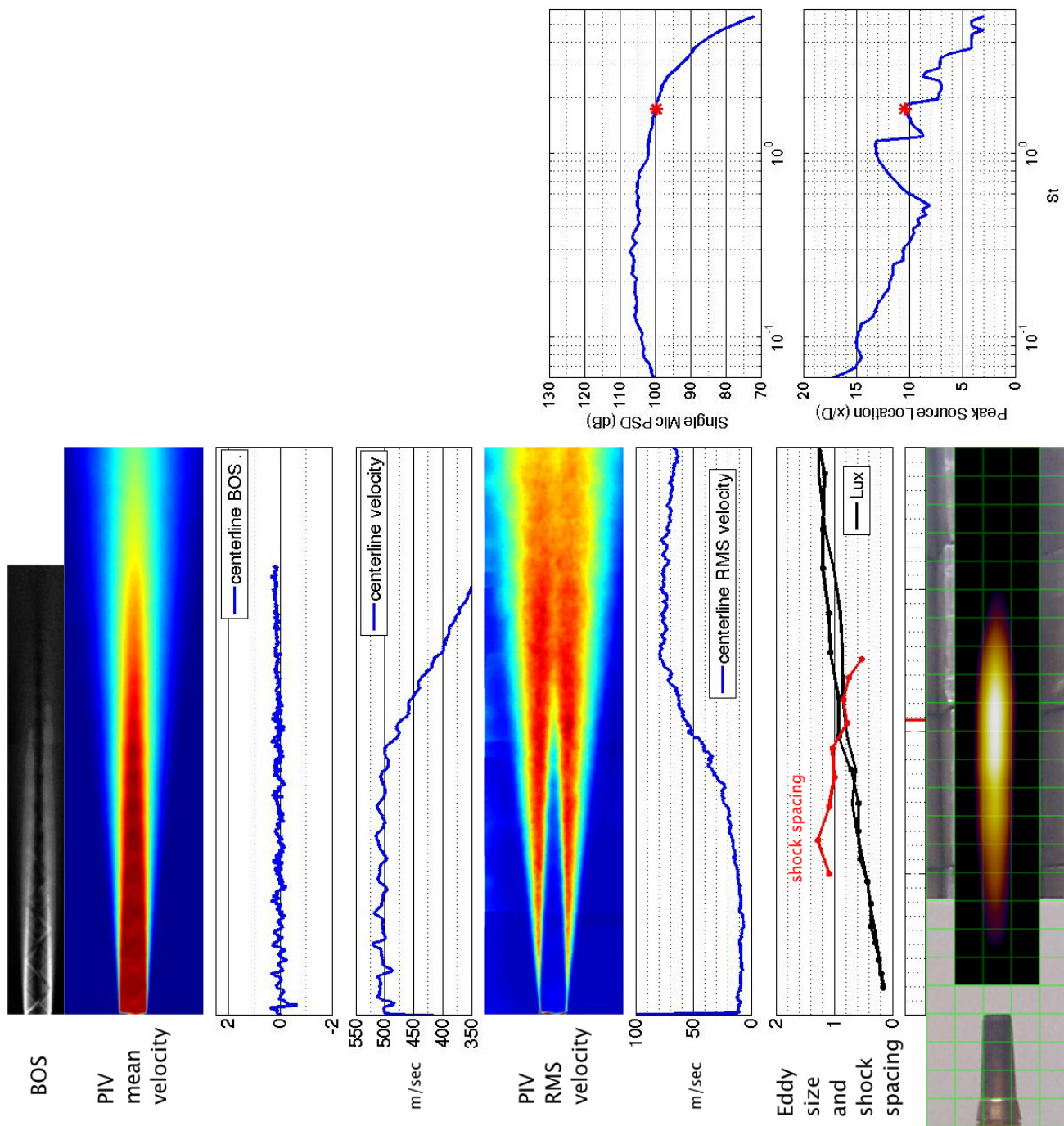
Figure 236.—SMC016; ideally-expanded; set point 11610; Mj=1.50; Mjdesign=1.50; St=1.739.
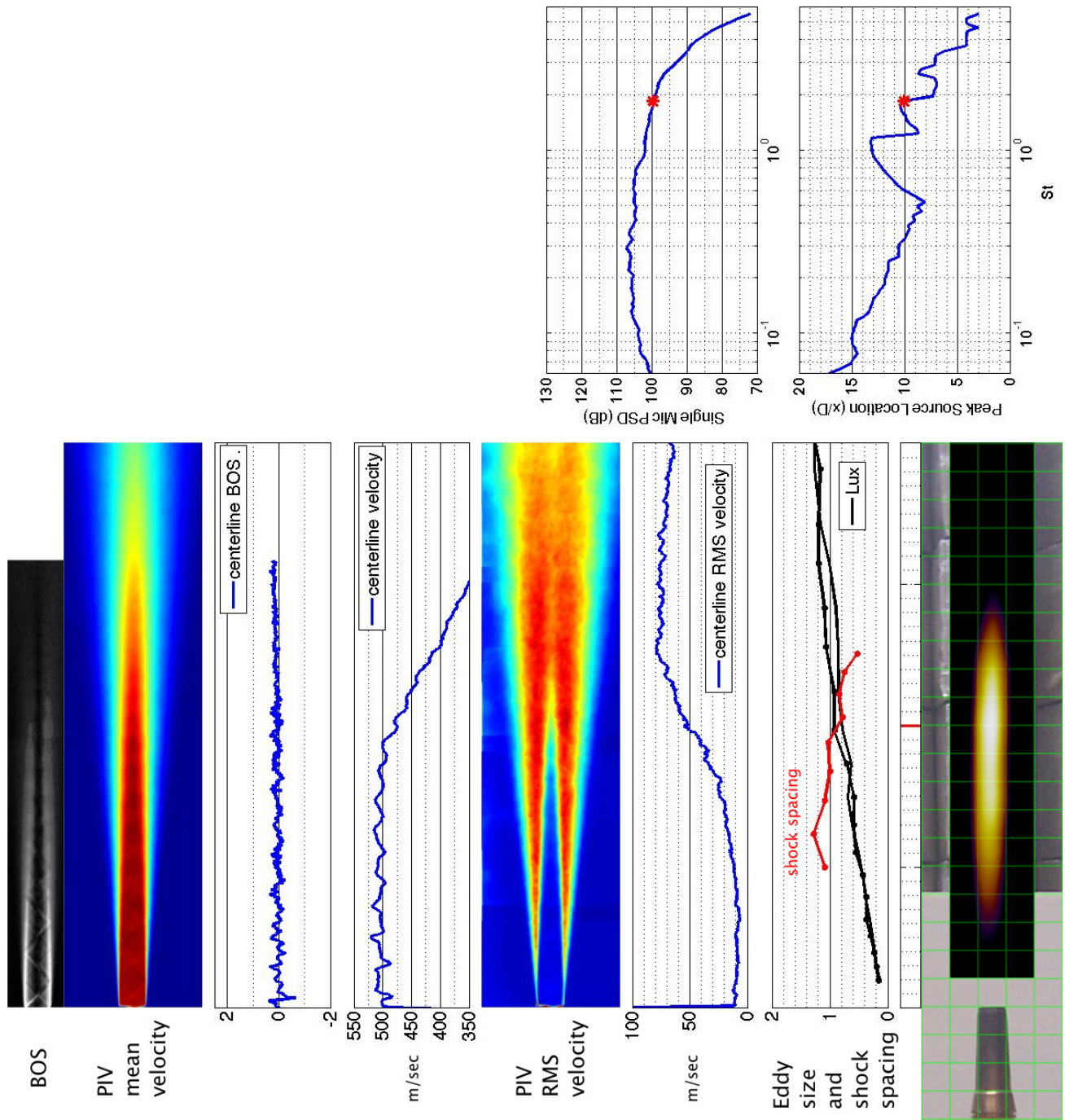
Figure 237.—SMC016; ideally-expanded; set point 11610; Mj=1.50; Mjdesign=1.50; St=1.850.
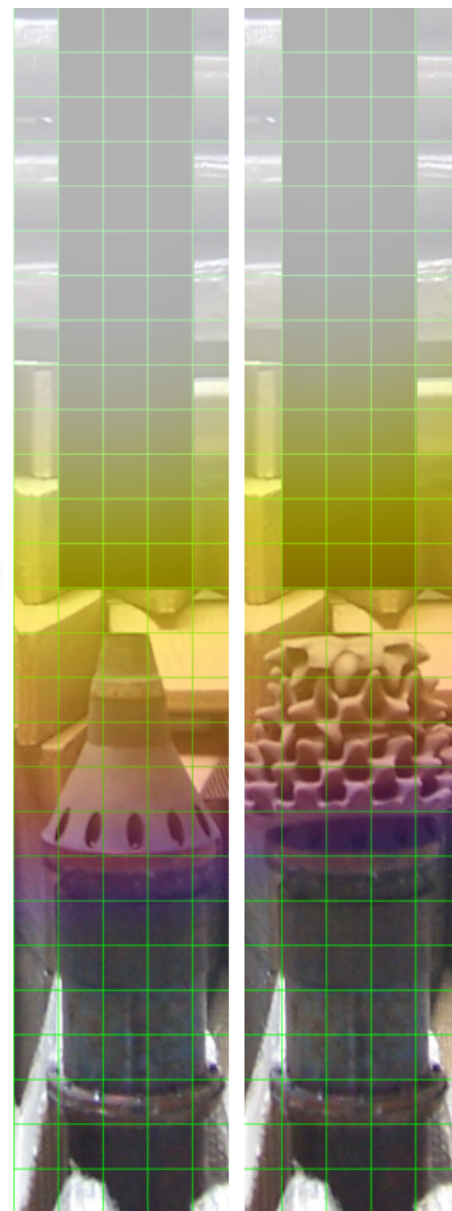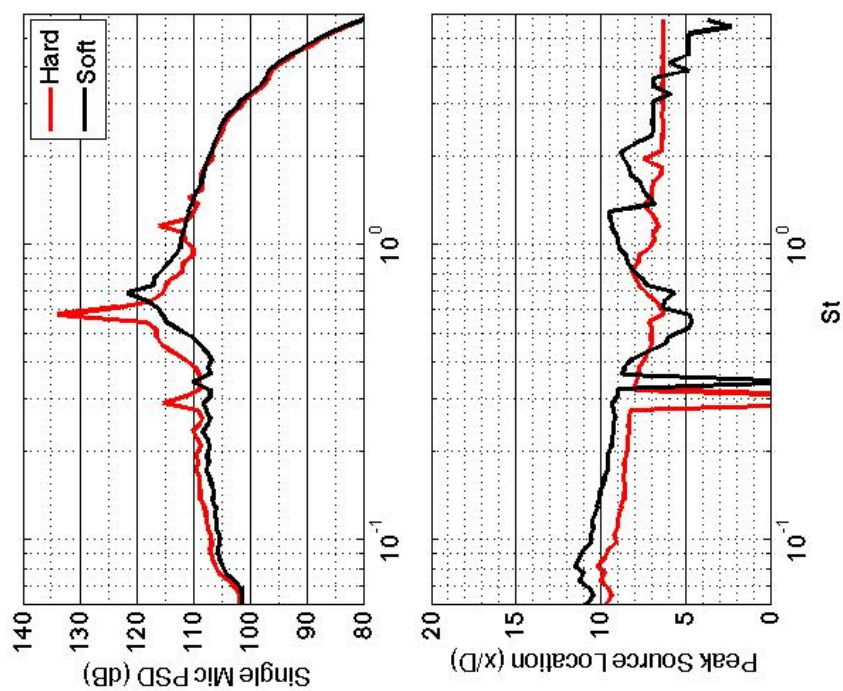
Figure 238.—SMC000; under-expanded; set point 9010; Mj=1.40; St=0.052.
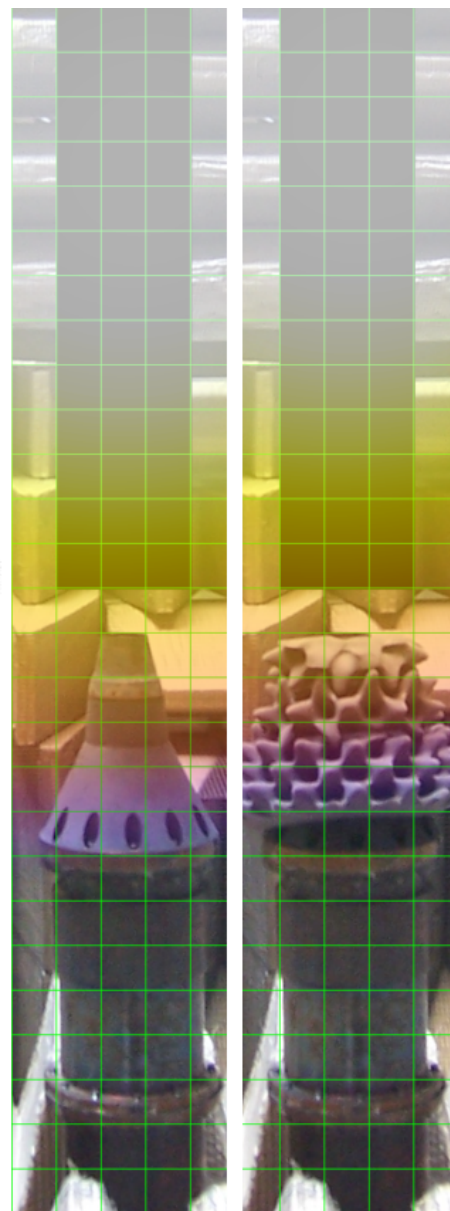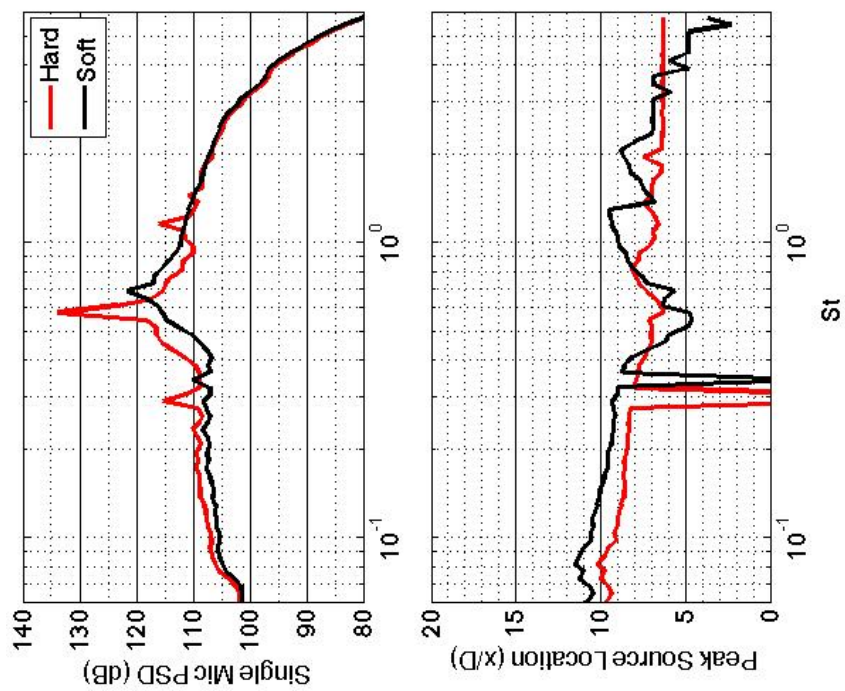
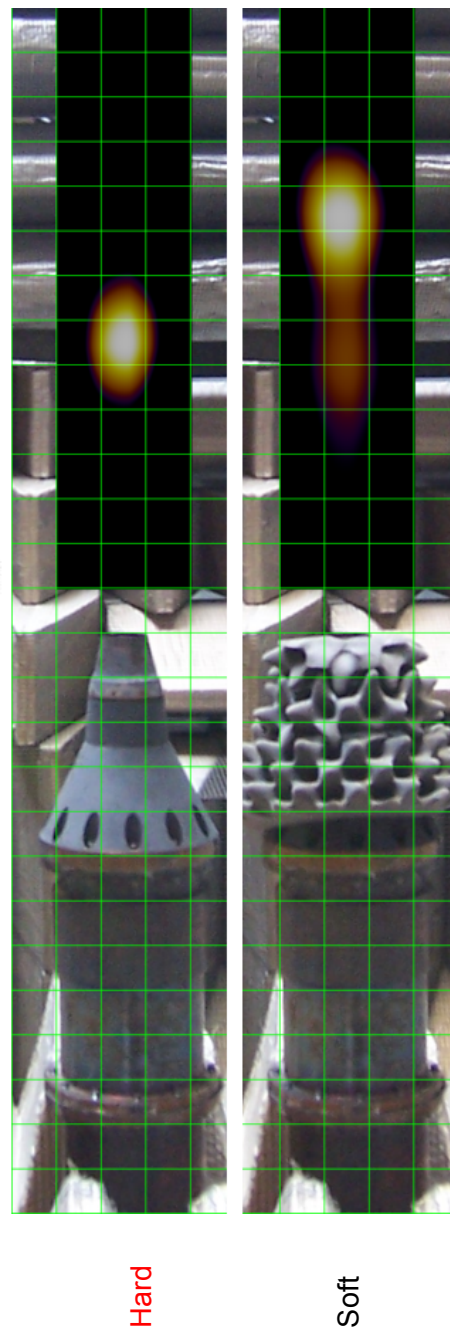Figure 239.—SMC000; under-expanded; set point 9010; Mj=1.40; St=0.055.
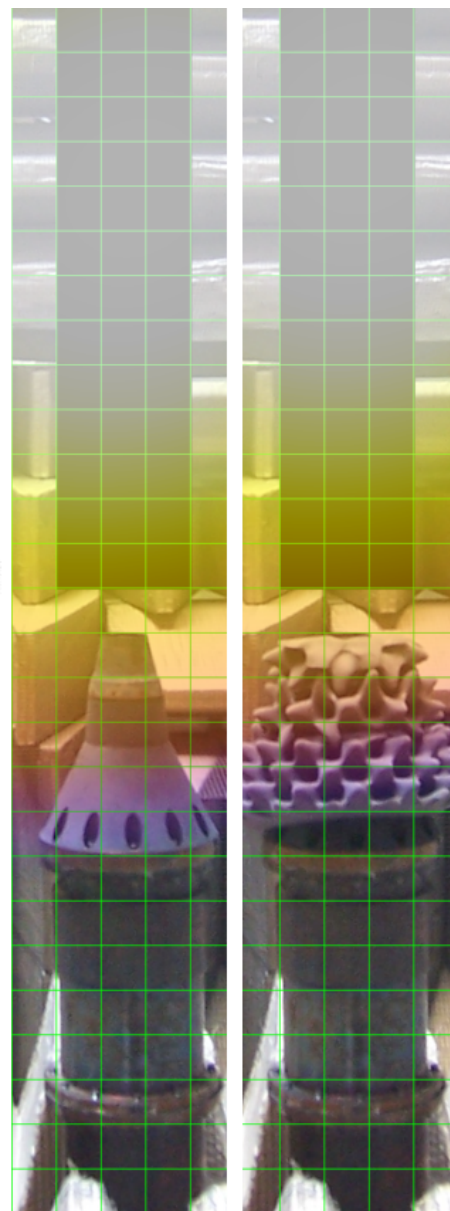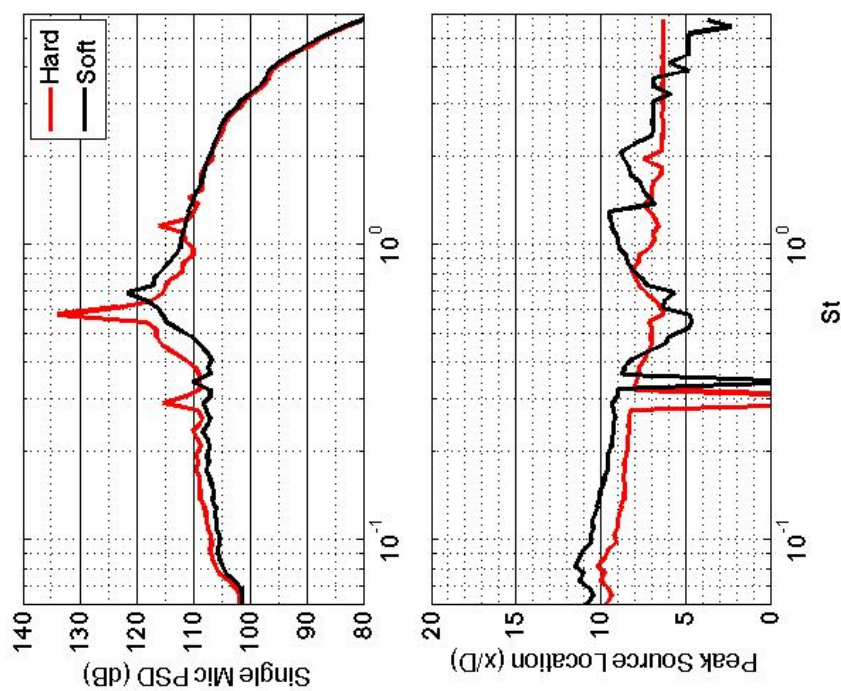
Figure 240.—SMC000; under-expanded; set point 9010; Mj=1.40; St=0.058.

Hard

Soft
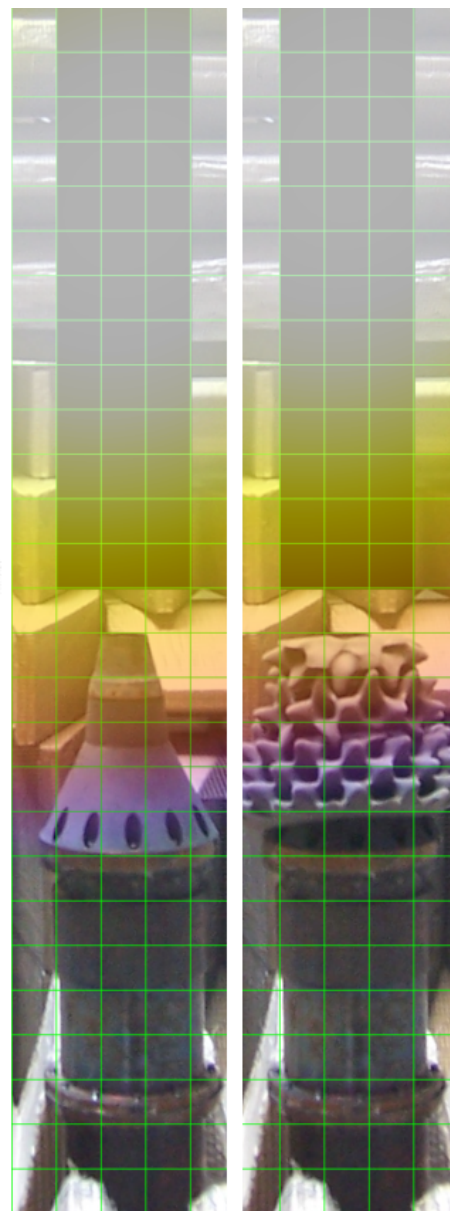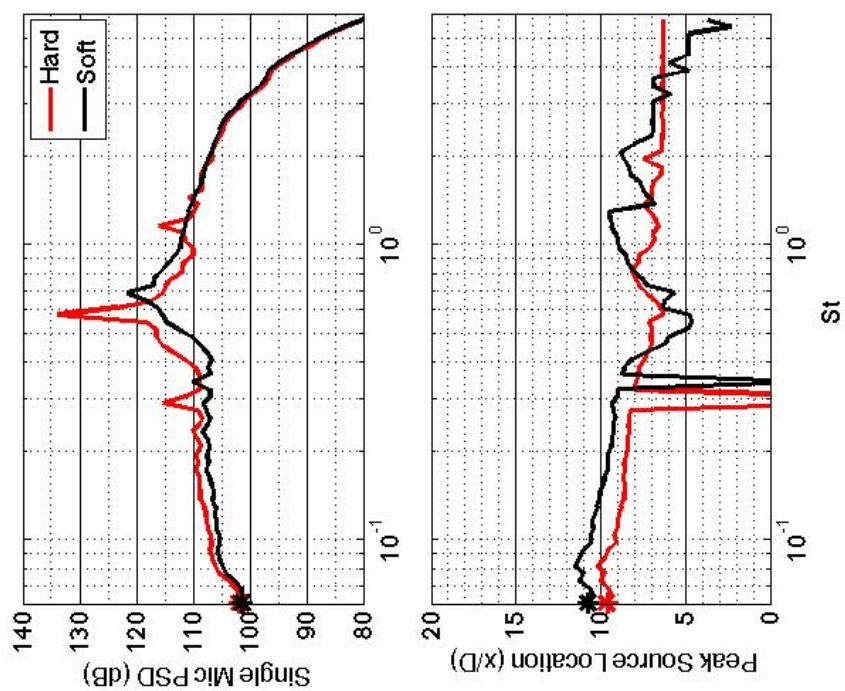
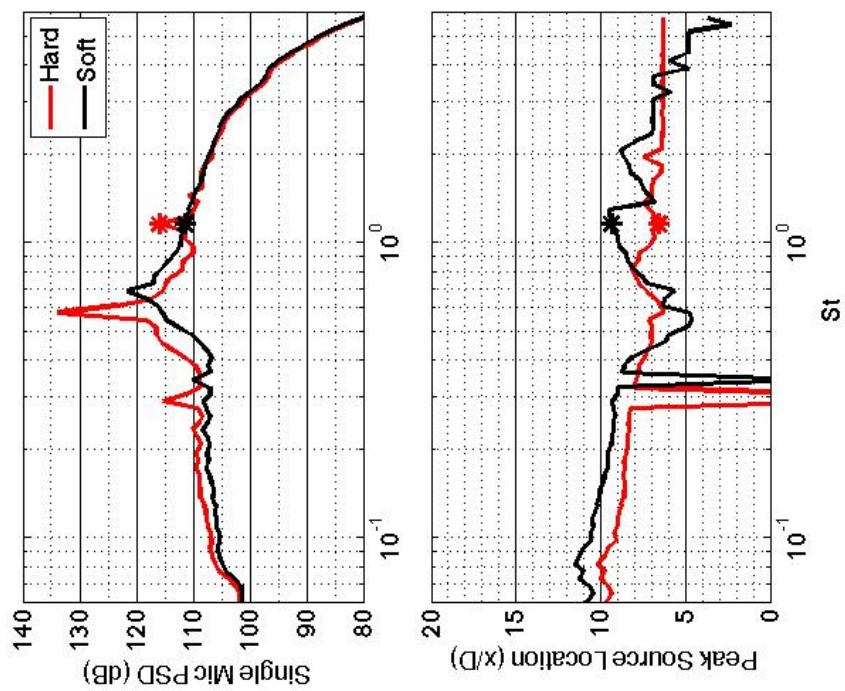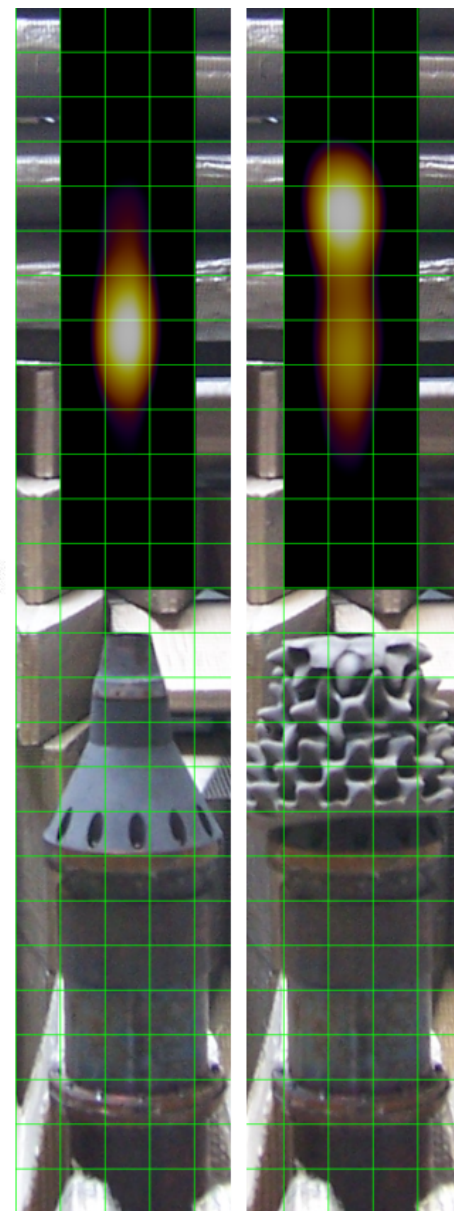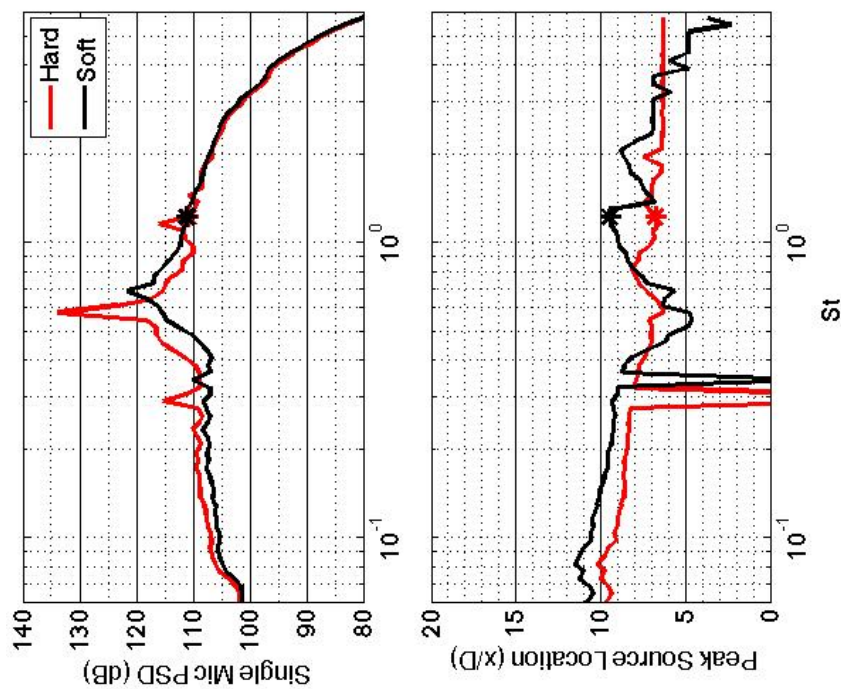Figure 241.—SMC000; under-expanded; set point 9010; Mj=1.40; St=0.061.

Hard

Soft
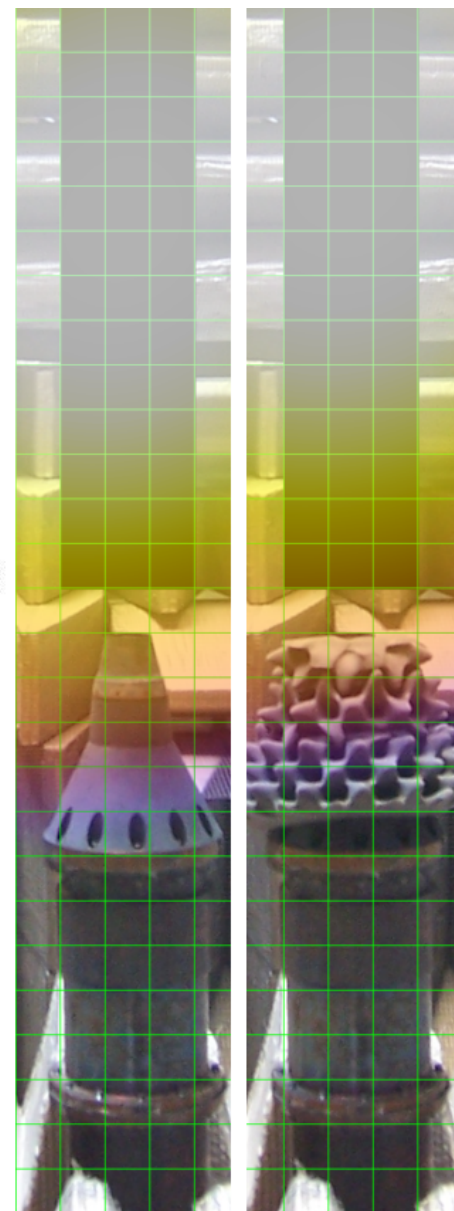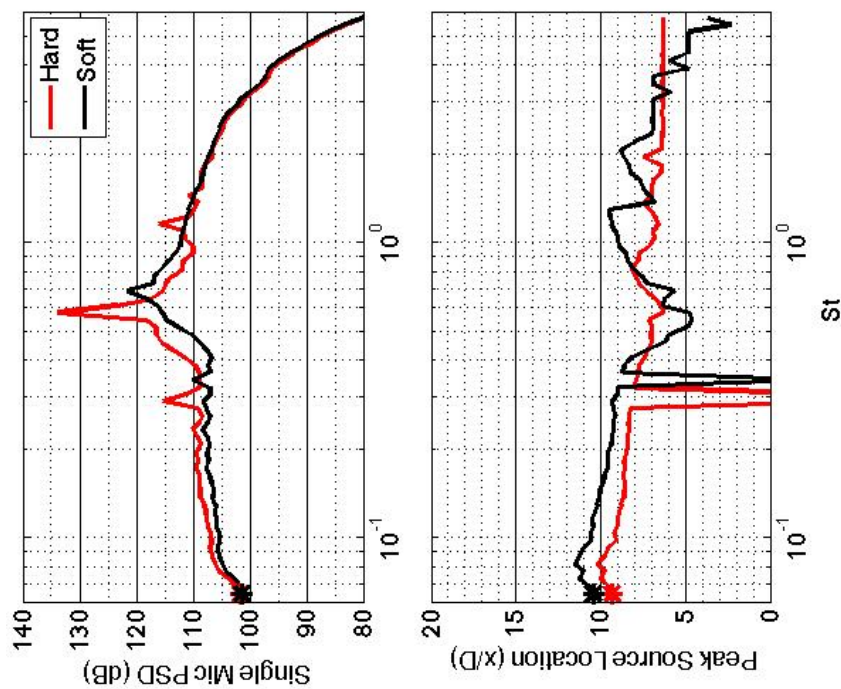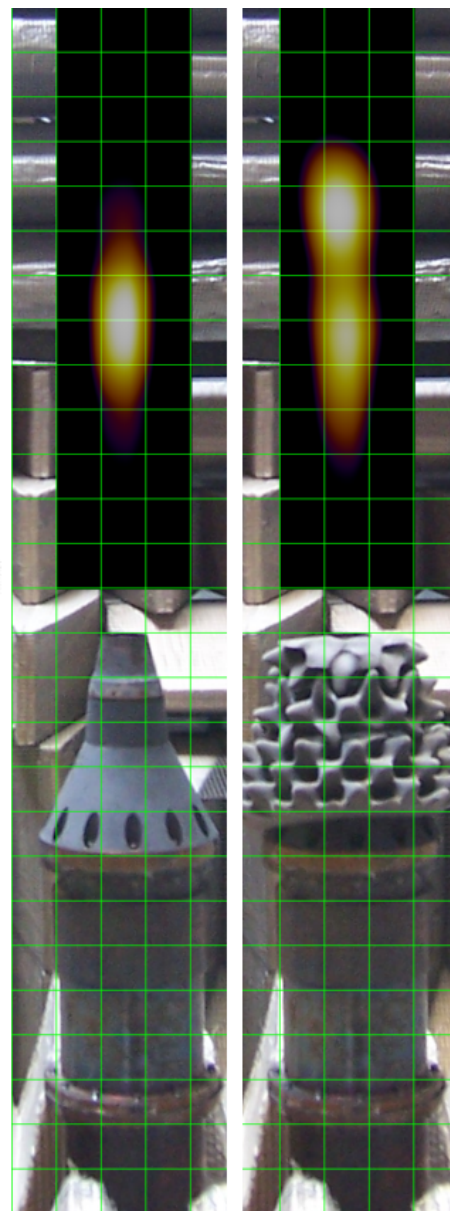
Figure 242.—SMC000; under-expanded; set point 9010; Mj=1.40; St=0.065.
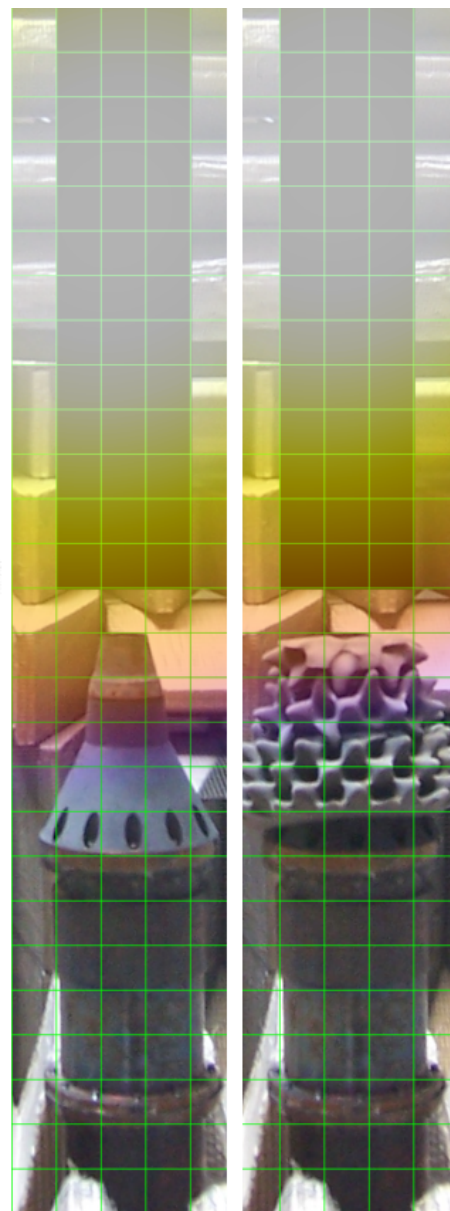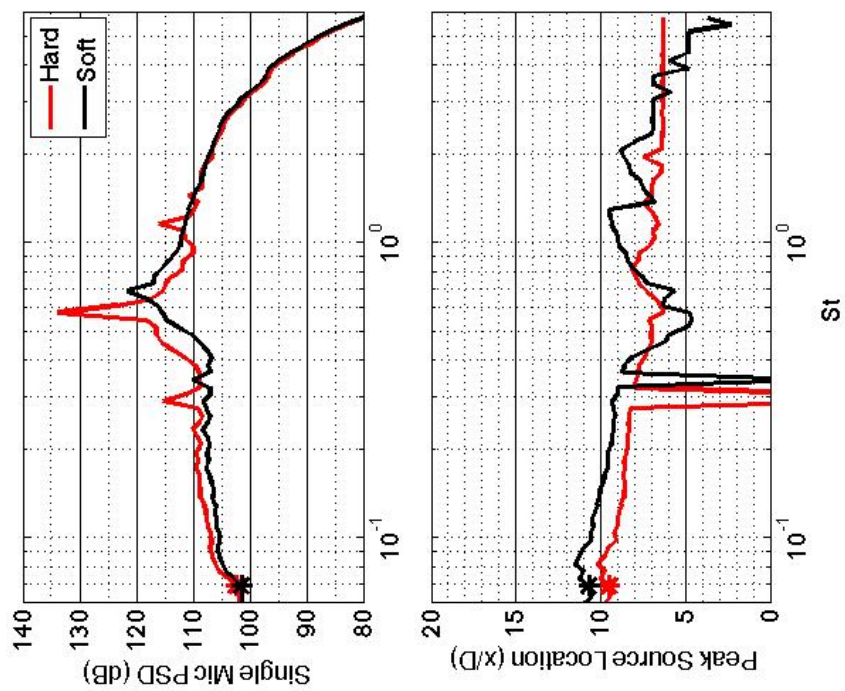
Figure 243.—SMC000; under-expanded; set point 9010; Mj=1.40; St=0.069.

Hard

Soft
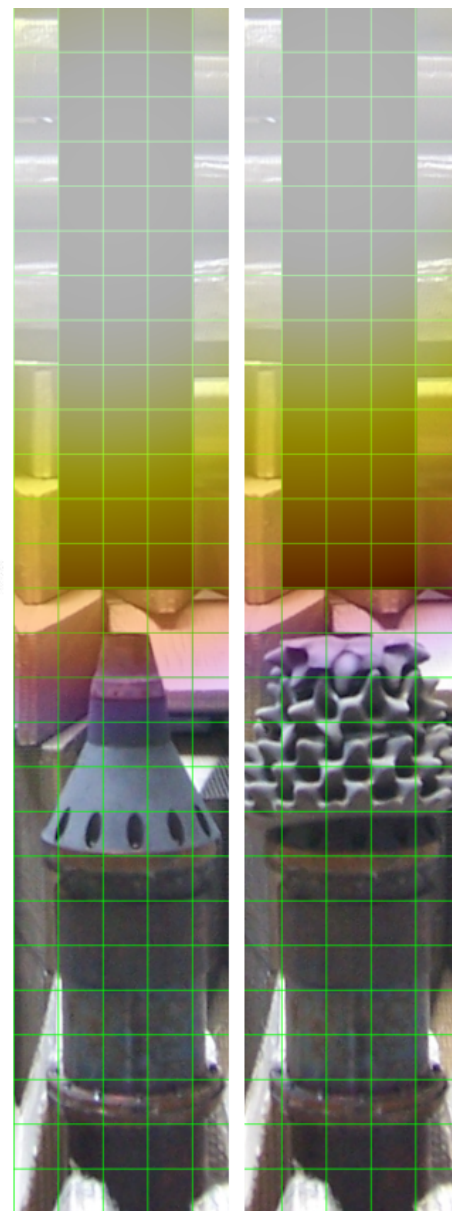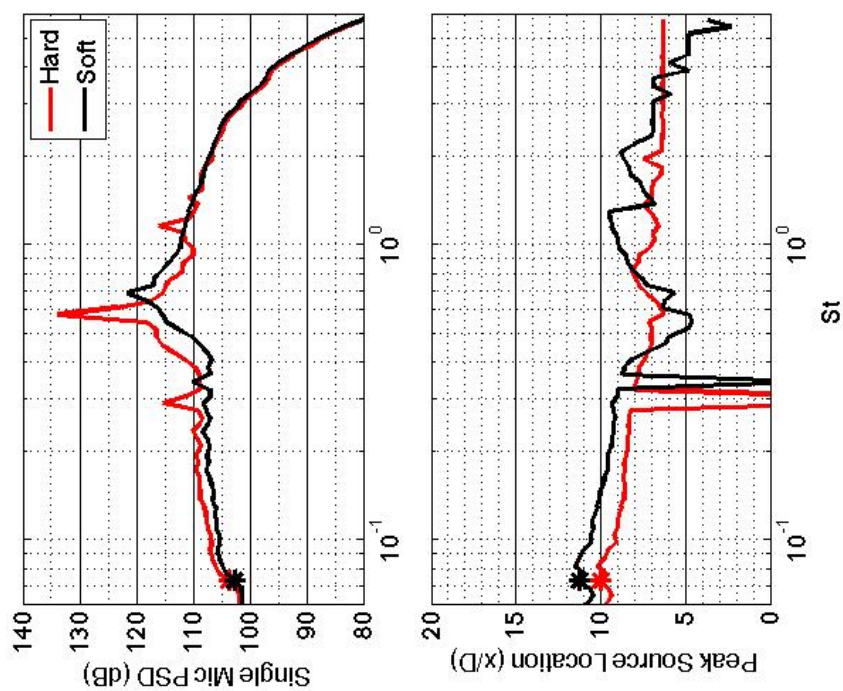
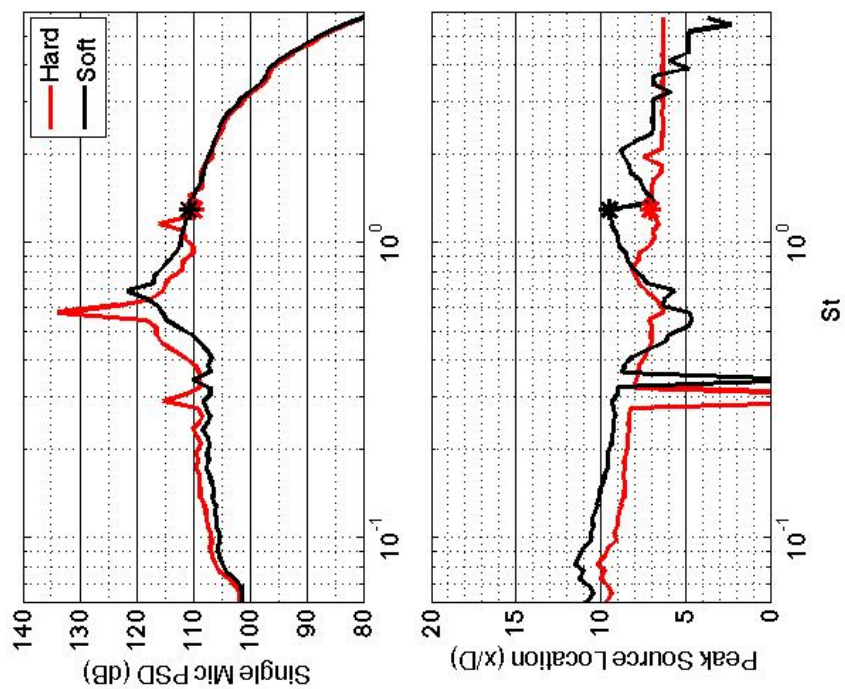
Figure 244.—SMC000; under-expanded; set point 9010; Mj=1.40; St=0.073.
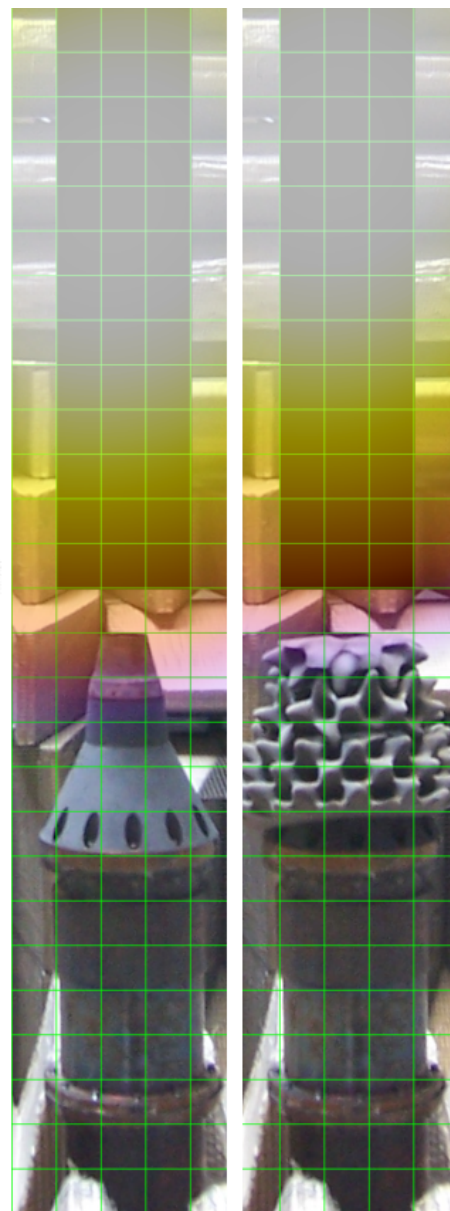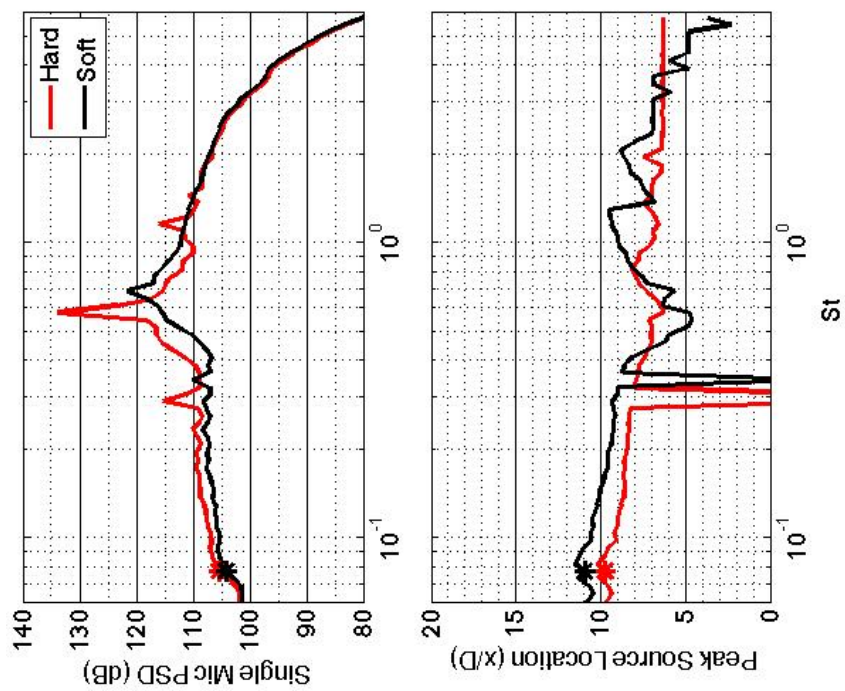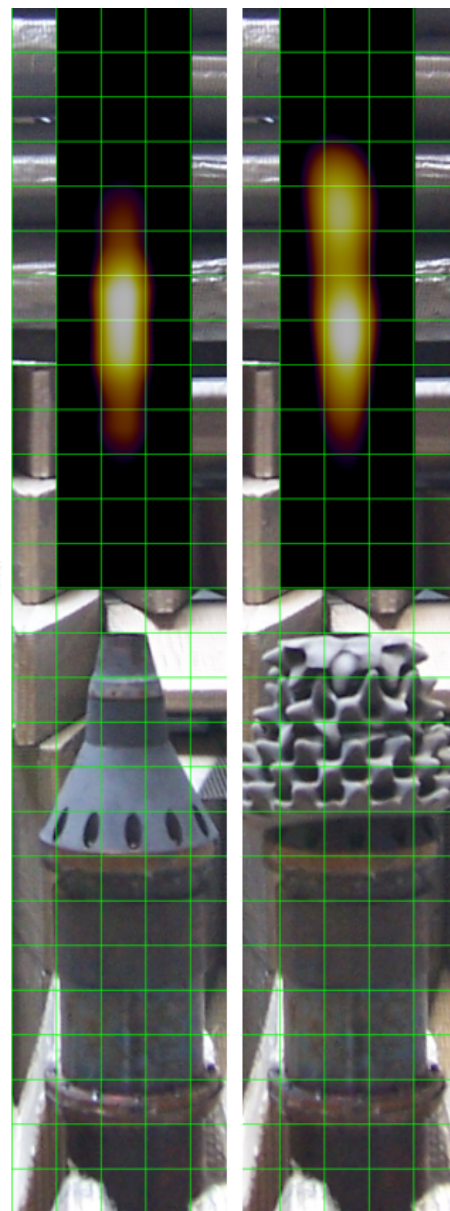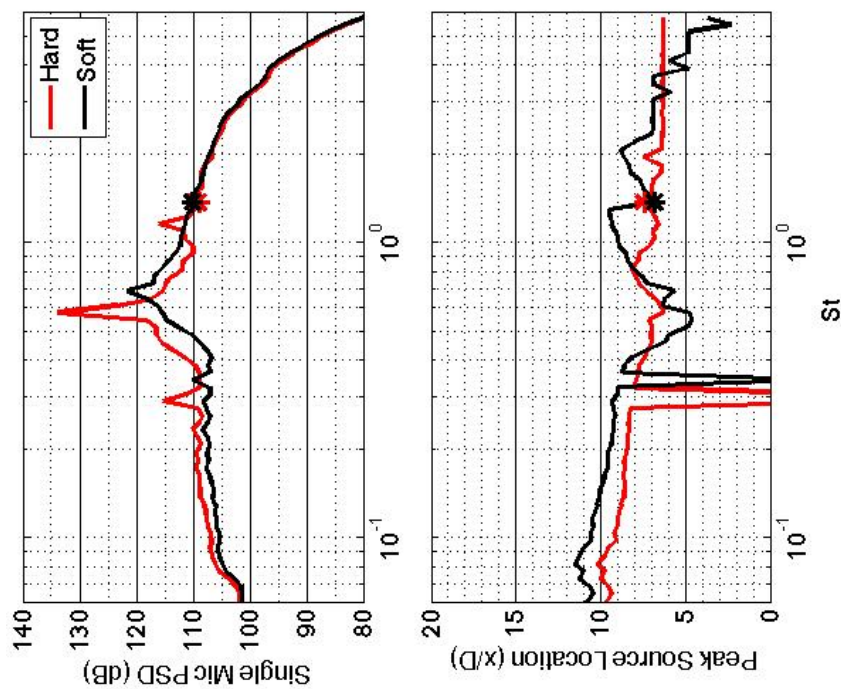
Figure 245.—SMC000; under-expanded; set point 9010; Mj=1.40; St=0.077 .
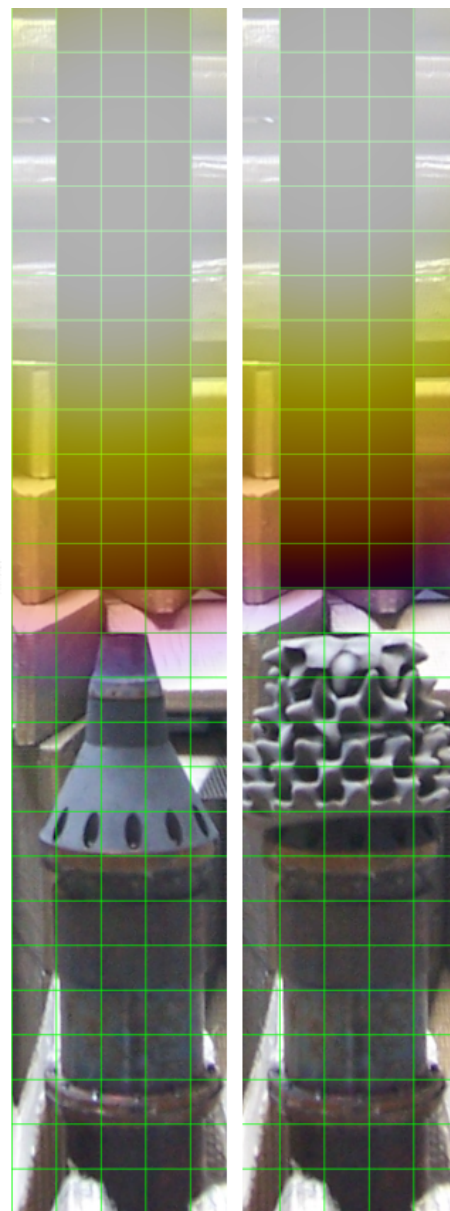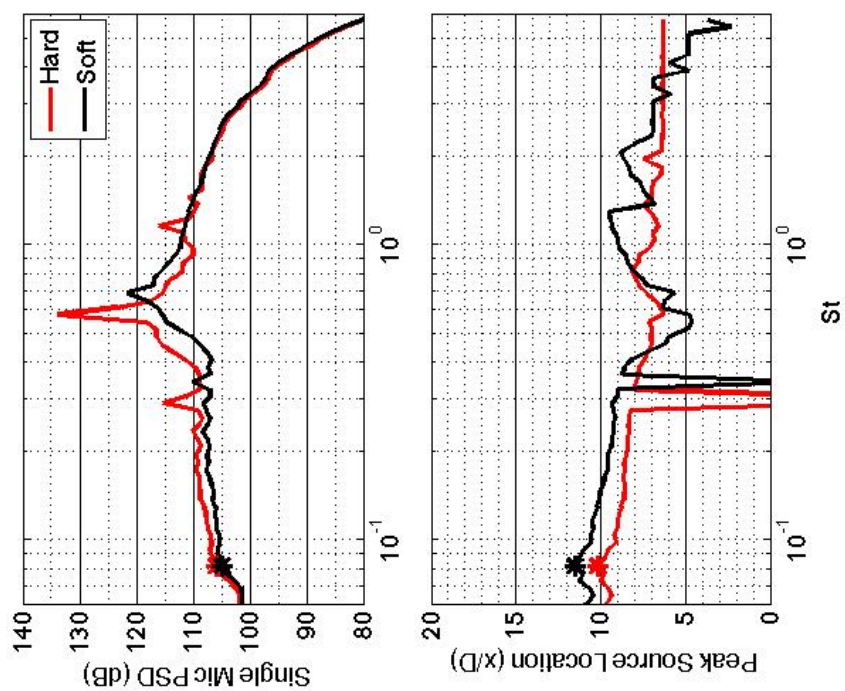
Figure 246.—SMC000; under-expanded; set point 9010; Mj=1.40; St=0.082.

Hard

Soft
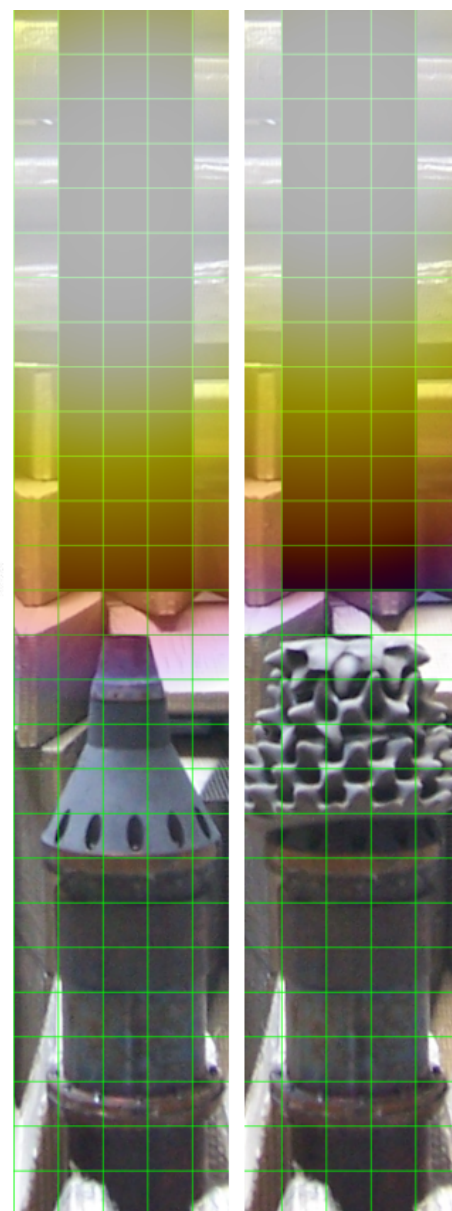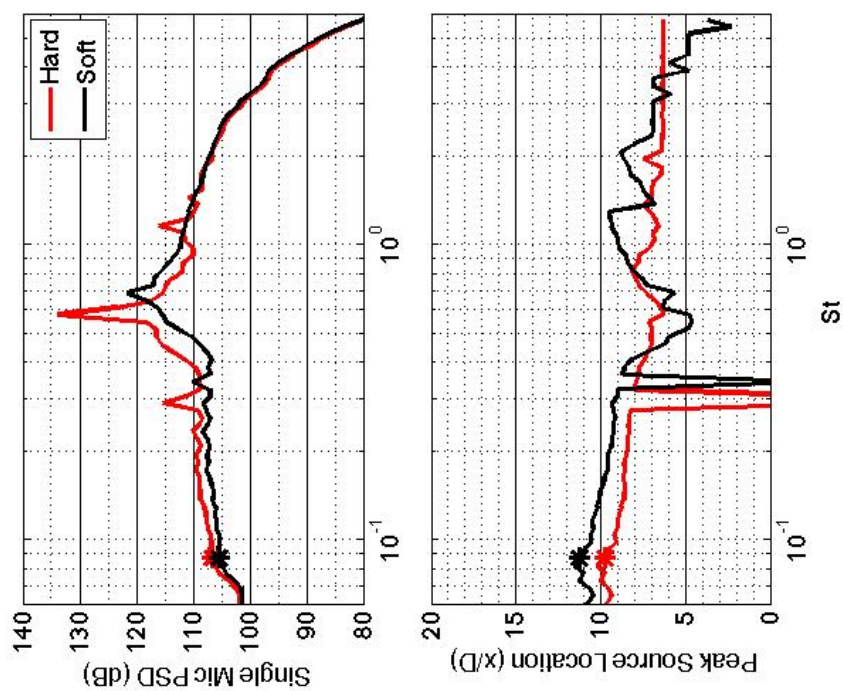
Figure 247.—SMC000; under-expanded; set point 9010; Mj=1.40; St=0.087.
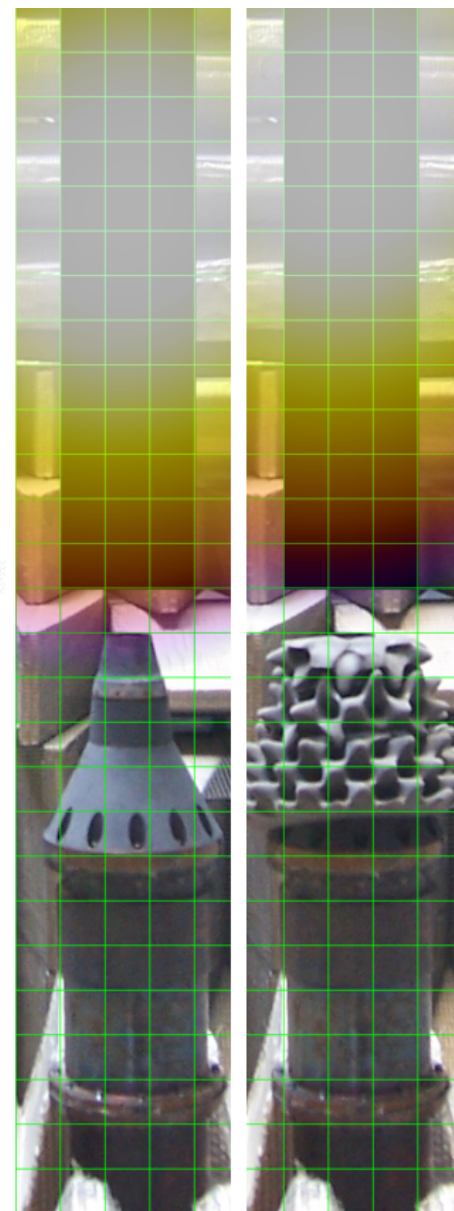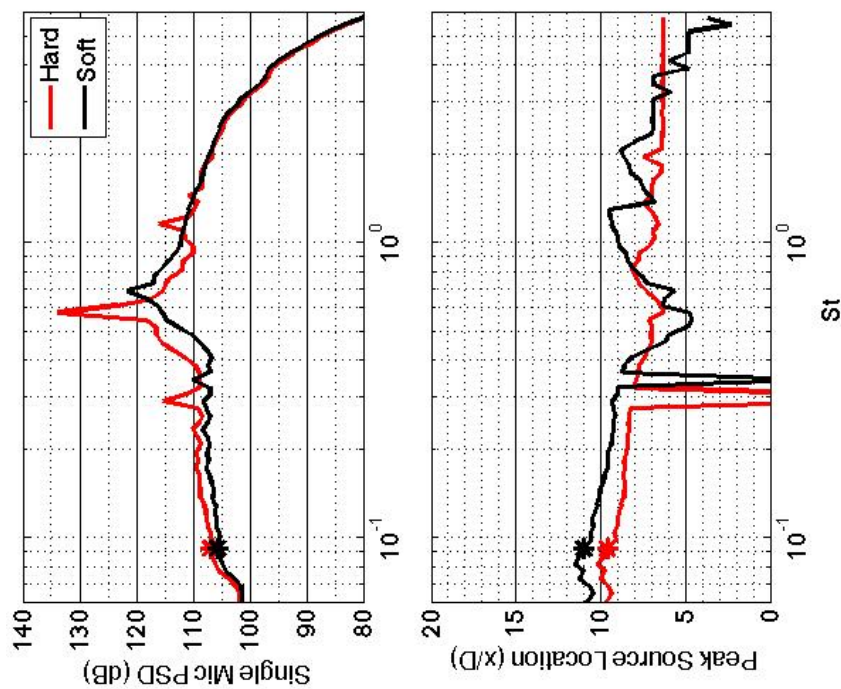
Figure 248.—SMC000; under-expanded; set point 9010; Mj=1.40; St=0.092.
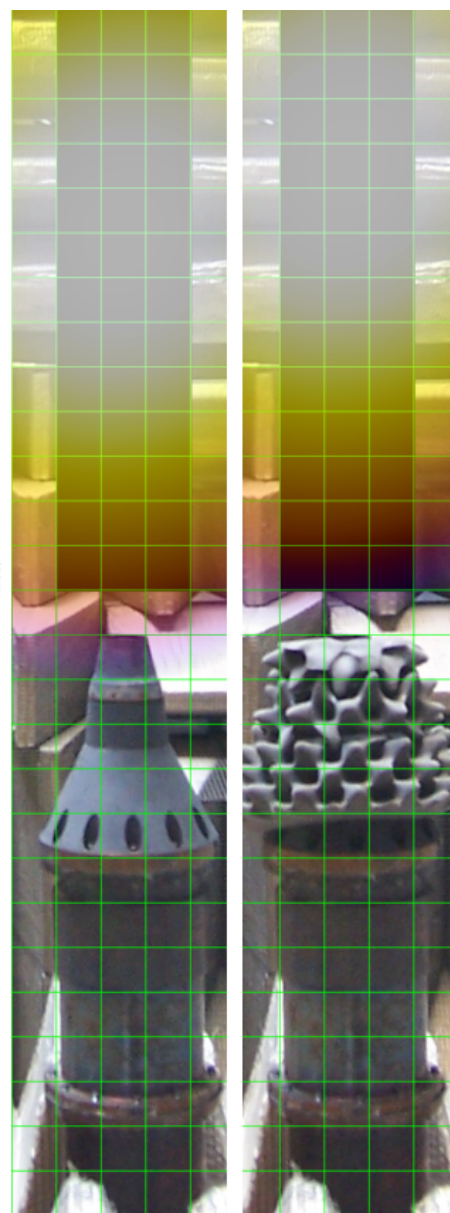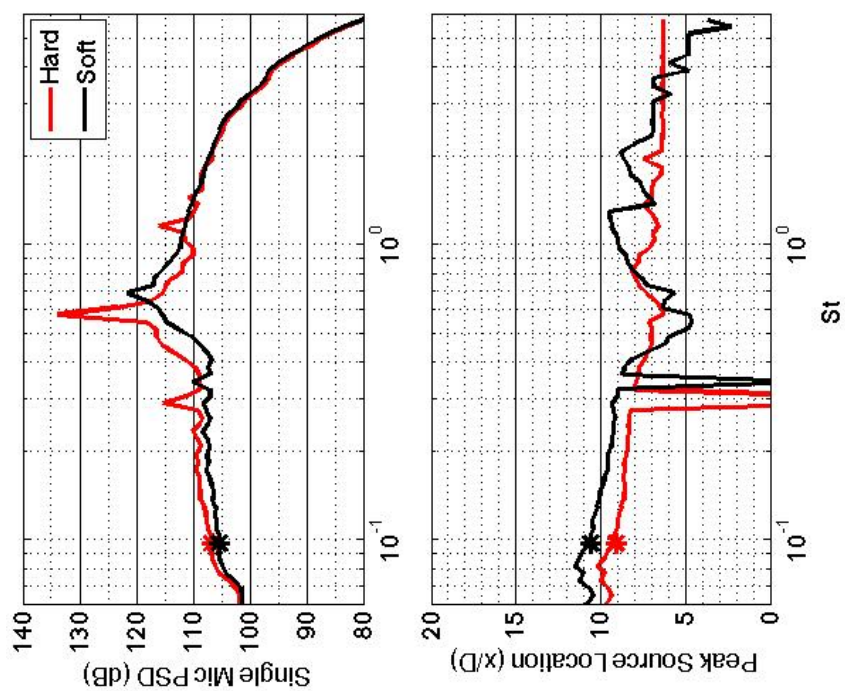
Figure 249.—SMC000; under-expanded; set point 9010; Mj=1.40; St=0.098.
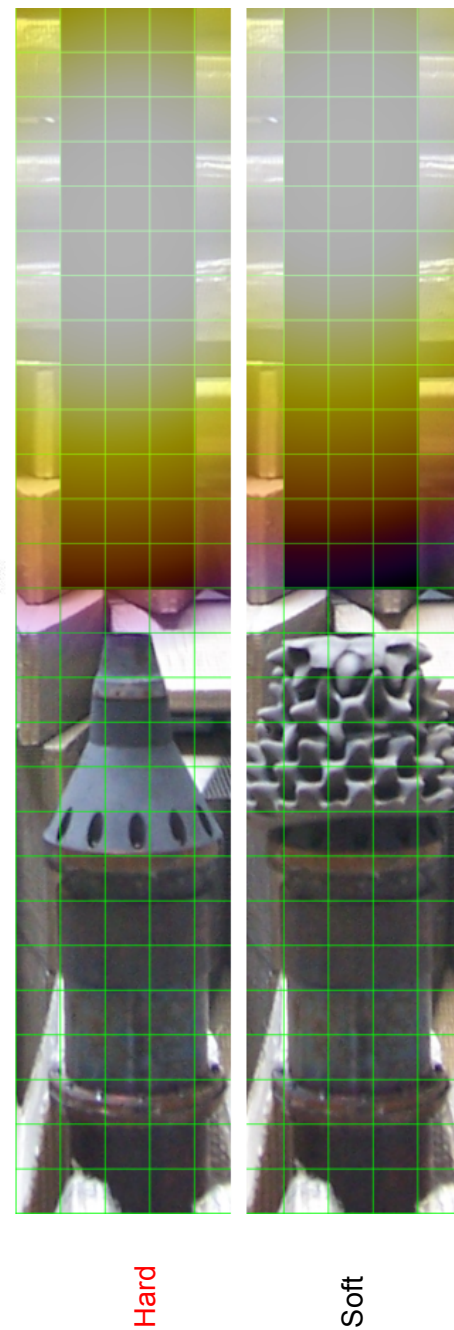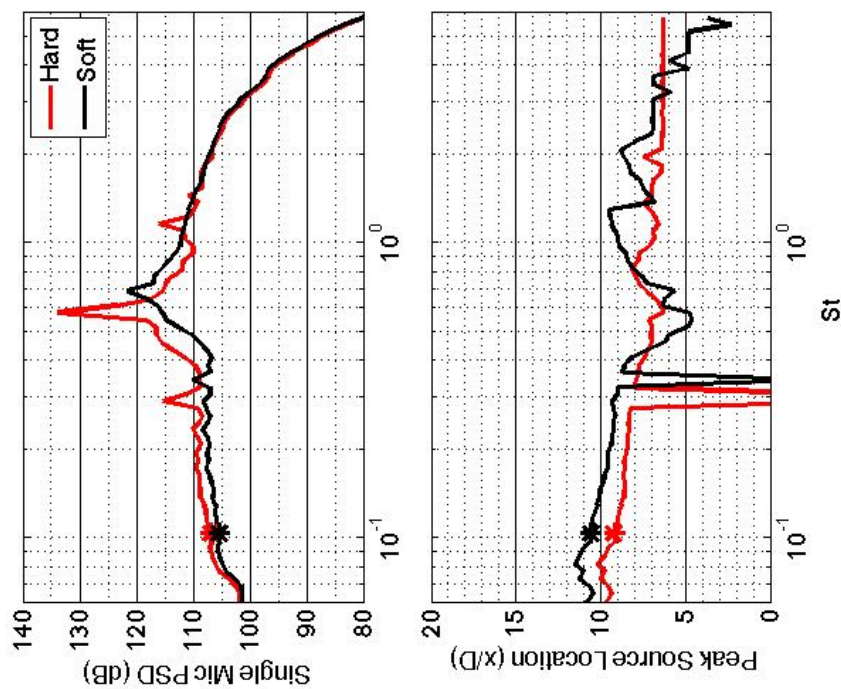
Figure 250.—SMC000; under-expanded; set point 9010; Mj=1.40; St=0.103.
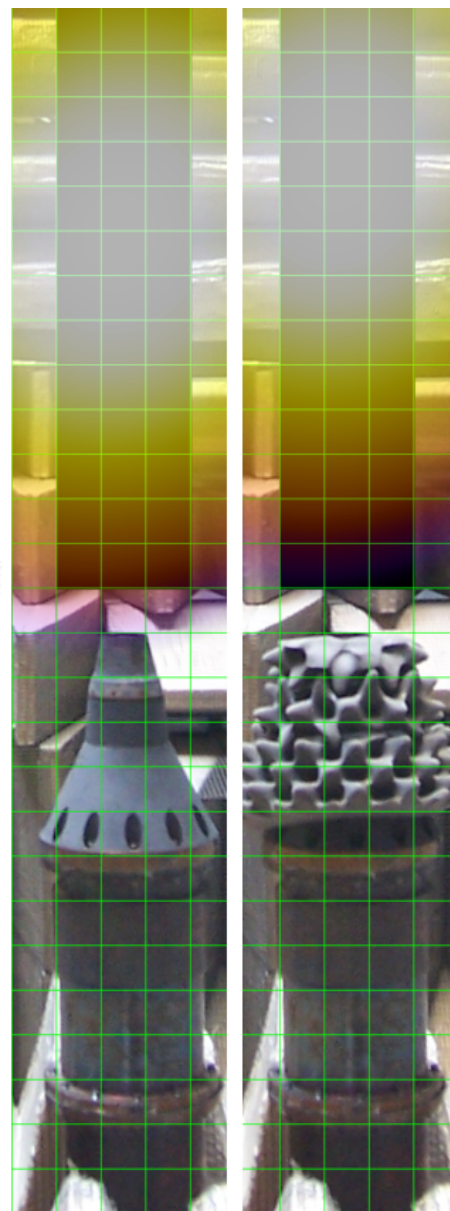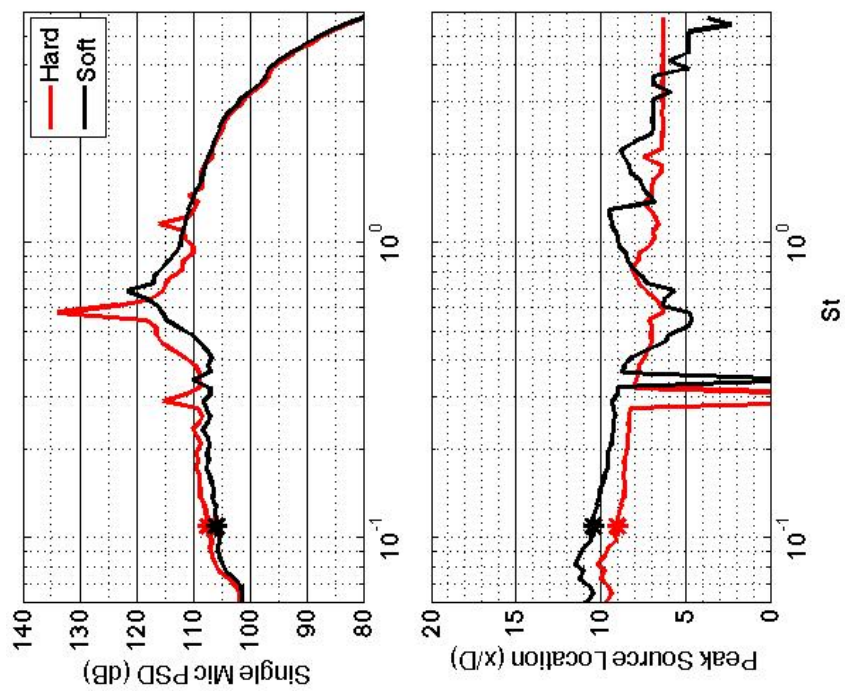
Figure 251.—SMC000; under-expanded; set point 9010; Mj=1.40; St=0.110.
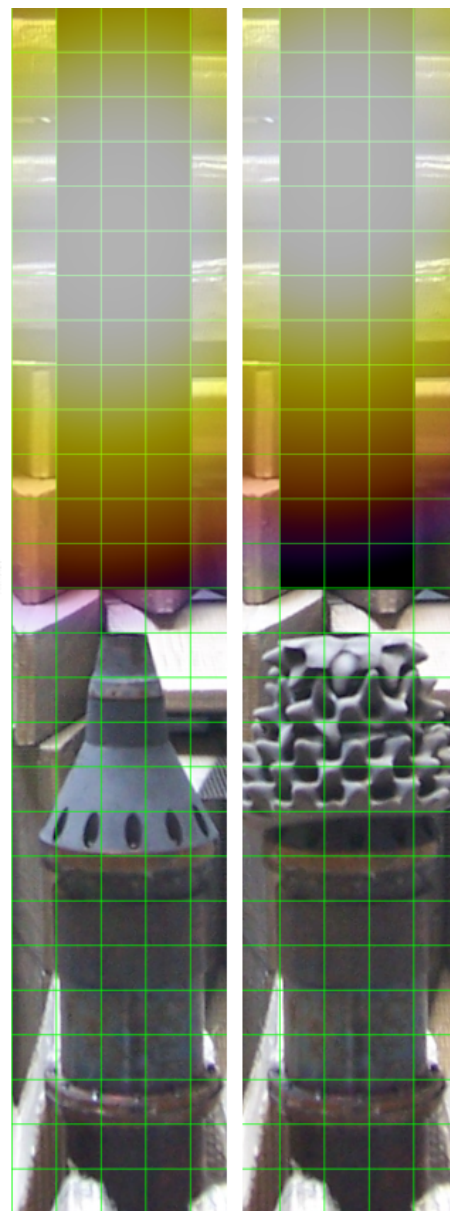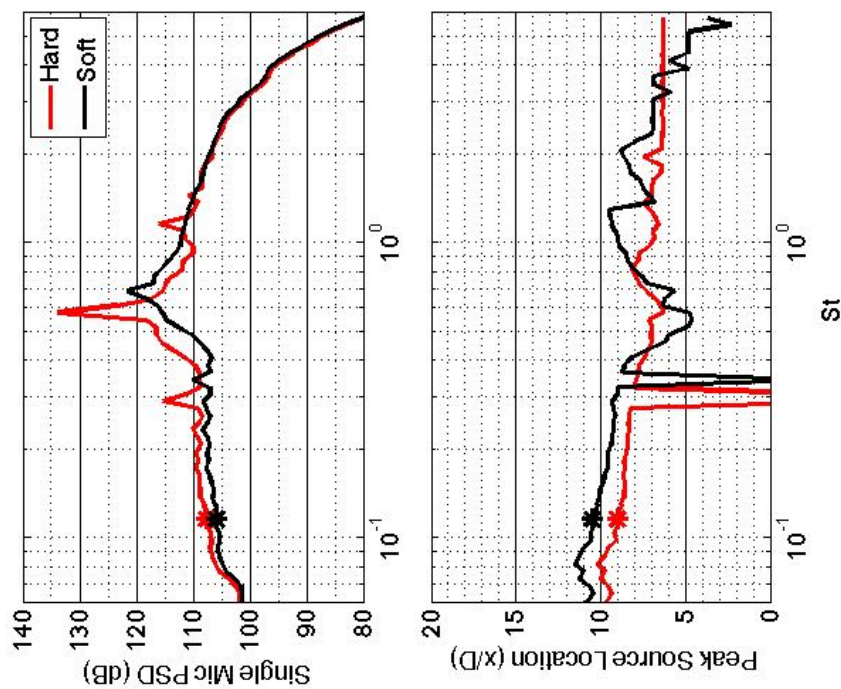
Figure 252.—SMC000; under-expanded; set point 9010; Mj=1.40; St=0.116.
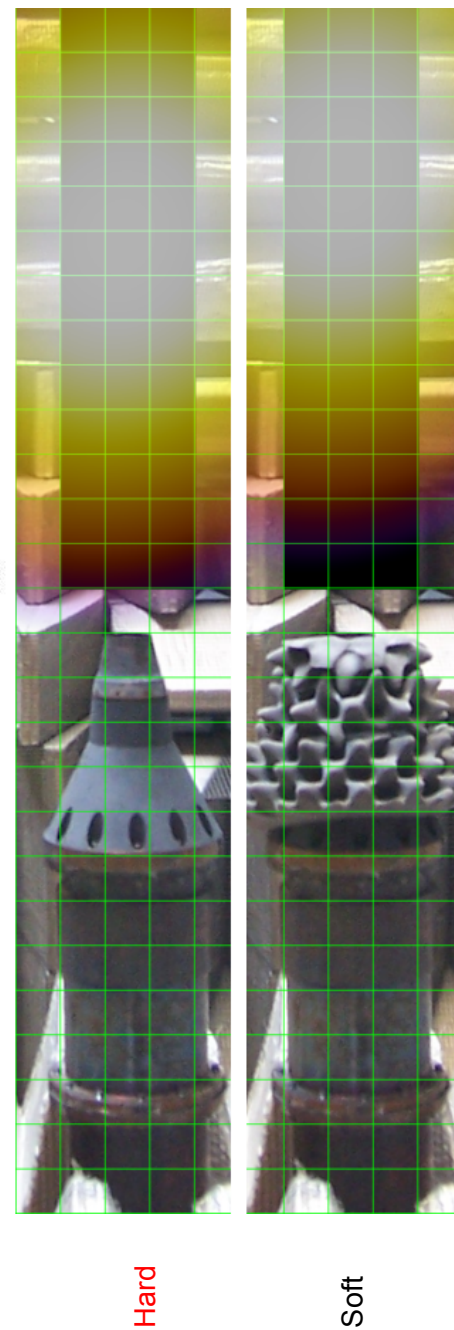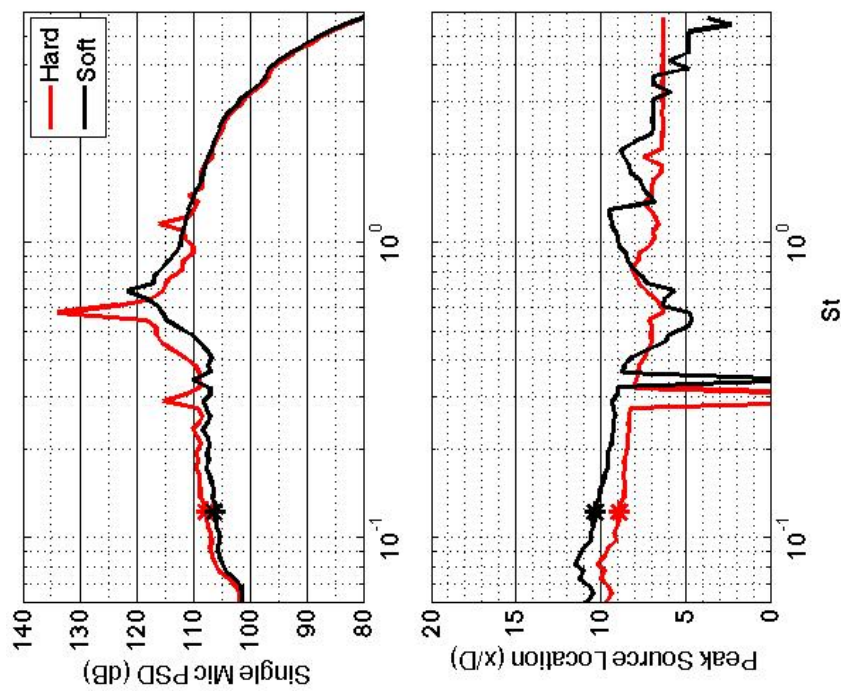
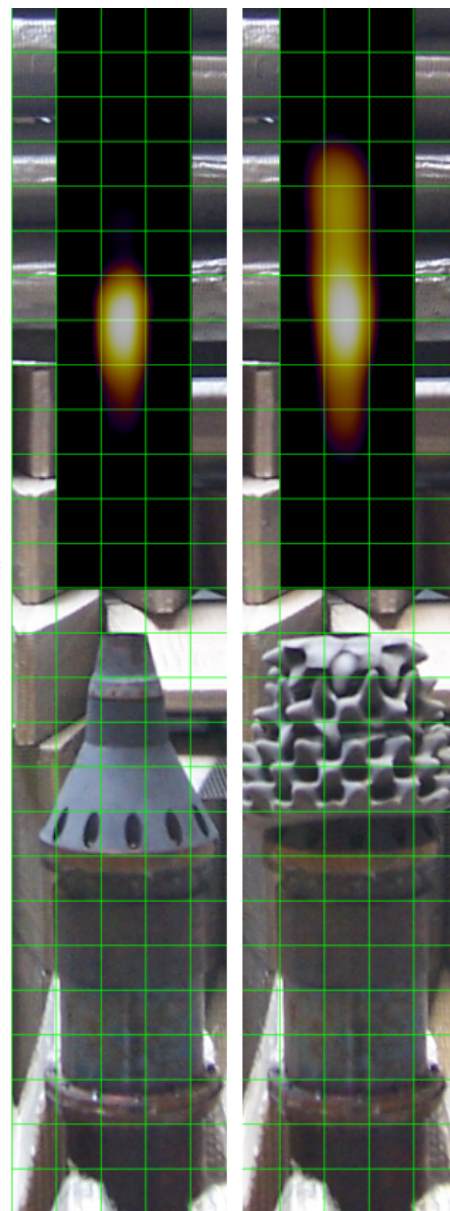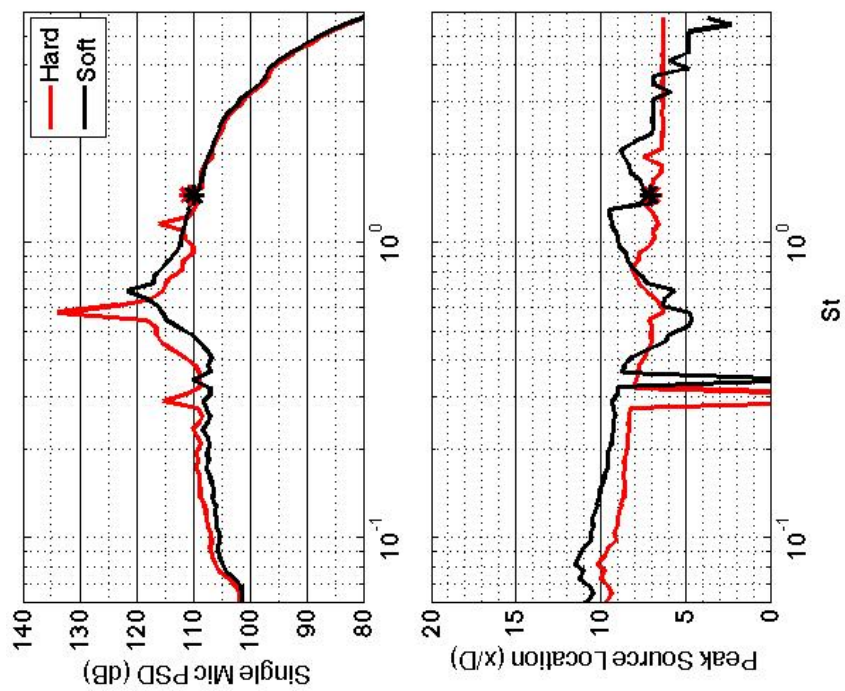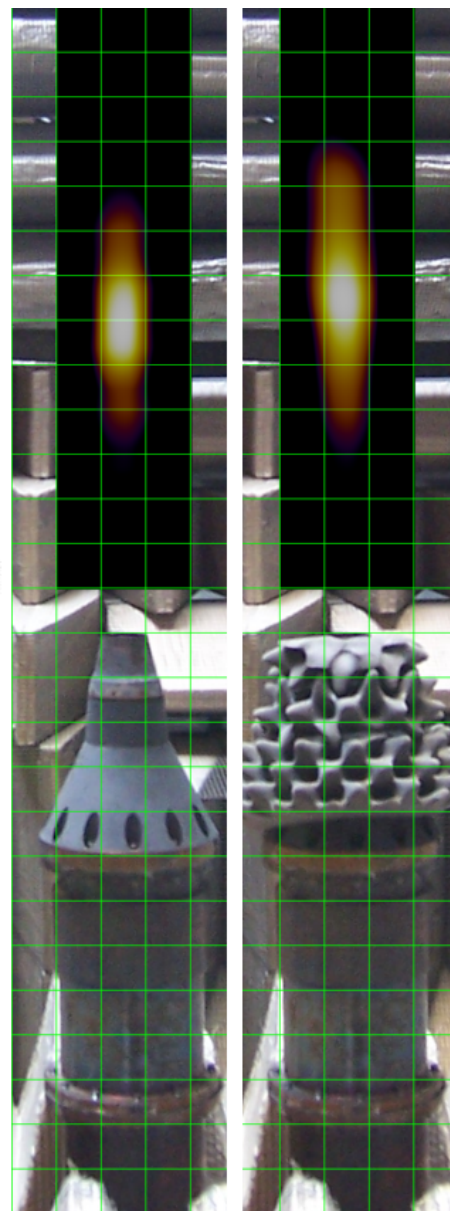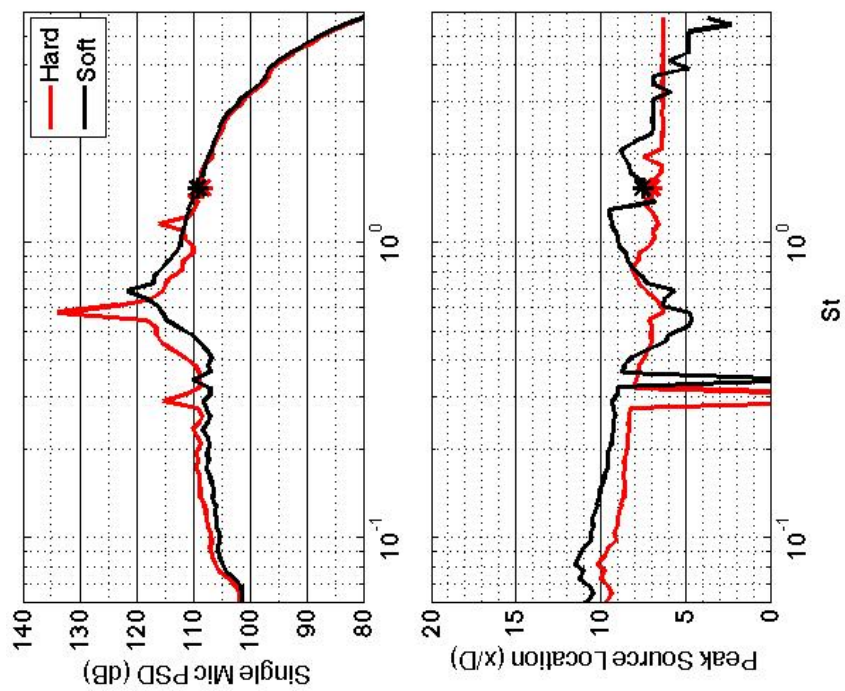Figure 253.—SMC000; under-expanded; set point 9010; Mj=1.40; St=0.122.

Hard

Soft
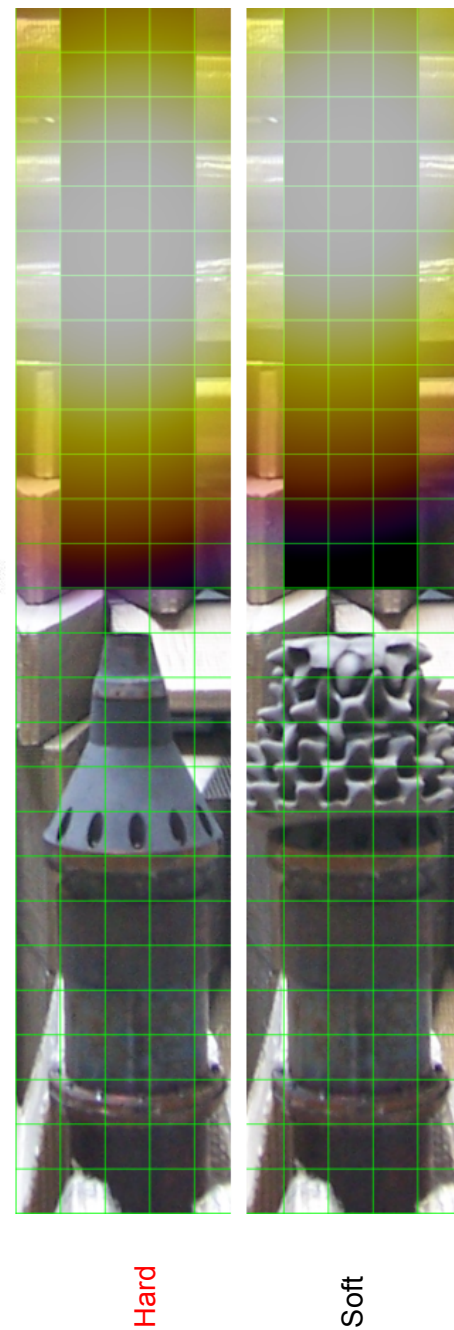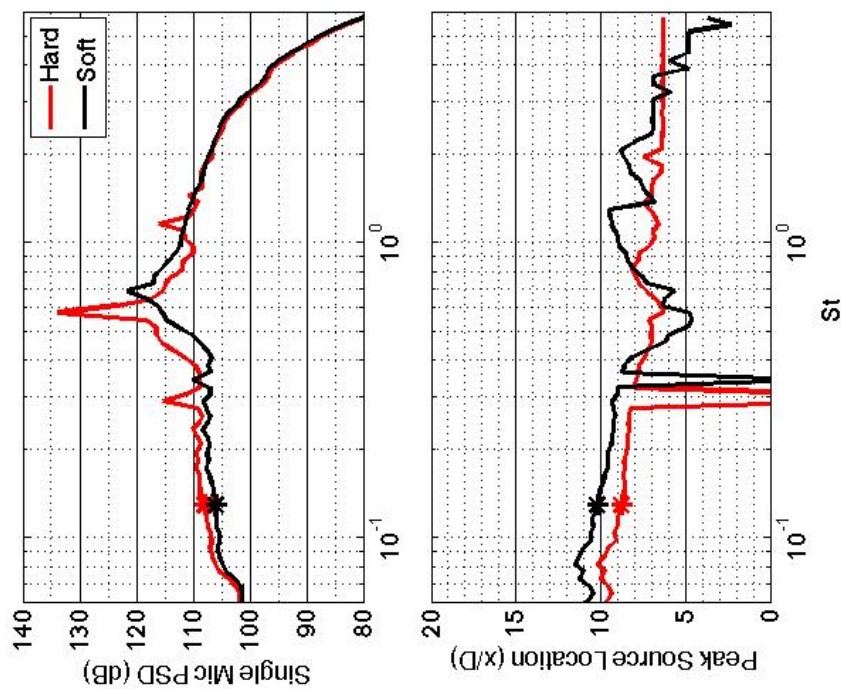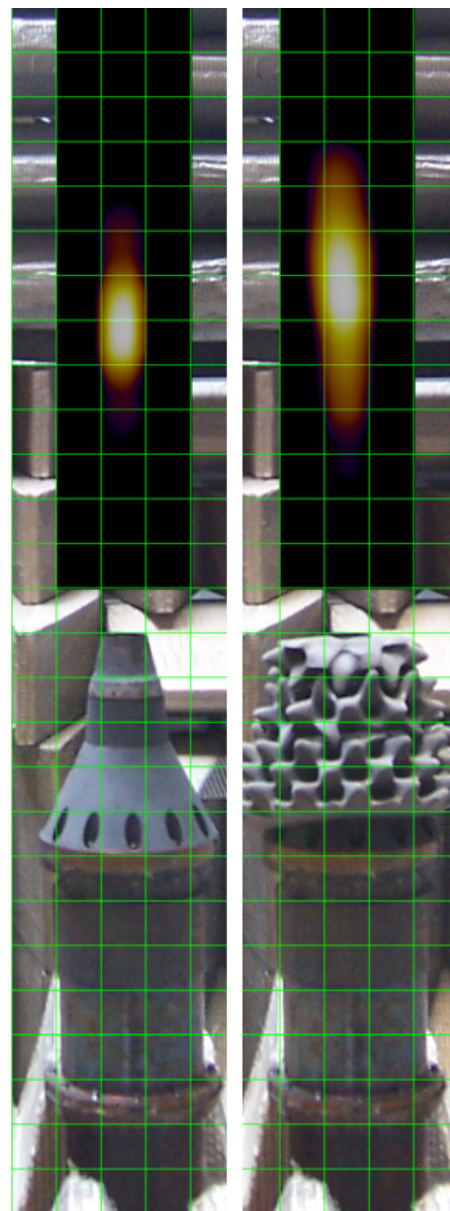
Figure 254.—SMC000; under-expanded; set point 9010; Mj=1.40; St=0.129.
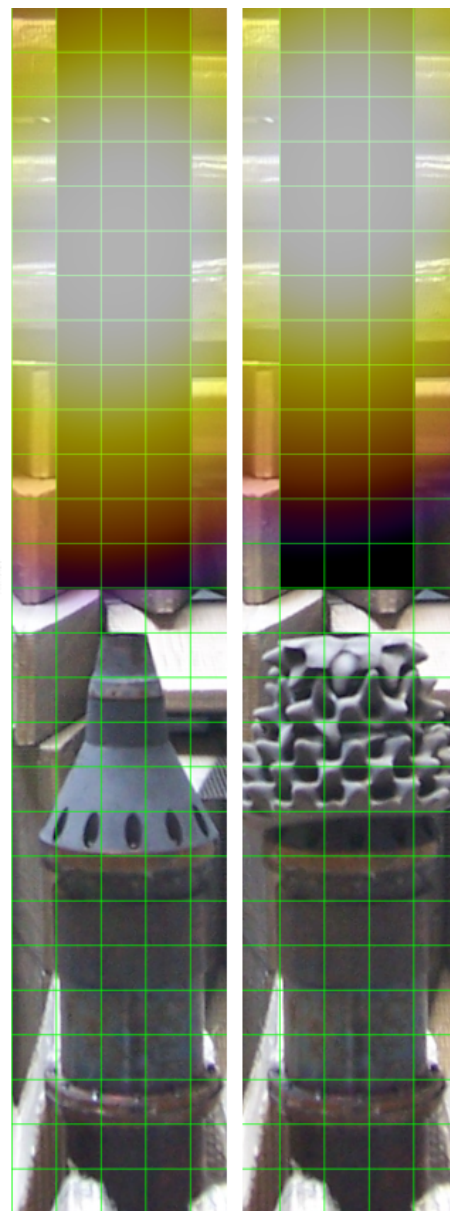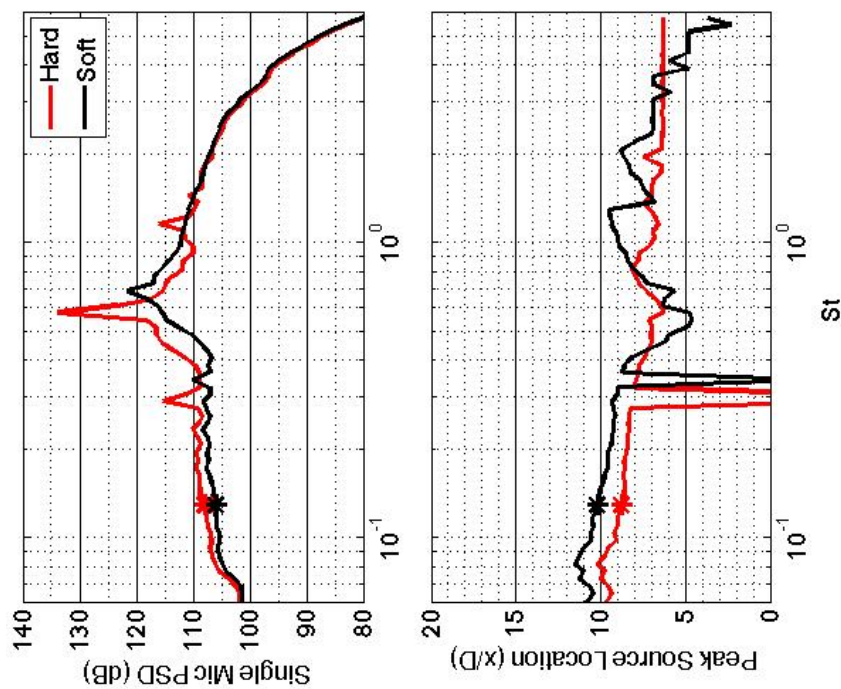
Figure 255.—SMC000; under-expanded; set point 9010; Mj=1.40; St=0.137.
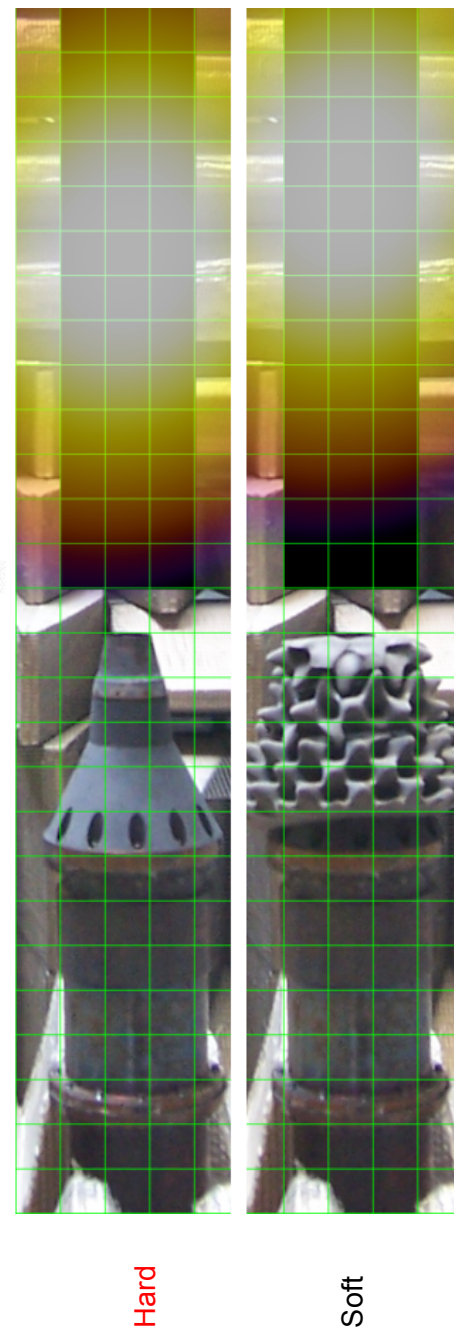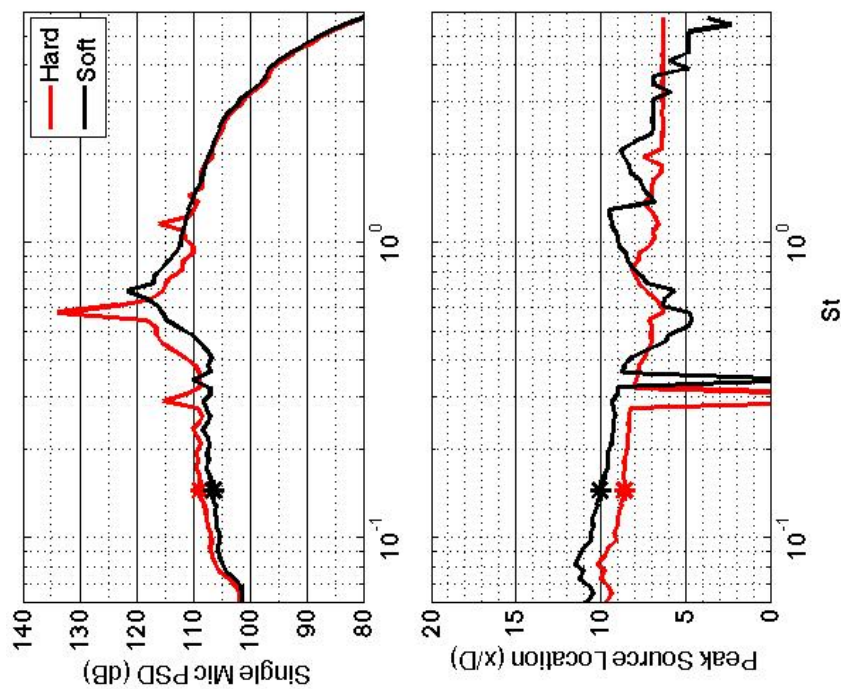
Figure 256.—SMC000; under-expanded; set point 9010; Mj=1.40; St=0.145.

Hard

Soft
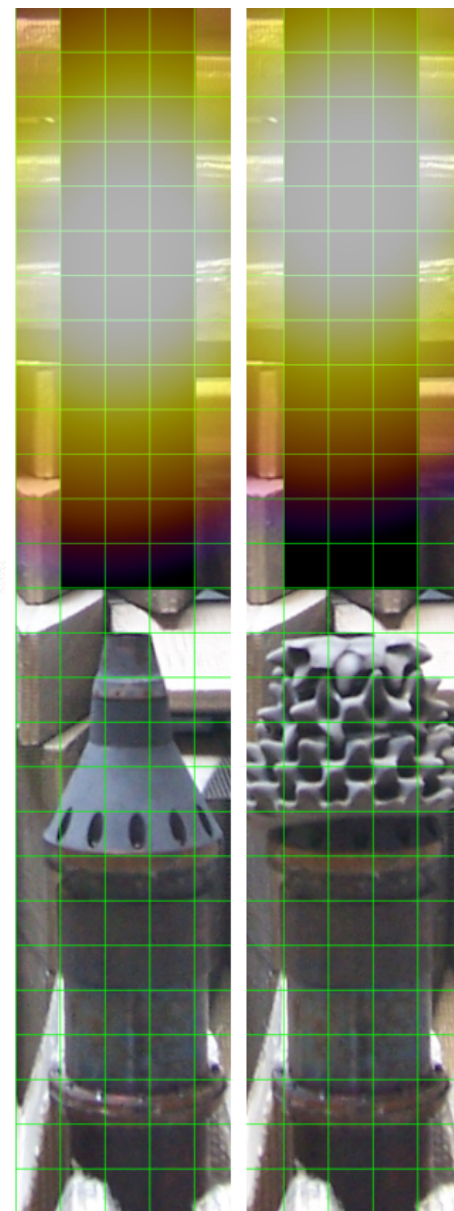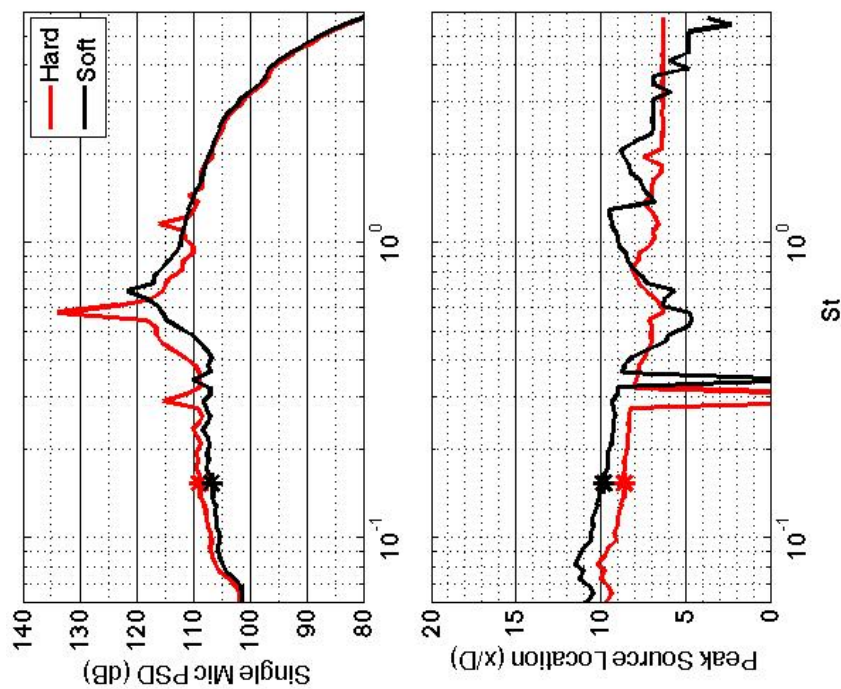
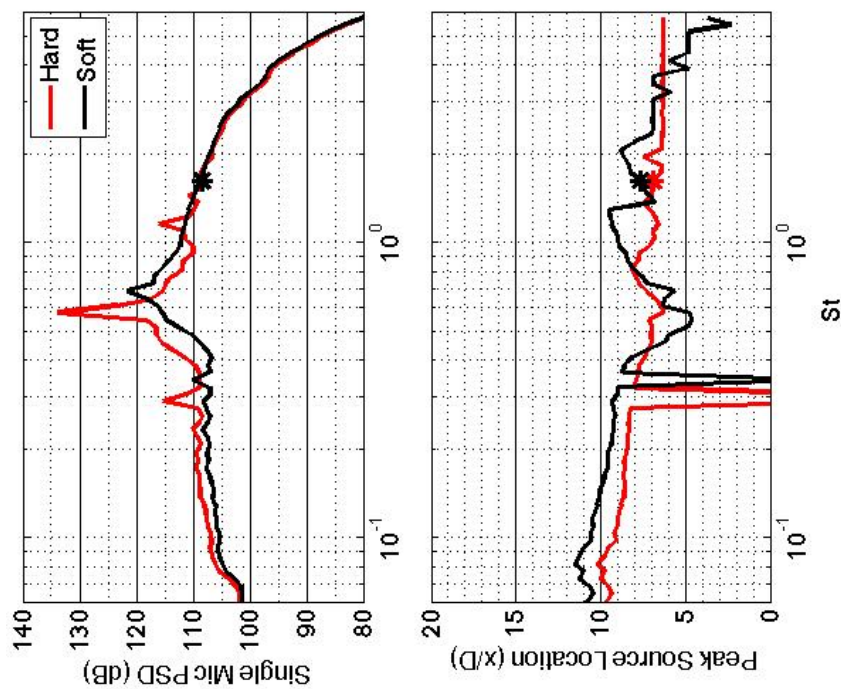Figure 257.—SMC000; under-expanded; set point 9010; Mj=1.40; St=0.153.
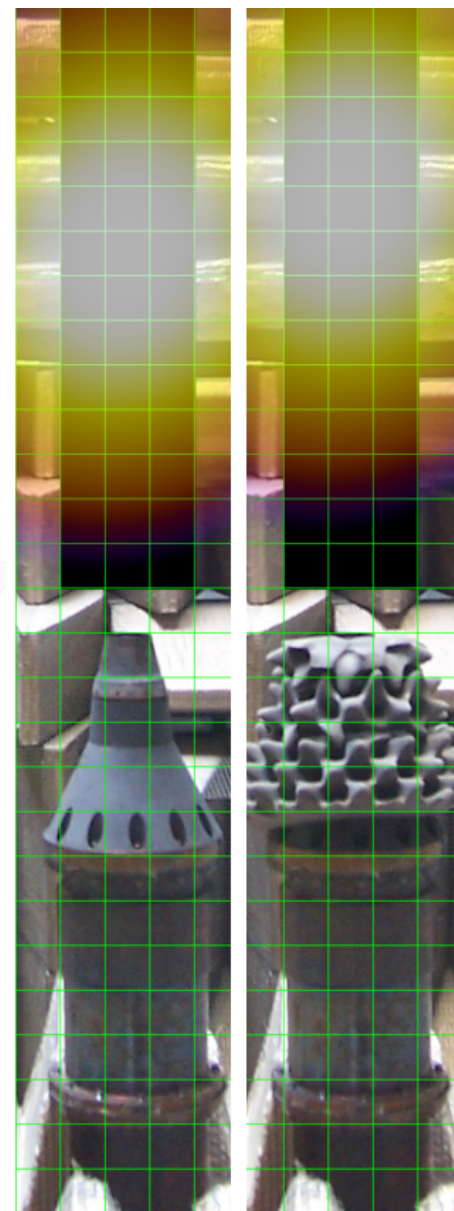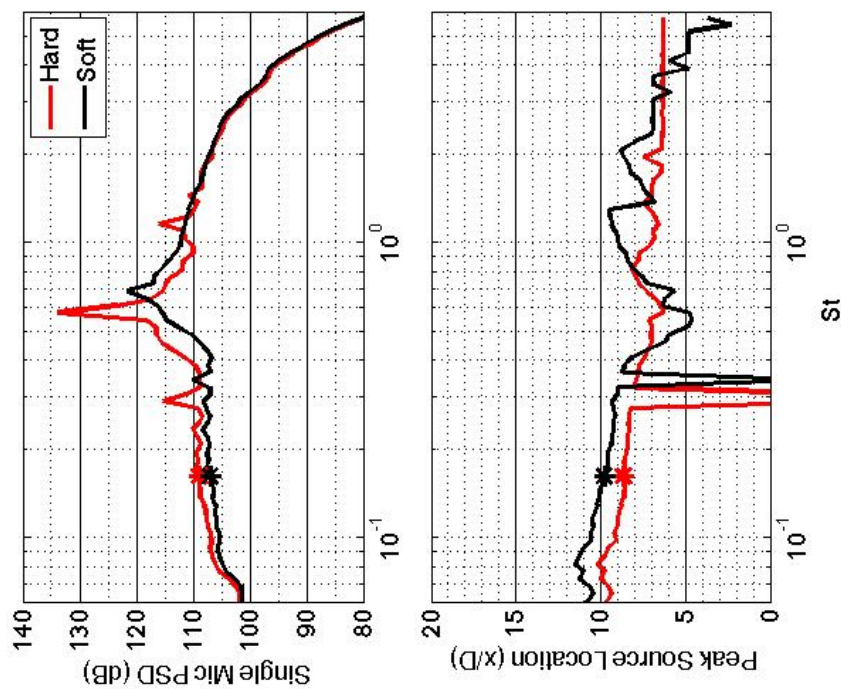
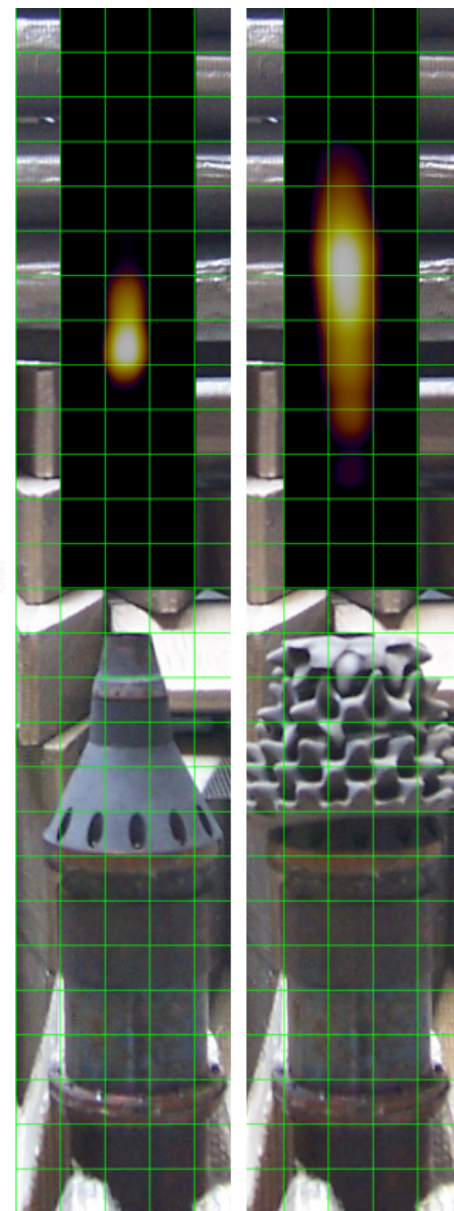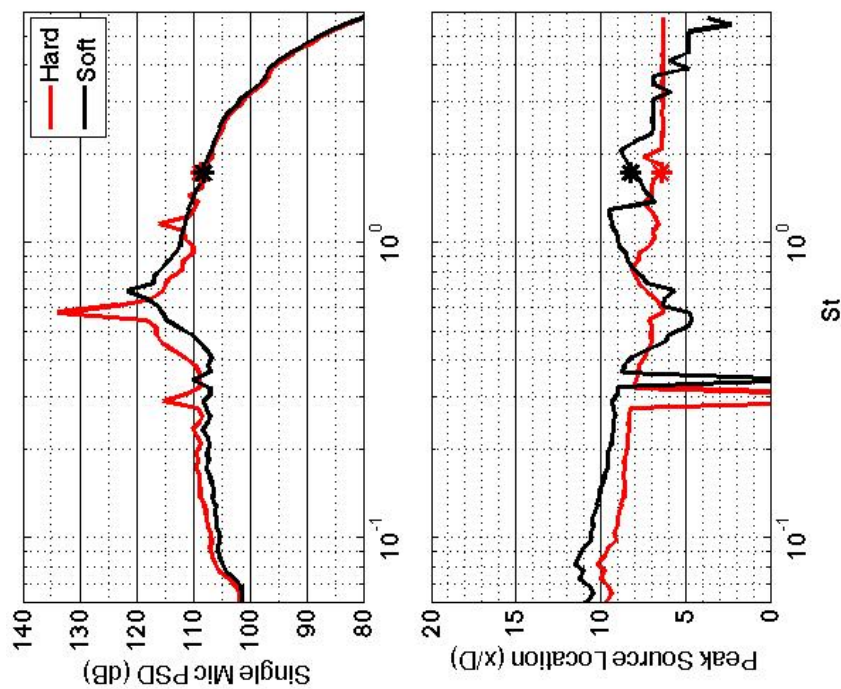Figure 258.—SMC000; under-expanded; set point 9010; Mj=1.40; St=0.162.
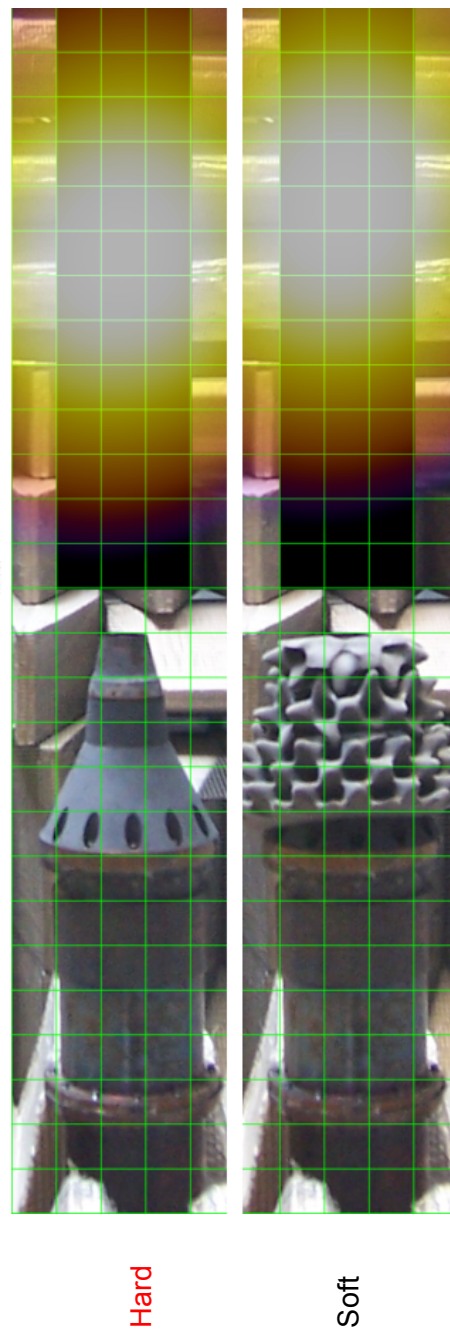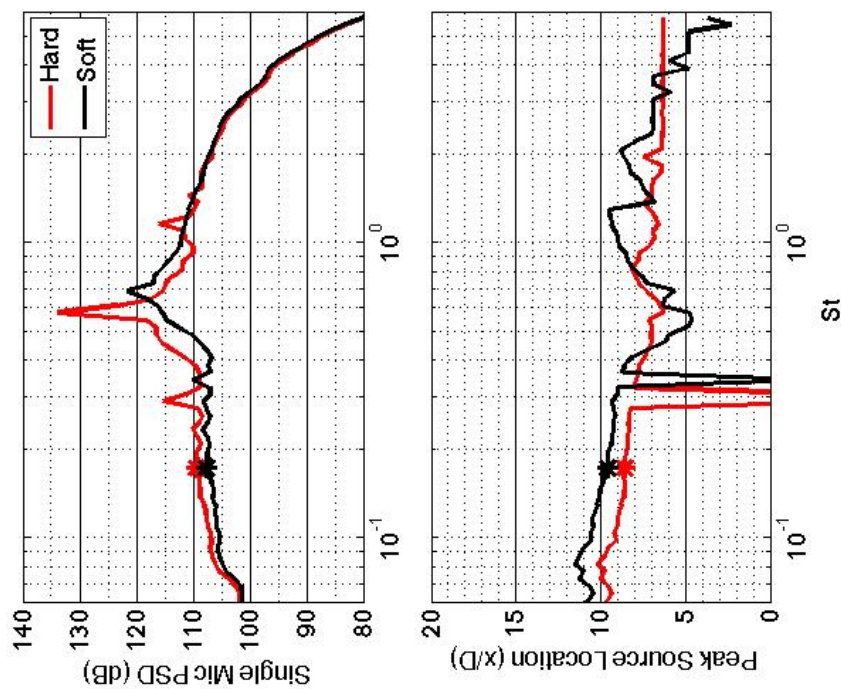
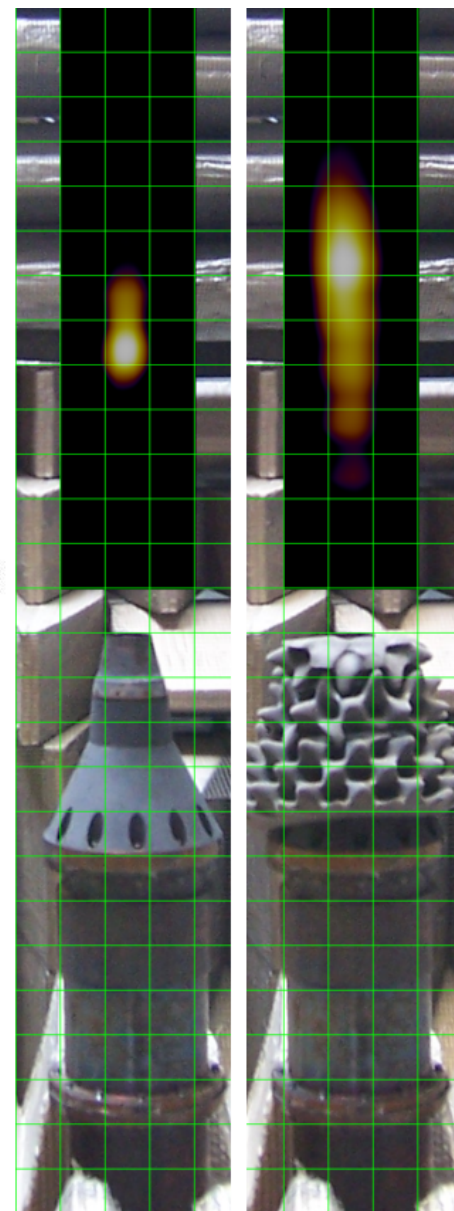Figure 259.—SMC000; under-expanded; set point 9010; Mj=1.40; St=0.172.
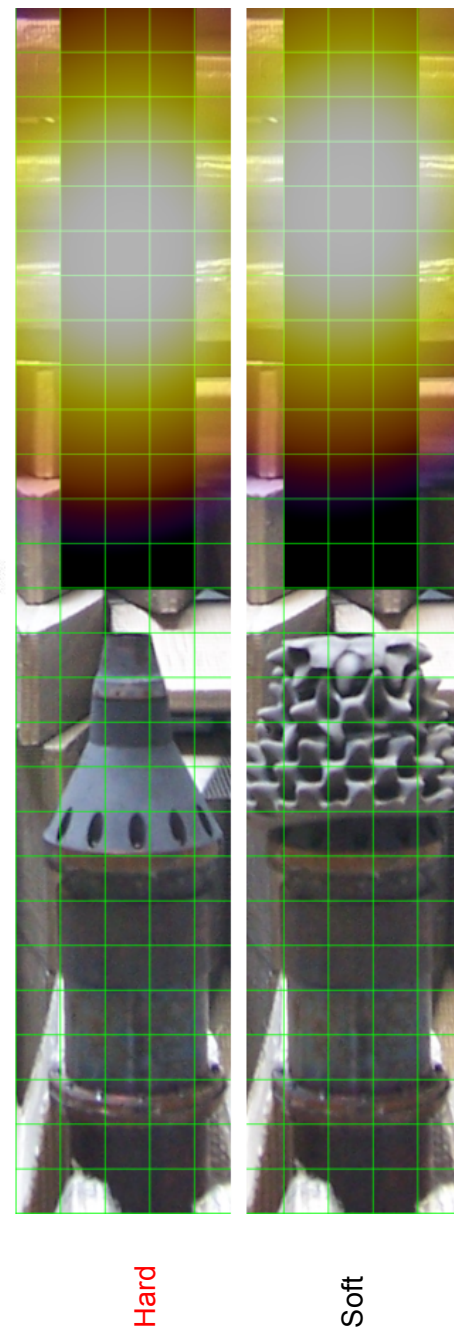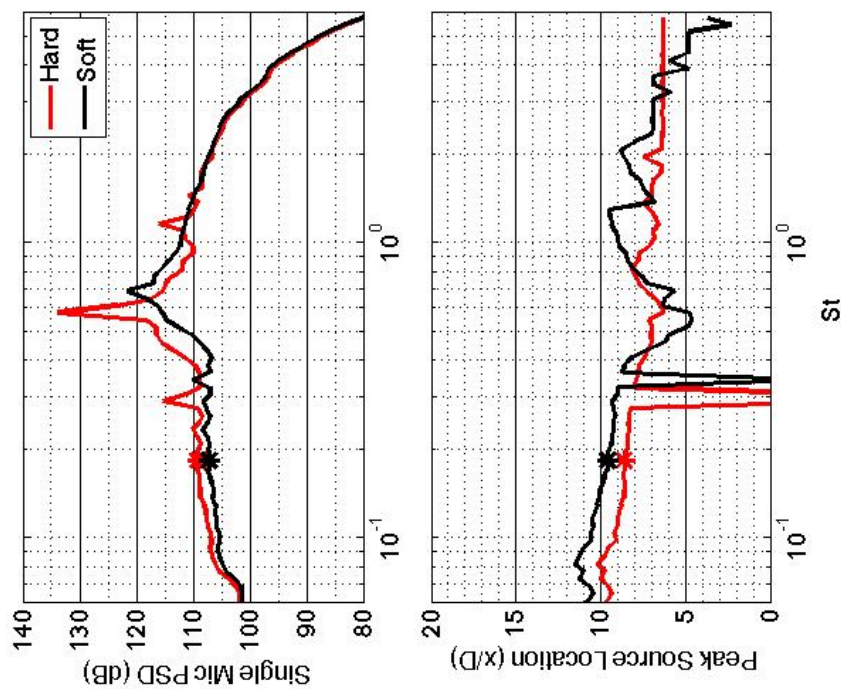
Figure 260.—SMC000; under-expanded; set point 9010; Mj=1.40; St=0.183.
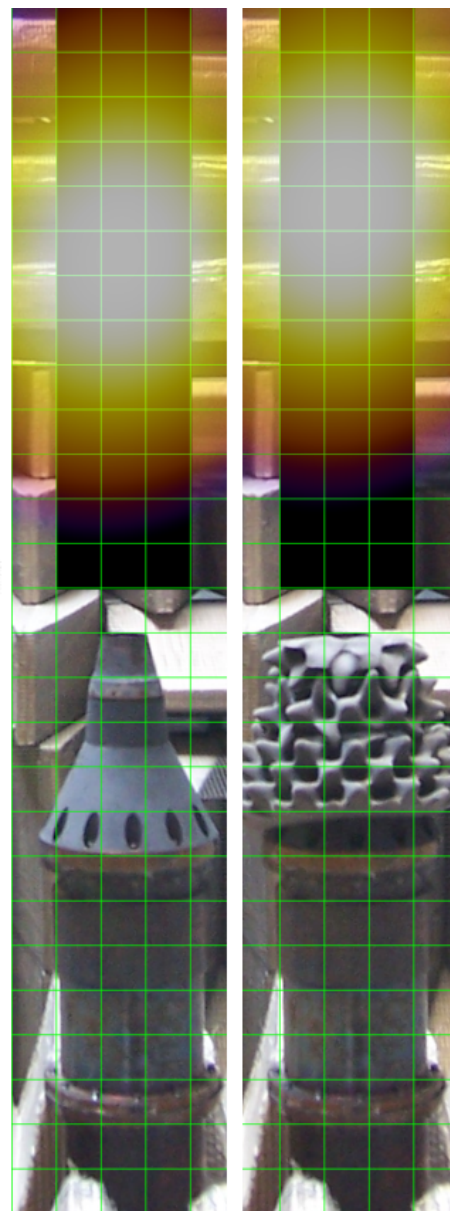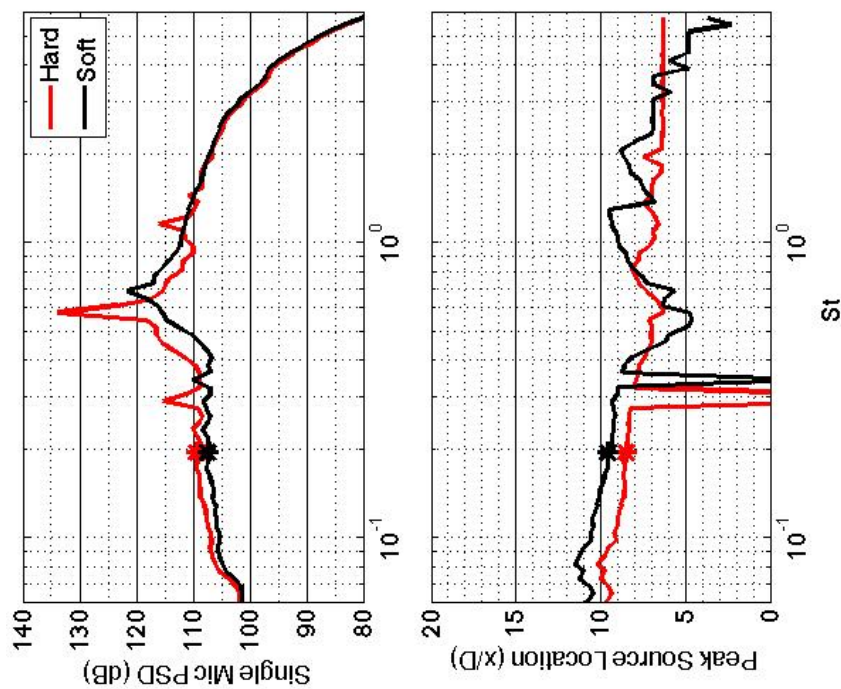
Figure 261.—SMC000; under-expanded; set point 9010; Mj=1.40; St=0.195.
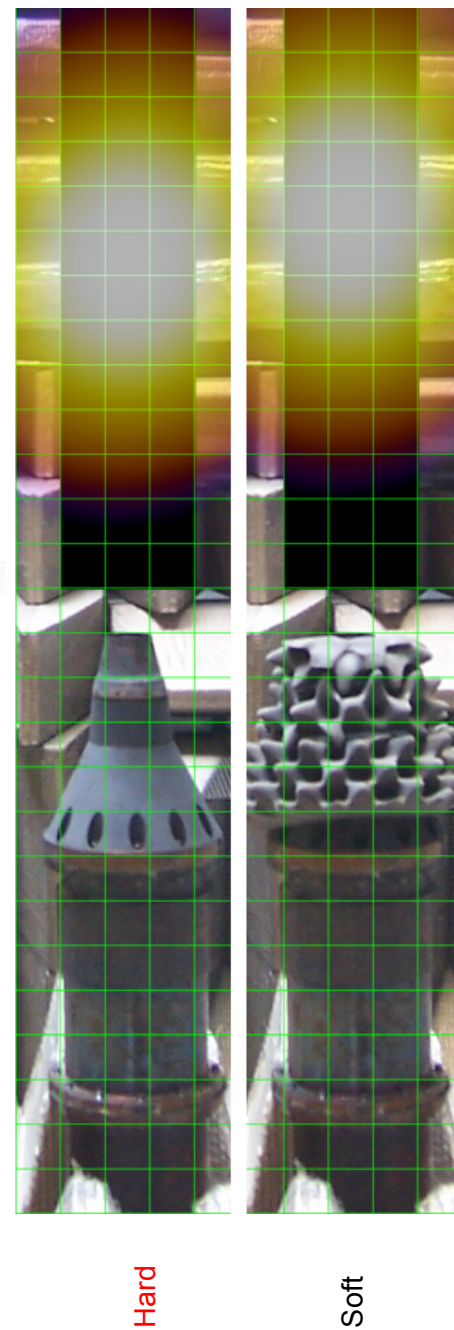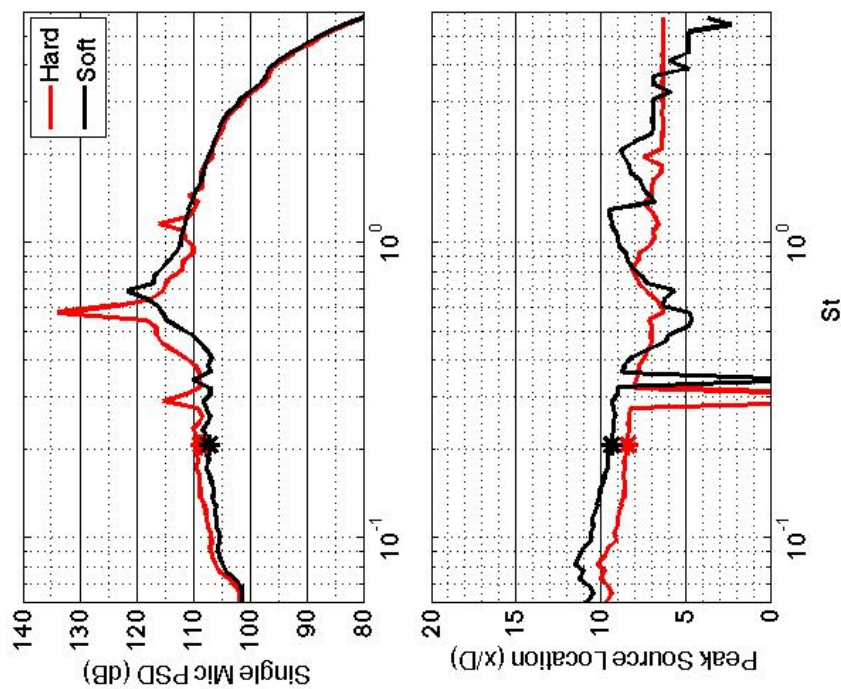
Figure 262.—SMC000; under-expanded; set point 9010; Mj=1.40; St=0.207.
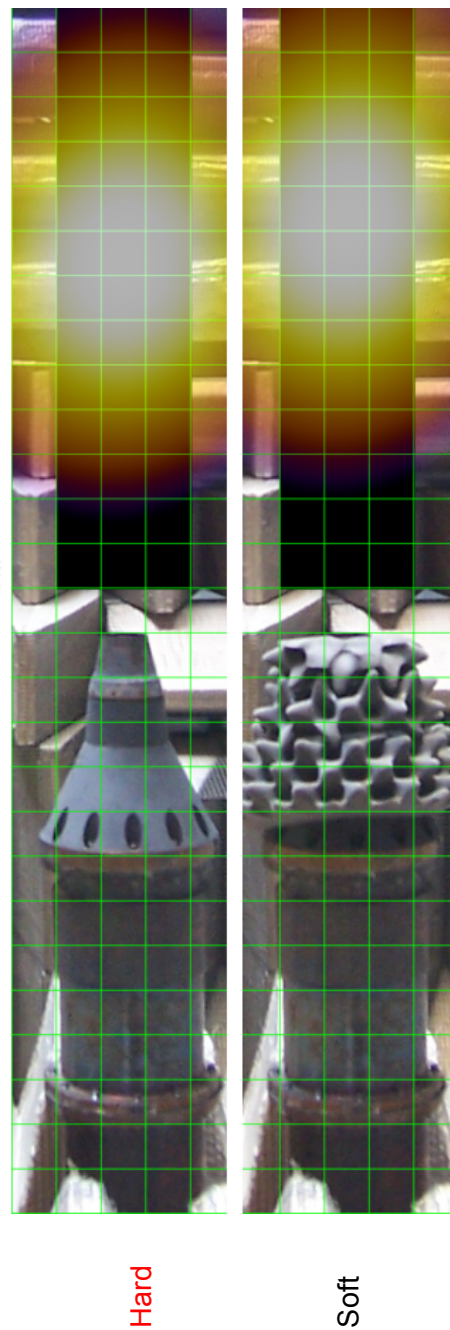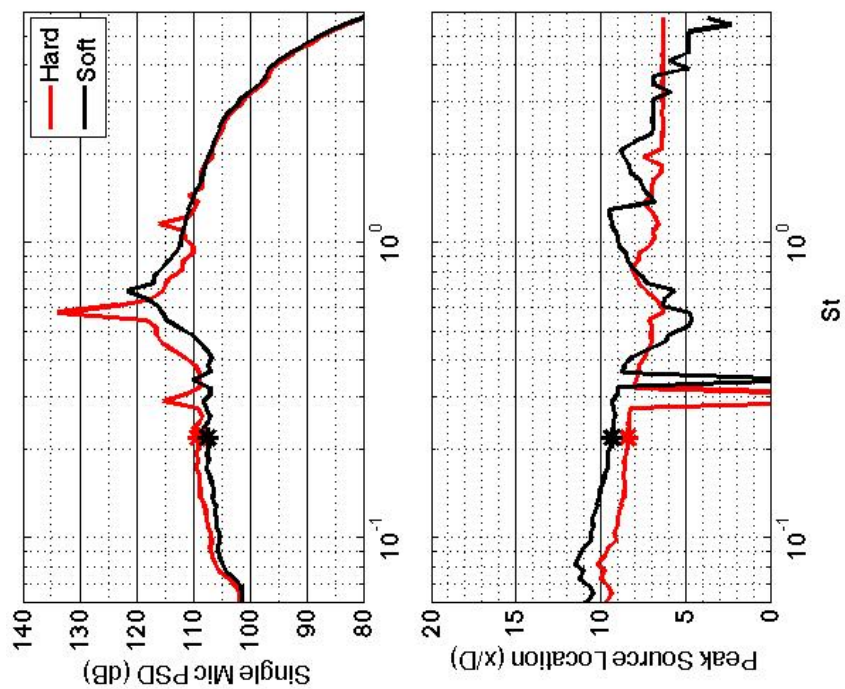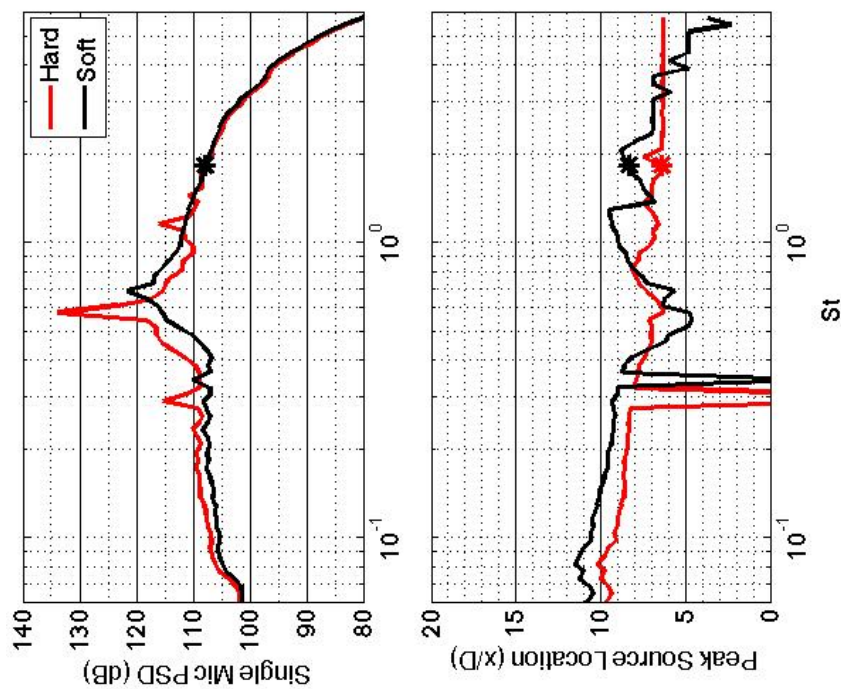
Figure 263.—SMC000; under-expanded; set point 9010; Mj=1.40; St=0.219.
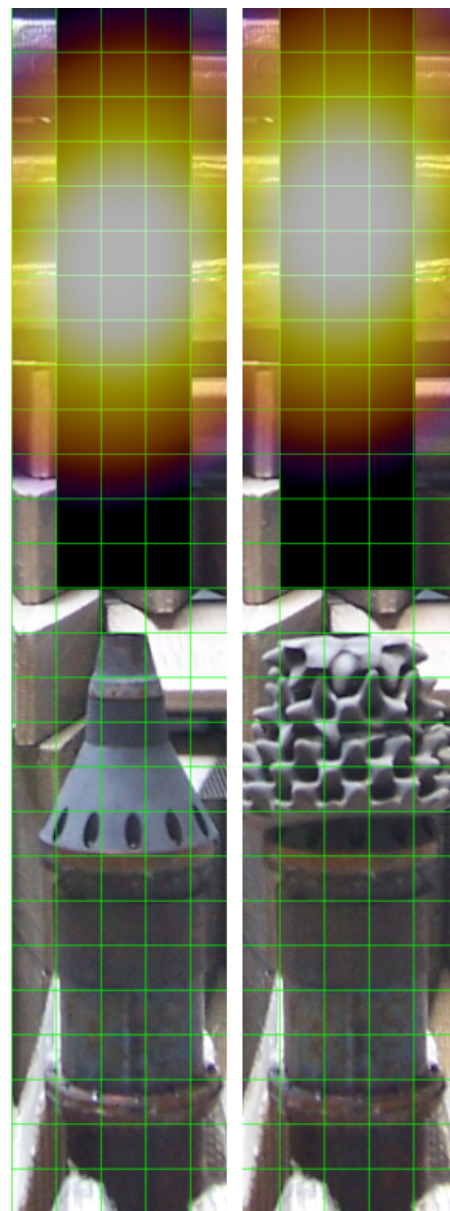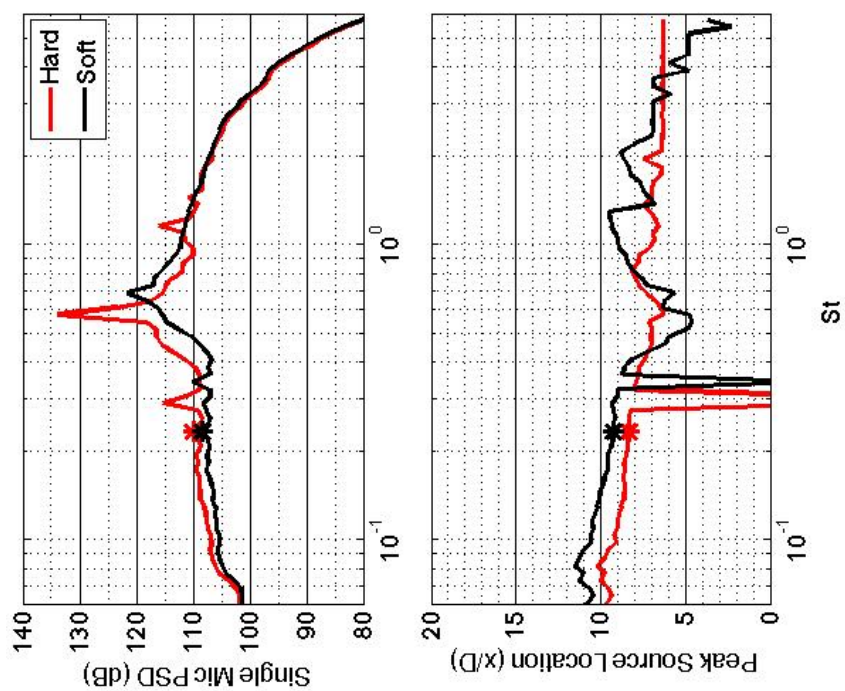
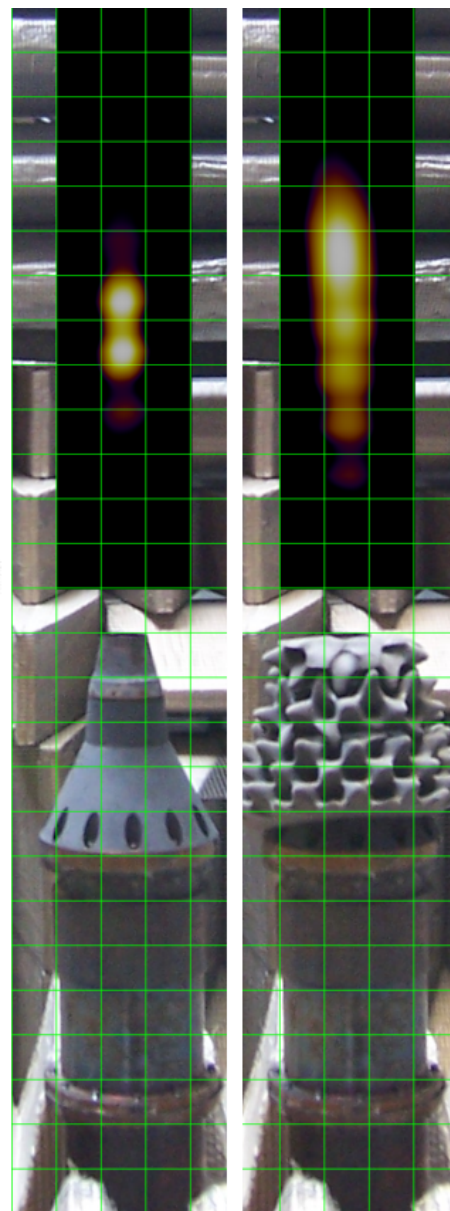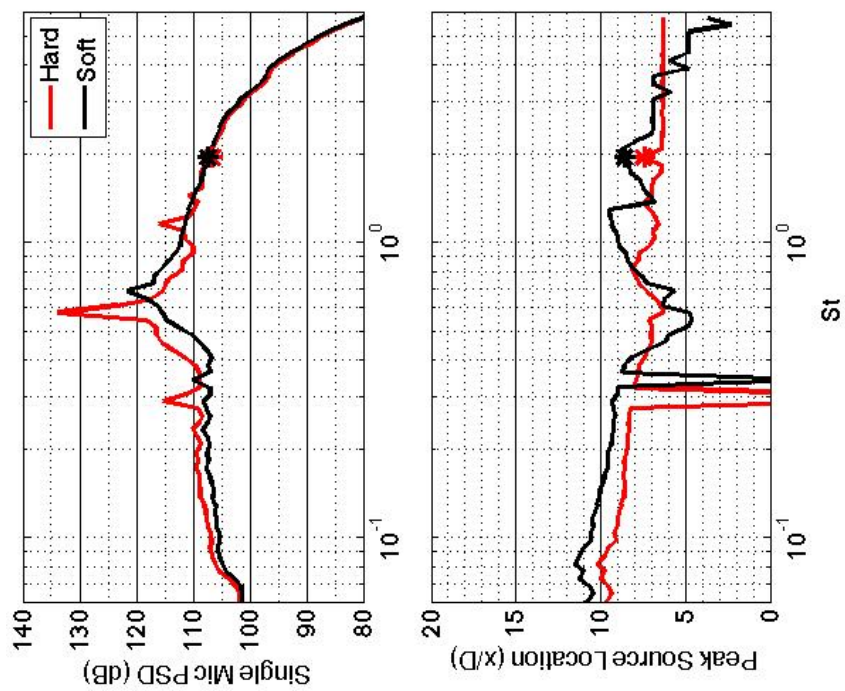Figure 264.—SMC000; under-expanded; set point 9010; Mj=1.40; St=0.232.
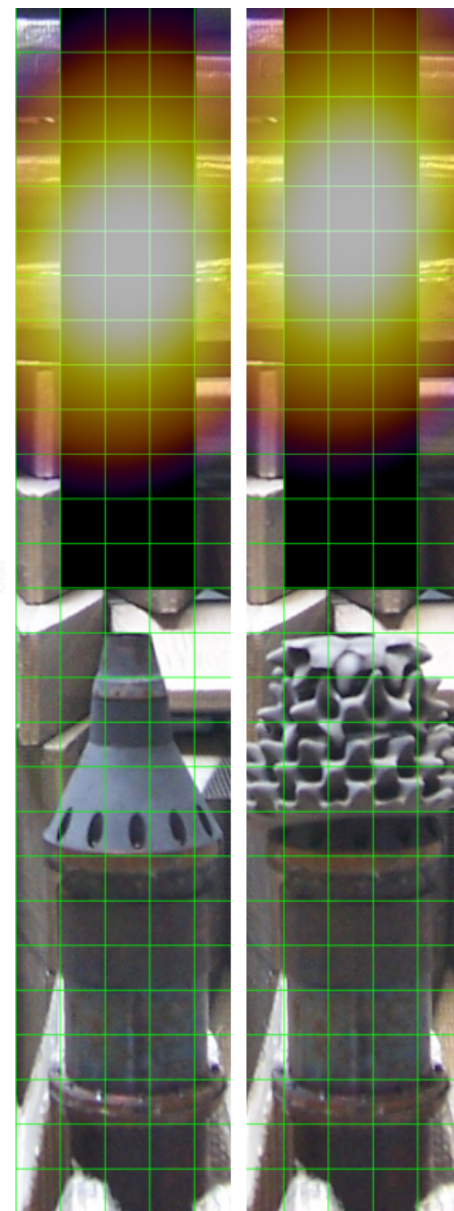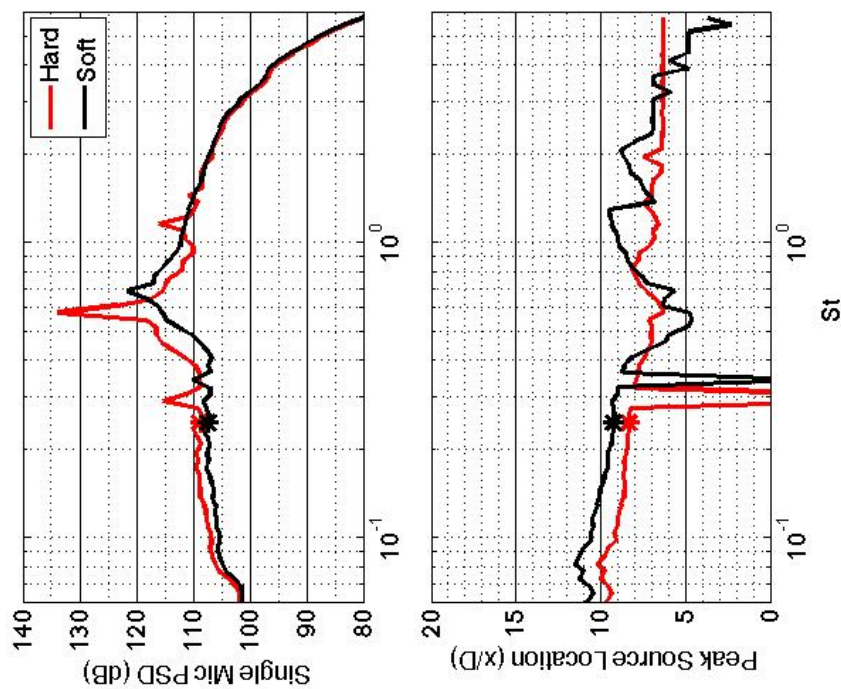
Figure 265.—SMC000; under-expanded; set point 9010; Mj=1.40; St=0.245.
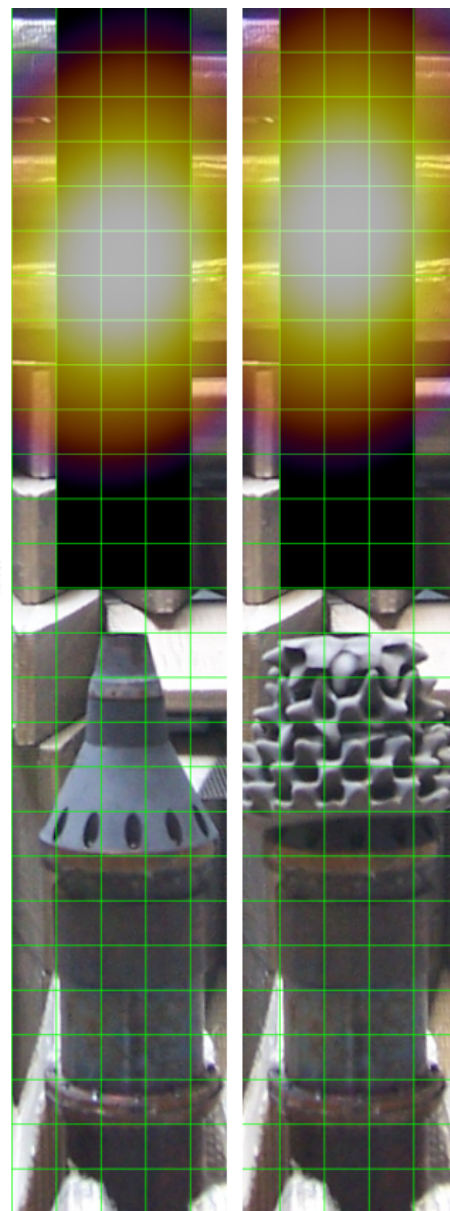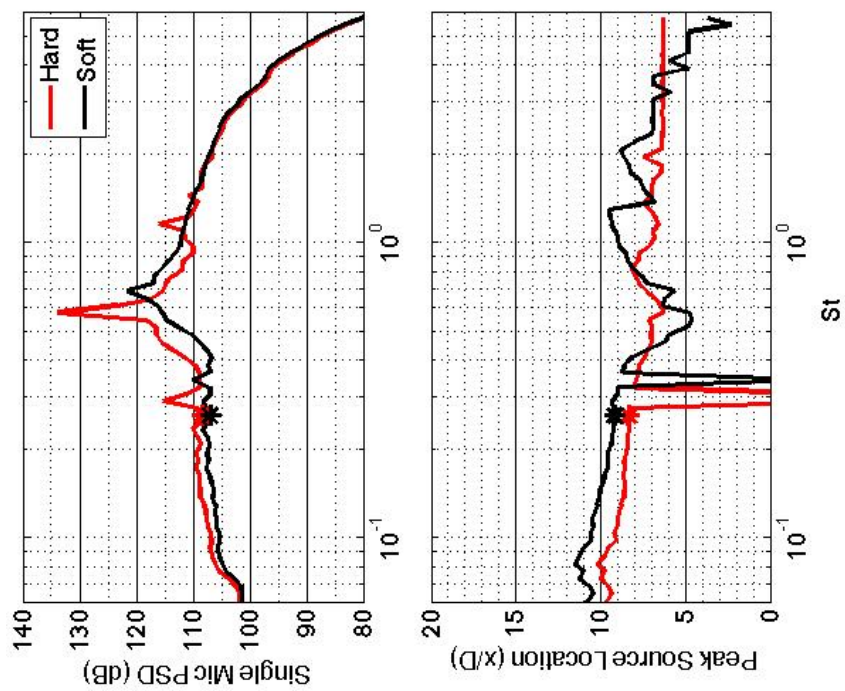
Figure 266.—SMC000; under-expanded; set point 9010; Mj=1.40; St=0.259.
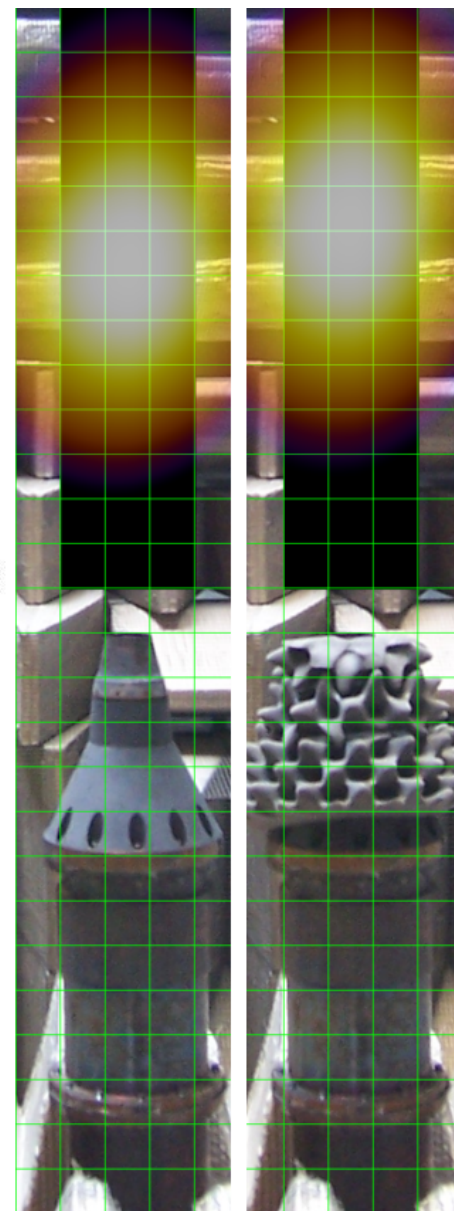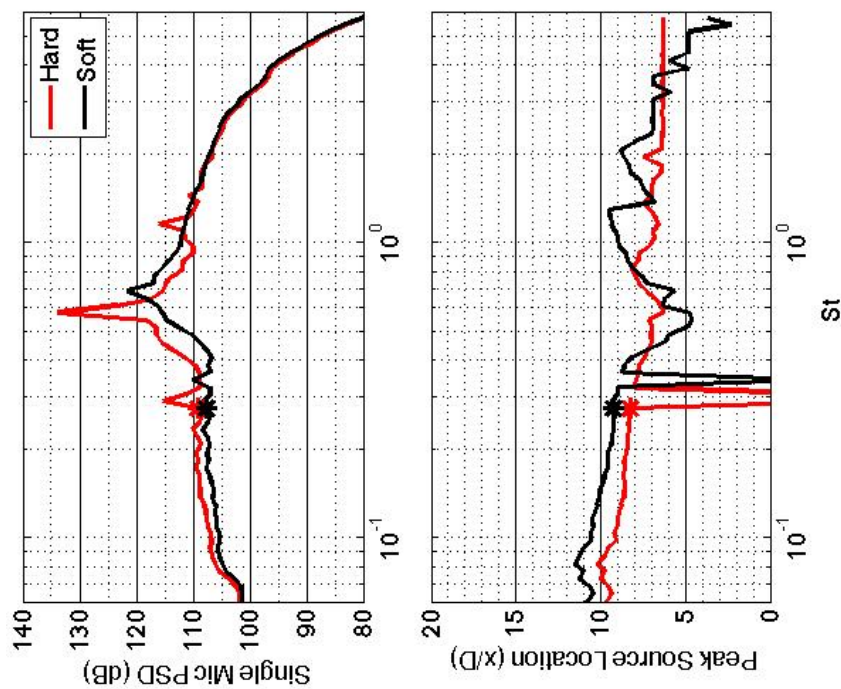
Figure 267.—SMC000; under-expanded; set point 9010; Mj=1.40; St=0.274.
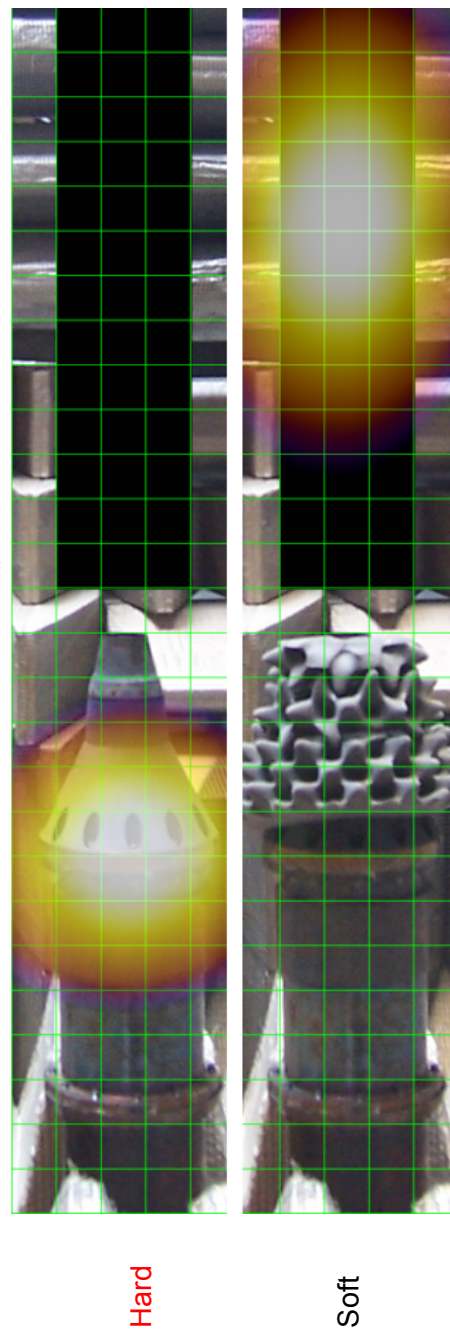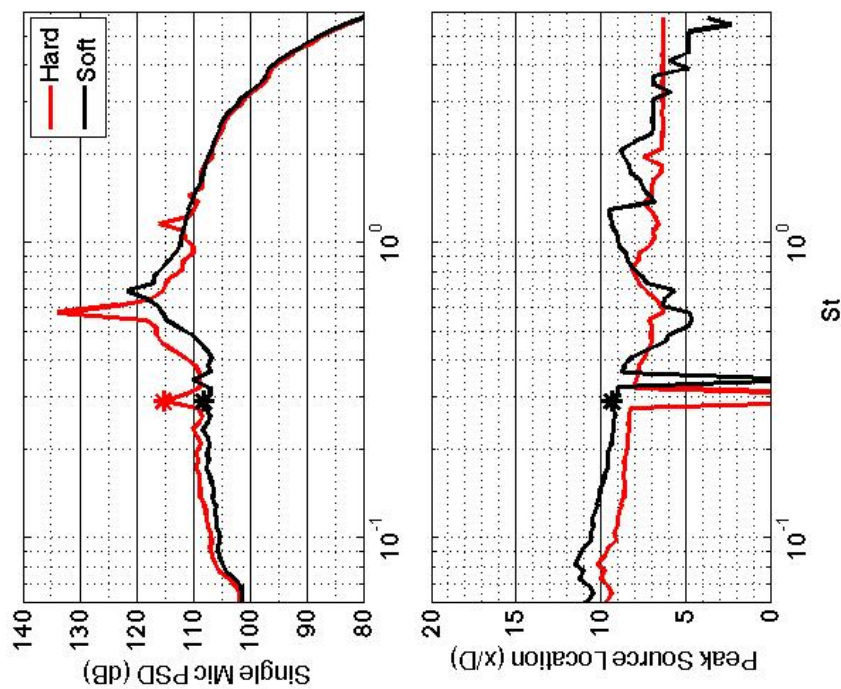
Figure 268.—SMC000; under-expanded; set point 9010; Mj=1.40; St=0.290.
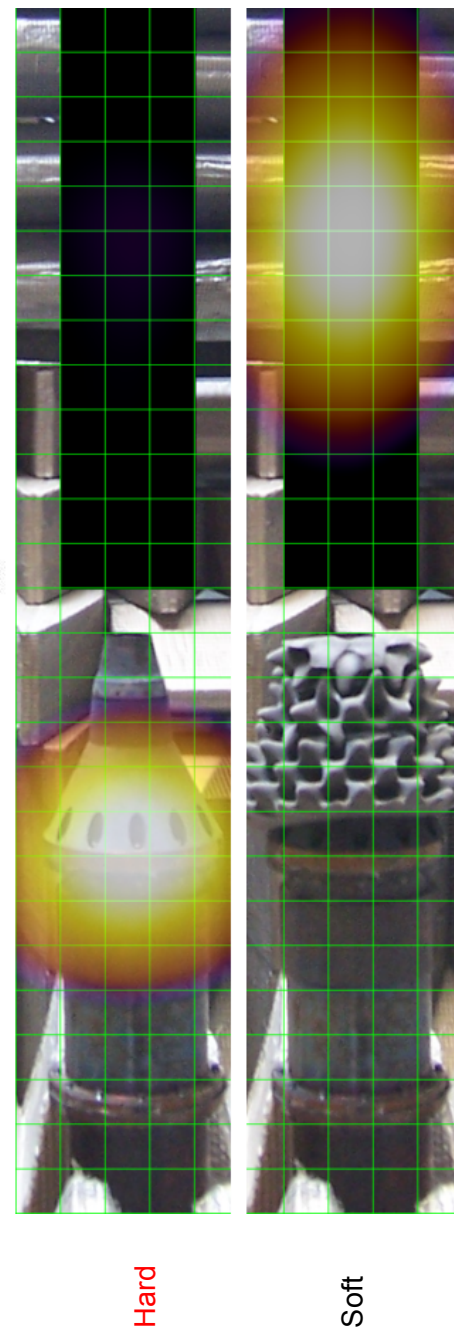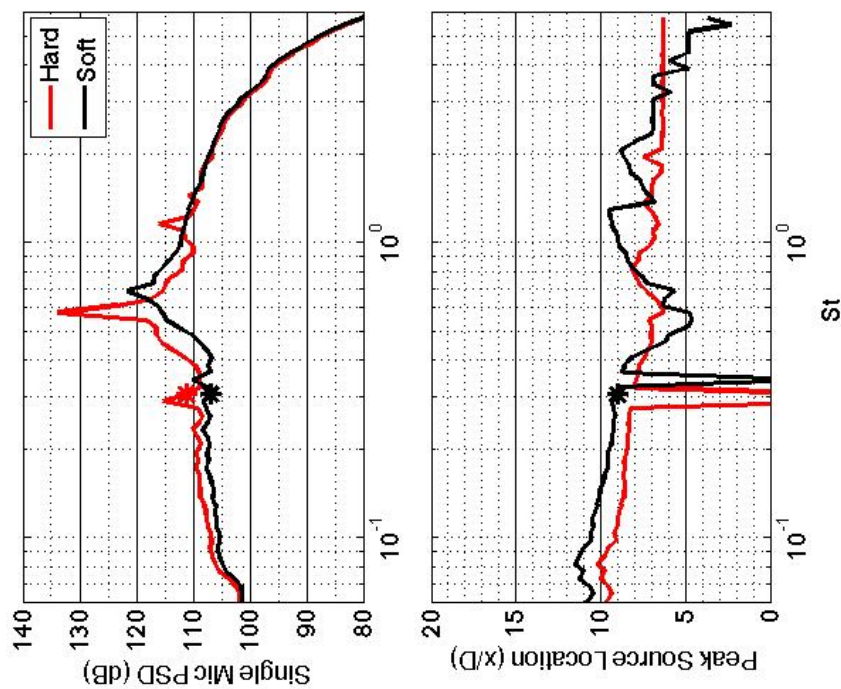
Figure 269.—SMC000; under-expanded; set point 9010; Mj=1.40; St=0.306.
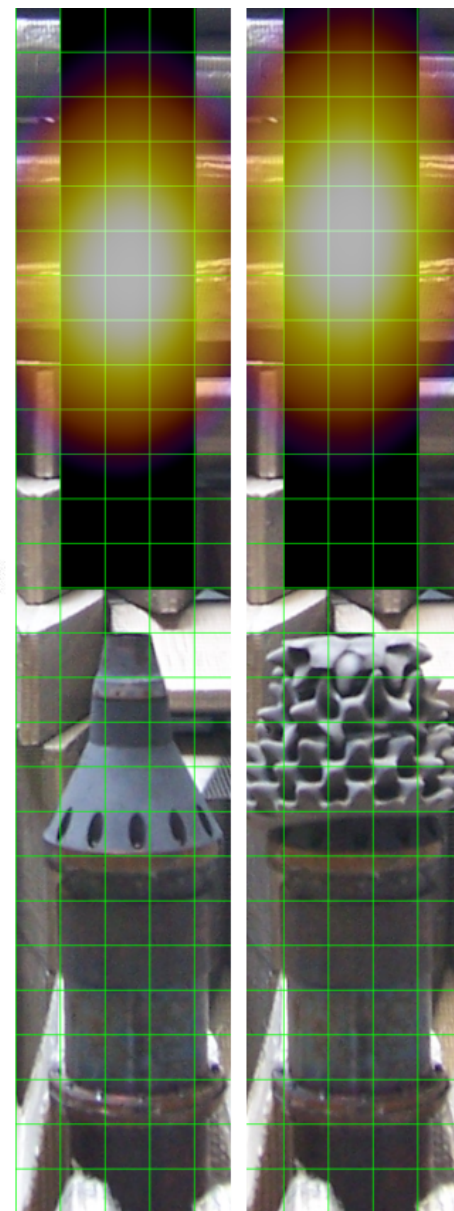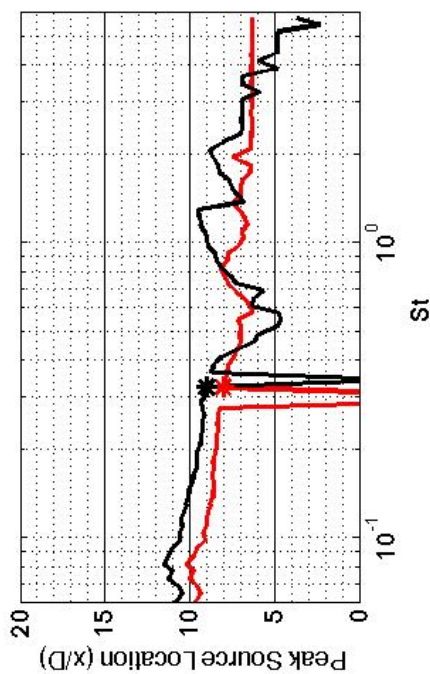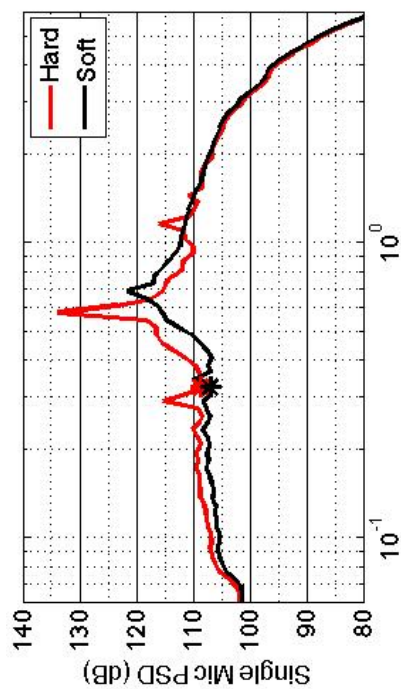
Figure 270.—SMC000; under-expanded; set point 9010; Mj=1.40; St=0.324.
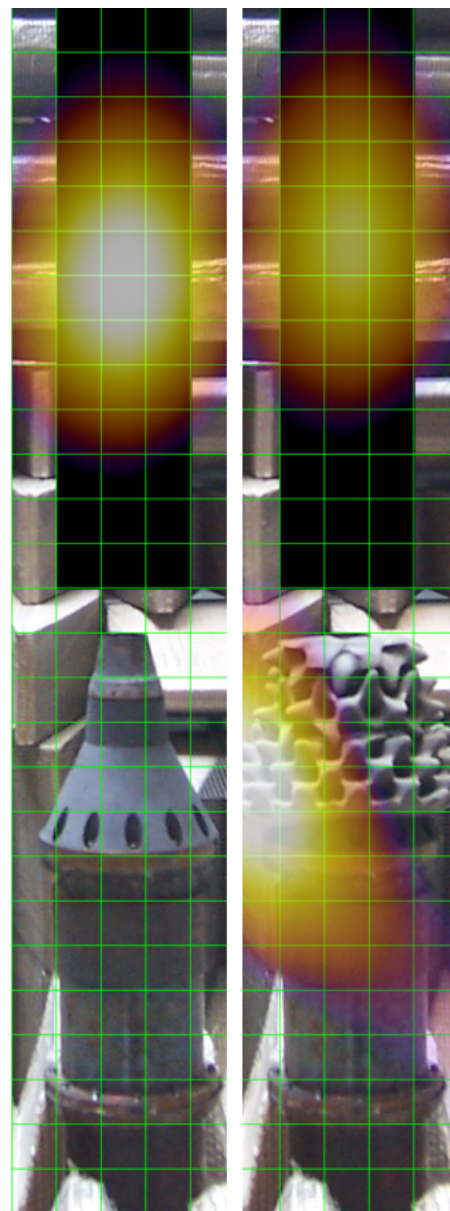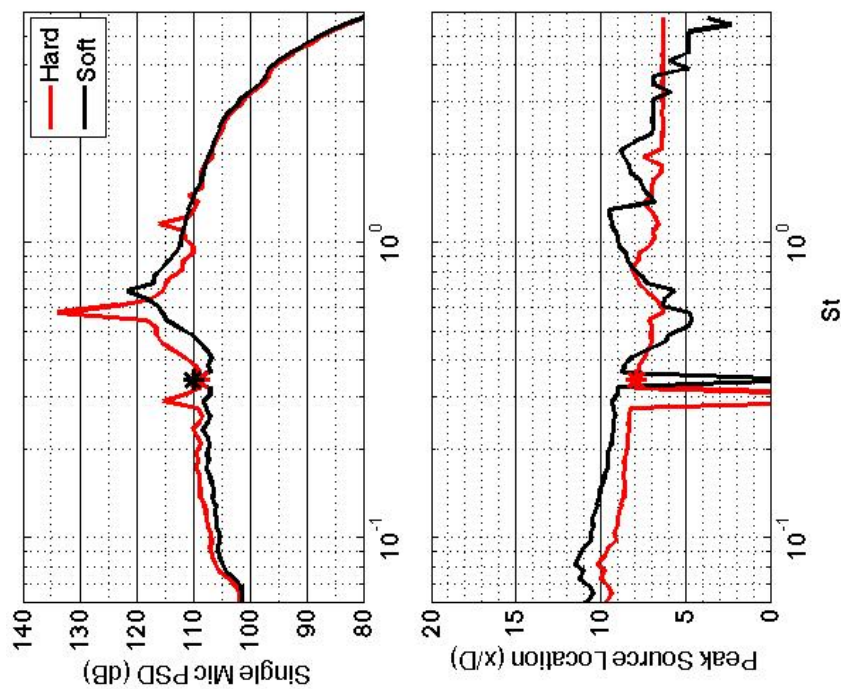
Figure 271.—SMC000; under-expanded; set point 9010; Mj=1.40; St=0.343.
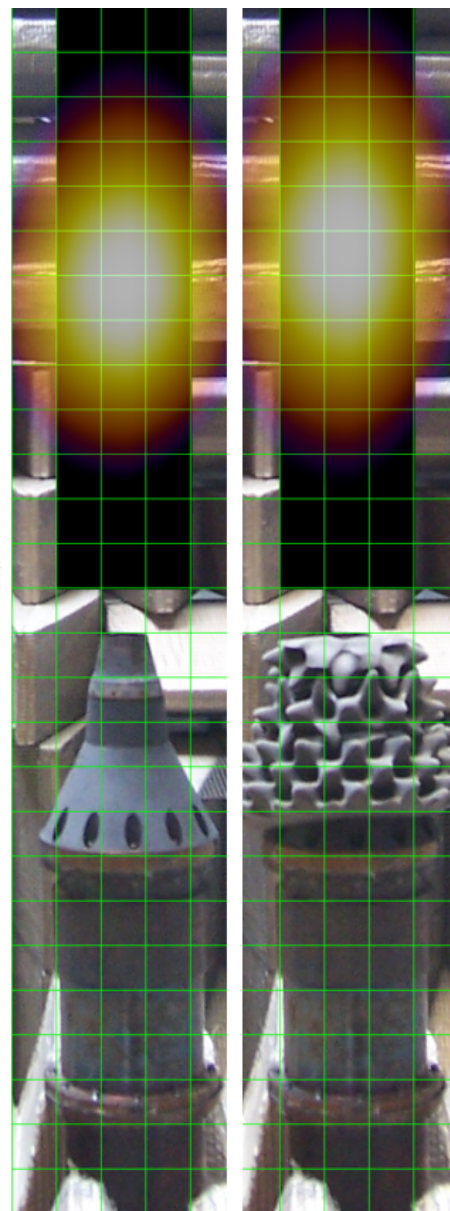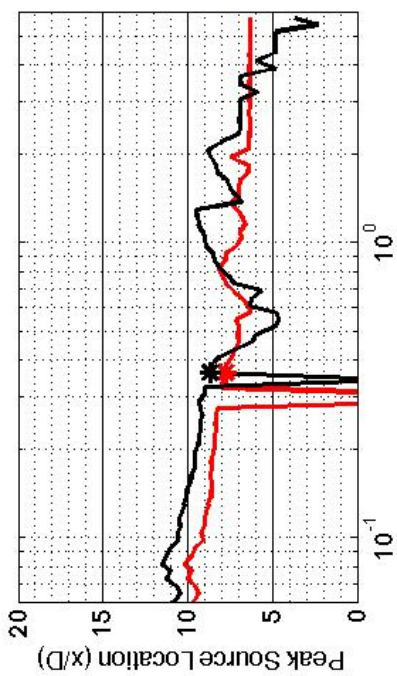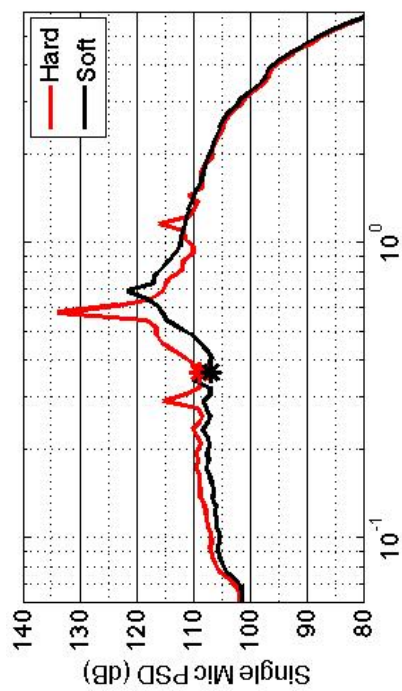
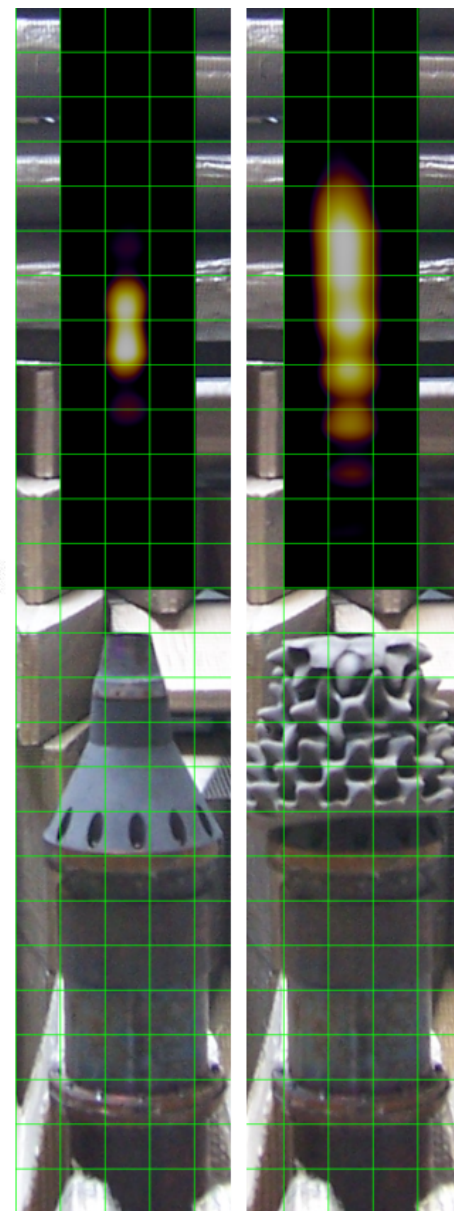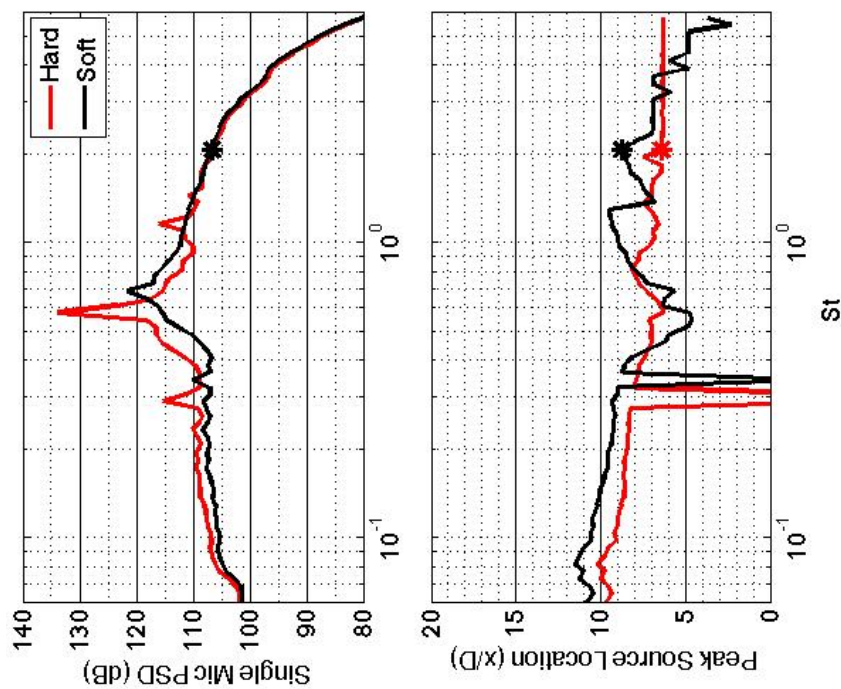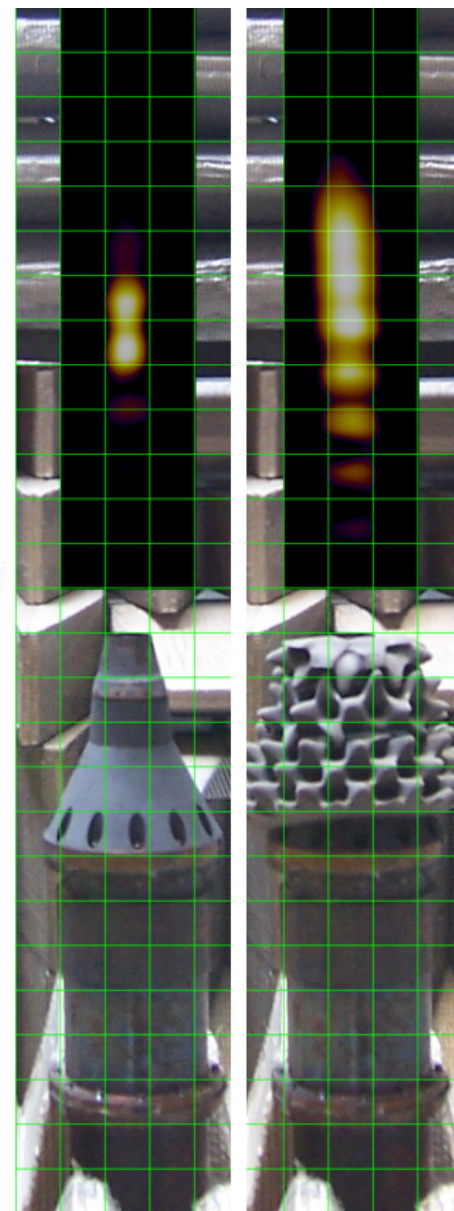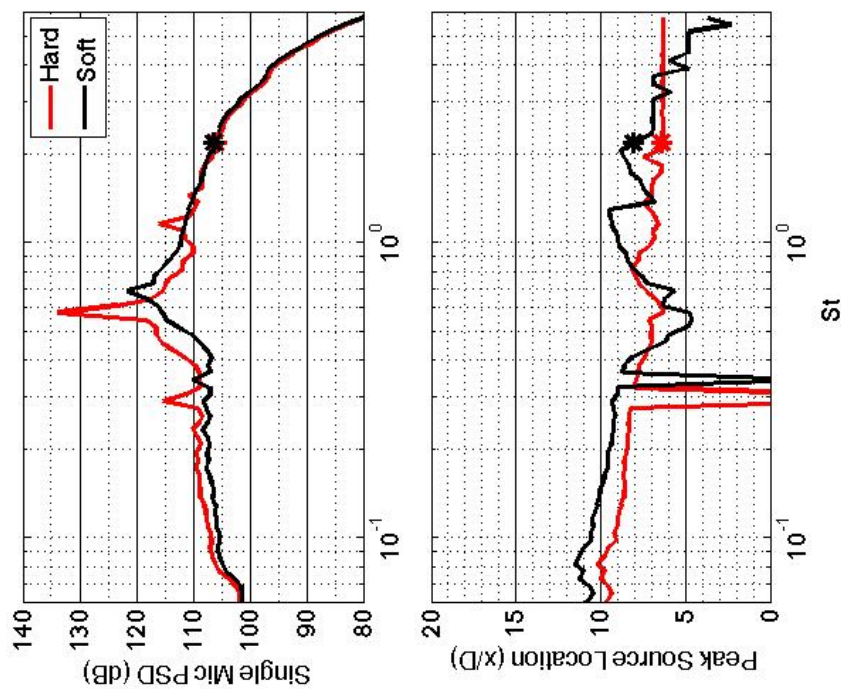Figure 272.—SMC000; under-expanded; set point 9010; Mj=1.40; St=0.363.
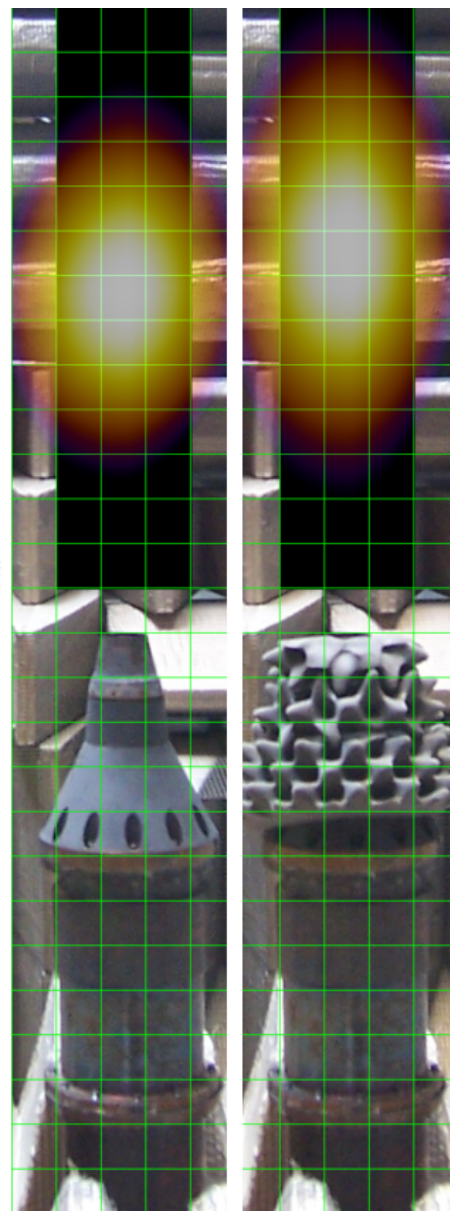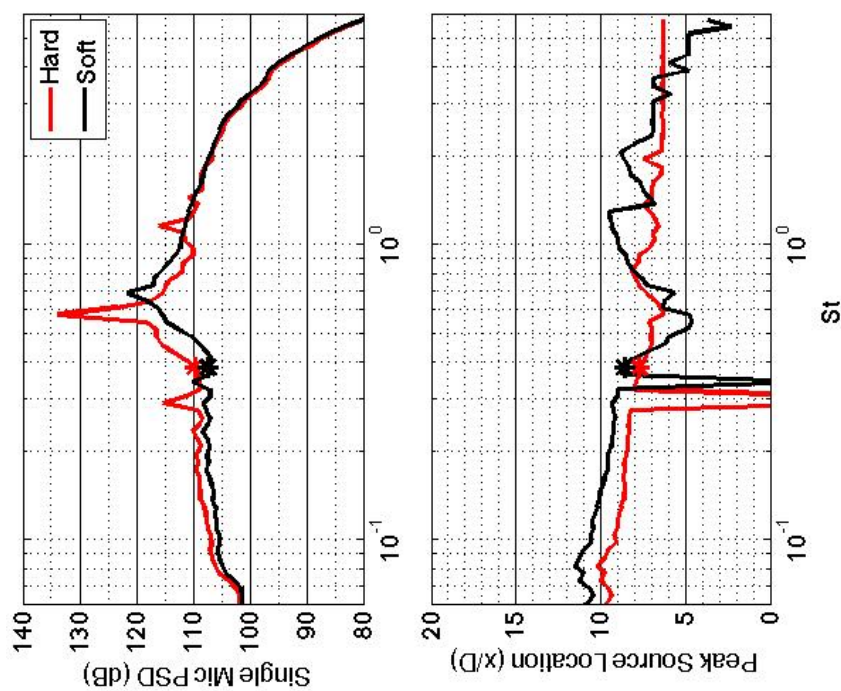
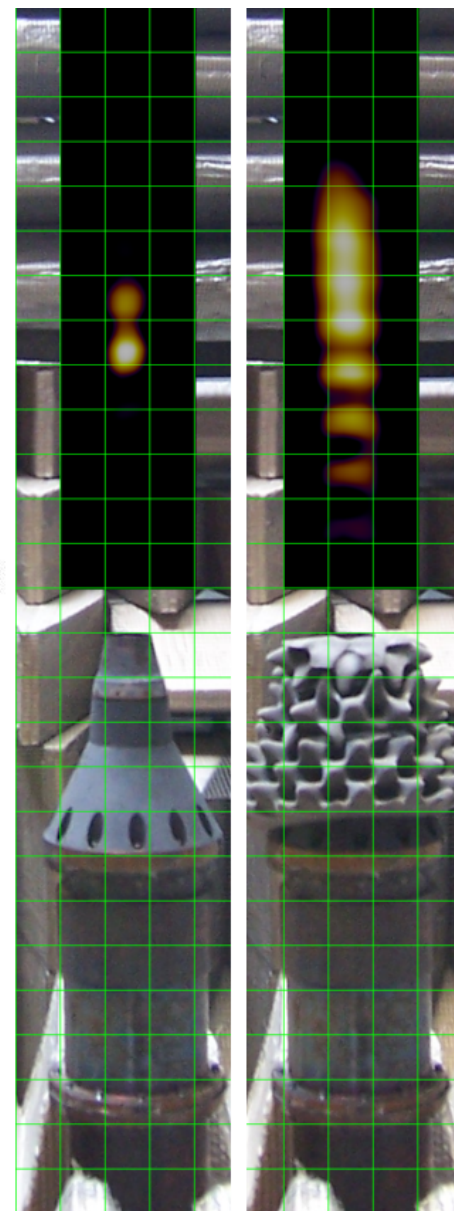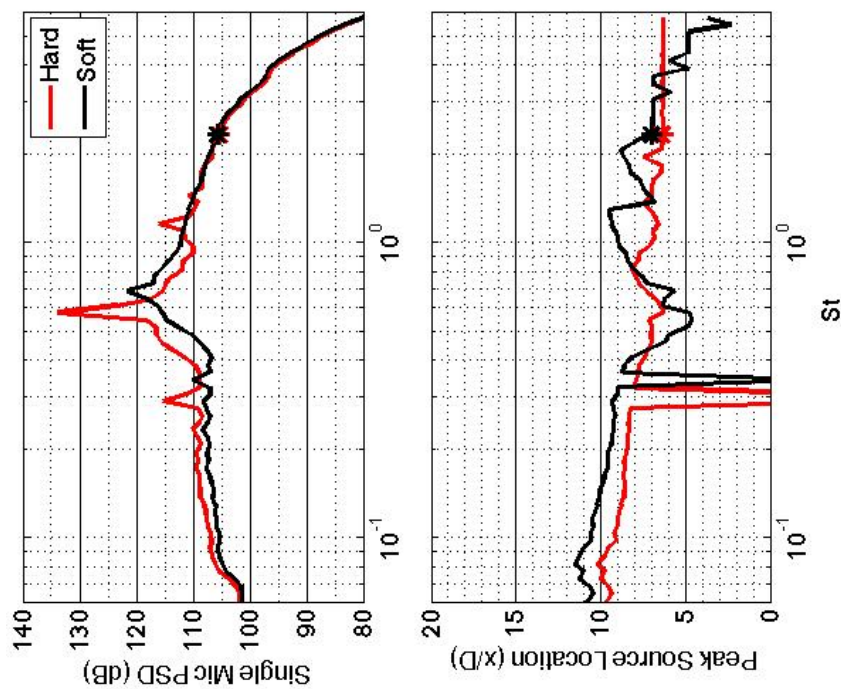Figure 273.—SMC000; under-expanded; set point 9010; Mj=1.40; St=0.385.
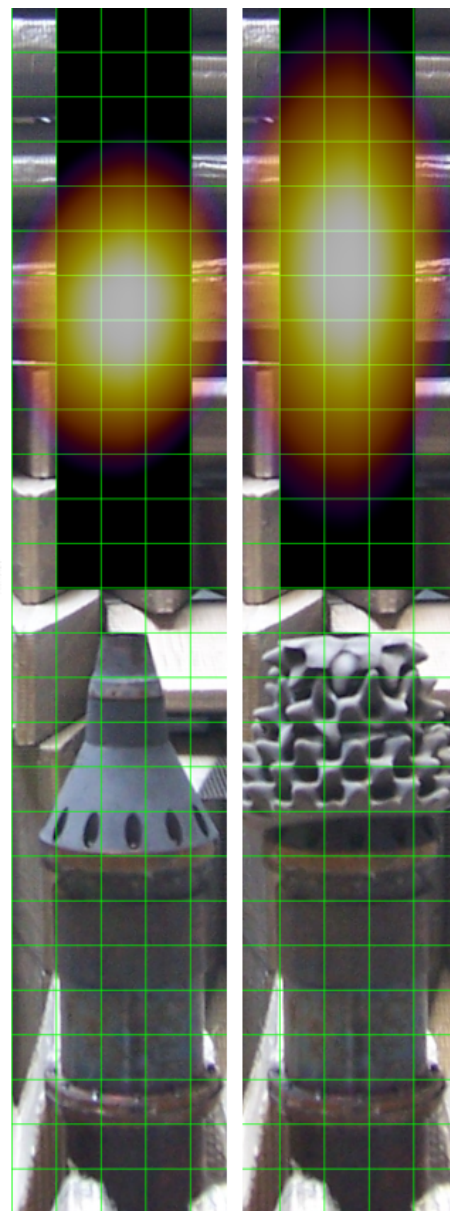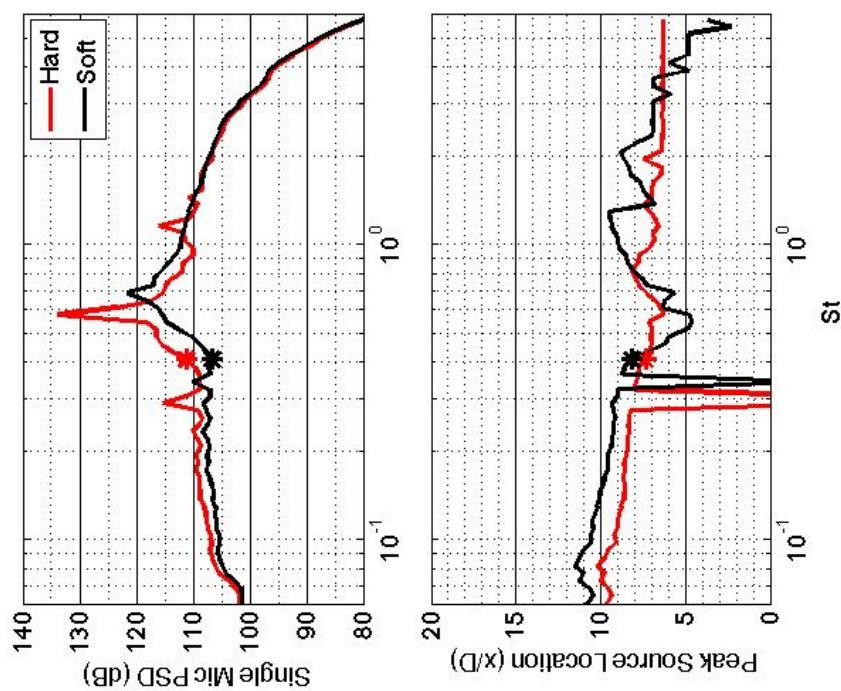
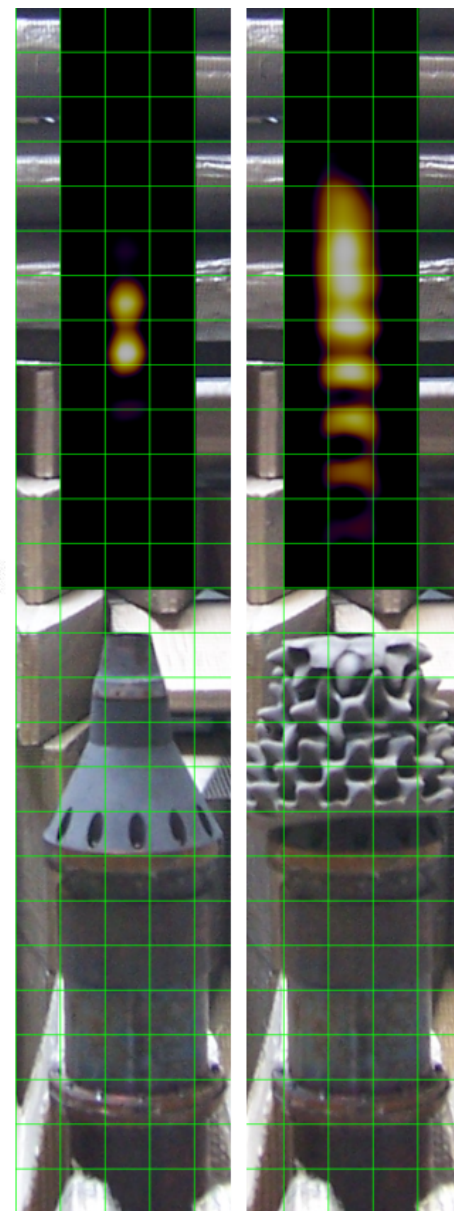Figure 274.—SMC000; under-expanded; set point 9010; Mj=1.40; St=0.408.
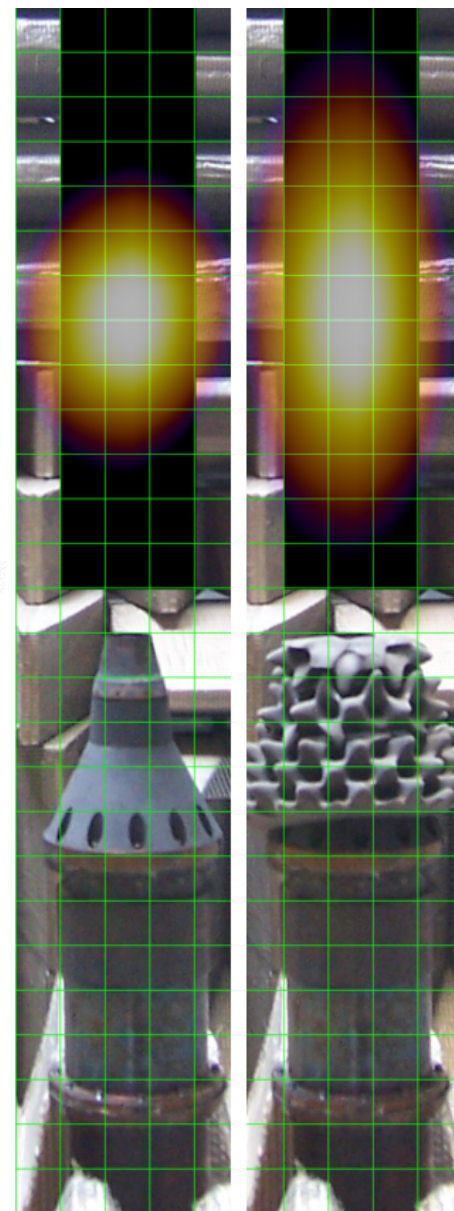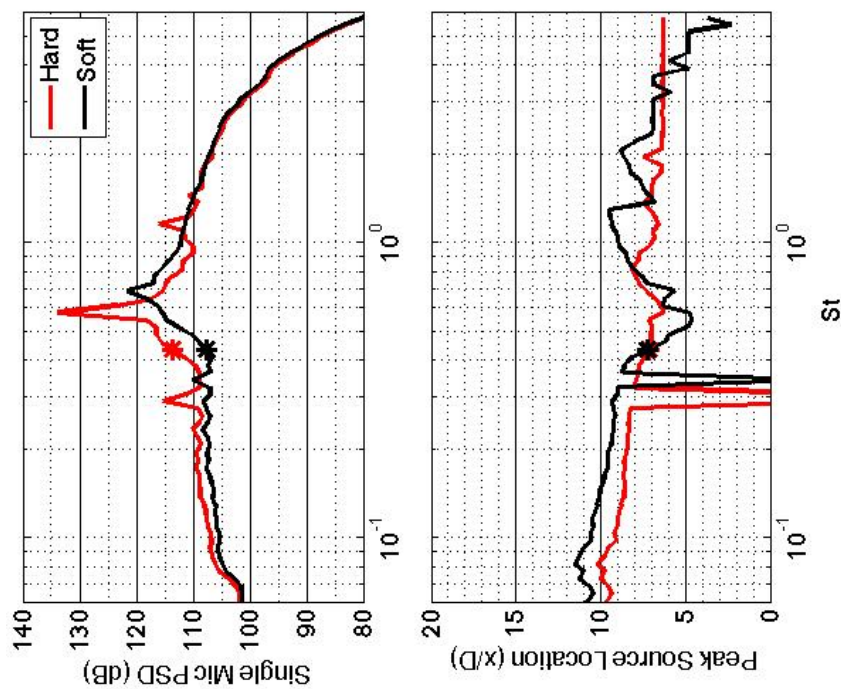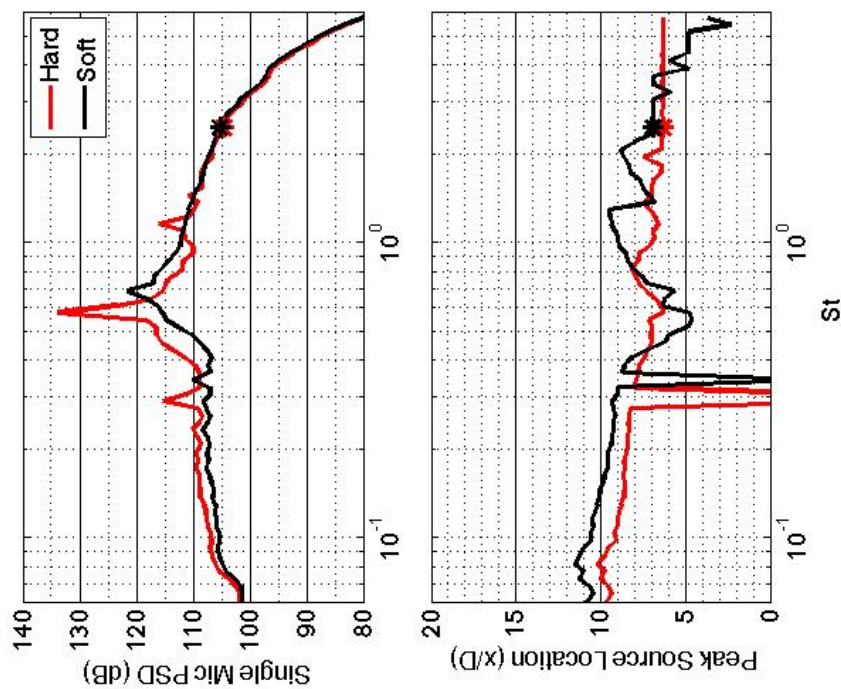
Figure 275.—SMC000; under-expanded; set point 9010; Mj=1.40; St=0.433.
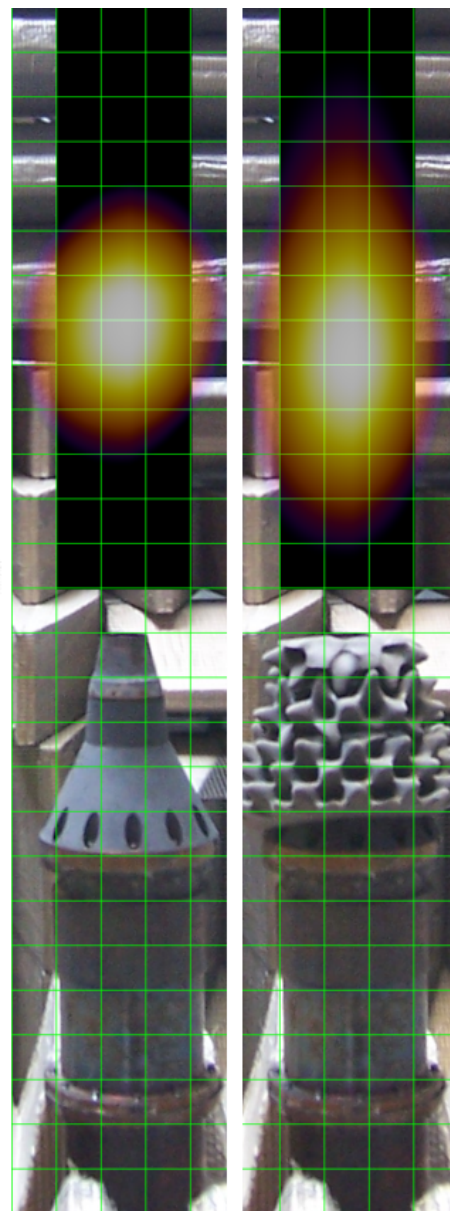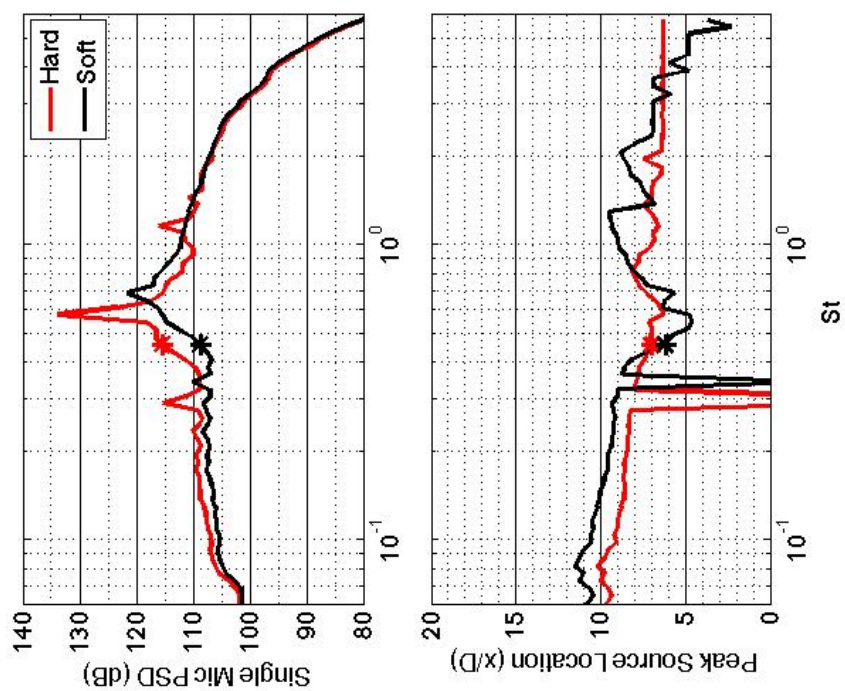
Figure 276.—SMC000; under-expanded; set point 9010; Mj=1.40; St=0.460.
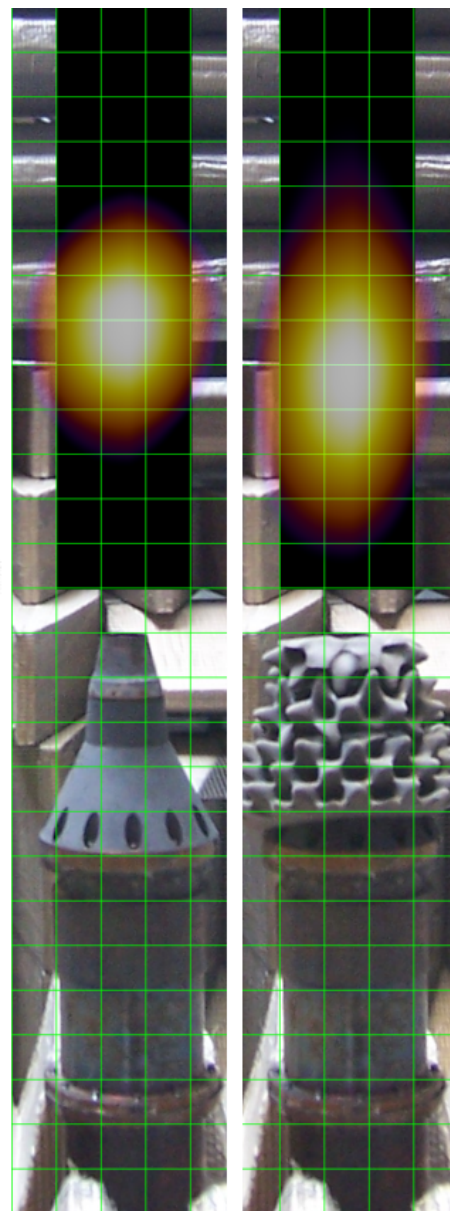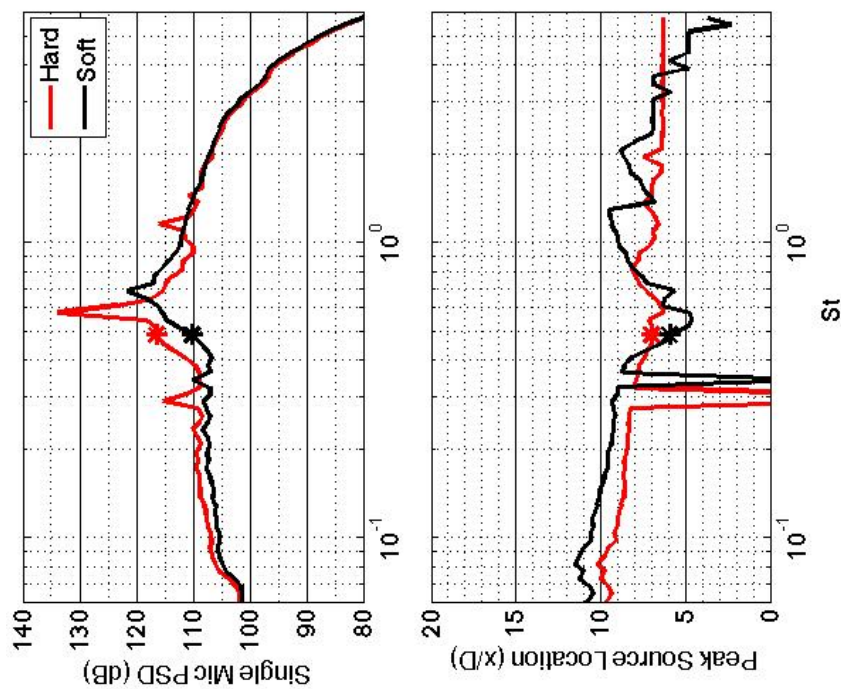
Figure 277.—SMC000; under-expanded; set point 9010; Mj=1.40; St=0.488.
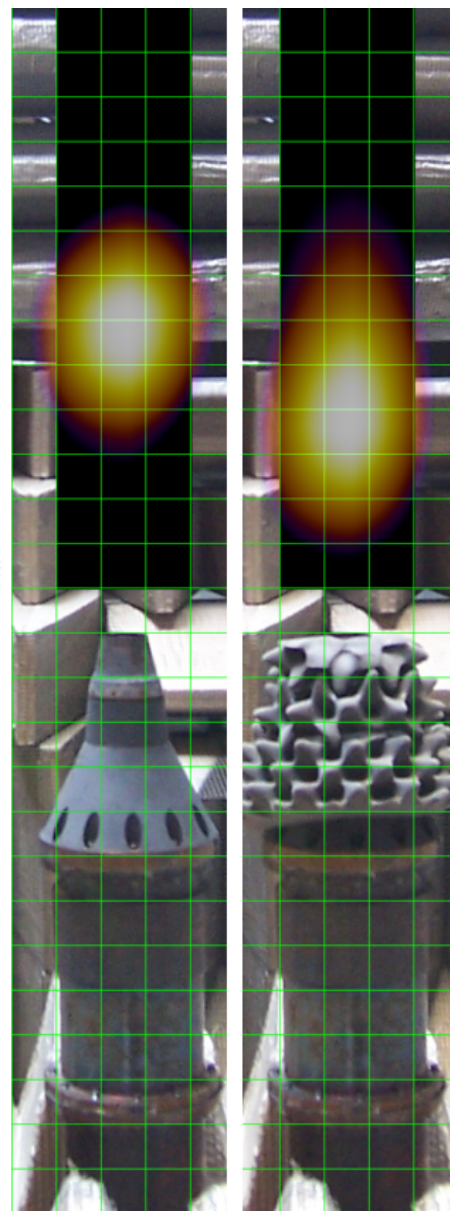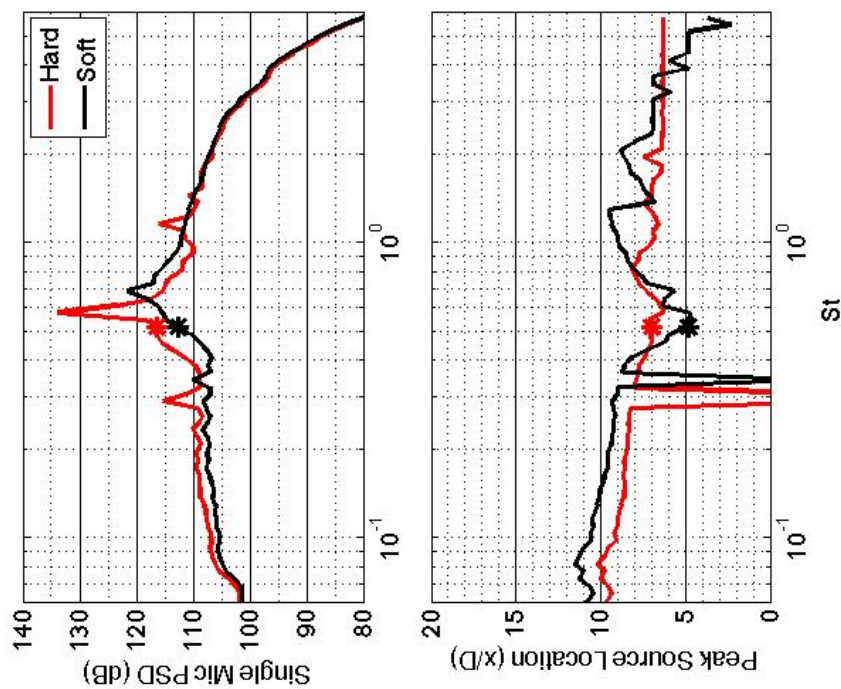
Figure 278.—SMC000; under-expanded; set point 9010; Mj=1.40; St=0.517.
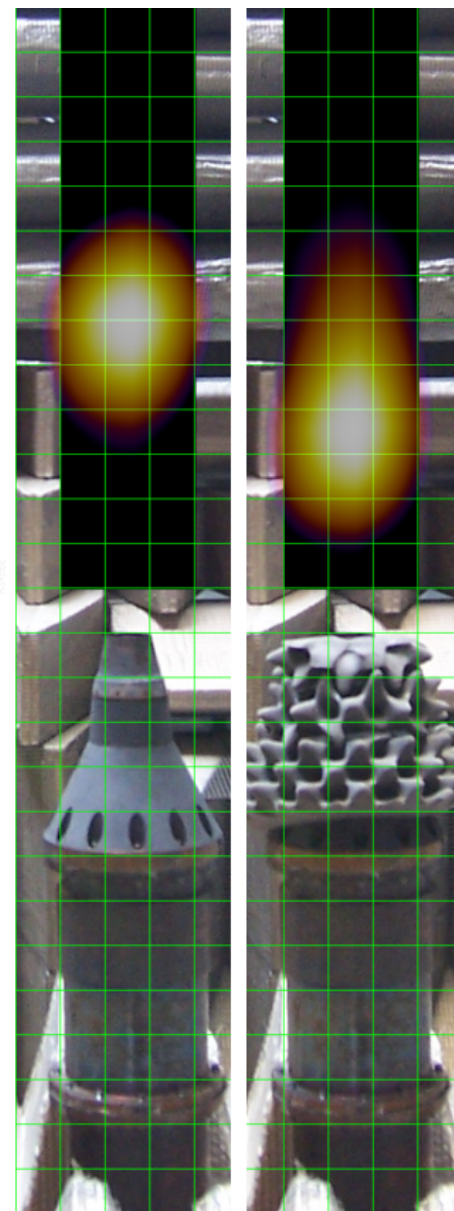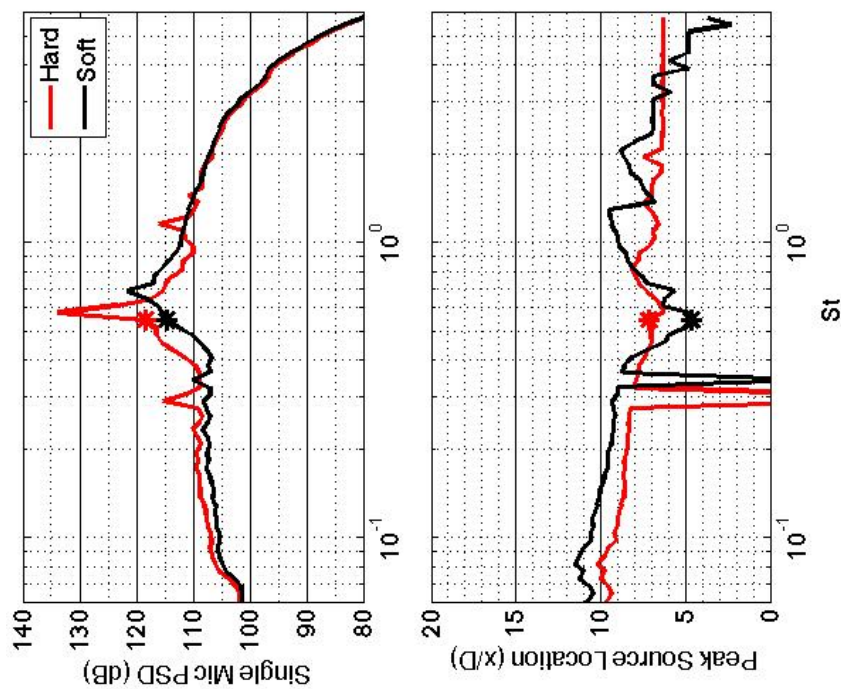
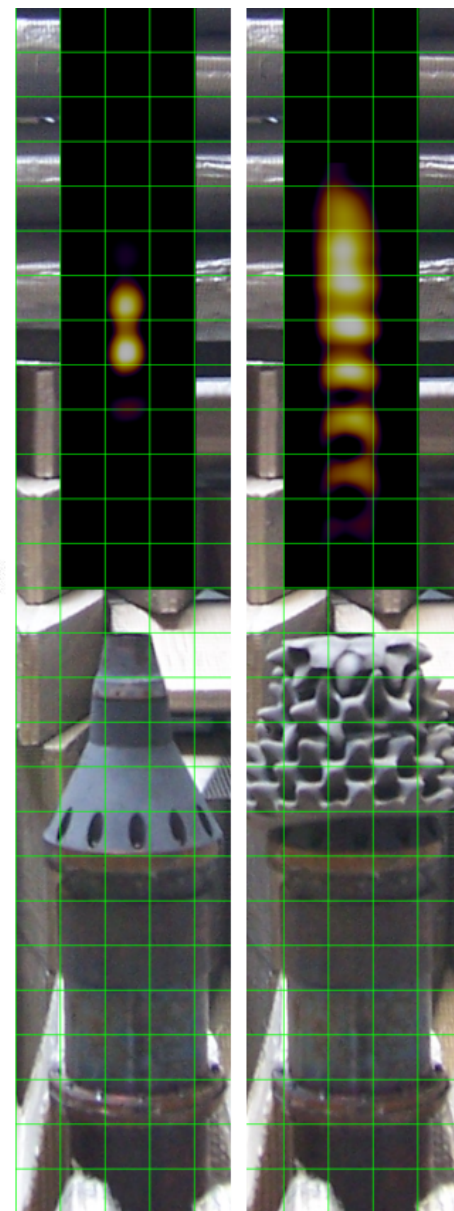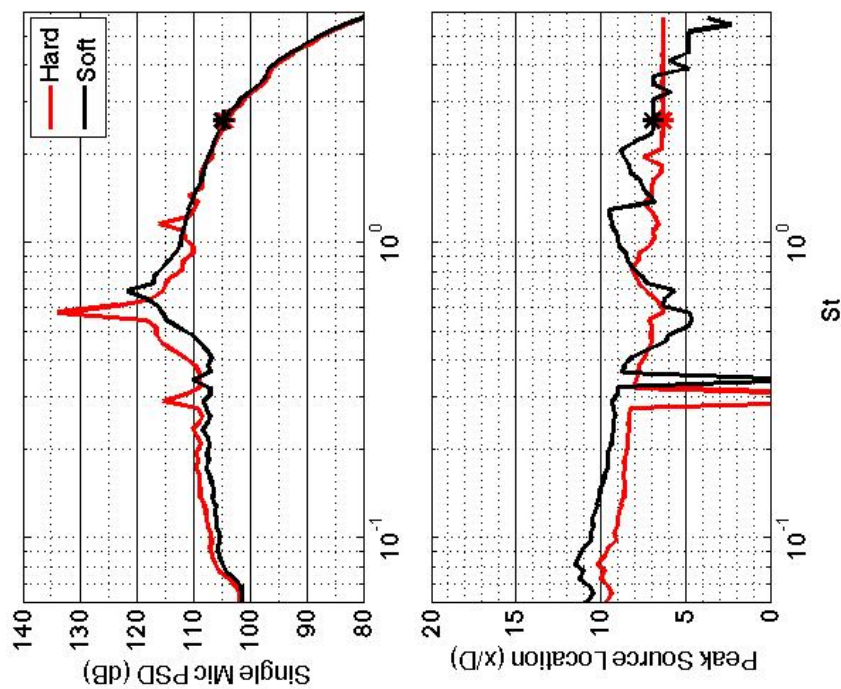Figure 279.—SMC000; under-expanded; set point 9010; Mj=1.40; St=0.548.
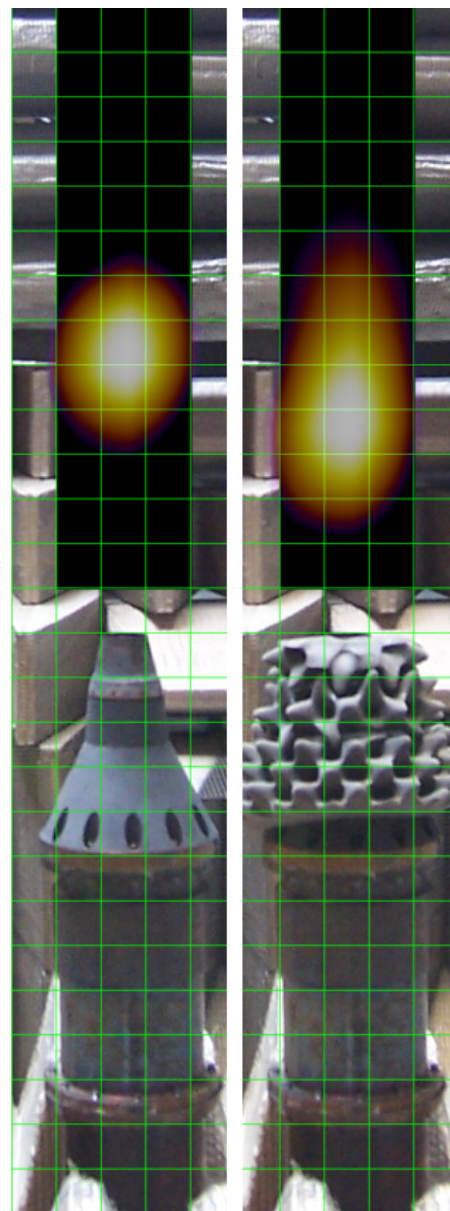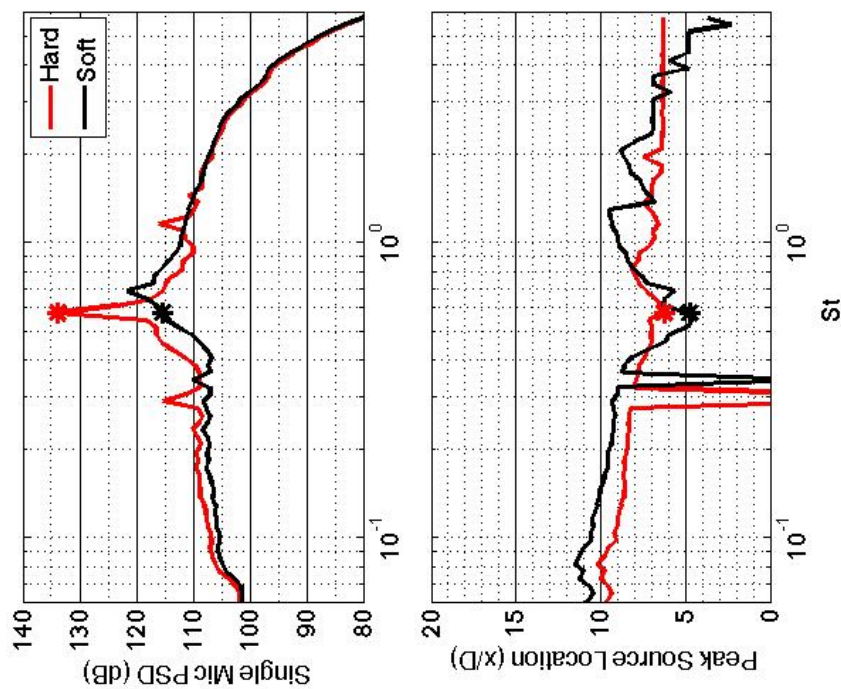
Figure 280.—SMC000; under-expanded; set point 9010; Mj=1.40; St=0.579.
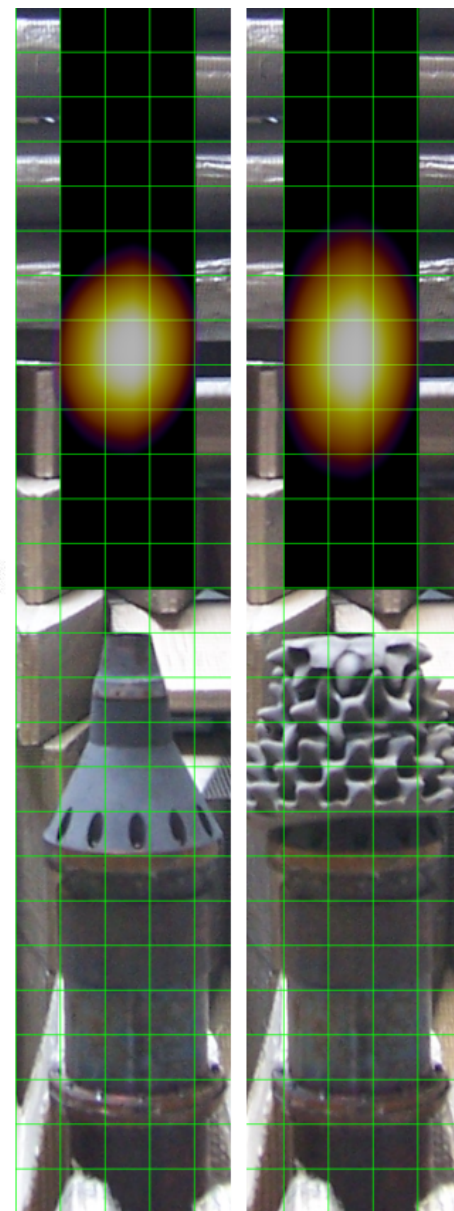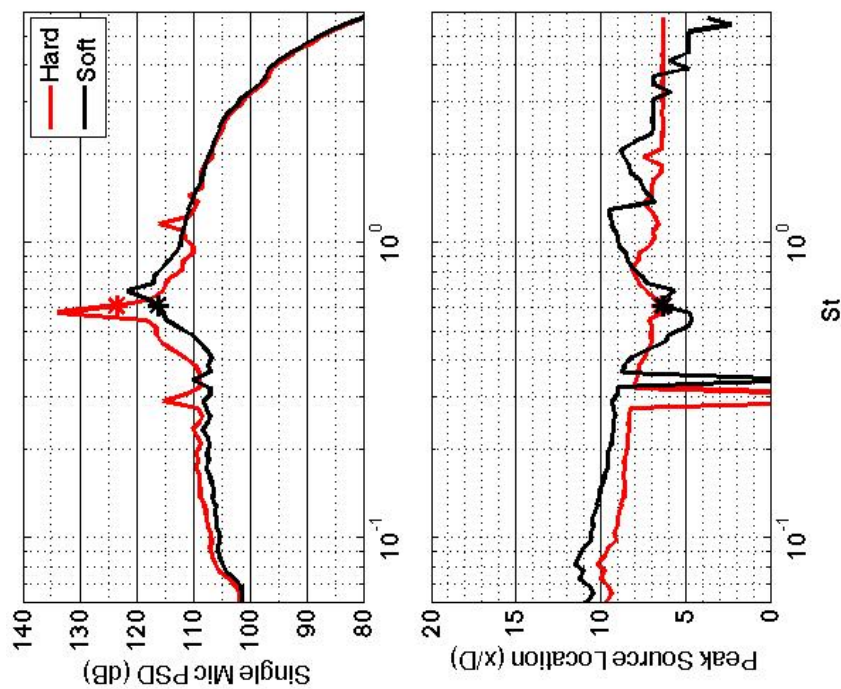
Figure 281.—SMC000; under-expanded; set point 9010; Mj=1.40; St=0.612.
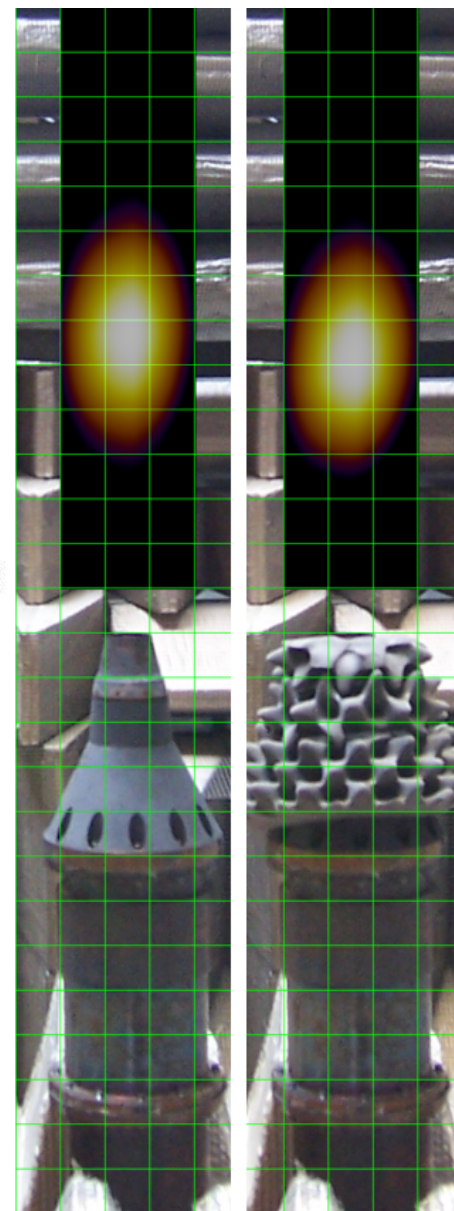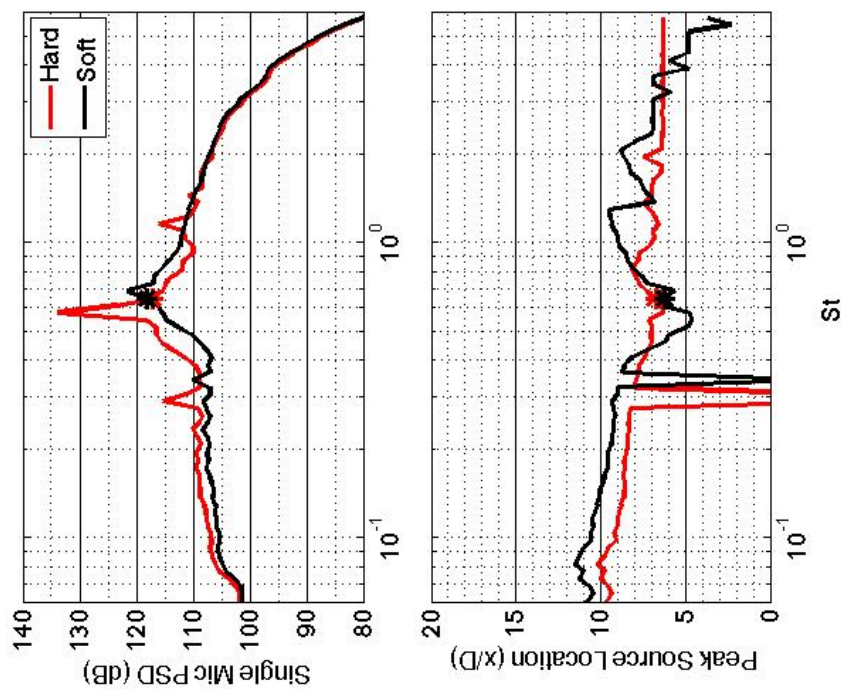
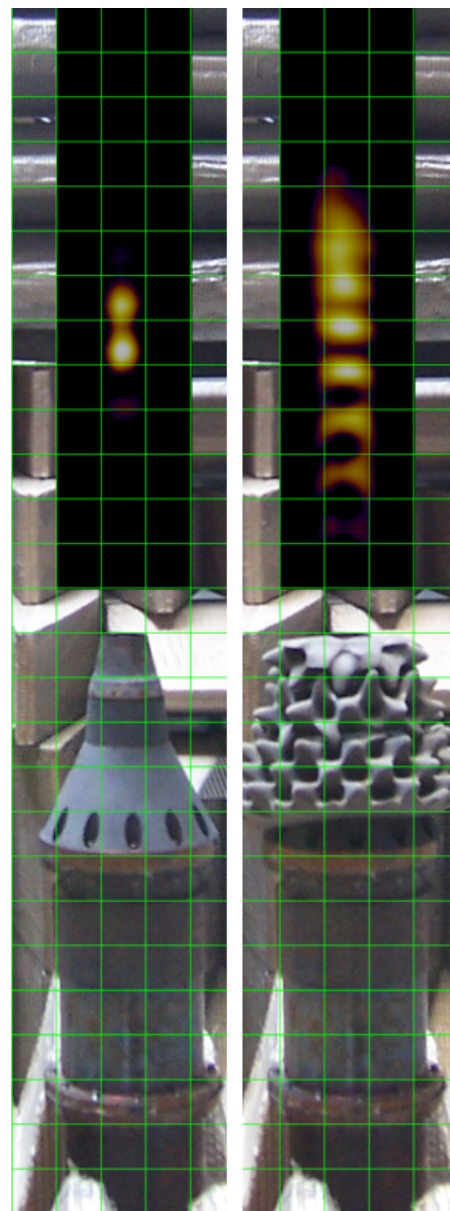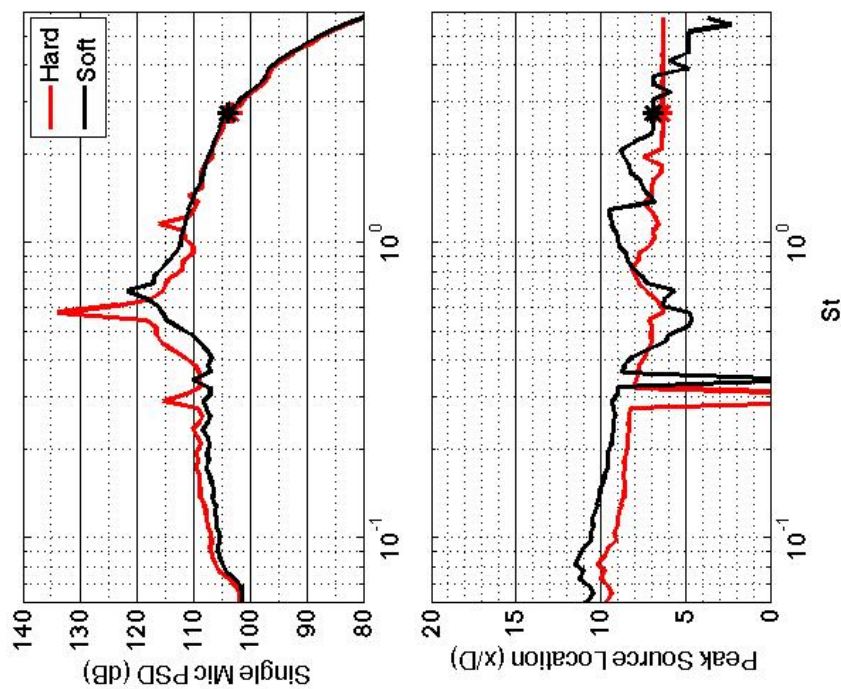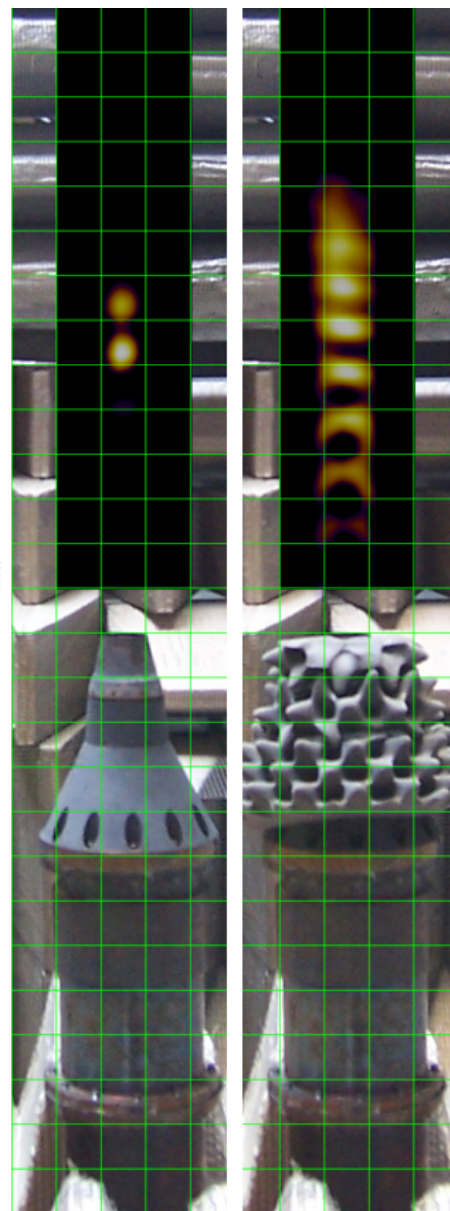Figure 282.—SMC000; under-expanded; set point 9010; Mj=1.40; St=0.648.
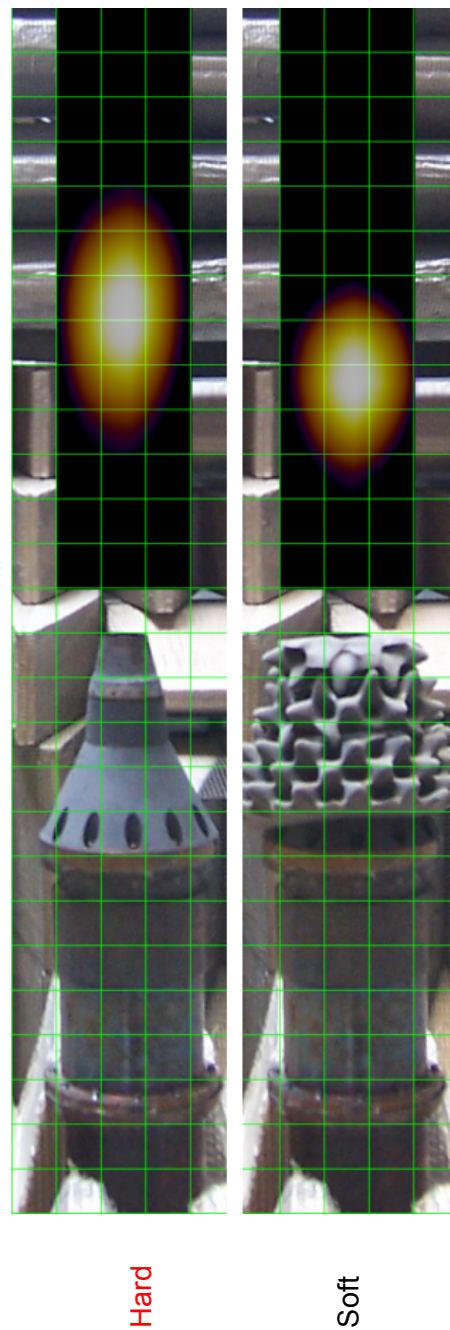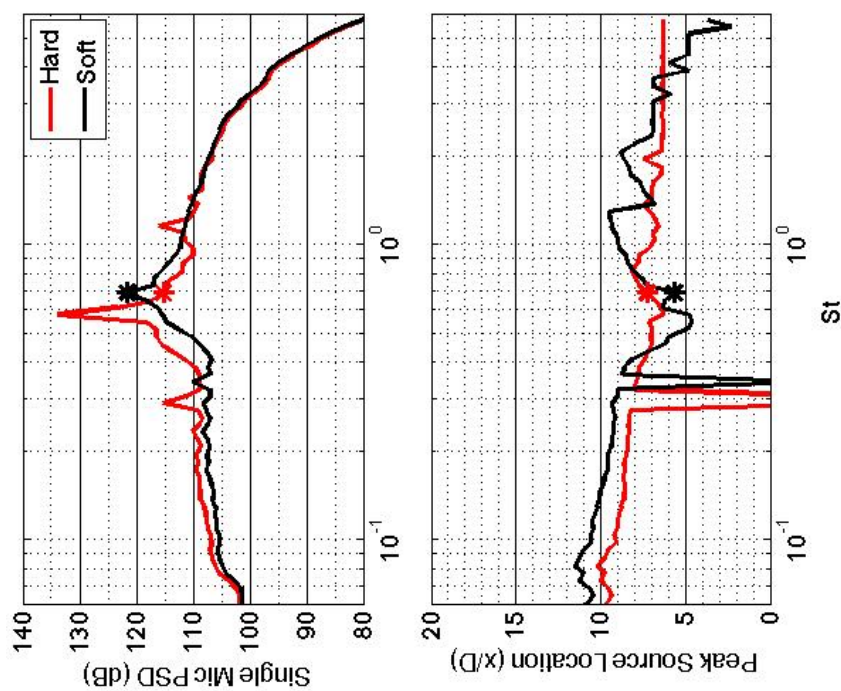
Figure 283.—SMC000; under-expanded; set point 9010; Mj=1.40; St=0.686.
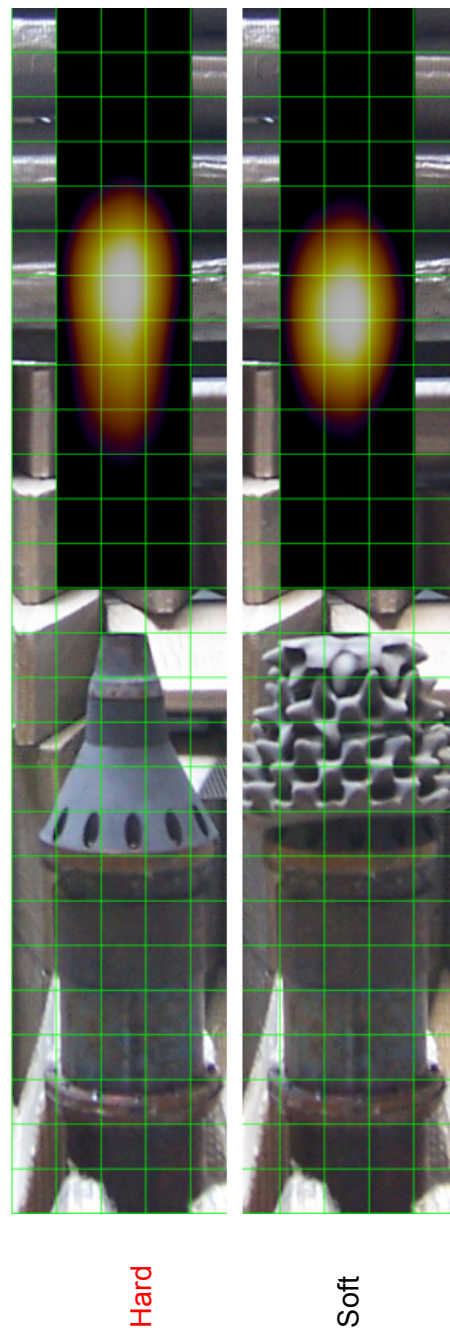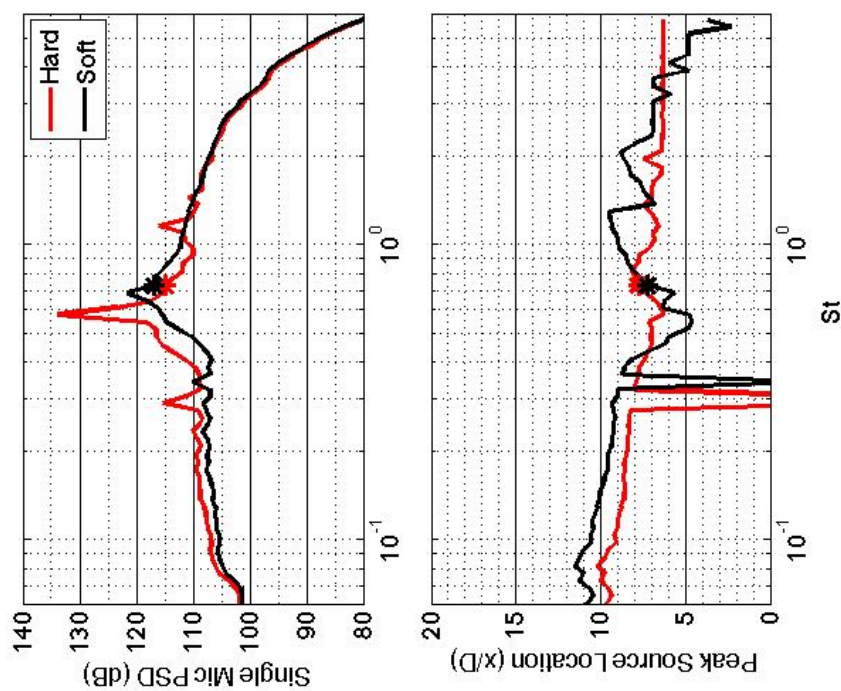
Figure 284.—SMC000; under-expanded; set point 9010; Mj=1.40; St=0.727.
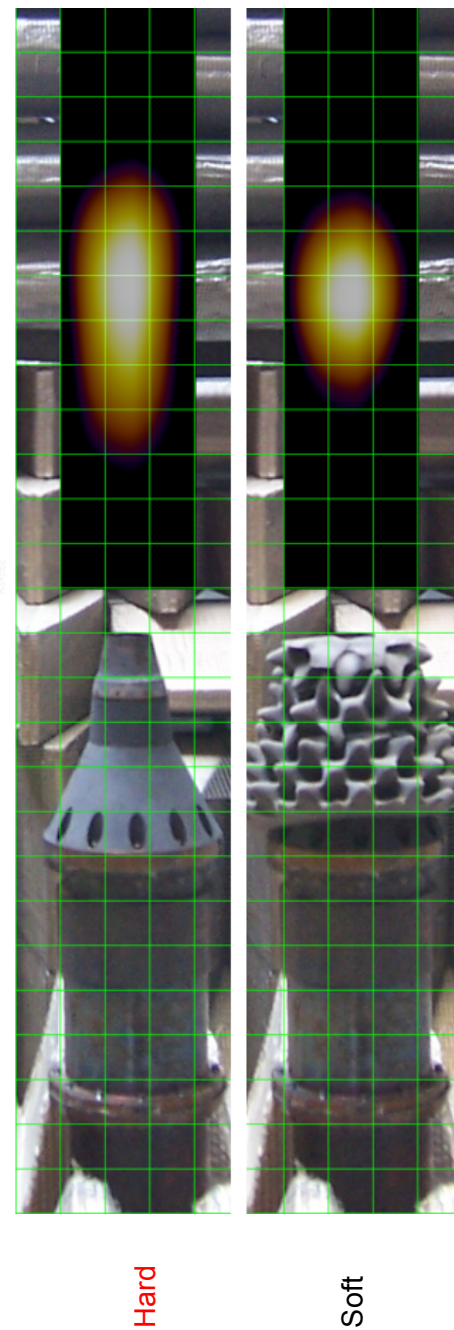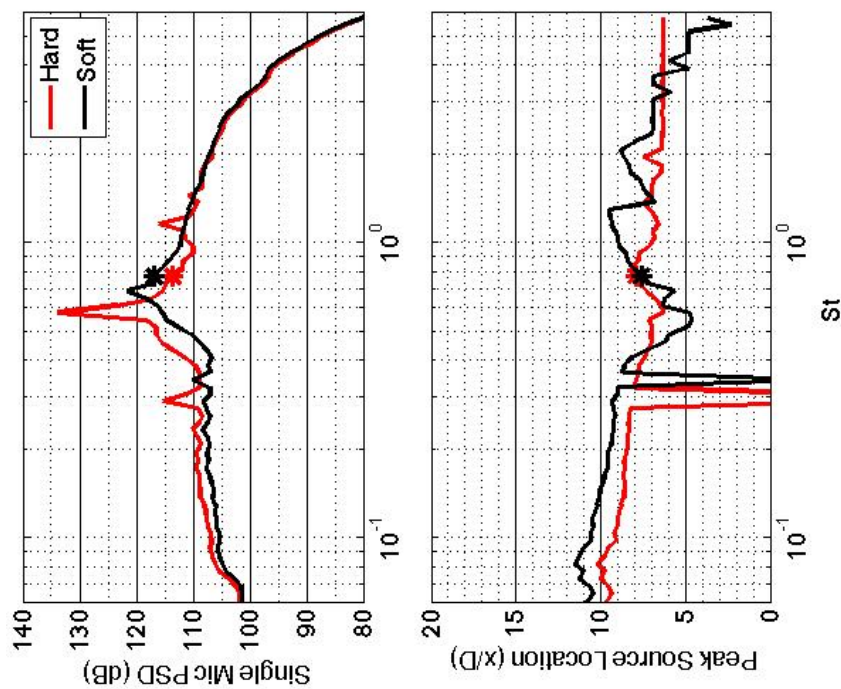
Figure 285.—SMC000; under-expanded; set point 9010; Mj=1.40; St=0.770.

Hard

Soft
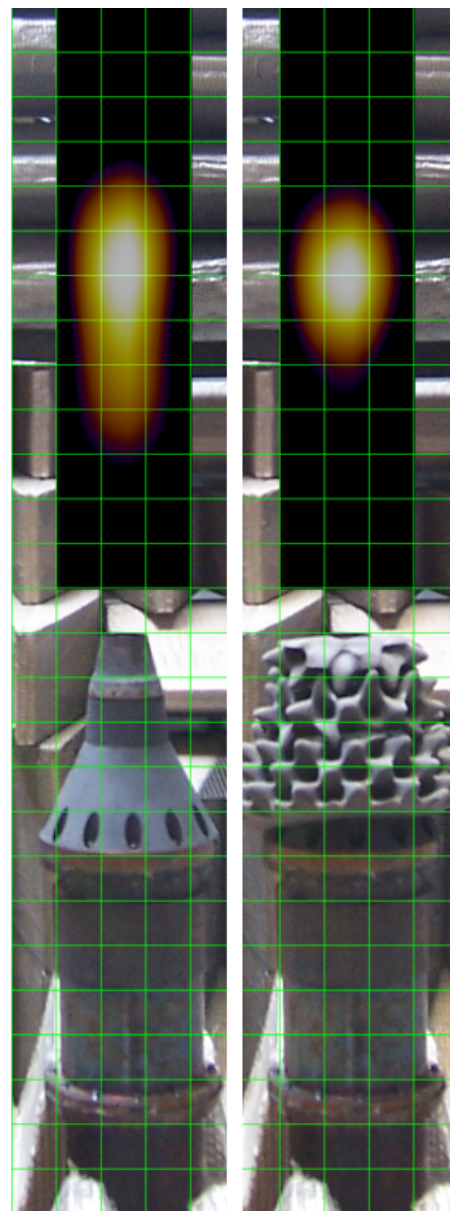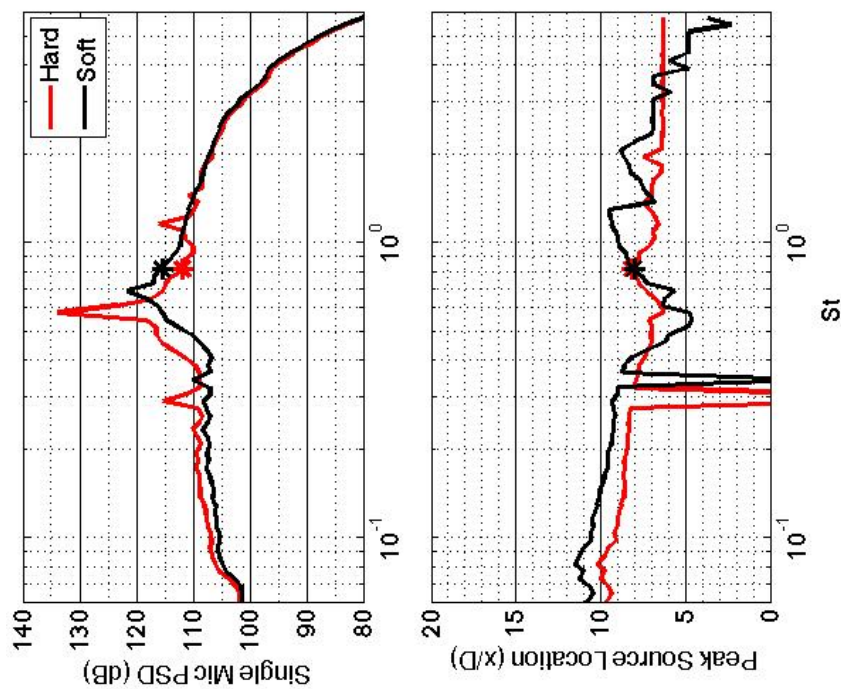
Figure 286.—SMC000; under-expanded; set point 9010; Mj=1.40; St=0.816.
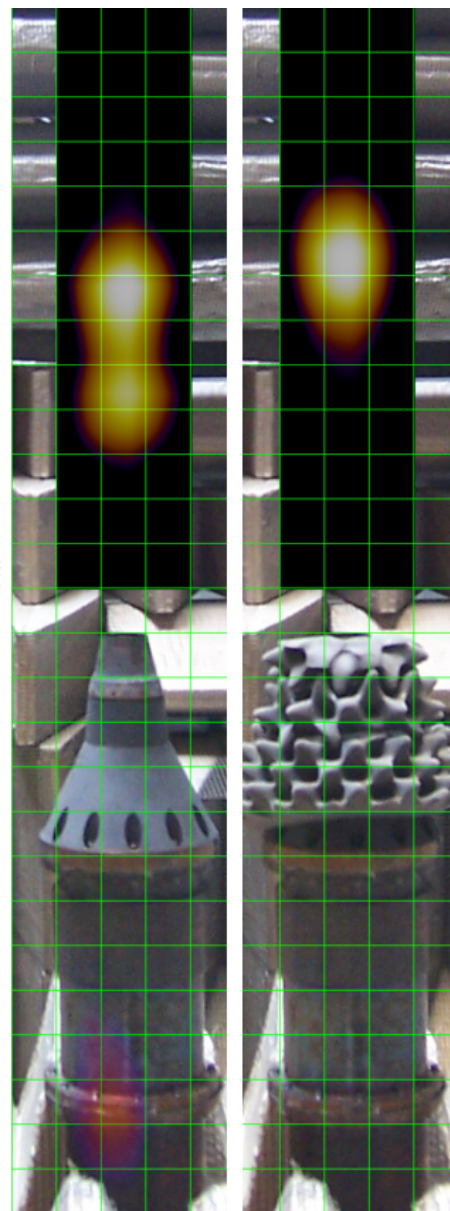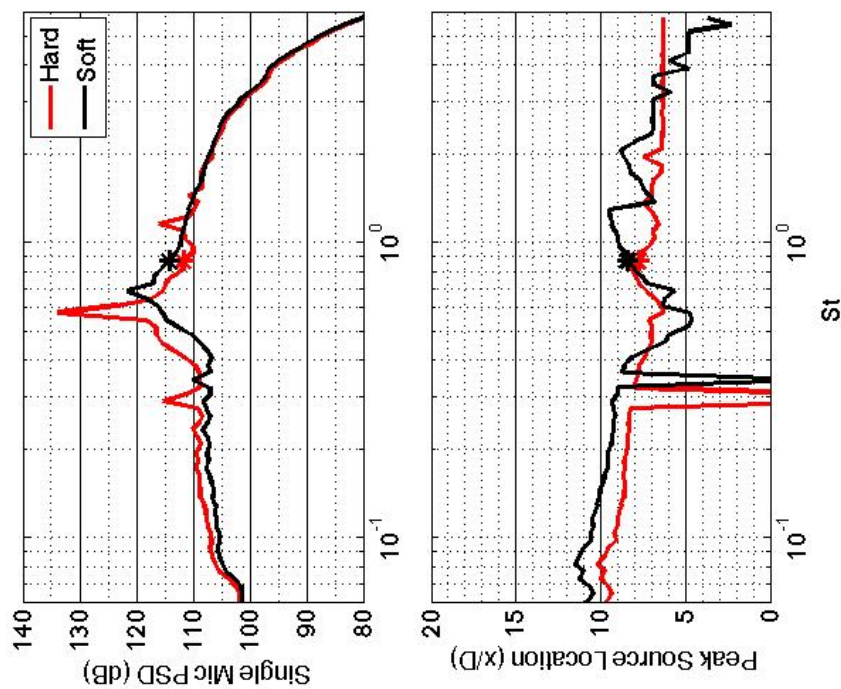
Figure 287.—SMC000; under-expanded; set point 9010; Mj=1.40; St=0.866.
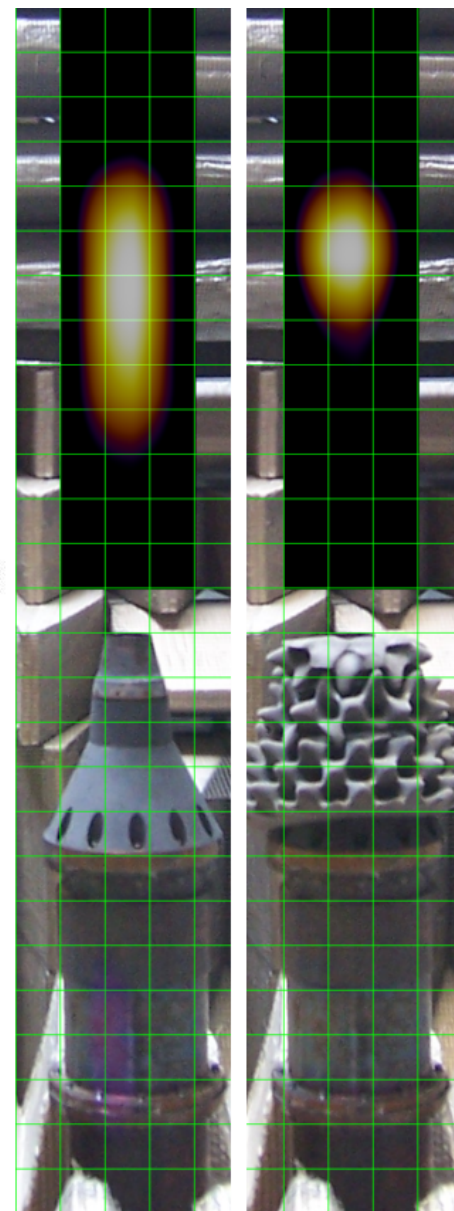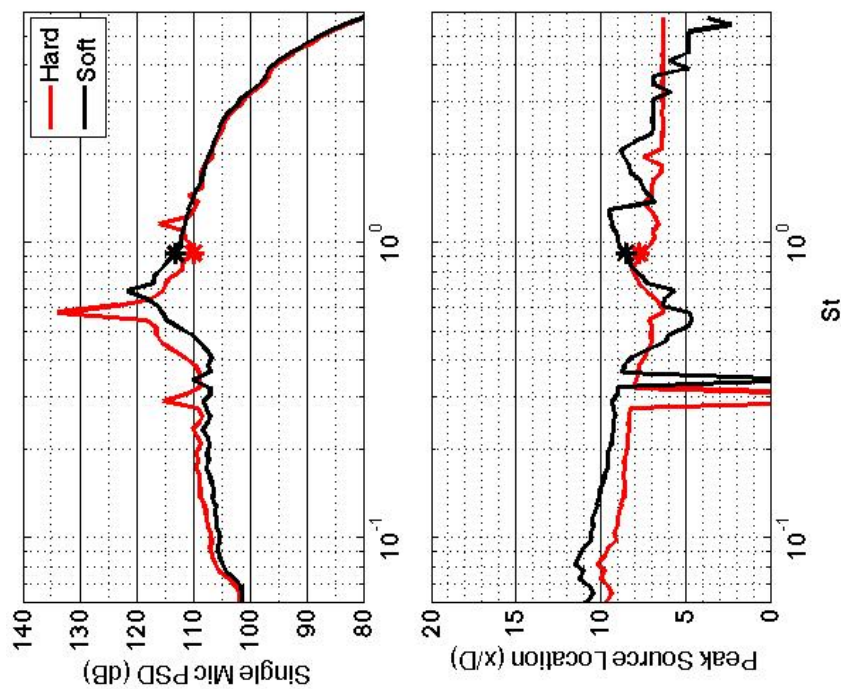
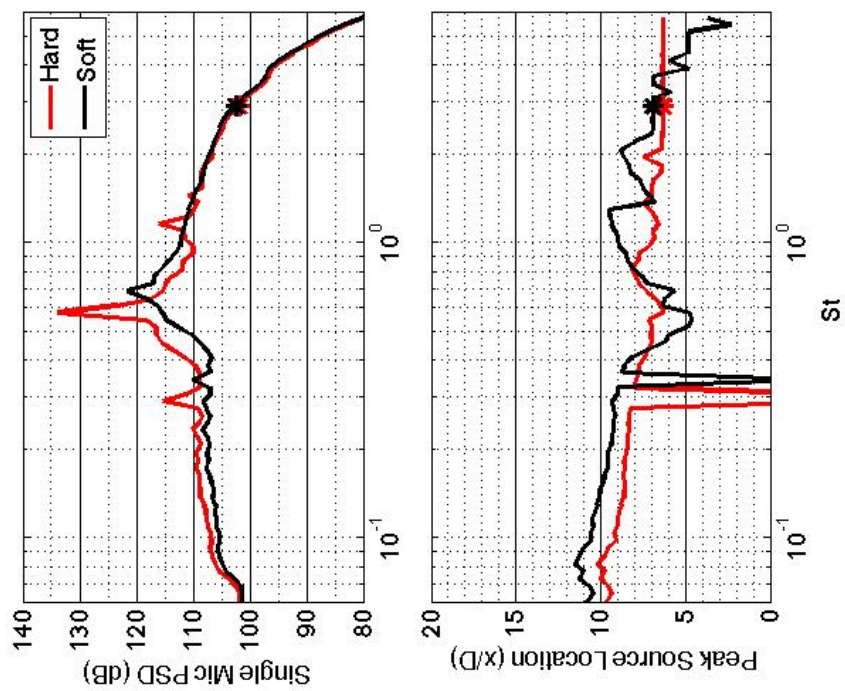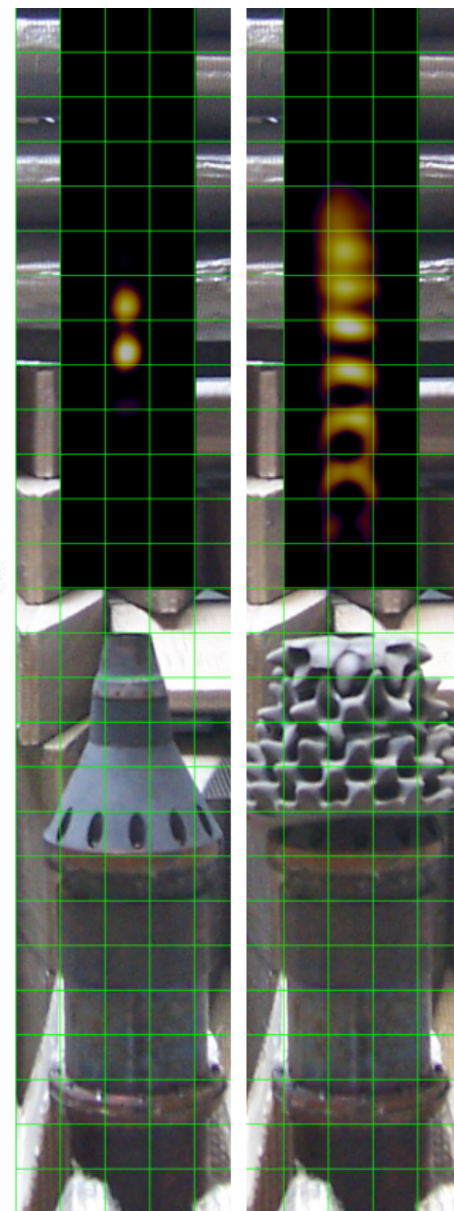Figure 288.—SMC000; under-expanded; set point 9010; Mj=1.40; St=0.919.
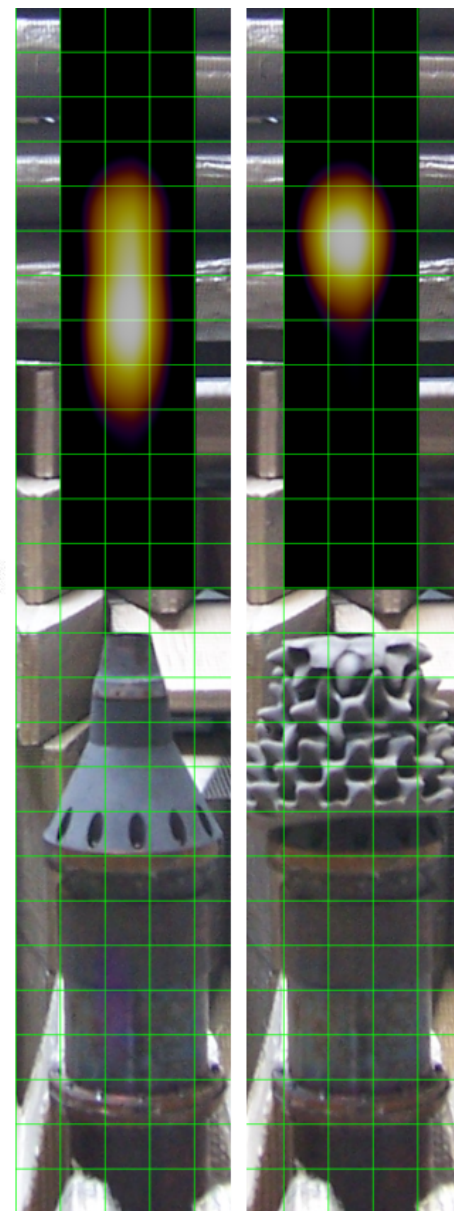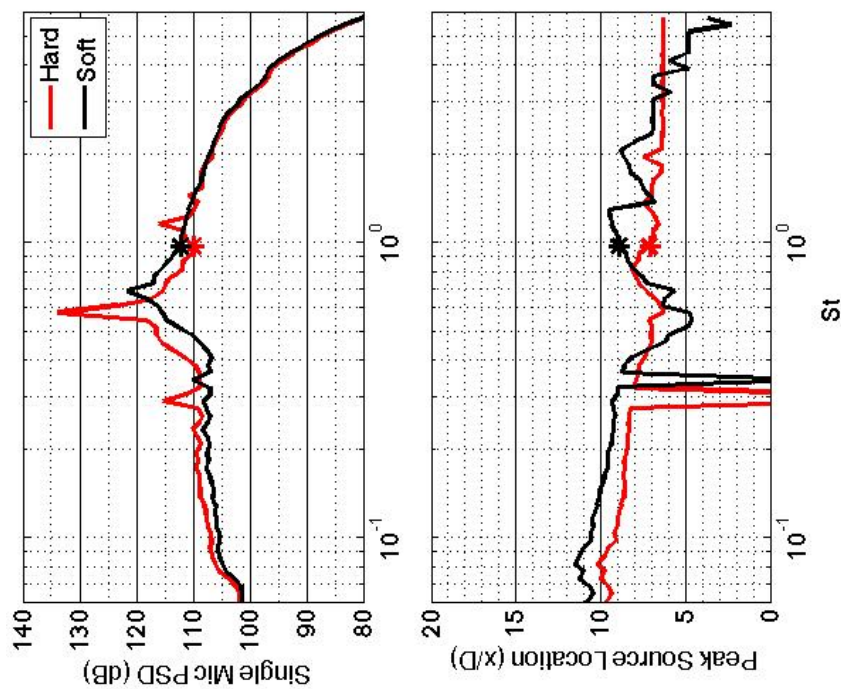
Figure 289.—SMC000; under-expanded; set point 9010; Mj=1.40; St=0.976.
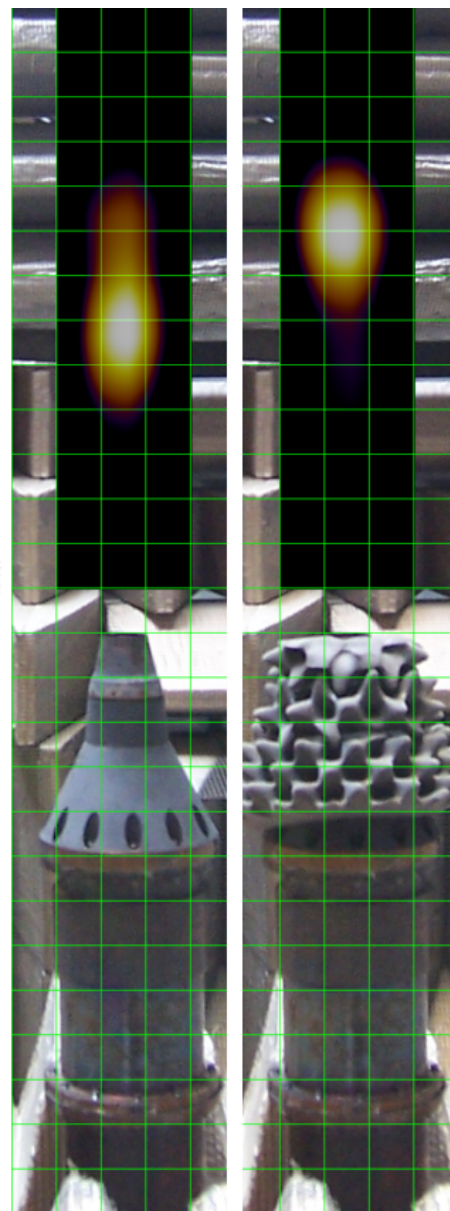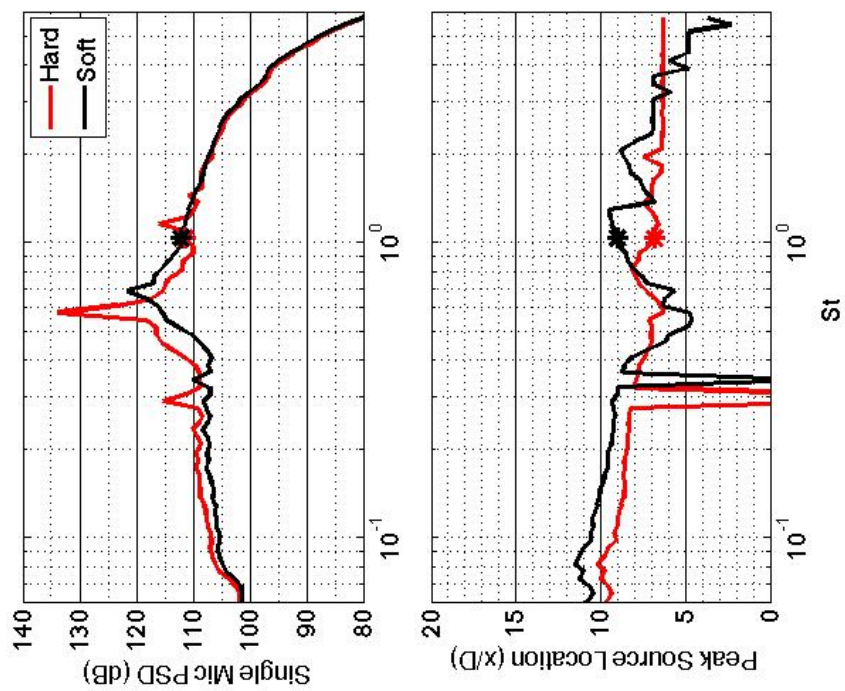
Figure 290.—SMC000; under-expanded; set point 9010; Mj=1.40; St=1.035.
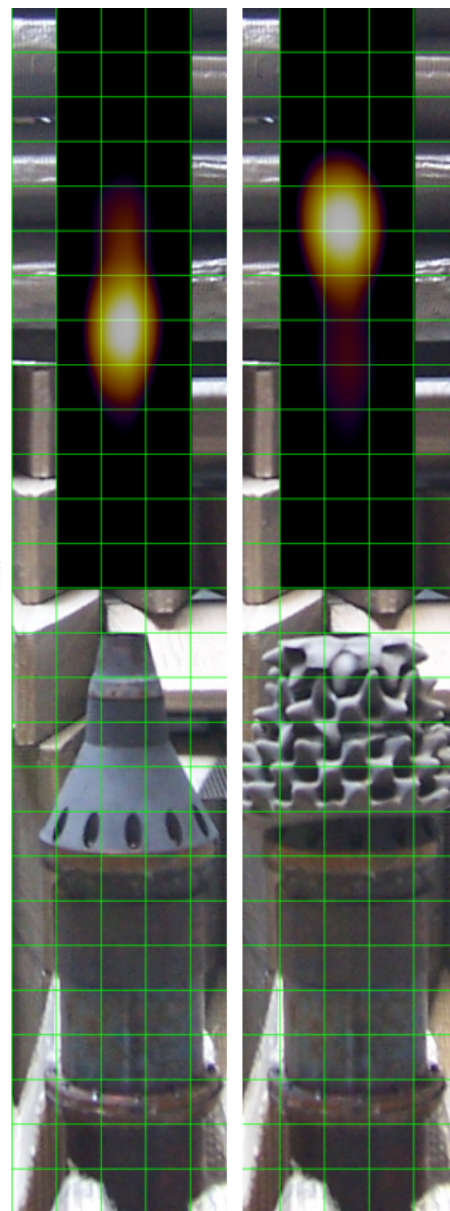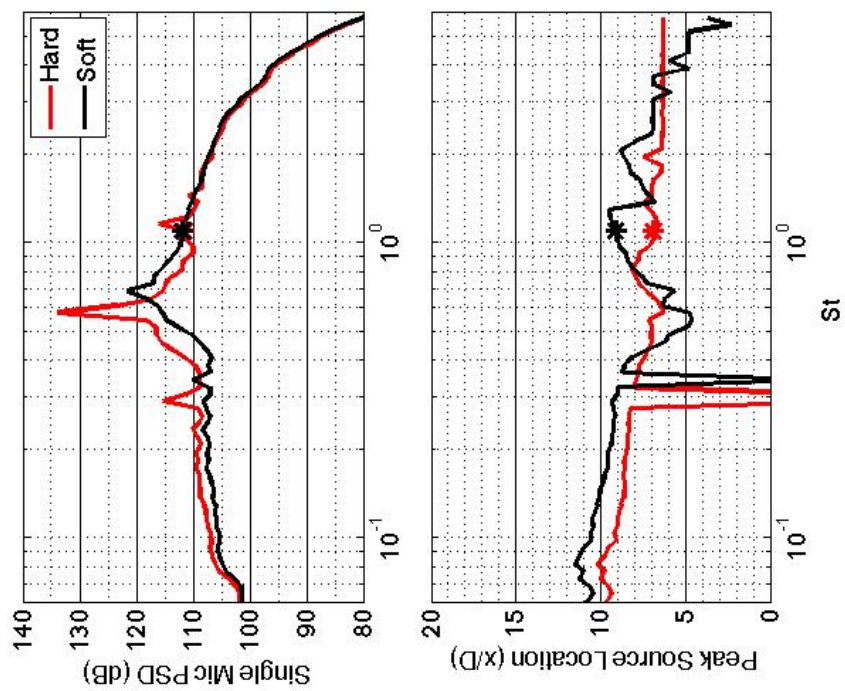
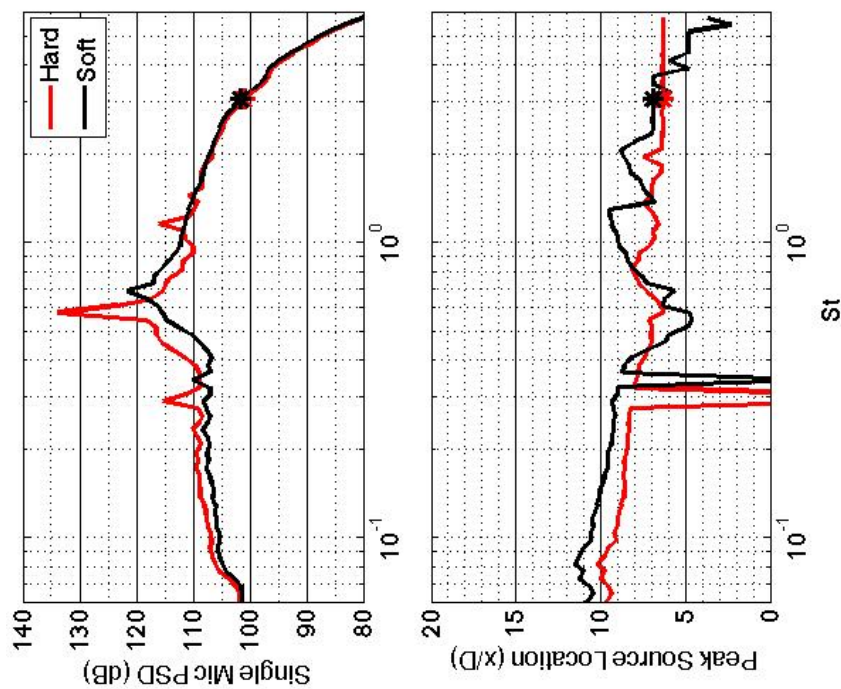Figure 291.—SMC000; under-expanded; set point 9010; Mj=1.40; St=1.095.

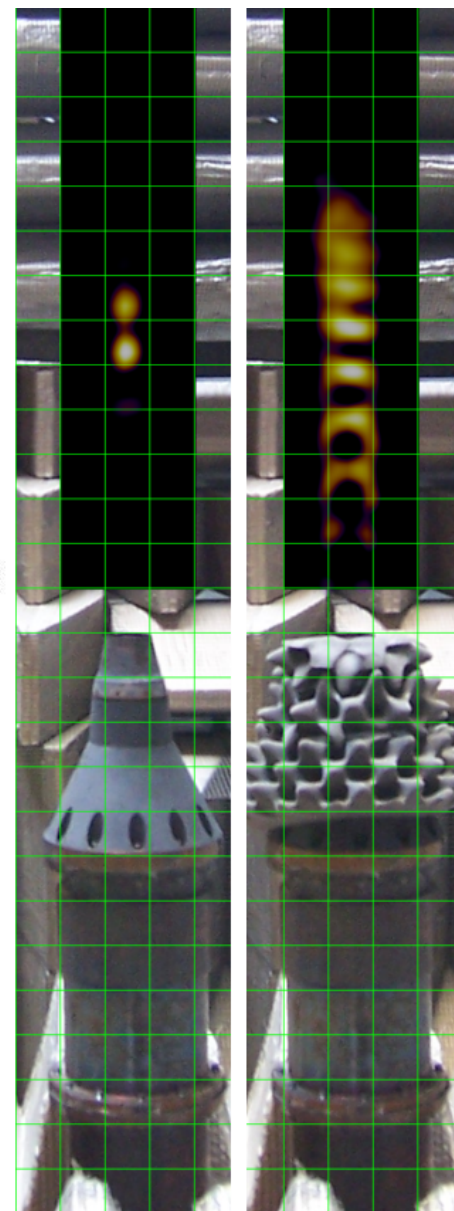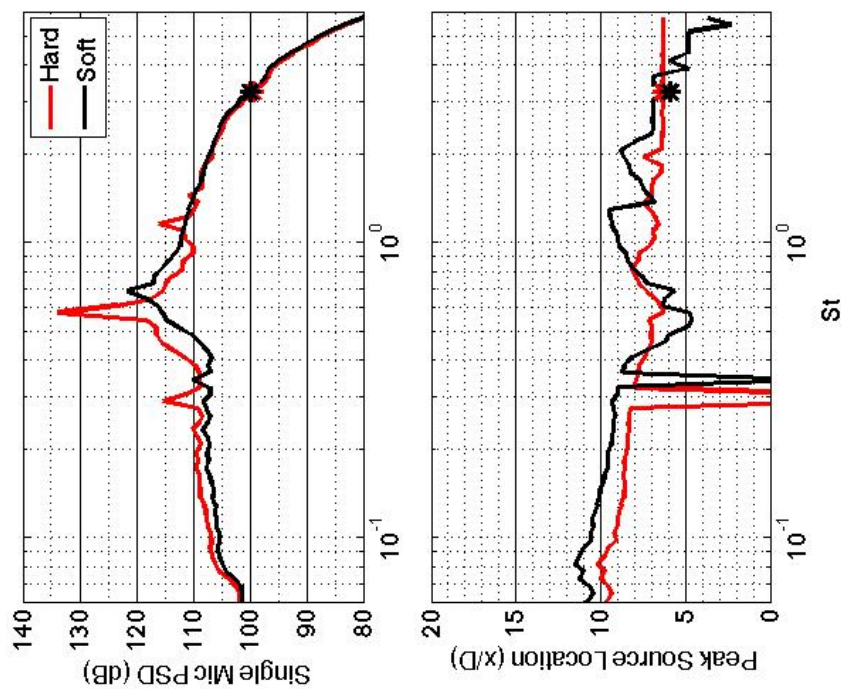Figure 292.—SMC000; under-expanded; set point 9010; Mj=1.40; St=1.158.

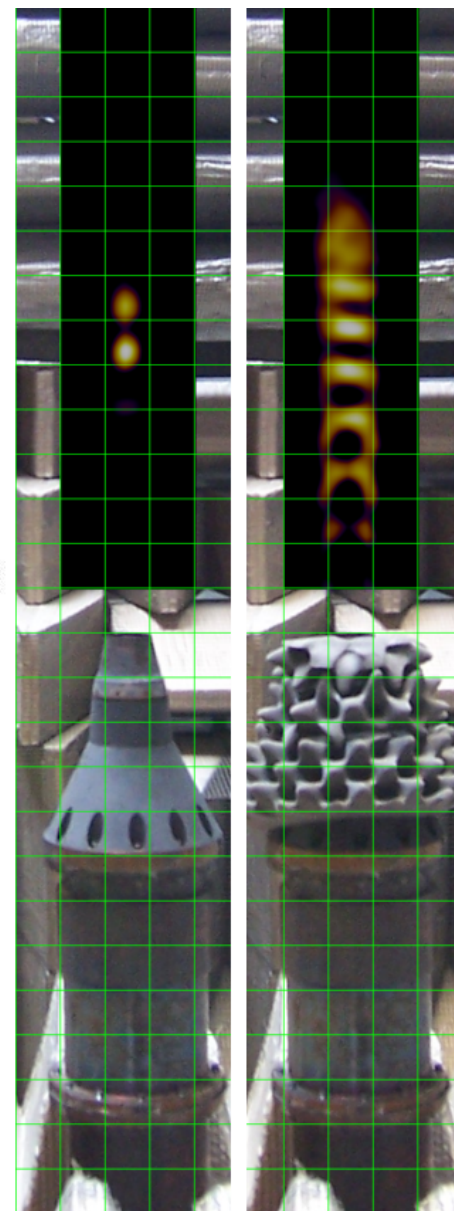Figure 293.—SMC000; under-expanded; set point 9010; Mj=1.40; St=1.225.

Figure 294.—SMC000; under-expanded; set point 9010; Mj=1.40; St=1.295.

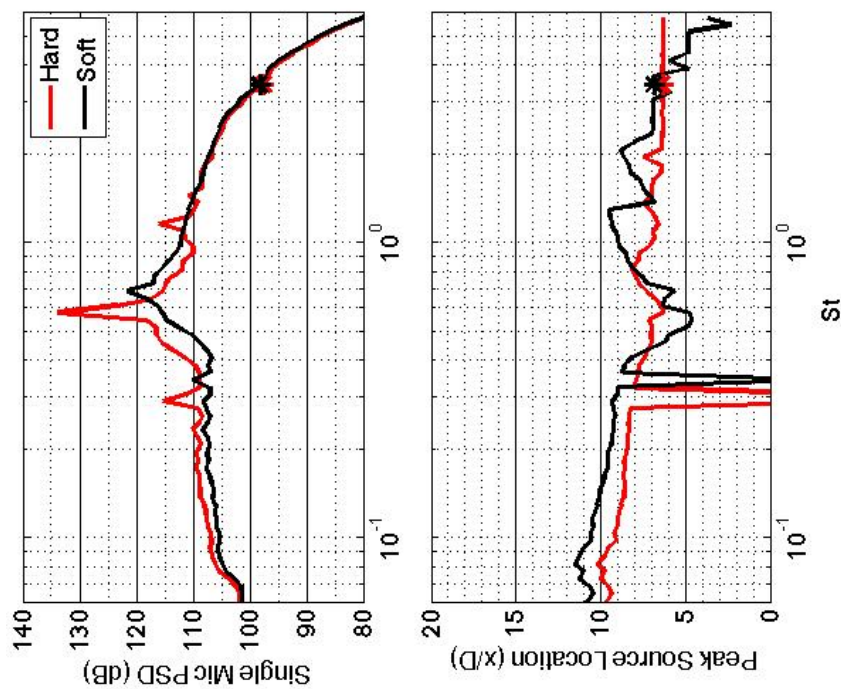Figure 295.—SMC000; under-expanded; set point 9010; Mj=1.40; St=1.369.

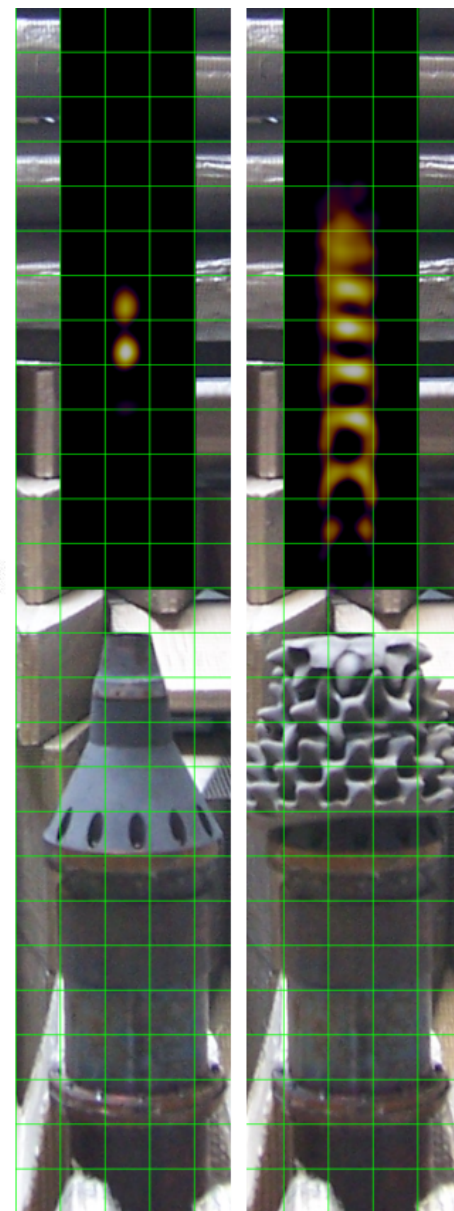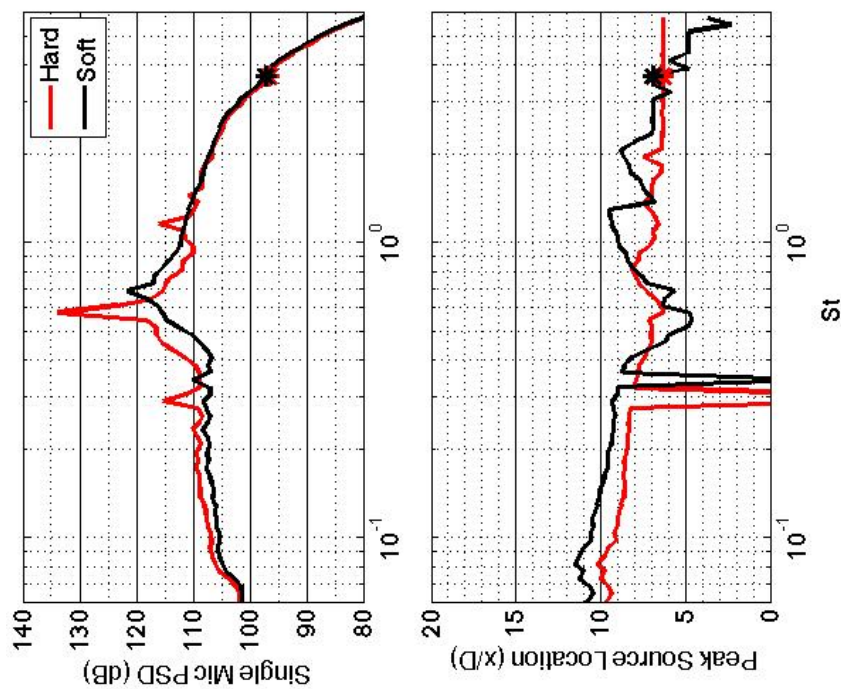Figure 296.—SMC000; under-expanded; set point 9010; Mj=1.40; St=1.448.

Figure 297.—SMC000; under-expanded; set point 9010; Mj=1.40; St=1.531.

Figure 298.—SMC000; under-expanded; set point 9010; Mj=1.40; St=1.621.

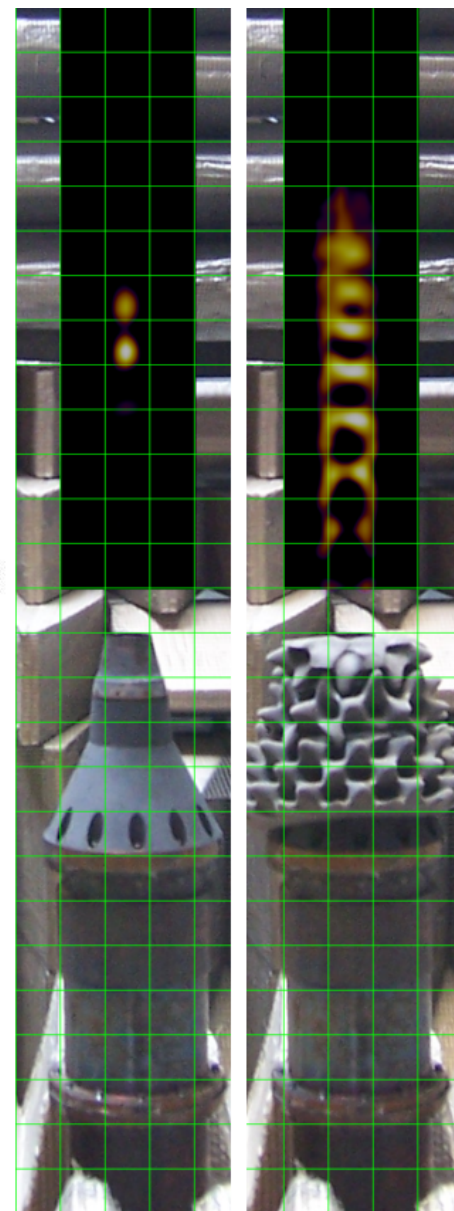Figure 299.—SMC000; under-expanded; set point 9010; Mj=1.40; St=1.722.

Figure 300.—SMC000; under-expanded; set point 9010; Mj=1.40; St=1.831.
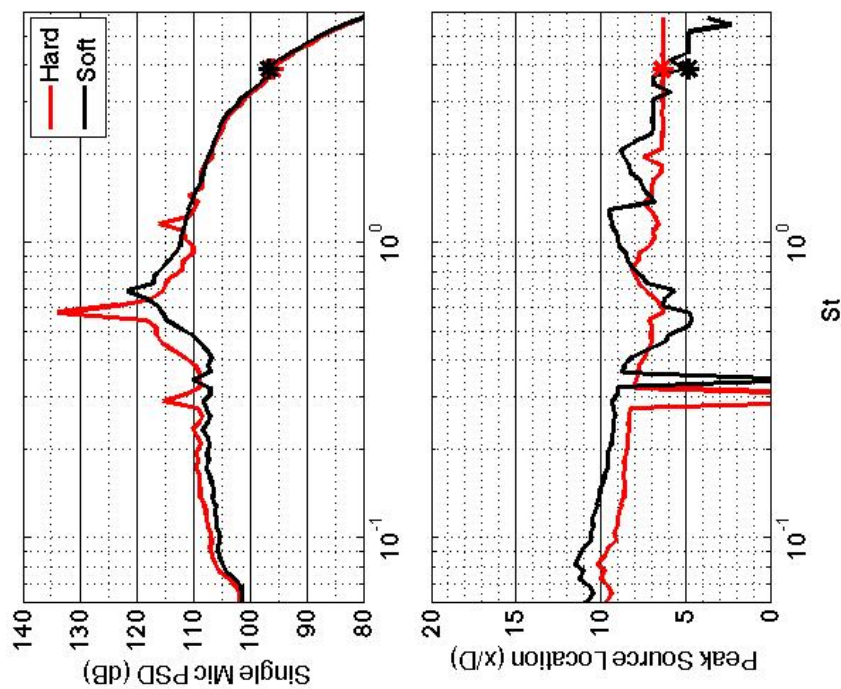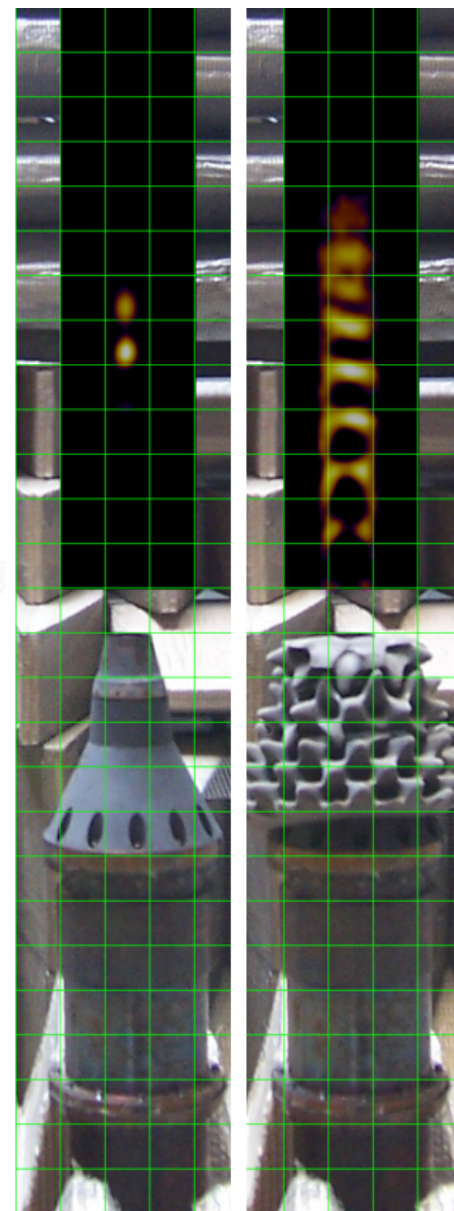
Figure 301.—SMC000; under-expanded; set point 9010; Mj=1.40; St=1.948.

Figure 302.—SMC000; under-expanded; set point 9010; Mj=1.40; St=2.069.

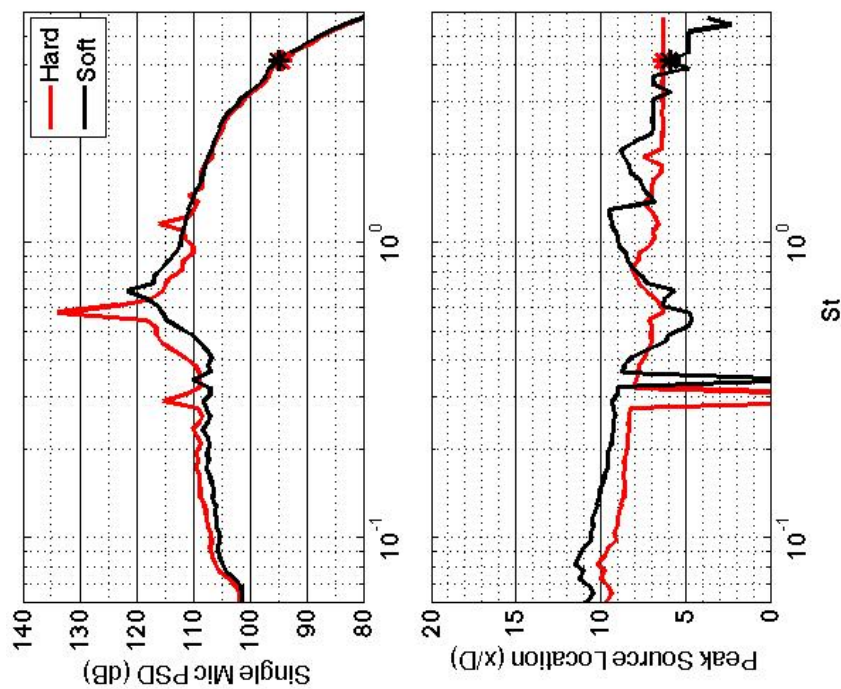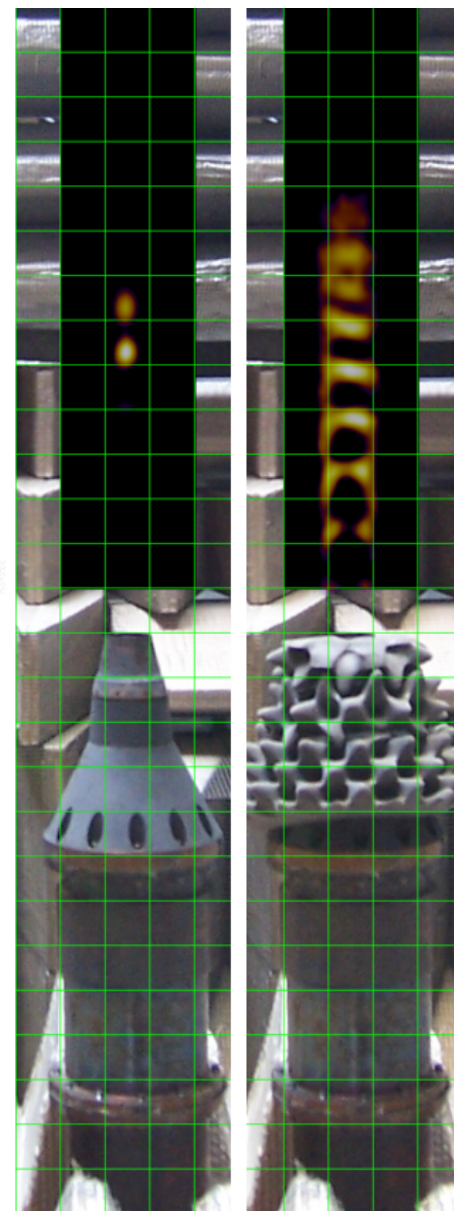Figure 303.—SMC000; under-expanded; set point 9010; Mj=1.40; St=2.191.

Hard

Soft
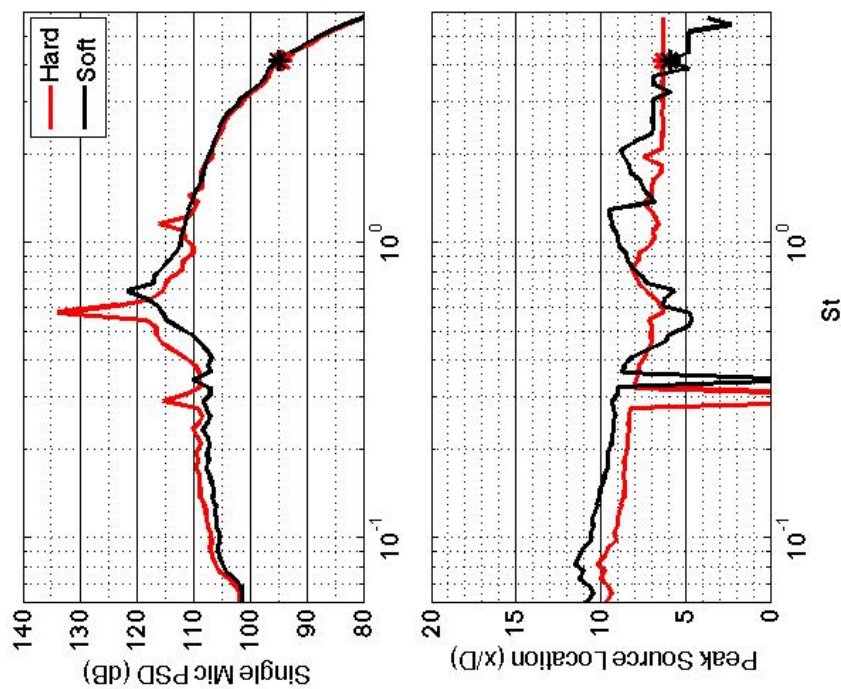
Figure 304.—SMC000; under-expanded; set point 9010; Mj=1.40; St=2.316.

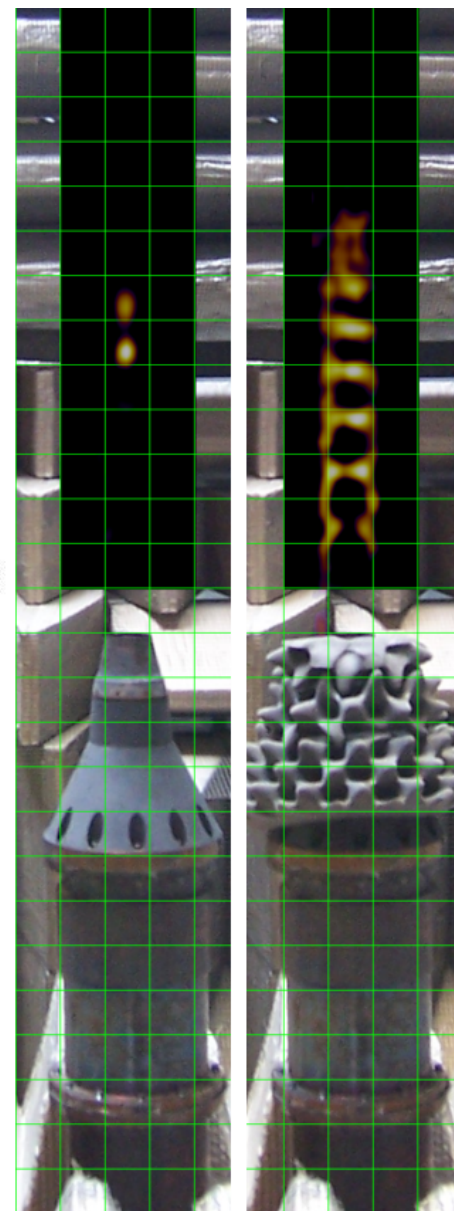Figure 305.—SMC000; under-expanded; set point 9010; Mj=1.40; St=2.449.
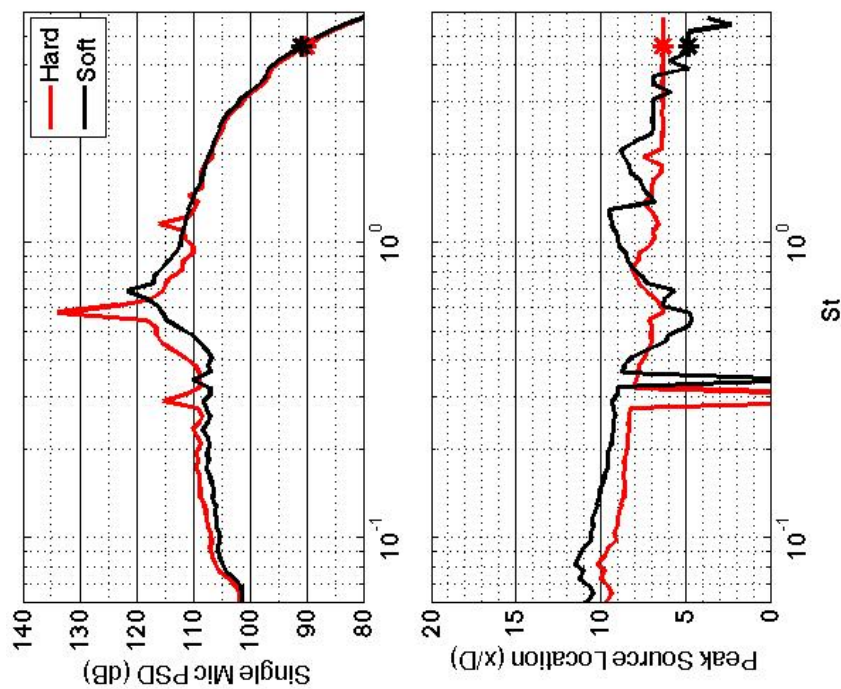
Figure 306.—SMC000; under-expanded; set point 9010; Mj=1.40; St=2.590.

Figure 307.—SMC000; under-expanded; set point 9010; Mj=1.40; St=2.738.

Figure 308.—SMC000; under-expanded; set point 9010; Mj=1.40; St=2.895.

Figure 309.—SMC000; under-expanded; set point 9010; Mj=1.40; St=3.061.

Figure 310.—SMC000; under-expanded; set point 9010; Mj=1.40; St=3.242.

Figure 311.—SMC000; under-expanded; set point 9010; Mj=1.40; St=3.443.

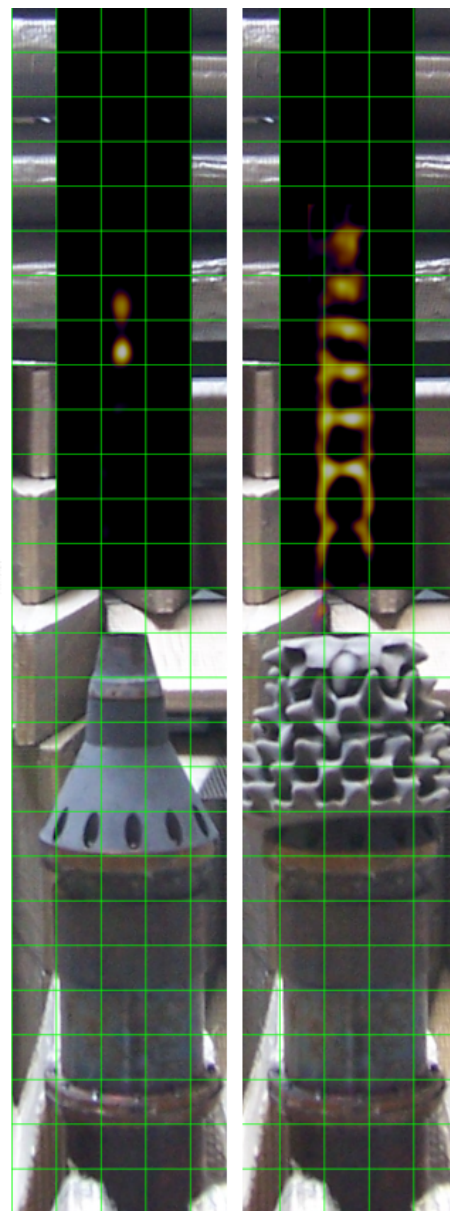Figure 312.—SMC000; under-expanded; set point 9010; Mj=1.40; St=3.663.

Figure 313.—SMC000; under-expanded; set point 9010; Mj=1.40; St=3.896.

Hard

Soft

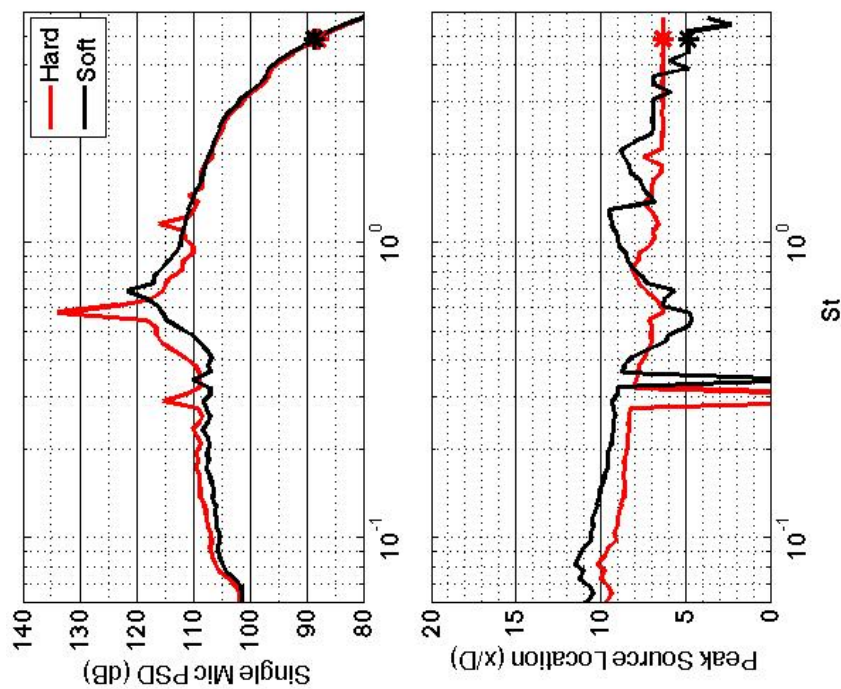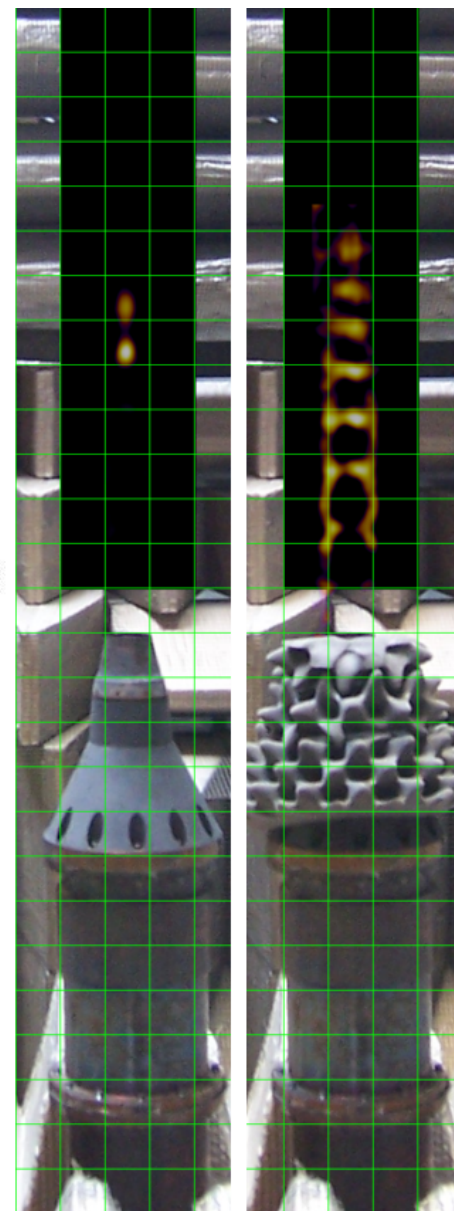Figure 314.—SMC000; under-expanded; set point 9010; Mj=1.40; St=4.138.

Hard

Soft

Figure 315.—SMC000; under-expanded; set point 9010; Mj=1.40; St=4.381.

Figure 316.—SMC000; under-expanded; set point 9010; Mj=1.40; St=4.633.

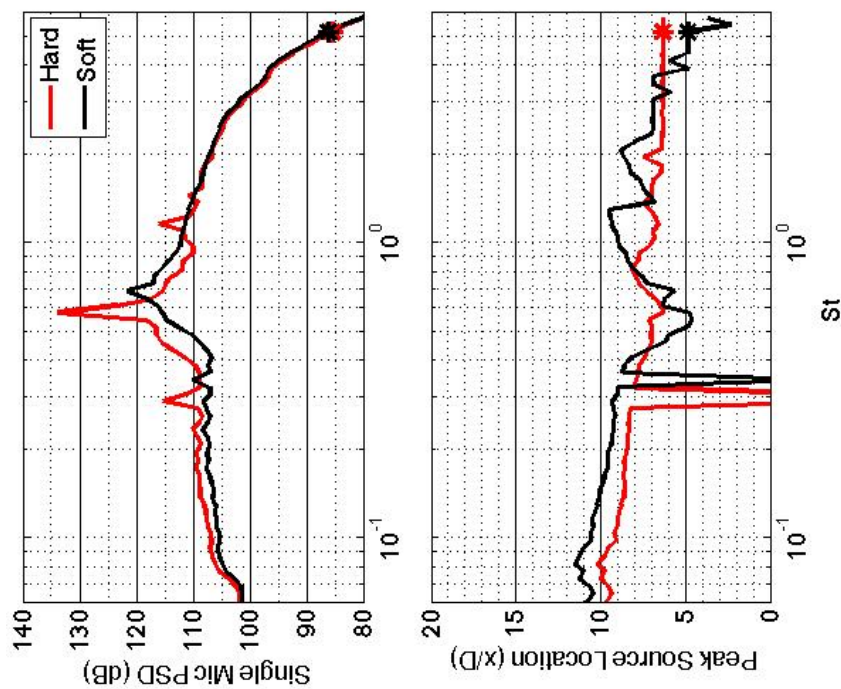Figure 317.—SMC000; under-expanded; set point 9010; Mj=1.40; St=4.898.

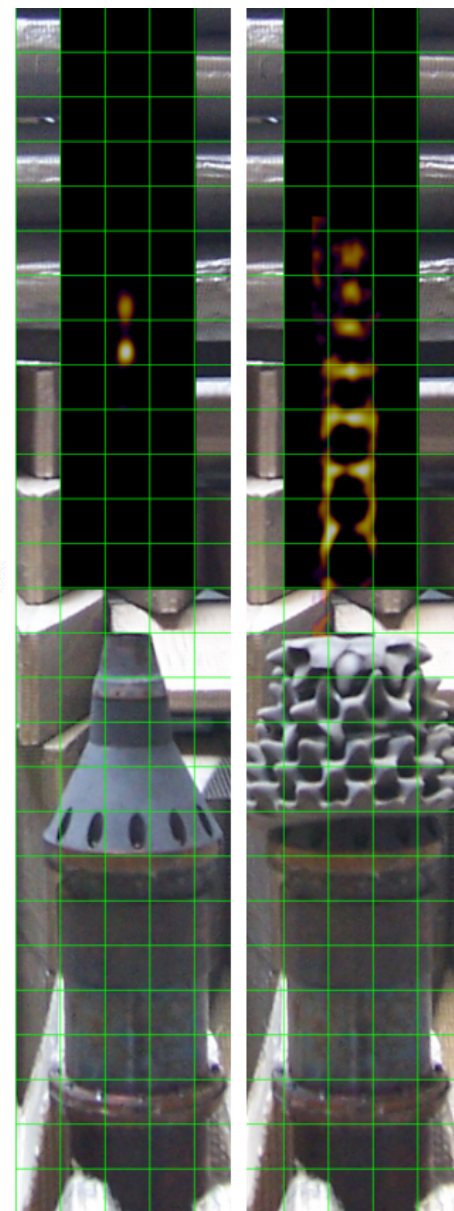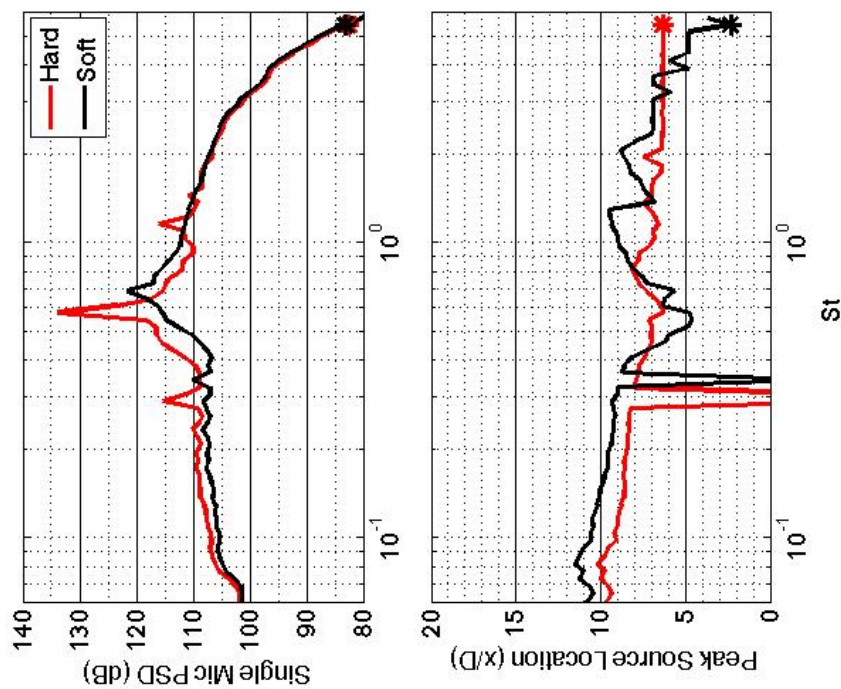Figure 318.—SMC000; under-expanded; set point 9010; Mj=1.40; St=5.179.

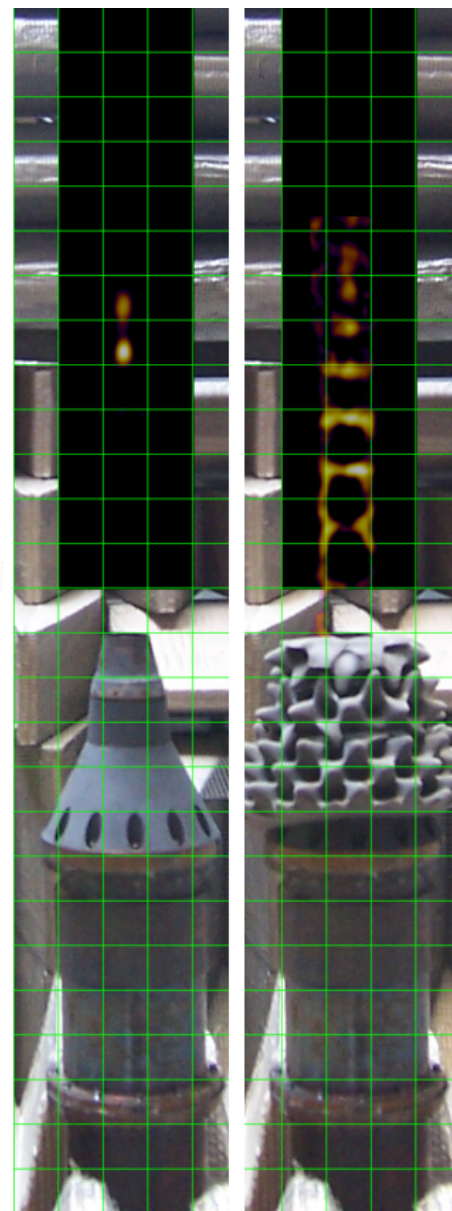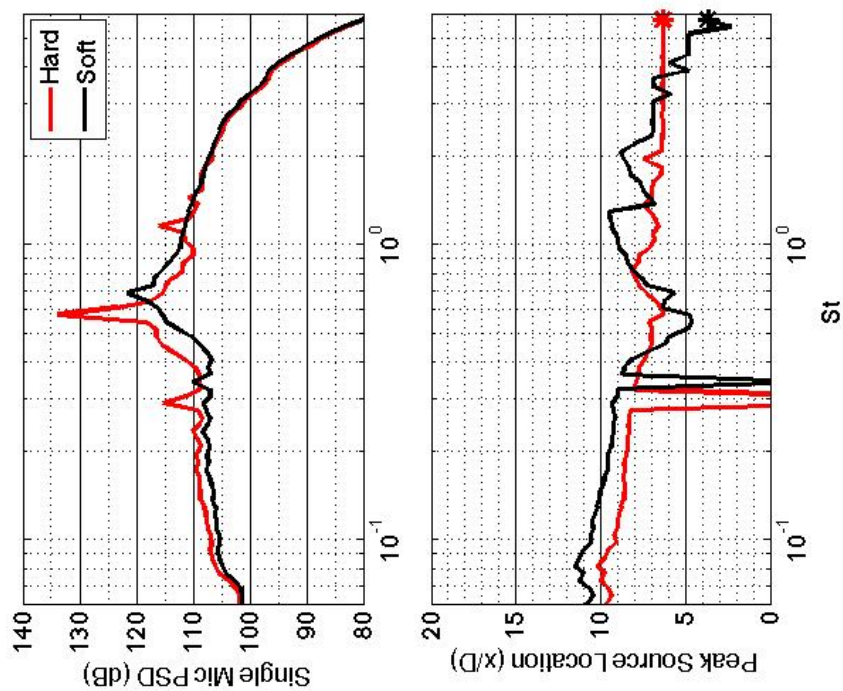Figure 319.—SMC000; under-expanded; set point 9010; Mj=1.40; St=5.476.

Figure 320.—SMC000; under-expanded; set point 9010; Mj=1.40; St=5.791.